The University Of Sheffield.

Dissecting the Links between Morphology and ECM Dynamics in the Developing Zebrafish Heart

Juliana Sánchez-Posada

A thesis submitted in partial fulfilment of the requirement
for the degree of Doctor in Philosophy

The University of Sheffield
Faculty of Science
School of Biosciences

September 2022

ACKNOWLEDGEMENTS

A mis abuelos, Omaira y Jaime,

a quienes extraño y recuerdo con amor.

I packed my bags and left Colombia with a dream, to become a Doctor! And here I am writing the acknowledgements of my thesis after four years of embarking on this adventure. And what an adventure! I am not going to say it was easy. Surely, there were moments of frustration, fatigue, overwhelm, tears, anger, heartbreak, and a lot of homesickness, but also it was full of excitement, joy, friendship, wonder, biscuits and most of all accomplishment! And thankfully, throughout this whole journey, I was not alone. There are so many people I would like to thank for sharing a piece of this adventure with me, so here I go.

Emily, *the SuperVisionary!* Thanks for taking the risk of taking an engineer living on the other side of the world as one of your students. You are the best supervisor I could have asked for. Your constant guidance, support and encouragement throughout these years have made me become a better scientist, researcher, and person and for that, I am deeply grateful. Thanks for all the endless meetings we had discussing exciting science. I am sure we always came out of them with more questions and experiments to do. Your passion and excitement for the research we do are truly contagious, and it was, in part, what kept me going all along. This journey would not have been the same without you! Thanks!

¡Mamá, Papá y Cata, la mejor familia! Gracias por apoyarme en todos y cada uno de los momentos de este proceso. Tenerlos lejos todo este tiempo, definitivamente no fue fácil, pero su apoyo y amor, así fuera en mensajes, llamadas, notas de voz, y en las cortas visitas a Colombia, fueron incondicionales y constantemente me mantuvieron en pie. Gracias por creer en mi y apoyarme siempre.

Pallollito. Este proceso no hubiera sido el mismo sin tu compañía. Gracias por cruzar el océano para acompañarme y poder compartir este proceso juntos. Gracias por ser mi patito de hule mientras que desarrollaba *morphoHeart* y descifraba mis datos. Infinitas gracias por alimentarme, y sobre todo consentirme y abrazarme en todos los momentos en que de verdad lo necesitaba. ¡Tus locuras constantes me hacen sonreír! Me siento muy afortunada de tenerte a mi lado.

The Noël lab: Chris, Eric, Emma, and Philippa. There is no better lab I could have landed on. The best science family, with the most amazing, friendly and biscuit-filling lab meetings. It was the best place to grow as a scientist. Thanks for all your support, friendship, and feedback throughout these years. You all owe me a carrousel/horse tornado ride!

Ana. I am so happy I met you in the first months of my PhD. You, Phil and later Sofia became the closest thing to a family for us in the UK and I am ever so grateful for that! Looking forward to a long and wonderful friendship.

Tata, *la cuñada más consentidora.* Gracias por siempre estar pendiente de mi desde el día cero que llegué a UK. Gracias por siempre ser tan especial y buscar la forma de subirme el ánimo con paquetes de amor con sabor a Colombia.

Paulis. La primera doctora de la familia y la que siempre estuvo pendiente de mi bienestar, sabiendo todo lo que significaba hacer un doctorado. Gracias por siempre estar ahí, con una sonrisa dispuesta a escucharme, apoyarme y darme consejos. ¡Por muchas más aventuras como las primas doctoras!

La raza, la familia Europea. Viajar a verlos siempre fue una recarga de energía. ¡Por muchos más años de amistad, fiestas y aventuras juntos!

Katie, Keivan, Dan, Ruth, Hubashia, Piece, James V and James M. I am really grateful to have had the opportunity of sharing this PhD experience with you. You have all become friends for life. Looking forward to future gatherings and adventures together.

Finally, I would like to thank Martin Zeidler and Tanya Whitfield, my PhD advisors, for their valuable input into this work and the aquarium team for taking care of my fish and keeping them healthy and happy during these four years.

THESIS SUMMARY

During development, the heart tube comprises two cellular layers, an outer-myocardium and an inner-endocardium, between which lies a layer of extracellular matrix (ECM). This cardiac ECM creates specialised extracellular environments that mediate the chemical and biomechanical signals that shape the heart tube into a three-dimensional (3D) organ. Visualising and linking ECM and tissue morphology is challenging since sample processing may impact matrix hydration and tissue structure.

To understand the spatiotemporal dynamics of the ECM and its role in cardiac morphogenesis, I developed *morphoHeart,* an image analysis tool that allows the 3D segmentation of the heart layers -including the ECM- from *live* embryos. Using *morphoHeart*, I was able to provide the first 3D morphological characterisation of all three layers of the zebrafish developing heart -the myocardium, endocardium and cardiac ECM- at pre-, during- and post-looping stages. Quantification of heart size revealed that wild-type hearts increase in size as they transition from a linear tube to a looped organ, and the atrium compacts down once cardiac looping is completed. Analysis of cardiac jelly distribution confirmed that the atrial-specific left-sided ECM expansion we had previously described at tube stage (26hpf) is maintained as the heart undergoes looping and ballooning morphogenesis.

To understand if defects in heart tube lateralisation result in abnormal ECM-regionalisation and disrupted morphogenesis, I investigated zebrafish hearts in which *spaw* (zebrafish homolog of *Nodal* - responsible for left-right laterality) is disrupted. 3D reconstruction of *spaw* mutant hearts revealed that 'middle' loopers undergo looping morphogenesis but in a dorso-ventral direction. In addition, interrogation of cardiac and ECM remodelling in *spaw* mutants pinpointed roles for Nodal regulating cardiac tissue volume and chamber-specific ECM remodelling during morphogenesis. Detailed investigation of cardiac ECM distribution identified that irrespective of looping direction, the ECM asymmetry of Nodal mutants in the tube translates into a highly regionalised ECM in the atrial outer-curvature at looping stages, suggesting a possible link between the axis of ECM asymmetry and the direction of looping and chamber ballooning.

In situ hybridisation and immunofluorescence assays identified regionalised expression/deposition of the *hyaluronan and proteoglycan link protein 1a* (*hapln1a*) in zebrafish at tube stage, overlapping the ECM expansion and suggesting Hapln1a protein may be involved in its modulation. Analysis of *hapln1a* promoter mutants, which lack *hapln1a* transcript, revealed that despite the defects in atrial ECM expansion, the left-sided atrial ECM asymmetry is reduced yet maintained, suggesting *hapln1a* is not the only component involved in its establishment.

Together I propose a model whereby laterality cues orient an early asymmetric cardiac ECM that, mediated by Hapln1a's protective cross-linking properties, intrinsically sets an axis for chamber growth and looping morphogenesis to occur, ensuring robust dextral cardiac morphogenesis.

DECLARATION OF AUTHORSHIP

September 2022

I, Juliana Sánchez-Posada, confirm that the work presented here

"Dissecting the links between morphology and ECM dynamics in the developing zebrafish heart"

is to the best of my knowledge and belief, original and the results of my own investigations, except as acknowledged and has not been submitted, either in part or whole, for a degree, diploma or other qualification at this or any other university or other institute of higher learning.

GENERAL TABLE OF CONTENTS

Abbreviations Used

#	2D	Two dimensions (x,y)
	3D	Three dimensional (x,y,z)
	4D	Four-dimensional (x,y,z and time)
A	AIC	Atrium's inner curvature
	ALPM	Anterior lateral plate mesoderm
	AOC	Atrium's outer curvature
	AP	Antero-posterior
	AVC	Atrio-ventricular Canal
B	BDM	2,3-Bu-tanedione 2-monoxime
	BM	Basement membrane
	bp	base-pairs
C	cDNA	coding DNA
	CHD	Congenital Heart Disease
	CRISPR	Clustered regularly interspaced short palindromic repeats
	CS	Chondroitin Sulfate
	CSPG	Chondroitin Sulfate Proteoglycan
D	D/V	Dorso-Ventral
	DDW	Double Distilled Water
	dpf	days post-fertilisation
E	E	Embryonic day (mouse)
	ECM	Extracellular Matrix
	EMT	Epithelial to mesenchymal transition
F	FHF	First heart field
	Fwd	Forward
G	GAG	Glycosaminoglycan
	gDNA	genomic DNA
	gRNA	guide RNA (crRNA + tracrRNA)
H	HA	Hyaluronan/Hyaluronic Acid
	hpf	hours post-fertilisation (zebrafish)
	HS	Heparan Sulphate
	HSPG	Heparan Sulphate Proteoglycan
I	IC	Inner curvature
	IECM	Interstitial Extracellular Matrix
	IFT	Inflow tract
	IHC	immunohistochemistry
	IND	internuclear distance
	inX	Incross (mating of fish with identical genetic background)
	ISH	*in situ* hybridisation

K	KD	Knockdown
	KO	Knockout
	KV	Kupffer's Vesicle
L	L/R	Left-Right
	LPM	Lateral plate mesoderm
M	MaPS	Macroscopic Phase Stamping
	MIP	Maximum intensity Z-projection
	MO	Morpholino
O	OC	Outer curvature
	OC-to-IC	Outer-curvature to Inner-curvature
	OFT	Outflow tract
	outX	Outcross (mating of fish with different genetic background)
P	PCR	Polymerase Chain Reaction
	PGs	Proteoglycans
R	Rev	Reverse
	ROI	Region of interest
S	SAN	Sinoatrial node
	SHF	Second Heart Field
	SPIM	Selective Plane Illumination Microscopy
V	VIC	Ventricle's inner curvature
	VOC	Ventricle´s outer curvature
W	WT	wild-type

LIST OF FIGURES

LIST OF TABLES

Chapter 1. Introduction

---

1 INTRODUCTION

Heart morphogenesis is a complex dynamic process during embryogenesis that requires a series of events to be tightly orchestrated and integrated in space and time to drive molecular, cellular and tissue-level events, which together create a mature and properly formed heart. Changes or disruptions in the process can lead to the development of congenital heart defects (CHD), a major cause of infant morbidity and mortality and the most common cause of congenital abnormalities worldwide (Bruneau, 2008; van der Linde *et al.*, 2011; Hoffman, 2013). Thus, characterising the series of events that lead to proper morphogenesis of a healthy heart has significant repercussions on our understanding of the causes of congenital heart diseases, which is relevant for its early diagnosis, prevention where feasible, and treatment with state-of-the-art therapies (Nakanishi *et al.*, 2016).

2 AN OVERVIEW OF VERTEBRATE HEART DEVELOPMENT

Various animal models are used to understand the morphogenetic events and underlying mechanisms that drive cardiac morphogenesis. Although the architecture of the final mature cardiovascular system differs between the models, the basic morphological programme triggered by specific signalling molecules and mediated by multiple tissue-specific transcription factors has been shown to be evolutionarily well conserved (Srivastava and Olson, 2000; Jensen *et al.*, 2013).

During embryonic development, the heart is the first organ to function, even before it has acquired its mature structure, and its correct formation is essential to ensure the distribution of nutrients and oxygen and the removal of waste in the developing foetus (Koefoed *et al.*, 2014; Lindsey, Butcher and Yalcin, 2014; Sylva, Van den Hoff and Moorman, 2014). Heart development is a complex process.

In humans, initially, two bilateral fields of mesodermal cardiac cells, also known as the primary or first heart field (FHF), fuse to form the primitive heart tube at about 3 weeks of gestation (Fig 1.1Ai). The posterior-dorsal end of the tube corresponds to the venous pole through which blood enters the heart tube, while the anterior pole, located on the antero-ventral side, is the arterial pole through which blood leaves the heart flowing to the rest of the developing body (Fig 1.1Aii) (Baldwin and Dees, 2012). At this point, the heart tube is comprised of an outermost cell layer, the myocardium, lined by a thick layer of extracellular matrix (ECM), referred to as cardiac jelly, and by an inner cell layer of specialised endothelial cells termed the endocardium (Baldwin and Dees, 2012; Gittenberger-de Groot *et al.*, 2013; Buijtendijk, Barnett and van den Hoff, 2020) (Fig 1.2). At about 4 weeks of gestation, the heart tube goes through a series of morphological rearrangements that break the tube's bilateral asymmetry, transitioning from a simple linear tube to a looped tube with a rightward helical loop in a process called *cardiac looping* (Fig 1.1Aiii). This highly asymmetric looping process is critical for ensuring the correct alignment of the future chambers as well as the inflow and outflow tracts of the mature heart (Moorman et al., 2003; Baldwin and Dees, 2012; Schleich *et al.*, 2013). Ventricular trabeculation, which consist of the formation of a network of trabeculae (i.e. luminal projections of myocardial cells covered by an endocardial layer), is initiated during the last stages of looping as a mechanism to increase the myocardial muscle mass, surface area and wall stiffness (Fig 1.1Aiv). The increase in surface area during this process aids nutrition and oxygen uptake of the cells comprising the embryonic heart prior to the formation of the coronary vasculature, while the build-up in muscle mass leads to an increase in cardiac output of the developing heart (Moorman, Brown and Anderson, 2010; Baldwin and Dees, 2012). Following onset of trabeculation, the septation of the chambers and formation of the valves transform the heart into a four-chambered organ with unidirectional flow. Development of the conduction system and the coronary circulation follow, and at about 9 weeks of gestation structural organogenesis of the heart is complete (Srivastava and Olson, 2000; Moorman, Brown and Anderson, 2010; Baldwin and Dees, 2012; Schleich *et al.*, 2013).

[*Note#1.1:* It is important to note, that most of what is known about the early stages of human heart development come from the extension of studies performed in avian and mouse models (Baldwin and Dees, 2012). The development of new technologies is allowing every day earlier and earlier visualisation of the developing human heart and will aid the future validation of results derived from non-human model organisms].

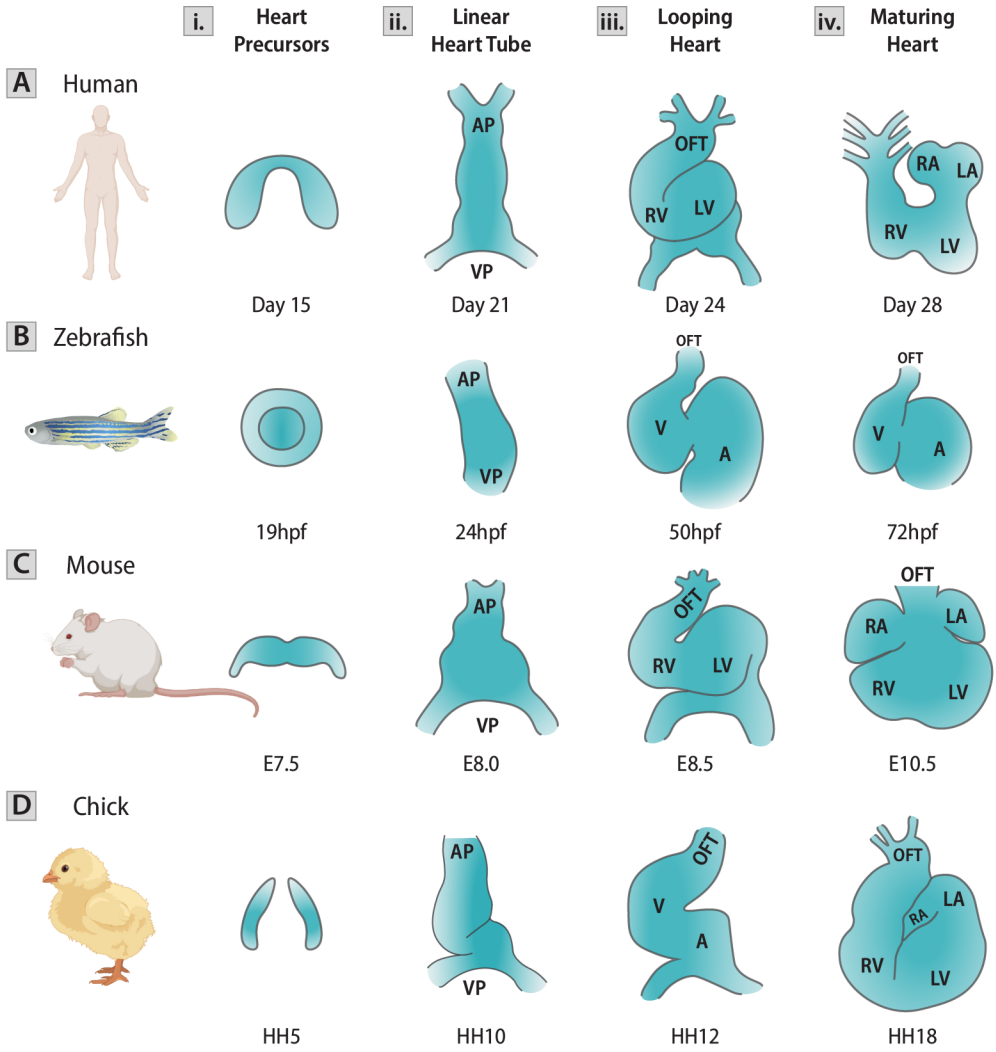

Fig 1.1. Early heart morphogenesis in different vertebrate models.
A-D. Schematic representing the ventral view of the heart at key stages of development in humans (A), zebrafish (B), mice (C), and chick (D) and its corresponding developmental times (see text for details). AP: arterial pole, VP: venous pole, A, atrium, V: ventricle, LA: left atrium, LV, left ventricle, RA: right atrium, RV: right ventricle, OFT: outflow tract. Adapted from (De La Cruz, Sánchez-Gómez and Palomino, 1989; Srivastava and Olson, 2000; Epstein, Aghajanian and Singh, 2015; Brown *et al.*, 2016; Wittig and Münsterberg, 2016; Shewale and Dubois, 2021).

Similar to humans, heart morphogenesis in mice, chick and zebrafish start with the specification of the cells comprising the FHF (Fig 1.1B-Di). Soon after their specification, these cardiac cells converge along the ventral midline of the embryo to form the linear heart tube (Fig 1.1B-Dii). While the cardiac precursors that form the primitive heart tube initially coalesce in different shapes in the different organisms (mice: crescent, chick: two wings of cardiac mesoderm, zebrafish: disc) (Ivanovitch, Temiño and Torres, 2017), the linear heart tube stage is a highly conserved morphological landmark in the development of the heart in all vertebrates (Fig 1.1B-Dii), where the differential gene expression along its length already exhibits patterning related to specific structures that will later emerge (Harvey, 2002; Srivastava, 2006; Meilhac

and Buckingham, 2018; Shewale and Dubois, 2021). In all three organisms, like in humans, the linear heart tube (mice: embryonic day (E) 8.5e, chick: Hamburger-Hamilton stage (HH) 9, zebrafish: 24 hours post-fertilisation (hpf)) is comprised of a myocardial and endocardial layer, between which lies a layer of cardiac jelly (Fig 1.2).

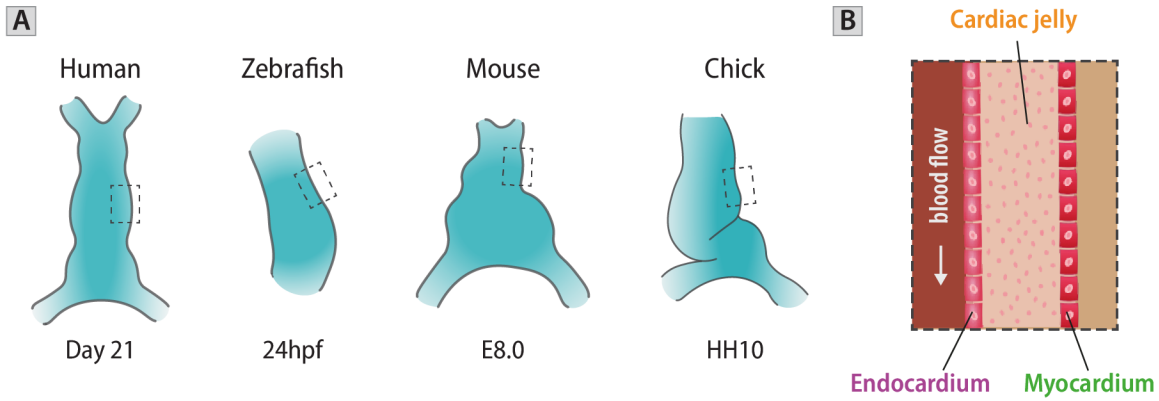

Fig 1.2. The heart tube is comprised two cellular layers, an outer myocardium and an inner endocardium, between which lies a layer of extracellular matrix known as cardiac jelly.
The linear heart tube stage is a highly conserved morphological landmark in the development of the heart in all vertebrates. **A.** Schematic depicting the linear heart tube of humans, zebrafish, mice and chicks (from left to right). **B.** Schematic depicting the three layers of the heart tube: endocardium, cardiac jelly and myocardium of the dotted squares in A.

At E8.5f in mice, HH10 in chick and 30hpf in zebrafish, cardiac looping takes place (Fig 1.1B-Diii). In chick, looping occurs in three distinct phases: dextral looping (also known as c-looping), formation of the primitive s-loop, and formation of the mature s-loop (Männer, 2000, 2009). Dextral-looping is the stage where the embryo breaks its bilateral symmetry and is characterised by the transformation of the straight linear heart tube into a tube with a c-shape loop, whose convexity points towards the right side of the embryo (Fig 1.1Diii). At this stage, the c-looped heart becomes a structure with morphologically distinct primitive atrium, ventricle and outflow tract. During the primitive s-loop phase, the distance between the poles of the c-shaped heart tube shortens, and the primitive ventricle shifts from a cranial to a caudal position with respect to the developing atrial chambers. The s-loop maturation involves the growth of the chambers, the morphological appearance of the future great arteries and the shift of the outflow tract to its final definitive position ventral to the right atrium (Männer, 2000, 2009; Wittig and Münsterberg, 2020). In mice, a leftward displacement of the venous pole makes both heart poles become asymmetrically positioned, resulting in a rightward tilt of the heart tube (Fig 1.1Ciii). This first asymmetrical event, combined with elongation of the tube, give rise to a helical looped heart (Desgrange, Le Garrec and Meilhac, 2018). In zebrafish, the heart tube undergoes cardiac looping by gradually bending at the boundary between the ventricle and the atrium, creating a flat S-shape loop and thus positioning the ventricle to the right of the atrium (Bakkers, 2011) (Fig 1.1Biii). During heart looping, while proliferation plays a minor role in this initial growth phase, elongation of the heart tube is mainly driven by the addition of cells to either end of the heart tube from a pool of highly proliferative mesodermal progenitor cells known as the second heart field (SHF) (de la Cruz *et al.*, 1977; Mjaatvedt *et al.*, 2001; Waldo *et al.*, 2001; Domínguez *et al.*, 2012; Shewale and Dubois, 2021). Whilst in zebrafish, the major contribution of the SHF is to the single ventricle with a lesser contribution to the atrium (de Pater *et al.*, 2009; Hami *et al.*, 2011; Colombo *et al.*, 2017), in mice and chick, cells added to the arterial pole will contribute to the outflow tract (OFT), right ventricle (RV) and interventricular septum (IVS), and those added to the venous pole, will form the developing atria and the atrial septum (Meilhac *et al.*, 2004; Kelly, Buckingham and Moorman, 2014).

Onset of trabeculation occurs in mice at E9.5, in chick at HH16-17 and in zebrafish at 60hpf (Liu *et al.*, 2010; Peshkovsky, Totong and Yelon, 2011; Captur *et al.*, 2016; Wittig and Münsterberg, 2020). By E10.5 in mice and HH14 in chick, the heart has acquired well-defined chambers (Fig 1.1B-Div); by E14.5, HH25-34, these chambers become separated as a result of septation and valve formation. During this time window, chambers are also connected to the pulmonary trunk and aorta, establishing the pulmonary and systemic circulations (which will be fully separated for mice after birth) (Buckingham, Meilhac and Zaffran, 2005; Wittig and Münsterberg, 2020).

Formation of the valves and maturation of the chambers are processes that takes place in hearts which experience correct flow patterns resulting from having undergone looping morphogenesis appropriately. These observations imply that the early processes of morphogenesis in the heart, particularly those driving looping morphogenesis, are critical in building the necessary elements of form and function to generate a functional healthy heart (Srivastava and Olson, 2000; Harvey, 2002; Bruneau, 2008; Männer, 2009). Consequently, investigating the mechanisms that drive early heart development could help better understand the aetiology of defects, setting up the basis for better diagnostics and the development of treatments for current and future patients with CHDs.

3 Heart Looping, an Essential Process in Cardiac Development

Regardless of the model organism being investigated, looping morphogenesis has been defined as essential for ensuring the correct positioning and alignment of the cardiac chambers with the vasculature and thus for the subsequent processes of maturation into a multi-chambered functional organ (Srivastava and Olson, 2000; Ramsdell, 2005; Baldwin and Dees, 2012; Schleich *et al.*, 2013; Koefoed *et al.*, 2014). The heart is an asymmetric organ, and the position of the chambers and its other structures are anticipated in the embryo during the process of heart looping. In humans, deviations of the normal pattern of left/right (L/R) asymmetries result in a wide spectrum of laterality phenotypes broadly classified as situs inversus, heterotaxia or visceral isomerism, and commonly associated with severe malformations and defects in the organs that are affected (Männer, 2004; Levin, 2005; Campione and Franco, 2016). As in most species, the majority of individuals exhibit the same directional asymmetry, suggesting a tightly controlled mechanism that drives rightward looping of the linear heart tube must be in place (Levin, 2005).

Numerous intrinsic and extrinsic mechanisms have been shown to promote specific aspects of asymmetric heart morphogenesis. Intrinsic mechanisms, which refer to the behaviour of cells and tissues within the heart tube, include regionalised extracellular matrix (ECM) remodelling, cell growth, and changes in cell shape and size (Auman *et al.*, 2007; Desgrange, Le Garrec and Meilhac, 2018; Grassini *et al.*, 2018; Lombardo *et al.*, 2019). External signalling pathways, physical constraints from the neighbouring regions, and organ growth by the addition of cells from the surrounding tissues are all extrinsic factors that act on the heart tube and also contribute to the looping process (Bakkers, Verhoeven and Abdelilah-Seyfried, 2009; Noël *et al.*, 2013; Desgrange, Le Garrec and Meilhac, 2018). Interestingly, all these intrinsic and extrinsic cellular and tissue behaviour mechanisms take place in an already beating and regionally patterned heart tube and come together appropriately, enabling processes of regionalisation and functional specialisation of the developing heart (Glickman and Yelon, 2002; Lindsey, Butcher and Yalcin, 2014). How these processes integrate to drive cardiac looping is not well understood; however, they must be subject to tight spatiotemporal regulation in order for this complex asymmetric morphological process to take place correctly.

Molecular asymmetries are established early within the embryo by the L/R organiser at around E8.0 in mice, HH7 in chick and 14hpf in zebrafish. Despite the structural variations within the animal model (i.e. node in mouse, Hensen's node in chick and Kupffer's vesicle in zebrafish), the coordinated movement of cilia that generates asymmetric fluid flow towards the future left-side of the embryo (in mouse and

zebrafish) (Brennan, Norris and Robertson, 2002; Bakkers, Verhoeven and Abdelilah-Seyfried, 2009; Grimes and Burdine, 2017) or the leftward movement of cells around the node (in chick) (Gros *et al.*, 2009) result in the up-regulation of Nodal, a conserved signalling ligand of the TGF-β (*Transforming growth factor β*) family in the lateral plate mesoderm (LPM) (Long, Ahmad and Rebagliati, 2003; Shiratori and Hamada, 2014). Once initiated, the asymmetric expression of Nodal spreads and remains along the left-LPM by a self-enhancement and lateral-inhibition mechanism in concert with LEFTY proteins which are expressed in the embryonic midline (Bakkers, Verhoeven and Abdelilah-Seyfried, 2009; Grimes and Burdine, 2017). Although Nodal expression itself is transient during early heart development, it initiates the expression of genes such as Pitx2 whose expression persists in the heart as development progresses.

As the zebrafish tube undergoes elongation, its venous pole is displaced towards the left, while the arterial pole remains in the embryonic midline in a process known as cardiac jogging. Previously, the directionality of looping morphogenesis in zebrafish was said to be predicted by the direction of jogging, as in all cases where the heart jogged to the left, the hearts underwent dextral looping (Chen *et al.*, 1997; Noël *et al.*, 2013). Disruption of L/R patterning in the embryos impacts jogging direction, resulting in the majority of embryos exhibiting a 'middle jogged' heart and suggesting L/R patterning as an inducer of asymmetry in the heart (Noël *et al.*, 2013; Grimes *et al.*, 2020). Surprisingly, despite L/R patterning disruption and 'middle jogging', a significant proportion of embryos undergo dextral looping, suggesting that in addition to L/R patterning, another mechanism may be in place to help drive robust dextral looping.

Supporting the existence of an additional mechanism, studies of cardiac looping in mice, chick and zebrafish have all shown that even in the absence of extrinsic laterality cue (i.e. disrupted L/R patterning), the heart still undergoes the morphogenetic process of cardiac looping, often in the correct direction (Chang *et al.*, 2000; Fujiwara *et al.*, 2002; Long, Ahmad and Rebagliati, 2003; Furtado *et al.*, 2008; Mine, Anderson and Klingensmith, 2008; Lenhart *et al.*, 2013; Noël *et al.*, 2013). All these have led to the suggestion that intrinsic information within the tissues of the developing heart must provide directional cues promoting fine-tuning of organ shape and robust dextral looping morphogenesis (Desgrange *et al.*, 2020).

4 ZEBRAFISH AS A MODEL ORGANISM TO STUDY HEART DEVELOPMENT

Zebrafish have been shown to be a valuable vertebrate model for the study of heart development. Although its heart is much simpler than that of humans (composed of two chambers instead of four), the cellular and signalling processes that drive heart development in zebrafish are closely related to those which occur in the human heart (Brown *et al.*, 2016). Comparison of zebrafish and human genomes demonstrates that zebrafish have at least one orthologous gene for approximately 70% of the human genes, making it a highly affordable and suitable vertebrate model to study heart development in healthy and pathological scenarios helping us understand the mechanistic activity of disease-related- genes in humans (Howe *et al.*, 2013). Moreover, when zebrafish hearts are compared to mammalian hearts, most of the specialised cell types (i.e. myocardium, endocardium, neural crest cells, second heart field, fibroblasts), and structures comprising the heart (valves -atrioventricular and aortic, pacemaker, trabeculae and coronary vasculature), as well as the signalling pathways driving its early heart development, are conserved (Staudt and Stainier, 2012; Shewale and Dubois, 2021; Bowley *et al.*, 2022).

Additional advantages offered by the zebrafish model are inherent to its biology. External egg fertilisation combined with a clear embryo with transparent chorion facilitates live-cell visualisation and imaging using light microscopy can be applied throughout development and aids the study of the heart and its function during morphogenesis. Rapid embryonic development means the whole morphogenetic process of heart development occurs in 5 days, and as the development of the embryo itself is independent of heart function, it allows the screening of severe cardiovascular defects without causing embryonic death

(Bakkers, 2011; Brown *et al.*, 2016). Finally, the fully sequenced and well-annotated genome allows the use of multiple techniques for genetic manipulation to study the localisation and function of specific genes and proteins during development (Holtzman *et al.*, 2016).

4.1 Zebrafish Heart Development

4.1.1 Specification, Differentiation and Fusion of the Heart Fields

Heart development in zebrafish starts with the specification of myocardial and endocardial progenitors at about 5hpf (Stainier, Lee and Fishman, 1993). While the two pools of myocardial progenitors (atrial and ventricular) are located in the lateral marginal zone of the blastula, the two pools of endocardial progenitors are distributed throughout the marginal zone without any spatial organisation. As development progresses, at about 14 somites (16hpf), cardiac progenitor cells located in the anterior lateral plate mesoderm (ALPM) enter into cardiogenic differentiation, and expression of sarcomeric genes like *myosin light chain polypeptide 7* (*myl7*) start to be observed in some cells. More specifically, while ventricular cells initiate the expression of *myosin heavy chain 7-like* (*myh7l*, previously *ventricle myosin heavy chain* or *vmhc*), atrial cells start expressing *myosin heavy chain 6* (*myh6*, previously *atrial myosin heavy chain* or *amhc*) (Bakkers, 2011; Brown *et al.*, 2016). Between 16 and 19hpf, the linearly arranged cardiomyocytes migrate towards the embryonic midline and fuse, forming a cardiac disc (Holtzman *et al.*, 2007). During this process, endocardial cell migration precedes that of the myocardium, resulting in a cardiac disc with endocardial cells positioned to the middle, lined by ventricular and atrial cardiomyocytes (Fig 1.3A-A'') (Bussmann, Bakkers and Schulte-Merker, 2007; Holtzman *et al.*, 2007; Bakkers, 2011).

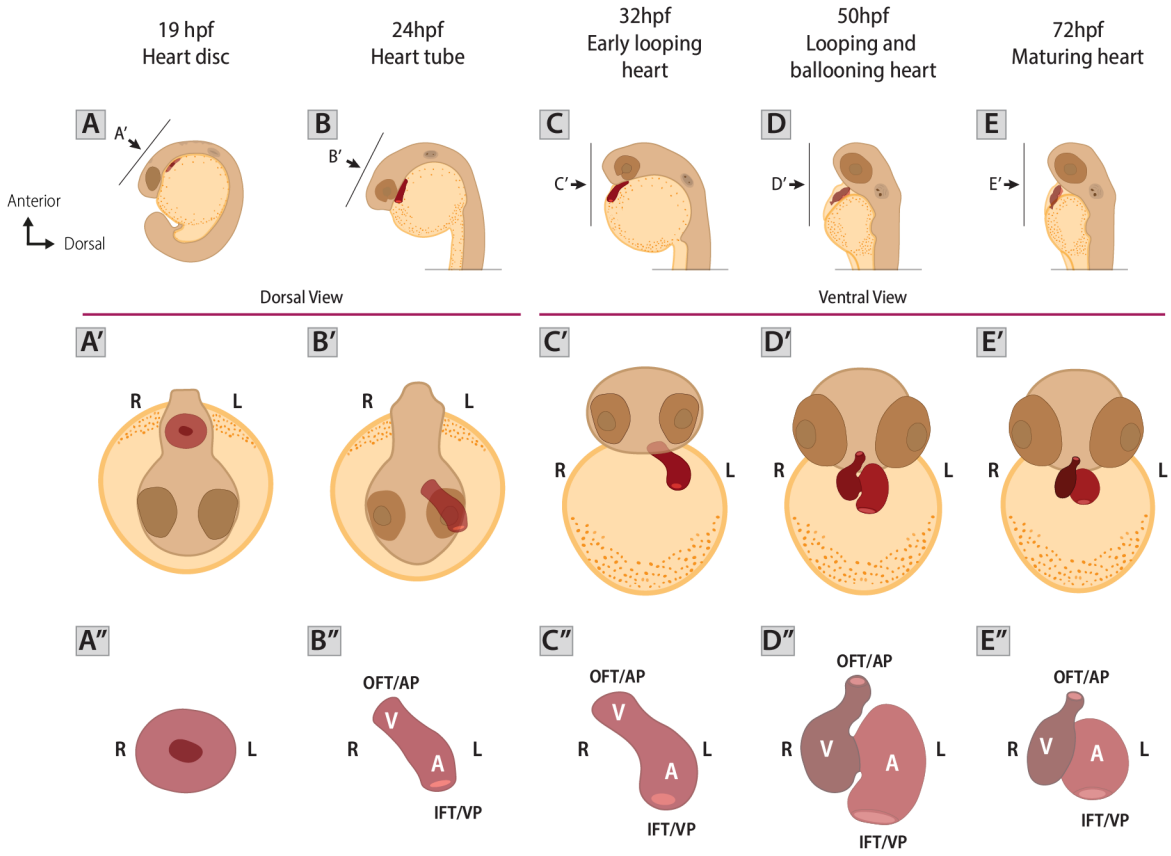

Fig 1.3. Development of the zebrafish heart.
A-E''. Schematic of key stages of zebrafish heart development. At 19hpf, the zebrafish heart is a disc located in the midline of the embryo (A-A''). Between 19 and 24hpf, this tube rotates and involutes to the left side of the embryo forming a heart tube positioned underneath the left eye (24hpf, B-B''). As development progresses the heart tube descends ventrally over the yolk sac (32hpf, C-C'') and starts to undergo looping and ballooning

morphogenesis. At 50hpf, the heart has acquired a flat S-shape loop and each chamber a bean-shaped morphology (D-D''). At 72hpf the heart starts to undergo maturation processes such as trabeculation and valvulogenesis, ending with a mature heart at about 5hpf. A-E: Left view of the embryo illustrating the position of the heart. A'-E': Schematic of the embryo and heart viewed from the position of the arrows depicted in A-E. A''-E'': Close up of the hearts shown in A'-E'. A'-B', A''-B'': Dorsal view. C'-E', C''-E'': Ventral view. L: left, R: right, A: atrium, V: ventricle, OFT/AP: outflow tract/arterial pole, IFT/VP: inflow tract/venous pole.

4.1.2 HEART JOGGING: FROM A DISC TO A TUBE

Formation of the heart tube initiates when the heart disc undergoes a clockwise rotation (from a dorsal view) and a simultaneous asymmetric involution or folding of the right-posterior region of the disc epithelium towards the anterior-left side of the embryo, in a process referred to as *heart jogging* (Bakkers, 2011) (Fig 1.3B-B''). As a consequence of the involution and rotation of the myocardial tissue, the original basal surface of the heart disc becomes the lumen of the tube ,and the bilateral (i.e. L/R) myocardial cells populations in the heart disc become the dorso-ventral (D/V) regions of the heart tube (Rohr, Otten and Abdelilah-Seyfried, 2008; Smith *et al.*, 2008; Guerra *et al.*, 2018). During this process, the resulting cardiac tube has the arterial pole still located in the embryonic midline while the venous pole is located on the anterior left side.

The mechanism underlying the asymmetric involution and folding of the heart disc to form the heart tube has been actively studied in the past years (Rohr, Otten and Abdelilah-Seyfried, 2008; Smith *et al.*, 2008; Lenhart *et al.*, 2013; Veerkamp *et al.*, 2013; Kidokoro *et al.*, 2018). Preceding the formation of the heart disc, at 14hpf as a result of Kupffer's vesicle activity, the expression of the L/R signalling gene *southpaw* (*spaw*, a Nodal-related gene) is asymmetrically induced in the posterior lateral plate mesoderm (LPM) and propagated anteriorly through the left LPM in an autoregulatory manner (Long, Ahmad and Rebagliati, 2003; Bakkers, Verhoeven and Abdelilah-Seyfried, 2009). At 20hpf, *spaw* expression in the anterior LPM induces the asymmetric expression of downstream targets of Nodal signalling, such as *has2* (*hyaluronan synthase 2*) and *bmp4* (*bone morphogenetic protein 4*), which are expressed asymmetrically in the LPM adjacent to and in the heart disc itself (Rohr, Otten and Abdelilah-Seyfried, 2008; Smith *et al.*, 2008). Nodal-induced upregulation of *has2* expression on the left compartment of the disc which downregulates Bmp4 activity. This reduction in Bmp signalling on the left establishes L/R differences in migration speeds of the cardiomyocytes, through regulation of the expression of non-muscle myosin. Together, higher cell motility of the cardiomyocytes on the left compartment when compared to the right result in a clockwise rotation of the heart disc during heart tube formation and reorientation of the left-right axis of the heart disc to the dorso-ventral axis of the tube (Smith *et al.*, 2008; Lenhart *et al.*, 2013; Veerkamp *et al.*, 2013). Concomitantly to these rotation and involution events, cells from the SHF get are recruited to the venous pole of the forming tube (19-34hpf) (de Pater *et al.*, 2009).

4.1.3 FROM A TUBE TO A LOOPED ORGAN

The linear heart tube at 24hpf is comprised of cells from the FHF. At around 28hpf, the tube starts to undergo looping morphogenesis, while progenitor cells from the SHF are recruited to both poles, in a process that has been shown to be conserved with mice and chick (de la Cruz *et al.*, 1977; Mjaatvedt *et al.*, 2001; de Pater *et al.*, 2009; Hami *et al.*, 2011; Kelly, Buckingham and Moorman, 2014). Within the next day, as the heart descends over the yolk, cells are added to the distal portion of the arterial pole of the heart (34-48hpf), becoming part of the ventricle (Fig 1.3C-C'') (de Pater *et al.*, 2009; Hami *et al.*, 2011).

During looping morphogenesis, the two chambers become morphologically distinct in a process known as chamber ballooning, where each chamber acquires a bean-shaped morphology with clear inner and outer curvatures (Fig 1.3D-D''). To form this asymmetrically positioned heart, cardiomyocytes in each chamber undergo differential shape changes which are particularly confined to the developing outer and inner curvatures, facilitating its ballooning (Auman *et al.*, 2007). Interruption of blood flow and contractility

impact cellular changes in the ventricle, suggesting the requirement of a tight balance between extrinsic and intrinsic biomechanical forces to ensure the correct shaping of the chambers (Sehnert *et al.*, 2002; Auman *et al.*, 2007).

Concurrent with chamber ballooning, a constriction between the chambers known as the atrioventricular canal (AVC) is formed. At this stage, the expression of specific genes has been shown to pattern the different structures of the developing heart. Similar to the mammalian heart, the T-box transcription factor 2 (*Tbx2*, in zebrafish *tbx2b*) aids the establishment of the expression domains of the working myocardium by presenting an expression domain reciprocal to *natriuretic peptide type A* (*Nppa,* in zebrafish *nppa*). The repressive complex formed by *Nkx2.5-Tbx2* competes with the complex formed *Nkx2.5* and T-box transcription factor 5 (*Tbx5*, in zebrafish *tbx5a*), which positively regulates the expression of *Nppa* in the working myocardium (Harvey, 2002; Auman *et al.*, 2007; Bruneau, 2008; Jensen *et al.*, 2013). In zebrafish, failure to restrict the expression of *nppa* and *nppb* (expressed more tightly in the outer curvatures of the chambers), resulted in a spectrum of cardiac defects, impacting heart morphology and the formation of the atrioventricular canal (Auman *et al.*, 2007).

The heart tube begins to function and drive circulation as soon as it forms, supplying organs and tissues with oxygen and nutrients and removing waste. At 48hpf, the heart is connected to a more developed vasculature. Oxygenated blood leaves the heart to the circulatory system through a series of aortic arches that enter the anterior and posterior circulatory loops. Deoxygenated blood returns to the developing atrium through the common cardinal vein over the yolk completing the circulatory loop (Warren and Fishman, 1998; Eberlein *et al.*, 2021).

4.1.4 Valvulogenesis

During looping morphogenesis, the AVC is visible as the constriction between the atrium and the ventricle. The first molecular indication of AVC specification occurs at around 37hpf with the restriction of *bmp4* and *versicana* expression in the myocardial cells at the AVC (Walsh and Stainier, 2001). Subsequently, *notch1b*, which was previously expressed in the entire ventricular endocardium, becomes restricted to the endocardial cells at the AVC at about 45hpf (Westin and Lardelli, 1997; Milan *et al.*, 2006; Lagendijk *et al.*, 2011, 2013). Within this time frame, the endocardial and myocardial cells located in the AVC differentiate morphologically. Specifically, the endocardial cells undergo a transition from a squamous to a cuboidal cell shape and start expressing the cell-adhesion molecule, Dm-grasp. Subsequently, these cuboidal endocardial cells undergo what has been described as an incomplete epithelial to mesenchymal transition (EMT) transition or a direct invagination, forming protrusions that extend into the cardiac jelly, which results in the formation of endocardial cushions (Beis *et al.*, 2005; Bakkers, 2011; Staudt and Stainier, 2012). To ensure a proper formation of the valve, oscillating blood flow through the heart is required to induce the shear-responsive gene *klf2* in the endocardial cushions. Induction of *klf2,* which acts upstream of Notch1, is required to stimulate cell shape changes involved in the formation of the endocardial cushions (Vermot *et al.*, 2009; Heckel *et al.*, 2015). Following a remodelling process of the endocardial cushions, primitive valve leaflets are formed at about 76hpf, blocking regurgitation (i.e. backflow into the atrium when the ventricle contracts) and creating unidirectional flow through the heart (Brown *et al.*, 2016). By 105hpf, the primitive valve leaflets have enlarged and matured into mature valve leaflets that have expended into the lumen of the ventricle, composed of two layers of cells separated by a layer of ECM rich in fibronectin (Bakkers, 2011).

Mutations in various components that have been recognised as constituents of the cardiac jelly during valve formation (e.g. fibronectin, versican, and hyaluronan) result in severe impairment of the endothelial cell invasion process to the cardiac jelly, abrogating the formation of the endocardial cushions (Yamamura *et al.*, 1997; Mjaatvedt *et al.*, 1998; Camenisch *et al.*, 2000; Walsh and Stainier, 2001; Lagendijk *et al.*, 2011; Hatano *et al.*, 2012; Gunawan *et al.*, 2019). Together, these studies suggest that precise composition

of the cardiac ECM in the AVC is a conserved requirement for promoting valve differentiation and development.

4.1.5 HEART MATURATION

Once the heart has undergone looping, aspects of cardiac remodelling and maturation include trabeculation and the development of the conduction system (Fig 1.3E-E'') (Samsa, Yang and Liu, 2013).

VENTRICULAR TRABECULATION

Trabeculation in zebrafish starts when an inner layer of cardiomyocytes delaminates from the ventricular wall creating luminar protrusions over their neighbouring cells. These protrusions then gradually reduce their abluminal surface to move closer to the trabecular layer while the neighbouring cells move into the space left behind by the protruding cell maintaining a cohesive compact layer (Staudt *et al.*, 2014). As previously described, this highly organised process increases ventricular myocardial mass and internal surface area. Similar to chamber growth, its correct progression requires an active cross-talk between the myocardial and endocardial layers (Uribe *et al.*, 2018). Moreover, studies in mice, chick and zebrafish have shown that endocardial signals cross the cardiac jelly to activate cardiomyocyte delamination and proliferation (in the case of mice) (Icardo and Fernandez-Terán, 1987; Stankunas *et al.*, 2008; Rasouli and Stainier, 2017; del Monte-Nieto *et al.*, 2018). This signalling is enhanced when degradation of the cardiac ECM in the ventricle starts, suggesting a tight correlation between ECM dynamics and the onset of this maturation process in zebrafish (Rasouli and Stainier, 2017).

CONDUCTION SYSTEM DEVELOPMENT

Initial coordinated contractions with a peristaltic wavelike pattern propel blood out of the heart tube at about 24hpf. As development progresses and the heart undergoes looping, these contractions become coordinated with each chamber showing distinct contractile pulses (36hpf) (Warren and Fishman, 1998; Goenezen, Rennie and Rugonyi, 2012). The pacemaker or sinoatrial node (SAN) in zebrafish is located at 24hpf in the inner curvature of the venous pole and is comprised of SHF cells actively expressing *isl1* (de Pater *et al.*, 2009; Arrenberg *et al.*, 2010). Between 36 and 48hpf, a reduction of the electrical pulse is observed in the AVC, causing a contraction delay (or AV delay) that results in a sequential contraction of the atrium followed by the ventricle. As the heart loops and the ventricle trabeculates, an immature fast conduction network develops in the ventricle (72-96hpf), which later on fully matures into a fast conduction network with an apex-to-base activation pattern (Neil C Chi *et al.*, 2008).

5 THE EXTRACELLULAR MATRIX

Cardiac morphogenesis requires tight spatiotemporal coordination of chemical and biomechanical signals that shape the early heart tube into a three-dimensional (3D) organ. During this highly complex process of morphogenesis, the heart tube is comprised of two cellular layers, an outer myocardium and an inner endocardium, between which lies a layer of specialised ECM or cardiac jelly. Mediating signalling at cellular and tissue levels and providing structural support, the ECM has been shown to play multiple important roles in development (Rozario and DeSimone, 2010; Keeley *et al.*, 2020; Walma and Yamada, 2020).

5.1 THE ECM COMPOSITION

The extracellular matrix (ECM) is a complex array of highly cross-linked macromolecules that provides structural support to cells and tissues and defines the physical and chemical interactions that modulate cellular physiology and homeostasis (Byron, Humphries and Humphries, 2013; Mouw, Ou and Weaver, 2014). Being a dynamic structure, ECM components are continuously deposited, modified and degraded

in response to developmental processes, injury and disease (Lu *et al.*, 2011; Humphrey, Dufresne and Schwartz, 2014; Sivakumar *et al.*, 2018; Derrick and Noël, 2021). Additionally, being in close contact with cells, the ECM can influence many cellular functions such as differentiation, migration, adhesion, growth, and survival. At the same time, the ECM plays structural functions such as providing tissues with mechanical strength and flexibility and cells with anchoring support (Humphrey, Dufresne and Schwartz, 2014; Walma and Yamada, 2020).

The ECM is formed by a complex array of tissue-specific macromolecules produced intracellularly by resident cells and secreted via exocytosis into the extracellular space (Mouw, Ou and Weaver, 2014). As the resident cell's role is to produce its own ECM, every organ has a unique ECM composition, and its deposition is intended to serve a particular tissue-specific purpose (Frantz, Stewart and Weaver, 2010; Walker, Mojares and del Río Hernández, 2018). In this way, to maintain homeostasis, the cells in contact with the ECM sense its properties through different receptors and focal adhesions. Depending on the tissue-specific needs, they regulate the expression and deposition of ECM components and enzymes into the ECM. This continuous sensing and regulation of ECM-specific gene transcription create a feedback loop mechanism where cells respond to the ECM's biophysical and biomechanical cues and influence its composition, resulting in the maintenance of tissue homeostasis (Cox and Erler, 2011; Handorf *et al.*, 2015; Walker, Mojares and del Río Hernández, 2018). Therefore, dysregulation of ECM remodelling exhibited either by excess ECM deposition or increased stiffness has been shown to affect homeostasis maintenance and cell fate resulting in fibrotic conditions (Cox and Erler, 2011).

The dynamic structure of the ECM can be divided into two distinct entities: the basement membrane (BM) and interstitial ECM (IECM), both of which are intimately interconnected (Fig 1.4). While the basement membrane underlines epithelial and endothelial cells providing a barrier and physical support and connections between the cells and the interstitial matrix (Sekiguchi and Yamada, 2018; Boland, Quondamatteo and Van Agtmael, 2021), the interstitial ECM constitutes most of the extracellular mass, providing structure to spaces between cells and modulating inter-cellular and inter-tissue interactions (Fig 1.4).

[*Note#1.2:* As the present thesis deals primarily with interstitial matrix components, I will only focus on describing with more detail those in here (for reviews on BM proteins, see (Sekiguchi and Yamada, 2018; Boland, Quondamatteo and Van Agtmael, 2021))].

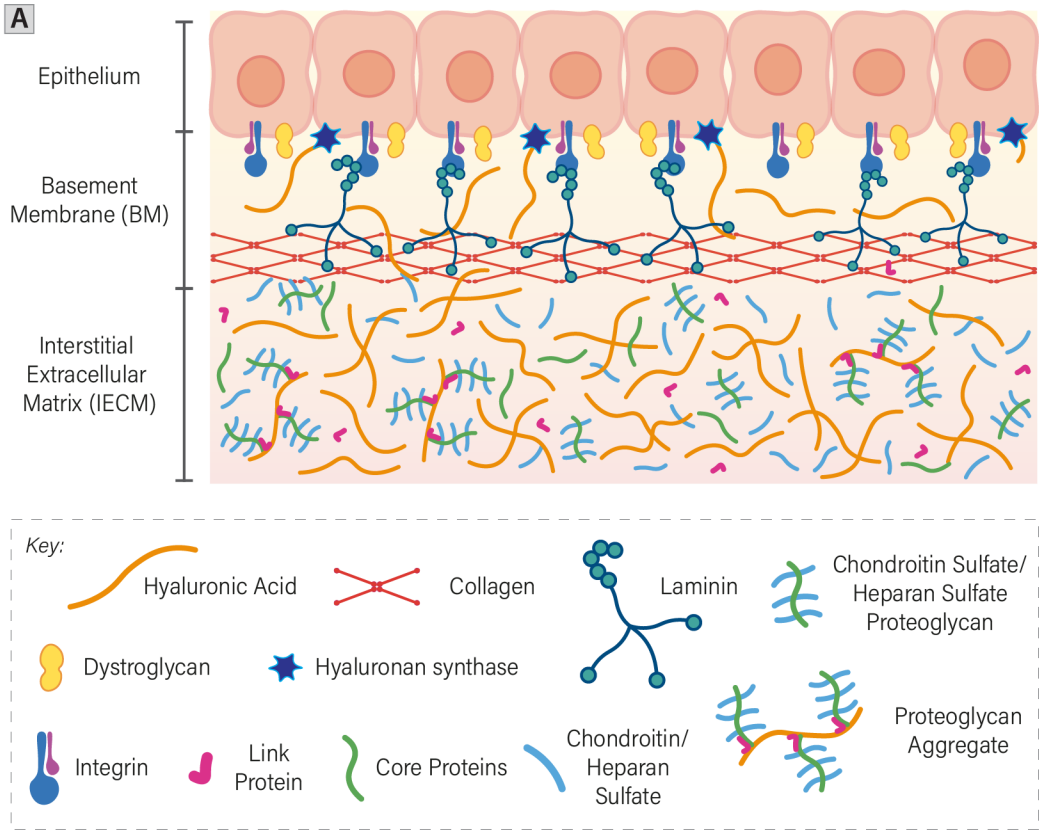

Fig 1.4. The extracellular matrix.
A. Schematic illustrating the basic structure of the extracellular matrix surrounding an epithelium. The basement membrane (BM) provides physical support to the cells via direct attachment. Beneath the BM, the interstitial ECM (IECM) provides a structural scaffold to the tissues and modulates inter-cellular and inter-tissue interactions.

The interstitial cardiac jelly is composed of two main classes of macromolecules: proteoglycans (PGs) and fibrous proteins (Frantz, Stewart and Weaver, 2010; Mouw, Ou and Weaver, 2014).

5.1.1 PROTEOGLYCANS

Proteoglycans (PG) are composed of a *core protein* linked to a long, linear chain of disaccharide repeats, referred to as glycosaminoglycans (GAG). The biochemical and hydrodynamic characteristics of the GAGs give proteoglycans their primary biological function, which is to bind water and provide hydration and compressive resistance to the ECM (Frantz, Stewart and Weaver, 2010; Rozario and DeSimone, 2010; Attili and Richter, 2013; Mouw, Ou and Weaver, 2014). Proteoglycans can vary in structure depending on multiple factors: 1) the type of GAG (or GAGs) that are attached to the core protein, 2) the actual number of GAGs attached, 3) the arrangement of sulfated residues found along the chain and 4) the stoichiometry of the GAGs chain substitution (i.e. attachment sites within the core protein vs actual attachment sites used by GAGs) (Merry *et al.*, 2022).

Proteoglycans are categorised according to the nature of their GAG chain and the density of these chains along the core protein and are generally named after their core protein (Mouw, Ou and Weaver, 2014; Merry *et al.*, 2022). The four classes of GAGs are hyaluronic acid (HA - also hyaluronan), chondroitin sulfate/dermatan sulfate (CS/DS), heparan sulfate (HS) and keratan sulfate (HS). While the synthesis of CS, KS and HS occurs in the Golgi apparatus and couples with the translation of the core protein, synthesis of HA occurs at the cell membrane where it is directly deposited (Lockhart *et al.*, 2011a; Mouw, Ou and Weaver, 2014; Walma and Yamada, 2020).

The most common PGs found in the ECM are chondroitin sulfate proteoglycans (CSPGs), heparan sulfate proteoglycans (HSPGs) and keratan sulfate proteoglycans (KSPGs) (Mouw, Ou and Weaver, 2014). HSPGs form a major part of the basement membrane and comprise syndecans, agrin and perlecan. CSPGs are found in the interstitial ECM. The most common CSPGs belong to a group of PGs called *lecticans* or *hyaladherins* and include aggrecan, neurocan, versican and brevican.

Although CSPGs can exist in isolation within the extracellular matrix and interact with other GAGs and PGs, they can also take the form of proteoglycan aggregates (Rodriguez and Roughley, 2006; Attili and Richter, 2013; Roughley and Mort, 2014). These PG aggregates are composed of a central filament of HA that is covalently linked to PGs by means of a link protein.

Together, the hydrodynamic characteristic of proteoglycans combined with the multiple forms and structures it can take, make the PGs important components of the ECM which in addition to its structural role, have been shown to have multiple biological functions within the ECM (Walker, Mojares and del Río Hernández, 2018; Merry *et al.*, 2022).

Aggrecan is the best studied core protein and across species is predominantly expressed in cartilaginous structures (Lockhart *et al.*, 2011a; Roughley and Mort, 2014). In aqueous solution, the high charged density present in aggrecan causes the molecules to swell, providing this PG the ability to generate elasticity and resist high compressive loads in the cartilage (Attili and Richter, 2013; Roughley and Mort, 2014; Merry *et al.*, 2022). Proteolytic degradation of aggrecan is commonly associated with the loss of tissue function which can result in arthritis and degenerative cardiac disease (Kiani *et al.*, 2002; Rodriguez and Roughley, 2006). Expression and deposition of neurocan and brevican are restricted to the central nervous system suggesting they play a role in the homeostasis of the ECM specifically in neural tissue (Yamaguchi, 2000; Hatano *et al.*, 2012).

Versican is a major component of many tissues and has been found to be expressed in the central and peripheral nervous systems, the luminal surface of glandular epithelia, blood vessels in normal and tumour tissues, dermis, and the proliferative zone of the epidermis, and embryonic tissue (Bode-Lesniewska *et al.*, 1996). Although versican is transiently expressed during development, this broad expression in different systems, suggest an important role for this proteoglycan in the ECM (Wu *et al.*, 2005; Lockhart *et al.*, 2011a).

5.1.2 Hyaluronic Acid

Hyaluronic acid (also known as hyaluronan) is a uniformly linear non-sulfated GAG with high molecular weight composed of D-glucuronic acid and N-acetylglucosamine repeating units. HA can vary in length from 2,000 to 25,000 disaccharides, depending on the tissue in which it is produced and can be found virtually in every tissue of vertebrates (Simpson *et al.*, 2022).

Three major characteristics of this GAG highlight its uniqueness and importance as part of the ECM in developing organisms: 1) its unique hydrodynamic properties grants this protein the ability to form hydrated voluminous structures in solution (Toole, 2001; Cyphert, Trempus and Garantziotis, 2015), 2) its interactions with structural extracellular hyaladherins, complements the hydration ability of this GAG producing more stable multi-component matrixes with variable mechanical properties (Toole, 1990), and 3) its instructive effect on cell signalling and behaviour generate a coordinated balance between cell-ECM dynamics (Toole, 2001; Feinberg and Weiss, 2009; Walker, Mojares and del Río Hernández, 2018).

Under physiological conditions, due to its ability to create hydrogen bonds between adjacent sugars and the repulsion force exerted between the negatively charged carboxyl groups, hyaluronic acid on its own can form a stiffened and expanded random coil, forming a continuous network (Toole, 2001; Cowman and Matsuoka, 2005; Simpson *et al.*, 2022). In addition to these interactions, and different to the other GAGs (i.e. chondroitin sulfate, heparan sulfate) HA is not covalently linked to core proteins, instead, it is linked

and stabilised to other proteoglycans (also called hyaladherins (Toole, 1990; Knudson and Knudson, 1993)) by HAPLNs, modifying its conformation and structure (Rodriguez and Roughley, 2006; Long *et al.*, 2018). Consequently, HA acts as a scaffold to build a network of proteoglycan aggregate structures adapted to specific tissues and functions (Simpson *et al.*, 2022).

As previously mentioned, HA is synthesised in the plasma membrane of cells, and this is accomplished by a family of membrane-bound glycosyltransferases known as *hyaluronan synthases* (HAS). HAS catalyse the addition of UDP-D-glucuronic-acid and UDP-N-acetyl-D-glucosamine monomers in an alternating fashion resulting in the assembly of long HA polymers (Toole, Yu and Underhill, 2001; Necas *et al.*, 2008). Interestingly, cell-based and mice studies identified that the three isoforms so far identified of HAS produce HA with different sizes. In general, HAS3 synthesises the shortest polymers, while HAS1 and HAS2 catalyse the formation of longer HA chains (Itano *et al.*, 1999). Furthermore, HAS genes have a different spatiotemporal expression throughout embryonic development, with HAS2 being the most commonly expressed throughout most of its stages (Tien and Spicer, 2005; Cyphert, Trempus and Garantziotis, 2015).

HA removal or turnover is facilitated by *hyaluronidases* (HYALs), a class of highly homologous endoglycosidases, which catabolise HA creating primary and shorter disaccharides (Necas *et al.*, 2008; Cyphert, Trempus and Garantziotis, 2015). Although HYALs promote the turnover of HA, its catabolic function is not strictly limited to HA, as studies have shown they can also degrade other GAGs like chondroitin sulfate (Cyphert, Trempus and Garantziotis, 2015). Aside from HYALs, turnover of HA can be performed by free radicals by a non-specific pathway in scenarios of inflammatory response (Rodriguez and Roughley, 2006; Cyphert, Trempus and Garantziotis, 2015).

Dysregulation of the expression of HAS or HYAL genes has important implications in the progression of development, injury and disease (Knudson and Knudson, 1993; Toole, Yu and Underhill, 2001; Cyphert, Trempus and Garantziotis, 2015). Taken together and consistent with all the biological roles attributed to HA, hyaluronan synthases and hyaluronidases regulate HA deposition and metabolism, establishing a tight balance of HA content in the ECM and maintaining tissue homeostasis (Lagendijk *et al.*, 2013; Cyphert, Trempus and Garantziotis, 2015).

5.1.3 LINK PROTEINS

A class of proteins that selectively bind hyaluronan and proteoglycans, creating proteoglycan aggregates are known as *hyaluronan and proteoglycan link proteins* (HAPLN) (Simpson *et al.*, 2022). Link proteins contain two homologous repeats of the link module and an immunoglobin-like globular domain, which makes them specifically able to interact with HA and PGs, respectively (Kohda *et al.*, 1996).

Link proteins are required in the process of PG aggregate formation promoting the interaction between the core protein and HA (Rodriguez and Roughley, 2006; Attili and Richter, 2013). Interestingly, the G1 domain of the newly synthesised core proteins is not able to interact with HA until the protein has undergone a conformational change. This conformational change in the core proteins has been shown to be induced and enhanced by link proteins, facilitating the formation and stabilisation of the proteoglycan aggregates (Melching and Roughley, 1990). Furthermore, attachment of PG to HA by HAPLN proteins limits the access of the relatively large HYALs to the HA chain, protecting the PG aggregates from degradation via HA catabolism (Rodriguez and Roughley, 2006). If concentration of HYALs or free radicals is increased the protection ceases, suggesting that link proteins can retard degradation but not abolish it (Rodriguez and Roughley, 2006).

5.2 THE ROLE OF THE ECM IN HEART DEVELOPMENT

Considering that the primitive heart is a simple tube-like structure with no valves and propelling blood with a peristaltic beat, early studies carried out in the 1940s proposed the cardiac ECM as an indispensable

layer in the heart tube to ensure effective pumping action of the tube (Barry, 1948). In this study, results using a simplified mathematical analysis of a cross-sectional area of a heart tube with and without cardiac jelly suggested that the thickened cardiac jelly allows the heart to close its lumen in every peristaltic beat, directing blood out of its arterial end and towards the developing embryo. Subsequently, as the myocardium relaxes, the resilient property of the cardiac jelly pulls the endocardium back, assisting the heart tube to *spring back* to its original open-lumen shape while drawing blood again into the heart and restarting the cycle (Barry, 1948). This pumping efficiency has been recently re-proposed in studies performed on chick embryos, in which harnessing the ability to obtain real-time *in vivo* images of biological samples, the cross-sectional changes of pulsating embryonic chick hearts were analysed (Männer *et al.*, 2008). Analysis of the cross-sections identified that as a consequence of the uneven distribution of cardiac ECM in the chick heart tube, the myocardial tube narrows and widens concentrically while the endocardial tube does it eccentrically. These results, combined with theoretical modelling of the beating heart with uneven distribution of ECM (Taber and Perucchio, 2000), suggested that the pumping efficiency of the heart tube is not solely achieved by the presence of a cardiac jelly but also by the fact that it is asymmetrically distributed (Männer *et al.*, 2008).

Another functional role was suggested by studies performed in the late 1970s. In these studies, successful isolation of the cardiac jelly from explanted embryonic chick hearts recognised that the cardiac ECM could maintain its hydrated shape and structure in the absence of myocardial tissue and in media with different ionic concentrations. These newly recognised abilities of the cardiac jelly were attributed to the high contents of GAGs that make up the cardiac ECM, suggesting it plays a structural morphogenetic role during cardiac morphogenesis (Nakamura and Manasek, 1978, 1981).

In addition to these early proposed roles, recent studies have shown that composition and remodelling of the embryonic ECM drive organ morphogenesis in mice, chick and zebrafish, revealing that deposition, cleavage and degradation of ECM substrates not only sculpt tissue architecture but also generate bioactive ECM fragments critical to specific developmental processes (Feinberg and Weiss, 2009; Kim *et al.*, 2018; Sivakumar *et al.*, 2018; Mittal *et al.*, 2019). Perturbation of expression of genes related to ECM components and remodelling factors has been shown to interfere with different processes involved in heart development, suggesting tight regulation of its spatiotemporal expression and turnover is essential during cardiac morphogenesis.

For instance, HA, the most common ECM component, has been shown to be one of the major constituents of the cardiac jelly (Lockhart *et al.*, 2011b) and its expression is conserved in the developing heart of different animal models (Camenisch *et al.*, 2000; Wirrig *et al.*, 2007; Grassini *et al.*, 2018). The development of an HA sensor in zebrafish (known as *ssNcan-GFP*) (De Angelis *et al.*, 2017) has allowed to follow HA deposition *live*, and multiple studies using the sensor have identified the presence of HA throughout zebrafish heart development (spanning from 24 to 120hpf), suggesting it is HA-rich (De Angelis *et al.*, 2017; Grassini *et al.*, 2018; Gunawan *et al.*, 2020; Derrick *et al.*, 2021).

Supporting the requirement for HA in cardiac morphogenesis, several studies in which Has2 was disrupted (directly or indirectly) have shown that HA plays multiple roles in different processes during heart morphogenesis, such as myocardial cell migration, heart looping and atrioventricular valve formation (Camenisch *et al.*, 2000; Lagendijk *et al.*, 2011, 2013).

Whilst disruptions in HA synthesis result in more profound heart defects, disruption in the synthesis of PGs or GAGs have shown defects mainly related to the formation of the AVC. Indeed, Walsh and Stainier identified a requirement for the *UDP-glucose 6-dehydrogenase* (*ugdh*), a synthetic enzyme involved in the synthesis of HA, HS and CS during looping morphogenesis. Loss of this component resulted in embryos that failed to pattern the AVC region correctly as a consequence of disrupted cell signalling within the cardiac tissues (Walsh and Stainier, 2001). Similarly, loss of *chsy1* (*chondroitin sulfate synthase 1*) resulted

in aberrant AVC patterning with loss of AVC constriction, together suggesting a functional requirement of PG during valvulogenesis (Peal *et al.*, 2009).

Aggrecan, recognised as the major CSPG in the articular cartilage, has been shown to be expressed in the epicardium and the mesenchyme of the AVC and OFT cushions in chick (Zanin *et al.*, 1999), suggesting that this PG plays an active role in valve and OFT development. Further confirming aggrecan's role in the maturation of the OFT, loss of *aggrecana* using morpholino oligonucleotides (MO) and CRISPR Cas9 mutagenesis in zebrafish disrupted the development of the OFT, resulting in embryos with aortic stenosis (Rambeau *et al.*, 2017).

Initial studies investigating the role of Versican in heart development identified that it, in conjunction with *bmp4*, is required for the specification of the zebrafish myocardium at the AVC (Mjaatvedt *et al.*, 1998). More recent studies have identified important roles in the deposition and remodelling of this PG in heart morphogenesis. Kim *et al.*, for instance identified the significance of proteolytic remodelling of the cardiac jelly for proper atrial chamber morphogenesis in mice. Failure of ECM degradation by the protease enzyme family ADAMTs resulted in enhanced atrial cardiomyocyte proliferation. Enhanced proliferation, in turn, contributed to a thickened atrial cardiac jelly, whereby excessive deposition of GAGs and core proteins (i.e. Versican) into the cardiac ECM impaired the elongation and polarisation of myocardial actin filaments in the atrium, resulting in disrupted atrial chamber expansion and morphology (Kim *et al.*, 2018). Mittal *et al.*, on the other hand, described the importance of versican expression in medaka heart morphogenesis. Medaka embryos lacking Versican exhibited arrest of cardiac development at the linear heart tube stage, with an absence of cardiac looping and no cardiac jelly or valves (Mittal *et al.*, 2019). Interestingly, these phenotypic characteristics are similar to those found in the hearts of Has2- and Versican-deficient mice (Yamamura *et al.*, 1997; Camenisch *et al.*, 2000; Hatano *et al.*, 2012), confirming the importance of these ECM components in the modulation of continued heart morphogenesis. Finally, supporting the role of proteoglycan aggregates as structural ECM components, HAPLN1-deficient mice exhibit mild structural malformations which are accompanied by decreased protein levels of Versican.

Together, these studies demonstrate that the cardiac ECM is a key component during cardiac morphogenesis, and that besides providing a structural role, its continuous deposition, remodelling and turnover are required to facilitate essential processes (e.g. looping, valvulogenesis, OFT maturation) in the development of a functional heart. A recently published comprehensive review discusses the requirement of these and some other ECM components in supporting heart morphogenesis in different animal models (Derrick and Noël, 2021).

6 HYPOTHESIS AND OBJECTIVES

Recent studies in the Noël lab have shown a conserved atrial-specific left-sided expansion of the zebrafish cardiac jelly before the heart tube undergoes looping morphogenesis (Fig 1.5) (Derrick *et al.*, 2021). Although other ECM asymmetries have been described at an analogous stage in chick (Taber and Perucchio, 2000; Männer *et al.*, 2008), the role of this regionalised expansion of cardiac jelly and its interaction with the surrounding tissues in the process of cardiac looping and in general during heart morphogenesis remains unknown. In light of the multiple roles that the ECM plays in organogenesis of the heart and other organs, I ***hypothesise that the regionalised differences observed in ECM expansion in the heart tube are required to provide tissue-intrinsic directional cues during cardiac morphogenesis***. Consequently, precise spatiotemporal regulation of the expression and turnover of the ECM components involved in that early expansion may be essential for normal embryogenesis.

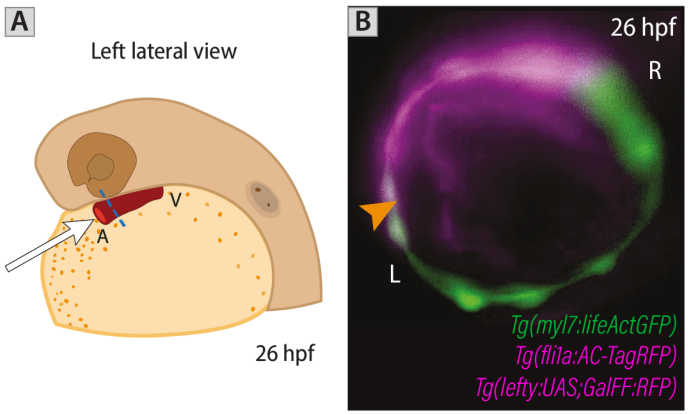

Fig 1.5. The ECM space between the myocardium and endocardium is expanded on the left side of the atrial heart tube.
A. Schematic of a zebrafish embryo showing the position and orientation of the heart tube at 26hpf. **B.** Optical cross-section through the blue dotted line in A of a *Tg(myl7:lifeActGFP; fli1a:AC-TagRFP; lefty:UAS; GalFF:RFP)* triple transgenic zebrafish heart tube (myocardium marked in green, endocardium and dorsal myocardium in magenta) identifies a left-side thickening of the ECM at early stages of development (orange arrow) (Derrick *et al.*, 2021).

Accordingly, the **main aim** of this thesis is to investigate the link between heart morphology and ECM dynamics in the developing zebrafish heart. This overarching aim will be broken down into the following objectives:

- Develop and establish an image analysis tool to segment and visualise the myocardium, endocardium **and** cardiac jelly of zebrafish hearts from high-resolution live images with state-of-the-art fluorescence microscopy.
- Develop and include within the tool 3D morphometric quantifications of the cardiac layers (myocardium, endocardium and cardiac jelly) and chambers (atrium and ventricle).
- Characterise early zebrafish heart development in 3D at early-, during- and post-looping stages.
- Characterise the cardiac ECM distribution dynamics during early zebrafish heart development.
- Characterise heart morphology in 3D during development in mutants with disrupted left-right patterning.
- Investigate the role of left-right patterning in ECM regionalisation.
- Identify possible ECM candidate genes driving the asymmetric expansion of the cardiac jelly.
- Using candidate-driven functional analysis, create promoter mutants of the candidate gene and interrogate its role in heart morphogenesis.

7 RATIONALE

Considering these hypothesis and objectives, throughout my PhD studies, I investigated the role of the cardiac ECM and its early asymmetric distribution in promoting zebrafish heart morphogenesis.

Initially, to precisely understand how the ECM drives morphogenesis, I needed to be able to describe comprehensively **in 3D** and **throughout development** *cardiac morphology* and *ECM-positioning* and use such information to link morphology and ECM dynamics to specific heart developmental processes. Consequently, I developed *morphoHeart*, a quantitative image analysis tool that allows the 3D segmentation of the heart layers -including the cardiac jelly- and quantification of heart morphology during development (Chapter 3). Using *morphoHeart,* I was able to characterise heart/chamber morphology and ECM distribution at early looping (between 34 and 36hpf), during looping and ballooning (between 48 and 50hpf) and post-looping or early maturing stages (between 72 and 74hpf) (Chapter 4). Having

characterised wild-type ECM dynamics throughout this time window, I moved on to investigate how wild-type ECM dynamics compare to embryos with defective L/R patterning (*spaw* mutants) (Chapter 4). Characterisation of wild-type embryos and *spaw* mutants combined with mRNA ISH analysis of interstitial ECM components allowed me to identify *hapln1a* as a candidate protein driving the regionalised cardiac jelly expansion. Finally, to investigate the role of Hapln1a in heart morphogenesis and ECM expansion, I generated *hapln1a* promoter mutants in which *hapln1a* transcription is prevented. 3D morphometric analysis of these mutants allowed me to identify the spatiotemporal requirement for this hyaluronan and proteoglycan link protein in heart morphogenesis (Chapter 5).

In summary, this work begins to define the role of an asymmetric cardiac ECM as a tissue-intrinsic mechanism of the heart driving asymmetric morphogenesis during cardiac development.

CHAPTER 2. MATERIALS AND METHODS

1 ZEBRAFISH HUSBANDRY

1.1 ZEBRAFISH STRAINS, HANDLING AND HUSBANDRY

All the experiments were performed at the University of Sheffield and conducted in accordance with UK Home Office Regulations under the Home Office Project Licenses 70/8588 and PA1C7120E held by Prof. Timothy Chico and Emily S. Noël, respectively. Adult zebrafish were fed twice a day and maintained in circulating water at 28.5°C, at a maximum density of one fish per 0.25L, and in a 14-hour day:10-hour night cycle. When adult fish were no longer required for future experiments, fish were euthanised by immersion in an overdose of Tricaine (MS222, overdose concentration: 1.33g/L). The following zebrafish lines were used in this work:

Table 2.1. Wild-type and transgenic zebrafish lines

Line	Fluorophore localisation	Reference / Notes
Wild-type (AB) / Wild-type (TL)	N/A	-
Tg(myl7:lifeAct:GFP)	Actin-tagged GFP in the myocardium	(Reischauer *et al.*, 2014)
Tg(fli1a:AC-TagRFP)^{sh511}	Actin-localised RFP in the endothelial cells	(Savage *et al.*, 2019)
Tg(-5.1myl7:DsRed2-NLS)	DsRed2 localised in the nuclei of myocardial cells	(Rottbauer *et al.*, 2002)
Tg(kdrl:Hsa.HRAS-mCherry)	mCherry labelling the membrane of endothelial cells	(Neil C. Chi *et al.*, 2008)
Tg(myl7:lck-EGFP)^{md71}	EGFP labelling the cytoplasm of cardiomyocytes (myocardium)	(Weber *et al.*, 2017)
Tg(myl7:Gal4; UAS:TFP)	TFP localised in the cytoplasm of cardiomyocytes producing Gal4	Generated in this study from an incross of *Tg(myl7:Gal4FF)* (Strate, Tessadori and Bakkers, 2015) and *Tg(UAS:TFP)* (Lagendijk *et al.*, 2017)
Tg(UAS:hapln1a, cryaa:CFP)^{sh584}	CFP in eye structures (lens and solid lens vesicle)	Generated in this study to mis-express *hapln1a. cryaa:CFP* was used to screen for embryos in which the *UAS:hapln1a* construct was present

Table 2.2. Mutant zebrafish lines

Line	Description of mutation	Reference
hapln1a^{promΔ241} (allele designation *hapln1a*^{sh580})	Excision of 241bp removing the *hapln1a*'s annotated promoter* and the initiating ATG (see Fig 5.5)	Generated in this study (Derrick *et al.*, 2021)
hapln1a^{promΔ187} (allele designation *hapln1a*^{sh611})	Excision of 187bp removing part of the *hapln1a*'s annotated promoter* and the initiating ATG (see Fig 5.5)	Generated in this study (Derrick *et al.*, 2021)
spaw^{t30973}	Single base pair change in the gene sequence that causes a Cys→Phe substitution at residue 401 of the carboxyl terminus of the mature TGFβ domain in the Spaw protein	(Noël *et al.*, 2013)

* Annotated promoter of *hapln1a* was identified using the Eukaryotic Promoter Database (Dreos *et al.*, 2017)

[*Note#2.1:* For simplification, the transgene allele numbers will be stated only in this Materials and Methods section.]

1.2 Embryo Collection and Staging

Embryos were collected from individually pair-mated fish within the hour of breeding. Fertilised embryos were staged according to morphological criteria (Kimmel *et al.*, 1995) and maintained in E3 media* at 28.5°C until required. Zebrafish embryos start to present pigmented cells from about 24hpf. To inhibit melanin production post 24hpf and improve signal detection, embryos that were going to be used for *in situ* hybridisation, immunohistochemistry or imaged live (in the light-sheet microscope) were transferred to E3+PTU* (Karlsson, von Hofsten and Olsson, 2001).

[*Note#2.2:* Henceforward, the composition of the solutions identified with * is described in Section 12 of this chapter.]

1.3 Fixation of Embryos

Prior to fixation, embryos remaining inside their chorion were dechorionated by hand using a dissecting microscope and Jewelers forceps (Dumont No.5). Embryos were fixed overnight at 4°C in 4% PFA* for mRNA *in-situ* hybridisation or 4% PFA+Sucrose* for immunostaining. Within three days after fixation, samples were washed into PBSTw* and transferred by a series of washes from PBSTw* to 100% Methanol (MeOH) [Fisher Scientific, M/4056/17] for long-term storage at -20°C.

When fixing embryos at shield stage (6hpf) or younger, to maintain embryonic structure, embryos were initially fixed inside their chorion overnight in 4% PFA, washed 3 times in PBSTw* for 5min at room temperature, manually dechorionated, and then serially washed into 100% MeOH for long term storage.

1.4 Embryo Rehydration

Prior to starting an *in situ* hybridisation or immunohistochemistry protocol, samples stored in MeOH at -20°C were serially rehydrated into PBSTw*.

1.5 Micro-injections into 1-Cell Stage Embryos

The injection needles used to micro-inject embryos were produced from Borosilicate Glass Capillaries [World Precision Instruments] using a P-1000 laming/Brown Micropipette Puller. On the day of the injections, needles were loaded with the injection solution using micro-loader tips and mounted into the needle holder on the micromanipulator of a PV820 Pneumatic PicoPump [World Precision Instruments]. To calibrate the volume of the solution being injected and ensure it is consistent for each embryo, the tip of the mounted needle was first gently cut off under a dissecting microscope using Jewelers forceps. With an open yet sharp needle tip, the needle was immersed into a drop of Mineral Oil [Sigma M5904] on a Stage Micrometer [Agar Scientific L4201]. Small amounts of the solution were injected into the Mineral Oil, and the size of the droplet was calibrated by adjusting the pressure and time settings of the microinjector until a droplet of 0.5nL was obtained.

Having calibrated the needles, embryos at 1-cell stage collected from pair-mating were carefully loaded and lined up in the troughs of a 1.5% agarose gel mould* using a transfer pipette and covered with E3 media* to prevent them from drying up. Using the micromanipulator to move the needle in and out of each embryo 1nL of injection solution was injected into each embryo's yolk. Following injections, embryos were transferred into a new dish with fresh E3 media and incubated at 28.5°C. Within the next hour of injection, embryos that appeared unfertilised or dead were discarded.

[*Note#2.3:* Details about the injection solutions used in this thesis are given in Sections 4.1.4].

2 MOLECULAR TECHNIQUES

2.1 ISOLATION OF TOTAL RNA FROM WILD-TYPE EMBRYOS

To isolate total RNA from wild-type embryos, 50 dechorionated embryos at the relevant stage were placed into an Eppendorf with TriReagent [Invitrogen AM9738] and homogenised with syringe and needles (wide and then fine). Following homogenisation, one-fifth of the homogenised volume of chloroform was added to the sample and mixed thoroughly. After a 5min incubation period at room temperature, sample was ultra-centrifuged at maximum speed (15,000rpm) and 4°C for 15min, resulting in a sample with two separated phases. The aqueous clear (top) phase was then moved to a new Eppendorf, where an equal volume of Propan-2-ol (Isopropanol) [Sigma I9516] was added, and vortex mixed. Following an incubation period of 15min at room temperature, a pellet containing the RNA was obtained by ultra-centrifuging at maximum speed (15,000rpm) and 4°C for 15min. The resulting pellet was washed twice with 75% Ethanol [Fisher Scientific, E/0600DF/17] and left to air dry at room temperature. The dry pellet was then resuspended in 30μL of double distilled water (DDW, RNAse free water), its concentration measured using a NanoDrop Spectrophotometer [ND-1000] and then diluted to 500ng/μL.

2.2 GENERATION OF CDNA

To generate cDNA by reverse transcription out of the isolated RNA, an initial mix containing RNA, dNTPs, OligodT primers [Invitrogen 12577-011] and MQ Water (Table 2.3) was prepared and incubated at 65°C for 5min to anneal the primers to the RNA template. Following the incubation period, the reverse transcription reaction mix (Table 2.4) was added and incubated at 42°C for 2min. 2μL of Superscript Reverse Transcriptase IV [ThermoFisher 18090010] was subsequently added, and incubated first for 50min at 42°C, and then for 15min at 70°C. To degrade the RNA template, 2μL of RNase H [ThermoFisher EN0201] was added and incubated at 37°C for 20min. The resulting cDNA was then diluted with 40μL of DDW and the concentration measured using a NanoDrop Spectrophotometer for reference.

Table 2.3. RT-OligodT Mix

Reagent	Volume (16μL Reaction)
2μg RNA	X μL
10mM dNTPs	2 μL
OligodTs (500ng/μL]	2 μL
MQ Water	12-X μL

Table 2.4. Reverse Transcription Reaction Mix

Reagent	Volume
5X First Strand Buffer	8 μL
25mM $MgCl_2$	8 μL
DTT (0.1mM)	4 μL
RNase Out	2 μL

2.3 DNA EXTRACTION

To extract the gDNA from zebrafish embryos, single dechorionated embryos were transferred into individual PCR wells containing 50μL of PK+SEL* (Proteinase K + SEL Buffer). Extraction of the gDNA was carried out by incubating the samples at 60°C for 1hour and then at 95°C for 15min to denature the Proteinase K. 1μL of the resulting gDNA was used as a template for PCR amplification (Section 2.4, 2.5 and 4.1.5).

2.4 Polymerase Chain-Reaction (PCR)

2.4.1 Primer Design

Primers were designed to amplify a region within the gDNA or cDNA of the zebrafish gene of interest using Primer 3 (http://primer3.ut.ee/). The top pairs of primers were assessed for their specificity using the *e!Ensembl* BLAST tool searching against *Danio rerio*, and final primers were selected from those that produced only one specific band. Once designed, primers were ordered from Integrated DNA Technologies (IDT), reconstituted at 100μM using MQ Water and stored at -20°C.

[*Note#2.4:* If designing primers for generating *in situ* hybridisation probes, primers were designed so that the amplified cDNA region had a length between 700 and 1000 base-pairs (bp)].

[*Note#2.5:* If designing primers to genotype a genetic deletion/mutation introduced into the embryos by CRISPR-Cas9, primers were designed so that they bind in a region upstream (forward primer) and downstream (reverse primer) region to the gRNA guide(s) used to generate the mutation].

2.4.2 PCR Using BioMix Red

To amplify a specific segment of the zebrafish DNA either to genotype individual embryos or generate *in situ* hybridisation probes, a standard PCR with a final volume of 10μL (or 60μL for Sanger sequencing, Section 2.5) using BioMix Red reaction mix [BiolineBIO25006] (Table 2.5) was carried out. The thermocycling programme was run in a Bio-Rad Thermocycler (Table 2.6) [Bio-Rad T100], in which the annealing temperatures and number of cycles were adjusted according to primers and genotyping protocol.

[*Note#2.6:* Tables 2.5 and 2.6 describe a predefined BioMix Red PCR mix and thermocycler program. To increase the yield of the PCR when genotyping specific mutations, primer concentrations and thermocycling programs were adjusted and these details are provided in Section 5].

Table 2.5. BioMix Red PCR Mix

Reagent	Volume (10μL Reaction)
cDNA / gDNA	1 μL
Forward (Fwd) Primer	0.5 μL
Reverse (Rev) Primer	0.5 μL
BioMix Red	5 μL
MQ Water	3 μL

Table 2.6. BioMix Red PCR Programme

Step	Temperature	Time
1	95°C	3min
2	95°C	30s
3	Annealing T° (55°C - 58°C)	30s/kb
4	72°C	1min
5	Repeat steps 2-4 29 times (30 in total)	
6	72°C	5min
7	5°C	5min

2.5 Sanger Sequencing

To sequence PCR products, a PCR reaction with a final volume of 60μL using BioMix Red (see Sections 2.4.2, 5) was carried out and purified using the QIAGEN PCR Purification kit [QIAGEN 28016]. Purified samples were then sent to sequence by Sanger at either the Sheffield University Genomics Core Facility (Sept 2018-Dec 2019) or Genewiz UK (Dec 2019-2022).

2.6 *IN-SITU* HYBRIDISATION (ISH) PROBE SYNTHESIS

To generate *in situ* hybridisation probes using polymerase chain reaction the outline described in Table 2.7 was followed.

Table 2.7. Outline for RNA probe synthesis

Step	Process Name [Methods Section(s)]	Process description	Start (main input reagents)	End (final products)
1	Design and order primers [Section 2.4.1]	Design primers to amplify the cDNA region to which the probe will bind	Gene of interest	Primers
2	Extract RNA [Section 2.1]	Extract/isolate RNA from zebrafish embryos at the stage where the gene of interest is expressed	Zebrafish Embryos	Isolated RNA
3	Generate cDNA [Section 2.2]	Generate cDNA out of the isolated RNA	Isolated RNA	cDNA
4	PCR Amplification [Section 2.4.2]	Using PCR, amplify region of interest utilising cDNA as a template and the designed primers (Step 1)	cDNA	Amplified cDNA specific to the gene of interest
5	TOPO-TA cloning and Bacterial Transformation [Section 2.6.1]	Clone the cDNA of interest into a plasmid, transform into TOP10 cells	Amplified cDNA specific to the gene of interest	TOP10 cells containing cloned plasmid with cDNA specific to the gene of interest
6	Extract plasmid [Section 2.6.1] and Sanger sequence	Confirm successful transformation, using colony PCR. Midi-Prep positive colonies and send to sequence to determine cDNA orientation within plasmid	TOP10 cells containing cloned plasmid with cDNA specific to the gene of interest	Circular DNA of cloned plasmid containing cDNA
7	Linearise plasmid [Section 2.6.2]	Digest plasmid to linearise it	Circular DNA of cloned plasmid containing cDNA	Linearised DNA (plasmid+gene cDNA)
8	Transcription and Clean-up [Section 2.6.2]	Transcribe and DIG-label the linearised plasmid, clean-up the final probe	Linearised DNA (plasmid+gene cDNA)	ISH Probe

2.6.1 TOPO-TA CLONING AND BACTERIAL TRANSFORMATION

TOPO-TA cloning was used to ligate the amplified cDNA into a plasmid and transform the resulting plasmid into bacterial cells. Prior to cloning, to determine the concentration of the PCR product, 5μL of the amplified cDNA (resulting PCR product from Step 4, Table 2.7) was analysed using electrophoresis in a 1% TAE* gel and the remaining volume was diluted accordingly with MQ Water. The diluted PCR product was then ligated into pCRII-TOPO [ThermoFisher 450640] (Table 2.8) at room temperature for 5 min. Following this incubation period, the mix was kept at 4°C until required.

Chemically competent TOP10 cells [ThermoFisher C404003] were thawed on ice and subsequently transformed by adding and gently mixing 1μL of the TOPO-TA reaction mix (Table 2.8). After incubation for 30min on ice, TOP10 cells were heat-shocked at 42°C for 30s and incubated on ice for 2min before adding 250μL of SOC medium [Sigma S1797]. Transformed cells were placed horizontally in a shaking incubator at 200-300rpm and 37°C for 90min, pelleted at low speed (3,000rpm) for 5min at room temperature and subsequently resuspended in 30μL of the SOC supernatant. Resuspended cells were plated on LB Agar [Sigma L7025] plates containing IPTG (0.1M) [Merck I6758], X-Gal (20mg/mL) [ThermoFisher R0404] and either Kanamycin [Sigma K1377] (50μg/mL), or Ampicillin [Sigma A0166] (100μg/mL) for blue-white selection, and incubated in a static incubator at 37°C overnight.

Table 2.8. TOPO-TA Reaction Mix

Reagent	Volume (3μL Reaction)
Diluted BioMix PCR Product▲	1 μL
Salt solution	0.5 μL
pCRII-TOPO	0.5 μL
MQ Water	1 μL

▲ Depending on the concentration of the PCR product, the volume added to the mix can vary. MQ Water volume is modified to obtain a final 3μL reaction.

To confirm successful ligation of the PCR product into the plasmid, white colonies were resuspended individually in 10μL of MQ Water. Half of the volume (5μL) was used as a template for colony PCR using the primers originally used to amplify the cDNA of the gene of interest (Step 1 and 4, Table 2.7) (Table 2.9 and 2.10). Positive colonies were revealed by running 10μL of the colony PCR product in a 1% TAE* gel. The remaining 5μL of resuspended positive colonies were used to inoculate 50mL of LB Broth [Sigma L7275] with relevant antibiotic and grown overnight at 37°C in a shaking incubator [New Brunswick Scientific, Innova 44] at 200-300rpm.

Isolation of the plasmid containing the inserted cDNA sequence was performed using a QIAGEN Midi-Prep kit [QIA 12143]. The concentration of the resulting plasmid was measured using a NanoDrop Spectrophotometer and diluted to a final concentration was 1μg/μL. The final plasmid was sequenced using M13 forward and reverse primers to identify the orientation of the insert in the vector and select the enzyme and transcription-polymerase to use in the linearisation and transcription of the anti-sense probe, respectively.

Table 2.9. Colony PCR mix

Reagent	Volume (20μL Reaction)
Colony resuspended in MQ Water	5 μL
Fwd Primer (10μM)	0.4 μL
Fwd Primer (10μM)	0.4 μL
BioMix Red	10 μL
MQ Water	4.2 μL

Table 2.10. Colony PCR Programme

Step	Temperature	Time
1	94°C	2min
2	94°C	20s
3	60°C (drops 1°C per cycle)	20s
4	72°C	45s
5	Repeat steps 2-4 9 times (10 in total)	
6	94°C	20s
7	50°C	20s
8	72°C	45s
9	Repeat steps 6-8 14 times (15 in total)	
10	72°C	3min
11	10°C	5min

2.6.2 RIBOPROBE SYNTHESIS AND CLEAN-UP FOR ISH

Following plasmid extraction, dilution and sequencing, the mRNA template for transcription of the *in situ* probe was generated by digesting overnight 10μg of plasmid DNA in a 50μL reaction. To confirm linearisation, a 1:10 dilution of undigested plasmid DNA and a 1:5 dilution of linearised plasmid were resolved on a 1% TAE* gel. The concentration of the linearised plasmid was assessed using a NanoDrop Spectrophotometer. If the measured concentration was at least 200ng/μL, the template was purified using a QIAGEN PCR Purification kit [QIAGEN 28016] and eluted into 30μL of MQ Water.

Following purification, transcription reaction mix (Table 2.11) was set up using 1μg of the linearised and purified template and digoxigenin-UTP [Roche 11277073910] to label the RNA probe and incubated at 37°C for 2 hours. After incubation, to remove the DNA template, 3μL of TURBO DNase [Invitrogen AM2238] was added to the mix and incubated at 37°C for 30min. RNA probe was recovered using Ammonium Acetate precipitation and ultracentrifugation at maximum speed (15,000rpm) for 15min at 4°C. The final pellet was resuspended in 10-20μL of DDW, and to confirm RNA integrity 1:5 dilution of the RNA was resolved by gel electrophoresis.

Table 2.11. Transcription Reaction Mix

Reagent	Volume (20μL Reaction)
10X Reaction Polymerase Buffer	2 μL
Digoxigenin-UTP mix	2 μL
Linearised and Purified DNA [1μg]	X μL
RNA Polymerase▲	2 μL
RNAse Out	1 μL
MQ Water	13-X μL

▲ RNA transcription polymerase [New England BioLabs, SP6: M0207S, T7: M0251S] was chosen according to insert orientation in the vector.

2.6.3 PROBES GENERATED AND USED FOR THIS STUDY

Information regarding the primers, vectors, enzymes, and transcription polymerases used to generate new mRNA *in-situ* hybridisation probes are detailed in Table 2.12. For probes generated by others, information concerning the enzymes and transcription polymerases used is described in Table 2.13.

Table 2.12. Probes generated for this work

Target gene	Primers (→ : Fwd, ← : Rev)	Vector	Enzyme / Transcription Polymerase ▲	Plasmid No. ❖
vcana (E1-E4)	→ GTCAGTGGCTTGTTGTCTGG ← CAGCCATAATCACAGCGGTC	pCRII-TOPO	NotI / SP6	146
vcana (E9-E11)	→ CAGCCGGACAGTTTCTTCTC ← TGGTGTCTTCGTCTGTGTACA	pCRII-TOPO	SpeI / T7	216

▲ Linearisation Enzyme [New England BioLabs] / Polymerase used for Transcription.
❖ Noël Lab Databases

Table 2.13. Probes used in this worked and generated by others

Target gene (*previous name*)	Enzyme / Polymerase▲	Plasmid No.❖	Made by / Reference (if applicable)
acana	NotI / SP6	209	C. Derrick
acanb	NotI / SP6	210	C. Derrick
bmp4	EcoRI / T7	54	(Chen *et al.*, 1997)
cemip	SpeI / T7	183	P. Paizaki
cemip2	NotI / SP6	184	P. Paizaki
chsy1	BamHI / T7	105	C. Derrick
hapln1a	SpeI / T7	11	E. Noël (Derrick *et al.*, 2021)
hapln1b	BamHI / T7	74	E. Noël
has2	NotI / T3	53	C. Derrick (Derrick *et al.*, 2021)
hyal1	NotI / SP6	186	P. Paizaki
hyal2a	NotI / SP6	187	P. Paizaki
hyal2b	NotI / SP6	188	P. Paizaki
hap2b	NotI / SP6	185	P. Paizaki
myl7 (cmlc2)	NotI / T7	143	(Yelon, Horne and Stainier, 1999)
myh6 (amhc)	PstI / T7	2	Bakkers Lab
myh7l (vmhc)	NotI / T7	81	Bakkers Lab
nkx2.5	EcoRI / T7	58	Bakkers Lab
notch1b	HindIII / T7	142, 145	Rob Wilkinson, (unpublished)
nppa (anf)	NotI / SP6	57	(Berdougo *et al.*, 2003)
spaw	SpeI / T7	88	Michael Rebagliati (Long, Ahmad and Rebagliati, 2003)
tbx2b	NotI / SP6	82	C. Derrick
tbx5a	NotI / SP6	83	C. Derrick
vcanb	SacII / SP6	T. Whitfield's Lab	(Geng *et al.*, 2013)

▲ Linearisation Enzyme [New England BioLabs] / Polymerase used for Transcription.
❖ Noël Lab Database

3 Other Wet-Lab Techniques

3.1 mRNA *in-situ* Hybridisation

3.1.1 3-Day Protocol (based on Thisse and Thisse, 2008)

On day 1, rehydrated embryos (Section 1.4) were washed twice in PBSTw* and permeabilised at room temperature with PK+PBSTw* (Proteinase K in PBSTw) with concentration of the permeabilisation solution and length of incubation determined according to embryonic stage (Table 2.14). After incubation, embryos were rinsed with PBSTw, refixed in 4% PFA* or 10% Buffered Formalin [VWR Q-Path Chemicals 11699404] for 20min at room temperature and pre-hybridised in Hyb+* at 70°C for at least 1hour.

Following pre-hybridisation, Hyb+* was removed from the samples, and probes diluted in Hyb+ (1:200) (Table 2.12, 2.13) were added to the embryos and incubated overnight at 70°C.

Table 2.14. Timings for PK-PBSTw treatment

Stage (hpf)	0-10	10-19	19-22	22-24	26	30	36	48-50	55-72	72-96	96-120
Time (min)	0	1	3	5	6	8	10	12	13	15	20
PK+PBSTw concentration	10µg/mL										20µg/mL

On the next day (day 2), probes were removed from the samples, embryos were briefly washed with Hyb-*, serially washed from 100% Hyb- into 2xSSCT*, and subsequently washed twice in 0.2xSSCT* (all at 70°C). Following this step, samples were washed stepwise from 0.2xSSCT* into PBSTw, washed twice in PBSTw, and blocked in Blocking Buffer* for at least 2hours (all at room temperature). After the blocking period, Blocking Buffer was removed, embryos were incubated with pre-incubated Anti-DIG-AP conjugated antibody* overnight at 4°C and protected from the light for the remainder of the protocol.

On day 3 samples were washed at room temperature a minimum of 8 times in PBSTw for a period of 2-3hours. Following these washes, samples were washed three times in AP Staining Buffer* (AP: Alkaline Phosphatase) and incubated with AP Staining Solution* at room temperature. When sufficiently developed staining was identified upon visual inspection, embryos were rinsed three times in PBSTw, fixed in 4% PFA or 10% Buffered Formalin overnight at 4°C, and then stepwise washed into 100% MeOH for long term storage at 4°C.

[*Note2.7:* Throughout all the described steps in the protocol, samples were gently agitated to ensure all embryos were homogeneously exposed to each solution].

Generation of the pre-incubated anti-DIG-AP antibody was performed by homogenising embryos at multiple developmental stages in PBSTw with a syringe and needle(s). Homogenised sample was then incubated with Anti-Digoxigenin-AP [Roche 11093274910] for at least 1hour at room temperature. Sample was then ultra-centrifugated at maximum speed (15,000rpm) for 15min at 4°C. The resulting aqueous supernatant, containing the pre-incubated antibody, was then transferred to a new Eppendorf into which Sodium Azide [Sigma S8032] was added to obtain a final concentration of 0.02%. Pre-incubated anti-DIG-AP antibody was stored at 4°C until required.

3.1.2 IMAGING ISH

Following an *in situ* hybridisation protocol, embryos were imaged in Murray's Medium (BBA*) on an Olympus BX51 Microscope. If genotyping of the embryos was required, the steps described in Section 5 were followed after the acquisition of the images.

3.2 IMMUNOHISTOCHEMISTRY (IHC)

3.2.1 PROTOCOL

On day 1, rehydrated embryos (Section 1.4) were washed three times into PBSTr* and blocked in IHC-Blocking Buffer* for at least an hour at room temperature. Following this, IHC-Blocking Buffer was removed and replaced with primary antibody solution (Table 2.15) at the required concentrations (Table 2.16) and incubated overnight at 4°C. On the next day, after removal of the solution containing the primary antibodies, samples were extensively washed in PBSTr for 2-3hours and incubated with the secondary antibody solution (Table 2.15) at the required concentrations (Table 2.17) overnight at 4°C and exposure to light was prevented for the remainder of the protocol. On day 3, following removal of the solution containing the secondary antibodies, embryos were extensively rinsed in PBSTr at room temperature and stored at 4°C until mounting.

[*Note2.8:* Throughout all the described steps in the protocol, samples were gently agitated to ensure all embryos were homogeneously exposed to each solution].

Table 2.15. Primary/Secondary Antibody Solution

Reagent	Volume (~200µL per sample)
IHC-Blocking Buffer	200 µL
DMSO (Final concentration 1%)	2 µL
Primary Antibody #1 / Secondary Antibody #1	see Tables 2.16, 2.17 for concentration
Primary Antibody #2 / Secondary Antibody #2	
Primary Antibody #... / Secondary Antibody #...	

3.2.2 Antibodies Used

Information regarding the primary and secondary antibodies used in this thesis are detailed in Tables 2.16 and 2.17.

Table 2.16. Immunohistochemistry Primary Antibodies

No.	Antigen	Species	Description	Dilution	Source or Reference
1	α-CT3	Mouse	Cardiac troponin T in the myocardium (Stored at 4°C)	1:100	Developmental Studies Hybridoma Bank (DSHB) CT3
2	α-Dm-grasp	Mouse	Cell membranes of cardiomyocytes and AV canal endocardial cells (Stored at 4°C)	1:100	DSHB # ZN-8 (Beis *et al.*, 2005)
3	α-DsRed	Rabbit	Boost DsRed2 signal (Stored at -20°C)	1:200	Takara Bio Clontech #632496
4	α-GFP	Chicken	Boost GFP signal (Stored at -20°C)	1:1000	Aves Labs #GFP-1010
5	α-Hapln1a	Rabbit	Zebrafish Hapln1a (targeted amino acids 117-134: DGMNDMTLEVDLEVQGKD) (Stored at -20°C)	1:100	Proteintech (Derrick *et al.*, 2021)
6	α-s46	Mouse	Atrial myosin heavy chain (Stored at 4°C)	1:100	DSHB # S46 (Stainier and Fishman, 1992)

Table 2.17. Immunohistochemistry Secondary Antibodies (Dilution 1:200)

No.	Conjugated Fluorophore	Species	Raised Against	Source
1	Cy2	Donkey	Chicken	Jackson ImmunoResearch #703-225-155
2	Cy3	Goat	Rabbit	Jackson ImmunoResearch #111-165-003
3	Cy5	Goat	Mouse	Jackson ImmunoResearch #115-175-166
4	Cy5	Goat	Rabbit	Jackson ImmunoResearch #111-175-144

3.2.3 Imaging Immunostainings

Following immunohistochemistry, individual embryos were dissected under a dissecting microscope in PBSTr and mounted using VectaShield [Vector Laboratories] between a coverslip [Menzel-Gläser 15787582] and a glass slide [VWR ROTHH870.1]. Mounted samples were stored at 4°C until required. Using a 40X oil immersion lens, embryos were imaged on Zeiss LSM880 AiryScan Confocal at the Wolfson

Light Microscopy Facility, University of Sheffield. If genotyping of the embryos was required, following image acquisition, the steps described in Section 5 were carried out.

4 TECHNIQUES TO INVESTIGATE GENE-FUNCTION

4.1 CRISPR-CAS9

Recent genome editing techniques such as CRISPR-Cas9 facilitate specific targeted mutagenesis to generate KO of genes aiding the interrogation of gene function (Hwang *et al.*, 2013; Liu *et al.*, 2017, 2019). The methodology used in this thesis to generate *hapln1a* promoter mutants, with the aim of interrogating the role of this gene in zebrafish cardiac morphogenesis will be described next.

4.1.1 GUIDE DESIGN FOR PROMOTER MUTATIONS

After having identified the annotated promoter of *hapln1a* using the Eukaryotic Promoter Database (https://epd.epfl.ch//index.php) (Dreos *et al.*, 2017), guide RNAs (gRNAs) targeting the deletion of the region comprising the identified promoter and the initiating ATG were designed using CHOPCHOP v3.0 (http://chopchop.cbu.uib.no/) (Labun *et al.*, 2019) and based on danRer11/GRCz11 (Cunningham *et al.*, 2022) assembly of the zebrafish genomic DNA. Suitable crRNA sequences were selected based on maximal efficiency and minimal off-targets, identified in CHOPCHOP in yellow colour. Custom crRNAs at 5nM and standardised tracrRNA at 5nM were ordered from Merck/Sigma with HPCL purification and reconstituted and stored as described in Section 4.1.2 [tracrRNA: TRACRRNA05N-5NMOL].

The following crRNA guides were designed and used in this work:

Table 2.18. CRISPR-Cas9 gRNAs used in this study▲

No.	Target gene	crRNA sequence (PAM) (Direction, → : Fwd, ← : Rev)	Primers to test gRNA efficiency (Direction, → : Fwd, ← : Rev)
1	*hapln1a (pre-promoter)*	→ GATGATTGCTCTGTTTTCTG(TGG)	→ EN281: ACATTTTGCATGCCCTCGAA ← EN282: TGCATCCTGGACCTTCATTCA
2	*hapln1a (post-ATG)*	→ TCGTCTCTCTCTAAGGGGAG(GGG)	

▲ All gRNAs were designed to create stable mutant lines, targeting the template strand of the gene
❖ Noël Lab Database

4.1.2 crRNA AND tracrRNA RECONSTITUTION AND STORAGE

The protocol used to reconstitute crRNA and tracrRNA pellets (both at an original concentration of 5nM) is described in the diagram below (Fig 2.1). Of note, throughout the reconstitution protocol, all samples were kept on ice.

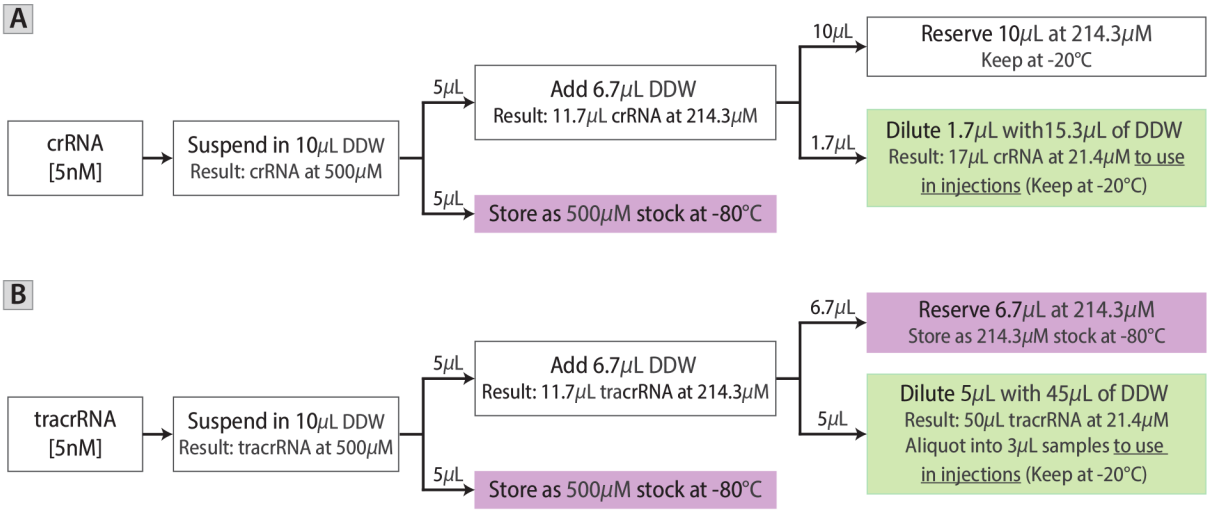

Fig 2.1. crRNA and tracrRNA reconstitution and storage.
A-B. Protocol followed to reconstitute and store crRNA (A) and tracrRNA (B) pellets into desired concentrations for CRISPR-Cas9 injections. Green boxes highlight the solutions at the concentrations used for injections, while purple boxes the solutions that were stored as stocks at -80°C.

4.1.3 Cas9 Protein Reconstitution and Storage

Cas9 protein (*S. pyogenes*) used for CRISPR Cas9 mutagenesis was ordered from NEB (20μM) [NEB M0386T] and diluted 1:3 with NEB Diluent B [NEB B8002S], resulting in a stock concentration of 6.67μM. To avoid contamination and ease set-up of injections, the stock solution was aliquoted and stored at -20°C until required.

4.1.4 Generation of Stable Zebrafish Mutant Lines

The promoter region of zebrafish *hapln1a* was targeted by injecting two-sequence-specific crRNAs (Table 2.18, No. 1 and 2) co-injected at an equimolar concentration with tracrRNA [TRACRRNA05N-5NMOL], and Cas9 Protein (Table 2.19) in a 1nL volume into the yolk of a 1-cell stage embryos obtained from an incross of *Tg(myl7:lifeActGFP)* (see Section 1.5 for details related to micro-injection method).

Table 2.19. CRISPR Cas9 injection solution

Reagent	Volume (6μL Reaction)
gRNA #1 (at 21.4μM)	1 μL
gRNA #2 (at 21.4μM)	1 μL
tracrRNA (at 21.4μM)	2 μL
Cas9 Protein (at 6.67μM)	1 μL
Phenol Red [Sigma P0290]	1 μL

The efficiency of the mutagenesis was assessed by extracting (Section 2.3) and amplifying individually the DNA of a subset of injected embryos at 1dpf using primers that were designed to bind to the region upstream of the first crRNA (i.e. Table 2.18, *hapln1a* EN281) and downstream of the second crRNA (Table 2.18, *hapln1a* EN282). Resulting PCR products were analysed by gel electrophoresis on 4% TBE* gels where the presence of PCR heteroduplexes indicated successful targeted mutagenesis. If mutagenesis was successful, a subset of the injected embryos was raised to adulthood (F0 generation) and, at about 3 months of age, screened by outcrossing to wild-type embryos to identify founders transmitting a suitable

germline mutation (using the same genotyping process previously described). PCR products with suitable deletions appraised by gel electrophoresis were sent to sequence by Sanger (Section 2.5), and the resulting sequence analysed to identify the nature of the lesion. F0 founders transmitting the suitable mutations were outcrossed to *Tg(myl7:LifeActGFP); Tg(fli1a:AC-TagRFP)* double transgenic wild-types to establish a stable F1 line. At 3 months of age, gDNA was extracted from F1 fish using fin biopsies (also known as fin-clips) to identify fish carrying the mutation in heterozygosity using PCR amplification and gel electrophoresis. To confirm the mutation, PCR products were analysed by Sanger sequencing (Section 2.5). F2 and stable lines were established by raising an outcross of the previous established generation (i.e. confirmed heterozygous carriers in F1 to generate F2, or in F2 to generate F3…) with wild-type embryos (i.e. ABs or *Tg(myl7:LifeActGFP); Tg(fli1a:AC-TagRFP)* double transgenic).

Embryos obtained from an incross of the F2 or F3 generation were used for all the experiments included in this thesis.

5 GENOTYPING PROTOCOL OF MUTANT LINES

To genotype embryos upon experiment completion (i.e. ISH - Section 3.1, immunohistochemistry imaging - Section 3.2, heart rate analysis - Section 7, light-sheet imaging -Section 8), gDNA of single embryos was extracted (Section 2.3) and 1μL of the resulting gDNA used as a template for PCR.

The primers, BioMix Red PCR Mix and thermocycling programmes used for each of the mutant lines used are described in Tables 2.20, 2.21, and 2.22, respectively. Gel electrophoresis was subsequently used to resolve differences in size of PCR product and identify the presence of a mutation either in heterozygosity or homozygosity (see specific details about gel electrophoresis for each mutation in Table 2.24 and Fig 2.2). In some cases, prior to gel electrophoresis, PCR products were digested and resulting fragments analysed on a high concentration agarose gel to aid the identification of mutations (Table 2.23, 2.24, and Fig 2.2C).

Table 2.20. Primers used for Genotyping Mutations

Mutation	Primers (→ : Fwd, ← : Rev)	Product size (wildtype / mutant)
hapln1a^{promΔ187}	→ EN281: ACATTTTGCATGCCCTCGAA ← EN282: TGCATCCTGGACCTTCATTCA	480bp / 293bp
hapln1a^{promΔ241}		480bp / 239bp
spaw▲	→ EN271: GGACATGATCGTGGAGGAGT ← EN272: TCAGGAGTCGCCACAGTAGA	258bp / ~239bp

▲ Primers introduce an *EcoRI* restriction site into the mutant strand.

Table 2.21. BioMix Red PCR Mix

Reagent	Volume (10µL Reaction)	
	hapln1a	*spaw*
gDNA	1 µL	1 µL
Fwd Primer (10µM)	0.5 µL	0.2 µL
Rev Primer (10µM)	0.5 µL	0.2 µL
Biomix Red	5 µL	5 µL
MQ Water	3 µL	3.6 µL

Table 2.22. BioMix Red PCR Programme

Step	Time	Temperature	
		hapln1a	*spaw*
1	3 min	95°C	95°C
2	30 s	95°C	95°C
3▲	30 s/kb	55°C / 56°C	53°C
4	1 min	72°C	72°C
5	Repeat steps 2-4:	29 times	45 times
6	5 min	72°C	72°C
7	5 min	5°C	5°C

▲ Annealing temperature varies depending on primers

Table 2.23. Digest for *spaw* PCR Product

Reagents	Volume (10µL Reaction)
PCR Product	8 µL
Enzyme (*EcoRI-HF*)	0.2 µL
Cut Smart	1 µL
MQ Water	0.8 µL

Table 2.24. Gel electrophoresis used for Genotyping Mutations

Mutation	Digest needed after PCR?	Gel Electrophoresis Details (Gel type, Voltage, Time, Ladder used)	Reference Fig
hapln1a^{promΔ187}	No	1% TAE, 110V, 35min, 50bp	Fig 2.2A
hapln1a^{promΔ241}			Fig 2.2B
spaw	Yes (see Table 2.23)	3% TAE, 110V, 35min, 50bp	Fig 2.2C

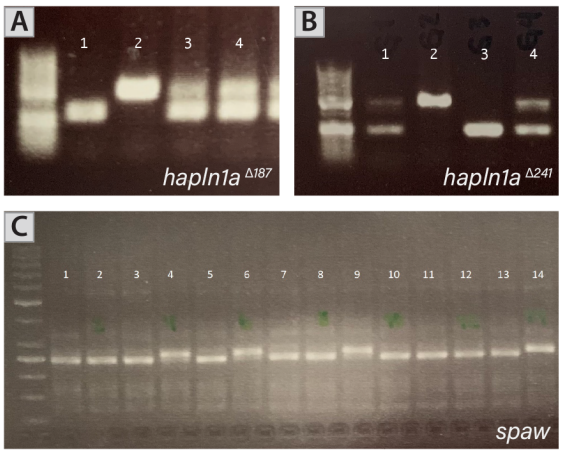

Fig 2.2. Genotyping mutations using gel electrophoresis.
A-C. Gel electrophoresis of gDNA extracted from an incross of *hapln1a*$^{Δ187/+}$ (A, sample 1-homozygous mutant, 2-wild-type, 3,4-heterozygous mutant), *hapln1a*$^{Δ241/+}$ (B, sample 1,4-heterozygous mutant, 2-wild-type, 3- homozygous mutant), and *spaw*$^{+/-}$ (C, 1,2,3,5,7,8,10,11,12,13: homozygous mutant, 4,6,9-heterozygous mutant, 14-wild-type) heterozygous fish. In all gels, 50bp ladder was run in the first well.

6 UAS-GAL4 SYSTEM

6.1.1 GATEWAY PLASMIDS USED IN THIS WORK

The following Gateway plasmids were used in this work (Table 2.25):

Table 2.25. Gateway plasmids used

Construct	Plasmid No.❖	Made by / Reference (if applicable)
p5E-UAS	N/A	S. Renshaw Lab (unpublished)
pME-hapln1a	130	C. Derrick (Derrick *et al.*, 2021)
p3E-poly(A)	45	(Kwan *et al.*, 2007)
pDestTol2-cryCFP	71	Rob Wilkinson, (unpublished)

❖ Noël Lab Database

6.1.2 GENERATION OF *UAS:hapln1a, cryaa:CFP* CONSTRUCT

To generate the *UAS:hapln1a, cryaa:CFP* construct (Noël Plamid No. 235) used in this work, the plasmids described in Table 2.25 were used as entry (*p5E-UAS, pME-hapln1a, p3E-poly(A)*) and destination (*pDestTol2-cryCFP*) vectors. Recombination of the construct via LR reaction, was carried out by incubating 20fM of *p5E-UAS, pME-hapln1a*, *p3E-poly(A)* and *pDestTol2-cryCFP* together with LR Clonase II Plus [ThemoFisher 12538120] (Table 2.26) overnight at 25°C. Following incubation 1μL of ProteinaseK (supplied with the Gateway kit) was added to the LR reaction and incubated for 10min at 37°C. Final solution was stored at 4°C until required.

Table 2.26. LR Reaction Mix

Reagent	Volume (10μL Reaction)
TE (pH 8.0)	4 μL
20fM p5E (*p5E-UAS*)	1 μL
20fM pME (*pME-hapln1a*)	1 μL
20fM p3E (*p3E-poly(A)*)	1 μL
20fM pDest (*pDestTol2-cryCFP*)	1 μL
LR Clonase II Plus	2 μL

3μL of the LR reaction solution was transformed into chemically competent TOP10 cells [ThermoFisher C404003] and grown overnight in a static incubator at 37°C on LB Agar [Sigma L7025] plates with Ampicillin [Sigma A0166] (100μg/mL). The next day, 5 colonies were picked from the plates and used to inoculate 3mL of LB Broth [Sigma L7275] grown overnight with relevant antibiotic at 37°C in a shaking incubator [New Brunswick Scientific, Innova 44] at 200-300rpm. Plasmid DNA was extracted from 2mL bacteria culture by QIAGEN Miniprep [QIA 27106]. To confirm recombination order of all the constructs and identify orientation of the final cassette in the vector, a diagnostic restriction digest was carried out. The colony containing the correct final plasmid was grown overnight at 37°C in 50mL of LB Broth with relevant antibiotic in shaking incubator. Plasmid DNA was extracted from cells using a QIAGEN Midi-Prep kit [QIA 12143], eluted into 100μL of MQ Water and its concentration measured using a NanoDrop Spectrophotometer [ND-1000]. To confirm correct recombination the final construct was sent to sequence by Sanger using the primers designed for *hapln1a* probe (Derrick *et al.*, 2021). Upon confirmation, plasmid was stored at -20°C until required.

6.1.3 GENERATION OF *Tg(UAS:hapln1a, cryaa:CFP)*

To generate *Tg(UAS:hapln1a, cryaa:CFP*) transgenic zebrafish the *UAS:hapln1a, cryaa:CFP* construct was co-injected with *tol2:mRNA* (Table 2.27) in a 1nL volume into the yolk of a 1-cell stage embryos obtained from an incross of wild-type fish (see Section 1.5 for details related to micro-injection method). Injected embryos were screened at 2dpf and those with CFP+ eyes grown to adulthood (F0 generation). At about 3 months of age, F0 fish were outcrossed to wild-type embryos and germline transmission was assessed by the presence of CFP eyes in the progeny. To confirm *hapln1a* mis-expression, CFP+ and CFP- embryos from potential F0 founders were separated, fixed, and evaluated using *hapln1a* ISH. If *hapln1a* mis-expression was identified in CFP+ embryos whilst *hapln1a* wild-type expression remained in the CFP-ones, germline transmission of construct together with CFP was confirmed. Confirmed F0 founders were outcrossed to wild-type and CFP+ embryos grown to adulthood establishing a stable *Tg(UAS:hapln1a, cryaa:CFP*) line.

Table 2.27. *UAS:hapl1a, cryaa:CFP* injection mix

Reagent	Volume (4μL Reaction)
UAS:hapln1a, cryaa:CFP (200ng/μL)	1 μL
tol2:mRNA (200ng/μL)	1 μL
Phenol Red [Sigma P0290]	1 μL
MQ Water	1μL

7 HEART RATE ANALYSIS

Dechorionated embryos at the required stage were carefully placed a 1.5% agarose gel mould* using a transfer pipette and gently oriented to obtain a clear image of the embryo from a lateral view (Fig 2.3A). Videos focusing on the embryonic heart were acquired with a High-Speed Camera [CM3-U3-13Y3C-CS 1/2" Chameleon®3 Color Camera, Teledyne FLIR] mounted on a dissecting microscope [Leica MZ16], using SpinView [FLIR] imaging software. Videos were recorded at 120fps for 5s, setting the balance ratio to 0.7 and the auto-exposure and auto-capture rates off. Following image acquisition, to genotype the embryos the steps described in Section 5 were carried out.

To quantify the heart rhythm of the embryos from the acquired videos, using ImageJ (Schindelin *et al.*, 2012) a line 1-pixel wide was drawn across the ventricle where the clearest moving border of the beating chamber was identified (see red line in Fig 2.3A). Using this line, a kymograph was obtained in which multiple full-cardiac-cycles (or heartbeats, HB) were recognised (Fig 2.3B). To measure the heart rate using the kymograph, a new line positioned parallel to the time direction and at a height in which individual heartbeats could be identified was drawn and its plot profile obtained (ImageJ's Plot Profile tool) (horizontal cyan line in Fig 2.3B). Peak identification of the plot profile aided the quantification of individual and average heart rates per embryo (Fig 2.C), which were subsequently compared between genotypes.

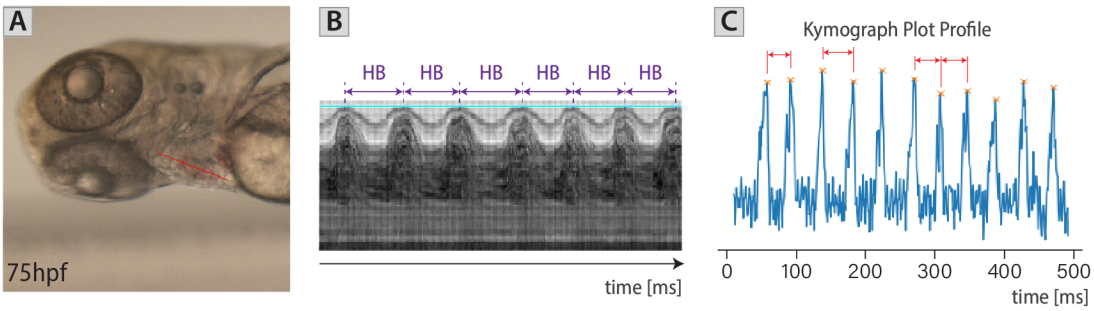

Fig 2.3. Heart rate analysis from high-speed camera videos.
A-C. Still from high-speed video illustrating the 1-pixel-wide line drawn on heart from which the Kymograph of the beating heart shown in B was obtained. Individual heartbeats (HB) can be identified by the repetitive pattern delimited by the double arrows. To quantify individual heartbeats, a new line parallel to the time axis is drawn on the kymograph at a height in which individual heartbeats can be recognised (cyan line) and analysed using ImageJ's Plot Profile tool obtaining the graph shown in C. Peak identification in C aids the quantification of the period per heartbeat and its corresponding rate.

---

8 LIGHT-SHEET IMAGING

To assess cardiac morphology at different developmental stages, live or fixed zebrafish embryos were imaged on a ZEISS Lightsheet Z.1 microscope. To stop the heartbeat of live embryos and aid image analysis, prior to mounting, 3 to 5 embryos were anesthetised by transferring them from a dish containing E3+PTU* to a new cooled dish containing E3 and 8.4% Tricaine [Sigma MS-222] (E3+Tricaine*). Anesthetised embryos were embedded in 1% low melting point agarose* with 8.4% of Tricaine in black capillaries (1mm diameter) [Brand 701904]. To ensure the heartbeat was arrested during the acquisition, the imaging chamber was filled with E3+Tricaine* and maintained throughout the experiment at 10°C. [*Note#2.9:* Similar settings, except those related to arrest the heartbeat were used for imaging fixed embryos post-immunohistochemistry].

All images were acquired using a 20X objective lens with 1.0 zoom. Single-side lasers with activated pivot scan were used for sample illumination. High-resolution images capturing the whole heart were obtained with 16-bit image depth, *1200 x 1200* pixel (*0.228µm x 0.228µm* pixel size resolution) image size and *0.469-0.7µm* z-stack interval. For double fluorescent transgenic embryos, each fluorophore was detected on separate channels. Details regarding the lasers, filters and mirrors used to image the different transgenic lines used in this thesis, are described in Table 2.28.

Table 2.28. Light-sheet imaging set-up used for different transgenic lines

Transgenic line	Fluorophore [Laser]	Filter	Mirror
Tg(myl7:lifeActGFP); Tg(fli1a:AC-TagRFP)	GFP [488nm], RFP [561 nm]	LBF 405/488/561	LP560
Tg(myl7:lifeActGFP); Tg(-5.1myl7:DsRed2-NLS)	GFP [488nm], DsRed2 [561 nm]	LBF 405/488/561	LP560
Tg(myl7:Gal4, UAS:TFP), Tg(UAS:hapln1a, cryaa:CFP), Tg(myl7:lifeActGFP)	TFP/CFP [405nm], RFP [561 nm]	LBF 405/488/561	LP560

If genotyping of the embryos was required, after image acquisition, embryos were gently dissected out of the agarose and the steps described in Section 5 were subsequently followed.

9 Endurance Swim Test

To assess cardiovascular function of adult zebrafish carrying a specific genetic mutation an endurance-swimming test was used.

9.1 Protocol

The day before the experiment, the evening feed of fish subject to swim tunnel analysis is withheld. The order in which fish were selected for testing was randomized and maintained throughout the study. On the morning of the experiment, fish were placed into individual labelled tanks to keep track of genotype and test order and transported to the swim tunnel room (Bateson Centre Aquarium Facility, University of Sheffield).

Individual fish were placed following the established order into the swim tunnel and acclimated at low flow speed (1.24L/min) for 5 min. Throughout the experiment the water flowing through the swim tunnel was maintained at 28°C. After this acclimation, fish were given an endurance-swimming test, during which water flow speed was increased gradually by 1.24L/min in 5 min steps until the fish became fatigued. The endpoint for each fish was reached when the animal reached exhaustion/fatigue, meaning the animal stopped swimming and rested against the back wall of the swim tunnel for at least 10s. Once exhaustion was observed, the fish was allowed another opportunity to re-enter the highest achieved flow speed by pausing the time, reducing the flow, allowing it to rest for 5min, and slowly increasing the current back to the fatigue flow speed, continuing with the experiment. The moment the fish stopped swimming, the time and flow speed was recorded. At this point, water flow was shut down and the fish was removed from the swim tunnel and placed in an individual tank with fresh water. Fish were allowed to recover in the individual tanks for two hours and behaviour was documented. After recovery, fish were anesthetised with 4.2% Tricaine in aquarium water, weighed and its body length measured. Following this, fish were placed into fresh water and allowed to recover from the anaesthesia.

Fish subject to swim tunnel analysis were individually housed post-testing to link repeat testing between subjects. Swim test was performed on the same fish three times. Two tests were performed in one week, allowing a recovery of at least 3 days between swim testing, and an additional test approximately two weeks after the first test had been done.

Solitary confinement for this period could lead to stress and/or increased impact upon health – all animals were monitored, and if necessary were housed with distinguishable companion fish (e.g. distinguishable female and male in same individual tank with tank divider). Upon completion of third swim test, fish recovery was monitored for 3-5 days, and the experimental fish were euthanised by Schedule 1 Killing Method. Each of the strains subject to test included a group of wild-type siblings as a control group.

9.2 Analysis

To compare the swimming endurance between fish, the critical swimming speed U_{crit}, of each embryo was calculated using the equation (Brett, 1964):

$$U_{crit} = U_i + \left[U_{ii} \cdot \frac{T_i}{T_{ii}}\right]$$

where, U_i [cm/s] was the highest flow speed the fish maintained for the whole 5 min period, U_{ii} the flow speed increment used in the experiment (6.58 cm/s), T_i [s] the time during which the embryo managed to swim at the fatigue flow speed, and T_{ii} the time between flow speed changes [5min]. To account for the

differences in size between sex (i.e. male, female) and phenotype, critical swimming speed was normalised by weight, standard length, and area of each fish, and resulting values compared between genotypes.

10 QUANTITATIVE METHODS

10.1 HEART LOOPING, HEART/CHAMBER AREA, OTHER CHAMBER PARAMETERS

To prevent bias during the quantification process, ISH images were initially blinded using the Blind Analysis ImageJ macro written by Christophe Leterrier v1.0[1].

In situ hybridisation mRNA expression analysis of the specific pan-cardiac marker *myosin light chain 7* (*myl7*), ventricular marker *myosin heavy chain 7-like* (*myh7l*) and atrial marker *myosin heavy chain 6* (*myh6*) were used to identify the heart, ventricle, and atrium of wild-type and mutant embryos. To quantify heart/chamber morphology and size the expression pattern of these genes was used and multiple morphological parameters like the ones illustrated in Fig 2.4 were measured using ImageJ.

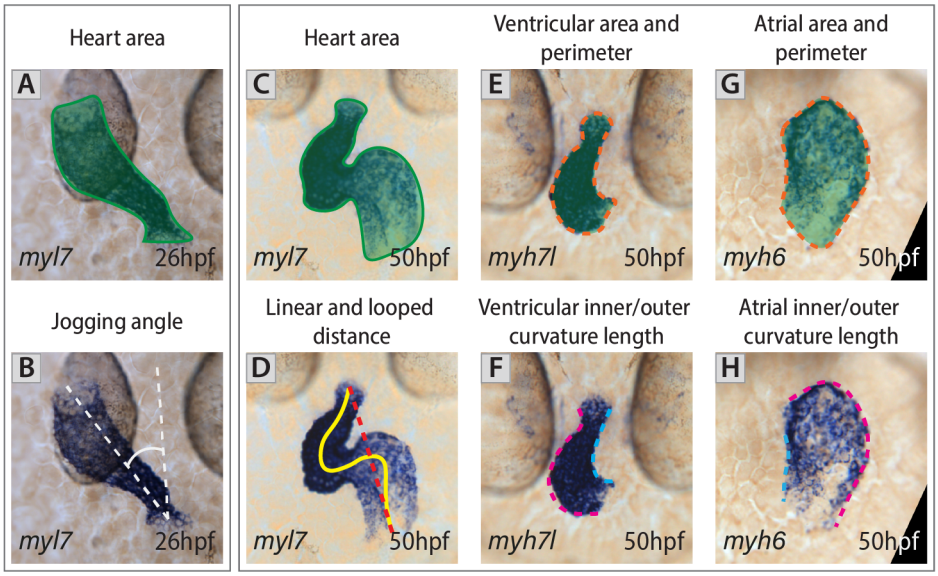

Fig 2.4. Quantification of heart/chamber morphology from ISH images.
A-D. Illustration of methods to quantify heart morphology and size from *myl7* ISH images at 26hpf (A-B) and 50hpf (C-D). Heart area as a proxy for heart size was quantified by tracing and measuring the area of the *myl7* expression domain represented by the green shaded area in A and C. Jogging angle of the early heart tube was measured by measuring the angle between the embryo's midline and the heart orientation (angle traced in B). Quantification of heart's looping ration was done by calculating the quotient of the looped (yellow line in D) and linear (red dotted line in D) lengths. **E-H.** Illustration of methods to quantify chamber morphology and size from *myh7l* (ventricle, E-F) and *myh6* (atrium, G-H) ISH images at 50hpf. Chamber area and perimeter were quantified by tracing and measuring the area (green shaded area) and perimeter (orange dotted trace) of the chamber-specific gene expression domain represented in E and G. Chamber-specific inner/outer curvature were measured by manually tracing the curvatures of the chambers and measuring their length (inner/outer curvatures represented by dotted line in light-blue/magenta in F and H).

[1] https://github.com/quantixed/FerriTag/blob/master/Blind_Analysis.ijm

11 Statistical Analysis

Quantitative data were analysed using a custom-written Python code using the *stats* module of the *scipy* package (Virtanen *et al.*, 2020) and *scikit_posthoc* package (Terpilowski, 2019). Embryos obtained from mutant incrosses were displayed as individual data points for data quantified from ISH or light-sheet images. In these datasets, when running statistical analysis, each embryo was considered an individual experimental unit subjected to minor experimental variations (i.e. genetic mutations).

All data groups were initially analysed for normality using the Shapiro-Wilk Normality test. In datasets containing two groups (e.g. wild-types and homozygous mutants) comparative statistics of normally-distributed datasets were carried out using Un-paired t-test, while non-normal datasets were analysed using Mann-Whitney test. In datasets containing more than 2 groups, comparative statistics of normally-distributed datasets were carried out using One Way ANOVA (*post-hoc:* Tukey's Multiple Comparisons), whilst non-normal data was analysed using Kruskal-Wallis (*post-hoc:* Dunn's Multiple Comparisons).

For all tests a statistical significance α of *0.05* was defined, and *p-value* by star denotation on graphs was stated as: ****: *p-value*<0.0001, ***: *p-value*<0.001, **: *p-value*<0.01, and *: *p-value*<0.05. Of note, a non-parametric test and Dunn's Multiple Comparisons (where appropriate) were run for variables that involved the quotient between two measured parameters, such as looping ratio. Violin plots throughout this thesis show median and interquartile ranges with different colours representing different repeats. Boxplots show error bars with 95% confidence interval of the mean. For data quantified from ISH images, a minimum of two biological repeats (including wild-type and mutant embryos) were performed. For data quantified from live/fixed light-sheet images, a minimum of 5 embryos per genotype were analysed.

12 LABORATORY SOLUTIONS

Table 2.29. Composition of laboratory solutions used in this thesis

Solution	Composition▲
General solutions	
PBS	5 Phosphate Buffered Saline tablets [Oxoid BR0014], 500mL MQ Water
10% Tween-20 (v/v)	5mL Tween-20 [Sigma P2287], 45mL PBS
PBSTw (0.2% PBS-Tween-20)	10mL 10% Tween-20, 490mL PBS
10% Triton-X (v/v)	5mL Triton-X [Sigma T8787], 45mL PBS
PBSTr (0.2% PBS-Triton-X)	10mL 10% Triton-X, 490mL PBS
Solutions for embryo related work	
E3 media (provided by Aquarium Facility)	0.29g NaCl, 0.13g KCl , 0.37g $CaCl_2$, 0.40g $MgSO_4$, MQ Water to 1L
7.5% PTU in DMSO	375mg 0.2mM 1-phenyl2-thiourea (PTU) [Sigma P7629], 5mL DMSO [Sigma 276855]
E3+PTU	460µL PTU in DMSO, 1L E3 media
2% Agarose Gel Mould (micro-injections)	10g Agarose [Meridian Bioscience BIO-41025], 50mL E3 media
Solutions for DNA extraction	
SEL Buffer	25mL KCl (1M), 1.25mL $MgCl_2$ (1M), 5mL Tris (1M, pH 8.3), 2.25mL 10% (v/v) NP40, 2.25mL 10% Tween-20, 50mL 0.1% (w/v) Gelatin, MQ Water to 500mL
PK+SEL (Proteinase K+SEL)	(1:100) Proteinase K (PK) (10mg/mL) [Ambion AM2542] : SEL Buffer
Solutions for in situ hybridisation (ISH)	
4% PFA	10mL 16% Paraformaldehyde (PFA) [Cell Signalling Technology 12606], 30 mL PBS
20X SSC (Saline sodium citrate), (pH 7.0)	87.5g NaCl [Sigma S7653], 44.19g Sodium Citrate [VWR 27833.360], MQ Water to 500mL
Hyb- (50mL)	25mL Formamide (50%) [Sigma 47671], 12.5mL 20X SSC, 460µL Citric Acid (1M, pH 6.0), 500µL 10% Tween-20, 11.54mL MQ Water
PK+PBSTw (10µg/mL)	Per tube: 0.5µL Proteinase K (PK) (10mg/mL) [Ambion AM2542], 499.5µL PBSTw
PK+PBSTw (20µg/mL)	Per tube: 1µL Proteinase K (PK) (10mg/mL) [Ambion AM2542], 499µL PBSTw
Hyb+	49mL Hyb-, 500µL tRNA (50mg/mL) Ref, 500µL Heparin (5mg/mL) Ref
2xSSCT (50mL)	4.95mL 20X SSC, 500µL 10% Tween-20, 44.5mL MQ Water
0.2xSSCT (50mL)	495µL 20X SSC, 500µL 10% Tween-20, 49mL MQ Water
Blocking buffer	2% Sheep Serum [Sigma S3772], 2mg/mL Bovine serum albumin (BSA) (100mg/mL) [Sigma A9418], PBSTw
Pre-incubated Anti-DIG-AP conjugated antibody	(1:500) Pre-incubated Anti-DIG-AP Antibody : Blocking Buffer
AP Staining Buffer (50mL)	5mL 1M Tris-HCL (pH 9.5) [Sigma T1503], 2.5mL 1M $MgCl_2$, 1mL 5M NaCl, 0.5mL 10% Tween-20, 41mL MQ Water
AP Staining Solution (50mL)	(1:50) NBT/BCIP (Nitro-blue tetrazolium/5-bromo-4-chloro-3-inodyl phosphate) [Roche 11681451001] : AP Staining Buffer

▲ Concentration presented in parentheses corresponds to the concentration of the original solution

Table 2.29. Composition of laboratory solutions used in this thesis (*continuation*)

Solution	Composition▲
Solutions for imaging ISHs	
BBA	(2:1) Benzyl benzoate [Sigma B6630]: Benzyl alcohol [Sigma 402834]
Solutions for immunohistochemistry	
4% PFA+Sucrose	40g Sucrose [Sigma S0389], 40g paraformaldehyde [Sigma 441244], 90.8mL 1M K_2HPO_4, 9.2mL 1M KH_2PO_4, 1.5mL 0.1M CaCl
IHC-Blocking Buffer	(1:10) Goat Serum [Invitrogen 10000C] : PBSTr
Solutions for electrophoresis (PCR gels)	
20X TAE	242g Tris-HCl, 18.61g EDTA, 57.1mL Glacial Acetic Acid, MQ Water to 1L
1X TAE	20mL 20X TAE, 980mL MQ Water
5X TBE	54g Tris-HCl, 27.5g Boric Acid, 20mL 0.5M EDTA, MQ water to 1L
1X TBE	200mL 5X TBE, 800mL MQ Water
Solutions for light-sheet imaging	
1% (w/v) low melting point agarose	1g of low melting point agarose [Sigma A9414], 100mL of E3 media
E3+Tricaine	

▲ Concentration presented in brackets corresponds to the concentration of the original solution

---

CHAPTER 3. *morphoHeart*

A NOVEL QUANTITATIVE TOOL TO PERFORM INTEGRATED 3D ANALYSES OF THE HEART AND ECM MORPHOLOGY DURING ZEBRAFISH DEVELOPMENT

1 STATE OF THE ART METHODS FOR IMAGING AND SEGMENTING TISSUES

Light-sheet microscopy, also known as Selective Plane Illumination Microscopy (SPIM) has emerged as a valuable *in vivo* imaging solution for understanding the highly dynamic processes of embryonic development (Huisken *et al.*, 2004). With its characteristic high-speed and excitation of one optical section at a time, this system allows the acquisition of high-resolution three-dimensional (3D) imaging of organs in live organisms over time, without causing any damage to the tissue nor interfering with its anatomical or physiological state (Hoebe *et al.*, 2007; Reynaud *et al.*, 2008; Power and Huisken, 2017; Taylor *et al.*, 2019).

To uncover the complex morphogenetic events and interactions happening in the early beating heart*, in vivo* imaging of the whole organ is required. Considerable research has been done trying to understand heart development using light-sheet microscopy and the zebrafish embryonic heart, the latter due to its small size and optical and genetic accessibility (Bakkers, 2011; Tu and Chi, 2012; Bowley *et al.*, 2022). Despite all the advantages presented by the technology and the animal model, challenges arise when trying to image the 3D spatial patterning of the embryonic heart while it is beating and pumping blood (Trivedi *et al.*, 2020; Schlaeppi *et al.*, 2021).

1.1 IMAGING OF A MOVING/BEATING ORGAN

Recent studies have devised distinct solutions to overcome the difficulties surrounding the imaging of the beating heart in zebrafish, either by suspending the heartbeat or developing computational strategies that control the acquisition or aid the post-processing of 3D images of beating hearts.

Strategies to suspend the heartbeat include the use of morpholinos (MO) (e.g. *silent heart* MO (Sehnert *et al.*, 2002)), drugs or toxins that act as chemical inhibitors of muscle contractions (e.g. BDM (Jou, Spitzer and Tristani-Firouzi, 2010; Chow *et al.*, 2018), α- bungarotoxin (Swinburne *et al.*, 2015)), anaesthetics that prevent the generation or conduction of nerve impulses (e.g. tricaine (Frazier and Narahashi, 1975; Kaufmann *et al.*, 2012)), and genetic modifications to optogenetically control the cardiac pacemaker cells (Arrenberg *et al.*, 2010), all allowing either continued or temporal cessation of the contractility of the heart. With the heart stopped, clean 3D image sequences of the heart can be acquired, removing the artefacts caused by the natural movement of the organ. Despite providing a solution, downsides to these approaches need to be considered and assessed in the context of the specific process of interest under study. Arresting the heartbeat allows capturing heart morphology only in a relaxed state, making all these approaches suitable for the study of processes in which capturing the dynamics of the beating heart is not essential. Additionally, as heart morphogenesis is a process driven by both genetic and biomechanical forces, stopping the heart at very early stages of development and/or for very long periods has shown to lead to heart defects and affect heart physiology (Kaufmann *et al.*, 2012; Mickoleit *et al.*, 2014), posing significant drawbacks that should be carefully considered when selecting the best strategy to use.

Consequently, recent studies have focussed on the development of retrospective (Mickoleit *et al.*, 2014; Akerberg *et al.*, 2019) and prospective (Taylor *et al.*, 2011, 2019; Lee *et al.*, 2012) computational approaches to obtain 3D images of the whole beating organ without affecting its anatomical nor physiological state. The retrospective approach initially acquires a series of continuous 2D movies of the beating heart at each *z*-position sequentially. Then, at a post-acquisition stage, assuming a periodicity of the heartbeat, synchronisation of the cardiac phase in each *z*-position movie results in a dataset containing the full 4D dynamics of the organ through at least a complete heart cycle (Mickoleit *et al.*, 2014; Akerberg *et al.*, 2019). Alternatively, the most recent prospective strategy (adaptive prospective optical gating) defines firstly a cardiac cycle phase of interest and then, aided by a live reference brightfield image sequence, computationally controls the fluorescent image acquisition process so that at each *z*-position,

the heart is captured at precisely the defined phase, resulting in a phase-locked 3D dataset comprising the whole heart morphology (Taylor *et al.*, 2019).

Though each approach facilitates imaging the whole heart in 3D (and even 4D), both techniques have advantages and limitations. Retrospective approaches excel at capturing the full 4D beating motion of the heart, which results useful for studies where the active contractility of the organ is important. However, its extended laser exposure might induce phototoxic and photobleaching effects on the embryo, proving unsuitable for time-lapse image acquisition. On the other hand, by acquiring one single fluorescent image per *z*-plane and timepoint, prospective techniques bring practical advantages such as minimising phototoxic damage and reducing data file sizes, offering the possibility of time-lapse image acquisition of live hearts across developmental time scales. In spite of these advantages, as the heart changes in position, size and shape throughout development, adaptable phase-locking algorithms, particularly in commercially available systems, remain challenging to implement.

Considering the advantages offered by both approaches, some studies have started combining both techniques using macroscopic-phase stamping (MaPS) (Trivedi *et al.*, 2020). This approach consists of the synchronous triggered recording per *z*-position of 1) a high-resolution optically-sectioned fluorescent 2D movie of the beating heart and 2) a low-resolution brightfield image that captures the macroscopic spatiotemporal information about the cardiac phase of the beating heart. Post-acquisition processing uses the brightfield images to assign to each fluorescent image (with known *z*-position) the instantaneous phase of the heart in which it was captured, obtaining a 4D dataset comprising the dynamics of the whole organ and contraction cycle. MaPS strategy combines the best of both approaches, capturing the full 4D beating motion of the heart with a post-acquisition enhanced synchronisation strategy in which assumptions such as periodicity of the heartbeat and sample spatial continuity in the *z*-direction can be quantitatively validated, obtaining a more accurate 4D representation of the periodic beating motion of the heart.

Continuous improvement of software and hardware to reduce file size and aid data acquisition and processing, as well as the development of more stable and less-phototoxic fluorophores (Chow and Vermot, 2017; Lischik, Adelmann and Wittbrodt, 2019), will remove most of the disadvantages in the presented approaches. These improvements will certainly enhance researchers' ability to capture 4D datasets of the beating heart as it develops granting a more detailed study of heart development and the onset of congenital heart defects (Truong *et al.*, 2020).

1.2 Obtaining 3D Morphological Readouts of the 3D Heart Remains Challenging

Cardiac malformations associated with tissue distortion are complex defects to diagnose and characterise using information in two-dimensions (2D). Thus, the ability to use light-sheet microscopes and any of the above approaches, combined with the use of zebrafish embryos to model human heart defects (Stainier *et al.*, 1996; Bakkers, 2011; Becker *et al.*, 2012; de Boer *et al.*, 2012; Akerberg *et al.*, 2019), has started to allow the description of cardiac abnormalities during ***live*** embryogenesis in ways not previously possible and calls for the analysis of heart morphogenesis in a more robust 3D way. However, available options for processing, segmenting and analysing datasets in 3D are computationally more demanding and objective quantification of such images remains limited (Rasse, Hollandi and Horvath, 2020; Kugler *et al.*, 2022).

Due to these challenges, even though most studies do acquire 3D high-resolution image sequences of the developing heart, they still rely either on subjective visual assessment of phenotypes or on simple quantifications taken from either 2D Maximum Intensity Projections (MIPs), individual or consecutive group of slices, failing to capture the wealth and complexity of the information contained in the original datasets and biasing the analysis towards obvious phenotypes.

Considering the complex morphogenetic events involved in heart development, segmentation of the 3D organ and its quantification is clearly preferable, but it is technically and computationally more challenging. Consequently, few zebrafish studies have reported 3D morphological and quantitative readouts of the zebrafish heart as it undergoes morphogenesis. For instance, when introducing the adaptive prospective optical gating approach, Taylor *et al.* reported an enlargement of the endocardial chamber of zebrafish hearts between 48 and 72hpf. They quantified these volume changes by surface rendering the 3D image datasets and cropping the rendered chambers at these two time points (Taylor *et al.*, 2019). Similarly, to understand zebrafish ventricular growth beyond 3 dpf, Kula-Alwar *et al.* rendered and measured the volume and different trabecular parameters of ventricles at 3 and 5 dpf (Kula-Alwar *et al.*, 2021). Trivedi *et al.*, focused on capturing the dynamic motion of the heart at 4.5 dpf throughout the beating cycle using MaPS and quantified the 3D changes in the volume of the whole myocardium and each heart chamber during a complete heartbeat (Trivedi *et al.*, 2020). While all of these quantifications give insights about changes undergone by the heart as it develops or pumps, most of them are limited to reporting the general metrics (i.e. surface area, volume) provided by commercially available software (e.g. Imaris, Oxford Instruments; Volocity, PelkinElmer), which fail in describing how each chamber and tissue layer change its 3D shape and organisation in the process of shaping this complex 3D organ.

Interestingly, some recent studies in non-zebrafish model organisms have started to use diverse 3D quantification methods to describe cardiac morphogenesis and the development of heart defects, evolving from simple descriptions of cardiac looping direction in 2D, to volumetric and 3D directional and orientational descriptions (Fei *et al.*, 2016; Ivanovitch, Temiño and Torres, 2017; Hoog *et al.*, 2018; Desgrange, Garrec, *et al.*, 2019; Desgrange, Lokmer, *et al.*, 2019).

All this demonstrates that the available metrics to quantify heart morphology and function remain very limited and unrefined, stressing the need for tools specifically tailored to the study of heart development in different animal models. The development of such 3D quantification tools in combination with continuous improvement of microscopes and acquisition algorithms will support not only a more detailed characterisation of the heart morphogenetic and patterning processes in wild-type and defective scenarios, but also the creation of higher resolution predictive models that provide novel insights into the mechanisms underpinning cardiac development (Heckel *et al.*, 2015; Le Garrec *et al.*, 2017; Vedula *et al.*, 2017; Desgrange, Garrec, *et al.*, 2019).

2 PROJECT AIM

The aim of this project is to investigate the link between morphology and ECM dynamics in the developing zebrafish heart. To fulfil this objective, we need to be able to describe **comprehensively in 3D** and **throughout development** cardiac morphology and ECM-positioning. Despite the great advances in high-resolution live imaging, to our knowledge no previous work had focused on characterising temporally in 3D the highly dynamic process of heart development in zebrafish using **both** the cellular (myocardium and endocardium), and acellular (ECM) tissue layers, revealing the need for a new tool that could provide quantifiable information regarding morphology and tissue composition and distribution through time. Consequently, I developed *morphoHeart*, an open-access comprehensive quantitative image analysis tool that allows the segmentation of the heart layers -including the cardiac jelly- and quantification of the tissue organisation and morphology throughout heart development.

Throughout this chapter I will give a detailed description of *morphoHeart*. I will start by describing the design principles that guided its development. Then, I will give an overview of the different phases involved in processing a zebrafish heart and illustrate the multiple morphological metrics included within the tool. Next, I will provide information regarding the precision and accuracy of *morphoHeart* and finish with the

future improvements that will be implemented to enhance the output measurements provided by the tool.

3 morphoHeart's Design Principles

The core design goal for *morphoHeart* was to generate a user-friendly visualisation and analysis software able to reconstruct in 3D the myocardium, endocardium and/or cardiac jelly of zebrafish hearts from fluorescently labelled images, facilitating a multi-parametric morphometric analysis of the tissue layers and whole heart morphology throughout development. To successfully deliver such outcome, this major design goal was split into three main design principles: i) reconstruction and visualisation, ii) quantification and iii) user experience and availability to the broader community (i.e. heuristic evaluation).

As previously discussed, the heart is a complex organ and therefore is poorly represented in 2D images. Therefore, *morphoHeart's* first major design goal was to enable the **segmentation and 3D reconstructions** of the heart from 3D image datasets where the myocardium, endocardium, and/or cardiac jelly are fluorescently labelled. Once the tissue layers have been segmented, *morphoHeart* provides the user with the **ability to interact with its 3D renderings**, facilitating a more in-depth exploration of the data.

To further enhance the understanding of the morphology of the heart and relate it to the biological process of cardiac morphogenesis, the second major design principle of *morphoHeart* was to **provide morphological quantifications** of the whole heart and its components. *morphoHeart*'s integrated toolset allows the complete geometric quantification of the tissue layers and chambers (e.g. volume, surface area, orientation), and the acquisition of metrics specifically tailored to the analysis of processes intrinsic to the formation of the heart (i.e. looping morphogenesis and chamber ballooning). *morphoHeart* also provides the functionality to perform **tissue thickness analysis** of the heart tissue layers facilitating the study of the relationship between tissue organisation and heart morphogenesis. Analysis of wild-type hearts at multiple developmental stages using *morphoHeart* permits a detailed characterisation and description of the changes in 3D shape, size, and morphology the heart, chambers and tissue layers undergo as it develops. Additionally, comparative analysis of wild-type and mutant hearts allows the identification of the time at which cardiac malformations originate, allowing much more detailed characterisation of previous incompletely described heart defects.

Lastly, *morphoHeart* was designed to be friendly with any type of user (independent of their programming experience) and available to the community. The community's adoption of *morphoHeart* will hopefully help close the gap between the rapidly evolving imaging technology and the available data analysis tools. Furthermore, it will aid and encourage researchers to make full use of the 3D image datasets they already acquire, extracting information relevant to answering the biological questions underpinning the development of this complex organ, having a significant impact on the advancement of the field.

4 morphoHeart Overview

morphoHeart offers the first standardised framework for characterising zebrafish heart morphogenesis, capturing spatiotemporal changes in heart and tissue morphology throughout development.

In general, the process of acquiring quantifiable information of a zebrafish heart using *morphoHeart* can be divided into 5 different phases (Fig 3.1). The initial phase corresponds to the image acquisition (Fig 3.1i). Even though *morphoHeart* can be used to process images of zebrafish hearts acquired in different microscope setups -if the myocardium and/or endocardium are fluorescently labelled-, recommendations regarding the acquisition process of the images are given to provide the best input into the tool. The processing and filtering of the RAW dataset is next required to enhance the tissue layer signal aiding its

segmentation (Fig 3.1ii). Tissue layer segmentation is then conducted by detecting and extracting the internal and external contours that delineate each tissue completely and constructing masks that contain the tissue layer of interest (Fig 3.1iii). Final masks are used to render 3D volumetric meshes of each tissue layer (Fig 3.1iv) where tissue distribution and morphology can be further quantified (Fig 3.1v).

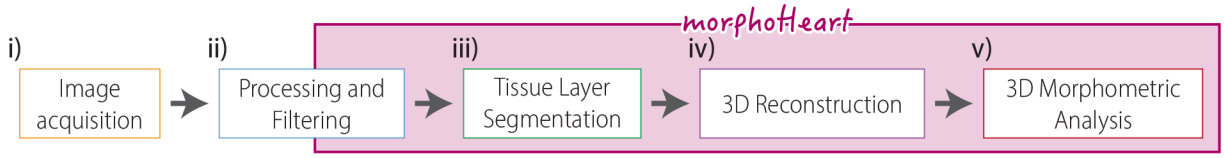

Fig 3.1. *morphoHeart* general overview.
Flow diagram describing the 5 phases involved in the process of acquiring morphometric data of a zebrafish heart using *morphoHeart*.

Throughout this chapter, this same flow diagram (Fig 3.1) is going to be presented at the beginning of each section, highlighting the phase being described.

4.1 IMAGE ACQUISITION

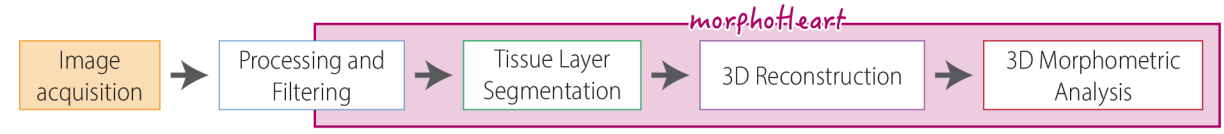

The imaging phase starts with the acquisition of *in vivo* serial dynamic images of single or double transgenic zebrafish embryos in the light-sheet microscope at the stage of interest. While many light-sheet microscope configurations exist it is recommended to use a hanging sample SPIM[2] (Fig 3.2A), which gives sufficient freedom of movement and rotation for the precise sample positioning (Schlaeppi *et al.*, 2021). To be able to segment the three tissue layers of the heart, the double transgenic zebrafish embryos used should have fluorescently labelled myocardium **and** endocardium, each tissue labelled with different fluorescent markers, allowing the demarcation of the two cellular tissue layers comprising the heart with fluorescent markers and the cardiac jelly as the acellular layer enclosed between them (Fig 3.2B). Using the brightfield setting of the light-sheet microscope, embryos are positioned and oriented within the chamber so that both eyes are in the focal plane, assuring a full ventral view of the heart (Fig 3.2C-E). As previously described, different image acquisition approaches have been devised and can be used to obtain 3D image sequences of the developing heart (Section 1.1). The z-stack range that covers the entire depth of the heart is next defined so that irrespective of the approach used to image the beating organ (e.g. suspending the heartbeat or using any of the described computational strategies), the outcome of this phase is a high-resolution 3D dataset of the single/double transgenic zebrafish that comprises the whole heart morphology at a sole cardiac phase and with fluorescent markers acquired as individual channels (Fig 3.2F).

[*Note#3.1*: Throughout this thesis the *Tg(myl7:lifeActGFP); Tg(fli1a:AC-TagRFP)* double transgenic line which expresses actin-tagged GFP in the myocardial layer (Reischauer *et al.*, 2014) and actin-localised RFP in the endothelium (Savage *et al.*, 2019), including the endocardial layer of the heart, will be used as the double transgenic line of preference. Additionally, to overcome the challenge of heart beating during the image acquisition phase, unless stated otherwise, the heartbeat of all the processed zebrafish hearts was temporarily stopped by combining low temperature (e.g. 10°C) and high dose of anaesthetic (8.4% of

[2] A hanging sample SPIM comprises one detection and two illumination lenses, all in a horizontal plane with the sample hanging vertically in the common focus (Reynaud *et al.*, 2008; Power and Huisken, 2017).

tricaine in E3) in the imaging chamber (for more details on the image acquisition process used see Chapter 2, Section 8)].

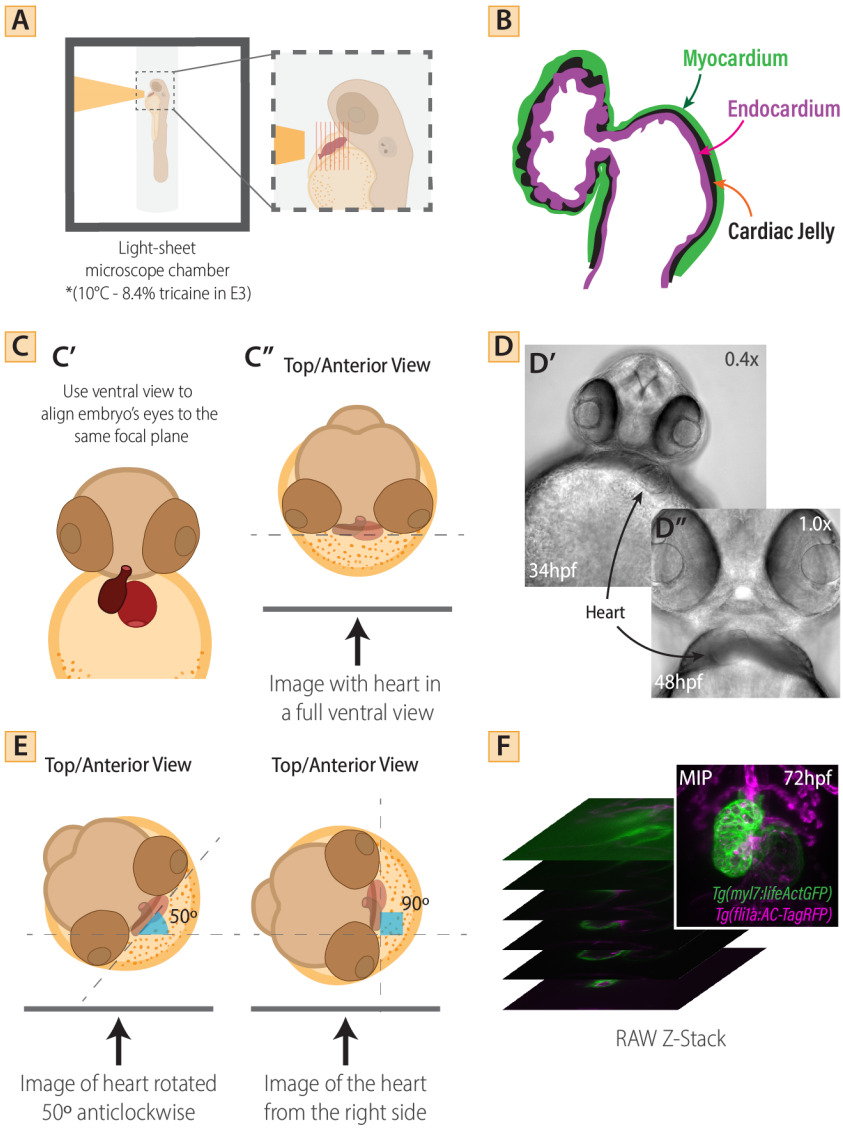

Fig 3.2. Image acquisition of *live* double transgenic zebrafish hearts in the light-sheet microscope.
A. Schematic depicting from a side view the sample positioning within the light-sheet microscope chamber and imaging conditions used in this thesis for stopping the zebrafish heartbeat (*). **B.** Schematic of a z-stack slice of a double transgenic zebrafish embryo depicting the two fluorescently labelled tissue layers needed to extract the cardiac jelly tissue layer (myocardium in green, endocardium in magenta, and cardiac jelly in black). **C.** For reproducible imaging and to facilitate orientation measurements of the heart in later analysis phases, it is recommended to position the embryos in the microscope chamber so that the embryo's eyes are completely aligned in the focal plane (C'), obtaining images from a full ventral view of the heart (C'-C''). **D.** Example of brightfield images of zebrafish embryos at 34hpf (D') and 48hpf (D'') positioned in the chamber and aligned with both eyes in the focal plane. If the embryo is kept in this orientation throughout the image acquisition, images of the heart will be taken from a full ventral view. **E.** If other orientation is preferred for the imaging, (e.g. if imaging from one side is desired) align the embryo's eyes first in focal plane (as described in C-D), and from that position rotate the fish in the desired direction measuring the angle deviation from the original full ventral view (E). Once the orientation of the embryo has been established, initial and last slices of a z-stack are defined to scan the heart completely. **F.** Output RAW z-stacks include information from both cellular tissue layers as individual channels, here illustrated in the z-stack representation and in the MIP by two different colours (myocardium in green, endocardium in magenta). B, D, F: Ventral views with anterior to the top. For more details on image acquisition go to Chapter 2, Section 8). MIP: Maximum intensity projection, hpf: hours post-fertilisation.

4.2 PRE-PROCESSING AND FILTERING

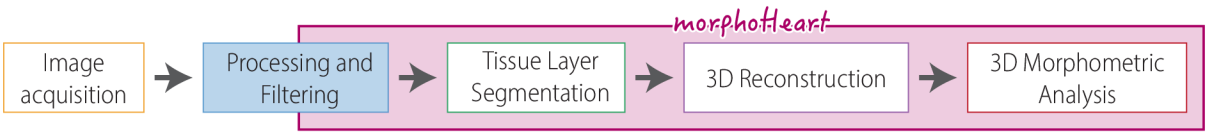

The *Processing and Filtering* phase involves the serial application of filters to the RAW individual channels to remove noise artefacts, accentuate details, and enhance tissue borders (Fig 3.3). Processing and filtering stages are performed using two different software, arivis Vision4D, V3.1.0 (arivis, Germany) (Fig 3.3A-K) and Fiji (Fig 3.3L-M) (Schindelin *et al.*, 2012; Legland, Arganda-Carreras and Andrey, 2016). [*Note#3.2*: All filters used for both stages were selected, and their parameters optimised to enhance the contrast of the signal coming from the GFP and RFP demarcating each tissue layer in the *Tg(myl7:lifeActGFP)*; *Tg(fli1a:AC-TagRFP)* double transgenic line and improve border delimitation].

Initially, to smooth the noise regions but still preserve the edges of each tissue layer, the arivis Vision4D *denoising filter (3D)* is applied to the RAW dataset (Fig 3.3D-E). This filter works in 3D, computing the final pixel values using the information from the pixel neighbourhood across x, y and z (slices/planes). Resulting images are then processed using the arivis' *Background Correction* filter (Fig 3.3F-G). This filter helps to eliminate variations in intensity present in the whole image set, setting the mean intensity value as the threshold to separate foreground from background pixels. arivis' *Morphology Filter* is used next to sharpen the tissue borders and prepare the dataset for the last filtering step in the pipeline (Fig 3.3H-I). To accomplish this, the *Morphology Filter* sharpens the boundaries of the regions with foreground pixels using a spherical structuring element (1 pixel in radius), resulting in individually processed channels with refined borders. The final filter applied within arivis Vision4D, *Membrane Enhancement*, is specially designed to boost the signal of membranes, producing clear slices with enhanced and sharpened borders in each channel (Fig 3.3J-K).

To enhance even more the heart tissue layer's signal and reduce file size, once individual channels have been processed through arivis Vision4D, images are processed in Fiji (Schindelin *et al.*, 2012) (Fig 3.3L-M). First the salt and pepper noise left in the images from previous filtering steps is removed by using the Fiji's integrated *despeckle* filter. An enhancement filter, also called normalisation filter, is then applied to both channels to improve the contrast of the images without distorting their grey level intensities. Finally, a Maximum Intensity Projection (MIP) of a composite containing both processed channels is used to define a square that contains the region of interest (ROI) comprising the heart. This ROI is then used to crop individually each of the processed channels reducing the image size used to segment the heart tissue layers.

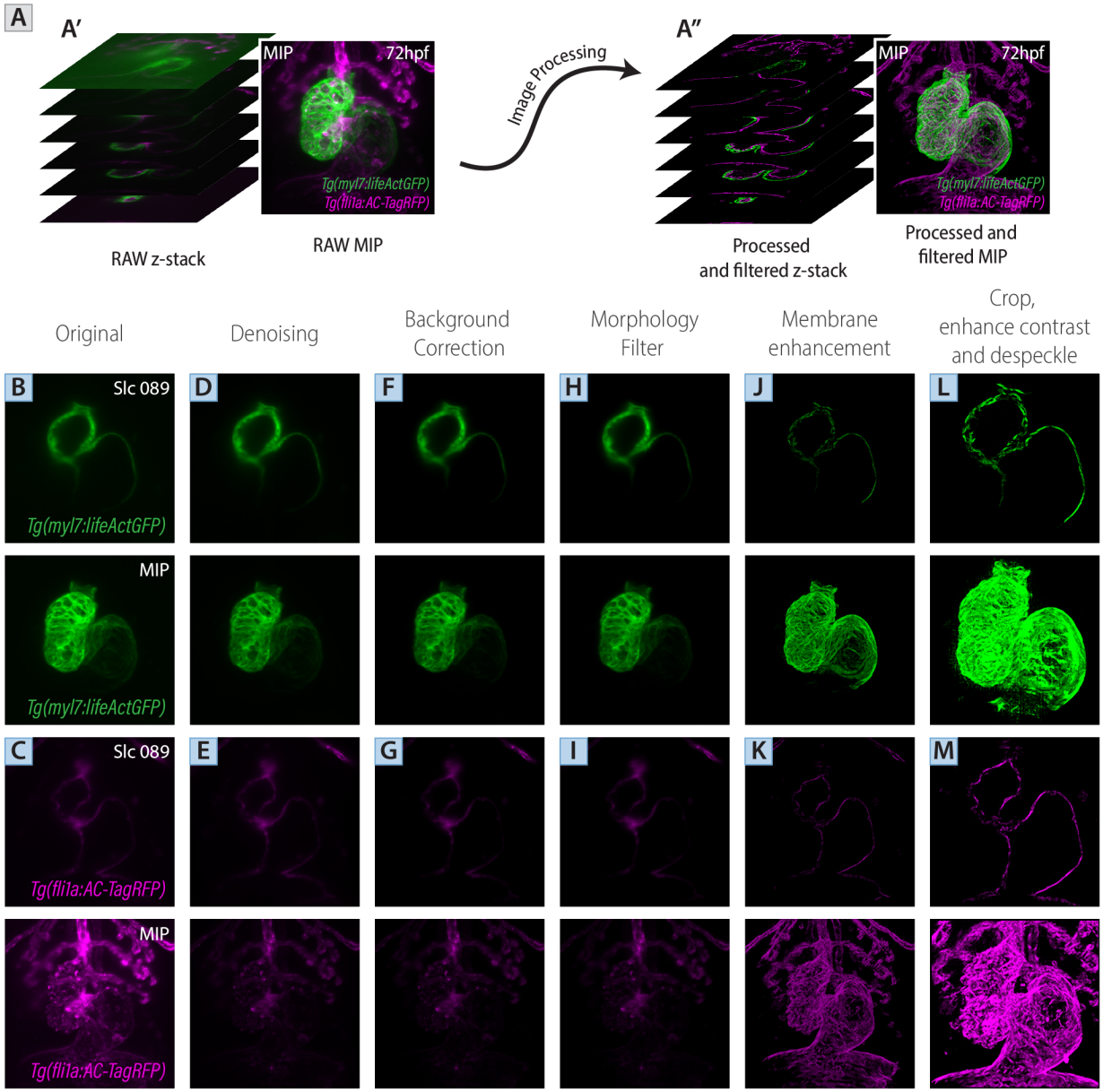

Fig 3.3. *morphoHeart's* image processing overview.

A. To prepare the images for tissue segmentation, RAW images obtained in the light-sheet microscope (**A'**) are processed and filtered, removing the noise, and enhancing the borders of each tissue layer. *Tg(myl7:lifeActGFP)* signal in green marks the myocardium and *Tg(fli1a:AC-TagRFP)* signal in magenta marks the endothelium. (**A''**). To illustrate the changes made when applying each filter, one slice of an example z-stack (Slc89, top image) and a MIP (bottom image) for each channel will be shown (B-M). **B-K.** RAW channels (B,C,) are first individually processed using arivis Vision4D image processing tools (myocardium: B,D,F,H,J,L and endocardium: C,E,G,I,K,M). **D-G.** Initially, a *denoising filter* (D-E) is applied to remove the noise artefacts from the image followed by a *background correction filter* (F-G) which eliminates variations in intensity, enhancing the signal coming from the tissue layers. **H-I.** The *morphology filter* is next applied to shrink the foreground pixels and reduce the hole sizes in each of the tissue layers. **J-K**. Lastly, the *membrane enhancement* filter of arivis Vision4D is used to heighten the tissue layers and thus ease subsequent processes of segmentation. **L-M.** arivis4D processed channels are then further processed in Fiji. Images are further filtered using *despeckle* and *enhance contrast* are used to accentuate details and remove noise added to the images from previous processing steps. Finally, filtered images are cropped to the region that contains the chambers to reduce the amount of information being processed and improve computational speed. A-M: Ventral views with anterior to the top.

4.3 TISSUE LAYER SEGMENTATION

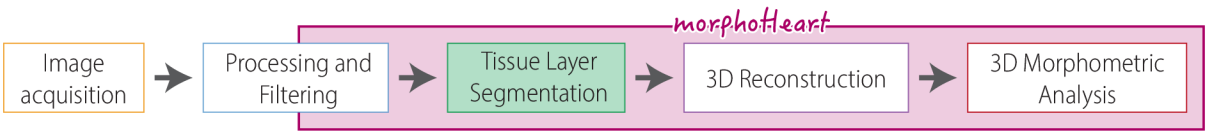

Filtered and cropped images are then imported into the next phase of *morphoHeart*: the *Tissue Layer Segmentation* phase (Fig 3.4 and 3.5A-C). This phase is divided in two stages. An initial stage in which the masks containing the myocardial and endocardial tissue layers are extracted and a second stage in which these masks are used to extract the cardiac jelly layer.

4.3.1 EXTRACTION OF MYOCARDIAL AND ENDOCARDIAL TISSUE LAYERS

To extract the myocardium and endocardium, individual slices making up each filtered channel go through a process of contour detection and selection, extracting all the contours that delineate the tissue layer completely (myocardium: Fig 3.4C and 3.5Ai, endocardium: Fig 3.4C' and 3.5Bi). Selected contours are then classified either as internal or external, depending on whether they outline the lumen or the external borders of the tissue, respectively. Classified internal and external contours are next used to create filled binarisation masks, one containing just the filled lumen of the tissue of interest (henceforth *filled internal contour* mask; myocardium: Fig 3.4E and 3.5Aiii, endocardium: Fig 3.4E' and 3.5Biii), and another containing both, the tissue layer and the filled lumen (henceforth *filled external contour* mask; myocardium: Fig 3.4D and 3.5Aii, endocardium: Fig 3.4D' and 3.5Bii). For each channel, external and internal contours masks are then combined applying an exclusive disjunction logical operator (XOR)[3] to obtain a final mask delineating just the tissue layer without its lumen (myocardium: Fig 3.4F and 3.5Aiv, endocardium: Fig 3.4F' and 3.5Biv).

[3] The exclusive disjunction operator or XOR is a logical operator that results in a value of true if exactly and only one of the operands has a value of true. The application of this operator to the filled external contour and filled internal contour masks will result in a mask with true values only where the tissue layer of interest is present (e.g. myocardium, endocardium).

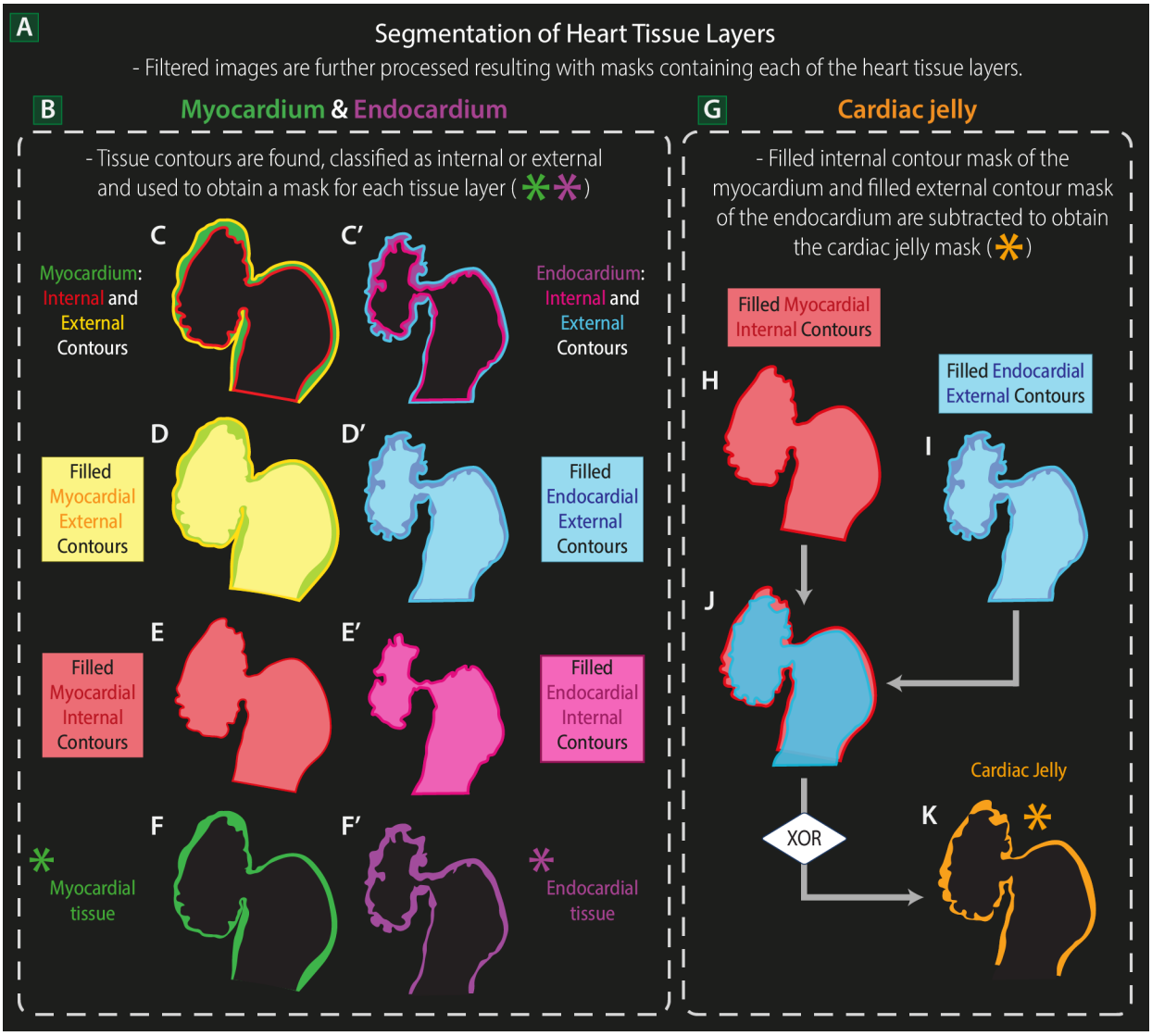

Fig 3.4. *morphoHeart's* heart tissue layer segmentation overview.
A. Overview of the steps required to segment each of the tissue layers of the heart. Filtered channels containing the myocardial and endocardial tissue signal are further processed to obtain masks containing each of the heart tissue layers, including the cardiac jelly. **B-E'.** For each channel, individually processed slices go through a process of contour detection and selection to extract all the contours that delineate the tissue completely (C-C'). Selected contours are then classified either as internal or external, depending on whether they outline the lumen (E-E') or the external borders (D-D') of the tissue, respectively. Internal and external contours are next used as binarisation masks for each channel, which are then combined, applying an exclusive disjunction logical operator (XOR) to obtain a final mask delineating each tissue layer without its lumen (F-F'). **F-F'.** Binarisation masks obtained for myocardial (F) and endocardial (F') slices, respectively for one example slice of the heart in Fig 3.2F, and Fig 3.3A. **G-J.** To segment the cardiac jelly per slice, the filled internal contour mask of the myocardium (E,H) and the filled external contour mask of the endocardium (D',I) are combined (J) applying an exclusive disjunction logical operator (XOR) obtaining a final mask that delineates the ECM (K). **K.** Binarisation mask obtained for the cardiac jelly in the same example slice as F-F'.

4.3.2 Extracting the ECM from the Negative Space Between Tissues

Recalling our interest in extracting the cardiac jelly layer of the heart, the same contour algorithm used to extract the cellular tissue layers' mask is followed to segment this ECM-rich layer. Despite the fact of not having a fluorescent marker to label the ECM, as the cardiac jelly lies between the myocardial and endocardial tissue layers (Fig 3.2B) (Lockhart *et al.*, 2011a; De Angelis *et al.*, 2017; Rasouli and Stainier, 2017; Derrick *et al.*, 2021), we can use the contour information obtained from the cellular tissue layers to extract the cardiac jelly tissue mask. In fact, classified external contours of the endocardium (Fig 3.4D',I)

outline the 'lumen' of the cardiac jelly while classified internal contours of the myocardium (Fig 3.4E,H) outline its external borders. Corresponding filled binarisation masks are then combined applying once again an exclusive disjunction logical operator (XOR) to obtain a final mask delineating just the ECM layer (Fig 3.4G, K, and 5C).

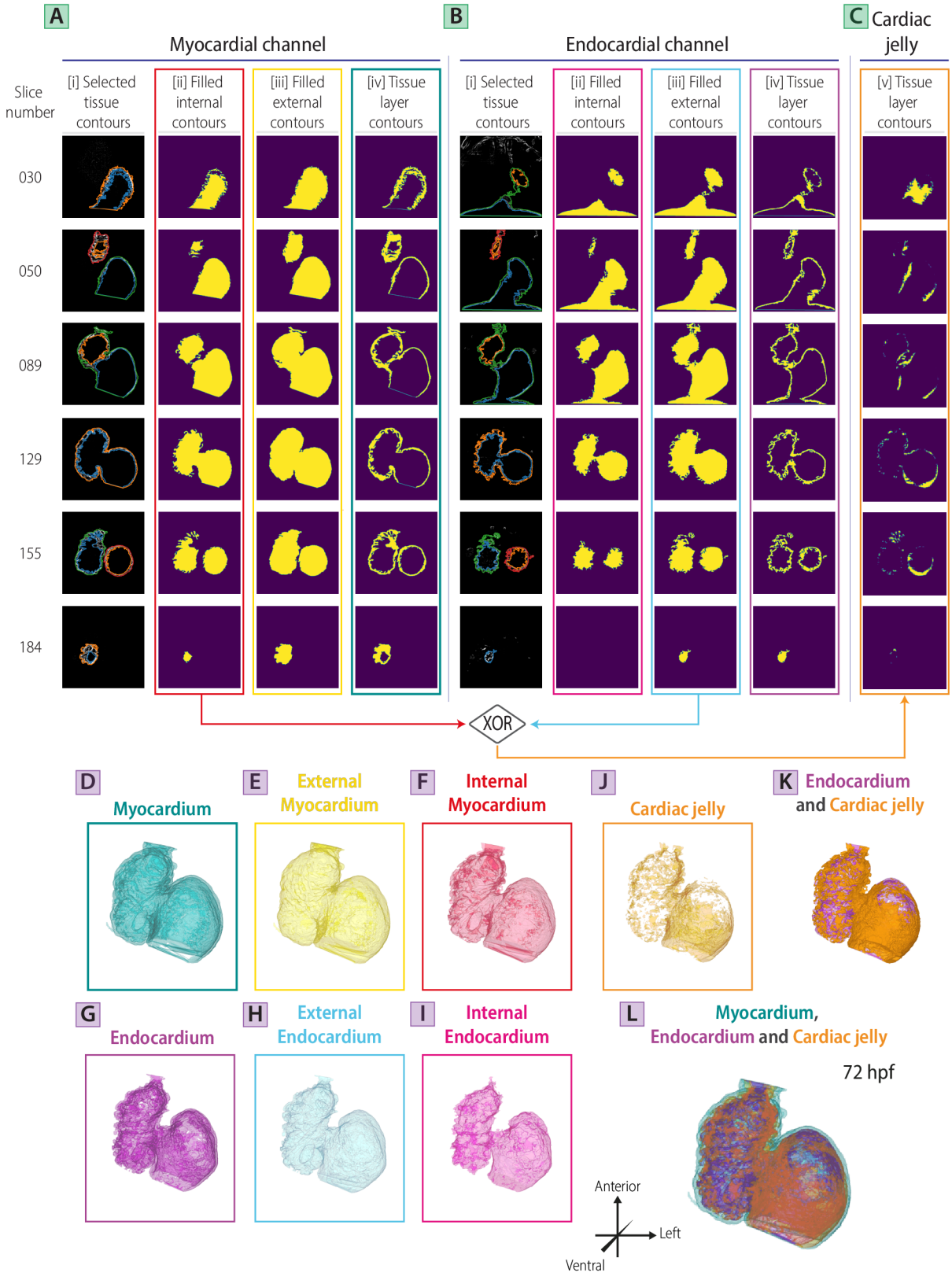

Fig 3.5. *morphoHeart's* heart tissue segmentation and 3D reconstruction overview.
A-B. Individually processed slices go through a process of contour detection (Ai, Bi), selection, and classification (internal and external) for each channel. Internal and external contours are next used independently to create

binarisation masks containing the tissue layer (Aiv, Biv), as well as the filled internal (Aii, Bii) and filled external (Aiii, Biii) versions for both the myocardial (A) and endocardial (B) channels. **C.** The filled internal contour mask of the myocardium (Aii, red box in A) and the filled external contour mask of the endocardium (Biii, light blue box in B) are then combined per slice to obtain the final mask that delineates the cardiac jelly tissue (Cv, orange box in C). **D-I**. Resulting masks are next used to create 3D/volumetric meshes of the different heart layers. As a reference, all resulting meshes and its surrounding squares are coloured according to the colour of the rectangle that surrounds the mask from which they were built in A-C. **D,G.** Resulting myocardial (D),and endocardial (G) tissue layers as 3D volumes. **E,H.** The filled external contours of the myocardium (Aiii, yellow box in A) and endocardium (Biii, light blue box in B) are used to create a 3D reconstruction of the filled tissue volume of each tissue layer (E: myocardium, H: endocardium). **F,I.** Similarly, the filled internal contours of the myocardium (Aii, red box in A) and endocardium (Bii, magenta box in B) are used to create a 3D reconstruction of the filled lumen of each tissue layer (F: myocardium, I: endocardium). **J.** Resulting cardiac jelly 3D volume. **K.** 3D endocardium and cardiac jelly volumes rendered together. **L.** 3D myocardium, endocardium and cardiac jelly volumes rendered together. A-C: Ventral view slices with anterior to the top. D-L: Ventral heart face with anterior to the top. Ai, Bi: Contours identified in each slice are coloured with random colours to aid the user's contour selection during processing.

4.4 3D Reconstruction

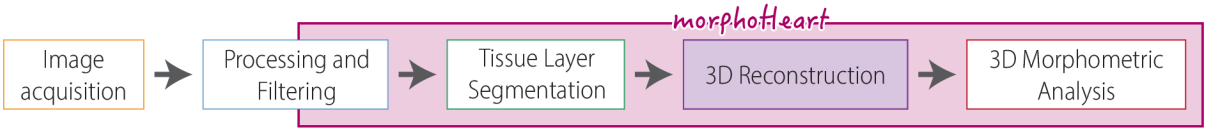

Resulting binarisation masks of each tissue layer are then used in the *3D Reconstruction* phase to create 3D volumes of each tissue layer (Fig 3.5 and 3.6), namely: the myocardium (Fig 3.5D and 6D-D''), endocardium (Fig 3.5E and 3.6E-E'') and cardiac jelly (Fig 3.5J and 3.6F-F''). When rendered the myocardial and/or endocardial volumes together with the cardiac jelly (Fig 3.5K, L), the ECM-rich layer is positioned as expected on the outside of the endocardium and the inside of the myocardium hence validating the segmentation process carried out for this layer.

Additionally, the filled external and internal contour masks of each tissue layer are used to construct 3D volumes of the filled tissue layer and its filled lumen, henceforth *external and internal myocardium/endocardium*, respectively (external myocardium: Fig 3.5E, internal myocardium: Fig5F, external endocardium: Fig 3.5H, internal endocardium: Fig 3.5I). These 3D reconstructions will be important when quantifying heart size, lumen size and tissue layer thickness in the *3D Morphometric Analysis* phase of *morphoHeart* (see Sections 4.5.3 and 4.5.4).

The obtained volumetric meshes that encompass the 3D information of the heart and each of its tissue layers will facilitate 3D morphological readouts to characterise and compare heart morphogenesis of wild-type and mutant embryos during development. As heart morphogenesis involves complex morphological tissue rearrangements, throughout the rest of the chapter, descriptions of the morphological measurements taken from these 3D volumes will be explained using a *Tg(myl7:lifeActGFP); Tg(fli1a:AC-TagRFP)* heart that was imaged at three key developmental stages: at tube/pre-looping (34hpf), looping and ballooning (50hpf) and at a maturing (72hpf) stage (Fig 3.6). Having an example of a segmented heart at these key developmental stages, will illustrate the way *morphoHeart* captures information regarding the morphological changes each tissue and chamber undergo throughout cardiac morphogenesis (Fig 3.6).

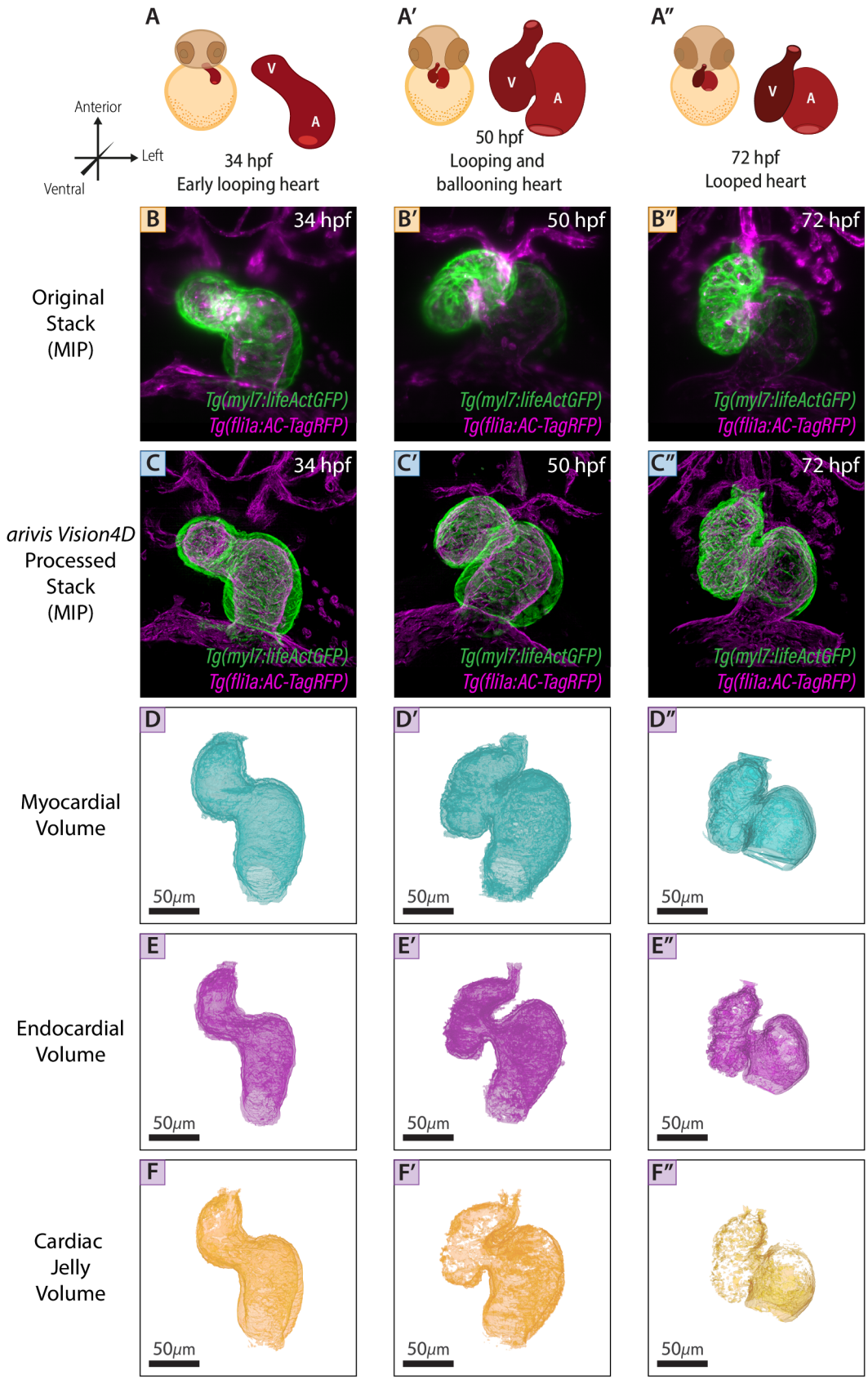

Fig 3.6. Application of *morphoHeart* phases 1-4 to zebrafish heart at early looping, during looping and ballooning, and at maturing stages.

A-A''. Schematic of the ventral face of a zebrafish and a zebrafish heart at the key developmental stages. The same embryonic heart carrying *Tg(myl7:lifeActGFP); Tg(fli1a:AC-TagRFP)* was imaged at 34hpf (B-F), 50hpf (B'-F') and 72hpf (D''-F'') and processed through arivis Vision4D and *morphoHeart* obtaining 3D reconstructions of the heart tissue layers. **B-B''.** MIPs of original z-stacks taken in the light-sheet microscope. **C-C''.** Resulting MIPs of processed images using arivis Vision4D pipeline. **D-F''.** Myocardial (D-D''), endocardial (E-E'') and cardiac jelly

(F-F'') 3D reconstructions of the processed stacks. B-B'',C-C'': Ventral views with anterior to the top. D-D'',E-E'',F-F'': Ventral heart face with anterior to the top. A: Atrium, V: Ventricle.

[*Note#3.3*: From this point onwards and throughout this thesis, the term '*view*' is going to be used when referring to the orientation with which one observes the embryo and '*face*' to refer specifically to the morphological/geographical surface of the heart that is being shown].

4.5 3D Morphometric Analysis Library

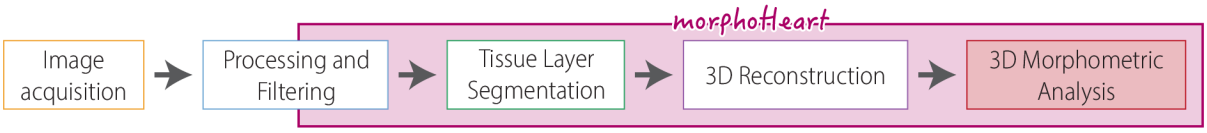

3D reconstructions of the developing heart obtained using *morphoHeart* open up the number of readouts available to characterise heart shape and morphology through time. To meet the needs for unbiased 3D analysis of morphology, for the last phase of *morphoHeart* I developed a 3D morphometric analysis library. This library provides different functions that allow the 3D quantification of heart/tissue size and distribution, as well as chamber morphology. It additionally includes metrics purposely tailored to quantify specific processes of heart morphogenesis such as heart looping and ballooning. A detailed description of the functions included within the library is given below.

4.5.1 Centreline Extraction

Centrelines have been identified as robust descriptors of the shape of tubular organs and have been used in different studies to investigate the spatial 3D morphology of the airways, gut, as well as arteries and veins within different organs (Piccinelli *et al.*, 2009; Smistad, Elster and Lindseth, 2014; Alazmani *et al.*, 2016; Bayer *et al.*, 2019; Kiruthika *et al.*, 2019; Üveges *et al.*, 2019; Stidham *et al.*, 2020). As the heart transitions from a linear tube to a looped organ during its initial developmental stages, the use of a centreline to describe and characterise the spatial and temporal morphogenetic changes is promising (Fig 3.7).

In general, centrelines are defined as the line between two lumen sections of a tube, whose minimal distance from the 3D boundary is maximal. To be able to define all the positions that make up a centreline, an internal Voronoi diagram of the surface is calculated (Fig 3.7B-B''). Such Voronoi diagram is composed of convex polygons whose vertices are the centres of all the maximal inscribed spheres that represent the surface's lumen. The radius of the maximal inscribed spheres provide information of the distance of each sphere to the surface's boundary, so that large spheres whose centres are in the deeper/central portion of the Voronoi diagram give information about the basic morphology of the surface while small spheres capture its small disturbances/roughness (Piccinelli *et al.*, 2009). The centreline is finally built by connecting the centres of all the maximal inscribed spheres along the centre path of the surface so that for every sphere there is a point belonging to the resulting centreline (Antiga *et al.*, 2008) (Fig 3.7C-C'').

To obtain the 3D centreline of the reconstructed heart, either the internal or external myocardial volume can be used as input surface. Internal Voronoi diagrams of the internal myocardium of the processed heart are shown in Fig 3.7B-BB'' while representations of the sequence of maximal inscribed spheres obtained from the Voronoi diagram in Fig 3.7C-C''. As the centre of the maximal inscribed spheres on either end of the heart's length don't reach all the way to the inflow and outflow tract, the connected centres of all the maximal inscribed spheres (obtained from the internal Voronoi diagram, Fig 3.7B-B'') define the central portion of the heart centreline. A final centreline is created by connecting this central centreline portion to pre-defined spheres positioned in the centre of the heart's inflow and outflow tract (blue and red circles in Fig3.7A-A'') obtaining the light blue splines shown in Fig 3.7D-D''. At this point, a segment connecting

these two spheres, (hereafter *linear heart length*), which provides information about whole heart orientation is also created.

Fig 3.7D-D'' illustrates the final centrelines (light blue) and linear heart length (light green) of the heart at different stages as 3D splines. The length of both splines can be measured and compared between different processed hearts. To assure unbiased analysis when using the centreline, all centreline splines -irrespective of their length-, are furthered refined and recreated with a constant number of points equally distanced to each other. [*Note#3.4*: All the analyses carried out in this thesis used centrelines obtained using the internal myocardium as surface and each centreline spline was refined to contain 300 points].

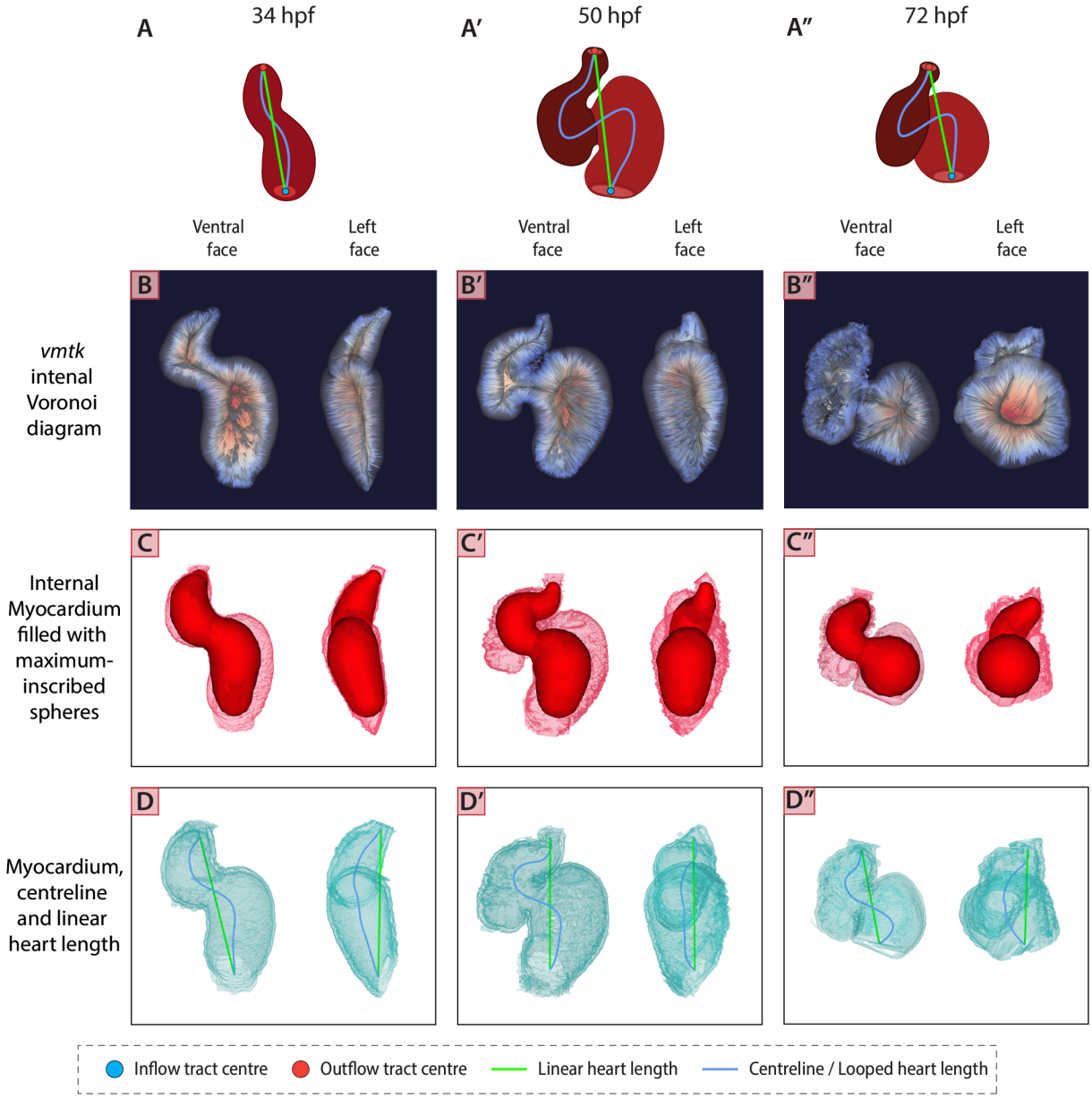

Fig 3.7. The 3D centreline, a shape descriptor for heart looping and ballooning.
A-A''. Schematic of the ventral face of a zebrafish heart with the centreline (light blue line) and the linear heart length (green line) at 34hpf (A), 50hpf (A') and 72hpf (A''). **B-B''.** Ventral and left heart face of the internal Voronoi diagram of the 3D internal myocardial mesh of a zebrafish heart at 34hpf (B), 50hpf (B') and 72hpf (B'') used to extract the 3D centreline. Colours represent the radius of maximal inscribed spheres (red: small, blue: large). **C-C''.** Ventral and left heart face of the internal myocardium meshes shown in B-B'' filled with the maximal inscribed spheres, whose centres make up the 3D centreline. **D-D''.** Ventral and left face of the centreline (light blue) and linear heart length (light green) of the hearts shown in B-B''. The linear length is obtained by creating a segment connecting the inflow and outflow tract centre points. This 3D segment also

holds information regarding the orientation/direction of the whole organ. B-B'',C-C'',D-D'': Ventral and left heart faces with anterior to the top.

4.5.2 Definition of Heart Sectioning

As previously described, during cardiac morphogenesis, multiple processes such as cell addition/ingression, cell proliferation, and changes in cell shape and size, shape this organ. These processes have been not only described to be distinct for each chamber and tissue layer (Auman *et al.*, 2007; de Pater *et al.*, 2009; Dietrich *et al.*, 2014; Kelly, Buckingham and Moorman, 2014; Le Garrec *et al.*, 2017) but also for different regions within them (Manasek, Burnside and Waterman, 1972; Auman *et al.*, 2007; Dietrich *et al.*, 2014; Hoog *et al.*, 2018; Derrick *et al.*, 2021).

With the interest of characterising and understanding more deeply how chambers and tissues change in size and morphology throughout development, and reveal regionalised differences, two different heart sectioning functions were included as part of the 3D morphometric analysis library, both of which will be described next.

Atrium and Ventricle

All 3D volumes obtained (Fig 3.5D-J) can be divided into atrial and ventricular meshes or volumes. To obtain these chamber-meshes, a disc is created centred in a centreline point designated (by the user) as the atrio-ventricular canal (AVC) of the heart (Fig 3.8A-B''). The disc orientation is defined by calculating the direction of the 3D vector connecting the centreline points immediately adjacent to the designated AVC point and assigning such vector as the vector normal to the disc (i.e. vector perpendicular to the flat surface of the disc that defines its orientation in 3D). Depending on the heart morphology being analysed, the parameters of this disc can be further modified by the user rotating (moving) the initially created disc around (in) the x, y or z axes and changing the disc size. This results in the final disc being clearly positioned dividing the 3D heart volume into two individual chambers (Fig 3.8B-B''). Final atrial and ventricular meshes of each tissue layer can be stored and further quantified, obtaining more detailed information per chamber (Fig 3.8C-D''').

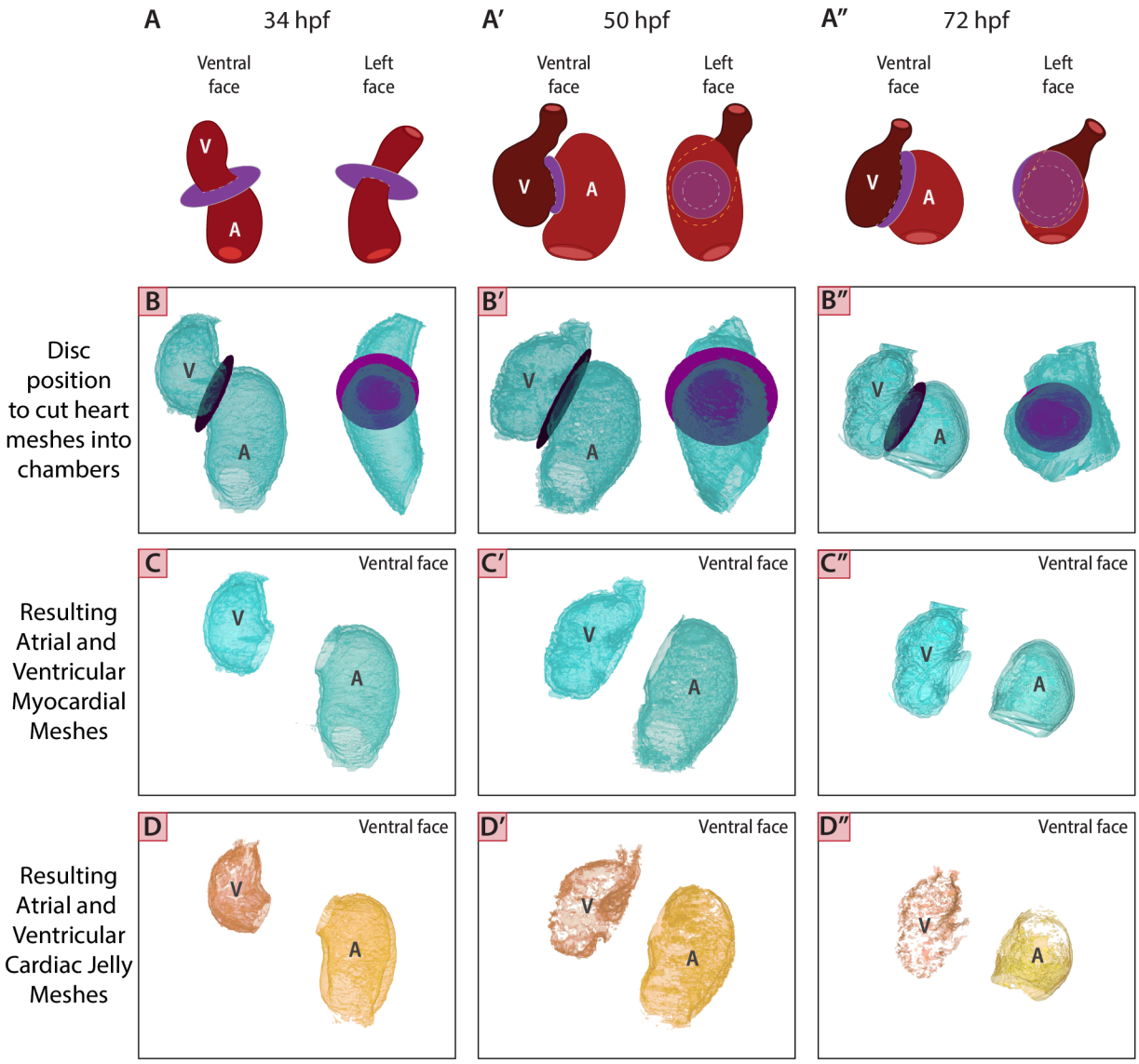

Fig 3.8. Dividing the heart into chambers to further characterise specific chamber morphology and tissue composition.

A-A''. Schematic of the ventral and left face of a zebrafish heart at 34hpf (A), 50hpf (A') and 72hpf (A'') depicting the way in which a disc (purple) is positioned to cut the heart tissue layers into chambers. **B-B''.** Ventral and left face of the myocardial tissue layer of a zebrafish heart at 34hpf (B), 50hpf (B') and 72hpf (B'') with the disc (purple) positioned for cutting the tissue layer into chambers. **C-C''.** Ventral face of the atrial and ventricular myocardial tissue meshes of the heart. These are the final meshes obtained when cutting the myocardial tissue with the disc shown in B-B''. **D-D''.** Ventral face of the atrial and ventricular cardiac jelly meshes of the heart. These are the final meshes obtained when cutting the cardiac jelly with the same disc shown in B-B''. B-B'': Ventral and left heart faces with anterior to the top. C-C'',D-D'': Ventral face of the heart chambers with anterior to the top. A: Atrium, V: Ventricle.

LEFT AND RIGHT

Similar to the chamber sectioning, all 3D volumes can be divided into left and right side meshes. To obtain these lateral meshes, initially each end of the 3D centreline (inflow and outflow tract portions) is extended further along the anteroposterior heart axis so that the new centreline spline endpoints are located outside the heart mesh. The direction in which each end is extended is directed by the orientation of the last centreline points adjacent to either the inflow or outflow tract centre points (light blue and red circles in Fig 3.7A-A''). This extended centreline is next projected through the dorsoventral plane of the heart creating a ribbon (pink ribbon in Fig 3.9A-B''') with which the heart mesh is going to be cut to obtain left

and right side meshes (Fig 3.9C'C'''). Resulting left and right side meshes of the cut tissue layer can be stored and further quantified, obtaining more detailed information for each side of the heart. Moreover, this method can be also applied to divide the individual chambers shown in Fig 3.8D-D'' into left and right sides, capturing more granular information regarding the distribution of this tissue layer per chamber and per side (Fig 3.9D-D'').

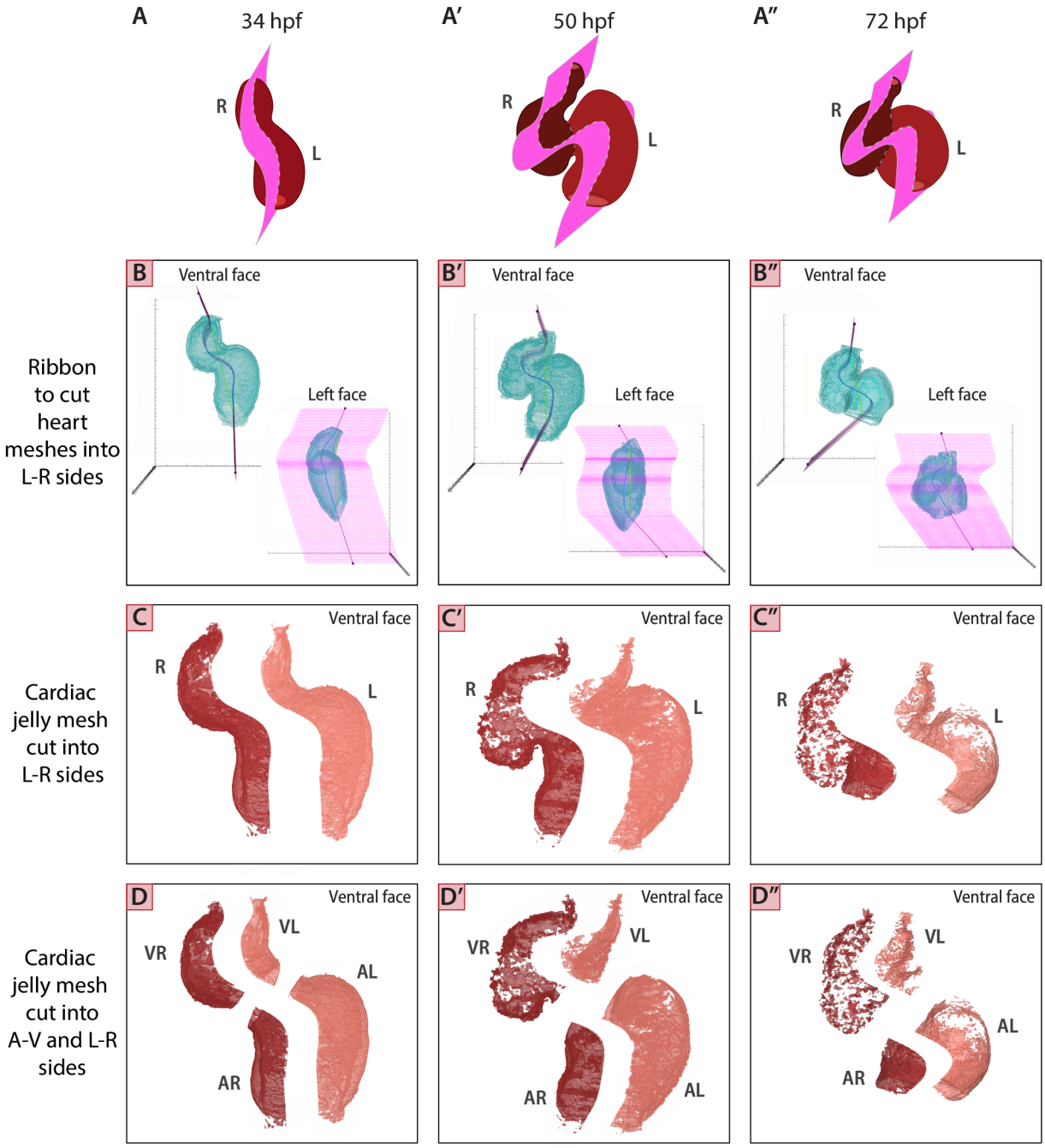

Fig 3.9. Dividing the heart cardiac jelly into left and right sides to further characterise cardiac jelly regionalisation.

A-A''. Schematic of the ventral face of a zebrafish heart at 34hpf (A), 50hpf (A') and 72hpf (A'') depicting the way in which the centreline has been extended dorso-ventrally creating a ribbon (pink) to cut any heart mesh into left and right sides. **B-B''.** Ventral and left face of the myocardial tissue layer of a zebrafish heart at 34hpf (B), 50hpf (B') and 72hpf (B'') with the ribbon (magenta) positioned for cutting the heart mesh into left and right sides. **C-C''.** Left and right sides of the cardiac jelly mesh of the heart shown in B-B''. These are the final meshes obtained when cutting the cardiac jelly with the same ribbon shown in B-B''. **D-D''.** Left and right side of the atrial and ventricular cardiac jelly mesh of the heart shown in B-B''. These are the final meshes obtained when cutting the chamber cardiac jelly meshes (Fig 3.8D-D'') with the same ribbon shown in Panels B-B''. B-B'':

Ventral and left heart faces with anterior to the top. C-C'',D-D'': Ventral face of the left and right side meshes with anterior to the top. A-V: Atrium-Ventricle, A: Atrium, V: Ventricle, L-R: Left-Right, L: Left, R: Right.

4.5.3 QUANTIFICATION OF MORPHOLOGICAL PARAMETERS

Once all the 3D meshes of interest for the analysis had been obtained, the *morphoHeart* 3D morphometric analysis library includes a series of functions to extract and quantify gross morphology and other metrics intentionally designed to understand cardiac development.

Table 3.30. *morphoHeart's* gross morphological measurements obtained from 3D reconstructions.

Measurement	Input structure	Output measurement
Surface Area	External Myocardium	Heart surface area
	Internal Endocardium	Lumen surface area
Volume	Myocardium	Myocardial tissue volume
	Atrial / Ventricular Myocardium	Atrial / Ventricular Myocardial tissue volume
	External Myocardium	Heart size
	Atrial / Ventricular External Myocardium	Atrial / Ventricular size
	Endocardium	Endocardial tissue volume
	Atrial / Ventricular Endocardium	Atrial / Ventricular Endocardial tissue volume
	Internal Endocardium	Lumen size
	Atrial / Ventricular Internal Endocardium	Atrial / Ventricular Lumen size
	Cardiac Jelly	Cardiac Jelly Volume
	Atrial / Ventricular Cardiac Jelly	Atrial / Ventricular Cardiac Jelly volume
	Left / Right Tissue Layer Mesh	Left / Right Tissue Layer volume[#]
Gross Chamber Morphology [▲] (Fig 3.10)	Atrial / Ventricular Myocardium	Atrial / Ventricular depth Atrial / Ventricular length Atrial / Ventricular width Atrial / Ventricular Asphericity [❖]
Looping Measurements	Centreline	Looped heart length
	Linear heart length	Linear heart length
	Centreline and Linear heart length	Looping Ratio = $\frac{\text{Looped heart length}}{\text{Linear heart length}}$

[#] Any tissue layer mesh can be divided into left and right sides using the method described in Section 2.6.2 (Left-Right) and the volume of each side can be further quantified.

[▲] To obtain morphological measurements of the chambers, ellipsoids are fit to each chamber and dimensions and properties of the resulting ellipsoid are noted (Fig 3.10).

[❖] Asphericity measures how different an ellipsoid is from a sphere. Values that are close to zero correspond to a more spherical object. If *a*, *b*, and *c* are the dimensions of the ellipsoid axes, the asphericity of the ellipsoid is defined by:

$$Asph = 4 \cdot \left[\left(\frac{a-b}{a+b} \right)^2 + \left(\frac{a-c}{a+c} \right)^2 + \left(\frac{b-c}{b+c} \right)^2 \right] / 3$$

Table 3.1 describes an initial set of functions to quantify gross morphological parameters of the 3D reconstructions, detailing the input structure being quantified and the measurement obtained.

Measurements such as surface area and volume are attributes measured directly from the 3D meshes and can be used as a proxy for heart/chamber/tissue size and shape. Additionally, surface area measurements can become particularly interesting when describing changes in trabeculation of the ventricle at stages of development over 72hpf, providing a way to quantify the increase in complexity of this tissue as it undergoes this essential maturation process (see Chapter 1, Section 4.1.5). Atrial and ventricular shape can be further quantified by measuring the dimensions and properties of the ellipsoid that best fits the specific chamber myocardial mesh (Fig 3.10). Additionally, similar to the looping ratio analysis in 2D (Derrick *et al.*, 2021), the length of the 3D splines representing the centreline and linear heart length (Fig 3.7D-D''') can be measured and the extent to which each heart has undergone looping can be further assessed and compared by quantifying its looping ratio in 3D (see Chapter 2, Section 10).

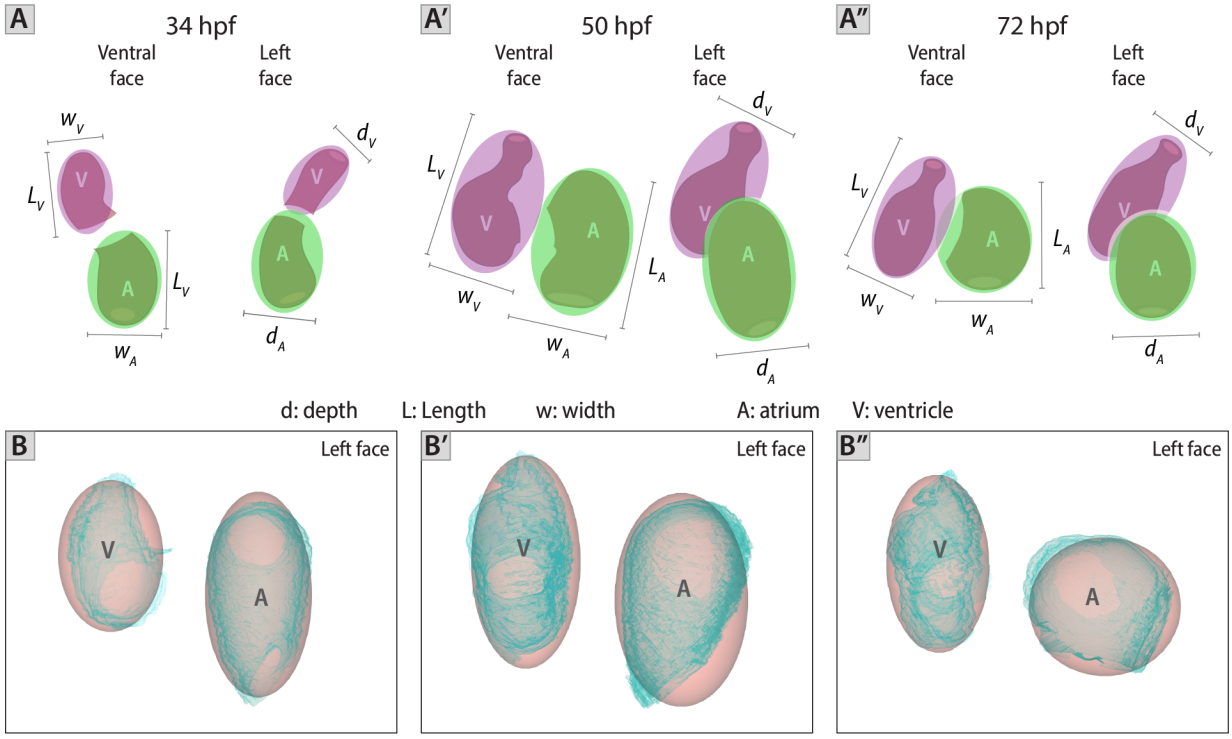

Fig 3.10. Characterising gross chamber morphology.
A-A''. Schematic of the ventral and left face of a zebrafish heart at 34hpf (A), 50hpf (A') and 72hpf (A'') depicting the way ellipsoids are fit to each chamber to obtain standardised measurements of its size and shape, such as length (*L*), width (*w*) and depth (*d*) (ellipsoids fitting the ventricle in magenta, ellipsoids fitting the atrium in green). To further quantify the chamber's shape, the asphericity of the fitted ellipsoid can be calculated obtaining a value between 0 and 1. Asphericity values closer to zero correspond to a more spherical ellipsoid. **B-B''.** Left face of the 3D atrial and ventricular myocardium circumscribed by the ellipsoid that best fits each chamber's shape. B-B'': Chambers' left face with anterior to the top. A: Atrium, V: Ventricle, d: depth, L: length, w: width.

Heart/Chamber Orientation

3D visual analysis from both the frontal and sagittal planes of the 3D hearts shows variation in terms of chamber orientation, confirming the previously described chamber realignments that occur during heart morphogenesis (Rohr, Otten and Abdelilah-Seyfried, 2008; Lombardo *et al.*, 2019; Tessadori *et al.*, 2021). To further describe chamber orientation and characterise topographically the relationship between the chambers at any stage, metrics regarding chamber orientation in both planes were included within the 3D morphometric analysis library. The evolution of these orientation parameters through development will aid the understanding of the processes that concomitant to chamber growth and expansion bring the developing heart chambers side-by-side forming an S-shaped loop.

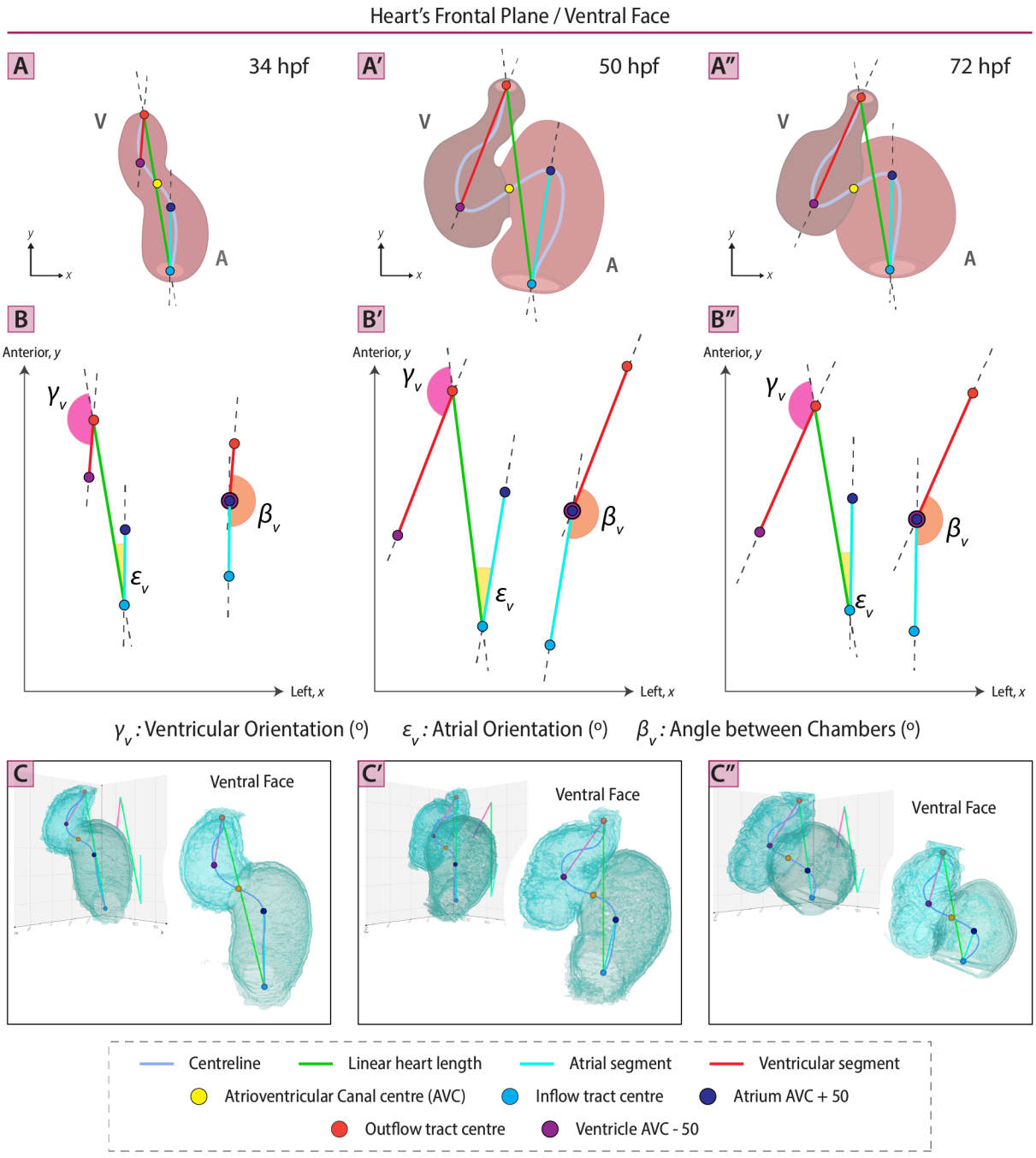

Fig 3.11. Measuring chamber orientation from the ventral view.
A-A''. Schematic depicting the segments used to measure chamber orientation with respect to the heart from the frontal plane at 34hpf (A), 50hpf (A') and 72hpf (A''). A line segment representing the atrial orientation (light blue) is defined by connecting a sphere in the centre of the inflow tract (blue sphere) with a sphere located in the centreline, around 50 points away from the AV canal (yellow sphere) towards the atrium (dark blue sphere). Likewise, the line segment that defines the ventricular orientation (red) is defined by connecting a sphere in the centre of the outflow tract (red sphere) with a sphere located in the centreline, around 50 points away from the AV canal (yellow sphere) towards the ventricle (purple sphere). **B-B''.** When these line segments and the linear heart length are projected in the *x,y* plane of the heart and viewed from the frontal face of the heart, angle measurements between them provide a quantitative readout of the orientation of each chamber (γ_v: ventricle, ε_v: atrium) and the angle between them (β_v) from the frontal plane of the heart (ventral face). **C-C''.** Top left images in panels show example of 3D atrial and ventricular myocardial chambers with defined orientation segments and linear heart length inside heart and projected in the *x,y* plane at different stages of development. Right images in panels show the ventral face of these same hearts. C-C''-(top left images in panels): 45° clockwise rotated ventral face around the y-axis with anterior to the top to see projected segments behind heart chambers. C-C''- (right images in panels): heart's ventral face with anterior to the top. A: Atrium,

V: Ventricle, AVC: Atrioventricular canal, AVC +/- 50: sphere positioned 50 centreline points away from the AVC centreline position in the direction of the atrium/ventricle.

_____

To measure chamber individual orientation in the frontal plane (from a ventral view, Fig 3.11) at any stage of development, a global heart reference coordinate system is first established by projecting the linear heart length (green segment) to the *x,y* plane. This projected segment eliminates bias in the measurement, ensuring all angles are measured with respect to the heart orientation. A line segment representing the atrial orientation (cyan segment) is defined by connecting a sphere in the centre of the inflow tract (blue sphere) with a sphere located in the centreline, around 50 centreline points away from the AVC sphere towards the atrium (dark blue sphere) (Fig 3.11A-A'''). Likewise, a line segment that defines the ventricular orientation (red segment) is defined by connecting a sphere in the centre of the outflow tract (red sphere) with a sphere located in the centreline, around 50 points away from the AVC sphere towards the ventricle (purple sphere) (Fig 3.11A-A'''). Chamber orientation segments are next projected to the *x,y* plane and ventral atrial and ventricular orientations (ε_v and γ_v, respectively, Fig 3.10B-B'') are measured with respect to the projected linear heart length segment (Fig 3.11B-B''). Finally, the angle between the projected atrial and ventricular orientation segments is measured (β_v, Fig 3.11B-B''), providing an idea of the chamber alignment from a ventral view.

Likewise, to measure chamber individual orientation in the sagittal plane (from a left view, Fig 3.12) at any stage of development, the linear heart length (green segment) is projected to the *z,y* plane, providing a reference segment with respect to which chamber angles will be measured. Line segments defining atrial and ventricular orientations (cyan segment and red segment, respectively, Fig 3.12) are now projected to the *z,y* plane and sagittal atrial and ventricular orientations (ε_s and γ_s, respectively) are then measured with respect to the projected linear heart length segment (Fig 3.12B-B''). Similarly, to measure the angle between chambers, the angle between the *z,y* projected atrial and ventricular orientation segments is measured, providing an idea of the rotation around the AVC these chambers experience as they develop (β_s).

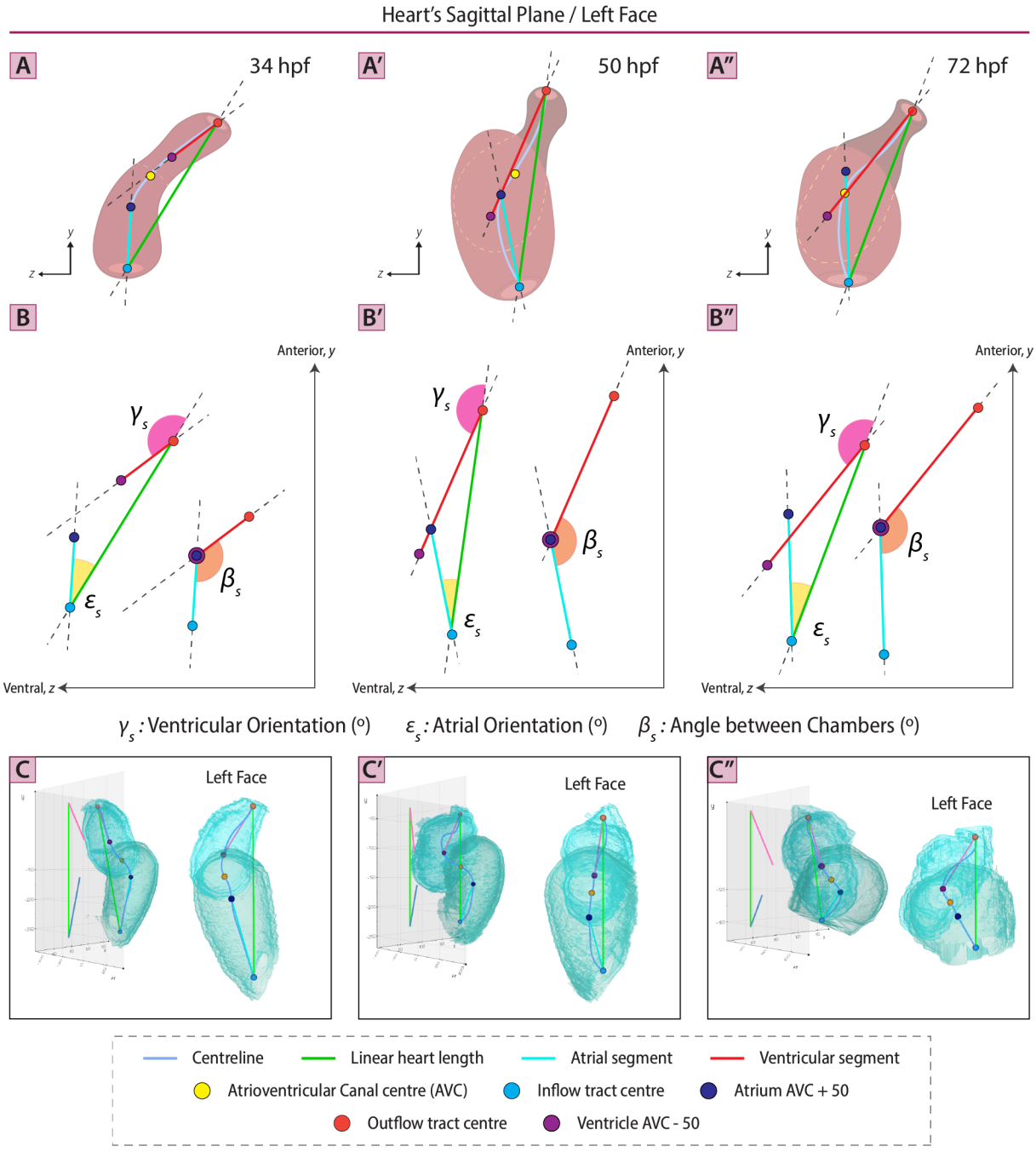

Fig 3.12. Measuring chamber orientation from the sagittal plane.
A-A''. Schematic depicting the segments used to measure chamber orientation with respect to the heart from the sagittal plane at 34hpf (A), 50hpf (A') and 72hpf (A''). A line segment representing the atrial orientation (light blue) is defined by connecting a sphere in the centre of the inflow tract (blue sphere) with a sphere located in the centreline, around 50 points away from the AV canal (yellow sphere) towards the atrium. Likewise, the line segment that defines the ventricular orientation (red) is defined by connecting a sphere in the centre of the outflow tract (red sphere) with a sphere located in the centreline, around 50 points away from the AV canal (yellow sphere) towards the ventricle. **B-B''.** When these line segments and the linear heart length are projected in the *z,y* plane of the heart and viewed from the left face of the heart, angle measurements between them provide a quantitative readout of the orientation of each chamber (γ_s: ventricle, ε_s: atrium) and the angle between them (β_s) from the sagittal plane of the heart (left face). **C-C''.** Top left images in panels show example of 3D atrial and ventricular myocardial chambers with defined orientation segments and linear heart length inside heart and projected in the *z,y* plane at different stages of development. Right images in panels show the left face of these same hearts. C-C''-(top left images in panels): 45° counter-clockwise rotated ventral face around the y-axis with anterior to the top to see projected segments on the left side plane of heart chambers. C-C''- (right images in panels): heart's left face with anterior to the top. A: Atrium, V: Ventricle, AVC:

Atrioventricular canal, AVC +/- 50: Sphere positioned 50 centreline points away from the AVC centreline position in the direction of the atrium/ventricle.

4.5.4 Tissue Layer Thickness Analysis

With the interest of characterising tissue distribution around the heart and identifying regions within the organ where more tissue is present compared to others, a detailed characterisation of heart tissue layer thickness has been included within *morphoHeart's* 3D morphometric analysis library.

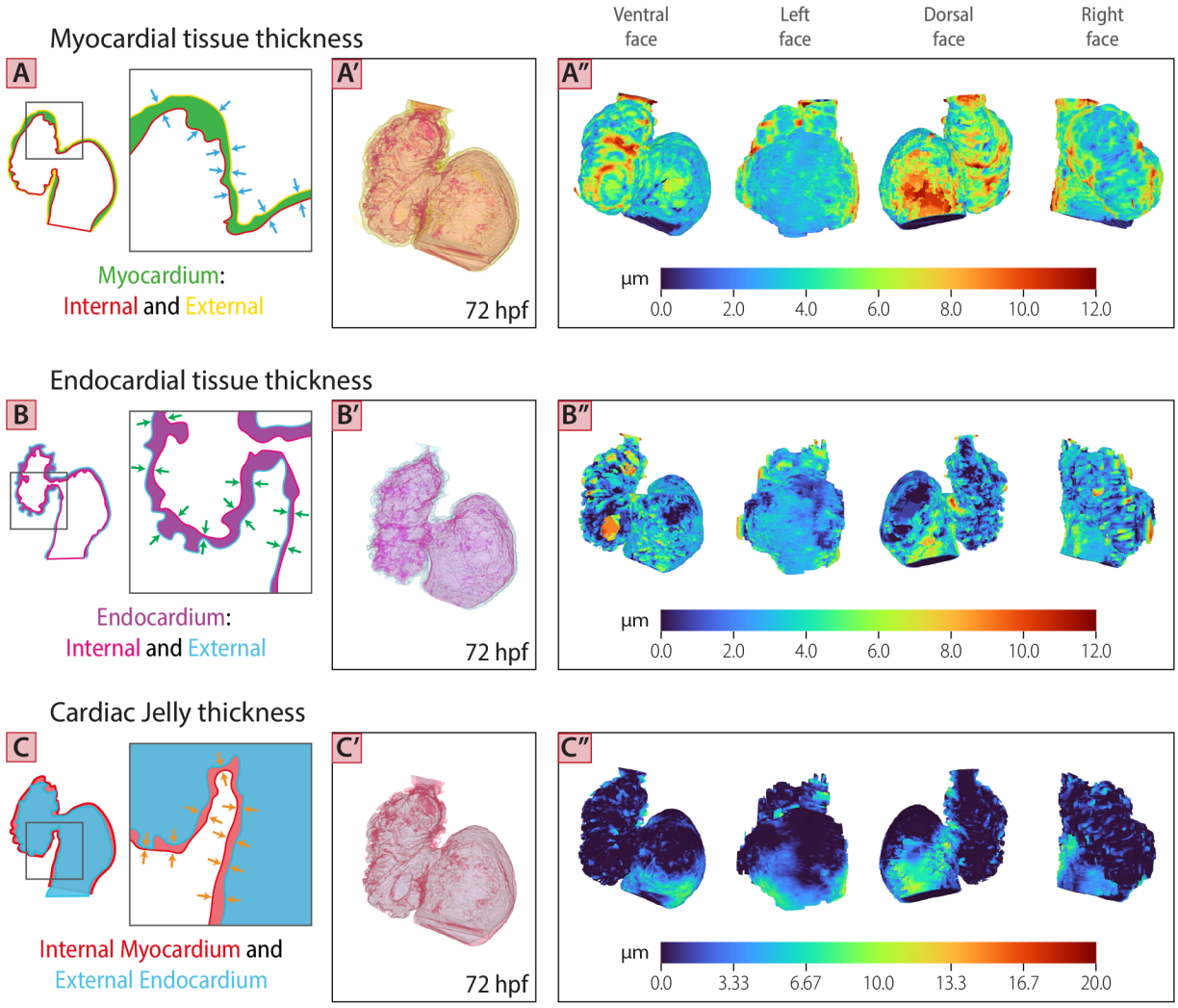

Fig 3.13. Colour coded tissue thickness heatmaps to quantify regional tissue distribution.
A-A''. Myocardial tissue thickness is calculated measuring the shortest distance between the external myocardium and the internal myocardium and colour coding the measured distances on the external myocardial mesh. **A.** Schematic representing with blue arrows the distance being measured between the external and internal myocardium. **A'.** 3D volume of the external (yellow) and internal (red) myocardium used to measure the myocardial thickness. **A''.** Ventral, left, dorsal and right face (left to right) of the external myocardium colour-coded by the myocardial thickness. B-B''. Similarly, the endocardial tissue thickness is calculated measuring the shortest distance between the external endocardium and the internal endocardium and the measured distances colour-coded on the external endocardial volume. **B.** Schematic representing with green arrows the distance being measured between the external and internal endocardium. **B'.** 3D volume of the external (blue) and internal (magenta) endocardium used to measure the endocardial thickness. **B''.** Ventral, left, dorsal and right face (left to right) of the external endocardium colour-coded by the endocardial thickness. C-C''. The cardiac jelly is sandwiched between the myocardium and the endocardium, as such the cardiac jelly tissue thickness is calculated measuring the shortest distance between the internal myocardial mesh and the external endocardial mesh and colour coding the measured distances on the internal myocardium. **C.** Schematic representing with orange arrows the distance being measured between the internal myocardium and external

endocardium. **C'.** 3D volume of the internal myocardium (red) and external (blue) endocardium used to measure the cardiac jelly thickness. **C''.** Ventral, left, dorsal and right face (left to right) of the internal myocardium colour-coded by the cardiac jelly thickness. A'-C': Heart's ventral face with anterior to the top.

To obtain tissue thickness values the external and internal meshes of the tissue of interest are used (e.g. myocardium [Fig 3.5E,F], endocardium [Fig 3.5H,I] or cardiac jelly [Fig 3.5F,H]) and the *signed distance field*[4] from the external to the internal mesh is calculated (Quammen, Weigle and Taylor II, 2011; Musy *et al.*, 2022). The thickness values obtained when using this approach correspond to the minimum distance between each of the points making up the external layer mesh and those making up the internal layer mesh of the tissue under study. Resulting thicknesses are mapped to the corresponding external mesh with colour-coded thickness ranges (Fig 3.13A-C'') and will be henceforth referenced as *3D thickness heatmaps*. This representation allows a simplistic yet detailed visualisation and assessment of the regionalisation of tissue layer thickness within the heart, providing insights into how its distribution varies around it. Moreover, if this thickness analysis approach is taken when analysing hearts at different developmental stages, comparative analysis of changes in tissue distribution can be made, offering information about the thickness/distribution changes each tissue layer undergoes during distinct developmental processes.

4.5.5 BALLOONING ANALYSIS

Taking advantage of the colour-coded representations created for the tissue thickness analysis, a new metric to quantify heart ballooning by measuring the extent to which each chamber had grown and modified its morphology from the primitive tubular shape could prove informative. To accomplish this, a similar methodology to the one previously described was taken, but this time calculating the *signed distance field* between the (external/internal) myocardial mesh and the heart centreline, mapping the obtained distances to the analysed myocardial mesh with colour-coded ballooning-distance ranges (Fig 3.14).

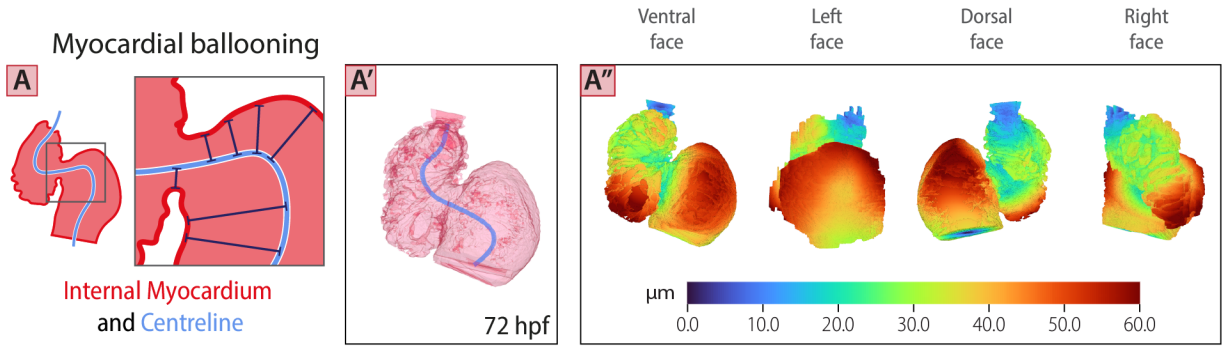

Fig 3.14. Colour coded ballooning heatmaps to quantify regional chamber growth.
A-A''. Myocardial ballooning is calculated measuring the shortest distance between the internal myocardium centreline and colour coding the measured distances on the internal myocardium. **A.** Schematic representing with capped segments (dark blue) the distance being measured between the internal myocardium and the centreline. **A'.** 3D volume of the internal myocardium (red) and the centreline (light blue) used to measure the myocardial ballooning. **A''.** Ventral, left, dorsal and right face (left to right) of the internal myocardium colour-coded by the myocardial ballooning measurement. A': Heart's ventral face with anterior to the top.

---

[4] A *signed distance field* is a function that takes a position as an input and outputs the distance from that position to the nearest part of a given input shape (Osher and Fedkiw, 2003; Quammen, Weigle and Taylor II, 2011).

This ballooning representation, hereafter termed *3D ballooning heatmaps*, allows a detailed 3D assessment of the regions within each chamber that have deviated to a major extent from the original tubular shape, becoming a valuable variable to use when characterising the morphogenesis of each chamber. [*Note#3.5*: In all the analyses carried out in this thesis the internal myocardium was used to obtain the ballooning heatmaps].

4.5.6 Unlooping, Unrolling and Straightening the Heart Heatmaps

3D heatmap representations for tissue thickness and ballooning increase the amount of detail perceivable from just observing individual 3D tissue layer meshes or the external myocardium mesh, revealing a great amount of information that was contained but not being measured within these 3D heart representations. Even though this wealth of information has been uncovered, comparative analysis of hearts at different stages and/or with different mutations using these 3D heatmap representations remains intricate and complex. Therefore, to be able to perform such comparative studies a method for unlooping and unrolling the 3D heatmaps into 2D projections was developed and included within the *morphoHeart* 3D morphometric analysis library.

To illustrate how this method works refer to Fig 3.15. Initially, the heart centreline spline (Fig 3.7D-D'') is extended anteriorly and posteriorly (anteriorly for the ventricular end and posteriorly for the atrial end) following the orientation of the last points making up the centreline in each pole (Fig 3.15A). Using the centreline position previously defined as the AVC centre (yellow sphere in Fig 3.11 and 3.12) and the disc used to section the heart into chambers (Fig 3.8), both the 3D heatmap and the extended centreline are divided into atrial and ventricular sections (Fig 3.15B). Each chamber's centreline is next projected to the dorsal face of the 3D heatmap chamber, establishing a reference line (or series of mesh points) -hereafter *3D dorsally projected centreline*- along the surface of the 3D volume from which the radial position of other points making the volume will be measured (white dotted line in Fig 3.15C). Once this reference line has been created, the extended centrelines of each chamber are used to create equally distanced planes that are centred and distributed along the centreline. The orientation of each plane at each centreline point is defined by calculating the direction of the 3D vector connecting the two points immediately adjacent to the assigned plane's centre and allocating such vector as the normal vector[5] of the plane. This process results in the creation of planes that are always perpendicular to the centreline orientation in each centreline position (Fig 3.15D). Each of these planes is then used to extract information of the 3D heatmap points that are intersected by each plane along the chamber (points in yellow dotted lines in Fig 3.15D and 3.15E), using as a reference for radial position (φ = 0°) the point of the *3D dorsally projected centreline* (blue circle in Fig 3.15E) and centring all radial measurements to the point of the extended centreline (green circle in Fig 3.15E). The radial coordinates (φ) of each mesh point, the thickness/ballooning values associated to it, and the plane number by which it was intersected are stored (Fig 3.15E). 2D projected representations of each chamber 3D heatmap is then created by plotting in a colour-coded way the thickness/ballooning values for each radial position ($x = \varphi$) against the plane number (*y = atrial/ventricular plane number*) (Fig 3.15F). As the reference spline defined by the *3D dorsally projected centreline* is in the dorsal face of the heart, the 2D projected heatmaps contain information of the thickness/ballooning values along dorsal face of the heart on its left and right edges, while ventral information is contained in the central section (see heatmap frame and key labels in Fig 3.15F).

[5] The *normal vector* to a surface is a vector that is perpendicular to a surface at any given point.

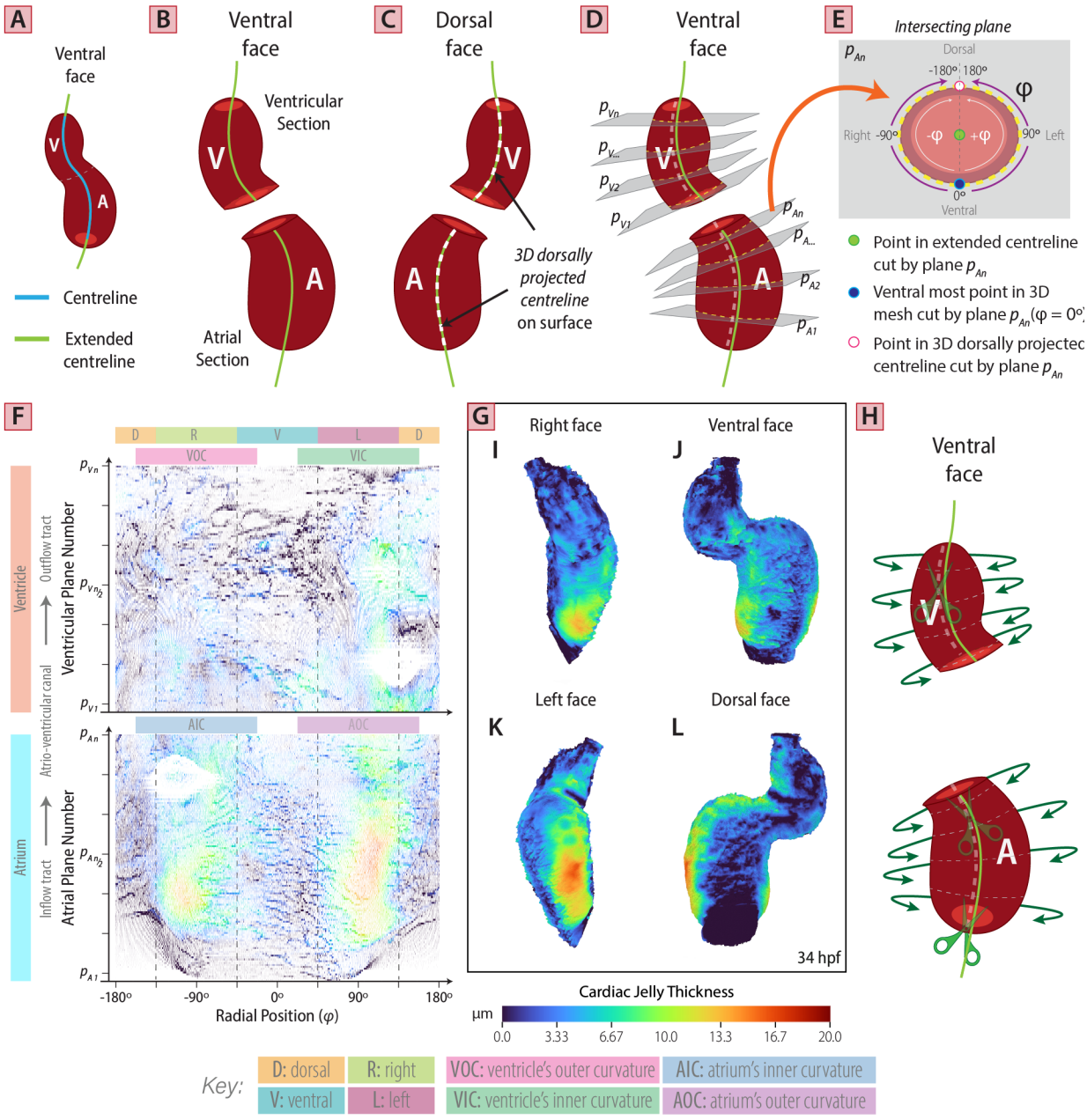

Fig 3.15. Unlooping and unrolling the heart: from 3D to 2D heatmaps.
A-G. Process followed to unloop and unroll heatmaps from 3D to 2D. **A.** The heart centreline is extended anteriorly in the ventricle (outflow tract) and posteriorly in the atrium (inflow tract), following the same orientation as the last points making up the centreline in each end. **B.** Extended centreline and 3D heatmap are split into chamber sections. **C.** Chamber-specific extended centreline is projected to the dorsal face of the 3D chamber heatmap, tracing a spline (white dotted line) on its surface. **D.** Each chamber's extended centreline is then used to create equally distanced planes that are distributed throughout the centreline's length and oriented perpendicular to the centreline's direction in each centreline position (for more details see description in text). **E.** Each of these planes is then used to extract information from the 3D heatmap points being intersected by each plane (e.g. radial coordinates φ and heatmap value) along the chamber. For each plane, the radial coordinates (φ) of each intersected mesh point are measured centred on the point of the extended centreline (green circle) and with respect to the point of the *3D dorsally projected centreline* (blue circle). **F.** 2D projected representations of each chamber 3D heatmap is then created by plotting in a colour-coded manner the thickness/ballooning values for each radial position ($x = \varphi$) against the plane number (*y = atrial/ventricular plane number*). This panel shows the planar projection of the 3D cardiac jelly thickness heatmap mesh shown in G. **G-L.** 3D cardiac jelly thickness heatmap of a 34hpf zebrafish heart colour-coded by thickness and shown in different orientations (I: right, J: ventral, K: left, L: dorsal face, all with anterior to the top). F and G share the same colour-coding range, shown on the bottom of panel G. **H.** *Unlooping*: Chamber-specific *3D dorsally projected centreline* is used to 'cut' the 3D heatmap along the chamber (see green scissors on the back of the

heart). *Unrolling*: 'Cut' heatmap chamber is then straightened and unrolled from the dorsal to the ventral face around the extended centreline to a planar projection, resulting in 2D heatmap plots like the ones shown in F. A,B,D,H: Heart's ventral face. C: Heart's dorsal face. A: Atrium, V: Ventricle. **2D Projected Heatmap**: D: Dorsal, R: Right, V: Ventral, L: Left, VOC: Ventricle's Outer Curvature, VIC: Ventricle's Inner Curvature, AOC: Atrium's Outer Curvature, AIC: Atrium's Inner Curvature.

In 3D what the methodology just described does is 'cut' the chamber specific 3D heatmap through the *3D dorsally projected centreline*, to then 'unroll' and straighten the cut surface from the dorsal to the ventral face all around the extended centreline (Fig 3.15H), finally obtaining 2D heatmap projections for each chamber. As initially mentioned, this methodology of unlooping, unrolling and straightening 3D heart heatmaps can be applied to any of the 3D heatmaps previously described in Sections 4.5.4 and 4.5.5 (as shown in Fig 3.16), allowing a standardised comparative analysis of tissue thickness or ballooning metrics to hearts not only at different developmental stages but with different mutations/defects.

[*Note#3.6:* All the 2D heatmaps projections presented in this thesis were created by obtaining information of the 3D chamber heatmap points cut into 152 planes. This number was selected as it gave the 2D heatmap projections a similar amount of perceived detail as the 3D heatmaps of the variable being measured (e.g. tissue thickness, myocardial ballooning). To illustrate this, compare the different views (faces) of the 3D cardiac jelly thickness heatmap in Fig 3.15G to the 2D heatmap in 3.15F, and all the 3D and 2D heatmaps shown in Fig 3.16].

[*Note#3.7*: Choosing a good colour scheme is integral to accurately and effectively displaying data, whereas a poor colour scheme can lead viewers to inaccurate conclusions or exclude those with colour deficiencies from proper analysis of the data. Considering this, throughout these thesis, 3D and 2D heatmaps are represented using *Turbo*, a recently developed colourmap that has the desirable properties of the commonly used *Rainbow/Jet* colourmap (i.e. show more detail due to its high contrast and allows quick visual assessment), while addressing some of its deficiencies (i.e. false detail and colour blindness ambiguity (Mikhailov, 2019)].

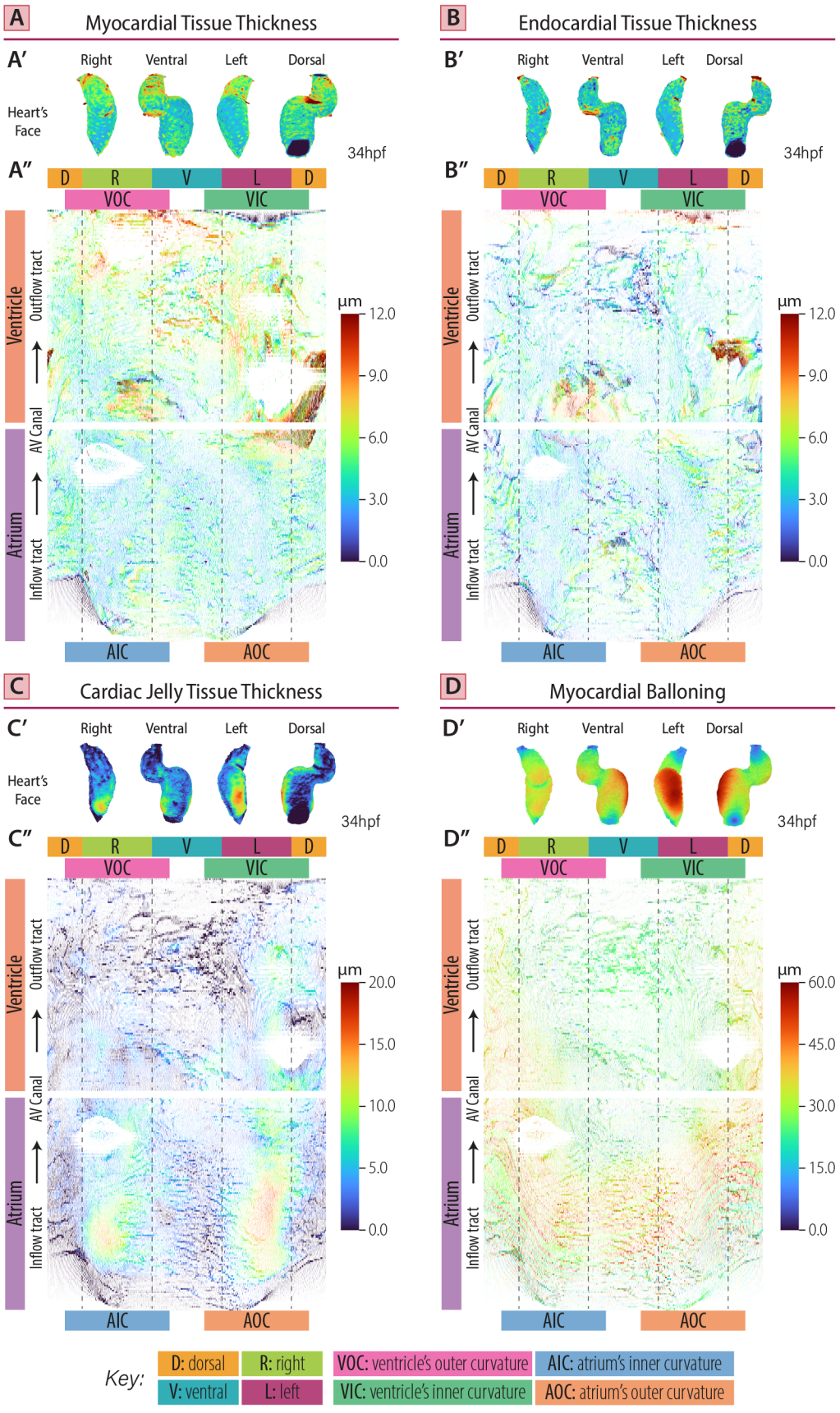

Fig 3.16. Heart layers' tissue thickness heatmaps and myocardial ballooning heatmap of a 34hpf zebrafish heart. **A-A''.** 3D and 2D representations of the myocardial thickness of a 34hpf zebrafish heart. **A'.** Right, ventral, left, and dorsal face (left to right) of the 3D colour-coded myocardium based on its thickness (colour-scale in A''). **A''.** Planar projection of the colour-coded myocardial thickness mesh shown in A'. **B-B''.** 3D and 2D representations of the endocardial thickness of a 34hpf zebrafish heart. **B'.** Right, ventral, left, and dorsal face (left to right) of the 3D colour-coded endocardium based on its thickness (colour-scale in B''). **B''.** Planar

projection of the colour-coded endocardial thickness mesh shown in B'. **C-C''.** 3D and 2D representations of the cardiac jelly thickness of a 34hpf zebrafish heart. **C'.** Right, ventral, left, and dorsal face (left to right) of the 3D colour-coded cardiac jelly based on its thickness (colour-scale in C''). **C''.** Planar projection of the colour-coded cardiac jelly thickness mesh shown in C'. **D-D''.** 3D and 2D representations of the myocardial ballooning of a 34hpf zebrafish heart. **D'.** Right, ventral, left, and dorsal face (left to right) of the 3D colour-coded myocardium based on its ballooning (colour-scale in D''). **D''.** Planar projection of the colour-coded myocardial ballooning mesh shown in D'. D: Dorsal, R: Right, V: Ventral, L: Left, VOC: Ventricle's Outer Curvature, VIC: Ventricle's Inner Curvature, AOC: Atrium's Outer Curvature, AIC: Atrium's Inner Curvature. A-D: Anterior to the top.

Comparative Analysis

Finally, as all hearts can now be mapped to equivalent 2D representations, to aid phenotypic comparison of these 2D heatmaps of hearts at different stages and/or with different mutations, a method to obtain average 2D heatmaps was included within the *morphoHeart* 3D morphometric analysis library. This function allows the illustration of the average tissue distribution (i.e. layer thickness heatmaps) or myocardial ballooning in hearts at the same developmental stage and with the same genotype (Fig 3.17), enabling a standardised and straightforward evaluation of the changes undergone by each of these variables through time and in defective scenarios.

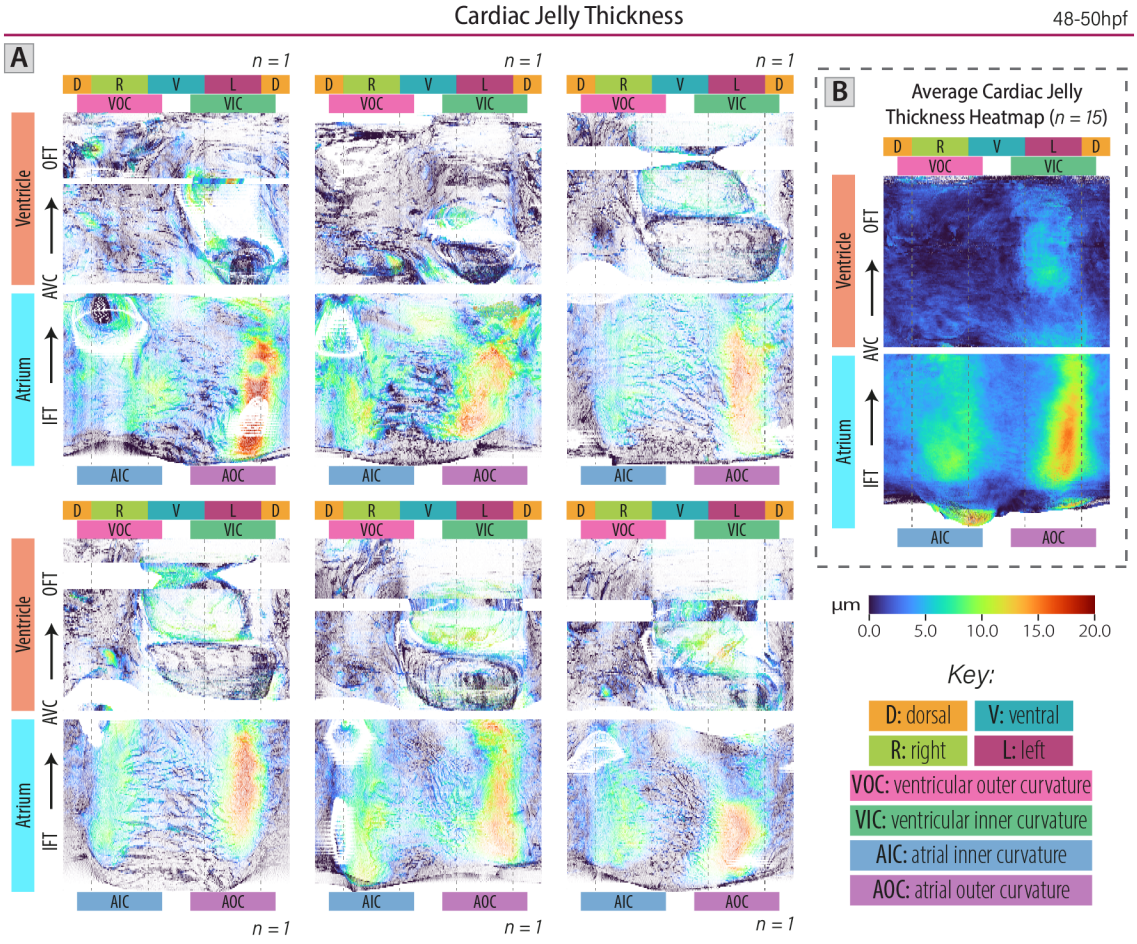

Fig 3.17. Average of 2D thickness/myocardial ballooning heatmaps of embryos with equivalent genotypes and stages evens out the noise allowing standardised phenotypic comparison of these variables.
A. Individual 2D representations of the cardiac jelly thickness of a six different zebrafish hearts at 48-50hpf. **B.** Average 2D cardiac jelly thickness heatmap of *n = 15* zebrafish embryos at 48-50hpf, including those presented in A. Averaging the cardiac jelly thickness of multiple hearts with same genotype and imaged at equivalent developmental stages, evens out the noise, and delivers a standardised 2D heatmap of this variable to use for phenotypic comparisons. IFT: Inflow-tract, AVC: Atrio-ventricular canal, OFT: Outflow-tract, D: Dorsal, R: Right,

V: Ventral, L: Left, VOC: Ventricle's Outer Curvature, VIC: Ventricle's Inner Curvature, AOC: Atrium's Outer Curvature, AIC: Atrium's Inner Curvature.

---

5 ACCURACY AND PRECISION ANALYSIS OF *MORPHOHEART*

As discussed in the introduction of this chapter, very few previous studies have attempted to quantitatively characterise in 3D heart morphology as the heart undergoes morphogenesis, exhibiting a lack of a 'gold-standard' data with which to compare the *accuracy* of *morphoHeart*'s 3D morphometric data.

However, to examine the *precision* of the tool, as wild-type hearts are expected to undergo similar morphological changes in size and shape as they develop, comparison of *morphoHeart*'s gross morphological metrics of embryos imaged at the same developmental stage, should inform the segmentation sensitivity and hence the precision of the tool. To make sure precision was the variable under evaluation, initially only embryos that had the same genotype, transgenic background and were imaged at the same developmental stage were analysed (i.e. wild-type, *Tg(myl7:lifeActGFP); Tg(fli1a:AC-TagRFP)* and 72hpf, respectively) (Fig 3.18A-D). Additionally, to evaluate the segmentation sensibility and precision of *morphoHeart* in the analysis of embryos with different transgenic backgrounds and imaging set-ups or approaches, a wild-type *Tg(myl7:lck:EGFP)^{md71}; Tg(kdrl:Hsa.HRAS-mCherry)* double transgenic embryo imaged at 50hpf using a retrospective approach was analysed at three different cardiac phases (Fig 3.18E). The *Tg(myl7:lck-EGFP)^{md71}; Tg(kdrl:Hsa.HRAS-mCherry)* expresses GFP in the cytosol of myocardial cells (Weber *et al.*, 2017) and mCherry in the plasma membrane of endothelial cells (Neil C. Chi *et al.*, 2008), labelling both cellular layers (analysed images were kindly provided by Anjalie Schlaeppi and Jan Huisken). Gross *morphoHeart* metrics of this heart were obtained and compared to the pool of 50hpf wild-type hearts presented throughout this thesis (Fig 3.18F-I).

Individual data points presented in each of the graphs in Fig 3.18A-D represent single zebrafish hearts at 72hpf processed by two different users. Fig 3.18F-I presents the same gross morphological variables presented in Fig 3.18A-D, but comparing the results obtained using different transgenic lines and imaging acquisition approaches in embryos at 48-50hpf. The fact that all the data points, independent of user, transgenic line or acquisition approach, cluster around a mean value confirms *morphoHeart*'s precision when providing morphometric parameters of the zebrafish heart. Interestingly, the myocardial volume is the only parameter in which segmentation of different transgenic lines appears not to cluster (Fig 3.18H). Two possible explanations could account for this phenomenon. The *Tg(myl7:lck:EGFP)^{md71}; Tg(kdrl:Hsa.HRAS-mCherry)* images were acquired in a beating heart, and retrospective processing was then used to synchronise the z-stack movies, obtaining a final 4D stack containing one full cardiac cycle (Weber *et al.*, 2017). The manual segmentation used to remove the added noise in some slices, induced by factors such as myocardial-fluorophore brightness, organ movement and synchronisation method, could have resulted in 'higher' myocardial volumes in the final 3D reconstruction of this layer. Another possibility could be associated with either transgenic line labelling different myocardial structures. The myocardial line used to segment the *Tg(myl7:lck:EGFP)^{md71}; Tg(kdrl:Hsa.HRAS-mCherry)* hearts labels the cytoplasm of the cardiomyocytes rather than the actin contained in them (i.e. *Tg(myl7:lifeActGFP); Tg(fli1a:AC-TagRFP)*), hence myocardial tissue volumes segmented using this cytoplasmic line could have resulted in 'higher' myocardial volumes, as the whole cell would be labelled with the fluorophore rather than only its actin. Both factors should be considered when designing the experiments in which to use *morphoHeart* and defining the most suitable comparative analysis, topics which will be briefly discussed in the next section (Section 6). Despite the differences obtained with this parameter, the clustered behaviour of the other variables, independent of user, transgenic line or acquisition approach, corroborates *morphoHeart*'s precision, validating its use.

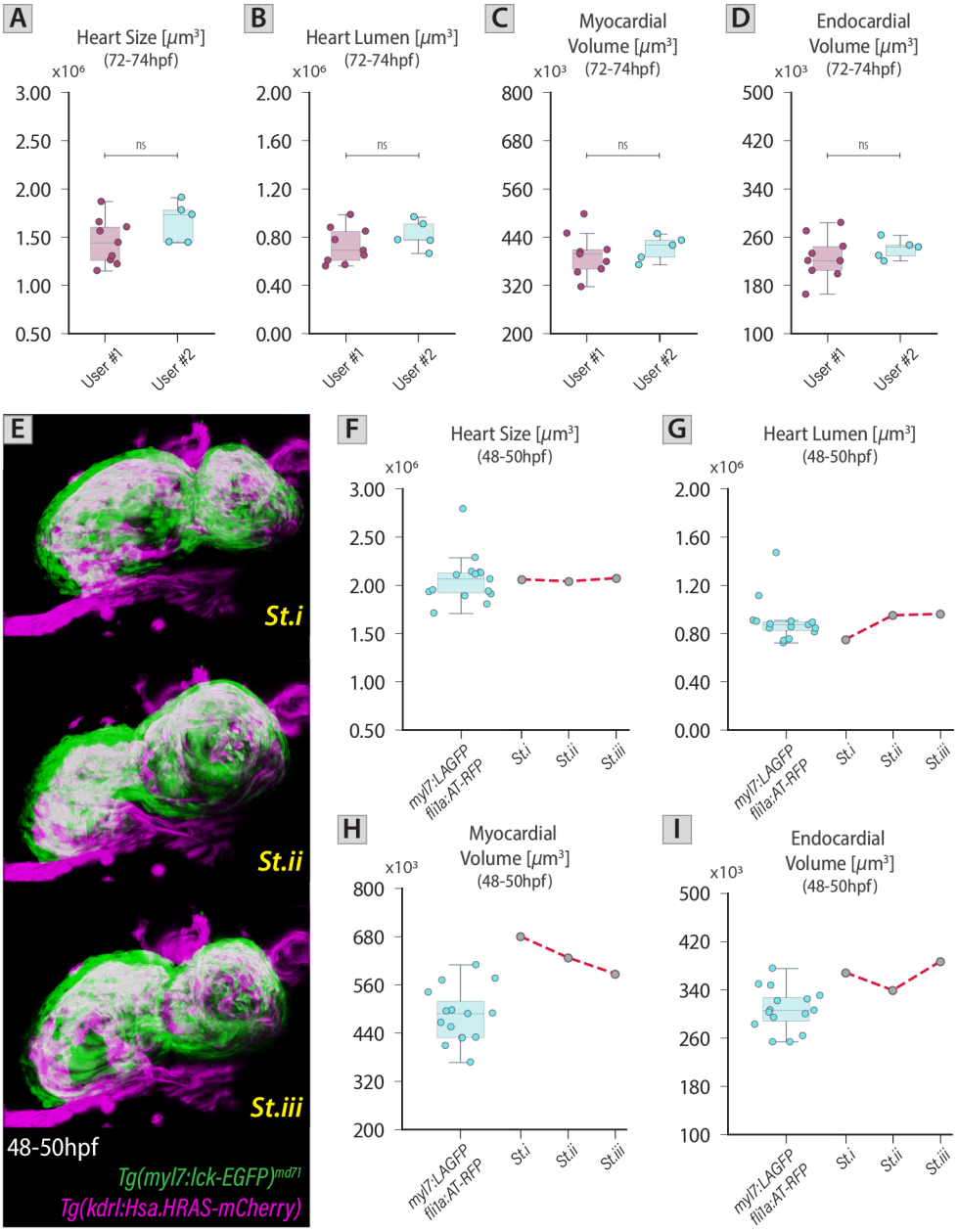

Fig 3.18. ***morphoHeart*** **provides precise morphometric parameters of the zebrafish heart independent of user, transgenic line, or acquisition approach.**

A-D. Comparison of the resulting morphometric values obtained for heart size (A), heart lumen (B), myocardial volume (C) and endocardial volume (D) from *Tg(myl7:lifeActGFP); Tg(fli1a:AC-TagRFP)* double transgenic wild-type hearts at 72hpf segmented by two different users. Individual data points represent different single zebrafish hearts. **E.** To evaluate the segmentation sensibility and precision of *morphoHeart* in the analysis of embryos with different transgenic backgrounds and imaging approaches, a wild-type *Tg(myl7:lck:EGFP)*^{md71}*; Tg(kdrl:Hsa.HRAS-mCherry)* double transgenic embryo imaged at 50hpf using a retrospective approach was analysed at three different cardiac phases (*St.i, St.ii,* and *St.iii*). **F-I.** Comparison of the resulting morphometric values obtained for heart size (F), heart lumen (G), myocardial volume (H) and endocardial volume (I) from segmenting 48-50hpf *Tg(myl7:lifeActGFP); Tg(fli1a:AC-TagRFP)* embryos (abbreviated as *myl7:LAGFP, fli1a:AT-RFP* in graphs) and the three different cardiac-phases of the 48hpf heart shown in E (referenced as *St.X* according to the stage of the cardiac cycle from which each variable was quantified). A-D;F-I: Error bars with 95% confidence interval of the mean. A-D: *User#1 n=9*, *User#2 n=5*. F-I: 72-74hpf: *myl7:LAGFP, fli1a:AT-RFP n=15*. ns: not significant.

Moreover, the ability of *morphoHeart* to capture size and tissue changes undergone by the heart/chambers during the cardiac cycle (as seen from the red point-plots presented on the right side of

panels F-I in Fig 3.18) suggests the use of this tool could provide valuable insights into the contractility dynamics of the heart, facilitating the understanding of the morphological changes experienced by the chambers and its comprising tissues (including the cardiac jelly) during the contraction cycle of wild-type and mutant hearts.

To further validate the segmentation abilities of *morphoHeart*, beads or 3D shapes with fully-known geometry could be imaged. The segmentation of these objects using *morphoHeart* tools and its further morphological characterisation could provide a quantitative notion of the precision and accuracy of the tool against the 3D world, validating its use.

6 DESIGNING THE EXPERIMENTS TO USE MORPHOHEART

morphoHeart offers the first comprehensive and standardised framework for characterising zebrafish heart morphogenesis, capturing spatiotemporal and morphological changes in the heart, its chambers and tissue layers throughout development. To obtain the most accurate data using *morphoHeart*, the transgenic line and image acquisition approach need to be carefully evaluated and selected according to the biological question of interest.

6.1 TRANSGENIC LINE SELECTION

The optical transparency of zebrafish embryos combined with the use of transgenic fluorescent reporters has made of this vertebrate model one of the key players in the study of the molecular basis underpinning cardiovascular disease (Brown *et al.*, 2016). A great number of zebrafish transgenic lines have been developed throughout the years labelling with fluorescent markers specific cell types or regions of the heart (e.g. *myl7* (Yelon, Horne and Stainier, 1999), *fli1a* (Thompson *et al.*, 1998), *kdrl* (Fouquet *et al.*, 1997), *flt1* (Grant *et al.*, 2017), *nppa* (Berdougo *et al.*, 2003), *isl1* (Cai *et al.*, 2003)). As the morphology of the cells that comprise each of heart cellular tissues is different (i.e. myocardial cells have constant thickness along its length, while endocardial cells are thicker around its nucleus and thinner at its junctions (Bornhorst *et al.*, 2019; Schlaeppi *et al.*, 2021)), and the cellular arrangement within the tissue changes as the heart develops (i.e. monolayer, multilayer), some transgenic lines are better suited to extract information regarding heart morphology and tissue distribution using *morphoHeart*. Accordingly, due to the morphology of endocardial cells, transgenic lines that label the cells membranes rather than its cytoplasm are recommended, avoiding the emergence of 'holes' in the image dataset in regions where the signal emission is very low due to thin cytoplasm (Schlaeppi *et al.*, 2021). Moreover, since image quality along the optical axis deteriorates when deeper sections of the heart are being imaged (e.g. imaging of the atrium at stages over 80hpf, where natural rearrangement of the chambers start to position the atrium posteriorly to the ventricle), the use of transgenic lines with bright and stable fluorophores is highly recommended. Lastly, the use of bright and stable fluorophores also applies to long time-lapse imaging, avoiding photo-bleaching and laser-induced phototoxicity in the sample throughout the imaging session (Jonkman *et al.*, 2020).

6.2 IMAGING METHOD CONSIDERATIONS

To acquire undisturbed z-stack comprising the morphology of the whole heart, multiple strategies to biologically arrest the heartbeat or computationally 'freeze' it have been developed. Though each approach facilitates imaging the whole heart in 3D (and even 4D), the advantages and limitations offered by each strategy (Section 1.1) make the approach of choice generally reliant on the researcher's available resources, length of the experiment, and the age of the fish to image.

Stopping the heart allows the analysis of the heart morphology only in a relaxed state, making this technique suitable when the contractility of the heart can be disregarded. However, stopping the heart at very early stages of development (e.g. by using MO or α- bungarotoxin) or for very long periods (e.g. by using tricaine or BDM) has been shown to be deleterious for the embryos and its cardiac function (Kaufmann *et al.*, 2012; Mickoleit *et al.*, 2014; Swinburne *et al.*, 2015; Taylor *et al.*, 2019). Thus, the former strategies are more appropriate for imaging embryos at early stages of development (~24-26hpf) -when cardiac defects have not yet manifested and cardiac function has not yet been impaired-, and the latter strategies at later stages when cardiac function can be restored after the image acquisition, if necessary, by washing the embryos into new media.

On the other hand, if analysis of the periodic beating motion of the heart is of interest, approaches to computationally 'freeze' the heartbeat are recommended. In this case, irrespective of the approach used to image the beating organ (Section 1.2), *morphoHeart* requires as input a 3D dataset (z-stack) comprised of individual channels containing the cellular tissue layer(s) and encompassing whole heart morphology at a single cardiac phase (see Section 4.1). Analysis of single hearts at multiple cardiac phases will give insights into the chamber and tissue dynamics thru a complete heart cycle.

[*Note#3.8:* Throughout this thesis, the approach used to obtain undisturbed 3D image datasets of the whole heart was to temporarily arrest the zebrafish heart by combining low temperature (e.g. 10°C) and a high-dose of anaesthetic (336mg/L of Tricaine [Sigma MS-222] in E3) in the imaging chamber (Fig 3.2A). All embryos, unless stated otherwise, were imaged at a single time point, and the length of the anaesthesia was carefully controlled so that the image acquisition of each embryo was done within 30 minutes of Tricaine exposure, reducing the possible deleterious effects caused by the anaesthetic in the analysis of heart morphology. Additionally, due to the approach used, all the processed zebrafish hearts are being analysed in the same 'relaxed' state. Although no contraction phases correspond in morphology to this 'relaxed' state - as the early heart behaves like a peristaltic pump which around 36-48hpf transitions into a more efficient sequential process of contraction of the atrium followed by the ventricle (Weber *et al.*, 2017) -, the use of this approach allows the analysis of all the processed embryos at an identical state, validating the use of this strategy for the present thesis].

7 morphoHeart Additional Modules

7.1 morphoCell Module

Numerous intrinsic and extrinsic mechanisms have been shown to promote specific aspects of cardiac morphogenesis. Intrinsic mechanisms, which refer to the behaviour of cells within the heart include cell proliferation, cell addition and cell changes in shape and size. To enhance our understanding of how each of the comprising tissues shape the heart as it undergoes morphogenesis, we need to be able to tell not only the number of cells that make up the cellular tissue layers but also quantify their size, shape and distribution throughout the tissue (Manasek, Burnside and Waterman, 1972; Auman *et al.*, 2007; Dietrich *et al.*, 2014; Lombardo *et al.*, 2019). To be able to acquire part of these metrics one of the additional modules that were included within *morphoHeart* was *morphoCell* (Fig 3.19, 3.20 and 3.21). This module allows counting of the number of cells that constitute a cellular tissue layer (e.g. myocardium or endocardium) and the quantification of the distance between adjacent nuclei. The distance between adjacent nuclei, hereafter *internuclear distance* (or IND) can be used as a proxy for cell size in cases where a transgenic line that labels cell membranes is not available, allowing an indirect measurement of this parameter. *morphoCell* analysis of these metrics (cell number and IND per chamber) aid the analysis of cell distribution within different chamber regions becoming an interesting tool to study the regionalised tissue reorganisation occurring during heart morphogenesis.

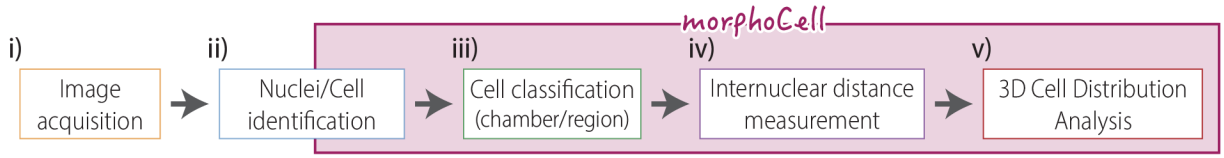

Fig 3.19. *morphoCell* module general overview.
Flow diagram describing the 5 phases involved in the process of counting cell number and quantifying cell size of a zebrafish heart using *morphoCell*.

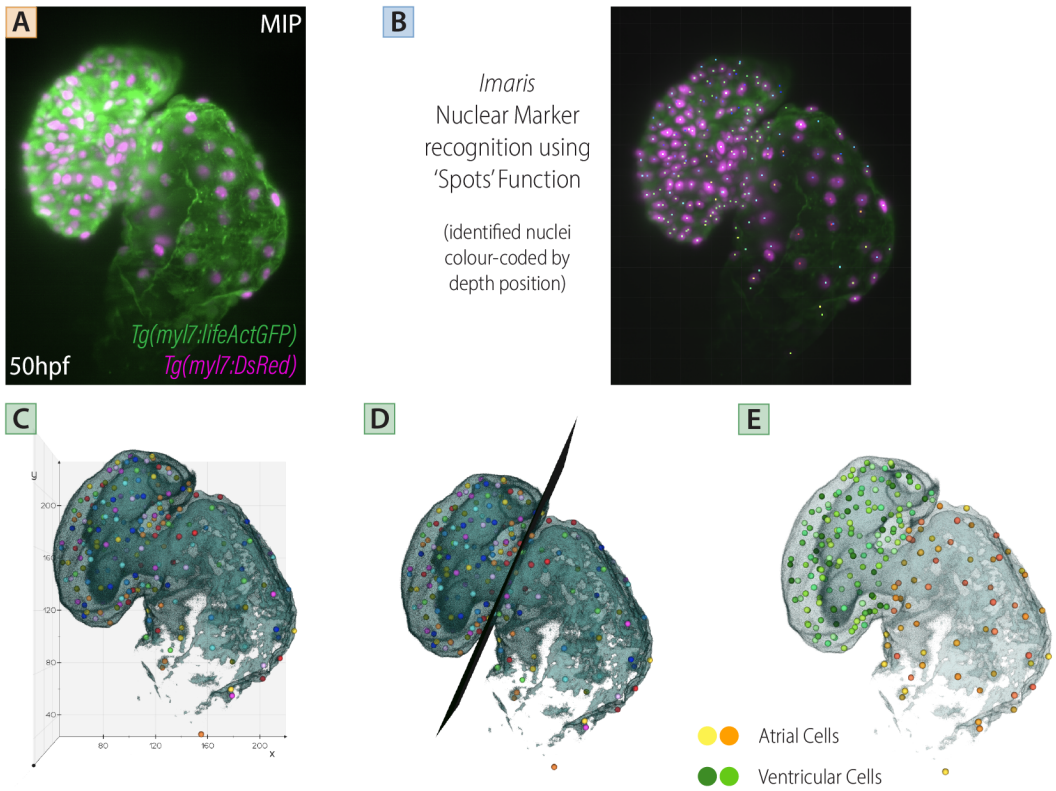

Fig 3.20. *morphoCell,* one of *morphoHeart*'s additional modules, enables cardiomyocyte counting in the zebrafish heart.
A. Double transgenic zebrafish embryos with myocardial tissue and nuclear marker are imaged on the light-sheet microscope. *Tg(myl7:lifeActGFP)* in green marks the myocardium and *Tg(-5.1myl7:DsRed2-NLS)* (Rottbauer *et al.*, 2002) signal in magenta marks the myocardial nuclei [henceforth *Tg(myl7:DsRed)*]. **B.** Fluorescent signal present in the nuclei is used to identify the position (x, y, z coordinates) of all the cells comprising the heart using free or commercially available software. In this case, Imaris 'Spot' function was used to identify the nuclei positions all around the heart. **C.** Coordinates of all the identified cells are imported into *morphoCell,* where they can be visualised and edited if needed. **D-E.** By means of a user-defined plane that roughly divides the heart into chambers (D), cells are classified as atrial/ventricular. Cell classification can be manually edited resulting in cells assigned either to the atrium (orange) or ventricle (green). A-B: Ventral views with anterior to the top. C-E. Heart's ventral face with anterior to the top.

Similar to *morphoHeart*, in general, the process of acquiring cell metrics using *morphoCell* starts with the acquisition of images obtained in the light-sheet microscope of zebrafish embryos in which the myocardial or endocardial tissue as well as its cell nuclei are fluorescently labelled with different fluorescent markers (Fig 3.19i, Fig 3.20A). To provide the best input into the tool, recommendations regarding the acquisition process of the images given for *morphoHeart* are also applicable to *morphoCell* (see Section 4.1). Next, RAW images are imported into Fiji or other commercially available software (e.g. Imaris) to identify the 3D coordinates that describe the position of each fluorescently labelled nuclei (Fig 3.19ii, Fig 3.20B). RAW

images and nuclei coordinates are then imported into *morphoCell*, where the acquired myocardial/endocardial signal is used to create a 3D rendering of the heart, and the input cell coordinates to position cells (represented by spheres) within it (Fig 3.20C). The 3D heart rendering provides a morphological reference to classify cells as atrial or ventricular cells providing distinct measurements per chamber (Fig 3.19iii, Fig 3.20D-E).

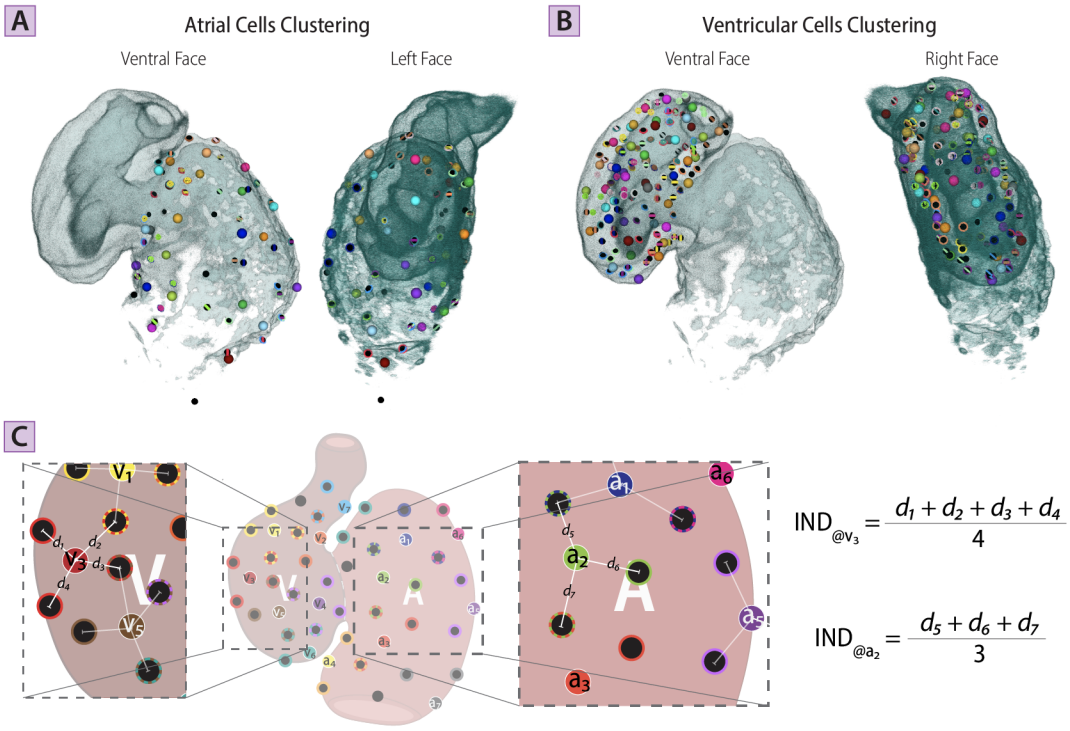

Fig 3.21. *morphoCell's* internuclear distance analysis of cardiomyocytes aids cell distribution analysis per chamber and chamber region in the zebrafish heart.
A-B. Cells identified in each chamber (atrium, ventricle) are clustered into distinct groups that are representative of cell organisation within the chamber (see details of clustering method in text) (A: atrial clusters, comprised of a central seed cell and 3 neighbouring cells, B: ventricular clusters, comprised of a central seed cell and 4 neighbouring cells). **C.** Schematic depicting the clustering process of *morphoCell* to calculate internuclear distance (IND) as a proxy for cell size. A subset of cells per chamber are iteratively assigned as central *seeds cells* and the number of clusters is maximised so that each cluster has a *seed cell* and a defined number of nearest neighbour cells (atrium: 3 neighbour cells, ventricle: 4 neighbour cells). The optimisation process is constrained in a way that *seed cells* (named here a_x and v_x and shown with different colours other than black) are only contained within one cluster while nearest neighbour cells can be shared between clusters. Neighbour cells are shown in black with an outline coloured according to the cluster (*seed cell(s)* colour) to which they are assigned. IND is calculated per cluster averaging the distances between the seed cell and all its assigned neighbour cells (here named d_x) as shown by the equations. Chamber clusters are further classified into distinct chamber regions: ventral, dorsal, inner curvature, and outer curvature in which internuclear distance between seeds and cluster members can be also quantified. A-B. Heart's ventral and left faces with anterior to the top.

Once cells have been classified, *morphoCell* quantifies cell size per chamber using the *internuclear distance* (IND) as a proxy (Fig 3.19iv). Lastly, to better understand cell distribution and size throughout each chamber, *morphoCell* also provides the ability to cluster cells into distinct groups that are representative of the cell organisation within the chamber (Fig 3.21A-C). To do so, a subset of cells per chamber are iteratively assigned as central *seeds cells* and the number of clusters is maximised so that each cluster has a *seed cell* and a defined number of nearest neighbour cells. The optimisation process is constrained in a way that *seed cells* are only contained within one cluster while nearest neighbour cells can be shared with

other clusters. If the result of the maximisation process identifies more than one cluster configuration, *morphoCell* allows the user to select the cluster to use for further 3D cell distribution analysis (Fig 3.19v). Resulting cell clusters which include most chamber cells (if not all), can be further sub-grouped and analysed as part of four different chamber regions: ventral, dorsal, inner curvature, and outer curvature.

All the metrics obtained by *morphoCell*, particularly the internuclear distances of chamber/region classified cells can be used to understand changes in cell distribution and size throughout different regions of the chambers which combined with tissue thickness heatmaps (Section 4.5.4, Fig 3.13), aids the analysis and understanding of regionalised tissue rearrangements occurring during heart morphogenesis.

8 REFERENCE OF USED PACKAGES

Built on Python's free and simple syntax *morphoHeart* takes advantage of the high-quality data processing and analysis packages available, as well as open-source tools directly aimed at (bio)image analysis. *morphoHeart* is written in Python 3.6 and depends on standard python packages such as *numpy* (Harris *et al.*, 2020), *matplotlib* (Hunter, 2007), and *pandas* (The pandas development team *et al.*, 2022). *scipy* (Virtanen *et al.*, 2020)and *scikit-image* (Walt *et al.*, 2014) combined with *cv2* (which allows the interaction of the user with the images) (Bradski, 2000) are used for the processing and filtering of the input channel stacks (Section 4.2) and segmenting the results and *vedo* as the rendering engine (Musy *et al.*, 2022). *vmtk* package, developed for the geometric analysis of image-based blood vessels (Antiga *et al.*, 2008) aids the centreline extraction of the heart within *morphoHeart*.

Finally, some of the packages used to enhance the user interaction with the tool are *playsound* (Marks, 2022) and *progress* (Verigakis, 2022).

9 CHAPTER CONCLUSIONS

- *morphoHeart* is a novel, comprehensive, and open-access quantitative image analysis tool that allows the segmentation of the heart layers and quantification of the tissue organisation and morphology throughout zebrafish heart development.
- *morphoHeart*'s segmentation approach using contours allows the 3D segmentation (from the negative space) and volumetric reconstruction of the cardiac jelly for the first time.
- *morphoHeart*'s capability to segment high-resolution images from ***live*** embryos aids the analysis of tissue and ECM distribution without complications induced by sample fixation and/or processing.
- *morphoHeart*'s open-access nature enhances the suite of tools and quantifications available in the biological field to characterise organ morphology and tissue distribution.

10 CHAPTER DISCUSSION

In this chapter I have presented *morphoHeart* -the first comprehensive open-access quantitative image analysis tool that allows the segmentation of the heart layers -including the cardiac jelly- and quantification of the tissue organisation and morphology throughout zebrafish heart development.

10.1 *MORPHOHEART*, A NOVEL COMPREHENSIVE IMAGE ANALYSIS TOOL

To date, a single tool or pipeline is not able to address all the processing and analysis needs in the analysis of 3D datasets. Although great effort has been invested in the development of free and commercially available software for segmenting and quantifying 3D objects from grey-scale images, fully automatic

segmentation approaches in 3D can be computationally demanding and can perform poorly on biological images due to their characteristic low local contrasts, high noise levels and numerous structures or artifacts surrounding the objects of interest (Andrey and Boudier, 2006; Rasse, Hollandi and Horvath, 2020). This poor performance sometimes forces researchers to manually segment the structures of interest, which aside from being a time-intensive task, might not provide the most accurate results.

Once the structures of interest have been segmented, either by fully automatic or manual segmentation, limited 3D object manipulation and quantification in both free (e.g. 3D Viewer (Schmid *et al.*, 2010), MorphoLibJ (Legland, Arganda-Carreras and Andrey, 2016), 3D Slicer (Fedorov *et al.*, 2012)) and commercially available software, allow only the extraction of few gross quantitative readouts, restricting the depth of the analysis that can be made. Some commercially available software specifically designed to analyse medical (e.g. Mimics Materialise, Belgium) or biological (e.g. arivis Vision 4D, Germany; Imaris, Oxford Instruments; Volocity, PelkinElmer) images provide a more extensive toolset for the morphological analysis of 3D objects. Nevertheless, aside from the high licensing cost, depending on whether the software was initially developed for medical or biological purposes, the available metrics might (just like in free software), not meet all the user-specific needs, requiring the use of additional tools to extract the quantifications of interest. However, handling the 3D objects between programmes (e.g. exporting, importing) can be tricky and require familiarity or resourcefulness from the user to find the tool that will meet his/her needs.

morphoHeart is an exciting alternative to both free and commercially available software, offering a comprehensive pipeline that provides semi-automated segmentation capabilities and improves the suite of tools and quantifications available in the biological field to characterise organ morphology and tissue distribution. *morphoHeart*'s 3D morphometric analysis library offers a suite of quantifications that to our knowledge allow the most complete morphological description of a zebrafish heart and its comprising parts (e.g. chambers and tissue layers).

The modular and open-source nature of *morphoHeart* will make the tool available to the broader community and allow new coding-experienced users to expand its functionalities, supporting user-specific needs that can be easily integrated within the tool.

As previously described, the segmentation of the cardiac jelly is challenging, especially if transgenic zebrafish that harbour fluorescently markers only in the *cardiac* ECM are not available. *morphoHeart* overcomes this difficulty taking advantage of the information contained in the fluorescently labelled heart cellular layers (myocardium and endocardium) obtaining for the first time a 3D reconstruction of the cardiac jelly. This novel ability to segment the cardiac ECM will allow the investigation of the links between morphology and ECM dynamics in the developing zebrafish heart.

While *morphoHeart* was initially developed for the study of zebrafish heart development, it can be applied to studying a wide range of morphogenetic processes in other organs and organisms, contributing to our understanding of the tissue organisation mechanisms and morphogenesis processes underpinning them. Similarly, *morphoHeart*'s methodology to obtain 3D reconstructions of the cardiac ECM from negative space can be also applied to other tissues or extracellular spaces for which fluorescent markers are not available as long as the inner and outer borders of such space can be extracted from other fluorescently labelled tissues/structures. Furthermore, morphological study of organs other than the heart in wild-type and defective scenarios using morphometric structures like the centreline in conjunction with 'ballooning' heatmaps could provide valuable insights regarding tissue morphology and pinpoint abnormalities in tissue organisation/size/shape which would be otherwise hard to identify.

10.2 COMBINING *MORPHOHEART*'S SEGMENTATION CAPABILITIES WITH ADDITIONAL MODELLING TOOLS

Heart malformations in human patients are often subtle disruptions to the shape of the developing heart, which affects its normal function. Tools such as *morphoHeart* that help to better identify, describe, and characterise the development of these defects in model organisms used in heart research make these findings more relevant and relatable to humans, pushing the study of congenital heart defects forward. In fact, the numerous advantages offered by zebrafish as a disease model organism (e.g. rapid external development, genetic modification toolbox, translucent larvae and imaging ease) in combination with *morphoHeart* will better establish the use of this animal model in the field. Current analyses of zebrafish in heart development studies lack sufficient detail when describing heart and tissue morphology, and the impact knockout or knock-in mutations have upon them. The use of *morphoHeart* in future similar studies will allow a more in-depth characterisation of heart malformations and the emergence of phenotypes, providing new and exciting insights into gene/protein function and setting new standards in the field for what analyses are now achievable with state-of-the-art microscopy.

In line with this, the morphological quantifications and resulting geometries provided by *morphoHeart*, which contain 3D information about the morphology of the organ and its tissue composition and distribution, could be fed into descriptive or predictive models to further understand the mechanisms (e.g. mechanical forces, cellular growth and rearrangements) that drive heart looping, chamber ballooning and ventricular trabeculation (Lee *et al.*, 2013; Le Garrec *et al.*, 2017; Vedula *et al.*, 2017; Honda, Abe and Fujimori, 2020; Honda, 2021).

Previous studies have used either finite element models (FEA) or 3D computational simulations to study the asymmetric process of looping morphogenesis (Le Garrec *et al.*, 2017; Honda, 2021). Using simple representations of the heart tube (e.g. cylindrical mesh with a defined thickness and a lumen, cylindrical surface and two discs at the extremities) and a combination of constraints and conditions, the models have recapitulated the bending and torsion of the heart, gaining insights into the internal and external forces involved in the formation of the mammalian helical loop. However, studies in different animal models have shown that one of the factors driving looping morphogenesis is changes in cell shape and size and that these changes are distinct in each tissue layer and chamber (Manasek, Burnside and Waterman, 1972; Auman *et al.*, 2007; Dietrich *et al.*, 2014; Bornhorst *et al.*, 2019). Hence, to better comprehend the roles of each cardiac tissue layer in this process, *morphoHeart* 3D reconstructions of the three cardiac tissue layers at early stages of development (<36hpf) could be provided as input meshes in new simulations predicting the mechanical forces acting in each of the comprising layers to transform the input early tubular geometry into a later looped morphology. As this type of image-based model would contain information not only about the geometry but also about the tissue distribution (e.g. cardiac tissue thickness, cell organisation and packing), novel insights into this complex process could be attained.

Much of the morphogenesis of the heart takes place while this organ is beating and pumping blood. To further understand the importance of blood flow and contractility throughout cardiac development, results of altered blood flow dynamics simulations could be compared to *morphoHeart* 3D reconstruction of hearts in which blood shear stress has been reduced (i.e. by injecting *gata1/gata2* MO (Lin, Swinburne and Yelon, 2012)) or contractility is absent (e.g. *tnnt2a* mutants (Sehnert *et al.*, 2002)). This comparison would provide interesting insights regarding the mechanisms by which blood flow regulates cardiovascular growth and development.

Combination of descriptive or predictive models with *morphoHeart* wild-type and candidate-driven functional analysis, like the ones just described will facilitate the comprehensive study of mechanisms behind heart morphogenesis proving new and exciting future research opportunities.

The validated comprehensive tool described in this chapter provides the foundation for investigating the link between ECM dynamics and tissue morphogenesis presented in the remainder of this thesis.

11 Limitations and Future Directions

The core aim design goal of *morphoHeart* was to develop an open-access comprehensive quantitative image analysis tool that allows the segmentation of all the cardiac tissue layers alongside quantification of whole heart morphology and tissue organisation throughout heart development. The scientific utility of *morphoHeart* in providing a better understanding of the mechanisms underpinning heart development will be demonstrated in the remaining chapters of this thesis. However, the lack of a 'gold-standard' to compare *morphoHeart* data corresponds to a limitation of the current study, and future work will be needed to examine this further.

As of today, *morphoHeart* has been developed as a series of scripts and has been used by five members of the Noël lab (other than myself), obtaining data that has been included in MSc and PhD thesis and as pilot data in successful grant applications, demonstrating its perceived contribution to the field.

To successfully achieve the last design principle of *morphoHeart* (see Section 3.1), make it user friendly and avoid unintentional modifications of the underlying code by the different users, I am planning on developing a Graphic User Interphase (GUI) through which users can interact with the tool and access all *morphoHeart*'s core functionalities. The development of this GUI will hopefully make *morphoHeart* a widely used tool, empowering scientists worldwide to make the most out of their data and providing a standardised framework for future analysis in the field.

Multi-user processing of multiple hearts using *morphoHeart* has pinpointed possible improvements to the current tool, which will be carefully considered for the release of its next version.

The process of 'unlooping and unrolling' the 3D ventricular thickness and myocardial ballooning in embryos over 48hpf show NaN (Not a Number or 'missing data') values in regions closer to the outflow tract (see horizontal stripes with incomplete data in the ventricular heatmaps of most of the embryos presented in Fig 3.17A). Although the reason behind this phenomenon is not yet confirmed, the current hypothesis is that abrupt changes in the curvature of the centreline between the ventricle and the outflow tract might change drastically the orientation of the planes used to cut the 3D colour-coded meshes, failing to map this region of the heart correctly. If this were the case, redesigning the methodology to map that particular region of the heart in a standardised way for embryos at all stages, would be the strategy of choice, consequently eliminating the potential artefacts that averaging of 2D heatmaps can induce in these regions and allowing its analysis.

To include the ability to measure heart orientation within the embryos, two approaches will be taken. If the transgenic line being used marks an additional anatomical structure other than the heart (e.g. aortic arches), segmentation of such structure within *morphoHeart* could provide a reference frame for the orientation analysis of multiple hearts. If a different anatomical structure is not available in the fluorescent channels acquired, the user will be asked to provide two brightfield images of the embryo: one from a full ventral view (i.e. recommended imaging orientation) and another from a full lateral view (i.e. orthogonal view to the imaging orientation) (Fig 3.2C-D). Both images will be used to measure the orientation of the embryo with respect to the *z*-axis from both views, obtaining a reference frame to use in the orientation analysis of multiple hearts.

Further improvements will be making *morphoHeart* a stand-alone application that can be simply downloaded and locally installed. For this to work, additional processing and filtering modules using *scikit-image* and other python packages will need to be developed to replace the processing currently performed using arivis Vision 4D and Fiji (Section 4.2). This change will make *morphoHeart* a much more

comprehensive and complete tool, enabling the analysis of RAW data from beginning to end using a single yet powerful tool.

12 AVAILABILITY

All *morphoHeart*'s code will be deposited on GitHub and will be freely available at https://github.com/jsanchez679/morphoHeart including detailed instructions for installation and use. Step-by-step workflows will be also available to illustrate the input and output of individual steps and modules. *morphoHeart*'s code will be free to modify and adapted by other researchers and users, facilitating its integration to particular labs' data, analysis pipelines and needs.

Even though *morphoHeart* has been created for the study of zebrafish heart development, its use can be further broadened for the analysis of other organs/tissues in which similar analysis are of interest (see Section 11).

Chapter 4. Characterisation of Early Zebrafish Heart Development

1 INTRODUCTION

Heart morphogenesis is a complex process that requires a series of events to be tightly orchestrated in space and time in order to end up with a mature and properly formed heart. Changes or disruptions in the process can lead to the development of congenital heart defects, a major cause of infant morbidity and mortality and the most common cause of congenital abnormalities worldwide (Bruneau, 2008; van der Linde *et al.*, 2011; Hoffman, 2013).

One of the most important stages in vertebrate heart development takes place when the heart undergoes cardiac looping and ballooning. In these processes, the linear heart tube undergoes a series of morphological rearrangements that break the bilateral symmetry of the tube, transitioning from a simple linear tube to a dextrally-looped and ballooned organ (Manasek, Burnside and Waterman, 1972; Christoffels *et al.*, 2000; Christoffels, Burch and Moorman, 2004; Männer, 2009; Le Garrec *et al.*, 2017; Lombardo *et al.*, 2019). Although many cellular events are known to be involved in these morphogenetic processes (e.g. ingression of cells from the SHF, changes in cell size) (see Chapter 1, Section 4.1), very few studies have exploited the advantages of zebrafish to characterise looping and ballooning morphogenesis in 3D, limiting our understanding not only about the way the chambers grow, expand and rearrange but also about the tissue layer transformations that accompany and support the shaping of this organ.

Here, I characterise zebrafish heart development between early looping (34hpf) and initial maturing stages (74hpf) using *morphoHeart* and its 3D morphometric analysis library (see Chapter 3 for details). I will describe how each of the morphometric parameters measured change as the heart undergoes looping and ballooning morphogenesis and link them to the already described mechanisms that assist the formation of a looped and maturing heart. As the ECM represents a key intrinsic factor in promoting heart development (Lockhart *et al.*, 2011a; Scuderi and Butcher, 2017; Cui *et al.*, 2019; Derrick *et al.*, 2021) and *morphoHeart* allows for the first time the acquisition and analysis of the cardiac jelly of live embryos in 3D, I will provide a detailed characterisation of the dynamics of the cardiac ECM and its pattern of regionalisation during early morphogenesis. This information will be then complemented and linked to an ISH screen looking specifically for interstitial matrix components that are likely involved in cardiac ECM volume regulation over the course of cardiac morphogenesis. Lastly, I will use this set of morphometric parameters to investigate heart morphology and morphogenesis in embryos with defective laterality (*spaw* mutants), generating a hypothesis regarding the relationship between lateralisation, cardiac ECM dynamics and heart morphogenesis in zebrafish.

This work begins to uncover zebrafish cardiac morphogenesis in 3D, providing detailed 3D morphological readouts that describe the chamber, tissue and ECM changes underpinning cardiac looping and ballooning, and its association to large scale embryo patterning.

2 ZEBRAFISH HEART MORPHOGENESIS THROUGHOUT DEVELOPMENT

To better characterise morphologically and in 3D the changes experienced by the heart through looping and ballooning morphogenesis, *Tg(myl7:lifeActGFP); Tg(fli1a:AC-TagRFP)* double transgenic embryos were imaged live on the light-sheet microscope at early looping (between 34 and 36hpf), during looping and ballooning (between 48 and 50hpf) and post-looping or early maturing stages (between 72 and 74hpf). The resulting images were processed using *morphoHeart*, obtaining 3D reconstructions of the three cardiac tissue layers of multiple hearts. Characterisation of the changes undergone by the whole organ, its chambers, and individual layers (including the cardiac ECM) was performed using *morphoHeart*'s 3D morphometric analysis library.

[*Note#4.1:* All the data presented throughout this chapter originates from embryos that came from crosses of families that I will use elsewhere in this thesis but that were genotyped as wild type.]

The ultimate purpose of a heart is to pump blood throughout the whole body via the circulatory system, ensuring the distribution of nutrients and oxygen and the removal of waste. As previously mentioned, oxygen diffusion in zebrafish larvae is sufficient to sustain life up until 7 days post-fertilisation (dpf), when they start to rely on circulating blood (Pelster and Bagatto, 2010). All the morphogenetic events happening before this time point need to proceed correctly to shape a healthy and functional organ with the right size and shape, ready to sustain all the embryos' needs.

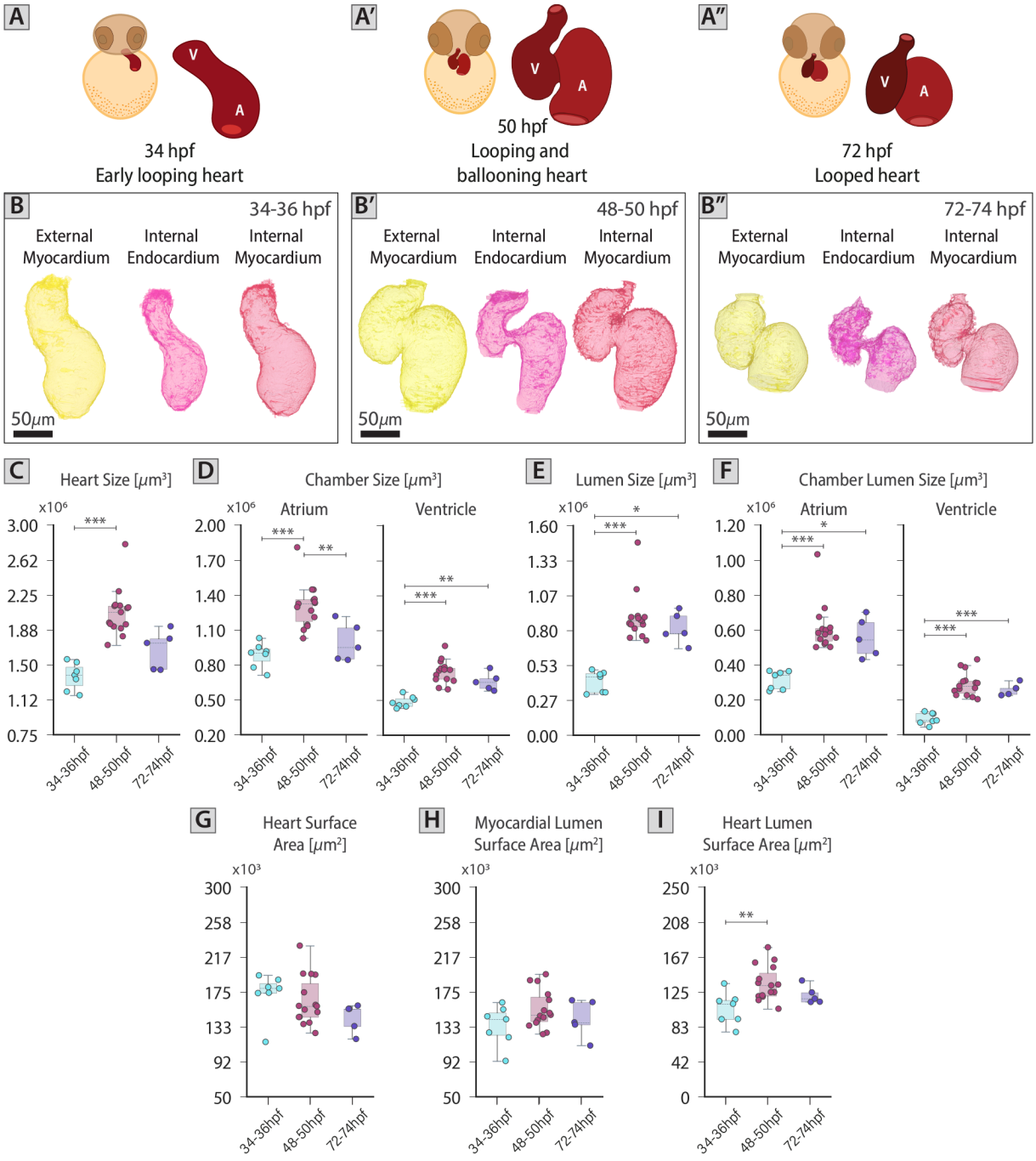

Fig 4.1. The embryonic heart grows as it loops and balloons. Then the atrium compacts as the heart starts to mature while maintaining its lumen capacity.

A-A''. Schematic of the ventral face of a zebrafish and a zebrafish heart at early looping (34-36hpf, A), during looping and ballooning (48-50hpf, A') and at maturing (72-74hpf, A'') stages. **B-B''.** Wild-type hearts at these three key developmental stages were imaged and processed using *morphoHeart* obtaining 3D reconstructions of the external myocardial mesh (yellow meshes), internal endocardial mesh (magenta meshes), and internal myocardial mesh (red meshes). **C.** Quantification of the external myocardial volume (yellow mesh) offers information about the space occupied by the heart within the embryo, acting as a proxy for heart size. Wild-type hearts grow as they transition from a linear early looped tube to a looped organ (34-36hpf vs. 48-50hpf:

p-value=0.00011) and compact once cardiac looping and ballooning processes are completed (50→74hpf). **D.** When the external myocardial meshes are divided into chambers (see Chapter 3. Section 4.5.2 for details), quantifications of the volume of each individual chamber gives information about its size. Similarly, to the whole heart, individual chambers grow as the heart is looping and ballooning (34-36hpf vs. 48-50hpf: atrium *p-value=0.00100*, ventricle *p-value=0.00100*), but only the atrium significantly compacts down as the heart starts maturing (48-50hpf vs. 72-74hpf: atrium: *p-value=0.00391*). **E.** Quantification of the internal endocardial volume (red mesh), offers information about the space occupied by the blood within the embryo's heart, proving as a proxy for heart's lumen size. As the heart loops and balloons, the lumen of the heart expands (34-36hpf vs. 48-50hpf: *p-value=0.00038*) and then is maintained as it continues to mature. **F.** When the internal endocardial meshes are divided into chambers, quantifications of the volume of each individual chamber provides information about its lumen size. Both, the atrial and ventricular lumen expand during looping and ballooning (34-36hpf vs. 48-50hpf: atrium *p-value=0.00034*, ventricle *p-value=0.00100*), and later maintain their size through the first stages of maturation. **G-H.** Surface area quantifications of the external (G, yellow meshes in B-B'') and internal (H, red meshes in B-B'') myocardial meshes, provide an idea of the changes in rugosity undergone by this tissue layer during heart morphogenesis. Despite the changes in whole organ volume, between 34 and 74hpf, the surface area of the whole heart (G) and the myocardial lumen (H) is maintained constant. **I.** Quantification of the internal endocardial surface area (magenta meshes in B-B'') conveys information about the surface area changes experienced by the endocardial tissue that is in contact with blood (i.e. heart lumen). As the heart loops and balloons, the surface area of the lumen of the heart significantly increases and is maintained as the heart transitions to an early maturing stage (34-36hpf vs. 48-50hpf: *p-value=0.00038*). A-B'': Heart's ventral face with anterior to the top. C-I: Error bars with 95% confidence interval of the mean. 34-36hpf: *n=7*, 48-50hpf: *n=15*, 72-74hpf: *n=5*. For details regarding the statistical analyses used to compare this set of data see *Note#4.2* (pg. 99). Only significant comparisons are shown. ***: *p-value*<0.001, **: *p-value*<0.01, *: *p-value*<0.05.

———————

[*Note#4.2:* All sample groups per stage (34-36, 48-50 and 72-74hpf) were analysed for normality using Shapiro-Wilk Normality test. For each analysed variable, if all groups were normally distributed, comparative statistics were carried out using ANOVA with Tukey's Multiple Comparisons as *post-hoc* test. When normal distribution could not be assumed, Kruskal-Wallis test with Dunn's Multiple Comparisons as *post-hoc* was used. For all tests a statistical significance α of *0.05* was defined].

To characterise the gross size changes undergone by the early developing heart, volumetric measurements of the whole and chamber-sectioned external myocardium (Fig 3.5E) and internal endocardium (Fig 3.5I) were taken from processed hearts over the course of looping morphogenesis and used as a proxy for heart and lumen size respectively (Fig 4.1). As the heart transitions from an early looping tube to a looped structure, the space occupied by the whole organ and its chambers (alongside its lumen) significantly increases, expanding the blood filling capacity of both chambers (Fig 4.1E,F). Interestingly, despite this growth, between 50 and 72hpf, the atrium undergoes a compaction process while the ventricle maintains its size (Fig 4.1D). Regardless of this reduction in atrial volume, the lumen size acquired by both chambers at 48-50hpf is maintained (Fig 4.1F), thus conserving both chambers' increased blood filling and pumping capacity at 72-74hpf.

As the heart changes in size and shape, the surface area of the organ that is exposed to the rest of the embryo and that that is in contact with blood also changes. To characterise these changes, the surface area of the external myocardium -proxy for total *heart surface area* (Fig 4.1G)- and the internal endocardium -proxy for the *heart lumen surface area* (Fig 4.1I)- were quantified and analysed. Total heart surface area (Fig 4.1G) is maintained constant between 34 and 50hpf, and points towards a slight but non-significant reduction between 50 and 74hpf. As expected by the increased and later maintenance of blood filling capacity (Fig 4.1E-F), as the heart undergoes looping and ballooning, the endocardial surface area in contact with blood increases during looping and ballooning and later is retained constant as the heart transitions to an early maturing state. Additional, surface area measurements for example, from the internal myocardium (Fig 4.1H) can also provide evidence of the tissue layer changes in morphological intricacy, especially when trabeculae start to form in the ventricle. Although ventricular trabeculation

starts in zebrafish embryos around 60hpf (Liu *et al.*, 2010; Peshkovsky, Totong and Yelon, 2011), suggesting an increase in myocardial lumen surface area between 50 and 74hpf, no significant differences are observed in this variable between these timepoints, possibly because of simultaneous reduction of the surface area due to atrial compaction. Evaluation of this variable per chamber could aid the differentiation between the two phenomena, providing a much more profound understanding of the morphological changes in surface area experienced individually by each chamber.

Changes in chamber morphology and size drive the process of growth and compaction of each heart chamber through looping and ballooning morphogenesis. To better understand the morphological changes experienced by each chamber during these developmental processes, ellipsoids were fit to the myocardial tissue chambers obtaining standardised measurements of their size and shape in 3D (for details about these morphometric parameters see Chapter 3, Section 4.5.3, Table 3.1, and Fig 3.10).

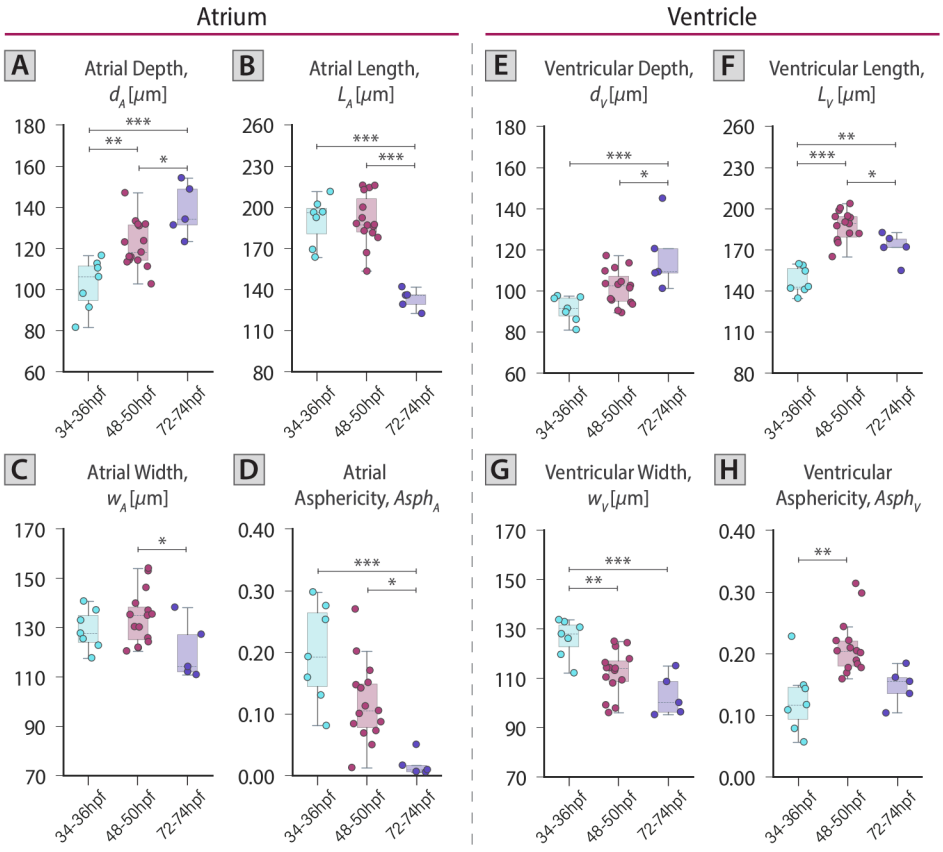

Fig 4.2. Heart chambers experience 3D morphological changes as the heart undergoes morphogenesis between 34hpf and 74hpf.

A-D. Quantifications of atrial depth d_A (A), length L_A (B), width w_A (C), and asphericity $Asph_A$ (D) of the fitted ellipsoids throughout development. As the heart tube undergoes looping and ballooning, the atrium elongates principally in the z-axis (d_A) (34-36hpf vs. 48-50hpf: d_A *p-value=0.00443*). Later on, as the heart starts maturing, this chamber keeps increasing its depth d_A (z-axis), while reducing its length L_A (y-axis) and width w_A (x-axis) transforming into an almost spherical chamber $Asph_A$ (48-50hpf vs. 72-74hpf: d_A *p-value=0.03334*, L_A *p-value=0.00100*, w_A *p-value=0.04791*, $Asph_A$ *p-value=0.02648*). **E-H.** Quantifications of ventricular depth d_V (E), length L_V (F), width w_V (G), and asphericity $Asph_V$ (H) of the fitted ellipsoids throughout development. As the heart tube undergoes looping and ballooning, the ventricular morphology changes in all directions transforming from a conical into an ellipsoidal shape (34-36hpf vs. 48-50hpf: L_V *p-value=0.00100*, w_V *p-value=0.00485*, $Asph_V$ *p-value=0.00459*). Following looping and ballooning, as the heart starts maturing, this chamber keeps increasing its depth d_V (z-axis), while reducing its length L_V (y-axis) transforming the already ellipsoidal shape into a more spherical chamber $Asph_V$ (48-50hpf vs. 72-74hpf: d_V *p-value=0.01934*, L_V *p-value=0.02379*). A-H: Error bars with 95% confidence interval of the mean. 34-36hpf: *n=7*, 48-50hpf: *n=15*, 72-74hpf: *n=5*. For details regarding the statistical analyses used to compare this set of data see *Note#4.2* (pg. 99).Only significant comparisons are shown. ***: *p-value*<0.001, **: *p-value*<0.01, *: *p-value* <0.05.

During looping, the atrium maintains the length and width observed at early looping tube stage, while increasing its depth (Fig 4.2A-D), suggesting this sole elongation in the *z-axis* is responsible for the significant increase in atrial size (Fig 4.1A). Meanwhile, the ventricle elongates and widens, transforming its shape from a tube to an ellipsoid with an enlarged volume (Fig 4.2E-H, Fig 4.1D). Once the heart has undergone looping and ballooning, the already described atrial compaction is driven by a continued increase in depth (Fig 4.2A), combined with a reduction in length and width (Fig 4.2B-C), resulting in an atrium with almost spherical morphology (Fig 4.2D) and a reduced size (Fig 4.1D). Concomitantly to the atrial compaction, between 50 and 74hpf, the ventricle increases its depth and reduces its length, both of which allow this chamber to maintain its size (Fig 4.2E-F, Fig 4.1D-E).

Over the course of chamber growth (between 36 and 50hpf), the heart is undergoing looping morphogenesis. During this process, a combination of ventricular elongation and widening (Fig 4.2F,G) and relocation of the outflow tract (OFT) moves the ventricle caudally (towards the embryo's tail), positioning it to the right of the atrium. These chamber and tissue reorganisations characterise looping morphogenesis, resulting in well-defined morphological chambers rearranged in an S-looped morphology, with a constriction in between known as the atrio-ventricular canal (AVC).

To quantify in 3D the rotations that characterise this chamber realignment, the atrial and ventricular orientations of processed hearts were acquired from the frontal and sagittal heart faces, and their values were analysed throughout development (for details about these morphometric parameters see Chapter 3, Section 4.5.3, Fig 3.11 and 3.12). These morphometric parameters describing chamber orientation, aim to characterise topographically the relationship between the chambers at any stage. Hence, the evaluation of how they evolve through development aids the understanding of the processes that concomitant to chamber growth and expansion bring the developing heart chambers side-by-side forming an S-shaped loop. [*Note#4.3:* To interpret these morphometric parameters easier, assume the outflow and inflow tract (IFT) of the heart are constrained to move only along the linear heart length so that changes in the orientations of the chambers result from the sole rotation of the chamber segments].

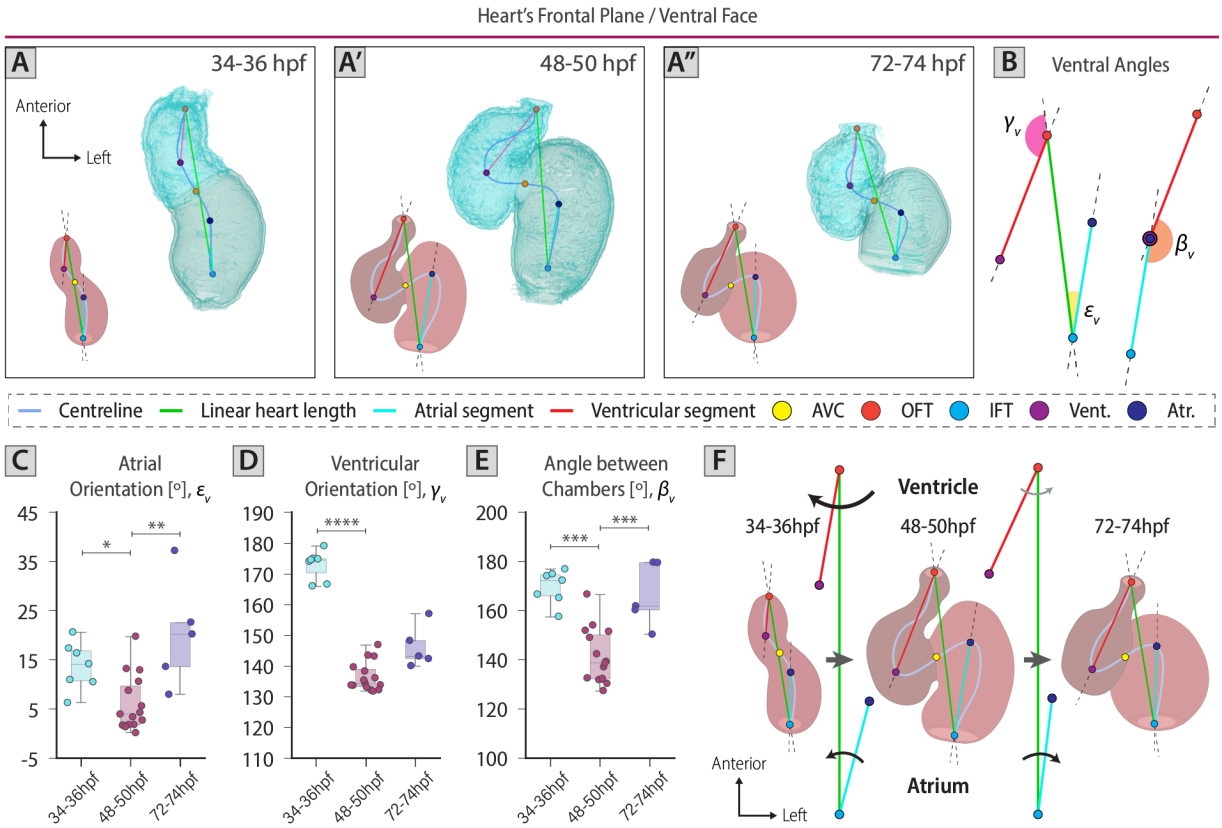

Fig 4.3. Distinct chamber rotations in the heart's frontal plane throughout development are linked to concurrent processes of looping, ballooning and chamber rearrangement.
A-A''. Representative 3D atrial and ventricular myocardial chambers with defined orientation segments and linear heart length inside the heart at different stages of development (34-36hpf: A, 48-50hpf: A', 72-74hpf: A''). When these segments are projected in the *x,y* plane of the heart (see schematic at bottom left corner in panels A-A'') measurements between them provide a quantitative readout of the orientation of each chamber and the angle between them from the frontal plane of the heart. **B.** Schematic depicting the ventral angles measured from the heart/chamber segments shown in A-A''. **C-E.** Quantification of atrial orientation ε_v (C), ventricular orientation γ_v (D), and angle between chambers β_v (E) between 34 and 74hpf. As the heart loops and balloons, the atrium 'rotates' towards the segment connecting the inflow and outflow tract centres (i.e. linear heart length in green) while the ventricle 'rotates' towards the right (away from the linear heart length). Both rotations result in a reduction in the angle between both chambers (34-36hpf vs. 48-50hpf: ε_v *p-value=0.03886*, γ_v *p-value=0.00006*, β_v *p-value=0.00100*). Later, as the heart undergoes maturation, the atrium 'rotates' back away from the linear heart length towards the left side of the embryo, while the ventricle maintains it orientation, resulting in an increased angle between chambers (48-50hpf vs. 72-74hpf: ε_v *p-value=0.00875*, β_v *p-value=0.00100*). **F.** Schematic summarising the ventral rearrangements undergone by the chambers between 34 and 74hpf. A-A',B,F: Heart's ventral face with anterior to the top. C-E: Error bars with 95% confidence interval of the mean. 34-36hpf: *n=7*, 48-50hpf: *n=15*, 72-74hpf: *n=5*. For details regarding the statistical analyses used to compare this set of data see *Note#4.2* (pg. 99). Only significant comparisons are shown. ****: *p-value*<0.0001, ***: *p-value*<0.001, **: *p-value*<0.01, *: *p-value*<0.05. AVC: Atrioventricular canal, OFT: Outflow-tract, IFT: Inflow-tract, Atr: sphere positioned 50 centreline points away from the AVC centreline position in the direction of the atrium, Vent: sphere positioned 50 centreline points away from the AVC centreline position in the direction of the ventricle.

Analysis of chamber orientation from the ventral face of the heart indicates that as the early heart tube undergoes looping, both chambers rotate towards the right side of the embryo or heart midline (Fig 4.3C,D,F). Since the ventricular rotation is higher than the atrial one, the angle measured between both chambers gets reduced (Fig 4.3E). This group of rotations, combined with chamber growth and the caudal translation of the OFT, deviates the ventricular segment from the linear heart length and the atrial orientation, setting the chambers in an arrangement that possibly aids its growth and ballooning while

acquiring their distinguishable bean shapes. At the same time, these set of rotations aid the establishment of both chamber apexes and the formation of a bend in the midline of the heart, where the future AVC will form. Having acquired this looped shape, as the heart transitions to a maturing stage, both chambers rotate back to the left side of the embryo (Fig 4.3C,D,F). This time the atrial rotation is higher than the ventricular one, causing the angle measured between chambers to increase (Fig 4.3E). These latter chamber rotations coupled with atrial compaction and linear heart length shortening feasibly ensure the heart maintains the already acquired looped morphology as it starts maturing.

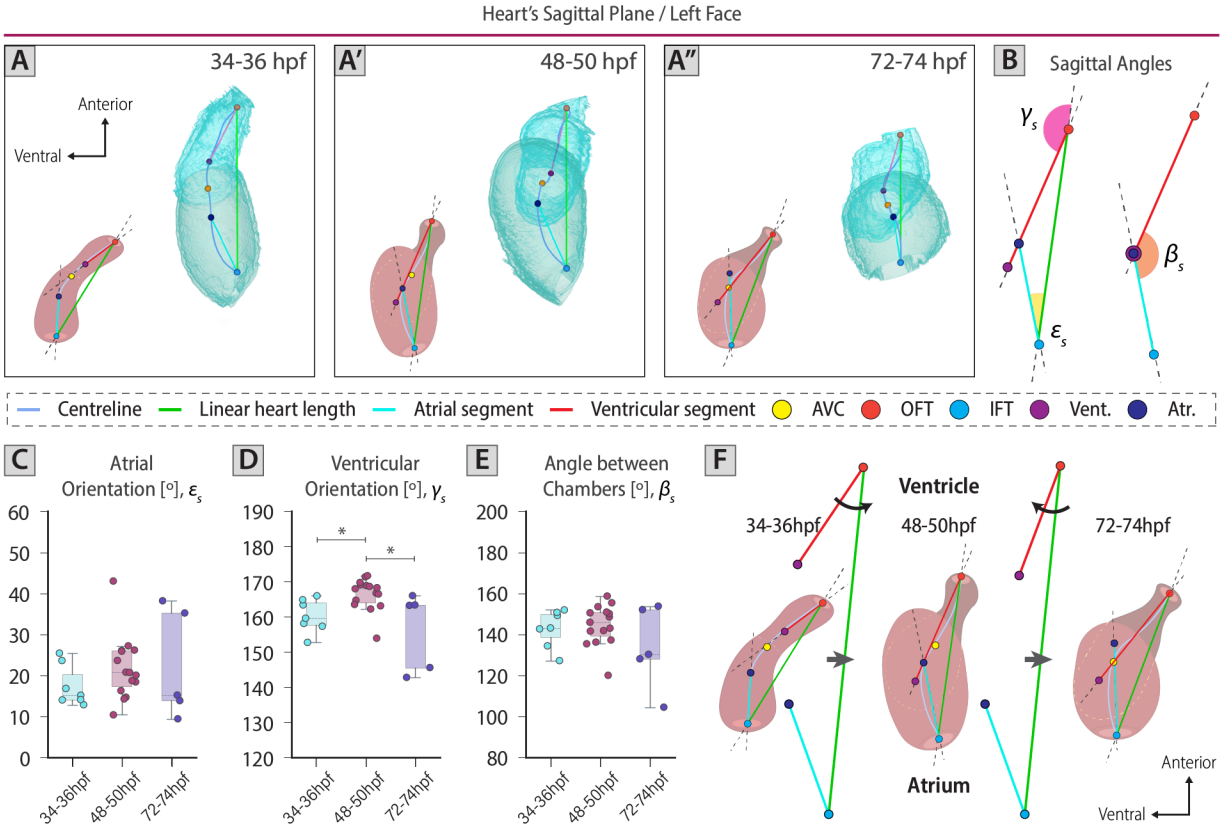

Fig 4.4. Rotations of the ventricle in the heart's sagittal plane repositions the outflow tract orientation suggesting they are required for efficient cardiac function.

A-A''. Representative 3D atrial and ventricular myocardial chambers with defined orientation segments and linear heart length inside the heart at different stages of development (34-36hpf: A, 48-50hpf: A', 72-74hpf: A''). When these segments are projected in the *z,y* plane of the heart (see schematic at bottom left corner in panels A-A'') measurements between them provide a quantitative readout of the orientation of each chamber and the angle between them from the sagittal plane of the heart (left face). **B.** Schematic depicting the sagittal angles measured from the heart/chamber segments shown in A-A''. **C-E.** Quantification of atrial orientation ε_v (C), ventricular orientation γ_v (D), and angle between chambers β_v (E) between 34 and 74hpf. As the heart loops and balloons, the atrium 'rotates' slightly (not significant) ventrally and away from the linear heart length while the ventricle 'rotates' dorsally towards the linear heart length (34-36hpf vs. 48-50hpf: γ_s *p-value=0.03801*), resulting in a constant angle between both chambers. As the heart undergoes maturation, the ventricle 'rotates' back away from the linear heart length, again maintaining constant the angle between chambers (48-50hpf vs. 72-74hpf: γ_s *p-value=0.04409*). **F.** Schematic summarising the sagittal rearrangements undergone by the chambers between 34 and 74hpf. A-A',B,F: Heart's left face with anterior to the top. C-E: Error bars with 95% confidence interval of the mean. 34-36hpf: *n=7*, 48-50hpf: *n=15*, 72-74hpf: *n=5*. For details regarding the statistical analyses used to compare this set of data see *Note#4.2* (pg. 99). Only significant comparisons are shown. *: *p-value* <0.05. AVC: Atrioventricular canal, OFT: Outflow-tract, IFT: Inflow-tract, Atr: sphere positioned 50 centreline points away from the AVC centreline position in the direction of the atrium, Vent: sphere positioned 50 centreline points away from the AVC centreline position in the direction of the ventricle.

Analysis of chamber orientation from the sagittal view identifies the ventricle as the main rotating chamber during looping morphogenesis (Fig 4.4). As the heart tube starts looping, along with the ventricular rotation in the frontal heart plane (Fig 4.3D), the ventricle undergoes a rotation in the sagittal plane towards the linear heart length (Fig 4.4D,F). This rotation is probably the result of the chamber's growth and the caudal translocation of the OFT, facilitating the foundation of the heart bend and the distinct AVC constriction. After 50hpf, the ventricle starts rotating ventrally while the atrium maintains its orientation. These last rotations possibly support the reorientation of the OFT so that blood can be pumped efficiently out of this chamber (Shewale and Dubois, 2021).

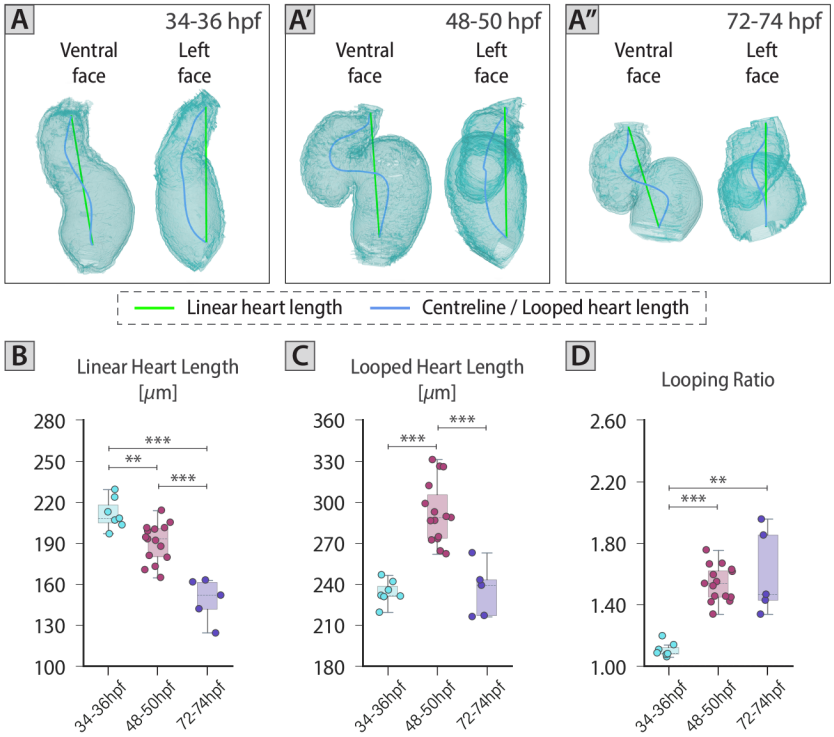

Fig 4.5. The heart undergoes looping morphogenesis between 34hpf and 50hpf and preserves this looped morphology as it matures.

A-A''. 3D reconstructions of the myocardium in wild-type hearts at early looping (34-36hpf, A), during looping and ballooning (48-50hpf, A') and at maturing (72-74hpf, A'') stages. Linear heart length (green line) and centreline (light blue spline) provide information about the length of the heart and its looped length, respectively, as it undergoes morphogenesis. **B.** Quantification of the linear heart length at these key developmental stages illustrates how the heart 'shortens' in length as it undergoes looping and ballooning (34-36hpf vs. 48-50hpf: *p-value=0.00742*) and keeps compacting as it starts maturing (48-50hpf vs. 72-74hpf: *p-value=0.00100*). **C.** Quantification of the looped heart length demonstrates an increase in the centreline length as the heart undergoes looping and ballooning (34-36hpf vs. 48-50hpf: *p-value=0.00100*) and a shortening as the heart matures (48-50hpf vs. 72-74hpf: *p-value=0.00100*). **D.** Quantification of looping ratio (quotient between looped heart length and linear heart length) confirms that between 34 and 50hpf the heart undergoes looping morphogenesis, transforming its shape from a tubular organ to a looped tube and increasing its looping ratio to values over 1.4 (34-36hpf vs. 48-50hpf: *p-value=0.00068*). As the heart undergoes the first stages of maturation (50→74hpf), despite the described compaction, looping ratio values are maintained, preserving the looped morphology. A-A'': Heart's ventral and left face with anterior to the top. B-D: Error bars with 95% confidence interval of the mean. 34-36hpf: *n=7*, 48-50hpf: *n=15*, 72-74hpf: *n=5*. For details regarding the statistical analyses used to compare this set of data see *Note#4.2* (pg. 99). Only significant comparisons are shown. ***: *p-value*<0.001, **: *p-value*<0.01.

All the chamber volume changes, rotations, and rearrangements just described constitute the basis of looping morphogenesis. To further quantify and characterise this process throughout these key developmental stages, the length of the line connecting the IFT and OFT (green line in Fig 4.5A-A'') and

that of the centreline (or looped heart length) (light blue spline in Fig 4.5A-A'') were acquired and the ratio between the looped and the linear length (i.e. looping ratio) was calculated. As expected, as the heart loops and balloons, the growth and rearrangement of the chambers results in them drawing closer to each other and forming the constriction at the AVC. This group of movements causes a shortening of the linear length of the heart (Fig 4.5B), and a lengthening of its looped length (Fig 4.5C), both of which result in looping ratio values over 1.4 (Fig 4.5D). Next, as the heart transitions into a maturing stage, the atrial compaction combined with further chamber realignments results in shorter linear and looped lengths. Interestingly, the looping ratio is maintained constant between 50 and 74hpf, suggesting the looped morphology already acquired by 48-50hpf is maintained while the heart undergoes early stages of maturation.

To get a more regionalised understanding of the 3D growth undergone by each heart chamber over the course of looping, ballooning and early maturing stages, 2D average myocardial ballooning heatmaps were obtained from the processed hearts at the three key developmental stages of interest (Fig 4.7A: 34-36hpf, B: 48-50hpf, and C: 72-74hpf). [*Note#4.4:* To aid the 2D heatmap analysis and comparison between stages, refer to Fig 4.6 where distinct 3D regions of the heart are colour matched to the corresponding 2D sections found in the planar projected heatmaps].

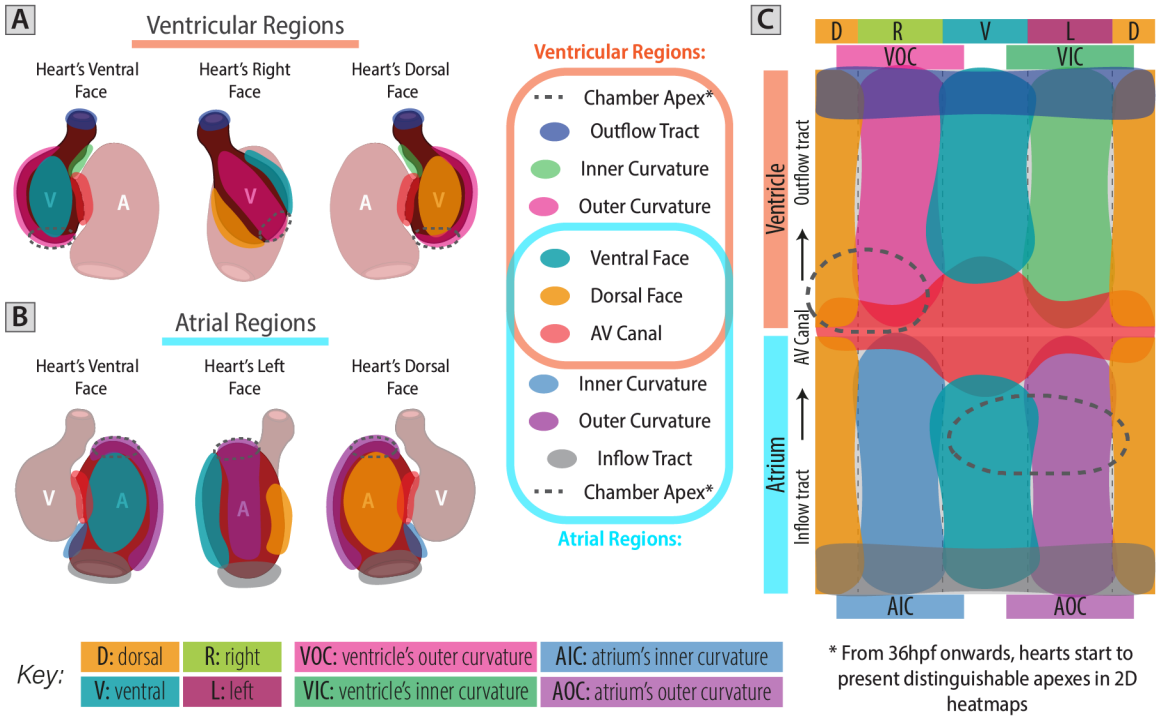

Fig 4.6. Schematic matching 3D heart regions to 2D heatmap sections.
A-B. Schematic illustrating with different colours and from different orientations the seven different ventricular (A) and atrial (B) regions that can be easily distinguished in the 3D heatmap representations. **C.** 2D heatmap format, highlighting with the same colours as in A and B, the different heart sections that can be identified in the heatmap planar projections. The use of this schematic throughout this thesis will aid 2D heatmap analysis and interpretation, allowing the matching of 2D sections to the corresponding 3D heart regions. D: Dorsal, R: Right, V: Ventral, L: Left, VOC: Ventricular Outer Curvature, VIC: Ventricular Inner Curvature, AOC: Atrial Outer Curvature, AIC: Atrial Inner Curvature, AV Canal: Atrioventricular Canal. A-B: Anterior to the top.

Analysis of the 2D myocardial ballooning heatmap at 34-36hpf (Fig 4.7A) identifies an early ballooning process of the atrium (red/orange tones forming a 'U' shape in the chamber's heatmap), -excluding the AVC region, which remains tubular (uniform light green colours). Changes in the depth of both chambers can also be observed at this early stage by comparing the colours on the dorsal and ventral regions of both

chambers. Darker red colours on the atrial dorsal-left and red tones on the ventricular dorsal-right also indicate the emergence of the characteristic outer curvatures of both chambers, confirming that heart tubes at 34-36hpf have already started to undergo ballooning and looping morphogenesis (looping ratio>1 in Fig 4.5D).

Comparative analysis of the 2D heatmaps between early looping (34-36hpf, Fig 4.7A) and looping and ballooning stages (48-50hpf, Fig 4.7B) corroborates the growth and expansion both chambers have undergone over the course of this time frame. The emergence of an apex is clearly distinguishable in the outer curvatures of both chambers (match regions enclosed by dotted lines in Fig 4.6 with Fig 4.7B'') as they continue to undergo morphogenesis.

As looping morphogenesis proceeds and the heart starts to transition into a maturing stage (72-74hpf, Fig 4.7C), chamber and tissue rearrangements are identified in the 2D myocardial ballooning heatmaps by the appearance of a constricted OFT (light blue colours in the top of the ventricular heatmap) and high ballooning values (dark red colours) in the apexes of both chambers as well as in the atrial dorsal and ventral faces. At this stage, a combination between the spherical morphology of the atrium (Fig 4.2E) and the orientation of the AVC, deviates the atrial centreline from the centre of the atrium, positioning its most concave section a little closer to the outer curvature of this chamber. This results in larger distances between the centreline and the inner curvature of the atrium when quantifying ballooning, hence making the myocardial ballooning heatmaps to characteristically display darker red colours in the atrial right face when compared to the left. [*Note#4.5:* As wild type heatmaps set up the basis for comparative analysis, the characteristic colour pattern of the 2D projected heatmaps described in this chapter will allow objective comparative analysis between embryos at different stages and/or genotypes, aiding the identification of defects in ballooning or tissue distribution].

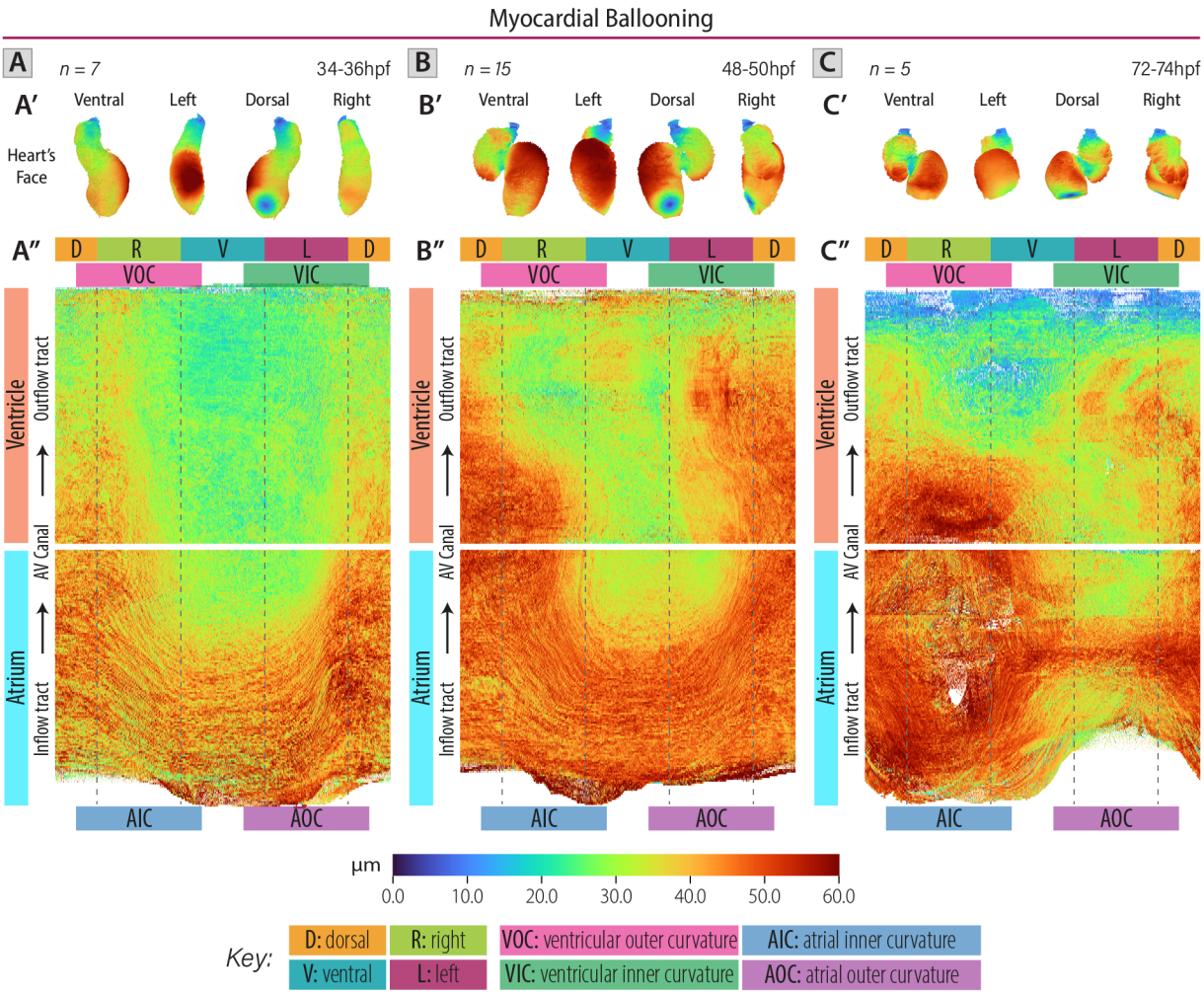

Fig 4.7. 2D planar projections of myocardial ballooning heatmaps reveals that heart tubes at 34-36hpf have already started to undergo both ballooning and looping morphogenesis.
A-C. 3D and 2D representations of the myocardial ballooning of a wild-type zebrafish heart at early looping (34-36hpf, A), during looping and ballooning (48-50hpf, B), and at maturing stages (72-74hpf, C). **A'-C'.** Right, ventral, left, and dorsal heart face (left to right) of 3D colour-coded internal myocardium meshes based on its ballooning values at key developmental stages (34-36hpf: A', 48-50hpf: B', 72-74hpf: C'). **A''-C''.** Average planar projections of the colour-coded myocardial ballooning 2D heatmaps of all the processed wild-type hearts at 34-36hpf (A'', *n=7*), 48-50hpf, (B'', *n=15*) and 72-74hpf (C'', *n=5*). As early as 34hpf, the atrium has already started to undergo ballooning, transforming its morphology from a tubular/conical shape to a more ellipsoidal shape. This can be seen in the atrial 2D heatmap at 34-36hpf (A'') where orange~light-red colours are present throughout the whole atrium except for the valve region. At 48-50hpf (B'') the already atrial ballooned regions at 34-36hpf have deviated more from the midline presenting darker red colours (compare A'' and B''), and accounting for a continued radial growth of this chamber. At this stage the ventricle also shows increased ballooning in the apex, inner curvature, and left-dorsal face of the chamber. After looping and ballooning, atrial ballooning is more prominent in the apex of the chamber, as well as the right face of the heart, while ventricular ballooning is maintained in the apex and left-dorsal face of this chamber. A-C: Anterior to the top. A-C' and A''-C'' share colour-scale presented with the key at the bottom of the figure. D: Dorsal, R: Right, V: Ventral, L: Left, VOC: Ventricular Outer Curvature, VIC: Ventricular Inner Curvature, AOC: Atrial Outer Curvature, AIC: Atrial Inner Curvature, AV Canal: Atrioventricular Canal.

Together, the morphometric parameters so far described illustrate the complexity of the alignment and morphological changes undergone by each chamber as the heart loops and balloons and then transition to an early maturing stage. Tight coordination of the chamber's growth and rearrangement ensures the precise chamber and looping morphology is set out at these early stages so that future maturation processes result in healthy and functional hearts.

Having characterised gross morphological changes in the developing heart, the next step was to study and describe the changes undergone by each cellular tissue layer over the course of looping, ballooning and early maturing morphogenesis. For this, volumetric measurements of the whole and chamber-sectioned myocardial and endocardial meshes were acquired and analysed (Fig 4.8).

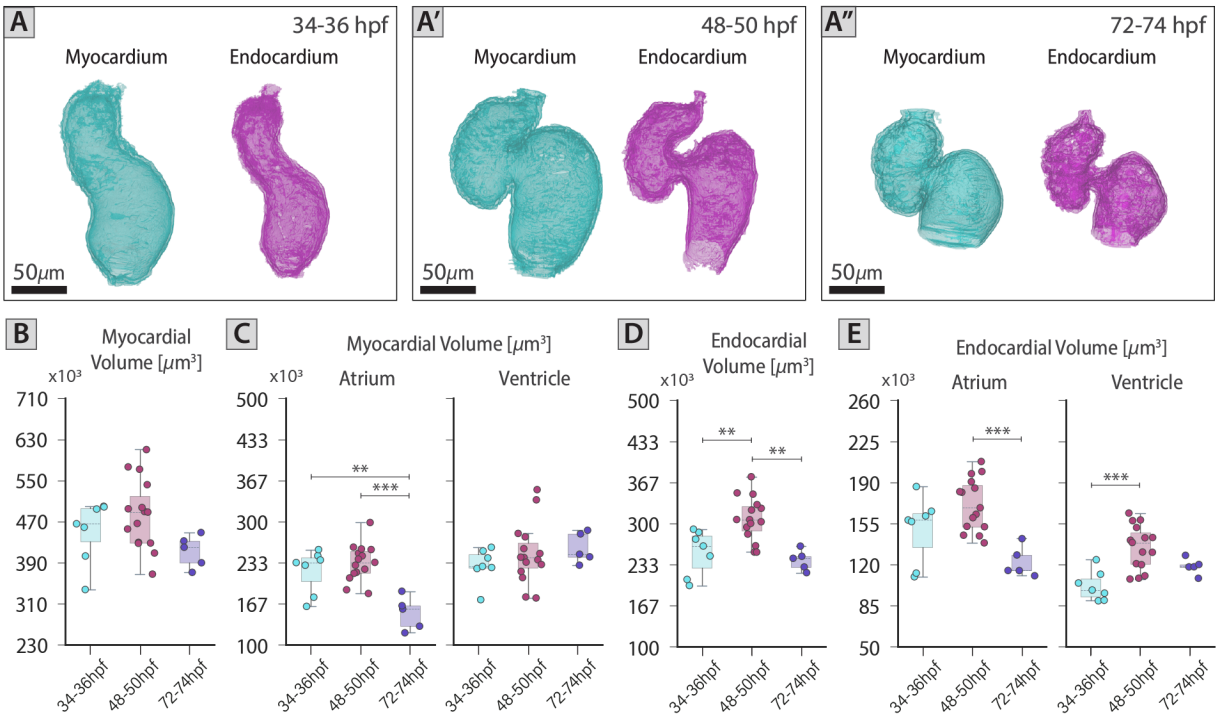

Fig 4.8. Chamber-specific changes in tissue volume happen in the myocardial and endocardial tissue layers as the heart undergoes morphogenesis.

A-A''. Representative 3D reconstructions of the myocardium (teal meshes) and endocardium (magenta meshes) in wild-type hearts at early looping (34-36hpf, A), during looping and ballooning (48-50hpf, A') and at maturing (72-74hpf, A'') stages. **B-C.** Quantification of the myocardial tissue volume of the whole heart (B) and its chambers (C). As the heart loops and balloons the total myocardial tissue volume remains constant (34hpf→48hpf) and decreases as it transitions to the maturing stage (50hpf→72hpf, not significant). This trend is significant for the atrium where a great reduction in myocardial tissue volume is observed between 50 and 74hpf (48-50hpf vs. 72-74hpf: *p-value=0.00100*), while the ventricle maintains its tissue volume throughout these stages. **D-E.** Quantification of the endocardial tissue volume of the whole heart (D) and its chambers (E). While the heart undergoes looping and ballooning, the total endocardial tissue volume increases due to an increase in this tissue volume mainly driven by the ventricle (34-36hpf vs. 48-50hpf: whole heart *p-value=0.00412*, ventricle *p-value=0.00100*). Later, as the heart transitions to a maturing stage, the total endocardial volume of the heart is reduced driven primarily by a reduction in the endocardial tissue in the atrium (48-50hpf vs. 72-74hpf: whole heart *p-value=0.00194*, atrium *p-value=0.00100*). A-A'': Heart's ventral face with anterior to the top. B-E: Error bars with 95% confidence interval of the mean. 34-36hpf: *n=7*, 48-50hpf: *n=15*, 72-74hpf: *n=5*. For details regarding the statistical analyses used to compare this set of data see *Note#4.2* (pg. 99).Only significant comparisons are shown. ***: *p-value*<0.001, **: *p-value*<0.01.

As the heart tube loops and balloons, the myocardial tissue volume is maintained in both chambers (Fig 4.8B,C). Interestingly, this is not the case for the endocardium, where an increase in tissue volume between 34 and 50hpf is observed particularly in the ventricle (Fig 4.8D,E). Later, as the atrium compacts between 50 and 72hpf, both cellular tissue layers exhibit a significant reduction in volume, suggesting a 'wall thinning' process occurs in this chamber which allows it to maintain its lumen capacity as it reduces its size (Fig 4.1D,F). In contrast cellular tissue volume reductions are not observed in the ventricle between 50 and 72hpf. This chamber-specific differences may arise from the onset of trabeculation in the ventricle

resulting in a slight but not-significant increase in the myocardial mass and a maintenance of the endocardial volume between these stages.

To complement this tissue volume analysis and understand the distribution of each tissue layer around the heart, average 2D tissue thickness heatmaps of both the myocardium and endocardium were acquired and analysed at the key developmental stages of interest (Fig 4.9 and Fig 4.12, respectively).

Analysis of the 2D myocardial thickness heatmap at early stages of looping morphogenesis (34-36hpf, Fig 4.9A) identifies a ventricle with thicker myocardial tissue (*~6-10µm*) when compared to the atrium (*~3-6µm*). This thicker myocardium is scattered throughout the chamber but mainly positioned on the OFT as well as the ventral, left, and dorsal faces of the ventricular chamber. As the heart tube undergoes looping and ballooning, the thickness of the myocardial tissue gets reduced across both chambers, with the ventricle maintaining an average thicker myocardium when compared to the atrium. Following the conservation of mass principle, for chambers to grow and expand (Fig 4.1 and 4.2) while maintaining its myocardial tissue volume constant (Fig 4.8B,C), the myocardial tissue thickness across the whole heart would need to be reduced. This reduction in tissue thickness is confirmed by the information presented in the 2D heatmaps when comparing the 34-36hpf and 48-50hpf stages (Fig 4.9A'' and B'').

Later, as the heart transitions to a maturing stage, thicker and thinner myocardial regions become more defined rather than homogeneously spread throughout both chambers (compare B'' and C'' in Fig 4.9). In the ventricle, as the myocardial tissue volume is maintained between 48 and 74hpf (Fig 4.8C), the myocardial tissue gets reorganised and concentrated in certain regions of the chamber, specifically in the ventral (close to the OFT) and dorsal face where average myocardial thicknesses of up to *12µm* can be found. This thicker myocardial regions in this chamber may represent areas of this cellular layer in which trabecular cardiomyocytes (also known as trabecular seeds) are starting to emerge as the ventricle starts to mature, suggesting the thickness values obtained for these regions correspond to the width of two cardiomyocytes sitting one on top of each other. On the contrary, between these same time-points, the atrium experiences a reduction in myocardial tissue volume (Fig 4.8C) while compacting in size (Fig 4.1D). This results in an atrial-wide reduction of myocardial thickness, confirming the already suggested 'wall thinning' process experienced by this chamber. However, at these later stage, patches of thicker myocardium remain in the ventral and dorsal regions of the atrium (Fig 4.9C'').

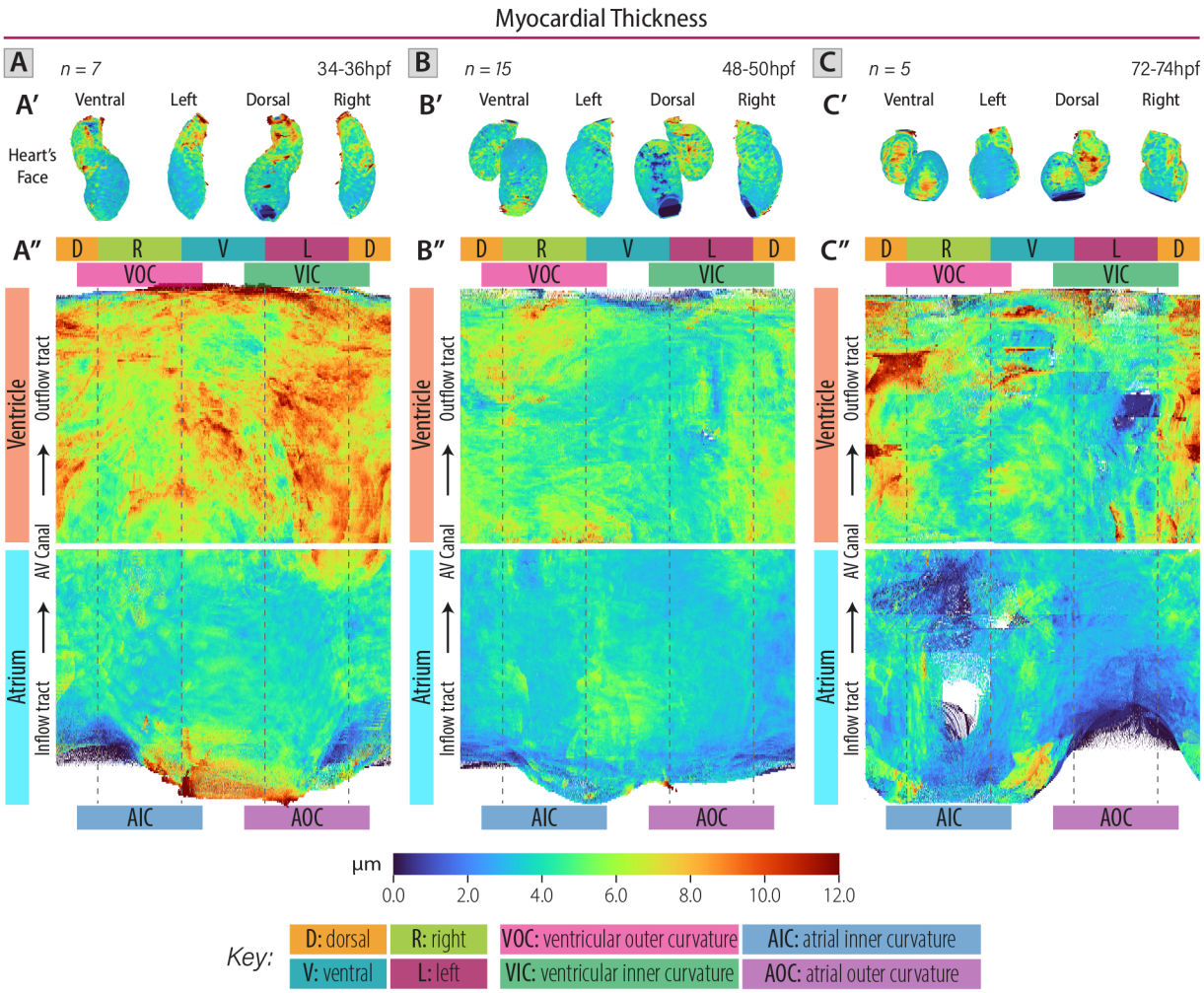

Fig 4.9. Despite its constant tissue volume, the myocardial thickness is dynamic over the course of looping and ballooning morphogenesis.

A-C. 3D and 2D representations of the myocardial thickness of a wild-type zebrafish heart at early looping (34-36hpf, A), during looping and ballooning (48-50hpf, B), and at maturing stages (72-74hpf, C). **A'-C'.** Ventral, left, dorsal and right heart face (left to right) of 3D colour-coded myocardial meshes based on its thickness values at key developmental stages. **A''-C''.** Average planar projections of the colour-coded myocardial thickness 2D heatmaps of all the processed wild-type hearts at 34-36hpf (A'', *n=7*), 48-50hpf, (B'', *n=15*) and 72-74hpf (C'', *n=5*). At early looping stages (A'') the atrial myocardium is thicker in the ventral face close to the inflow tract (IFT), and in the dorsal face close to the atrioventricular canal (AVC), while the ventricular myocardium has thicker myocardial regions in the ventral, left and dorsal face of this chamber (regions in orange~light-red colours). As the heart loops and balloons (A''→B'') the myocardial thickness gets reduced throughout the whole heart (compare A'' and B''). At this later stage (48-50hpf, B'') the myocardial thickness becomes mostly uniform throughout the chambers, with the ventricle showing thicker myocardium (~6-7μm) than the atrium(~3-4μm). Nevertheless, at this stage, the atrium shows two spots of thicker myocardium in its ventral central face and in its dorsal face close to the AVC. As the heart transitions to a maturing stage (B''→C''), thicker and thinner regions become more defined rather than spread throughout both chambers (compare B'' and C''). In the ventricle, thicker regions get located mainly in the dorsal and top ventral (i.e. close to the outflow tract (OFT)) face of the chamber, while in the atrium these thicker regions are positioned to the ventral and dorsal face (C''). A-C: Anterior to the top. A-C' and A''-C'' share colour-scale presented with the key at the bottom of the figure. D: Dorsal, R: Right, V: Ventral, L: Left, VOC: Ventricular Outer Curvature, VIC: Ventricular Inner Curvature, AOC: Atrial Outer Curvature, AIC: Atrial Inner Curvature, AV Canal: Atrioventricular Canal.

To further understand the myocardial tissue changes happening over the course of looping morphogenesis, cell counts and internuclear distance analysis were performed in *Tg(myl7:lifeActGFP); Tg(-5.1myl7:DsRed2-NLS)* double transgenic wild-type zebrafish embryos at 50 and 72hpf using *morphoCell*

(Fig 4.10 and 4.11) (for details regarding *morphoCell* see Chapter 3, Section 7.1). *Tg(-5.1myl7:DsRed2-NLS)* (henceforth *Tg(myl7:DsRed)*) embryos express the fluorescent protein DsRed2 in myocardial nuclei (Rottbauer *et al.*, 2002). To make sure all the DsRed positive cells were being captured in the analysis, embryos were fixed at these two developmental stages, immunostained to boost both fluorescent signals (i.e. GFP and DsRed) and imaged in the light-sheet microscope (for more details on the methodology see Chapter 2, Section 8).

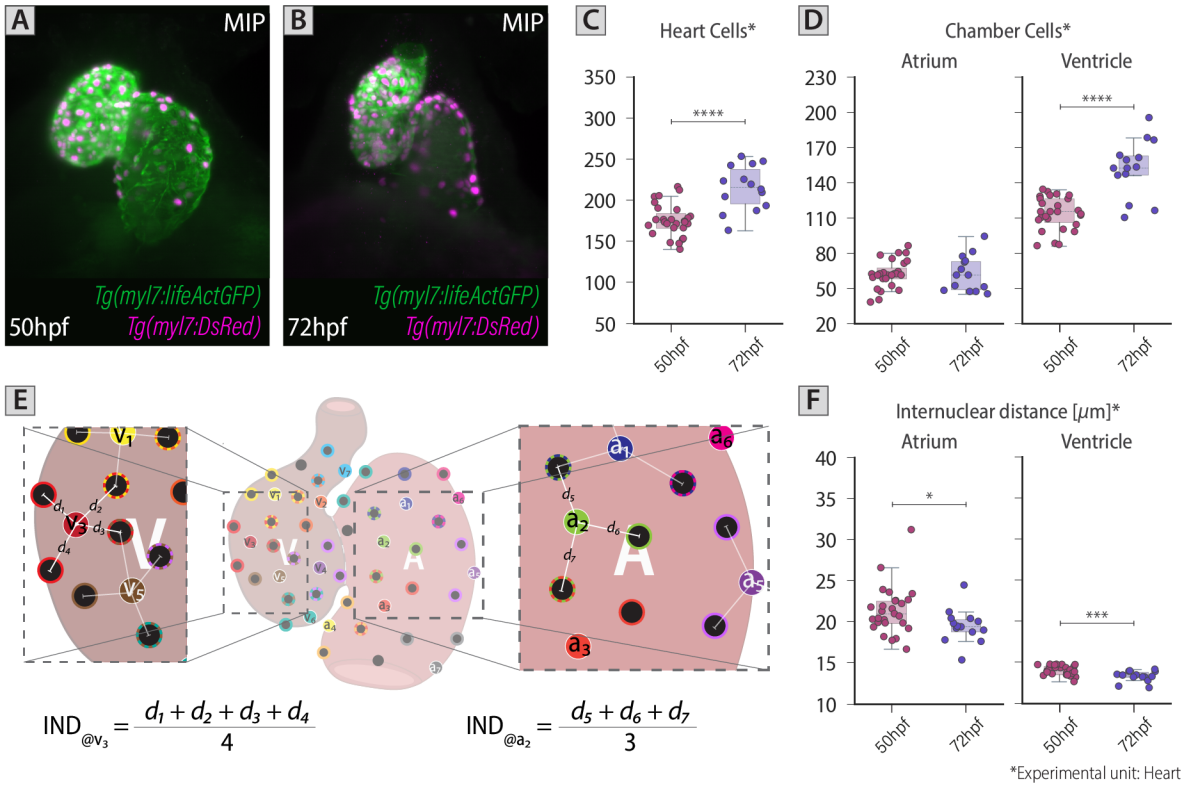

$$IND_{@v_3} = \frac{d_1 + d_2 + d_3 + d_4}{4} \qquad IND_{@a_2} = \frac{d_5 + d_6 + d_7}{3}$$

Fig 4.10. Internuclear distance analysis of cardiomyocytes suggest cell shrinking in both chambers is linked to chamber morphogenesis.
A-B. Double transgenic zebrafish embryos with myocardial tissue and nuclear marker are fixed at 50 (A) and 72hpf (B), immunostained to boost the fluorescent signals and imaged on the light-sheet microscope. *Tg(myl7:lifeActGFP)* in green marks the myocardium and *Tg(myl7:DsRed)* signal in magenta marks the myocardial nuclei. **C-D.** Quantification of cell number in the heart (C) and each chamber (D) using *morphoCell*. The number of cells making up the heart increases between 50 and 72hpf, driven mainly by an increase in the number of cells making up the ventricle (heart: *p-value*<0.00001, ventricle: *p-value*<0.00001). **E.** Schematic depicting the clustering process of *morphoCell* to calculate internuclear distance (IND) as a proxy for cell size (for more details regarding IND quantification method see Chapter 3, Section 7.1). **F.** Quantification of average IND per heart and chamber identifies a reduction in average cell size between 50 and 72hpf for both chambers (atrium: *p-value=0.02170*, ventricle: *p-value=0.00089*). A,B: Ventral views with anterior to the top. E. Heart's ventral face with anterior to the top. C,D,F: Error bars with 95% confidence interval of the mean. 50hpf: *n=27*, 72hpf: *n=14*. All sample groups per stage were analysed for normality using Shapiro-Wilk Normality test. For each variable, if all groups were normally distributed, comparison between stages was carried out using Unpaired t-test. When normal distribution could not be assumed, Mann-Whitney test was used. For all tests a statistical significance α of *0.05* was defined. Only significant comparisons are shown. ****: *p-value*<0.0001, ***: *p-value*<0.001, *: *p-value*<0.05. A: Atrium, V: Ventricle, IND: Internuclear-distance, MIP: Maximum intensity projection.

Between 50 and 72hpf, cell count analysis identifies an increase in total cardiomyocyte number, driven mainly by an increase in the number of cells making up the ventricle (while cell numbers in the atrium remain constant) (Fig 4.10C,D). Interestingly within this time frame, chamber size and myocardial tissue volume are reduced in the atrium while both are maintained in the ventricle (Fig 4.1D, Fig 4.8C). Combined,

these sets of information suggest a reduction in cell size in both chambers as the heart transitions to an early maturing stage. Internuclear distance (IND) analysis per chamber confirms this hypothesis, identifying significant reductions in cell size for both the atrium and ventricle (Fig 4.10F).

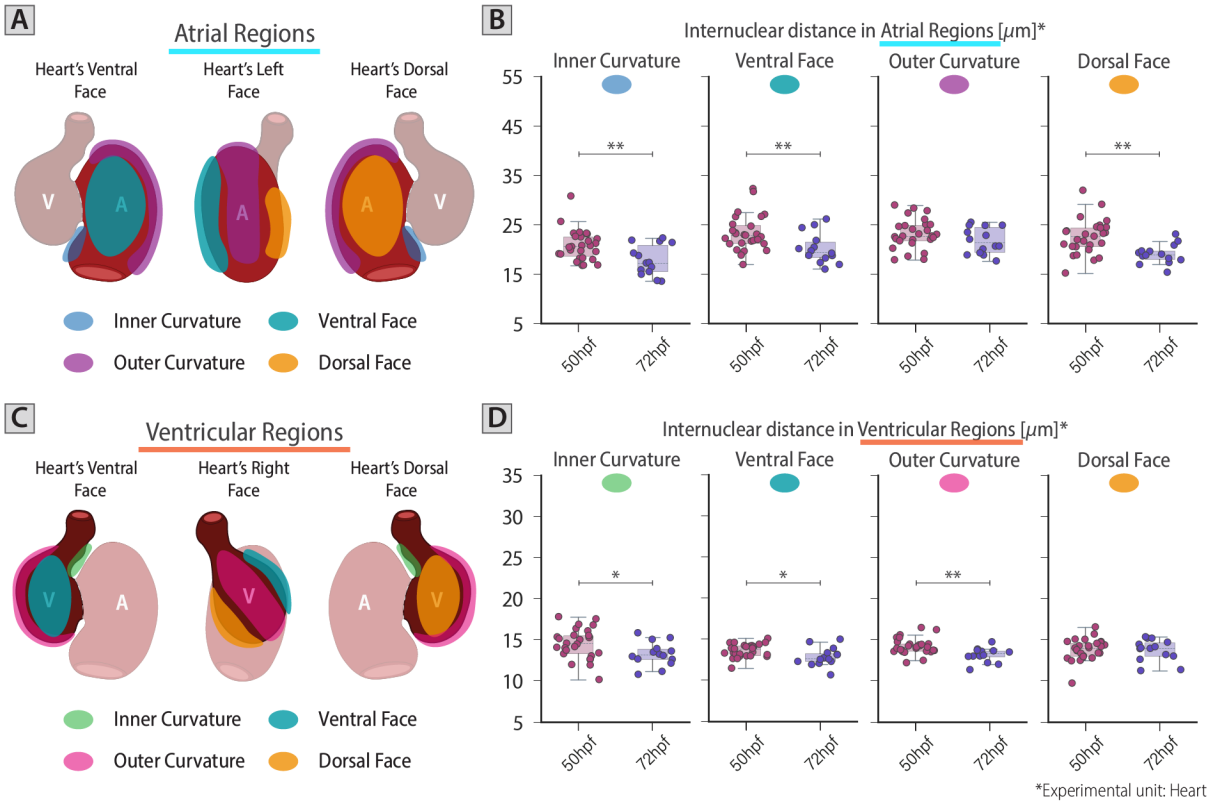

Fig 4.11. Internuclear distance analysis of cardiomyocytes suggests chamber-specific regional cell shrinking is linked to chamber remodelling between 50hpf and 72hpf.

A. Schematic illustrating with different colours the four different chamber regions into which atrial cells can be further classified to better understand cell distribution and size in this chamber. **B.** Quantification of average internuclear distance (IND) of atrial cells positioned in the inner curvature, ventral face, outer curvature, or dorsal face of this chamber. Between 50 and 72hpf reduction in cell size occurs mainly in the cells positioned in the ventral and dorsal face as well as the inner curvature of the atrium (inner curvature: *p-value=0.00865*, ventral face: *p-value=0.00861*, dorsal face: *p-value=0.00150*). **C.** Schematic illustrating with different colours the four different chamber regions into which ventricular cells can be further classified to better understand cell distribution and size in this chamber. **D.** Quantification of average internuclear distance (IND) of ventricular cells per region. Between 50 and 72hpf reduction in cell size occurs mainly in the cells positioned in the inner and outer curvatures as well as the ventral face of the ventricle (inner curvature: *p-value=0.02979*, ventral face: *p-value=0.01814*, outer curvature: *p-value=0.0.00163*). B,D: Error bars with 95% confidence interval of the mean. 50hpf: *n=27*, 72hpf: *n=14*. For details regarding the statistical analyses used to compare this set of data see details in legend of Fig 4.10). Only significant comparisons are shown. **: *p-value*<0.01, *: *p-value*<0.05. A: Atrium, V: Ventricle.

Further IND analysis per chamber and region revealed regional chamber-specific reductions in cell size (Fig 4.11). Interestingly, the most profound reductions in atrial cell size between these two time-points occur in the inner curvature and across the dorso-ventral axis of this chamber (Fig 4.11A,B). This data nicely matches the observations made from the 2D myocardial thickness heatmaps at 72-74hpf. As the atrium is compacting in size (Fig 4.1D), reductions in cell size (i.e. IND) happen in the same regions where the myocardium is identified as thicker (inner curvature/right, dorsal, and ventral faces, Fig 4.9 C), suggesting cardiomyocytes are reducing their planar size and compensating this change by heterogeneously yet regionally changing their thickness. At the same time, the IND between cells in the outer curvature (left side) of this chamber is maintained while the myocardial tissue gets thinner (50→72hpf, Fig 4.9), indicating

these myocardial cells maintain their planar size but get thinner to support this chamber remodelling process.

The most profound reductions in ventricular cell size happen in the ventral face and across the chamber's left-right (inner-outer curvature) axis while allowing the cells positioned in the dorsal face to maintain their size (Fig 4.11C,D). This data correlates well with the onset of trabeculation (between 60 and 65hpf) in specific regions of the ventricle, such as the outer curvature and the dorsal face, suggesting that part of the newly identified DsRed positive cells in this chamber (Fig 4.10D) are added to these ventricular regions within this time frame (Priya *et al.*, 2020), thus increasing their cellular-packing (Fig 4.11D). As the inner curvature of the ventricle does not start to trabeculate as early as the rest of the chamber (Rasouli and Stainier, 2017), cell size reductions in this region can possibly take place by the combination of the shortening of this chamber (Fig 4.2H) and the addition of new cells from the SHF, resulting also in increased cellular packing within this ventricular region. All these mechanisms of cell addition and tissue rearrangement explain the increase in ventricular cell number while the chamber's size and lumen capacity remain constant (Fig 4.1D, F).

Together, analysis of cell counts, and IND combined with myocardial tissue volume, thickness, and chamber morphology, suggests regional planar cell shrinking may contribute to chamber-specific remodelling post-looping and ballooning morphogenesis.

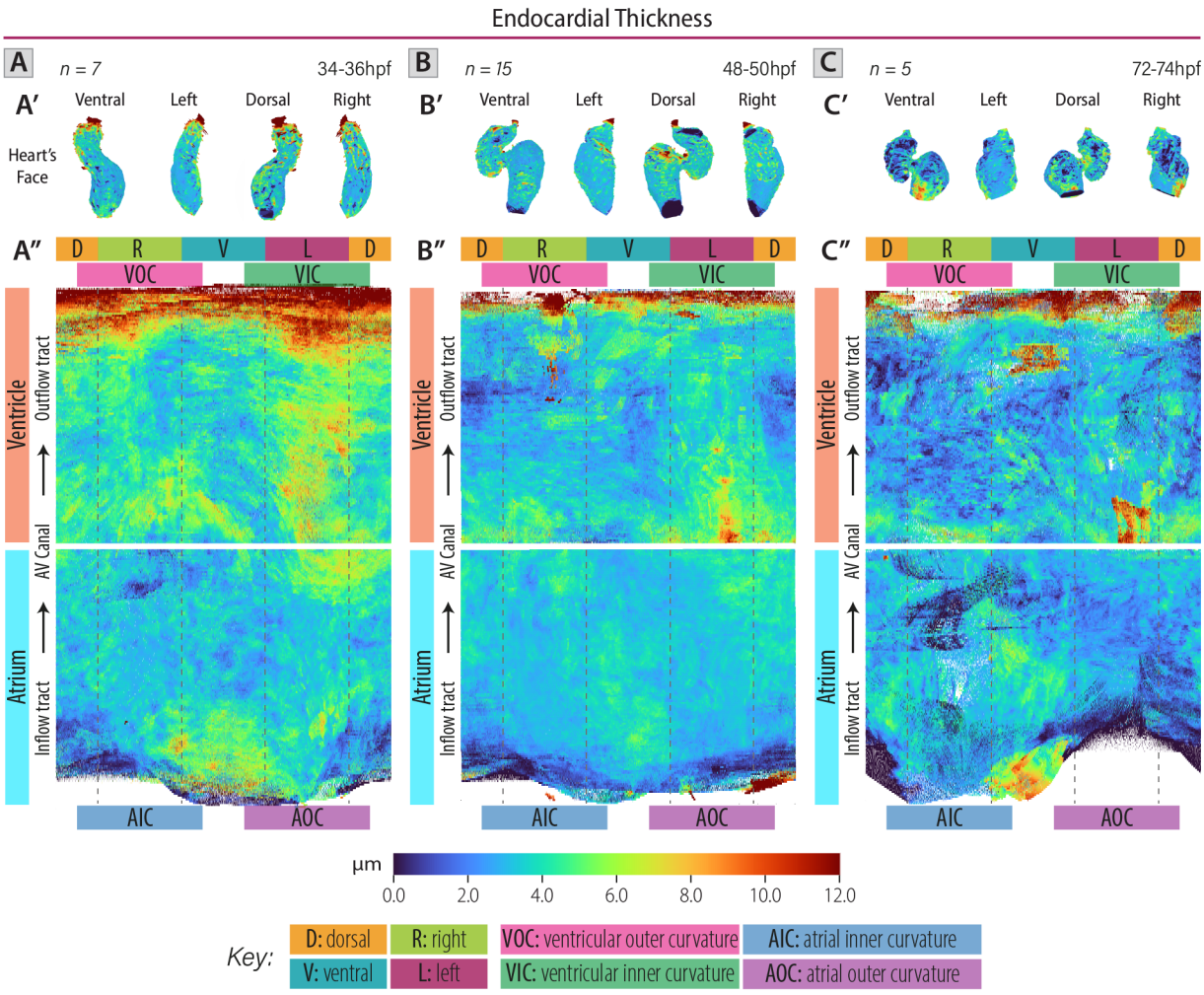

Fig 4.12. 2D heatmap thickness analysis of the endocardium matches its 3D volume dynamics over the course of looping and ballooning morphogenesis.
A-C. 3D and 2D representations of the endocardial thickness of a wild-type zebrafish heart at early looping (34-36hpf, A), during looping and ballooning (48-50hpf, B), and at maturing stages (72-74hpf, C). **A'-C'.** Ventral, left, dorsal and right heart face (left to right) of 3D colour-coded endocardial meshes based on its thickness values

at key developmental stages. **A''-C''.** Average planar projections of the colour-coded endocardial thickness 2D heatmaps of all the processed wild-type hearts at 34-36hpf (A'', *n=7*), 48-50hpf, (B'', *n=15*) and 72-74hpf (C'', *n=5*). At early looping stages (A'') the atrial endocardium is thicker in the ventral face close the inflow tract (IFT), and in the dorsal face close to the atrioventricular canal (AVC), while the rest of the chamber has uniform thickness. The ventricular myocardium, on the other hand, shows thicker regions in the right, dorsal and left faces of this chamber. As the heart loops and balloons (A''→B'') the endocardial thickness gets reduced throughout the whole heart (compare A'' and B''). At this later stage (48-50hpf, B'') the endocardial thickness becomes mostly uniform in the atrium (~3-4μm), while the ventricle presents thicker endocardium in the left and right faces closer to the atrioventricular canal (AVC). As the heart transitions to a maturing stage (B''→C''), thicker and thinner endocardial regions become more defined rather than spread throughout both chambers (compare B'' and C''). In the ventricle, thicker regions are located mainly in the ventral face close the outflow tract (OFT) while maintaining thicker endocardium in the left and right faces closer to the AVC, while in the atrium this get positioned in the ventral and right-dorsal face of this chamber. A-C: Anterior to the top. A-C' and A''-C'' share colour-scale presented with the key at the bottom of the figure. C'': Thick region identified in the ventricular ventral top appears to be an artefact of the heatmap averaging process. D: Dorsal, R: Right, V: Ventral, L: Left, VOC: Ventricular Outer Curvature, VIC: Ventricular Inner Curvature, AOC: Atrial Outer Curvature, AIC: Atrial Inner Curvature, AV Canal: Atrioventricular Canal.

———————

Analysis of the 2D endocardial thickness heatmap at early looping morphogenesis (34-36hpf, Fig 4.12A) identifies an atrium with thicker endocardium in the ventral face close to the IFT and the left-dorsal face close to the AVC, while the rest of the chamber maintains a uniform thickness. The endocardium in the ventricle is thicker across the left-right axis of the chamber and very pronounced around the OFT. The pronounced thickness close to the OFT can be explained by the challenge of segmenting a lumen that either is closed/collapsed due to the arrested heartbeat or hard to identify due to the characteristic diffuse and unsharp images obtained of this heart section and at these early stages when the ventricle is still positioned deep in the embryo underneath its left eye.

As the early looping heart tube undergoes looping and ballooning, the thickness of the endocardial tissue gets reduced across both chambers, whilst maintaining a thicker tissue layer around the AVC (Fig 4.12B). Looking into the ventricle in more detail, this chamber's growth between these time-points (Fig 4.1 and 4.2) counterbalances the increased ventricular endocardial volume (Fig 4.8D,E), resulting in a reduction in this tissue layer's thickness throughout this chamber (Fig 4.12B'').

Next, as the looped heart transitions to a maturing stage, the endocardial tissue layer becomes thinner throughout both chambers (compare B'' and C'' in Fig 4.12). In the compacting atrium (Fig 4.1C), the endocardial tissue volume gets reduced between these two stages (Fig 4.8E), confirming the wall in this chamber is getting thinner, possibly to preserve the chamber's blood filling capacity (Fig 4.1F). The ventricle on the other hand, maintains its size and endocardial tissue volume (Fig 4.1F, 4.8E), suggesting this observed reduction in thickness might result from the reorganisation of the tissue as this chamber is starting to undergo trabeculation. However, thicker endocardium can still be identified in the ventricle in its ventral face close the outflow tract (OFT) and across the left-right axis close to the AVC.

As previously described (Chapter 1, Section 4.1.4), valvulogenesis of the heart happens between 36 and 56hpf. At 48hpf the endocardial cells lining the AVC change their morphology from squamous to cuboidal, while maintaining this tissue as a monolayer (Beis *et al.*, 2005). Interestingly, the endocardial thickening observed close to the AVC between 48 and 74hpf (Fig 4.12B'' and C''), captures this valvulogenesis process the endocardial tissue is undergoing in this specific heart region.

Together, dynamic changes in myocardial and endocardial tissue volume and distribution support chamber-specific processes of growth and remodelling as the heart undergoes early cardiac morphogenesis.

3 THE ECM IN ZEBRAFISH HEART DEVELOPMENT

Having characterised chamber and tissue specific dynamics of the developing heart between pre-looping (34hpf) and early maturing stages (74hpf), the next step entailed the characterisation of the cardiac ECM. To initially describe the gross changes undergone by the cardiac jelly over the course of looping, ballooning and early maturing morphogenesis, volumetric measurements of the whole, and chamber-sectioned cardiac jelly meshes were acquired and analysed (Fig 4.14).

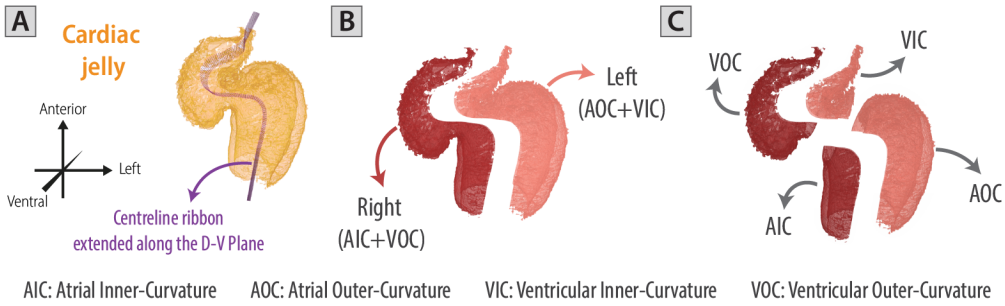

Fig 4.13. Dividing the cardiac jelly into left-right, atrial-ventricular sections to further characterise cardiac jelly regionalisation.
A. Ventral face of the cardiac jelly tissue layer of a zebrafish heart at 48-50hpf with its centreline ribbon (magenta) positioned to cut the tissue layer mesh into left and right sides. **B.** Left and right sides of the cardiac jelly mesh obtained when cutting the cardiac ECM layer in A with the centreline ribbon. **C.** Further division of the left and right sides into chambers (atrium and ventricle) results in four cardiac jelly sections which allow a more detailed characterisation of the ECM distribution throughout the heart. A-C: Heart's ventral face with anterior to the top. D-V: dorso-ventral, AIC: Atrial Inner Curvature, AOC: Atrial Outer Curvature, VIC: Ventricular Inner Curvature, VOC: Ventricular Outer Curvature.

Analysis of ECM volume throughout heart morphogenesis reveals that during cardiac looping and chamber ballooning, as the heart and individual chambers increase their size (Fig 4.1C-D) the cardiac jelly volume expands (Fig 4.14B). This expansion is mainly driven by an increase in the amount of cardiac jelly found in the atrium, while the ventricular ECM volume remains unchanged (Fig 4.14C). However, as the heart transitions to chamber remodelling and maturation stages, the cardiac ECM is significantly reduced in both chambers (Fig 4.14B,C). The timing of this decrease in ECM volume between these two time-points (50 and 74hpf) correlates to chamber-specific processes of growth and remodelling important for chamber maturation, such as the onset of ventricular trabeculation (characterised and linked in multiple studies to ECM degradation (Stankunas *et al.*, 2008; Rasouli and Stainier, 2017; del Monte-Nieto *et al.*, 2018)) and the newly described process of atrial compaction (described throughout this chapter but not previously investigated). Interestingly, over the course of these key developmental stages, the cardiac jelly volume in the atrium is always higher than that in the ventricle (compare atrial and ventricular cardiac jelly volumes per time-point in Fig 4.14C).

To confirm our previous published observations (Derrick *et al.*, 2021) (Appendix 1), where we had described a left-sided atrial-specific expansion of the cardiac ECM prior to the onset of heart looping (26hpf), and understand whether this phenomenon is maintained during looping and ballooning morphogenesis, 3D cardiac jelly meshes were divided into left and right sides (Fig 4.13A,B) and their volume quantified (Fig 4.14D). Similar to the total ECM dynamics, left cardiac ECM volume increases as the heart loops and balloons and reduces as it matures. Excitingly, this early expansion dynamics are not followed by the right cardiac ECM, where the ECM volume is maintained as the heart loops and only gets reduced as the heart matures. To further quantify differences between left and right, the ratio between left and right ECM volume was calculated per heart and at each time-point. A value greater than 1 for this ratio (red dotted line in Fig 4.14E) represents a left-sided thickening of this ECM layer. Analysis of this ratio

confirms that the left-sided specific expansion is maintained not only throughout looping and ballooning but also as the heart undergoes early stages of maturation (Fig 4.14E).

To deepen our understanding about the extent of this asymmetry within the chambers, right and left cardiac jelly meshes were divided into atrial and ventricular sections (Fig 4.13C), their volumes quantified, and the ratio between left and right chamber-specific volumes calculated (Fig 4.14F-I). Not surprisingly, the total ECM dynamics already described (Fig 4.14B) were followed by the atrial- and ventricular-left cardiac jelly volumes. Unexpectedly, the atrial-right cardiac jelly volume remains constants throughout the analysed time frame, indicating that the atrial cardiac jelly volume dynamics (Fig 4.14C) are mainly driven by the deposition and degradation of the cardiac jelly present on the left side of this chamber. However, like the total right cardiac jelly volume (Fig 4.14D), the ventricular-right cardiac ECM does not get expanded as the heart loops and balloons, but its volume does get reduced as it matures (Fig 4.14H). Left-to-right ratios per chamber confirmed this left-to-right ECM asymmetry is driven throughout development by the atrial cardiac jelly (Fig 4.14G), while the left and right volumes of the ventricular ECM are maintained relatively equivalent.

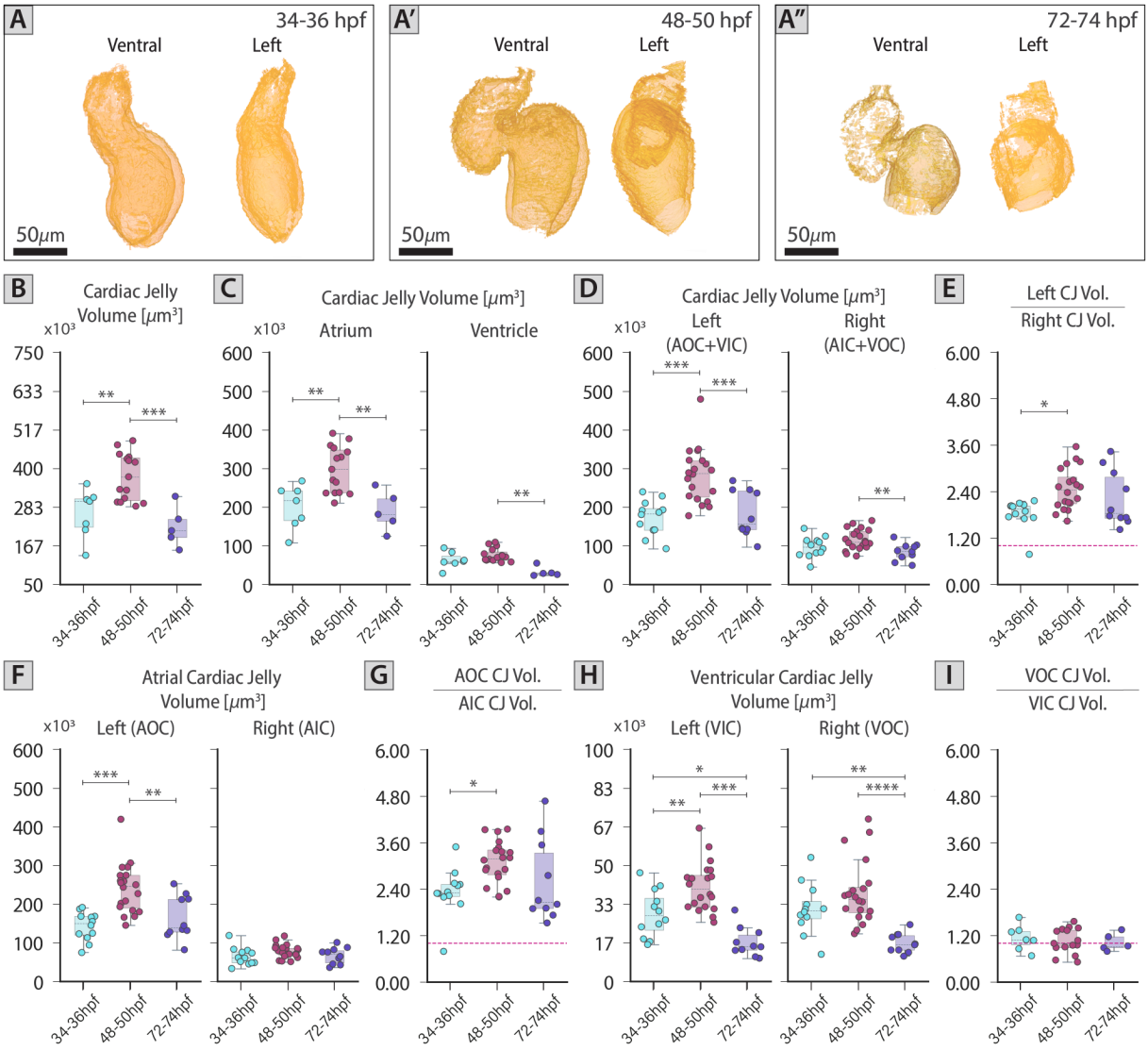

Fig 4.14. The left-sided atrial-specific expansion of the cardiac ECM is established in the early looping heart and maintained as the heart undergoes looping and ballooning morphogenesis.
A-A''. Representative 3D reconstructions of the cardiac jelly (orange meshes) in wild-type hearts at early looping (34-36hpf, A), during looping and ballooning (48-50hpf, A') and at maturing (72-74hpf, A'') stages. **B-C.** Quantification of the cardiac jelly tissue volume of the whole heart (B) and its chambers (C). As the heart

transitions from a tube to a looping and ballooning organ the total cardiac jelly volume increases, driven mainly by an increase in cardiac jelly in the atrium (34-36hpf vs. 48-50hpf: heart *p-value=0.00588*, atrium *p-value=0.00340*). Later, as the heart starts maturing, the amount of cardiac jelly present throughout the heart gets significantly reduced (48-50hpf vs. 72-74hpf: heart *p-value=0.00100*, atrium *p-value=0.00386*, ventricle *p-value=0.00125*). **D.** Quantification of cardiac jelly volume on the left and right sides of the heart throughout these key developmental stages. The trend observed for the total cardiac jelly volume is maintained when measuring the cardiac jelly volume on the left side of the heart (i.e. volume increase between 34-36 and 48-50hpf and decrease between 48-50 and 72-74hpf) (34-36hpf vs. 48-50hpf: left *p-value=0.00100*, 48-50hpf vs. 72-74hpf: left *p-value=0.00100*). The cardiac jelly volume on the right side is maintained as the heart loops and gets reduced as the heart matures (48-50hpf vs. 72-74hpf: right *p-value=0.00749*). **E.** Quantification of the quotient between left and right cardiac jelly volumes in the heart between 34 and 74hpf. A value greater than one (red dotted line) denotes a left-sided expansion of the cardiac jelly. Throughout these stages, the cardiac jelly is asymmetrically expanded on the left side of the heart (34-36hpf vs. 48-50hpf: *p-value=0.01011*). **F,H.** Quantification of cardiac jelly volume on the left and right sides of the atrium (F) and ventricle (H) throughout these key developmental stages. A similar trend to the one observed for total cardiac jelly is observed only for the left- atrial and -ventricular cardiac jelly (i.e. volume increase between 34-36 and 48-50hpf and decrease between 48-50 and 72-74hpf) (34-36hpf vs. 48-50hpf: atrial-left *p-value=0.00100*, ventricular-left *p-value=0.00555*; 48-50hpf vs. 72-74hpf: atrial left *p-value=0.00323*, ventricular left *p-value=0.00100*). The cardiac jelly volume on the atrial-right side is maintained throughout these key developmental stages, while the ventricular-right gets reduced as the heart transitions to an early maturing stage (48-50hpf vs. 72-74hpf: ventricular-right *p-value=0.00003*). **G,I.** Quantification of the quotient between atrial (G) and ventricular (I) left and right cardiac jelly volumes in the heart between 34 and 74hpf. A value greater than one (red dotted line) denotes a left-sided expansion. The left-sided expansion of the ECM is atrium specific and is maintained as the heart loops, balloons and matures (AOC/AIC, 34-36hpf vs. 48-50hpf: *p-value=0.02422*). A-A'': Heart's ventral and left face with anterior to the top. B-I: Error bars with 95% confidence interval of the mean. 34-36hpf: *n=7*, 48-50hpf: *n=15*, 72-74hpf: *n=5*. For details regarding the statistical analyses used to compare this set of data see *Note#4.2* (pg. 99). Only significant comparisons are shown. ****: *p-value*<0.0001, ***: *p-value*<0.001, **: *p-value*<0.01, *: *p-value*<0.05. CJ: Cardiac jelly, Atr: Atrial, Vent: Ventricular, Vol: Volume, AIC: Atrial Inner Curvature, AOC: Atrial Outer Curvature, VIC: Ventricular Inner Curvature, VOC: Ventricular Outer Curvature.

To complement this ECM volume analysis and understand more granularly the distribution of the cardiac jelly around the heart, average 2D tissue thickness heatmaps of the cardiac ECM were acquired and analysed at the same stages as the previous quantitative analysis (Fig 4.15A: 34-36hpf, B: 48-50hpf, and C: 72-74hpf).

Examination of the cardiac jelly thickness during early cardiac morphogenesis reveals the cardiac ECM is regionalised throughout the heart, but this regionalisation manifests differently in each chamber and changes as the heart develops and the chambers remodel. Analysis of 2D cardiac jelly thickness heatmap at 34-36hpf confirms the already described left-sided ECM expansion, revealing thicker ECM regions on the left side of both chambers when compared to the right (Fig 4.15A''). Interestingly, despite this asymmetry, the cardiac jelly volume found in the right side of the atrium is not negligible (*5-7µm*) and is distinguishable from the ventral and dorsal regions of this chamber, where a homogenous but thin ECM layer (*2-3µm*) is present. At these early stages, the ventricle displays thicker ECM regions only closer to the AVC, particularly on its left side.

As the heart tube undergoes looping and the chambers balloon, the thicker ECM regions that were initially on the left and right sides of the atrium and lower-left side of the ventricle (Fig 4.15A'') widen, capturing the whole length of the corresponding chamber's curvatures. Additionally, as the cardiac jelly volume of the atrium expands (Fig 4.14C,D) the thickness of this layer gets enhanced across the left-right axis of this chamber (in Fig 4.15 compare A'' and B''), presenting ECM thickness values of around *15µm* on the atrial outer curvature (or left side). Between these two time-points (34 and 50hpf), the ventricular-left ECM thickening gets also re-positioned to the central region of this chamber's inner curvature while maintaining a homogeneous and thin ECM throughout the rest of the chamber.

Later, as the heart transitions to a maturing stage and the atrium compacts (Fig 4.15C''), the ECM volume that remains in this chamber (Fig 4.14C,F) gets mainly positioned to the dorsal face (*~16µm)* and apex of this chamber (*8-10µm*) (Fig 4.15C''). Simultaneously, the ongoing ventricular ECM volume reduction (Fig 4.14C,H) occurs chamber-wide except on the chamber's inner-curvature where the thickened ECM is maintained and distributed in patches *~3-5µm* thick along the length of this region (Fig 4.15C''). Interestingly the timing of this ECM volume reduction correlates with the appearance of the first trabeculae in the outer curvature of the ventricle by 60hpf (Rasouli and Stainier, 2017). Additionally, the conservation of the inner-curvature ECM between these timepoints (50 and 74hpf) correlates nicely with the literature, where this region has been described as the last one to undergo trabeculation in zebrafish heart (Rasouli and Stainier, 2017), confirming ECM maintenance is important to avoid the early onset of this maturation process in this ventricular region.

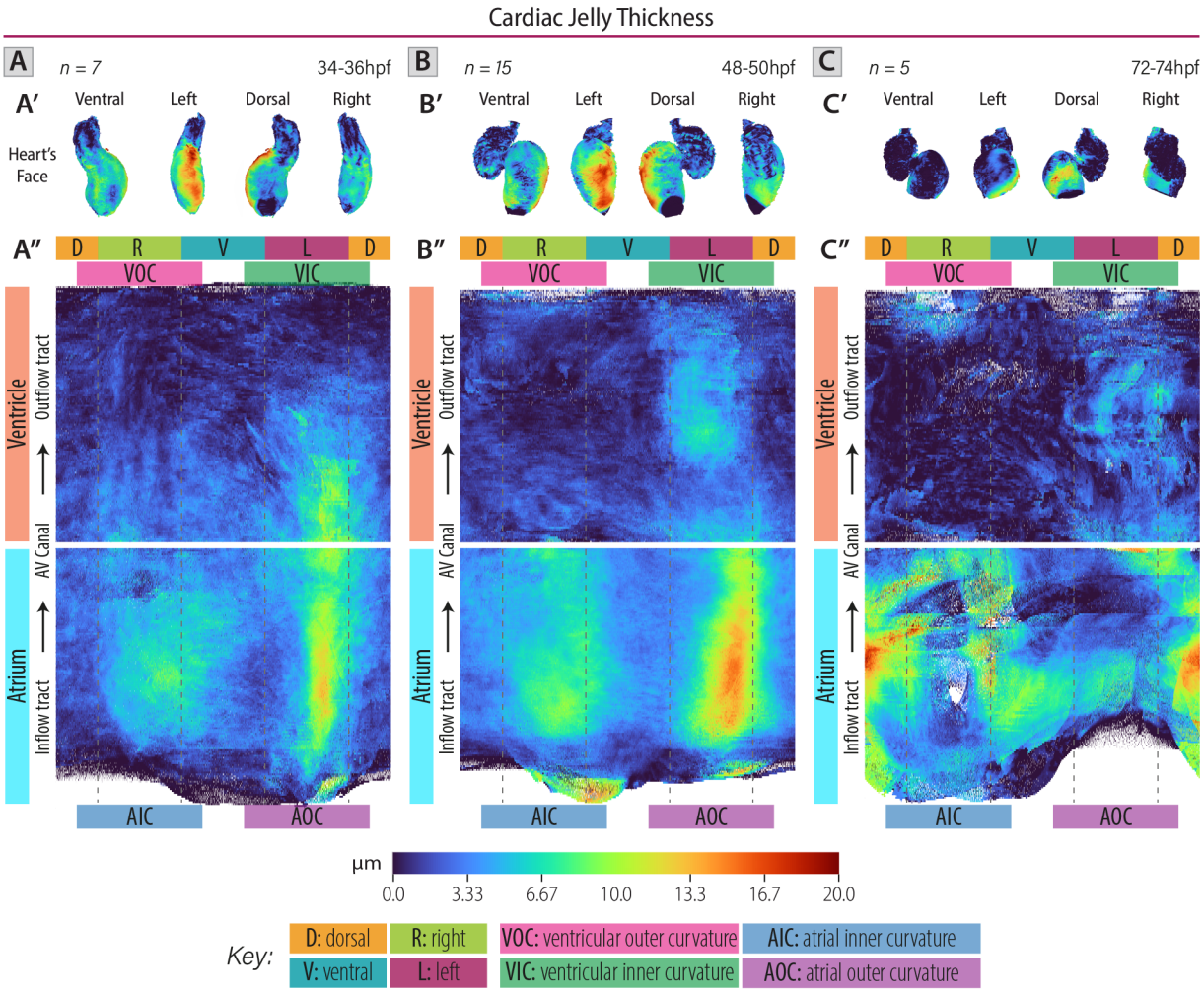

Fig 4.15. The ECM is dynamic and highly regionalised during early cardiac morphogenesis.
A-C. 3D and 2D representations of the cardiac jelly thickness of a wild-type zebrafish heart at early looping (34-36hpf, A), during looping and ballooning (48-50hpf, B), and at maturing stages (72-74hpf, C). **A'-C'.** Ventral, left, dorsal and right heart face (left to right) of the 3D colour-coded cardiac jelly based on its thickness values at key developmental stages. **A''-C''.** Average planar projections of the colour-coded cardiac jelly thickness 2D heatmaps of all the processed wild-type hearts at 34-36hpf (A'', *n=7*), 48-50hpf, (B'', *n=15*) and 72-74hpf (C'', *n=5*). During early cardiac development, the ECM is regionalised throughout the heart, but this regionalisation manifests differently in each chamber and changes as the heart develops. During early looping stages (A''), the atrial regionalisation encompasses a thickening in the inner and outer curvatures, while in the ventricle the ECM is specifically thicker in the inner curvature, closer to the atrioventricular canal (AVC). As the heart undergoes looping and ballooning (A''→B'') while the outer curvature region gets even more regionalised (presenting thicker ECM regions), the atrial inner curvature region with high regionalisation at early stages (A'') expands to the whole right face of the chamber (compare A'' and B''). As the heart starts maturing (B''→C''), ECM thickness

gets reduced throughout the ventricle and highly regionalised ECM is maintained in the apex and central dorsal face of the atrium. A-C: Anterior to the top. A-C' and A''-C'' share colour-scale presented with the key at the bottom of the figure. D: Dorsal, R: Right, V: Ventral, L: Left, VOC: Ventricular Outer Curvature, VIC: Ventricular Inner Curvature, AOC: Atrial Outer Curvature, AIC: Atrial Inner Curvature, AV Canal: Atrioventricular Canal.

Together, analysis of ECM dynamics during early cardiac morphogenesis, reveals that while initial heart looping and chamber growth is associated with an increase in cardiac ECM volume, chamber remodelling and the onset of ventricular trabeculation is coupled with a dramatic reduction in cardiac ECM in both chambers. Total heart and chamber left-right distribution analysis confirms our previously published observations of an atrial-left-sided expansion of the cardiac ECM and demonstrates **for the first time** that this expansion is maintained as the heart undergoes looping, ballooning, and early maturing. Additional to left-right asymmetry, ECM thickness analysis uncovers the high regionalisation of the cardiac jelly between pre- and post-looping stages, revealing it is chamber- and stage-specific, and allowing the linkage of the cardiac ECM dynamics to chamber-distinct remodelling and maturation processes.

3.1 CARDIAC JELLY COMPOSITION IN HEART DEVELOPMENT

While multiple studies have examined the composition of the cardiac jelly in the adult regenerative zebrafish hearts (Chen *et al.*, 2016; DeLaughter *et al.*, 2016; Jam *et al.*, 2018; Notari *et al.*, 2018; Sun *et al.*, 2022), very few studies have described the composition of the embryonic interstitial ECM, including the components that assist its synthesis and degradation. Consequently, whole-mount mRNA *in situ* hybridisation (ISH) screen of interstitial ECM components was carried out between 19 and 72hpf to identify possible proteins that are likely involved in cardiac ECM regionalisation and volume regulation as the heart undergoes early morphogenesis and link this information back to the ECM dynamics previously described.

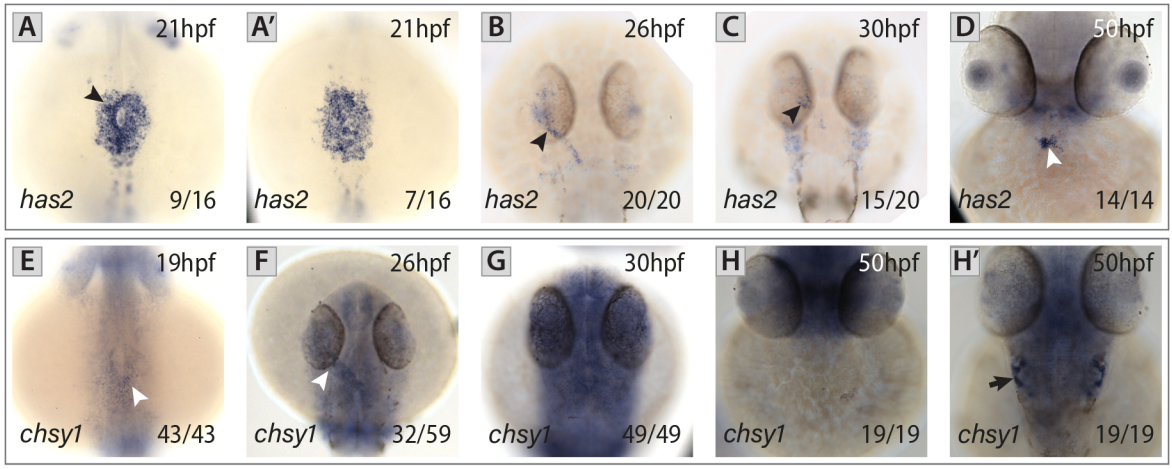

Fig 4.16. The GAG synthases *has2* and *chsy1* are dynamically expressed throughout cardiac morphogenesis. **A-D.** mRNA *in situ* hybridisation analysis of *has2* at 21hpf reveals its expression patterns is either elevated on the left side (arrowhead in A) or homogeneously distributed in the heart disc (A'). At 26hpf, *has2* expression is uniform throughout the linear heart tube endocardium (B) and as developments progresses, gets restricted to the presumptive AVC at 30 and 50hpf (C-D). **E-H'.** mRNA *in situ* hybridisation analysis of *chsy1* at 19 (E), 26 (F), 30 (G), and 50hpf (H-H'). *chsy1* is expressed at low levels in the early heart disc (E) and heart tube (F) but becomes absent in the heart at 30 (G) and 50hpf (H), where it is highly expressed in the developing ear (H'). A-H': Heart-specific expression is indicated by arrowheads, while expression in other embryonic structures is pointed by arrows. The number of embryos matching the image shown is indicated at the bottom right of each image. ISH images shown in B and C were kindly provided by Christopher Derrick. A,A',B,C,E,F,G,H': Dorsal Views with anterior to the top. D,H: Ventral views with anterior to the top.

The interstitial cardiac jelly is composed of two main classes of macromolecules: proteoglycans (PGs) and fibrous proteins (Frantz, Stewart and Weaver, 2010; Mouw, Ou and Weaver, 2014). As previously described, PGs consist of glycosaminoglycan (GAG) chains that are covalently linked to specific core proteins. The highly negative charge of GAG chains allows PGs to sequester water and ions, making them fill the majority of the interstitial space in the form of a hydrated gel, providing shape and structure to this cardiac layer (Nakamura and Manasek, 1981; Frantz, Stewart and Weaver, 2010; Attili and Richter, 2013) (see Chapter 1, Fig 1.3). Being of such importance in the integral structure of the ECM, the expression patterns of molecules involved in the synthesis of GAGs and specific core proteins were the first genes examined by mRNA ISH at early stages of heart development (disc/cone: 19/21hpf, tube: 26/30hpf, looping heart: 48/50hpf, post-looping: 61/72/96hpf).

Previous studies have identified Hyaluronic Acid (HA) and Chondroitin Sulfate (CS) as key cardiac jelly GAGs involved in cardiac development (Camenisch *et al.*, 2000; Peal *et al.*, 2009; Lagendijk *et al.*, 2011; Grassini *et al.*, 2018; Derrick *et al.*, 2021). Confirming previous studies, *has2*, the major cardiac HA synthesising enzyme displays a distinctly elevated left-sided expression in the heart disc at 21hpf in most of the analysed embryos (Fig 4.16A) (Smith *et al.*, 2008; Veerkamp *et al.*, 2013). Expression of *has2* in the heart is maintained and homogeneously distributed in the endocardium as the heart forms a tube (Fig 4.16B) and gets restricted to the AVC during looping and ballooning stages (Fig 4.16C,D) where its requirement for valve development has been shown (Lagendijk *et al.*, 2011). Analysis of *chondroitin sulfate synthase 1* (*chsy1*) expression identifies it is present in low levels in the heart at disc and tube stages (Fig 4.16E,F). No detection of *chsy1* is observed in the heart at stages later than 30hpf suggesting the transcription of this gene is no longer required in the cardiac ECM as the zebrafish heart undergoes looping, ballooning or early maturing (Fig 4.16G,H).

Proteoglycans are categorised according to the nature of their GAG chain and named after their core protein. As expected by the heart-specific expression of *chsy1* at early stages of heart development (Fig 4.16E-F), proteoglycans containing chondroitin sulfate as their GAG (known as chondroitin sulfate proteoglycans or CSPGs) have been identified as important ECM components during cardiac morphogenesis (Peal *et al.*, 2009). In line with this, two putative CS core proteins have been described to be expressed in the developing vertebrate heart: Versican and Aggrecan (Zanin *et al.*, 1999; Walsh and Stainier, 2001; Kang *et al.*, 2004; Rambeau *et al.*, 2017; Mittal *et al.*, 2019). However, as none of these studies have fully characterised the expression dynamics of these two core proteins during early stages of heart development, mRNA ISH expression analysis of the two paralogs genes of *aggrecan* (*acana*, *acanb*) and *versican* (*vcana*, *vcanb*), were performed.

mRNA ISH expression analysis of the two paralog *aggrecan* genes in zebrafish identifies neither of the genes are expressed in the heart prior to maturing stages (Fig 4.17 *acana:* A-E, *acanb:* F-J). At 72hpf both genes become expressed in the pharyngeal arches and ventral aorta with *acana* expression present also in the presumptive bulbus arteriosus (Fig 4.17E) as previously described (Rambeau *et al.*, 2017). Different to *aggrecan,* ISH analysis of *versican* identifies both genes exhibit dynamic, non-overlapping and complementary expression patterns during early heart morphogenesis (Fig 4.17 *vcana:* K-N, *vcanb:* O-Q). Prior to tube formation, both genes are expressed: while *vcana* is uniformly expressed in the myocardium at cardiac disc stage (Fig 4.1KI), *vcanb* is expressed only in a small ring of cells at the centre of the heart disc (Fig 4.17O). At 26hpf, *vcana* is expressed homogeneously throughout the heart tube (Fig 4.17L), whilst *vcanb* expression is restricted to the arterial pole (Fig 4.17P) where cardiomyocytes from the SHF are migrating into the heart (de Pater *et al.*, 2009). As expected, as the heart loops and balloons, *vcana* expression becomes limited to the AVC (Fig 4.17M), while *vcanb* cardiac-specific expression is absent in the heart (Fig 4.17Q). As the heart starts maturing, no expression of either *versican* is specifically observed in the heart suggesting none of them are required for further stages of heart development (Fig 4.17N). The combined observations indicate that the two CS core proteins Versican and Aggrecan are expressed

in unique patterns during zebrafish cardiac morphogenesis and suggest they play different roles in development.

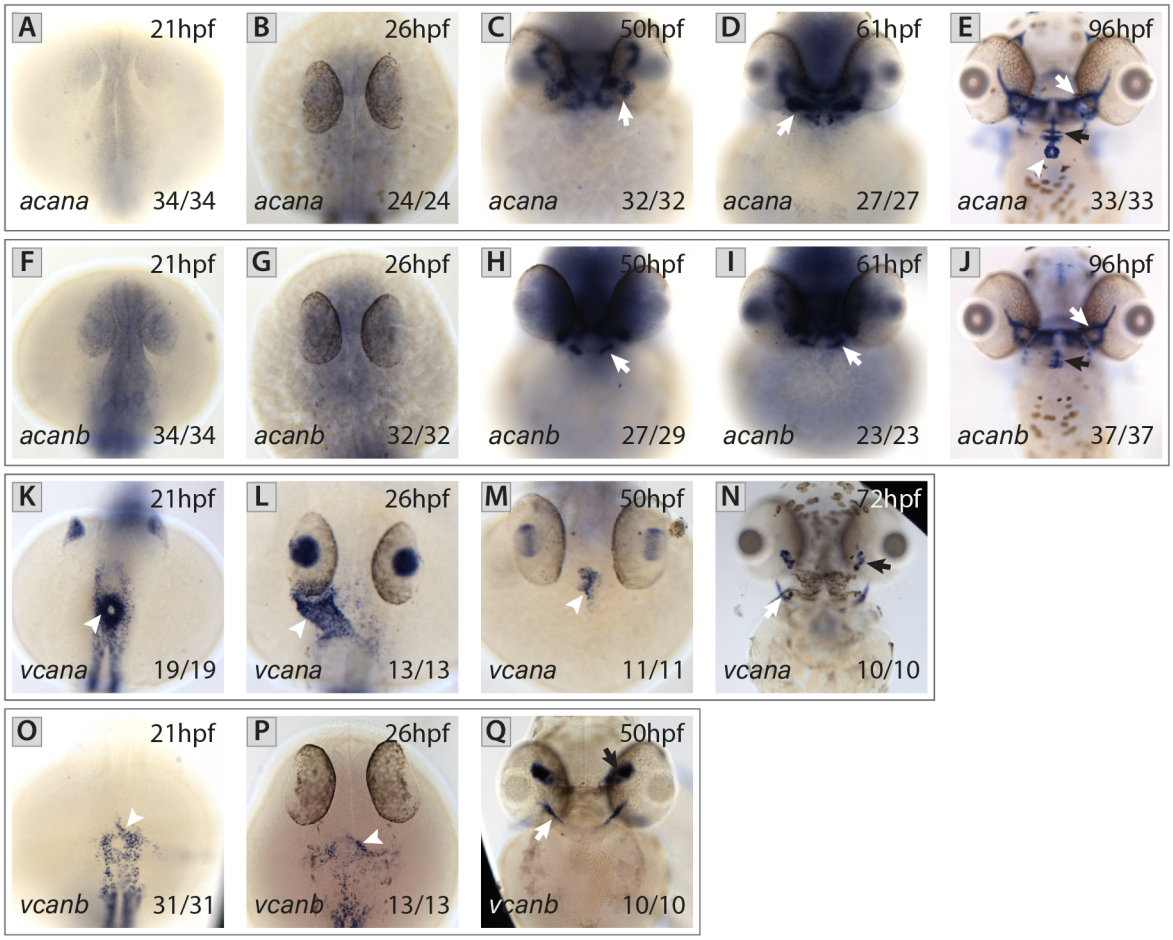

Fig 4.17. mRNA of the core proteins *aggrecan* and *versican* display distinct patterns of expression throughout heart development.
A-E. mRNA *in situ* hybridisation analysis of *acana* at 21 (A), 26 (B), 50 (C), 61hpf (D) and 96hpf (E). *acana* expression is absent from the heart between 21 and 61hpf. At day 4 (96hpf), *acana* becomes expressed in the pharyngeal arches and the ventral aorta (white and black arrow, respectively, E) and in the future bulbus arteriosus (arrowhead, E). **F-J.** mRNA *in situ* hybridisation analysis of *acanb* at 21 (F), 26 (G), 50 (H), 61 (I) and 96hpf (J). Similar to *acana*, *acanb* expression is absent from the heart throughout the analysed stages (21-96hpf, F-J), but is expressed in the pharyngeal arches and ventral aorta between 50 and 96hpf (white and black arrow, respectively, J). **K-N.** *vcana* mRNA *in situ* hybridisation analysis reveals *vcana* is expressed throughout the heart disc (21hpf, I) and heart tube (26hpf, J) while being restricted to the AVC at 50hpf (K). At 72hpf, *vcana* is no longer expressed in the heart, but appears to be present in the cranial cartilage (white arrow) and in the developing ear (black arrow). **O-R.** mRNA *in situ* hybridisation analysis of *vcanb* identifies *vcanb* is expressed only in a small ring of cells at the centre of the heart disc at 21hpf (O), and in the outflow tract of the heart tube at 26hpf (P). As development progresses *vcanb* is no longer expresses in the heart but gets restricted to the developing ear (black arrow) and cranial cartilage (Q). A-Q: Heart-specific expression is indicated by arrowheads, while expression in other embryonic structures is pointed by arrows. The number of embryos matching the image shown is indicated at the bottom right of each image. ISH images shown in E and J were kindly provided by Christopher Derrick. A,B,F,G,K,L,O,P: Dorsal Views with anterior to the top. C,D,E,H,I,J,M,N,Q: Ventral views with anterior to the top.

Within the ECM, when HA gets covalently linked to PG by means of a link protein, they form what is known as a PG aggregate (Faltz *et al.*, 1979; Aspberg, 2012). Having already characterised the expression dynamics of the HA synthase *has2* and the molecules that comprise CS proteoglycans (Fig 4.16 and 4.17), the PG aggregate components that have not yet been characterised are the link proteins. Also known as

hyaluronan and proteoglycan link proteins or Haplns, zebrafish Haplns consists of five members (Spicer, Joo and Bowling, 2003), two of which have been reported to be expressed in the heart at early stages of development (*hapln1a* and *hapln1b*, paralogs of the mammalian gene *Hapln1*) (Kang *et al.*, 2008; Derrick *et al.*, 2021; Sun *et al.*, 2022). Similar to the mRNA ISH expression analysis of *versicana* and *versicanb*, *hapln1a* and *hapln1b* exhibit complementary expression patterns during early heart morphogenesis (Fig 4.18 *hapln1a:* A-C, *hapln1b:* D-F). At 21hpf, both *hapln1a* and *hapln1b* are primarily expressed in the posterior region of the disc (Fig 4.18A and D, respectively). At 26hpf, *hapln1a* gets restricted to the myocardium (Fig 4.18B) while *hapln1b* appears to be expressed mainly by the endocardium and with lower levels of expression in the myocardium (including the SHF cells entering the venous pole) (Fig 4.18E). Interestingly, at this stage both paralogs, irrespective of the tissue by which they are expressed, have an elevated domain of expression on the left side of the heart tube compared to the right. As the heart loops and balloons, expression of *hapln1a* gets restricted to the AVC (Fig 4.18C), whilst the endocardial expression of *hapln1b* is still maintained throughout the whole heart endocardium (Fig 4.18F). As development progresses *hapln1a* is no longer expressed in the heart, while *hapln1b* expression is preserved in the developing endocardium.

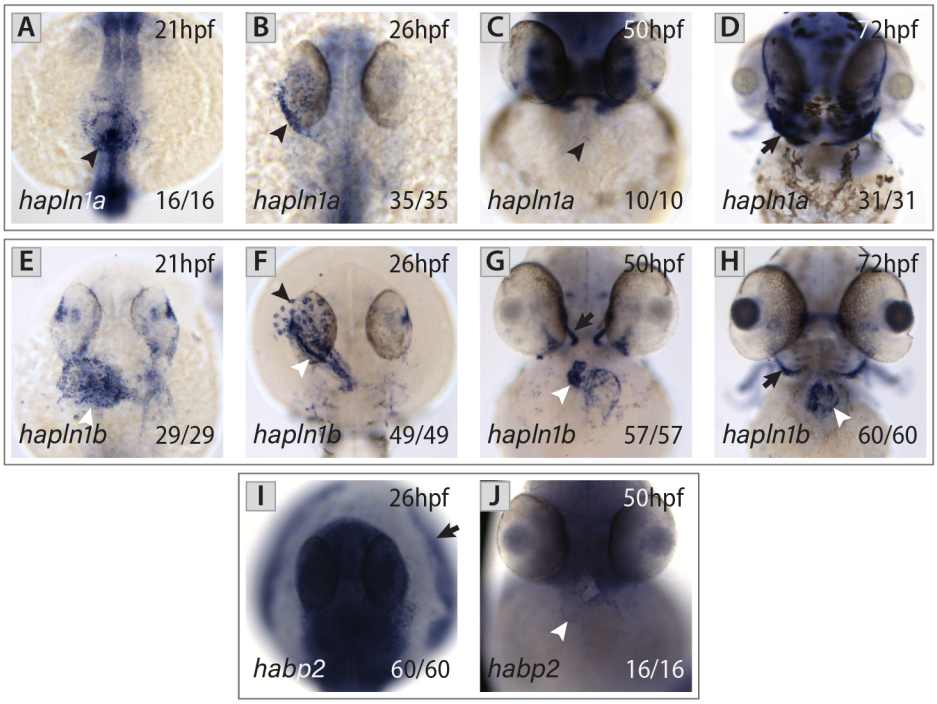

Fig 4.18. *hapln1a* and *hapln1b* link proteins have tissue-specific expressions and are asymmetrically expressed in the zebrafish heart at tube stage.
A-D. mRNA *in situ* hybridisation analysis of *hapln1a* at 21 (A), 26 (B), 50 (C) and 72hpf (D). At 21hpf, *hapln1a* is predominantly expressed in the posterior region of the heart disc (A). At 26hpf, *hapln1a* mRNA is present throughout the heart tube, with elevated levels on the left side of the tube when compared to the right (B). At 50hpf, *hapln1a* expression is restricted to the AVC region of the heart (C), and as development progresses, it becomes absent from the heart and restricted to the pharyngeal arches (black arrow, D). **E-H.** mRNA *in situ* hybridisation analysis of *hapln1b* at 21 (E), 26 (F), 50 (G) and 72hpf (H). Prior to the formation of the heart tube, *hapln1b* is expressed throughout the heart field, with higher expression in its posterior region (E). At tube stage *hapln1b* is expressed throughout the endocardium and in the inflow tract of the heart, with elevated levels on the left side of the tube when compared to the right (F). As the heart loops and balloons and transitions to an early maturation state *hapln1b* expression is maintained in the endocardium in both heart chambers (G-H). **I.** mRNA *in situ* hybridisation analysis of *habp2* at 26hpf reveals it is not expressed in the early heart tube. **J.** At 50hpf *habp2* is expressed in the inner and outer curvatures of the ventricle and outer curvature of the developing atrium. A-J: Heart-specific expression is indicated by arrowheads, while expression in other embryonic structures is pointed by arrows. The number of embryos matching the image shown is indicated at

the bottom right of each image. A,B,E,F,I: Dorsal Views with anterior to the top. C,D,G,H,J: Ventral views with anterior to the top.

_____

In addition to the Haplns, hyaluronan binding proteins have been described to be part of the interstitial ECM. mRNA ISH of *hyaluronan binding protein 2* (*habp2)* identifies the expression of this protein in the inner and outer curvatures of the developing ventricle and outer curvature of the atrium at 50hpf (Fig 4.18J). Interestingly, this expression coincides with the onset of cardiac ECM volume reduction in the heart (50→72hpf) suggesting Habp2 synthesis within these chamber regions is required to modify HA and support ongoing morphogenesis of this organ.

Together, the expression patterns of molecules that comprise proteoglycan aggregates in the interstitial ECM have shown to be highly dynamic throughout these early stages of heart morphogenesis. The cardiac-specific expression of ECM components such as *has2*, *chsy1*, *vcana*, *vcanb*, *hapln1a*, and *hapln1b* at stages as early as 21hpf suggests interstitial ECM synthesis is required prior to tube formation. Interestingly, the expression of most of these genes is maintained heart-specific as the cardiac tube forms. Asymmetric expression of *hapln1a* and *hapln1b* between 21 and 26hpf, suggests that early posterior expression of these genes in the disc becomes repositioned to the left side of the heart tube (Smith *et al.*, 2008; Guerra *et al.*, 2018) where it may interact with Versican a and HA creating an expanded cardiac ECM, and supporting our previous studies where an asymmetric expansion of the cardiac ECM at tube stage was described (Derrick *et al.*, 2021). The restriction of genes such as *has2*, *vcana* and *hapln1a* around the AVC during looping and ballooning suggest that at this stage the synthesis of these components is required for valve formation and no longer for the ongoing process of looping and ballooning. This confirms that the AVC has a conserved mechanism by which different mechanical and transcriptional cues converge to create a unique ECM environment that supports precise valvulogenesis (Steed, Boselli and Vermot, 2016).

While all the previously described expression analyses provide information about the interstitial composition of the cardiac ECM during early cardiac morphogenesis, multiple studies have shown that it is a tight coordination of the deposition, cleavage and degradation of these ECM components what is critical during development (Feinberg and Weiss, 2009; Lu *et al.*, 2011; Humphrey, Dufresne and Schwartz, 2014; Kim *et al.*, 2018; Sivakumar *et al.*, 2018). In line with this, and considering that the proteoglycan aggregates structure requires HA, the expression patterns of molecules likely to be involved in the degradation of HA, and other GAGs were next examined at 26 and 50hpf using ISH (Fig 4.19).

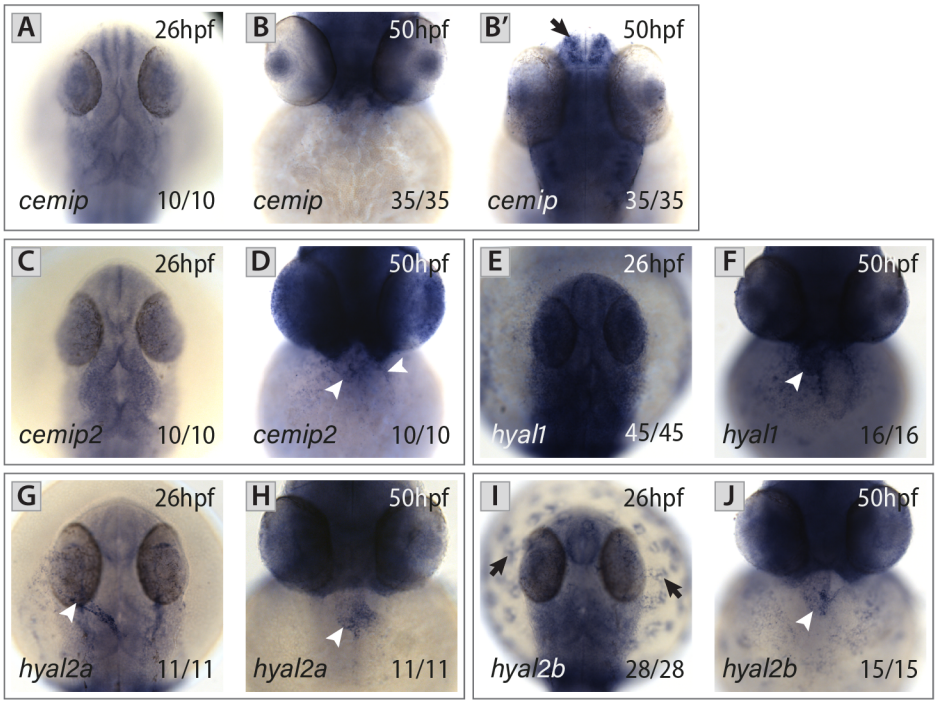

Fig 4.19. *cemip2*, *hyal1*, *hyal2a* and *hyal2b* are expressed in the looping and ballooning heart at 50hpf.
A-B'. mRNA *in situ* hybridisation analysis of *cemip* at 26 (A) and 50hpf (B-B') reveals *cemip* is not expressed in the heart at early stages of cardiac development but is expressed in the developing eyes and nose (arrow in B') at 50hpf. **C-D.** mRNA *in situ* hybridisation analysis of *cemip2* at 26hpf identifies *cemip2* is absent at the early heart tube (C). At 50hpf *cemip2* is expressed in the outer curvatures of the atrium and ventricle of the developing heart (D). **E-F.** mRNA *in situ* hybridisation analysis of *hyal1* at 26hpf reveals *hyal1a* expression is absent in the early heart tube (E). At 50hpf *hyal1* becomes expressed throughout the ventricle and inner and outer curvatures of the developing atrium (F). **G-H.** mRNA *in situ* hybridisation analysis identifies that *hyal2a* is specifically expressed by the endocardium in the heart tube at 26hpf (G) and in the AVC at 50hpf (H). **I-J.** mRNA *in situ* hybridisation analysis of *hyal2b* at 26 and 50hpf, reveals this hyaluronidase is not expressed in the heart tube at 26hpf (I) but is expressed in the ventricular curvatures and AVC at 50hpf (J). At both stages *hyal2b* is distinctively expressed in the yolk syncytial cells (black arrow in I). A-J: Heart-specific expression is indicated by arrowheads, while expression in other embryonic structures is pointed by arrows. The number of embryos matching the image shown is indicated at the bottom right of each image. A,B',C,E,G,I: Dorsal Views with anterior to the top. B,D,F,H,J: Ventral views with anterior to the top.

---

mRNA ISH expression analysis of multiple hyaluronidases identified heart-specific expression of *hyal2a* at tube stage (Fig 4.19G) and of *cemip2, hyal1, hyal2a* and *hyal2b* at looping and ballooning stages (Fig 4.19D,F,H, and J, respectively). The expression of this group of hyaluronidases at 50hpf supports the reduction in cardiac ECM volume identified in both chambers between 50 and 72hpf (Fig 4.14B-D) and suggests remodelling of the ECM via the regional degradation of HA might be important and required in succeeding processes involved in cardiac maturation. Additionally, the early expression of *hyal2a* when the zebrafish heart is a tube may indicate that in order to enable precise morphogenesis of the organ, synthesis and degradation of the cardiac ECM needs to be tightly controlled by different players throughout development.

Together, expression analysis of interstitial ECM components demonstrates dynamic spatial and temporal changes in the composition of the cardiac jelly in the different tissues and structures of the heart as the organ develops, remodels, and matures. Early expression of GAG synthases, core proteins, and link proteins at disc and tube stages suggests the synthesis of heart-specific ECM may be required early in development to set up an ideal and asymmetric ECM environment that supports subsequent processes of looping and ballooning morphogenesis. The specific expression of particular hyaluronidases by specific

tissues in the chambers at 50hpf supports the hypothesis that the cardiac ECM undergoes regional degradation as the heart loops, balloons and transitions to an early maturing state. All in all, demonstrating the requirement of a tight spatiotemporal control of the composition of the cardiac ECM to ensure the correct morphogenesis of this organ.

4 TIGHT CONTROL OF THE CELLULAR AND A-CELLULAR HEART LAYERS IS REQUIRED FOR PROMOTING HEART MORPHOGENESIS

Tight regulation of the heart layers' volume and distribution have been shown to be important in promoting distinct aspects of cardiac morphogenesis such as looping (Lagendijk *et al.*, 2011; Dietrich *et al.*, 2014; Grassini *et al.*, 2018; Mittal *et al.*, 2019), ballooning and chamber remodelling (Wirrig *et al.*, 2007; Chowdhury *et al.*, 2017; Crucean *et al.*, 2017; Dewan *et al.*, 2017; Kim *et al.*, 2018; Miao *et al.*, 2020; Rahman *et al.*, 2021). To further investigate the composition dynamics of the heart over the course of early cardiac morphogenesis, percentage composition of each heart and chamber component was calculated (Fig 4.20 and 4.21, respectively). Percentage composition of each heart component (e.g. myocardium, endocardium, cardiac jelly, and lumen) was calculated per embryo and defined as the ratio of the volume of that component to the total heart volume. Panel A in Fig 4.20 shows the different heart components or meshes -myocardium in teal (i), endocardium in magenta (ii), cardiac jelly in orange (iii) and lumen in red (iv)- making up the total heart volume or filled external myocardium shown in yellow (v). This same method was followed to define percentage composition per chamber (Fig 4.21, atrium: A-B, ventricle: C-D).

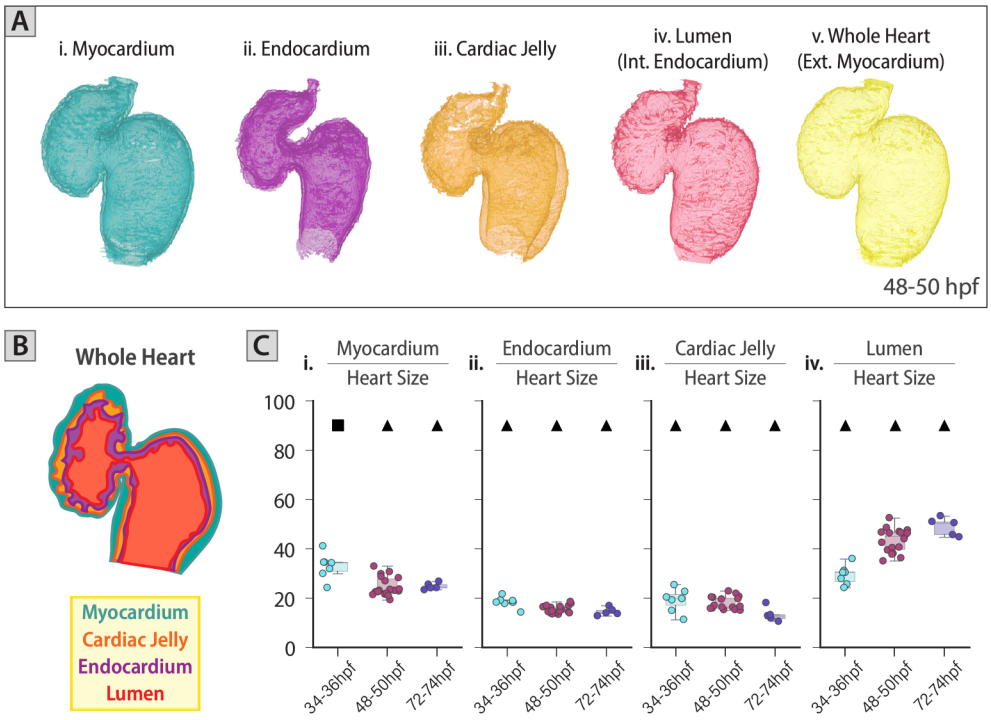

Fig 4.20. Percentage composition analysis of the whole heart suggest tissue and lumen growth is tightly controlled to support the ongoing processes of heart morphogenesis.
A. 3D reconstructions of the whole heart (v) and each of its components: i. myocardium ii. endocardium, iii. cardiac jelly, and iv. lumen. **B.** 2D schematic illustrating how the different heart layers presented in A (from i to iv) are contained within the heart. **C.** Percentage composition of the myocardium (i), endocardium (ii), cardiac jelly (iii), and lumen (iv) over the course of cardiac morphogenesis. A-B: Heart ventral face with anterior to the top. C: Error bars with 95% confidence interval of the mean. 34-36hpf: *n=7*, 48-50hpf: *n=15*, 72-74hpf: *n=5*. Symbols on top of each bar group indicate the standard deviation range of each group. ■ <10% ▲ <5%.

Percentage composition analysis of the heart (Fig 4.20) and chambers (Fig 4.21) revealed data from independent embryos per stage cluster around the same value (standard deviation <10% for all data groups), suggesting the process of tissue and lumen expansion and compaction is somehow tightly controlled to support the ongoing processes of morphogenesis. To further interpret this percentage composition data and put into context its biological significance, stacked bar plots per stage were created for the whole heart and its chambers (Fig 4.22).

As described, the zebrafish heart grows during looping and ballooning morphogenesis and appears to shrink as chamber remodelling and heart maturation progresses (Fig 4.1C). Analysis of the stacked bar plots presented in Fig 4.22 in which the different heart layers have been normalised to the total heart (or chamber) size, allows to evaluate if the changes in volume previously described for each of its comprising layers are proportional to the total growth or compaction experienced by the heart (or its chambers), hence gaining a deeper understanding of the morphogenesis of this organ.

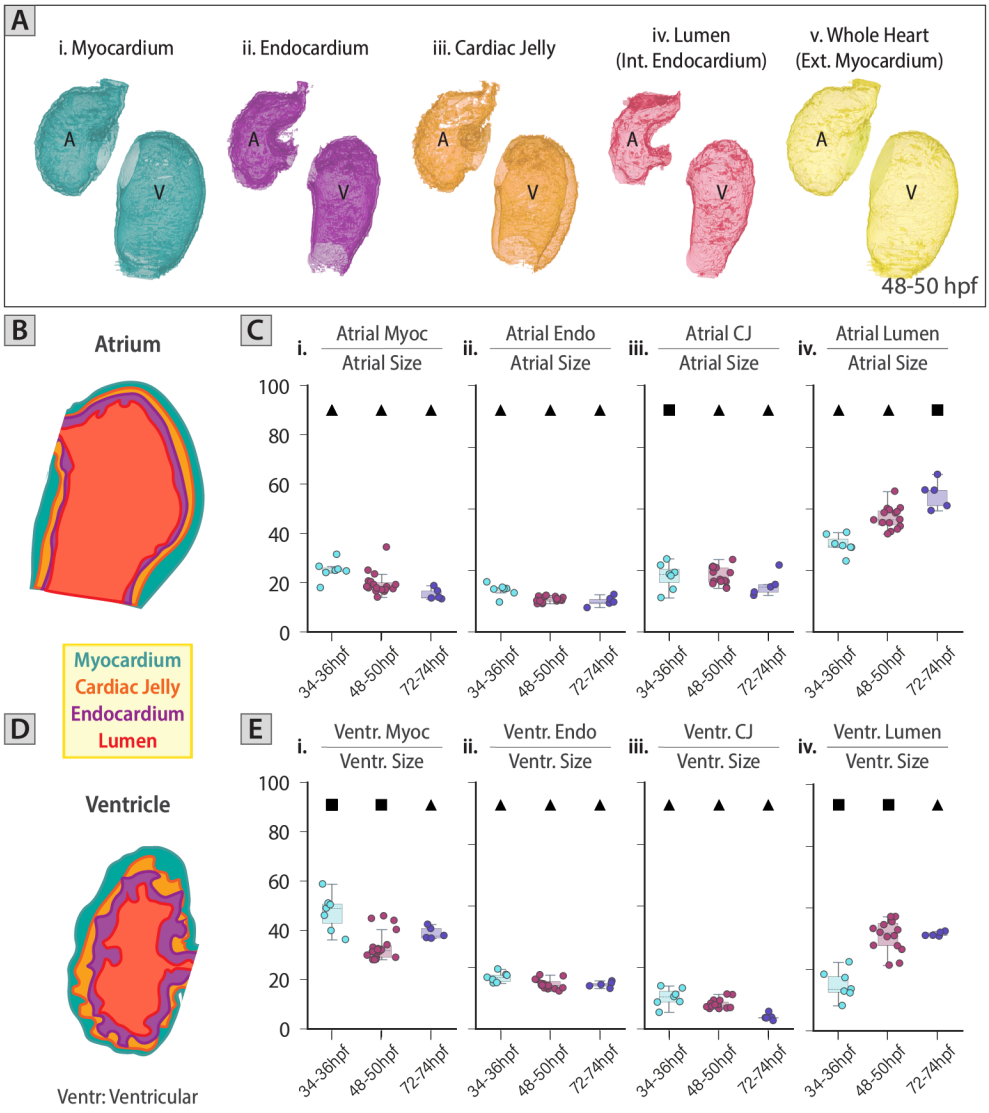

Fig 4.21. Tight control of chamber composition appears to be essential to maintain homeostasis over the course of heart morphogenesis.

A. 3D reconstructions of the whole atrium and ventricle (v) and each of its components: i. atrial and ventricular myocardium ii. atrial and ventricular endocardium, iii. atrial and ventricular cardiac jelly, and iv. atrial and ventricular lumen. **B,D.** 2D schematic of the atrium (B) and ventricle (D) illustrating the different heart layers making up each chamber. **C,E.** Percentage composition of the atrial (C) and ventricular (E) myocardium (i), endocardium (ii), cardiac jelly (iii), and lumen (iv) over the course of cardiac morphogenesis. A,B,D: Chamber's ventral face with anterior to the top. C, E: Error bars with 95% confidence interval of the mean. 34-36hpf: *n=7*,

48-50hpf: *n=15*, 72-74hpf: *n=5*. Symbols on top of each bar group indicate the standard deviation range of each group. ■ <10% ▲ <5%. A: atrium, V: ventricle.

Irrespective of heart size, throughout the key developmental stages here presented, the lumen of the whole heart and chambers grow, becoming the 'most predominant component' of the heart, atrium, and ventricle for this analysis. This phenomenon was expected: as the embryo grows and develops, its body size and oxygen requirements increase; and therefore, it is within this first week of development where the blood-filling capacity of the heart needs to increase to sustain its life (Pelster and Bagatto, 2010). To increase the percentage composition of the lumen of the heart, at least one of the other three comprising heart layers need to be reduced. This is exactly what happens to both the myocardial and endocardial percentage composition in the atrium between 34 and 74hpf (Fig 4.22B) and to the heart and ventricle between 34 and 50hpf (Fig 4.22A,C). Surprisingly, even though the myocardial volume is maintained throughout the heart between 48 and 74hpf (Fig 4.8B-C), the percentage composition reduction of the ventricular cardiac jelly results in an increased myocardial percentage composition within this chamber. Interestingly, the percentage composition of the cardiac jelly on the heart and atrium is practically maintained between 34 and 50hpf, suggesting that the cardiac jelly that is newly deposited as the heart loops and balloons (Fig 4.14C) is proportional to the growth undergone by the chamber between these two stages (Fig 4D). Moreover, and different to the atrium, the percentage composition of the ventricular cardiac jelly between the analysed timepoints is progressively reduced. This can be explained by the initial maintenance and later reduction of cardiac jelly volume (Fig 4.14C) in a growing and then unchanged-size chamber (Fig 4.1D).

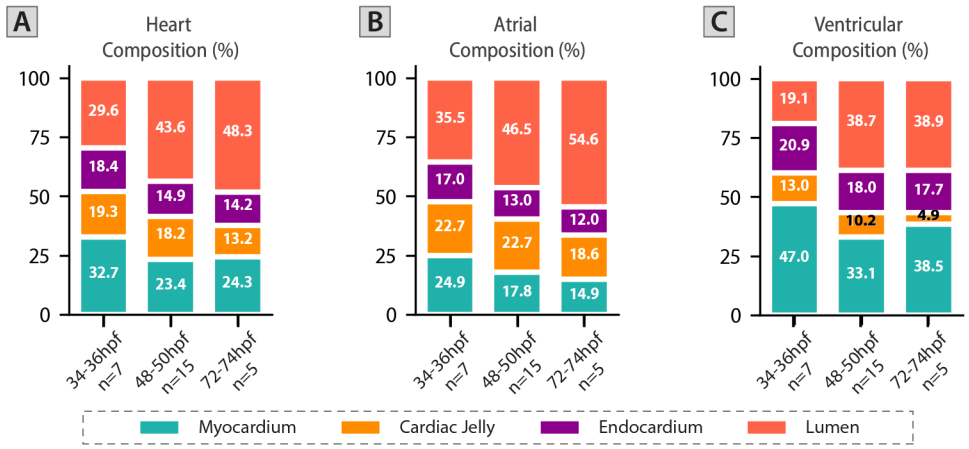

Fig 4.22. Atrial and ventricular composition are different and dynamic over the course of heart morphogenesis. A-C. Percentage composition of the whole heart (A), atrium (B) and ventricle (C) over the course of cardiac looping, ballooning and early stages of maturing, using staked bars graphs per stage. The stacked graph bars were created using the averages of the percentage composition of each analysed heart at each stage. 34-36hpf: *n=7*, 48-50hpf: *n=15*, 72-74hpf: *n=5*.

Together, the percentage composition analysis presented (Fig 4.20 and 4.21) suggests that some mode(s) of intra-organ communication between each layer, (including that which represents the space occupied by the blood), serves to coordinate the orchestrated growth of the different layers of the heart during the early stages of cardiac morphogenesis. This coordinated process of growth, which has been suggested to be activated and driven by biochemical and/or mechanical signals (Staudt and Stainier, 2012; Dietrich *et al.*, 2014; Bornhorst *et al.*, 2019), allows the heart to undergo morphological rearrangements and adaptations in size and volume while maintaining its homeostasis as it is undergoing morphogenesis.

5 Defective Left-Right Patterning

Studies of cardiac looping in mice, chicks and zebrafish have all shown that even in the absence of extrinsic laterality cues, for instance, when there is a disruption of the genetic pathways required for the establishment of left-right (L/R) laterality, the heart still undergoes looping morphogenesis, often in the correct direction (Brennan, Norris and Robertson, 2002; Noël *et al.*, 2013; Desgrange, Garrec, *et al.*, 2019). All these studies have led to the hypothesis that intrinsic information within the tissues of the developing heart must promote heart tube morphogenesis and provide directional cues. Nevertheless, the nature of this information and how it orchestrates robust dextral looping morphogenesis remains a topic of active study.

We have identified a left-sided atrial-specific expansion of the cardiac ECM that is established when the heart is a tube (26hpf) (Derrick *et al.*, 2021) (Appendix 1) and is maintained as the heart undergoes looping, ballooning, and early maturing (Fig 4.14 and 4.15). Knowing that looping morphogenesis is a highly asymmetric process, it is tempting to hypothesise that the left-right contrasting patterns of ECM thickening within the primitive and developing heart could promote distinct changes in ECM physical properties, tissue structure and signalling, which in turn could potentially provide directional cues and drive asymmetric and robust dextral looping morphogenesis. To test whether cardiac ECM asymmetry is linked to the direction of looping morphogenesis, zebrafish hearts in which *spaw* (zebrafish homolog of Nodal, responsible for L/R patterning) is disrupted (Long, Ahmad and Rebagliati, 2003; Noël *et al.*, 2013) were investigated.

5.1 Implications on General Heart Morphogenesis

spaw mutants lack asymmetric Nodal expression prior to asymmetric organ morphogenesis, resulting in midline positioning of the heart tube, which resolves in both normally and abnormally lateralised heart loops (Baker, Holtzman and Burdine, 2008). These abnormally lateralised loops include what has been described in the literature as mirror-imaged sinistrally looped hearts, and hearts that have failed to loop, where both cardiac chambers remain positioned along the midline (also called 'non-loopers' or 'midline loopers') (Chen *et al.*, 1997). The fact that *spaw* mutant hearts still undergo looping morphogenesis, makes them a good model to understand if defects in L/R patterning and looping directionality result in abnormal ECM-regionalisation and hence disrupted morphogenesis. To test this hypothesis, an incross of *Tg(myl7:lifeActGFP); Tg(fli1a:AC-TagRFP)* double transgenic *spaw* heterozygous carriers were imaged live on the light-sheet microscope at early looping (34-36hpf), looping and ballooning (48-50hpf) and early maturing stages (72-74hpf) (Fig 4.23).

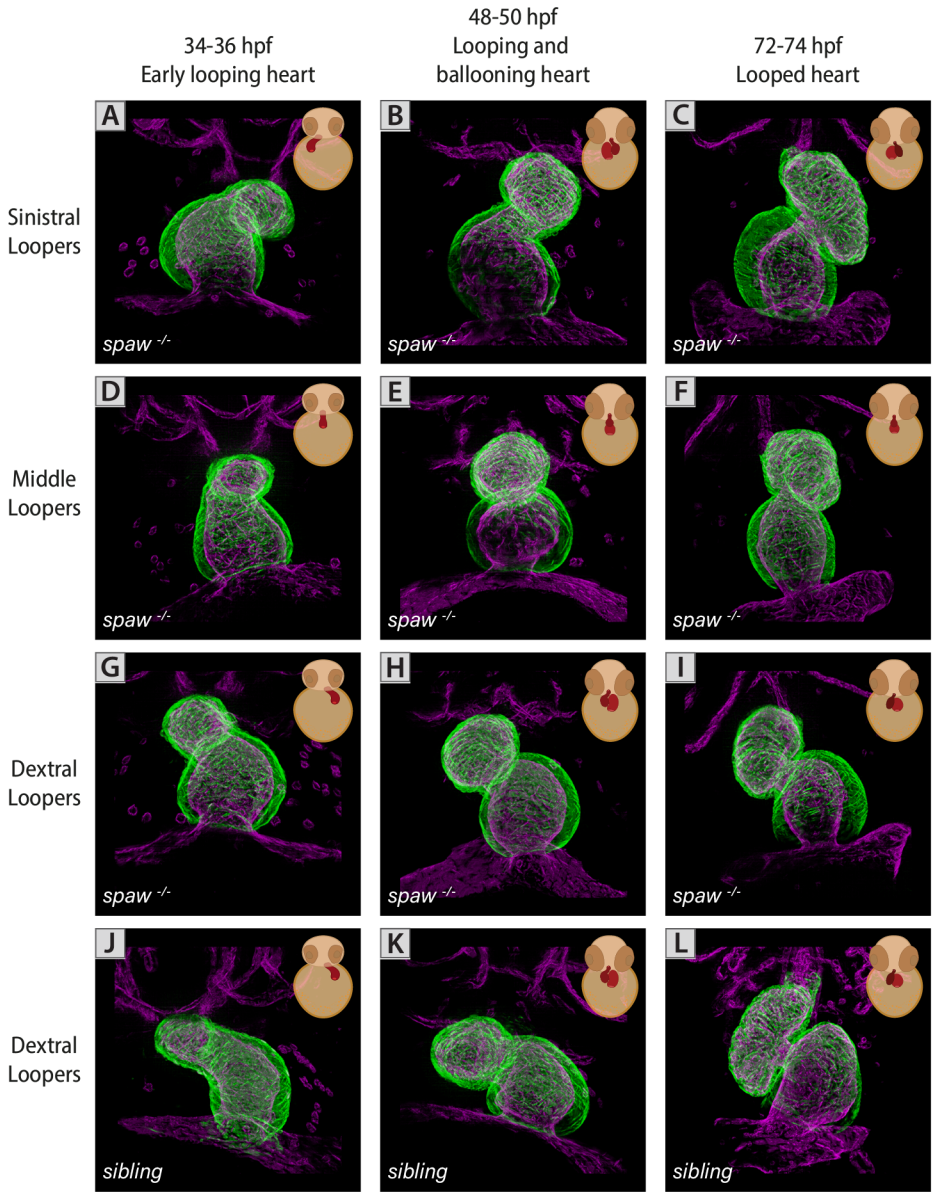

Fig 4.23. Light-sheet imaging of *spaw* mutants throughout early stages of heart development in which left-right asymmetry is disrupted.
A-L. MIPs of processed light-sheet z-stacks of an incross of live *Tg(myl7:lifeActGFP); Tg(fli1a:AC-TagRFP)* transgenic *spaw* heterozygous carriers at 34-36hpf (A,D,G,J), 48-50hpf (B,E,H,K) and 72-74hpf (C,F,I,L). *spaw* homozygous mutants (A-I) are classified according to their direction of looping as: sinistral (A-C), middle (D-F) and dextral (G-I) loopers. A-L: Ventral views with anterior to the top.

While descriptions of morphology in zebrafish with Nodal mutations have remained relatively simplistic (i.e. 2D description of looping directionality) (Noël *et al.*, 2013; Grimes *et al.*, 2020), analyses of mouse models of laterality have revealed more complex heart morphologies in the absence of Nodal (Desgrange, Lokmer, *et al.*, 2019; Desgrange *et al.*, 2020). To describe the morphological impact disrupted L/R patterning has in the zebrafish heart and understand the altered morphogenetic dynamics characteristic of hearts with different looping directionalities, at each of the developmental stages of interest, a set of *spaw* homozygous mutant (also referred to as *spaw*$^{-/-}$) hearts that had looped in each direction (i.e. sinistral, middle, and dextral loopers) were selected, and their cardiac morphology and ECM distribution was analysed using *morphoHeart*.

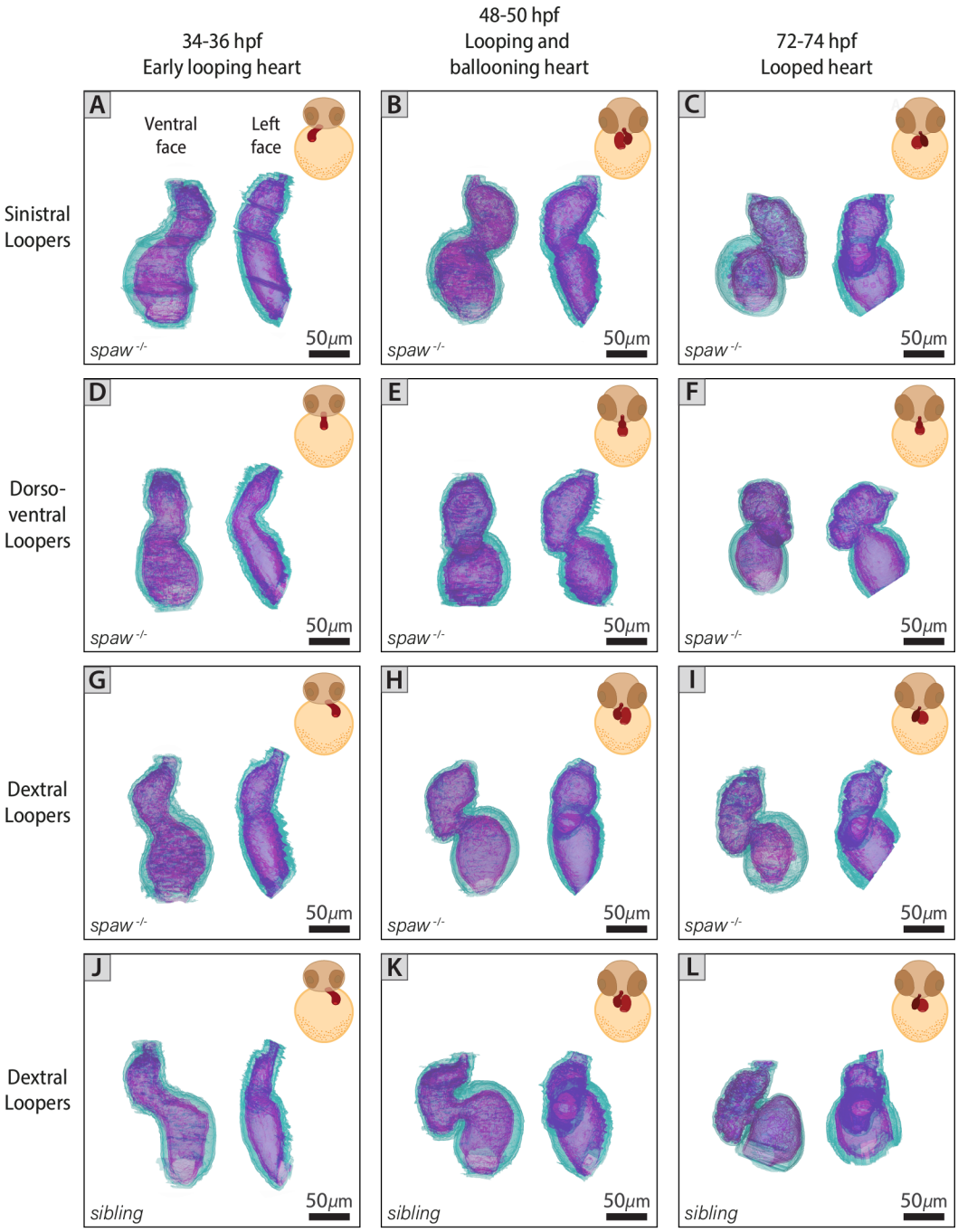

Fig 4.24. 3D reconstructions of *spaw* mutant hearts identifies that previously described 'non-loopers' exhibit dorso-ventral looping behaviour.

A-L. 3D reconstructions of the myocardium (teal) and endocardium (magenta) of *spaw*$^{-/-}$ (A-I) and sibling (J-L) hearts at key developmental stages (34-36hpf: A,D,G,J; 48-50hpf: B,E,H,K; and 72-74hpf: C,F,I,L). *spaw* homozygous mutants (A-I) are classified according to their direction of looping as: sinistral (A-C), middle (D-F) and dextral (G-I) loopers. A-L: As described by the labels in Panels A and B, all panels show the ventral face (on the left) and left face (on the right) of each of the hearts shown in Fig 4.23 with anterior to the top.

3D visual analysis of heart morphology of *spaw*$^{-/-}$ dextral loopers using *morphoHeart* (Fig 4.24G-I) identifies the heart morphology of these mutants to be the closest to the control phenotype (Fig 4.24J-L). Despite the progression of looping morphogenesis is in the correct direction, *spaw*$^{-/-}$ dextral loopers display abnormal rearrangement of the chambers as the heart loops, balloons and matures (48-74hpf, Fig 4.24H-I), characterised by what appears to be a failure to compact around the AVC and between the two poles. Interestingly, the heart morphology of *spaw*$^{-/-}$ sinistral loopers appears to be a mirror image of *spaw*$^{-/-}$

dextral loopers morphology (compare in Fig 4.24 A-C with G-I), in which despite looping morphogenesis proceeding in the *correct* left-right axis, the ventricle of this heart's is positioned to the left side of the atrium. Gross morphological inspection suggests that these hearts, similar to *spaw*$^{-/-}$ dextral loopers, have a defect in chamber rearrangement and compaction. 3D analysis of heart morphology of *spaw*$^{-/-}$ 'middle' loopers at tube stages (Fig 4.24D) shows these hearts do not display a distinguishable lateralised looping direction at these early stages. Additionally, contrary to published literature (Chen *et al.*, 1997), analysis of these 'middle' loopers between 48 and 74hpf identifies that these mutant hearts do undergo looping morphogenesis, but in the dorso-ventral axis, positioning the ventricle ventral to the atrium (see *left face* of the hearts presented in Fig 4.24E-F).

[*Note#4.6:* Having identified this morphologic characteristic, 'middle' loopers will be henceforth referenced as 'dorso-ventral' loopers].

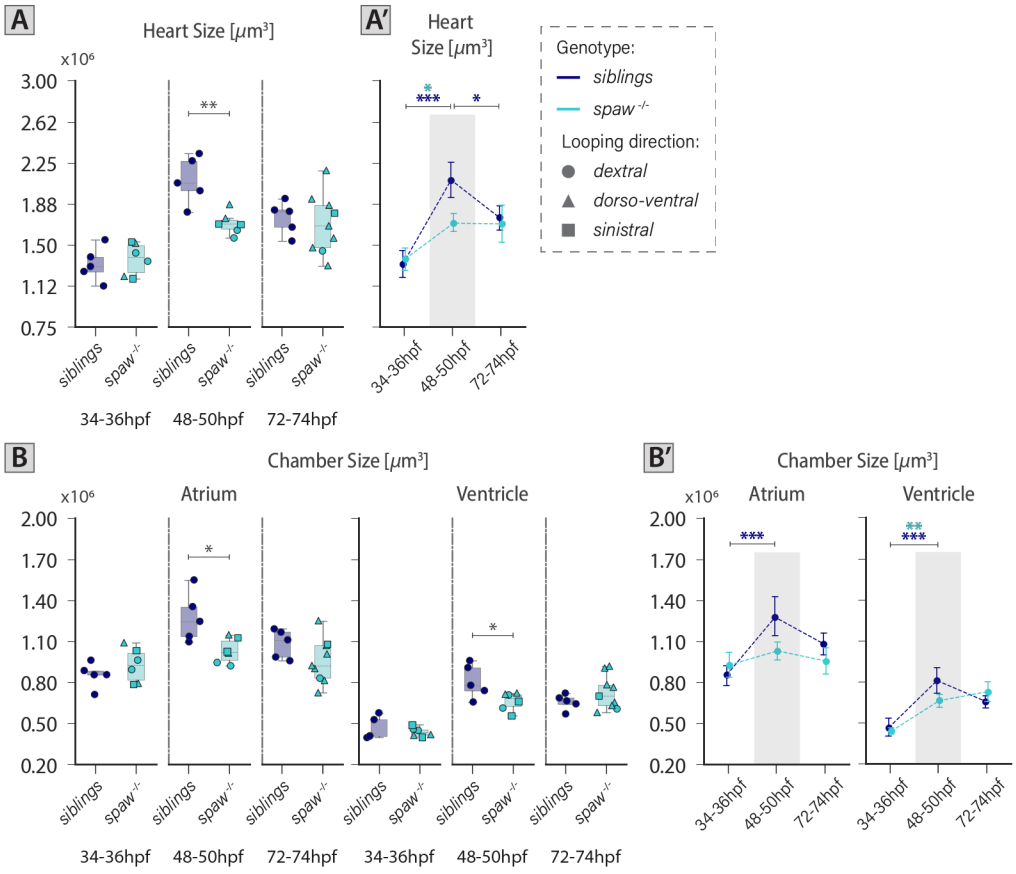

Fig 4.25. *spaw* mutant hearts fail to grow during looping and ballooning morphogenesis.
A-B'. Quantification of heart (A-A') and chambers (B-B') size using *morphoHeart* in *spaw* mutants and siblings at 34-36hpf, 48-50hpf and 72-74hpf. At 48-50hpf, the heart, atrial and ventricular sizes are significantly reduced in *spaw* mutants when compared to their siblings (heart: *p-value=0.00315*, atrium: *p-value=0.01737*, ventricle: *p-value=0.03348*). A' and B' are point-plots of the data presented in A and B, respectively (see *Note#4.9* below). A-B': Error bars with 95% confidence interval of the mean. 34-36hpf: *siblings n=5*, *spaw*$^{-/-}$ *n=6* (*sinistral n=2*, *dorso-ventral n=2*, *dextral n=2*); 48-50hpf: *siblings n=5*, *spaw*$^{-/-}$ *n=6* (*sinistral n=2*, *dorso-ventral n=2*, *dextral n=2*); 72-74hpf: *siblings n=5*, *spaw*$^{-/-}$ *n=9* (*sinistral n=1*, *dorso-ventral n=7*, *dextral n=1*). For details regarding the statistical analyses used to compare this set of data see *Note#4.7* (pg. 131). Only significant comparisons are shown. **: *p-value*<0.01, *: *p-value*<0.05.

[*Note#4.7:* All sample groups per stage and genotype (*spaw*$^{-/-}$ and *siblings*) were analysed for normality using Shapiro-Wilk Normality test. For each variable, if all groups were normally distributed, comparison between genotypes per stage were carried out using Un-paired t-test. When normal distribution could not be assumed, Mann-Whitney test was used. For all tests a statistical significance α of *0.05* was defined].

[*Note#4.8:* To identify if morphometric parameters of *spaw*$^{-/-}$ sinistral, dorso-ventral, and dextral loopers behave differently throughout development, throughout the rest of this thesis, box plots like the ones shown in Fig 4.25A will show different marker symbols to represent the datapoints coming from hearts that have looped in each direction].

[*Note#4.9:* To focus the comparisons between different genotypes through time, point-plots such as the ones shown in Fig 4.25A' will be included throughout the remaining chapters of this thesis. In these point-plots , for each genotype (identified by colour), dotted lines join the points representing the data's mean value per stage. Using this extra representation of the data allows the analysis of the changes experienced by each variable through time, facilitating the comparison of the temporal dynamics of each variable between genotypes. Additionally, to complement this new plot representation, stages where statistically significant differences were found between genotypes will be highlighted with a grey box (see for instance grey box in Fig 4.25A'), while statistically significant differences between stages (per genotype) will be shown with brackets and corresponding coloured stars].

Having segmented the 3D representations of *spaw*$^{-/-}$ hearts and their siblings, the gross size changes undergone by the early developing heart were characterised. Comparative analysis of heart size revealed that although there are no differences in organ size at early stages of development (32-34hpf), regardless of looping direction *spaw*$^{-/-}$ hearts fail to grow as they undergo looping and ballooning, and then maintain their smaller looped and ballooned size as they transition to an early maturing stage (Fig 4.25A-A'). Chamber-specific analysis identifies this growth defect between 34 and 50hpf is driven by reduced growth of both chambers (Fig 4.25B-B'). As the heart loops and balloons, the atrium of *spaw*$^{-/-}$ hearts maintains its volume while the ventricle grows but not to the extent nor at the rate of a sibling ventricle. As the chambers remodel and transition to an early maturing stage (50→72hpf), the atrial volume of *spaw* mutants is conserved, whilst the ventricular volume appears to sustain growth but at a slower rate (when compared to their earlier growth rate) (Fig 4.25B-B'). Interestingly, and despite the identified growth defects, these later events between 50 and 72hpf result in no organ nor chamber size defects in *spaw* mutants at 72hpf when compared to their siblings.

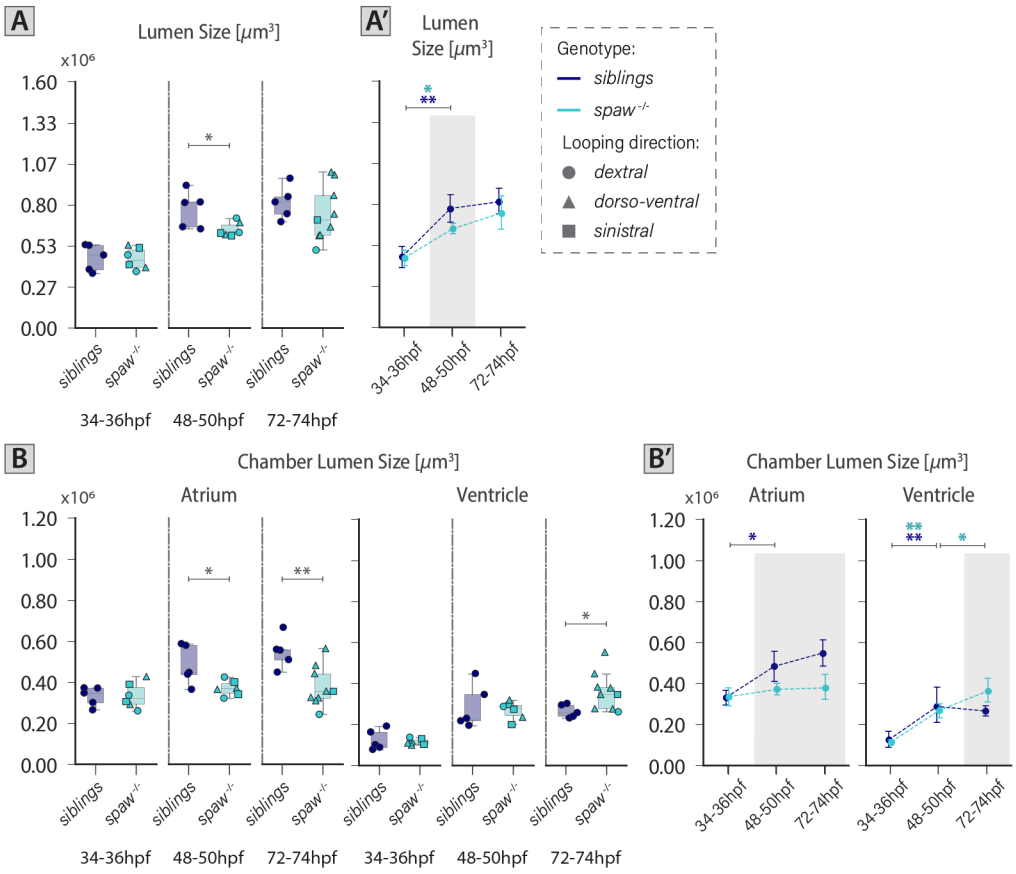

Fig 4.26. *spaw*$^{-/-}$ hearts exhibit distinct defects in chamber lumen size during and post-looping.
A-B'. Quantification of lumen size of the heart (A-A') and its chambers (B-B') using *morphoHeart* in *spaw* mutants and siblings at 34-36hpf, 48-50hpf and 72-74hpf. At 48-50hpf the total heart and atrial lumen size are significantly reduced in *spaw* mutants compared to their siblings (heart: *p-value=0.03414*, atrium: *p-value=0.02659*). At 72hpf, while the atrial lumen size (B) of *spaw* mutant hearts is significantly reduced compared to their siblings (*p-value=0.00662*), ventricular lumen size (B) is significantly expanded (*p-value=0.04481*). A' and B' are point-plots of the data presented in A and B, respectively. A-B': Error bars with 95% confidence interval of the mean. 34-36hpf: *siblings n=5*, *spaw*$^{-/-}$ *n=6* (*sinistral n=2*, *dorso-ventral n=2*, *dextral n=2*); 48-50hpf: *siblings n=5*, *spaw*$^{-/-}$ *n=6* (*sinistral n=2*, *dorso-ventral n=2*, *dextral n=2*); 72-74hpf: *siblings n=5*, *spaw*$^{-/-}$ *n=9* (*sinistral n=1*, *dorso-ventral n=7*, *dextral n=1*). For details regarding the statistical analyses used to compare this set of data see *Note#4.7* (pg. 131). Only significant comparisons are shown. **: *p-value*<0.01, *: *p-value*<0.05.

The identified failure to grow and expand of *spaw*$^{-/-}$ hearts during looping and ballooning morphogenesis translates directly into a defect in lumen size and hence a reduced blood filling capacity. As expected, analysis of lumen size throughout these timepoints reveals a defect in total heart lumen size at 48-50hpf (Fig 4.26A-A'). Intriguingly, is spite of having identified a defect in growth in both chambers (Fig 4.25B-B'), analysis of lumen size of individual chambers at 48-50hpf pinpoints the atrium of *spaw*$^{-/-}$ hearts as the sole driver of this heart lumen defect, while the ventricle presents the same lumen size and lumen growth rate (34→50hpf) as a sibling ventricle (Fig 4.26B-B'). Two events could explain the ventricular lumen expansion despite the chamber's growth failure: either the small chamber growth observed between 50 and 72hpf (Fig 4.25B') is sufficient to grant this increased lumen capacity, or a thinning of one or multiple cardiac layers could occur between these timepoints to allow such expansion. Analysis of myocardial and endocardial tissue volume at this stage confirmed *spaw*$^{-/-}$ have significantly reduced ventricular tissue layers (data not shown), advocating for this hypothesis. As the heart transitions to a maturing stage (50→72hpf), *spaw*$^{-/-}$ hearts retain their already acquired looped and ballooned size. This results in *spaw*$^{-/-}$ hearts having a significantly reduced atrial lumen size at 72-74hpf when compared to their siblings.

Interestingly and possibly due to the continued increase of ventricular size between 50 and 72hpf (Fig 4.25B-B'), the ventricular lumen of *spaw*$^{-/-}$ hearts at 72hpf is significantly bigger than that of their siblings, where ventricular lumen size is maintained between 50 and 72hpf.

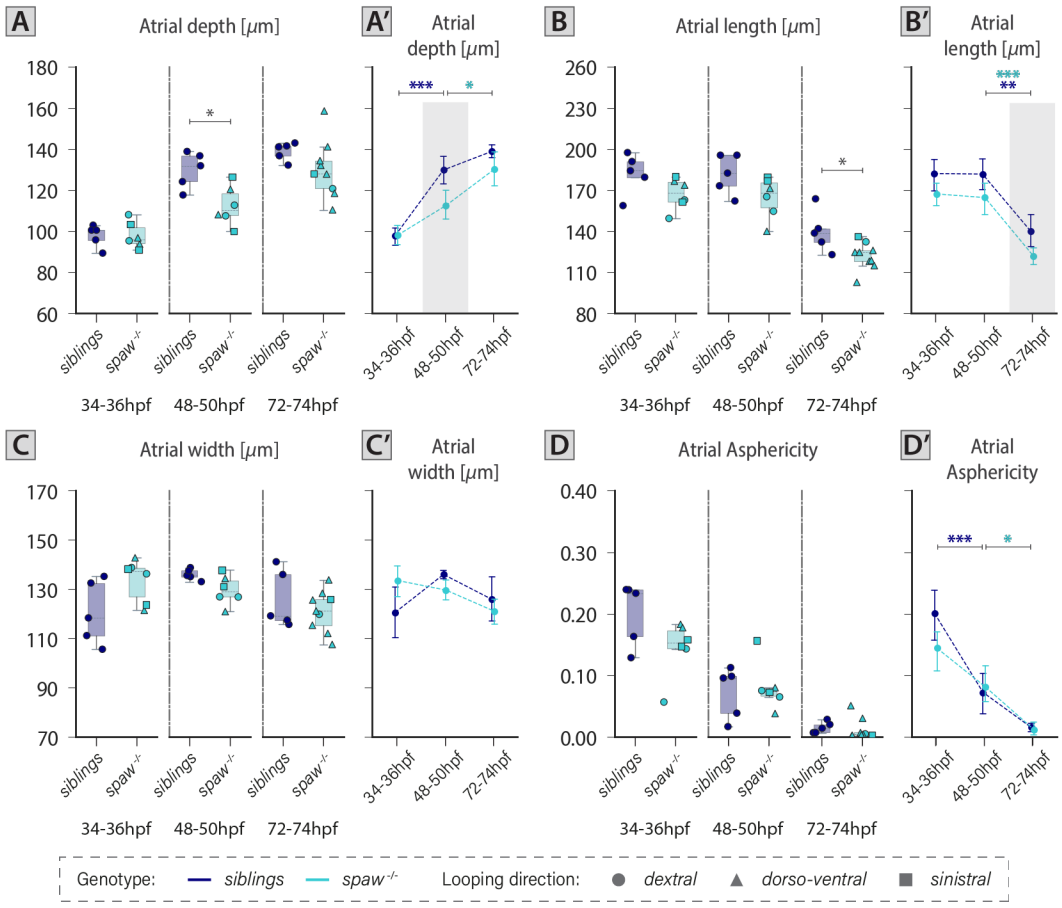

Fig 4.27. *spaw*$^{-/-}$ hearts have slightly affected atrial morphology during early cardiac morphogenesis.
A-D'. Quantifications of atrial depth (A-A'), length (B-B'), width (C-C'), and asphericity (D-D') using *morphoHeart* in *spaw* mutants and siblings at 34-36hpf, 48-50hpf and 72-74hpf. At 48-50hpf the depth of the atrium in *spaw* mutant hearts is significantly reduced when compared to their siblings (*p-value=0.01292*). Later, as the heart transitions to early maturation stages (72-74hpf), the length of the atrium is significantly reduced in *spaw* mutants when compared to its their siblings (*p-value=0.01993*). A-D': Error bars with 95% confidence interval of the mean. 34-36hpf: *siblings n=5*, *spaw*$^{-/-}$ *n=6* (*sinistral n=2*, *dorso-ventral n=2*, *dextral n=2*); 48-50hpf: *siblings n=5*, *spaw*$^{-/-}$ *n=6* (*sinistral n=2*, *dorso-ventral n=2*, *dextral n=2*); 72-74hpf: *siblings n=5*, *spaw*$^{-/-}$ *n=9* (*sinistral n=1*, *dorso-ventral n=7*, *dextral n=1*). For details regarding the statistical analyses used to compare this set of data see *Note#4.7* (pg. 131). Only significant comparisons are shown. ***: *p-value*<0.001, **: *p-value*<0.01, *: *p-value*<0.05.

To further analyse changes in chamber size of *spaw*$^{-/-}$ hearts from a morphological viewpoint, similar to the wild-type analysis, ellipsoids were fit to the myocardial tissue chambers obtaining standardised measurements of their size and shape in 3D (Fig 4.27 and 4.28). Analysis of chamber morphology throughout development reveals that the atria of 48-50hpf *spaw*$^{-/-}$ hearts are flatter (i.e. have a reduced depth, Fig 4.27A-A') and the ventricles are narrower (Fig 4.28C-C') when compared to their siblings. The reduction in each of these dimensions per chamber at looping and ballooning stages corroborates the defects in chamber volume previously identified (Fig 4.25B-B'), and supports the idea that changes in chamber morphology accompany chamber growth during morphogenesis. At 72-74hpf, the atrial length of *spaw*$^{-/-}$ becomes shorter than that of the siblings; nevertheless, rearrangements of this chamber in the other two dimensions as it transitions to an early maturing stage (50→72hpf) result in atria with spherical

morphology comparable to the controls. Loss of asymmetric Nodal activity appears to have no other effect on ventricular morphology in the *spaw*$^{-/-}$ hearts.

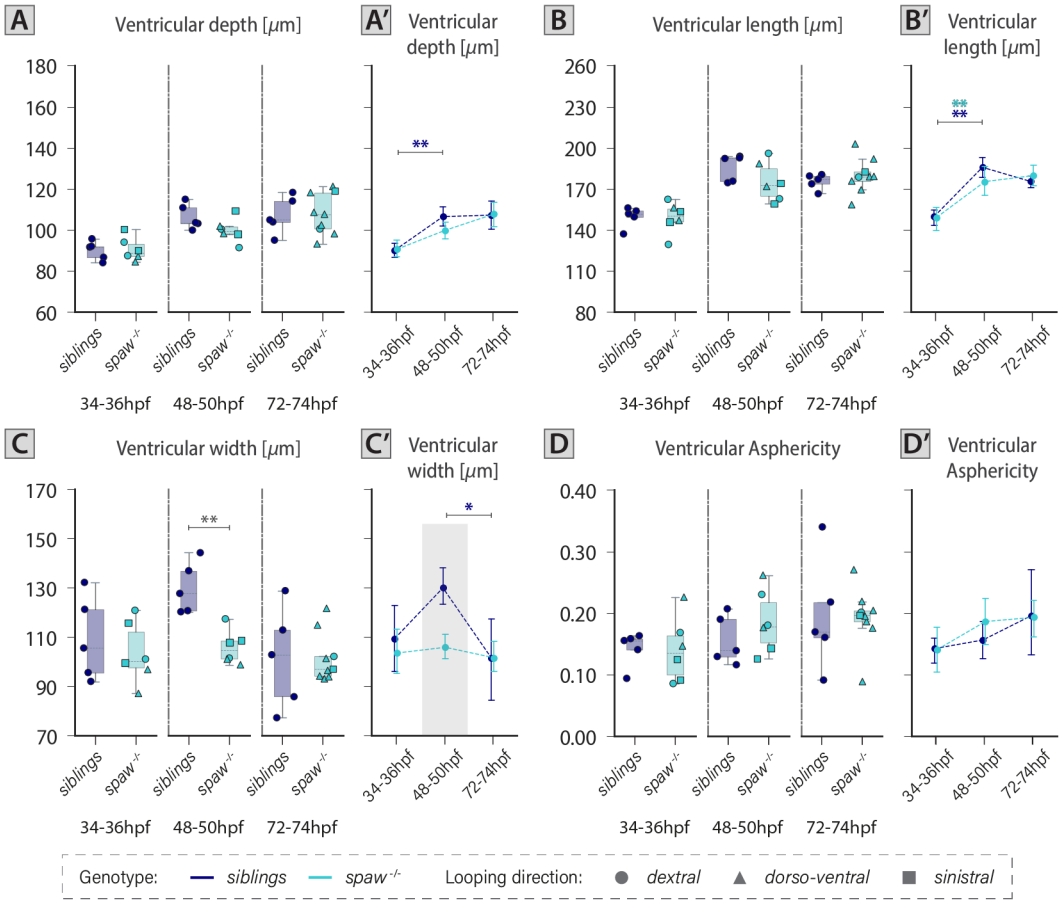

Fig 4.28. Ventricular failure to grow during looping and ballooning is exhibited by narrower ventricles in *spaw* mutant hearts.

A-D'. Quantifications of ventricular depth (A-A'), length (B-B'), width (C-C'), and asphericity (D-D') using *morphoHeart* in *spaw* mutants and siblings at 34-36hpf, 48-50hpf and 72-74hpf. At 48-50hpf the ventricular width in *spaw* mutant hearts is significantly reduced when compared to their siblings (*p-value=0.00129*). A-D': Error bars with 95% confidence interval of the mean. 34-36hpf: *siblings n=5*, *spaw*$^{-/-}$ *n=6* (*sinistral n=2*, *dorso-ventral n=2*, *dextral n=2*); 48-50hpf: *siblings n=5*, *spaw*$^{-/-}$ *n=6* (*sinistral n=2*, *dorso-ventral n=2*, *dextral n=2*); 72-74hpf: *siblings n=5*, *spaw*$^{-/-}$ *n=9* (*sinistral n=1*, *dorso-ventral n=7*, *dextral n=1*). For details regarding the statistical analyses used to compare this set of data see *Note#4.7* (pg. 131). Only significant comparisons are shown. **: *p-value*<0.01, *: *p-value*<0.05.

Notably, no defects in heart size are identified in *spaw*$^{-/-}$ hearts at early looping (34-36hpf) nor early maturing stages (72-74hpf) (Fig 4.25A-B'). Nevertheless, analysis of these mutant hearts at an intermediate stage (48-50hpf) recognises a growth defect in both chambers, which translates into defects in other morphological parameters at looping, ballooning and early maturing stages (Fig 4.26-4.28). Despite the absence of size defects at 72-74hpf, the identified growth defect at intermediate stages suggests *spaw*$^{-/-}$ hearts fail to undergo the same morphological changes and rearrangements a wild-type heart experiences during looping and ballooning morphogenesis, which possibly results in *spaw*$^{-/-}$ hearts with dissimilar cellular and tissue organisations at early maturation stages. Recognising this defect early in the analysis of *spaw*$^{-/-}$ hearts defined a newly informed perspective from which to analyse the phenotype of these mutants at early maturing stages.

Together, morphometric analysis of heart and lumen size as well as chamber morphology identifies not previously described defects in chamber growth in *spaw*$^{-/-}$ hearts, regardless of looping direction,

suggesting a dysregulation of chamber growth as a result of altered L/R patterning and consequently a role for Nodal in timely chamber growth as the heart loops and balloons and in chamber remodelling as it matures.

The fact that midline *spaw*$^{-/-}$ heart tubes resolve their looping in a dextral, dorsal, or sinistral direction raises additional questions about the chamber morphological changes involved in driving heart looping in a specific direction. Interestingly, parameter dynamics underlying chamber morphology of *spaw*$^{-/-}$ hearts appear to behave similarly throughout early development irrespective of looping direction (Fig 4.27-4.28), suggesting that a combination of specific changes in chamber dimensions/morphology, **is not the only** mechanism responsible for driving concurrent processes that ensure robust dextral looping and ballooning morphogenesis. Additional mechanisms, such as 3D chamber rotations and chamber/region-specific changes in cell size and shape, might need to be in place to aid simultaneous looping morphogenesis in the correct direction and support the ongoing morphogenesis of this organ.

To characterise the 3D chamber rotations that give rise to different looping directions and compare them to those driving the morphogenesis of wild-type hearts, analysis of chamber orientation of *spaw*$^{-/-}$ and their siblings through time was performed. To make the analysis uniform regardless of the orientation of the heart within the embryo (i.e. heart looping direction), the methodology to quantify the 3D chamber orientation was modified for dorso-ventral *spaw*$^{-/-}$ hearts: 'ventral' angles were measured by projecting the chamber segments to the plane in which both chambers are side to side (Fig 4.29A-C), and 'sagittal' angles by projecting them to the plane in which the atrium is in front of the ventricle (Fig 4.29D-F).

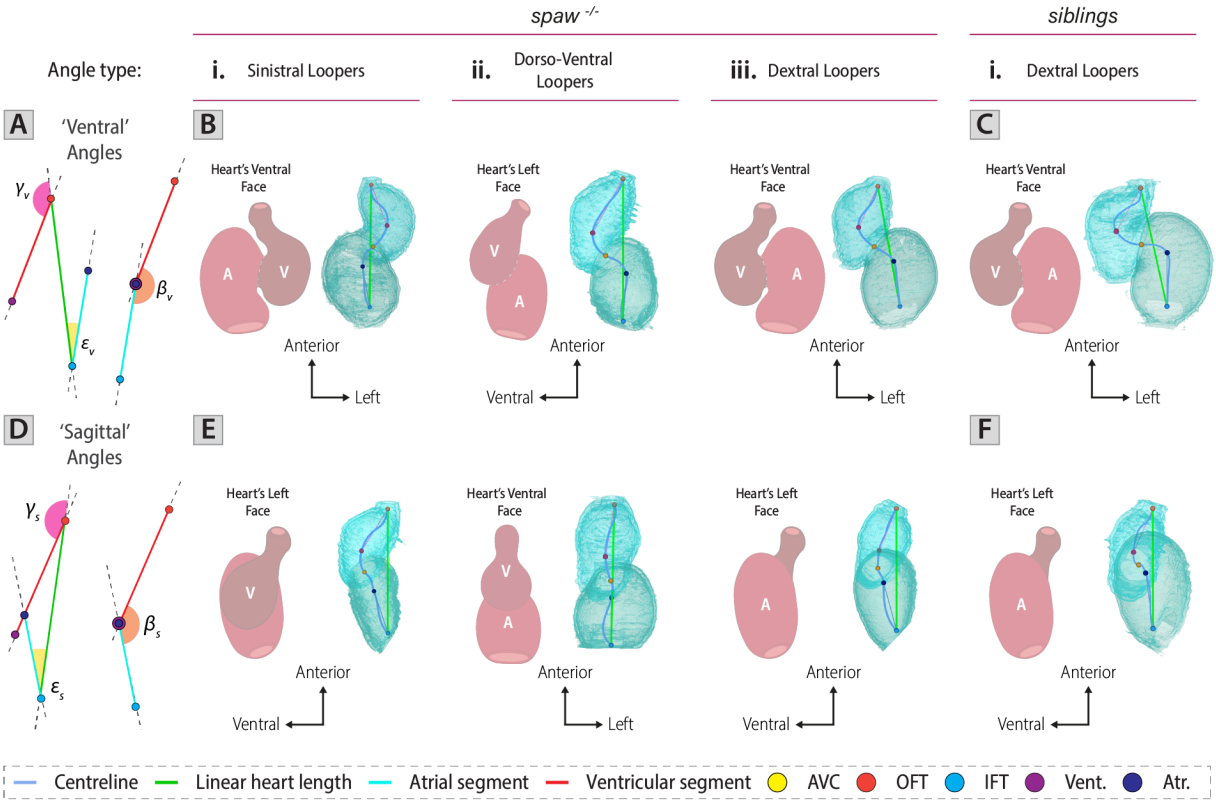

Fig 4.29. Schematic to illustrate 'ventral' and 'sagittal' angle standardisation in *spaw*$^{-/-}$ hearts with distinct looping directions.

A-F. Schematic depicting the way 'ventral' (A-C) and 'sagittal' (D-F) angles are measured using the heart/chamber segments in *spaw*$^{-/-}$ hearts with different looping directions (B,E, sinistral: i, dorso-ventral: ii, dextral: iii) and siblings (Ci, Fi). 'Ventral' angles are measured by projecting the chamber segments to the plane in which both chambers are side to side (equivalent to the frontal plane of a wild-type dextral looper) (A-C), while 'sagittal' angles by projecting them to the plane in which the atrium is in front of the ventricle (equivalent to the sagittal plane of a wild-type dextral looper) (D-F). B,C,E,F: Anterior to the top. AVC: Atrioventricular canal, OFT: Outflow-tract, IFT: Inflow-tract, Atr: sphere positioned 50 centreline points away from the AVC centreline

position in the direction of the atrium, Vent: sphere positioned 50 centreline points away from the AVC centreline position in the direction of the ventricle.

_____

Analysis of chamber orientation from the heart's ventral face through time reveals a clear division of the values for each measured parameter between two groups: the *spaw*$^{-/-}$ dorso-ventral and the *spaw*$^{-/-}$ dextral and sinistral loopers (i.e. lateralised loopers) (Fig 4.30). If comparisons are carried out individually between sibling hearts and lateralised loopers, not surprisingly, the ventral angles obtained for the *spaw*$^{-/-}$ appear to be the closest to the control phenotype, although still deviating at some stages from it. Despite undergoing looping morphogenesis in a lateralised manner, the identified deviations in 3D ventral chamber orientation of *spaw*$^{-/-}$ dextral and sinistral loopers when compared to their siblings, corroborates an abnormal rearrangement of the chambers.

When compared to their siblings, analysis of the 'ventral' angles of dorso-ventral loopers exposes the abnormal morphological rearrangements these hearts experience to undergo looping in the dorso-ventral axis. As the hearts loop, balloon and then transition to an early maturing stage, the atria of *spaw*$^{-/-}$ dorso-ventral loopers maintain their 'ventral' orientation (Fig 4.30B-B') while the ventricles rotate progressively clockwise (i.e. ventrally) and away from the midline (Fig 4.29Bii, Fig 4.30C-C'). This gradual ventricular rotation away from the midline results in a continued reduction of the 'ventral' angle between the chambers (Fig 4.30D-D'), which concurrently allows the ventricle of these dorso-ventral loopers to slowly grow (Fig 4.25B-B') and rearrange with the atrium. Interestingly and due to the particular orientation of these hearts within the embryo (see Fig 4.29Bii,Eii), these progressive rotations of the ventricle also allow *spaw*$^{-/-}$ dorso-ventral looper hearts to reposition the OFT so that blood can be pumped efficiently out of this chamber, resembling the rotations undergone by wild-type ventricles in the sagittal plane (Fig 4.4D), and all in all, resulting in the characteristic looped morphology these *spaw*$^{-/-}$ present in Fig 4.24E-F.

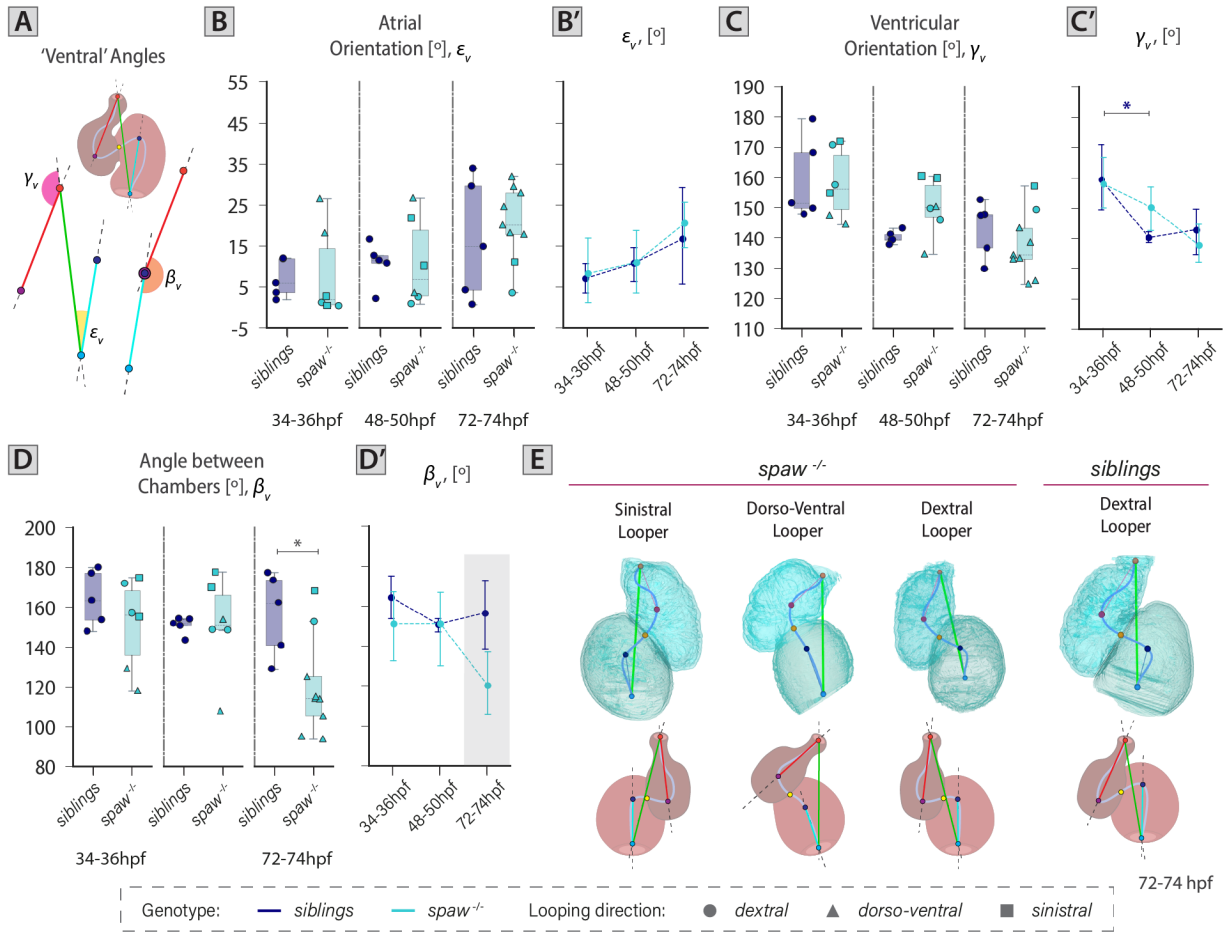

Fig 4.30. 'Ventral' angles of dorso-ventral loopers exposes the abnormal morphological rearrangements these hearts experience to undergo looping in the dorso-ventral axis.

A. Schematic depicting the 'ventral' angles measured from heart/chamber segments. **B-D'.** Quantification of atrial orientation ε_v (B-B'), ventricular orientation γ_v (C-C'), and angle between chambers β_v (D-D') in *spaw* mutants and siblings at 34-36hpf, 48-50hpf and 72-74hpf using the standardisation presented in Fig 4.29. At 72-74hpf the angle between chambers is significantly reduced in the *spaw* mutants when compared to their siblings (*p-value=0.01871*). **E.** Examples of 3D atrial and ventricular myocardial chambers with orientation segments and linear heart length in 72-74hpf *spaw*$^{-/-}$ and sibling hearts (top) and its corresponding schematics (bottom) illustrating the differences observed in 'ventral' angles in hearts with different looping directions. B-D': Error bars with 95% confidence interval of the mean. 34-36hpf: *siblings n=5*, *spaw*$^{-/-}$ *n=6* (*sinistral n=2*, *dorso-ventral n=2*, *dextral n=2*); 48-50hpf: *siblings n=5*, *spaw*$^{-/-}$ *n=6* (*sinistral n=2*, *dorso-ventral n=2*, *dextral n=2*); 72-74hpf: *siblings n=5*, *spaw*$^{-/-}$ *n=9* (*sinistral n=1*, *dorso-ventral n=7*, *dextral n=1*). For details regarding the statistical analyses used to compare this set of data see *Note#4.7* (pg. 131). Only significant comparisons are shown. *: *p-value*<0.05.

Like the 'ventral' angles, analysis of chamber orientation from the heart's 'sagittal' face throughout time (Fig 4.31) shows the same data division between *spaw*$^{-/-}$ lateralised and dorso-ventral loopers, with the 'sagittal' angles of lateralised loopers acting as the closest to the control phenotype. Analysis of the 'sagittal' angles of *spaw*$^{-/-}$ dorso-ventral loopers identifies an absence of rotation of both chambers throughout the analysed stages. As previously characterised, the combination of sagittal rotations undergone by wild-type chambers feasibly aids the reorientation of the OFT to pump blood efficiently out of the ventricle (Fig 4.4). Nonetheless, due to the orientation of the *spaw*$^{-/-}$ dorso-ventral loopers within the embryo, the set of rotations that allow the reorientation of the OFT in these mutants take place in the 'ventral' plane rather than the 'sagittal' one, corroborating the absence of rotations identified and confirming the results obtained for these set of parameters (Fig 4.31).

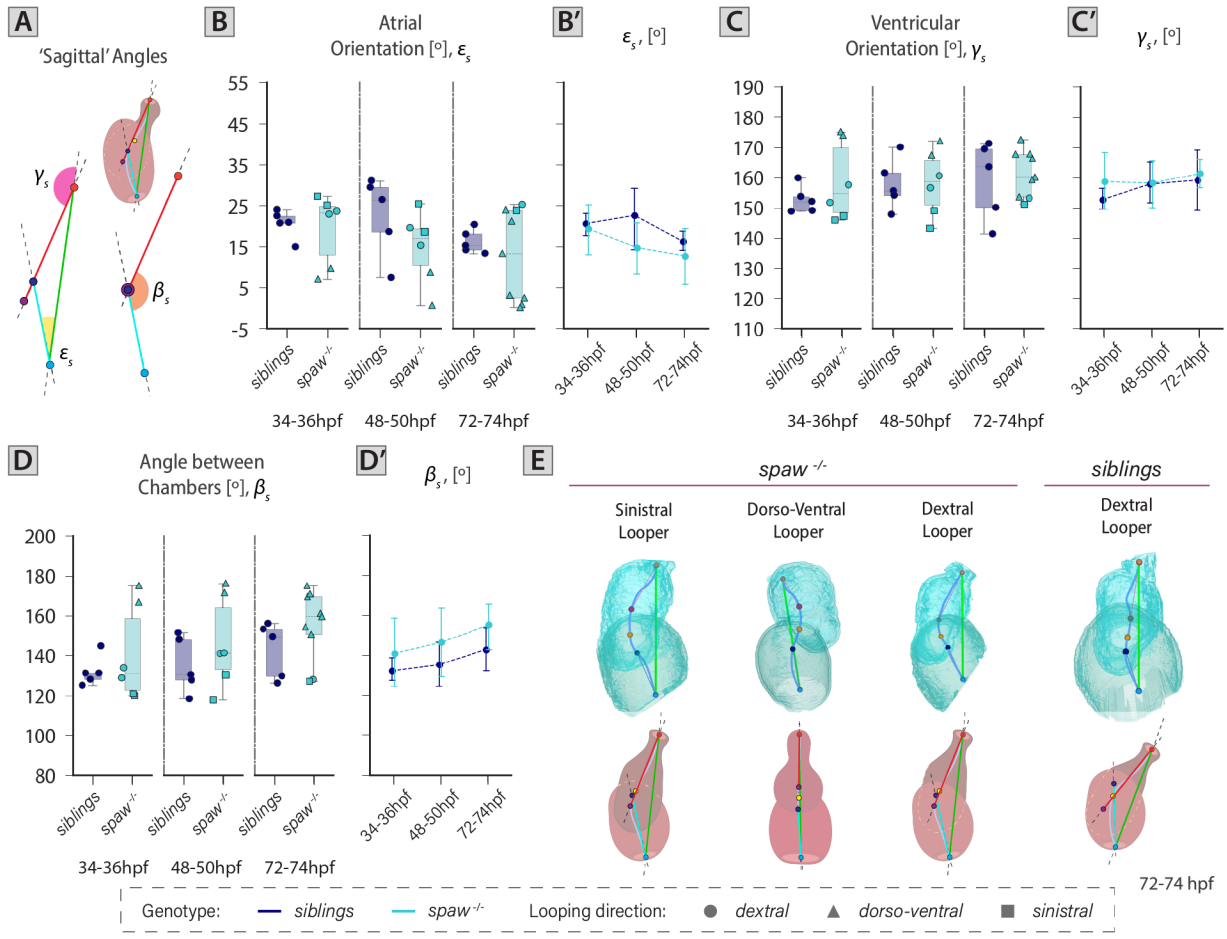

Fig 4.31. 'Sagittal' angle quantifications identify a division between *spaw*$^{-/-}$ lateralised and dorso-ventral loopers. **A.** Schematic depicting the 'sagittal' angles measured from heart/chamber segments. **B-D'.** Quantification of atrial orientation ε_v (A), ventricular orientation γ_v (B), and angle between chambers β_v (C) in *spaw* mutants and siblings at 34-36hpf, 48-50hpf and 72-74hpf using the standardisation presented in Fig 4.29. **E.** Examples of 3D atrial and ventricular myocardial chambers with orientation segments and linear heart length in 72-74hpf *spaw*$^{-/-}$ and sibling hearts (top) and its corresponding schematics (bottom) illustrating the differences observed in 'sagittal' angles in hearts with different looping directions. B-D': Error bars with 95% confidence interval of the mean. 34-36hpf: *siblings n=5*, *spaw*$^{-/-}$ *n=6* (*sinistral n=2*, *dorso-ventral n=2*, *dextral n=2*); 48-50hpf: *siblings n=5*, *spaw*$^{-/-}$ *n=6* (*sinistral n=2*, *dorso-ventral n=2*, *dextral n=2*); 72-74hpf: *siblings n=5*, *spaw*$^{-/-}$ *n=9* (*sinistral n=1*, *dorso-ventral n=7*, *dextral n=1*). For details regarding the statistical analyses used to compare this set of data see *Note#4.7* (pg. 131). Only significant comparisons are shown.

Taken together, *spaw*$^{-/-}$ lateralised and dorso-ventral loopers have distinct ways to rearrange and accommodate the chambers (i.e. left-right or ventral-to-dorsal configuration) which possibly assist these hearts in the rearrangement of the tissue during the concurrent processes of looping and ballooning morphogenesis. Likewise, the identification of the same 'ventral' rotation of the ventricle between 50 and 72hpf regardless of looping direction suggests that this chamber's reorientation is required for repositioning the OFT so that blood can be efficiently pumped out of this chamber into the rest of the developing embryo.

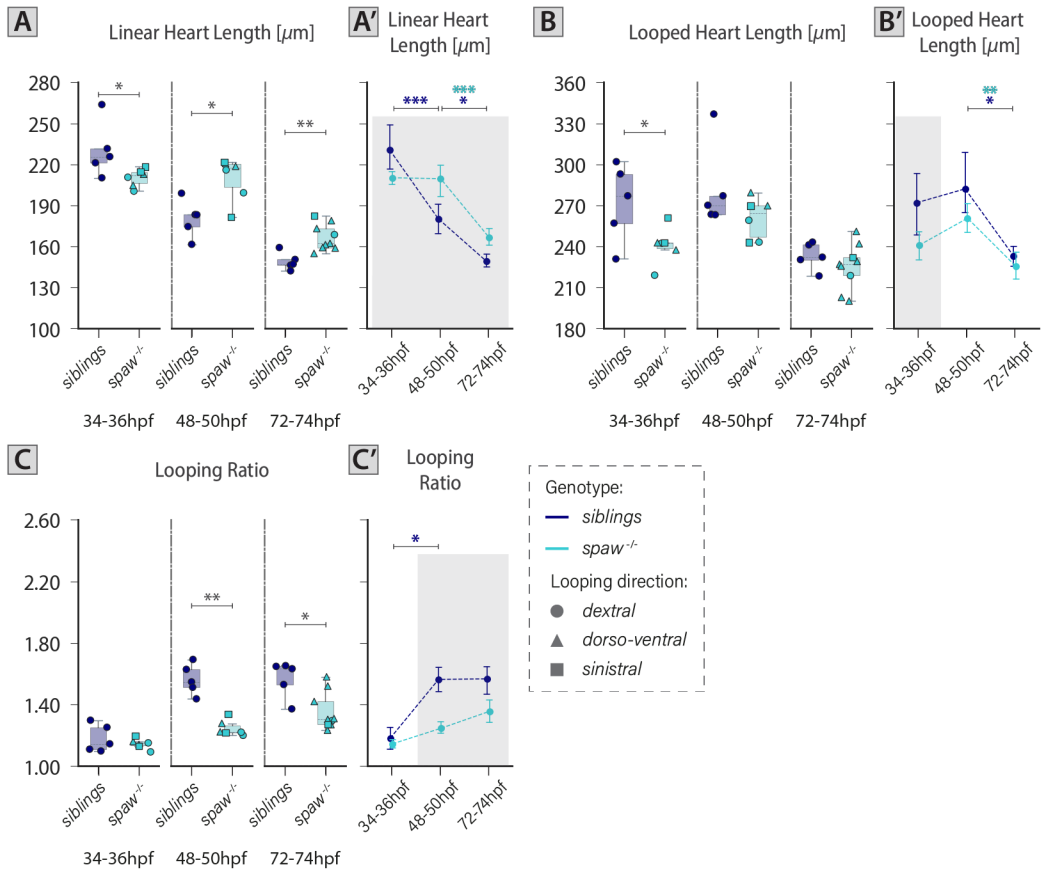

Fig 4.32. The chambers of *spaw*$^{-/-}$ hearts fail to move and rearrange side by side during looping morphogenesis presenting a loose and elongated configuration.

A-B. Quantification of the linear (A-A') and looped (B-B') heart length of the heart using *morphoHeart* in *spaw* mutants and siblings at 34-36hpf, 48-50hpf and 72-74hpf. At 32-34hpf the linear and looped heart length of *spaw* mutant hearts are significantly reduced when compared to their siblings (linear length: *p-value=0.04454,* looped length: *p-value=0.04116*). As the heart loops, balloons and transitions to an early maturing stage, the linear heart length of *spaw* mutant hearts is significantly increased when compared to their siblings (48-50hpf: *p-value=0.01058,* 72-74hpf: *p-value=0.00359*), suggesting *spaw* mutant hearts fail to compact during these stages. **C-C'.** Quantification of looping ratio (quotient between looped heart length and linear heart length) in *spaw* mutants and siblings at 34-36hpf, 48-50hpf and 72-74hpf. Failure in heart compaction, results in significantly reduced looping ratios for the *spaw* mutant hearts when compared to their siblings (48-50hpf: *p-value=0.00811,* 72-74hpf: *p-value=0.01640*). A-C': Error bars with 95% confidence interval of the mean. 34-36hpf: *siblings n=5*, *spaw*$^{-/-}$ *n=6* (*sinistral n=2*, *dorso-ventral n=2*, *dextral n=2*); 48-50hpf: *siblings n=5*, *spaw*$^{-/-}$ *n=6* (*sinistral n=2*, *dorso-ventral n=2*, *dextral n=2*); 72-74hpf: *siblings n=5*, *spaw*$^{-/-}$ *n=9* (*sinistral n=1*, *dorso-ventral n=7*, *dextral n=1*). For details regarding the statistical analyses used to compare this set of data see *Note#4.7* (pg. 131). Only significant comparisons are shown. ***: *p-value*<0.001, **: *p-value*<0.01, *: *p-value*<0.05.

The wild-type characterisation presented earlier in this chapter identified that it is the combination of chamber volume changes, rotations and rearrangements that constitutes the basis of looping morphogenesis. To further quantify the extent to which *spaw*$^{-/-}$ hearts undergo looping, the 3D linear and looped heart lengths of *spaw*$^{-/-}$ and their siblings were measured, and their looping ratio calculated (Fig 4.32). Analysis of these parameters initially identifies that *spaw*$^{-/-}$ hearts have a significantly shorter linear and looped heart length at early looping stages (34-36hpf, Fig 4.32A-B') when compared to their siblings.

In contrast to wild-type hearts in which looping and ballooning morphogenesis brings closer the heart poles, reducing the linear heart length and increasing the looped length (Fig 4.5B-C); when *spaw*$^{-/-}$ hearts undergo looping and ballooning their linear heart length is maintained constant and their looping length is slightly increased (Fig 4.32A-A'). This results in *spaw*$^{-/-}$ with a heart morphology in which despite the

formation of the AVC constriction, the chambers fail to move and rearrange into a tight side-by-side compacted shape maintaining a more 'relaxed', loose and elongated configuration of the chambers. Just like sibling hearts, as the hearts transition to an early maturation stage, the linear heart length of *spaw*$^{-/-}$ hearts continues to get shortened, but due to the early compaction defect, at 72-74hpf this length is maintained significantly longer than that of their siblings (Fig 4.32A-A').

Surprisingly, unlike the other variables, where the *spaw*$^{-/-}$ hearts appear to 'attain' the morphology of siblings' early maturing hearts (72-74hpf), the compaction failure identified in *spaw*$^{-/-}$ hearts results in linear heart lengths and looping ratios significantly different to that of their siblings. Interestingly, the looping defects and variable dynamics identified in the *spaw*$^{-/-}$ hearts characterise looping morphogenesis of this organ, irrespective of their looping direction, corroborating that *spaw*$^{-/-}$ dextral loopers, (similar to sinistral and dorso-ventral loopers and despite having looped in the *correct* direction), also have looping defects. This confirms the abnormal looping morphogenesis of *spaw* mutants regardless of looping direction, and highlights that these combined morphological assessments across time compared to traditional analyses (i.e. at single timepoints and with limited measurements) provide a much deeper understanding of the dynamic defects that characterise *spaw*$^{-/-}$ heart development.

To characterise with more detail the growth defects identified in the *spaw*$^{-/-}$ hearts and provide a more regionalised understanding of the effect of different looping directions in chamber morphology, the ballooning heatmaps of dextral, dorso-ventral and sinistral *spaw*$^{-/-}$ hearts were obtained and analysed at the three key developmental stages of interest (Fig 4.34A-B: 34-36hpf, C-D: 48-50hpf, and E-F: 72-74hpf). [*Note#4.10:* To assist the 2D heatmap analysis of *spaw*$^{-/-}$ hearts with different looping directions refer to Fig 4.33 where distinct cardiac 3D regions are colour matched to the corresponding 2D sections found in their corresponding planar projected heatmaps].

Analysis of chamber ballooning in *spaw*$^{-/-}$ hearts identifies distinctive colour patterns in the heatmaps for each looping directionality at each of the analysed stages, confirming the variety of heart morphologies found within this group of hearts. Ballooning heatmap examination at 34-36hpf, identifies similar colour patterns for the lateralised loopers (i.e. dextral and sinistral loopers) and the control heatmap (Fig 4.34Ai,Aiii and B). In these heatmaps, initiation of atrial ballooning in all three groups is confirmed by the redder colours forming a 'U' shape around the AVC region of the atrium, while the ventricle remains tubular in shape (ventral face in blue/green and dorsal face in a gradient of green, yellow, and orange). Interestingly, while the same characteristic colour pattern of a ballooning chamber is identified in the dorso-ventrally looped atrium, the ventricular colour pattern is different than that of any of the other hearts (Fig 4.34Aii). In this heart, a narrower and tubular ventricle can be identified by a uniform light green colour in all this chamber's heatmap, suggesting that at this stage this chamber has not yet started to grow nor balloon.

In general, analysis of 2D projected ballooning heatmaps at 48-50hpf highlights the defects in chamber growth previously identified, by presenting smaller ballooning values for both chambers in *spaw*$^{-/-}$ hearts when compared to their siblings. Evaluation of the colour patterns in *spaw*$^{-/-}$ heatmaps at 48-50hpf and 72-74hpf additionally supports the premise that sinistral loopers present a mirrored morphology to that of dextrally looped hearts (compare in Fig 4.34C and E the sinistral looper heatmaps (i) with that of the dextral loopers (iii)). Moreover, due to the particular chamber arrangement of dorso-ventral loopers, the ballooning heatmaps of these hearts feature a symmetrical colour pattern exhibiting the symmetrical appearance of the chambers around the heart's midline (Fig 4.34Cii,Eii). Interesting to note, some dorso-ventral loopers, despite undergoing looping morphogenesis in the dorso-ventral (D/V) axis, can have the atrial outer curvature (AOC) slightly oriented to either side of the embryo (e.g. the AOC of the heart in Fig 4.23E is slightly rotated to the left, whereas that in Fig 4.23F is slightly rotated to the right). This results in heatmaps that are not completely symmetric around the ventral face of these hearts (Fig 4.34Cii-Dii) which needs to be considered when examining the heatmaps of these hearts closer. At 72-74hpf, green colours

rather than blue in the OFT of **all** *spaw*$^{-/-}$ hearts suggest that unlike sibling hearts, *spaw*$^{-/-}$ have a wider OFT. Other than the characteristics just mentioned, the myocardial ballooning heatmaps *spaw*$^{-/-}$ hearts do not present additional morphological defects when compared to their dextrally looped siblings.

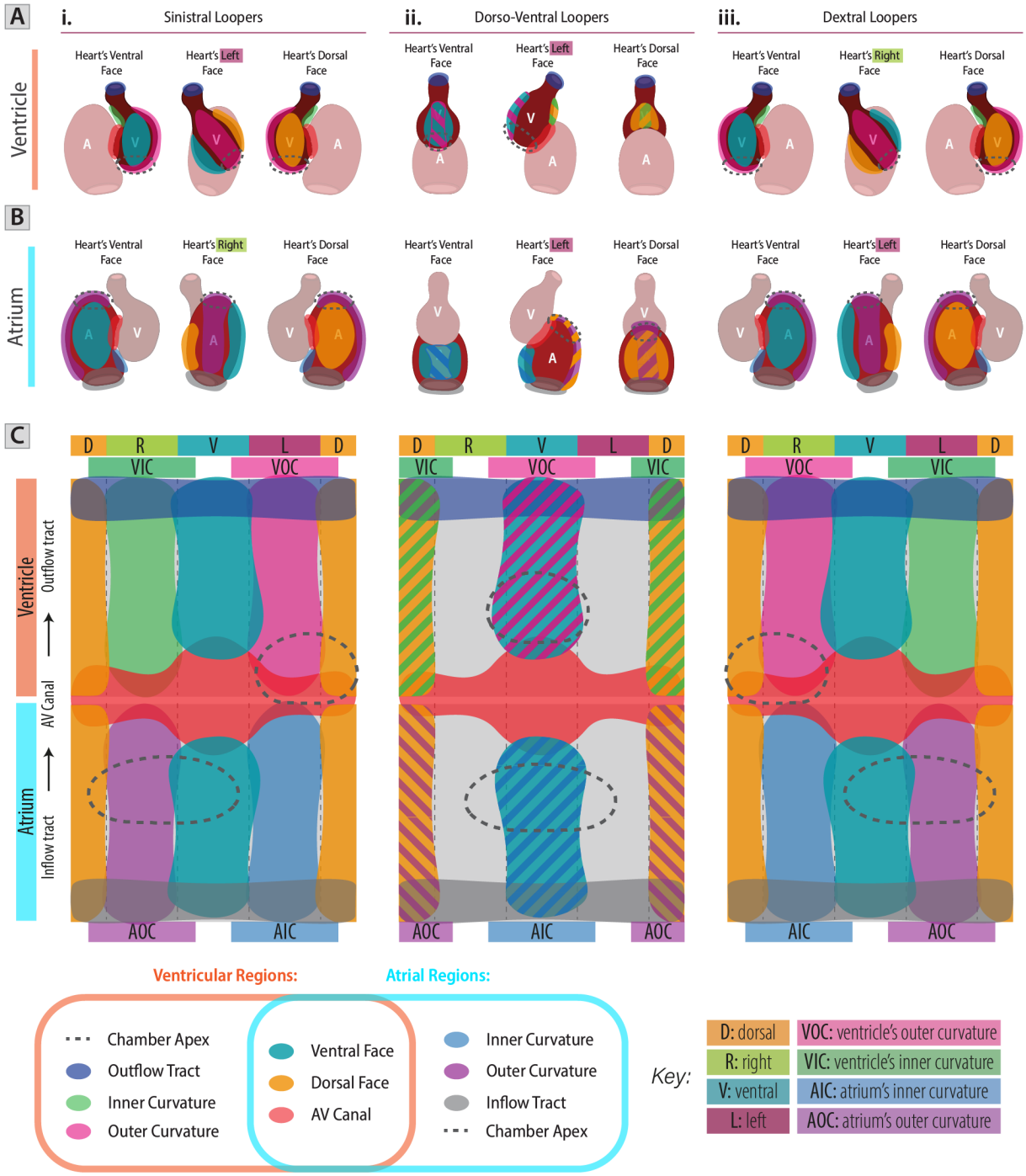

Fig 4.33. Schematic matching 3D heart regions in sinistral, dorso-ventral and dextral looping hearts to 2D heatmap sections.

A-B. Schematic illustrating with different colours and from different orientations the seven different ventricular (A) and atrial (B) regions that can be easily distinguished in the 3D heatmap representations of *spaw* mutant hearts that have a sinistral (Ai,Bi), dorso-ventral (Aii,Bii) and dextral (Aiii,Biii) looping directionality. **C.** 2D heatmap format, highlighting with the same colours as in A and B the different heart sections that can be identified in the heatmap planar projections. The use of this schematic throughout this thesis will aid the 2D heatmap analysis and interpretation of *spaw* mutant heatmaps, allowing the matching of 2D sections to the corresponding 3D heart regions. A-B: Anterior to the top. D: Dorsal, R: Right, V: Ventral, L: Left, VOC: Ventricular Outer Curvature, VIC: Ventricular Inner Curvature, AOC: Atrial Outer Curvature, AIC: Atrial Inner Curvature, AV Canal: Atrioventricular Canal.

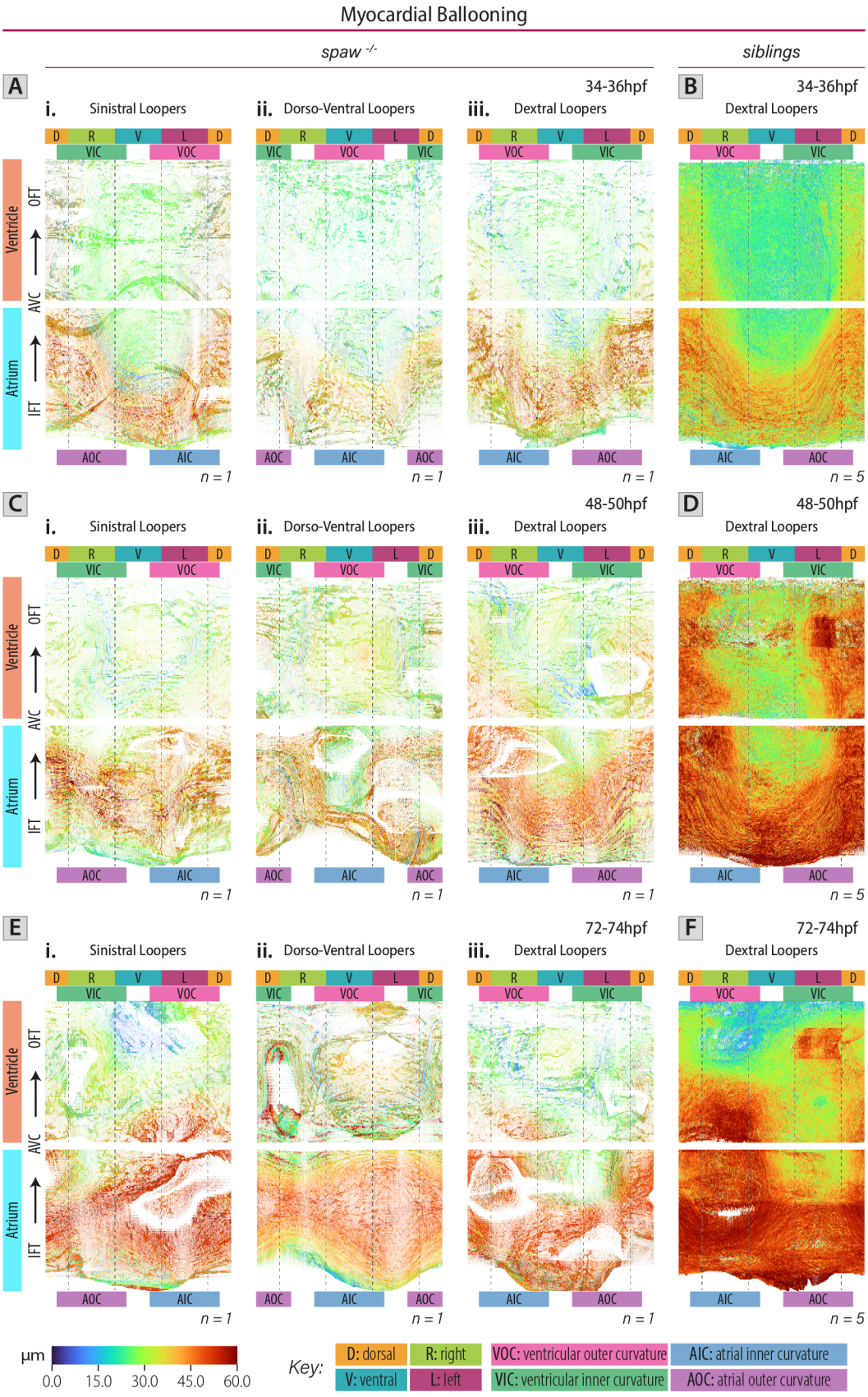

Fig 4.34. Myocardial ballooning heatmaps corroborate defective chamber growth in *spaw*$^{-/-}$ during looping and ballooning and confirm the mirror-imaged morphology of sinistrally looped mutants.
A-F. 2D representations of the myocardial ballooning of *spaw* mutant (A,C,E) and sibling (B, D, F) hearts at 34-36hpf (A-B), 48-50hpf (C-D) and 72-74hpf (E-F). *spaw* homozygous mutants are classified according to their

direction of looping as: sinistral (i), dorso-ventral (ii) and dextral (iii) loopers. While A, C and E show examples of planar projection plots of individual embryos, B, D and F show the average planar projections of all the processed siblings at all the indicated stages. A-F share colour-scale presented with the key at the bottom-left of the figure. D: Dorsal, R: Right, V: Ventral, L: Left, VOC: Ventricular Outer Curvature, VIC: Ventricular Inner Curvature, AOC: Atrial Outer Curvature, AIC: Atrial Inner Curvature, IFT: Inflow-tract, AVC: Atrioventricular Canal, OFT: Outflow-tract.

Together, all *spaw*$^{-/-}$ hearts, regardless of their looping direction, present a heart compaction failure and a dysregulation of chamber growth during looping and ballooning morphogenesis. This defective growth affects other morphological parameters not only at looping and ballooning stages but also at early maturing, suggesting L/R patterning has a significant role in timely chamber growth, rearrangement, and remodelling.

Additionally, the morphometric features so far described for *spaw*$^{-/-}$ hearts illustrate the subtle morphological alterations that characterise dextrally, dorso-ventrally, and sinistrally looped hearts. Dextrally looped *spaw*$^{-/-}$ present the closest morphology to that of a wild-type heart, however deviate from it. Detailed evaluation of chamber rotation and myocardial ballooning confirmed that the morphology of *spaw*$^{-/-}$ sinistrally looped hearts is the mirrored image of *spaw*$^{-/-}$ dextrally looped hearts. Likewise, the orientation of the heart within the embryo characterises the specific rotations and patterns of ballooning undergone by the chambers of dorso-ventral loopers.

5.2 Implications on Cardiac Jelly

Having characterised the gross morphological changes of *spaw*$^{-/-}$ hearts throughout early stages of development, the next step was to investigate the effect of aberrant L/R patterning in cardiac jelly dynamics and distribution, revealing more insights into the relationship between ECM regionalisation, abnormal looping direction, and disrupted morphogenesis. For this, volumetric measurements of the whole, and chamber-sectioned cardiac jelly meshes of *spaw*$^{-/-}$ hearts and their siblings (Fig 4.35) were acquired and analysed (Fig 4.36-4.40).

Initial inspection of the 3D reconstructions of the cardiac jelly does not reveal obvious defects in the cardiac jelly layer of *spaw*$^{-/-}$ hearts at early stages of development (32→50hpf, Fig 4.35). Interestingly, at 72-74hpf, the atrial cardiac jelly volume of dextrally and sinistrally looped *spaw*$^{-/-}$ hearts (Fig 4.35C,I) appears to be expanded in the outer curvature of this chamber.

Analysis of the total cardiac ECM volume throughout development identifies a not significant yet striking difference in the cardiac jelly volume found in *spaw*$^{-/-}$ hearts at 48-50hpf (Fig 4.36A-A'). Point-plot examination reveals that during the analysed stages, *spaw*$^{-/-}$ hearts maintain a relatively constant amount of cardiac jelly in the heart, suggesting *spaw*$^{-/-}$ embryos, fail to expand their ECM volume during looping and ballooning morphogenesis.

Excitingly, analysis of this variable in individual chambers identifies divergent progressions of ECM volume through time for each mutant chamber. Although no statistical differences were found in the atrial ECM volume between genotypes throughout the analysed stages, analysis of ECM volume dynamics in this chamber identifies a slower rate of ECM expansion in the *spaw*$^{-/-}$ hearts when compared to their siblings. Interestingly as the heart transitions to an early maturing state (50→72hpf), different to sibling atria in which the ECM begins to get degraded, the atria of *spaw*$^{-/-}$ sustain the slow production of ECM, resulting in what appears to be an expanded (yet not statistically significant) ECM volume in this chamber (Fig 4.36B-B'). Contrary to the atrial cardiac jelly, the ventricular ECM of *spaw*$^{-/-}$ hearts appears to be constantly degraded throughout the analysed stages, resulting in significantly reduced ECM volumes when compared to siblings from 48-50hpf onwards (Fig 4.36C-C'). Interestingly the reduction rate of the ventricular ECM

between 50 and 72hpf in *spaw*$^{-/-}$ hearts is similar to that in the siblings, probably indicating that the mechanisms of degradation or ECM turnover are not affected in these mutants.

The added effect of constant yet slow ECM expansion in the atrium with an accelerated ECM reduction in the ventricle results in the ECM dynamics identified for the total cardiac ECM (Fig 4.36A-A'), all in all suggesting a role for Spaw in regulating the cardiac ECM volume in a chamber-specific manner.

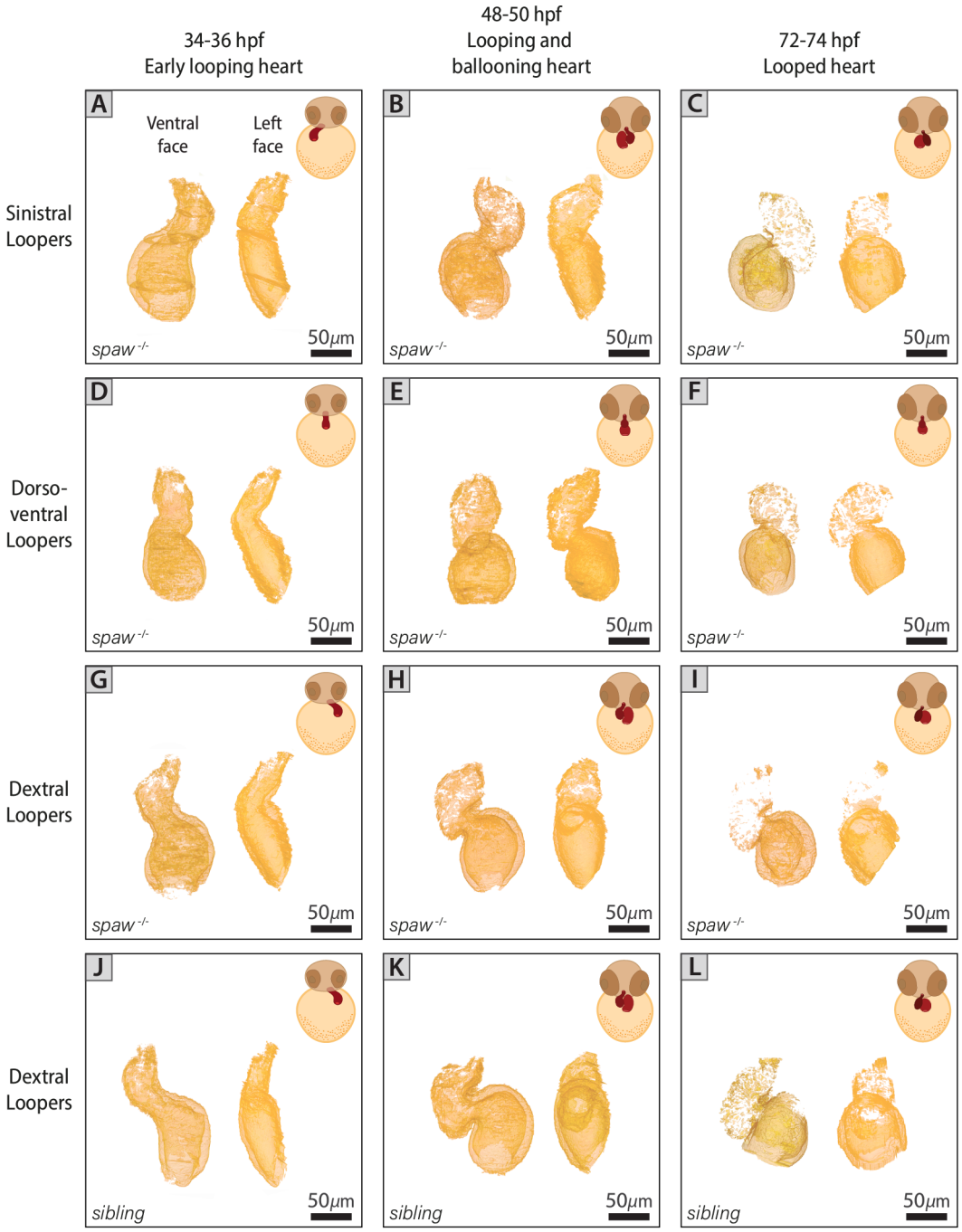

Fig 4.35. 3D cardiac jelly volumes of *spaw*$^{-/-}$ hearts do not show obvious ECM defects in these mutants.
A-L. 3D reconstructions of the cardiac jelly of *spaw*$^{-/-}$ (A-I) and sibling (J-L) hearts at key developmental stages (34-36hpf: A,D,G,J; 48-50hpf: B,E,H,K; and 72-74hpf: C,F,I,L). *spaw* homozygous mutants (A-I) are classified according to their direction of looping as: sinistral (A-C), middle (D-F) and dextral (G-I) loopers. A-L: As described by the labels in Panel A, all panels show the ventral and left face of each of the hearts shown in Fig 4.23 and 4.24 with anterior to the top.

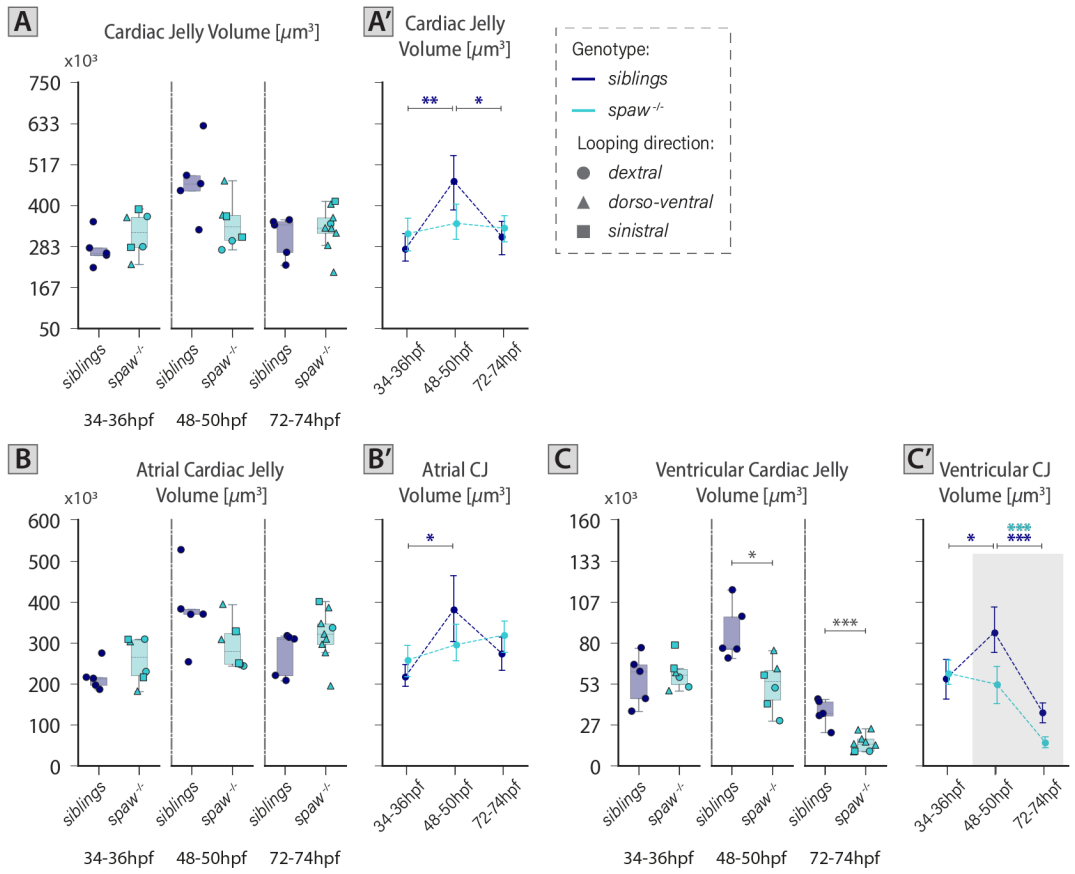

Fig 4.36. *spaw* regulates ECM volume in a chamber-specific manner throughout development.
A-B'. Quantification of cardiac jelly volume of the whole heart (A-A') and its chamber (B-B') in *spaw* mutants and siblings at 34-36hpf, 48-50hpf and 72-74hpf. The ventricular cardiac jelly is significantly reduced in *spaw* mutants at 48-50 and 72-74hpf when compared to their siblings (48-50hpf: *p-value=0.01065;* 72-74hpf: *p-value=0.00025*). A-B': Error bars with 95% confidence interval of the mean. 34-36hpf: *siblings n=5*, *spaw*$^{-/-}$ *n=6* (*sinistral n=2*, *dorso-ventral n=2*, *dextral n=2*); 48-50hpf: *siblings n=5*, *spaw*$^{-/-}$ *n=6* (*sinistral n=2*, *dorso-ventral n=2*, *dextral n=2*); 72-74hpf: *siblings n=5*, *spaw*$^{-/-}$ *n=9* (*sinistral n=1*, *dorso-ventral n=7*, *dextral n=1*). For details regarding the statistical analyses used to compare this set of data see *Note#4.7* (pg. 131). Only significant comparisons are shown. ***: *p-value*<0.001, **: *p-value*<0.01, *: *p-value*<0.05. CJ: Cardiac Jelly.

To further understand the ECM dynamics within different regions of the zebrafish heart and investigate whether the wild-type specific left-sided expansion of the ECM is linked to the dextral direction of looping morphogenesis, 3D cardiac jelly meshes of *spaw*$^{-/-}$ hearts were divided into the analogous left and right side regions of a wild-type heart (Fig 4.13B): a region comprising the outer curvature of the atrium (AOC) and inner curvature of the ventricle (VIC) (left: AOC,VIC) and a region comprising the inner curvature of the atrium (AIC) and outer curvature of the ventricle (VOC) (right: AIC,VOC) (Fig 4.37A-C'). The division of this mesh into these two newly defined heart ***sides*** standardises the regionalisation analysis into comparable regions regardless of the orientation of the heart within the embryo (i.e. direction of looping morphogenesis), allowing an unbiased analysis of this variable in *spaw*$^{-/-}$ hearts. Additionally, to identify if different looping directions alter the wild-type chamber-specific left-right ratio dynamics previously identified in wild-type embryos (Fig 4.14G,I), rather than analysing the left-to-right cardiac jelly volume ratio which might introduce some misleading differences for hearts with different looping directionalities, outer curvature-to-inner curvature (OC-to-IC) ratios per chamber will be presented.

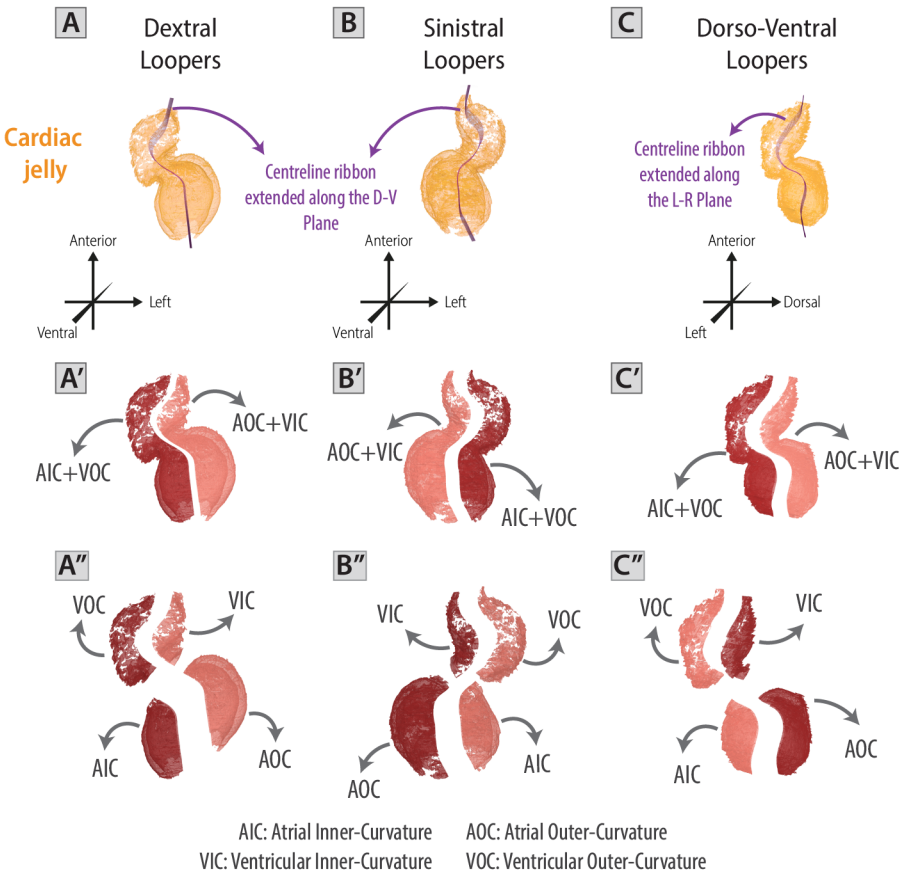

Fig 4.37. Dividing the cardiac jelly of dextral, sinistral and dorso-ventral loopers into side and chamber sections to further characterise cardiac jelly regionalisation.
A-C. Schematic illustrating the division of *spaw* dextral (A), sinistral (B), and dorso-ventral (C) loopers into side meshes corresponding to what was originally defined as left (from now termed AIC,VOC) and right (from now termed AOC,VIC) sides (see Fig 4.13B). Ventral face of the cardiac jelly tissue layer of a dextral (A) and sinistral (B) looped heart at 48-50hpf with its centreline ribbon (magenta) positioned to cut the tissue layer mesh into AOC,VIC and AOC,VIC sides. Left face of the cardiac jelly tissue layer of a dorso-ventral looped heart (C) at 48-50hpf with its centreline ribbon (magenta) positioned to cut the tissue layer mesh into the AOC,VIC and AOC,VIC sides. **A'-C'.** AOC,VIC and AOC,VIC regions of the cardiac jelly mesh obtained when cutting the cardiac ECM layer in A-C with the corresponding centreline ribbons. **A''-C''.** Further division of the resulting AIC,VOC and AOC,VIC regions into chambers (atrium and ventricle) results in four cardiac jelly sections which allow a more detailed characterisation of the ECM distribution throughout the heart. A-A'',B-B'': Ventral face with anterior to the top. C-C'': Left face with anterior to the top. D-V: dorso-ventral, AIC: Atrial Inner Curvature, AOC: Atrial Outer Curvature, VIC: Ventricular Inner Curvature, VOC: Ventricular Outer Curvature.

Quantification of the cardiac jelly volume in these newly defined *sides* identifies defects in the cardiac jelly of *spaw*$^{-/-}$ hearts characterised by an initially smaller ECM volume in the AOC,VIC region at 48-50hpf and a later expanded cardiac jelly volume in the AIC,VOC at 72-74hpf (Fig 4.38A-A'). Quantification of the ratio between the cardiac jelly comprising each *side* through time (similar to the left-to-right ratio presented earlier in the chapter, Fig 4.14E) identifies that despite having ratio values over 1 for all stages (indicating an AOC,VIC-sided thickening of this ECM layer), *spaw*$^{-/-}$ hearts present lower values for this ratio when compared to their siblings (Fig 4.39A-A'). To confirm whether these lower values for the *side* ratio (AOC,VIC/AIC,VOC) is the result of the combined dynamics of the cardiac jelly in each chamber (Fig 4.36B-C'), and deepen our understanding about the extent of the asymmetry within the individual chambers, AOC,VIC and AIC,VOC cardiac jelly meshes were divided into atrial and ventricular sections (Fig 4.37A''-C''), their volumes quantified, and the OC-to-IC ratio per chamber calculated (Fig 4.39B-C').

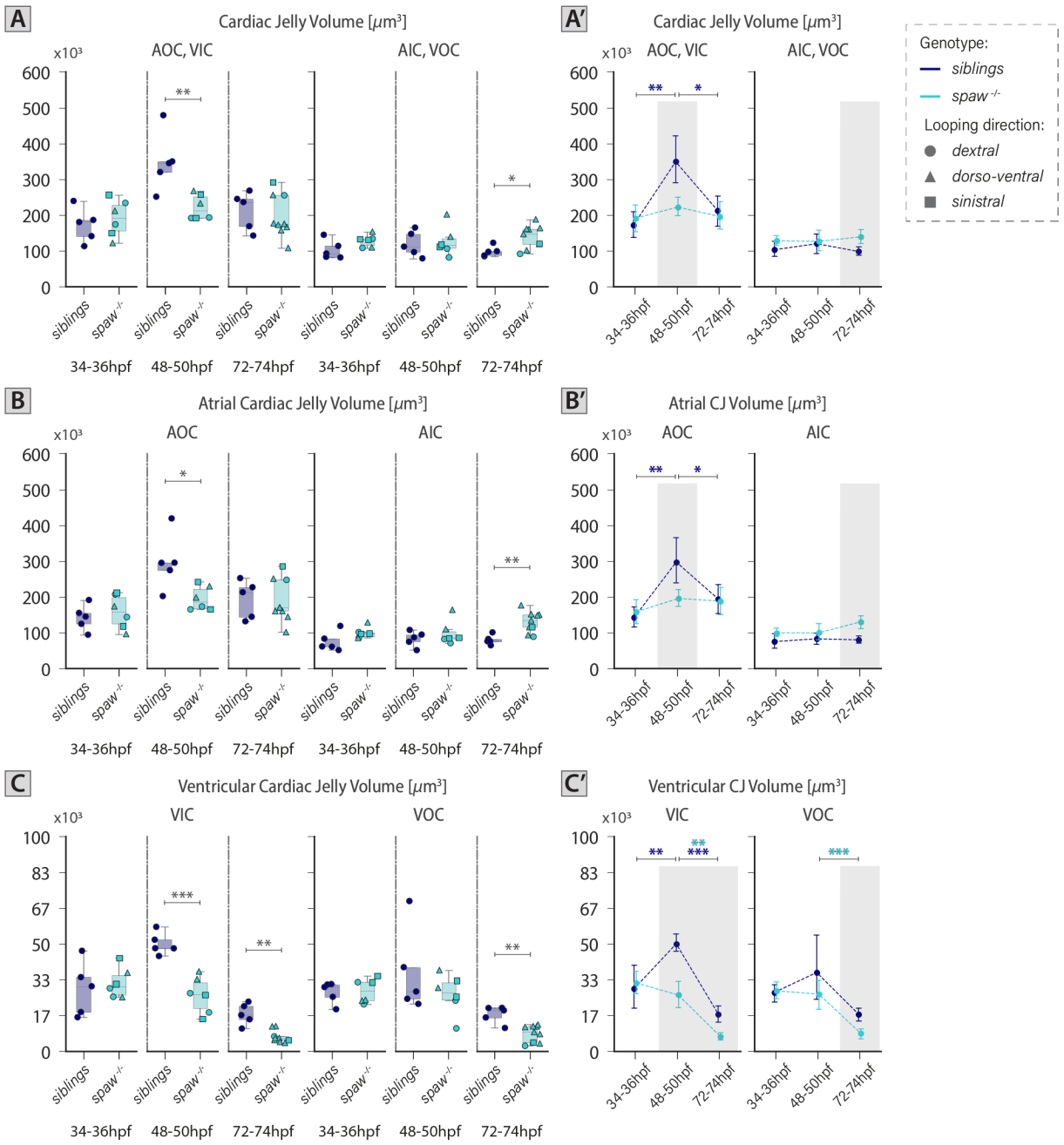

Fig 4.38. L/R patterning is required to regulate ECM dynamics in chamber and side specific regions throughout development.

A-A'. Quantification of the volume of cardiac jelly in the AOC,VIC and AIC,VOC in *spaw* mutants and their siblings at 34-36hpf, 48-50hpf and 72-74hpf. At 48-50hpf the AOC,VIC cardiac jelly volume is significantly reduced in *spaw* mutants when compared to their siblings (*p-value=0.00743*). At 72-74hpf the AOC,VIC cardiac jelly volume is significantly increased in *spaw* mutants when compared to their siblings (*p-value=0.02165*). **B-B'.** Quantification of the volume of the atrial outer curvature (AOC) and inner curvature (AIC) in *spaw* mutants and their siblings at 34-36hpf, 48-50hpf and 72-74hpf. At 48-50hpf the AOC cardiac jelly volume is significantly reduced in *spaw* mutants when compared to their siblings (*p-value=0.01746*). At 72-74hpf the AIC cardiac jelly volume is significantly increased in *spaw* mutants when compared to their siblings (*p-value=0.00363*). **C-C'.** Quantification of the volume of the ventricular outer curvature (VOC) and inner curvature (VIC) in *spaw* mutants and their siblings at 34-36hpf, 48-50hpf and 72-74hpf. At 48-50hpf the VIC cardiac jelly volume is significantly reduced in *spaw* mutants when compared to their siblings (*p-value=0.00041*). At 72-74hpf both the VOC and VIC cardiac jelly volumes are significantly reduced in *spaw* mutants when compared to their siblings (VOC: *p-value=0.00147;* VIC: *p-value=0.00766*). A-F: Error bars with 95% confidence interval of the mean. 34-36hpf: *siblings n=5*, *spaw$^{-/-}$ n=6* (*sinistral n=2*, *dorso-ventral n=2*, *dextral n=2*); 48-50hpf: *siblings n=5*, *spaw$^{-/-}$ n=6* (*sinistral n=2*, *dorso-ventral n=2*, *dextral n=2*); 72-74hpf: *siblings n=5*, *spaw$^{-/-}$ n=9* (*sinistral n=1*, *dorso-ventral n=7*, *dextral n=1*). For details regarding the statistical analyses used to compare this set of data see *Note#4.7*

(pg. 131). Only significant comparisons are shown. ***: *p-value*<0.001, **: *p-value*<0.01, *: *p-value*<0.05. CJ: Cardiac jelly, AIC: Atrial Inner Curvature, AOC: Atrial Outer Curvature, VIC: Ventricular Inner Curvature, VOC: Ventricular Outer Curvature.

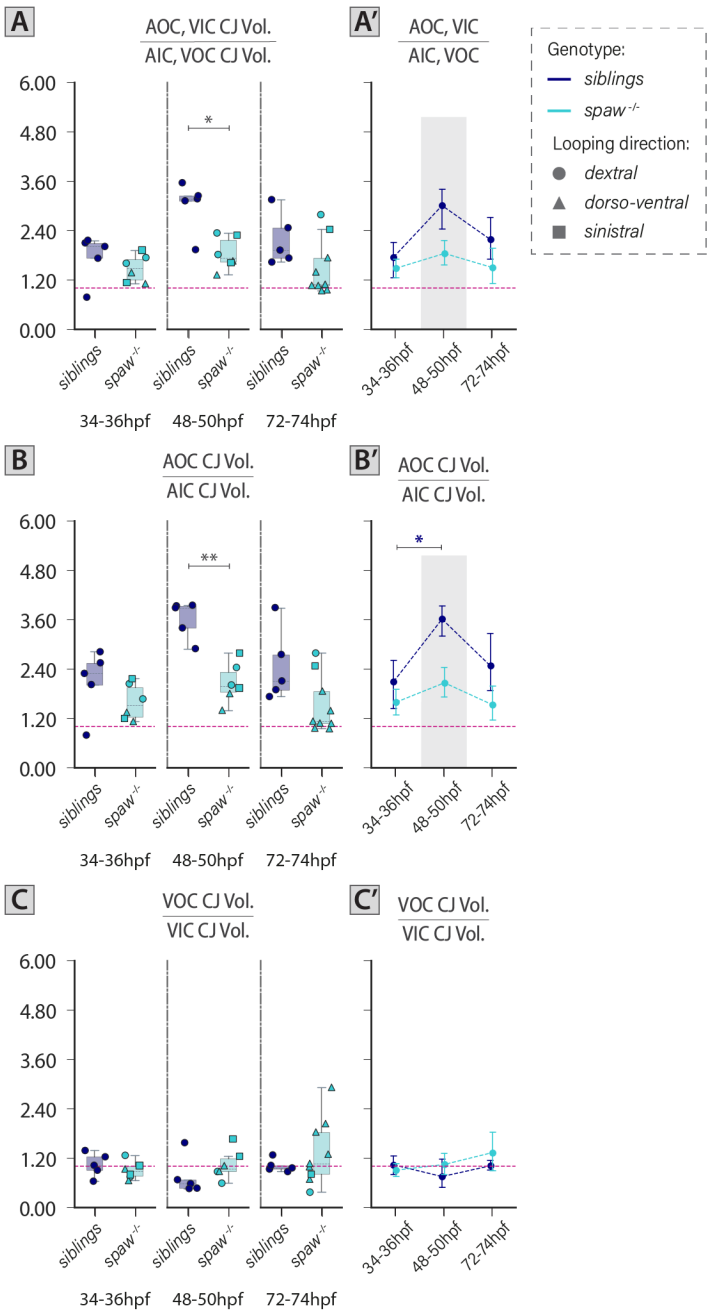

Fig 4.39. Spaw-driven L/R patterning is required for the correct establishment of the AOC-to-AIC ECM asymmetry in the developing heart.
A-A'. Quantification of the quotient between AOC, VIC and AIC, VOC cardiac jelly volumes in the heart in *spaw* mutants and their siblings at 34-36hpf, 48-50hpf and 72-74hpf (48-50hpf: *p-value=0.02248*). **B-B'.** Quantification of the quotient between AOC and AIC cardiac jelly volumes in the heart in *spaw* mutants and their siblings at 34-36hpf, 48-50hpf and 72-74hpf (48-50hpf: *p-value=0.00811*). **C-C'.** Quantification of the quotient between VOC and VIC cardiac jelly volumes in the heart in *spaw* mutants and their siblings at 34-36hpf, 48-50hpf and 72-74hpf. A-C': Error bars with 95% confidence interval of the mean. 34-36hpf: *siblings n=5*, *spaw$^{-/-}$ n=6* (*sinistral n=2*, *dorso-ventral n=2*, *dextral n=2*); 48-50hpf: *siblings n=5*, *spaw$^{-/-}$ n=6* (*sinistral n=2*, *dorso-ventral n=2*, *dextral n=2*); 72-74hpf: *siblings n=5*, *spaw$^{-/-}$ n=9* (*sinistral n=1*, *dorso-ventral n=7*, *dextral n=1*). For details regarding the statistical analyses used to compare this set of data see *Note#4.7* (pg. 131). Only significant comparisons are shown. **: *p-value*<0.01, *: *p-value*<0.05. CJ: Cardiac jelly, Vol: Volume, AIC: Atrial Inner Curvature, AOC: Atrial Outer Curvature, VIC: Ventricular Inner Curvature, VOC: Ventricular Outer Curvature.

Similar to the atrial cardiac jelly dynamics previously described (Fig 4.36B-B'), analysis of the cardiac ECM volume in the OC and IC of this chamber (AOC and AIC, respectively) identifies defects in the expansion and reduction of the ECM in *spaw$^{-/-}$* hearts when compared to their siblings (4.38B-B'). Interestingly, these defects are side-specific in this chamber (i.e. dynamics of ECM volume are differently affected in AOC and AIC) and occur in a non-simultaneous manner. Initially, as the heart undergoes looping and ballooning (36→48hpf), the slow ECM expansion is driven by the AOC while the cardiac ECM in the AIC remains constant. Later, as the heart transitions to an early maturing stage (50→72hpf), the slow cardiac jelly volume increase occurs in the AIC of *spaw$^{-/-}$* hearts, while the ECM in the AOC remains constant.

Examination of the ventricular cardiac ECM in the OC and IC identifies the same ECM degradation trend described for the ventricular ECM of *spaw*$^{-/-}$ hearts (Fig 4.36C-C') showing equal reduction rates through time for both curvatures of the chamber (Fig 4.38C-C'). The failure to expand the ECM in the ventricle results in a significantly smaller ECM volume in the VIC at 48-50hpf and in an overall reduced amount of cardiac ECM in both ventricular sides at 72-74hpf (Fig 4.38C-C').

OC-to-IC ratios per chamber confirms that despite the L/R patterning defect, *spaw*$^{-/-}$ hearts have an OC-to-IC ECM asymmetry (i.e. analogous to the left-to-right ECM asymmetry in wild-type heart, Fig 4.14E) that is driven throughout development by the atrial cardiac jelly (Fig 4.39B-C'), while the ventricular OC and IC ECM are maintained relatively equivalent. Analysis of the AOC-to-AIC ratio in *spaw*$^{-/-}$ hearts identifies that in spite of these ratio's values being in average always over 1, they are less than that of the control hearts, suggesting a role for Spaw in the correct establishment of the AOC-to-AIC ECM asymmetry. Surprisingly, despite the standardised division of the cardiac jelly mesh into analogous regions for different looping directions, a closer look at the AOC-to-AIC ratios identifies a segregation of these ratio's values between the lateralised (i.e. dextral and sinistral) and dorso-ventral loopers, with the ratios of the latter being always smaller than the former. This division in the AOC-to-AIC ratio values, indicates that *spaw*$^{-/-}$ dorso-ventral loopers have even less ECM asymmetry than *spaw*$^{-/-}$ lateralised loopers and suggests a more profound dysregulation of the atrial ECM dynamics is present when *spaw*$^{-/-}$ hearts fail to undergo a lateralised looping morphogenesis.

To complement this ECM volume analysis and confirm the asymmetries in the cardiac jelly of *spaw*$^{-/-}$ hearts regardless of their looping direction, 2D tissue thickness heatmaps of the cardiac ECM of *spaw*$^{-/-}$ hearts were acquired and analysed at the same stages of development (Fig 4.40A-B: 34-36hpf, C-D: 48-50hpf, and E-F: 72-74hpf). In general, similar to the analysis of myocardial ballooning heatmaps (Fig 4.34), the ECM thickness heatmap of dextrally looped *spaw*$^{-/-}$ look similar to that of a sibling heart and the ECM distribution of *spaw*$^{-/-}$ mutants sinistral loopers is almost the mirror image of the dextral loopers, with some minor variations depending on the heart.

Examination of the cardiac jelly thickness heatmaps of *spaw*$^{-/-}$ hearts during early cardiac morphogenesis reveals that despite the L/R patterning defects, the ECM of *spaw*$^{-/-}$ is regionalised, but this regionalisation manifests in different faces of the heart (i.e. ventral, left, right, or dorsal) depending on the heart's particular looping direction (Fig 4.40).

Closer analysis of the 2D **atrial** cardiac jelly thickness heatmaps identifies that *spaw*$^{-/-}$ hearts, **regardless of their looping direction, have thicker ECM regions in the OC of this chamber** (i.e. AOC). Subject to the looping direction of each heart, the OC of the atrium, hence the thicker ECM region, is positioned in the right, dorsal, or left heart face (sinistral, dorso-ventral and dextral loopers, respectively) (Fig 4.40). Not surprisingly, in all the analysed hearts, the next region presenting thicker ECM after the AOC is the AIC. The fact that sibling hearts have a heightened colour difference between these two atrial regions (AOC vs AIC) at 34-36 and 48-50hpf (Fig 4.40B,D), particularly when compared to the dorso-ventral loopers (Fig 4.40Aii,Cii), ratifies the lower OC-to-IC ratio values described for *spaw*$^{-/-}$ hearts (Fig 4.39B-B') and confirms that defective L/R patterning results in a reduction of atrial ECM asymmetry throughout early heart development. Additionally, abnormal atrial ECM expansion of *spaw*$^{-/-}$ hearts at 72-74hpf (Fig 4.36B-B') is confirmed when examining the thickness heatmaps of *spaw*$^{-/-}$ sinistral and dextral loopers (i.e. darker red colours in both the AOC and AIC in Fig 4.40Ei and Eiii, respectively), further supporting the hypothesis that timely regionalised ECM depletion is altered in *spaw*$^{-/-}$ hearts.

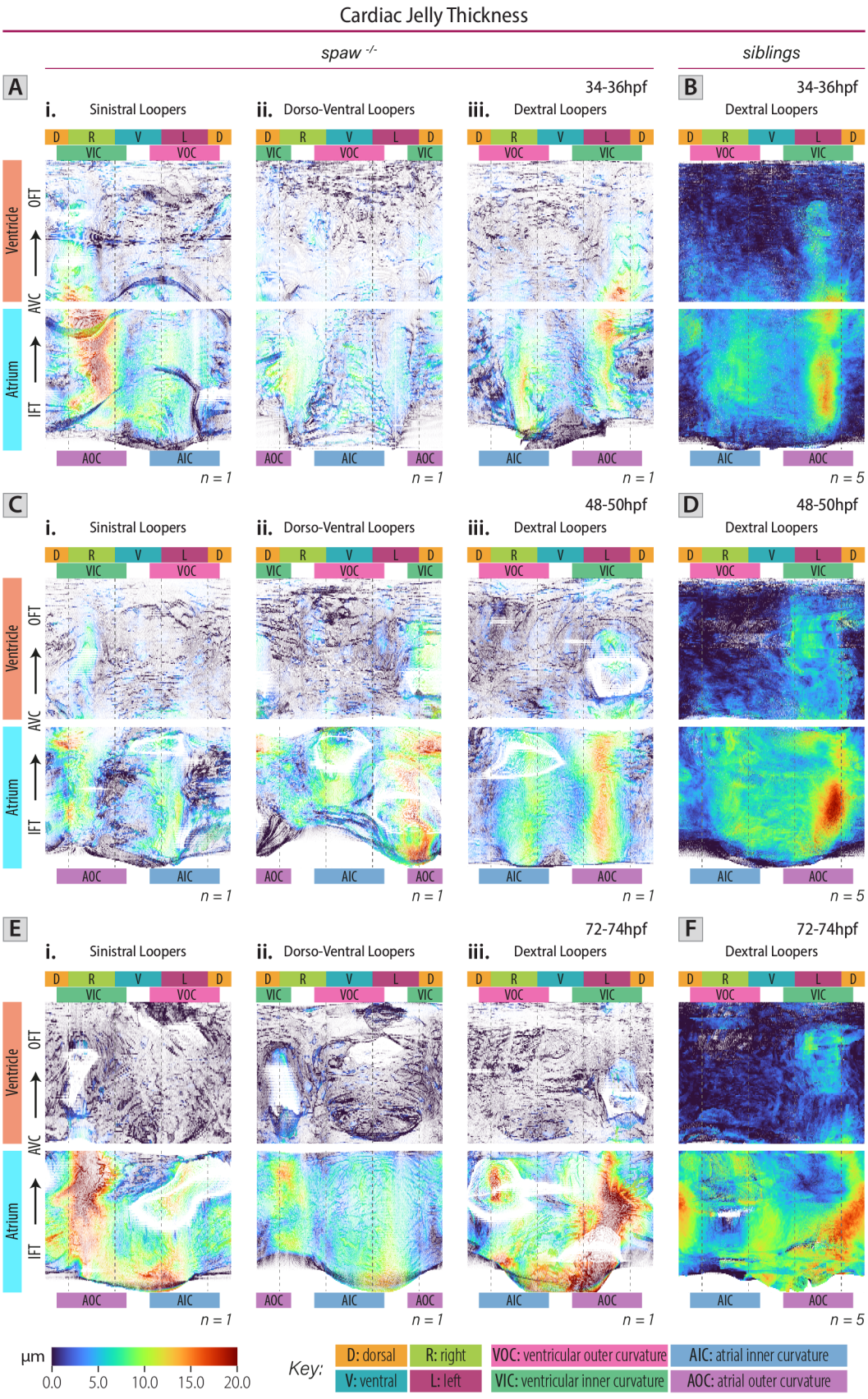

Fig 4.40. ECM regionalisation in the early *spaw* mutant hearts is maintained but mispositioned.
A-F. 2D representations of the cardiac jelly thickness of *spaw* mutant (A,C,E) and sibling (B, D, F) hearts at 34-36hpf (A-B), 48-50hpf (C-D) and 72-74hpf (E-F). *spaw* homozygous mutants are classified according to their direction of looping as: sinistral (i), dorso-ventral (ii) and dextral (iii) loopers. While A, C and E show examples of planar projection plots of individual embryos, B, D and F show the average planar projections of all the processed siblings at all the indicated stages. A-F share colour-scale presented with the key at the bottom-left

of the figure. D: Dorsal, R: Right, V: Ventral, L: Left, VOC: Ventricular Outer Curvature, VIC: Ventricular Inner Curvature, AOC: Atrial Outer Curvature, AIC: Atrial Inner Curvature, IFT: Inflow-tract, AVC: Atrioventricular Canal, OFT: Outflow-tract.

Due to the progressive reduction of cardiac jelly in the ventricle, the ventricular heatmaps of *spaw*$^{-/-}$ hearts between 48 and 74hpf show more regions with darker blue colours than the control hearts (Fig 4.40). However, similar to the atrium, throughout the stages of interest and irrespective of the looping direction, a ventricular region with thicker ECM is found in the IC of the ventricle (Fig 4.40). This ECM thickening pattern corroborates nicely with the literature where, as previously described, this region has been described as the last one to undergo trabeculation in zebrafish hearts (Rasouli and Stainier, 2017).

Together, analysis of ECM volume through time indicates that Spaw regulates the dynamics of ECM expansion and reduction in a chamber-specific manner (Fig 4.36B-C'). Interestingly, early looped *spaw*$^{-/-}$ hearts (34-36hpf) have no defects in the cardiac ECM volume in any of the investigated regions (i.e. AIC, AOC, VIC, VOC) when compared to their siblings (Fig 4.38B-C), suggesting Spaw's role comes into play after the early and native ECM has been set-up at tube stage, when it starts to be required for the regulation of the ECM volume in each chamber in a timely manner.

Quantification of *side* ratios in the heart and OC-to-IC ratios per chamber (Fig 4.39) confirms that even with disrupted L/R patterning, the ECM asymmetries in the heart are driven by the atrium. Standardisation of the regionalisation analysis into comparable regions regardless of the orientation of the heart (Fig 4.37) identified an AOC-sided thickening of the ECM layer throughout the analysed timeframe.

Together, analysis of the cardiac jelly volume distribution (Fig 4.36, 4.38, 4.39) and ECM thickness heatmap of hearts with different looping directions (Fig 4.40) identify that ECM regionalisation in *spaw*$^{-/-}$ hearts is maintained but mispositioned. This mispositioning of the ECM suggests that from 34hpf onwards, rather than an atrial-*left*-sided ECM expansion of the cardiac ECM, the cardiac jelly region that is specifically expanded, regardless of looping direction, is the atrial-*outer curvature*, proposing a model whereby in wild-type hearts laterality cues orient an early *left*-sided expansion of the cardiac ECM at tube stage (Derrick *et al.*, 2021), that translates into an atrial-*outer curvature* expansion as development progresses (Fig 4.14G, Fig 4.40C-F).

6 Chapter Conclusions

- *morphoHeart* analysis of wild-type zebrafish hearts at different developmental stages allowed the comprehensive description of *cardiac morphology* and *ECM-positioning* in 3D and throughout development.
- The characterisation of cardiac morphology and layer thickness/distribution throughout development aided the link between morphology and tissue dynamics to specific-heart developmental processes.
- While both chambers of the heart grow during looping and ballooning morphogenesis (34→50hpf), the atrium shrinks as the heart transitions to a maturing stage (50→72hpf).
- As the heart transitions to a maturing state (50→72hpf), atrial lumen volume is maintained despite atrium shrinkage.
- Looping and ballooning morphogenesis are concurrent processes in zebrafish heart development.
- Cardiac ECM expansion is associated with initial growth of the heart during looping morphogenesis (34→50hpf), and ECM degradation is subsequently linked to regionalised tissue shrinkage associated with chamber maturation (50→72hpf).

- The atrial-specific left-sided ECM expansion previously identified at 26hpf (Derrick et al., 2021) is maintained as the heart undergoes looping and ballooning, and its axis of regionalisation appears to be linked to the direction of atrial ballooning.
- Contrary to the established paradigm, 'middle' or 'non-looping' hearts with disrupted left-right patterning undergo looping morphogenesis in the dorso-ventral axis, positioning the ventricle ventral to the atrium.
- Asymmetric Nodal signalling regulates zebrafish chamber growth and regionalised ECM expansion in the AOC and VIC as the heart undergoes looping morphogenesis.
- Nodal mutants exhibit atrial ECM expansion in the AOC suggesting ECM-regionalisation is independent of Nodal signalling.
- Analysis of *spaw* mutant embryos suggests asymmetric Nodal signalling positions the axis of ECM asymmetry in the early zebrafish heart, influencing chamber-specific dynamics during heart growth and looping morphogenesis.

7 CHAPTER DISCUSSION

In this study, I present for the first time a **detailed 3D morphometric analysis of zebrafish heart development** that includes a thorough characterisation of the spatiotemporal changes undergone by the primitive heart, its chambers, and individual layers, offering novel quantitative insights into the relationship between tissue and ECM dynamics in organ morphogenesis.

7.1 3D MORPHOMETRIC ANALYSIS OF WILD-TYPE HEARTS AT MULTIPLE DEVELOPMENTAL STAGES REVEALS PREVIOUSLY NOT DESCRIBED MORPHOGENETIC EVENTS DURING ZEBRAFISH CARDIAC DEVELOPMENT

Heart morphogenesis is a complex asymmetric process that requires the timely coordination of distinct events to form a mature heart. One of the most important stages in vertebrate heart development takes place when the heart undergoes cardiac looping. In this process, the linear heart tube experiences a series of morphological rearrangements that breaks its bilateral symmetry, transitioning from a simple linear tube to an S-shaped dextrally-looped organ (Männer, 2009; Lombardo *et al.*, 2019). As cardiac looping progresses, the chambers of the heart expand anisotropically along their outer curvatures, acquiring a characteristic bean-shaped morphology in a process known as chamber ballooning (Christoffels *et al.*, 2000; Bakkers, 2011). The highly asymmetric process of looping morphogenesis is critical for ensuring the correct alignment of the future chambers and the inflow and outflow tracts of the mature heart (Srivastava and Olson, 2000; Ramsdell, 2005; Männer, 2009; Desgrange, Le Garrec and Meilhac, 2018) so that subsequent processes such as chamber septation and valve formation result in a multi-chambered functional organ. Since the ultimate purpose of a heart to pump blood throughout the whole body, distributing oxygen and nutrients and removing waste, and considering zebrafish start relying on their circulatory system at 7dpf (Pelster and Bagatto, 2010), all the morphogenetic events happening during these early stages of heart development might ensure the shape and size of this organ are sufficient to sustain the embryo's ongoing development and life.

Using *morphoHeart,* I have shown that the complex 3D morphological changes undergone by the zebrafish cardiac chambers and its tissue layers (myocardium, endocardium, **and cardiac jelly**) during cardiac development can be observed and characterised by performing a comparative analysis of 3D morphometric parameters in wild-type hearts at different key developmental stages.

Analysis of zebrafish cardiac morphogenesis using this tool allowed me to characterise gross changes in heart size, identifying growth of both chambers (and their lumen) as the heart transitions from a linear tube to a looped and ballooned organ (34→50hpf, Fig 4.1B-C). Logically, the growth and development of

an organ is normally accompanied by an increase in the tissue volume of its comprising tissue layers. Unexpectedly, analyses of myocardial and endocardial tissue volume per cardiac chamber between 34 and 50hpf identified that despite chamber growth, only the ventricular endocardium significantly increases its volume as the heart undergoes looping (Fig 4.8C,E). That myocardial tissue volume is maintained constant in both chambers between 34 and 50hpf suggests the need for a tight coordination of cardiomyocyte cell size in a growing heart where newly differentiated cells are being added to each chamber (de Pater *et al.*, 2009; Hami *et al.*, 2011; Lazic and Scott, 2011; Zhou *et al.*, 2011). Following this line of thought, hypertrophic growth of cardiomyocytes in the ventricle between 36 and 48hpf (Lin, Swinburne and Yelon, 2012) indicates the magnitude of chamber growth exceeds that of the newly added cardiomyocytes, possibly resulting in heterogeneous cardiomyocyte enlargement during looping and chamber ballooning to sustain the required chamber growth.

Previous studies have shown that within a similar timeframe (30→54hpf rather than 34→50hpf), endocardial chamber expansion involves cell proliferation and chamber-specific changes in cell surface area: atrial cells increase their surface area while ventricular cells decrease it (Dietrich *et al.*, 2014). These findings complement the endocardial tissue volume quantifications here presented and suggest that similar to the myocardium, a tight and chamber-specific balance between endocardial cell-proliferation and cell-size modifications is required to ensure chamber growth in a cellular tissue layer whose volume is either being increased (i.e. ventricular endocardium) or kept constant (i.e. atrial endocardium) (Fig 4.8E).

Together these findings suggest both cellular tissue layers undergo different chamber-specific processes of remodelling while the asymmetric processes of looping and ballooning are taking place in the heart.

Concurrent to these early processes of chamber growth and concomitant maintenance of tissue volume, the heart undergoes the highly asymmetric event of looping morphogenesis. Investigation of different morphometric parameters that characterise chamber morphology, orientation and heart looping aided the understanding of the compound morphogenetic events that need to occur for looping morphogenesis to take place and identified the ventricle as the main chamber driving this asymmetric process. In general, a combination of ventricular elongation, widening (Fig 4.2H,I) and sagittal and frontal rotations (Fig 4.3D, 4,4D) displace the ventricle caudally over the yolk, relocating the OFT and positioning the ventricle to the right side of the atrium. Alongside these ventricular movements, the atrium increases its depth (Fig 4.2B) while largely maintaining its frontal and sagittal orientation (atrial ventral rotations <10°), facilitating the foundation of the heart bend, the establishment of the chamber's apexes and curvatures and the distinct AVC constriction. This combination of frontal and sagittal rotations experienced by the ventricle suggests that, contrary to previous studies (Lombardo *et al.*, 2019), the deformation of the linear heart tube into an S-shaped loop does not solely take place in the embryo's frontal plane, exposing the three-dimensionality of the tissue rearrangements involved in looping morphogenesis. As measurements were not taken with a global reference point, it results challenging to confirm whether the morphological rearrangements involve a cranial shift of the atrium (pulling the ventricle into a new position), or a caudal movement of the ventricle (pushing down the atrium). Nevertheless, the assumption that the arterial (OFT) and venous (IFT) poles of the heart are *constrained* to move only along the linear heart length, identify that most of the orientation changes within this local coordinate system are driven by the ventricle, somehow confirming the ventricle as the main chamber driving the rearrangement of the heart during looping morphogenesis.

Studies in other animal models have not only corroborated the three-dimensionality of looping morphogenesis process by describing the sequential frontal (left/right) and transverse (cranial/caudal) rotations of the chamber segments and OFT (chick: (Thompson, Abercrombie and Wong, 1987), mouse: (Meilhac *et al.*, 2004; Bajolle *et al.*, 2006)) involved in the sub-processes/phases that comprise looping morphogenesis, but also described the principal role played by the ventricle during this asymmetric process of looping (Männer, 2000, 2009). Altogether this suggests that the ventricular shifts and rotations

underpinning chamber rearrangements during cardiac looping morphogenesis may be conserved across species.

Having identified the combination of rotations and chamber-morphology changes experienced by the heart during looping morphogenesis, this raises the question as to which mechanisms could be driving these ventricular rotations that constitute the basis of looping morphogenesis. Two recent complementary zebrafish studies have described a torsional winding of the heart tube that contributes to the S-shaped bending during cardiac looping (28-54hpf) (Lombardo *et al.*, 2019; Tessadori *et al.*, 2021). This cardiac twist, characterised by a rotation of the heart chambers in opposite directions around the AVC (and more strongly at the arterial pole, similar to what has been described in mouse (Le Garrec *et al.*, 2017)), suggests an active rearrangement of the ventricular tissue, which could result in the set of topographical relationships characterised by the ventricular rotations here described. Possible mechanisms underpinning this torsional winding, such as ingression of SHF cells to the embryonic cardiac poles (Zhou *et al.*, 2011; Kelly, Buckingham and Moorman, 2014; Le Garrec *et al.*, 2017), hemodynamic forces or heart contractility (Auman *et al.*, 2007), as well as anisotropic changes in cell shapes or sizes within the myocardial wall of the heart tube (Taber, 2006; Lin, Swinburne and Yelon, 2012; Shi *et al.*, 2014) were investigated as part of these studies.

Although addition of cardiomyocytes to the cardiac poles of the heart tube occurs within this timeframe (de Pater *et al.*, 2009; Hami *et al.*, 2011; Lazic and Scott, 2011; Zhou *et al.*, 2011) the fact that this cardiac twist still takes place in hearts in which addition of SHF cells has been avoided, either by explanting the heart tubes or by chemical inhibition, suggested that SHF ingression is dispensable for zebrafish cardiac looping at least between 28 and 38hpf (Tessadori *et al.*, 2021). Investigation of the cardiac twist and SHF addition at stages of development later than those studied by Tessadori *et al* (>38hpf), would confirm this mechanism is independent of cell ingression or, as others have described in zebrafish and mouse, dependent on it (de Pater *et al.*, 2009; Lazic and Scott, 2011; Zhou *et al.*, 2011; Le Garrec *et al.*, 2017). In a similar approach, evaluation of the torsional winding in hearts in which cardiac contractions were suppressed by injecting a *tnnt2a* MO (Lombardo *et al.*, 2019; Tessadori *et al.*, 2021), demonstrated that despite changes in the S-looped morphology of the hearts, blood flow and cardiac contractility is not required for cardiac twisting, and suggesting asymmetric changes in cardiomyocytes shape and size might be the driving force of this torsional rotation of the heart tube. Indeed, both studies identified that anisotropic growth of cardiomyocytes along the chamber's outer curvatures is the main mechanism that contributes to the torsional winding and the emergence of the S-shaped morphology of the zebrafish heart (Lombardo *et al.*, 2019; Tessadori *et al.*, 2021). Together this suggests that regionalised anisotropic cell shape changes accompany cardiac looping, setting the topographical relationship between the heart chambers described by the ventricular rotations here presented (Fig 4.3D, 4.4D). Interestingly, the cell count and IND analyses presented here are in tune with this concept of anisotropic changes in cell shapes or sizes within the myocardial wall and suggest that this intrinsic bending mechanism may be also one of the mechanisms driving the early maturation of the heart (Fig 4.10, 4.11).

Once the heart has undergone looping and ballooning morphogenesis, ongoing development involves a series of morphogenetic processes that adjust the positional relationship between chambers, so that maturation processes such as trabeculation can start to take place. While numerous studies have focussed in understanding the processes that drive looping morphogenesis, few have characterised the morphological characteristics of the chambers and their topographical relationship or investigated how these parameters evolve post-looping setting up an early maturing heart.

Here, I have shown that an interesting and previously not described atrial compaction and frontal rotation take place between 50 and 72hpf. Strikingly, despite this compaction event, the chamber preserves its blood filling and pumping capacity, suggesting other tissue layers make space to maintain this atrial lumen. Indeed, combinatorial analyses of myocardial and endocardial tissue volume and thickness heatmaps

identify an atrial-specific reduction in the tissue volume and overall thickness (Fig 4.8, 4.9C, 4.12C) of both tissue layers, which take place concomitant with atrial compaction. These findings suggest a myocardial and endocardial wall 'thinning' process is involved in the maturation of this compacting chamber. Maturation of the ventricle between this timeframe (50→72hpf) on the other hand, preserves the already attained chamber and lumen size (Fig 4.1D,F) with the volume of both cellular tissue layers also kept constant. Maintenance of cellular tissue volume in this chamber may be explained by the onset of trabeculation, altogether suggesting timely changes in myocardial and endocardial tissue volume and distribution support chamber-specific processes of remodelling as the heart undergoes early maturation.

7.2 Looping and ballooning are concurrent processes during zebrafish heart development

A novel way through which chamber growth can be investigated is by the use of 2D myocardial ballooning heatmaps, which, as shown throughout this chapter, provide a huge amount of information regarding chamber morphology and rearrangement (Fig 4.7,4.34).

Early studies carried out at the beginning of the 1900's defined cardiac looping and ballooning in animal models other than zebrafish. In these studies, cardiac looping was defined as the process that '*bring(s) the segments of the heart tube, and the developing great vessels approximately into their definitive topographical relationship*' (Männer, 2009). Interestingly, such a broad/general definition has generated a confusion in the field when defining the phases involved in cardiac looping, as a consensus has not been reached regarding the morphology that defines the 'pre-looped' and 'looped end-point' stages of this process, resulting in sometimes the inclusion of ballooning as a process that is either part or succeeding looping morphogenesis (Männer, 2000, 2009; Moorman et al., 2003).

Interestingly, when comparing the myocardial ballooning heatmap colour-pattern of the early looping zebrafish heart (34-36hpf, Fig 4.7A'') and that of a heart that is undergoing the commonly-defined transition between looping and ballooning (48-50hpf, Fig 4.7B''), one can clearly identify that both processes are occurring simultaneously between these two timepoint in the zebrafish heart. As early as 34hpf I was able to witness that both chambers of the developing heart not only have started to expand/grow deviating from its tubular shape (shown by a 'U' shape pattern across the ventral face of the heart) but also started to show a defined outer curvature indicating the onset of looping morphogenesis (also confirmed by looping ratio values >1, Fig 4.5D). Between 34 and 50hpf the ballooning process of both chambers becomes intensified, as depicted in the 2D heatmaps by a maintenance of the 'U'-shaped pattern, but with 'redder' colours. Simultaneous to ballooning, ongoing looping is also identified in the heatmaps by tissue rearrangements that lead to the emergence of outer and inner curvatures and apices in both chambers, while maintaining a constriction around the AVC. Ongoing looping is additionally confirmed by a progressive increase in looping ratio values between 34 and 50hpf (Fig 4.5D).

Due to the discrete approach taken in this study, the 'end-point' stage(s) to each of these processes after 50hpf remains unknown. What is known and has been revealed in this study is that by 72hpf, both looping and ballooning have finished: looping ratio is no longer increasing and is instead maintained (Fig 4.5D), and the atrium compacts while the ventricle preserves its acquired size (Fig 4.1D). Complementing this statement, a change in the 'U'-shaped pattern of the myocardial ballooning heatmap at 72-74hpf suggest these heatmaps are no longer representing the process of chamber ballooning characterised by chamber expansion, but of chamber and tissue remodelling characteristic of early maturation stages. Altogether, suggesting looping and ballooning morphogenesis in zebrafish hearts are simultaneous yet not sequential processes, which conclude at a stage between 50 and 72hpf, and are followed by chamber remodelling, including atrial compaction, and the onset of trabeculation.

7.3 REGIONAL CELL SHRINKING CONTRIBUTES TO CHAMBER-SPECIFIC REMODELLING POST-LOOPING MORPHOGENESIS

Combining the results obtained from the analyses of cardiomyocyte counts, IND (per chamber and region), myocardial tissue volume and thickness heatmaps has provided novel insights regarding the dynamics involved in regional maturation and rearrangement of the myocardium at 72hpf. Between 50 and 72hpf, cell count analysis identified an increase in total cardiomyocytes, driven mainly by an increase in the number of cells making up the ventricle (while cell numbers in the atrium remained constant) (Fig 4.10C,D). The difference in the increase in cell numbers making up the atrium and ventricle might be the result of the onset of chamber-specific refinement processes driven by different mechanisms. Two mechanisms that could be driving the ventricular increase in cardiomyocytes are: the addition of cells from the SHF to the arterial pole of the heart (Kula-Alwar *et al.*, 2021) and/or the proliferation involved in the formation of trabecular seeds and trabeculae (Liu *et al.*, 2010; Peshkovsky, Totong and Yelon, 2011; Uribe *et al.*, 2018; Kula-Alwar *et al.*, 2021).

Interestingly within this time frame, both the size and myocardial volume of the atrium are getting reduced while being maintained in the ventricle (Fig 4.1D, Fig 4.8C), suggesting a reduction in cell size in both chambers as the heart transitions to an early maturing stage. IND analysis per chamber confirms this hypothesis, identifying significant reductions in cell size in both chambers (Fig 4.10F).

To more granularly understand how these newly added cardiomyocytes and tissue rearrangements change the distribution or packing of cells within each chamber's tissue, chambers were divided into 4 distinct regions (i.e. dorsal face, ventral face, outer curvature, and inner curvature) and the IND distance within these regions at these two timepoints were analysed. Interestingly, comparison of regional IND between 50 and 72hpf revealed highly dynamic changes of cell size in distinct regions that nicely matched the changes observed in the myocardial tissue thickness heatmaps and the associated specific processes of maturation experienced by each chamber (atrial compaction and ventricular trabeculation). This suggests regional cell shrinking may contribute to chamber-specific remodelling post-looping and ballooning morphogenesis, and confirms these combinatorial analyses aids the understanding of regionalised tissue rearrangements occurring during heart development.

Indeed, as previously described, several lines of evidence suggest that anisotropic and heterogeneous epithelial remodelling is an important driver for tissue morphogenesis (Davis *et al.*, 2008; Lin, Swinburne and Yelon, 2012; Ray *et al.*, 2018; Lombardo *et al.*, 2019). In line with these studies, the anisotropic cardiomyocyte shrinking identified in the atrium between 50 and 72hpf, could be the driving force that aids simultaneously the compaction and frontal rotation of this chamber, in a direction opposite to that that had originally accompanied this chamber's growth (Fig 4.3).

Together, the analysis of 3D datasets like the ones here presented allowed the analysis of the 3D distribution of cells around the heart in a way in which details regarding cellular packing of the chamber regions could be uncovered and their dynamics analysed. Since the heart is a 3D organ, analysis like the ones presented in this thesis could improve upon analyses done using 2D image projections, and could help identify and describe more accurately distinct cellular processes involved in tissue morphogenesis (e.g. cell intercalation, cellular size changes, wall 'thinning') and bring them back into a tissue/organ level context. For example, a combination of multi-colour mosaic labelling tools (Staudt *et al.*, 2014; Foglia *et al.*, 2016; Lombardo *et al.*, 2019), prospective gating imaging set-ups and the 3D processing ability provided by *morphoHeart* would allow a more in-depth description of the highly dynamic 3D changes of cell morphologies within chambers and regions, gaining a better understanding of their contribution to tissue growth/rearrangement and organ morphogenesis.

7.4 A LEFT-SIDED ATRIAL-SPECIFIC EXPANSION OF THE CARDIAC ECM CHARACTERISES EARLY ZEBRAFISH HEART DEVELOPMENT

The cardiac ECM, which lies between the outer myocardial tube and inner endocardial layer (Lockhart *et al.*, 2011a; De Angelis *et al.*, 2017; Rasouli and Stainier, 2017; Derrick *et al.*, 2021), is like other ECMs a complex array of highly cross-linked macromolecules that provides structural support to cells and tissues and defines the physical and chemical interactions that modulate cellular physiology and fate (Byron, Humphries and Humphries, 2013; Mouw, Ou and Weaver, 2014). Being a dynamic structure, the ECM is continuously deposited, modified and degraded in response to developmental processes, injury and disease (Lu *et al.*, 2011; Humphrey, Dufresne and Schwartz, 2014). Given the importance of the ECM during development, to better characterise cardiac ECM dynamics and understand how this cardiac ECM helps sculpt the heart during early cardiac morphogenesis, I used *morphoHeart* to extract the first 3D reconstructions of the ECM-space from a live embryo at different key developmental stages.

Analysis of cardiac jelly volume and gross distribution suggests ECM expansion in both chambers is associated with the initial growth of the heart during looping and ballooning morphogenesis (34→50hpf), while ECM reduction possibly driven by degradation is subsequently linked to chamber-specific processes of remodelling important for chamber maturation.

ECM thickness analysis allowed a more granular inspection of cardiac jelly organisation and distribution additionally revealing that the cardiac ECM is regionalised in both chambers, but this regionalisation manifests differently in each chamber. In general, as looping and ballooning progresses, in the atrium, the cardiac jelly regionalisation encompasses a thickening in the outer and inner curvatures (left and right sides), with the former region presenting thicker ECM. In the ventricle on the other hand, the cardiac ECM gets specifically thicker along this chamber's inner curvature, while the rest of the chamber presents a homogeneously thinner ECM. Ongoing maturation modifies the distribution of the atrial ECM, relocalising the outer curvature thickening to the dorsal face as the chamber remodels.

Further detailed investigation of these thickness heatmaps identified thickening of the ECM in specific regions which could be linked to ongoing morphogenetic and functional processes in each heart chamber, two of which will be described below.

Examination of the cardiac jelly thickness heatmaps at 34-36 and 48-50hpf exposes a distinct region with thickened ECM in the inner curvature of the atrium, close to the venous pole, and exactly in the same area where previous studies have located the zebrafish pacemaker/sinoatrial node cells (de Pater *et al.*, 2009; Arrenberg *et al.*, 2010). Consistent with this observation, studies in other animal models have identified that the nodal cells comprising the sinoatrial node are embedded within a biochemically and biomechanically distinct ECM that serves as a protective scaffold to the pacemaker cardiomyocytes reducing the mechanical strain and mechanotransduction they would experience from continuous contractions every time the heart beats (Gluck *et al.*, 2017).

Reductions in the cardiac jelly throughout the heart identified by ECM volume quantifications (Fig 4.14) and cardiac jelly thickness heatmaps (Fix 4.15), are in line with previous studies in mice, chick, and zebrafish in which reduction of the cardiac ECM during development was described (Stankunas *et al.*, 2008; Rasouli and Stainier, 2017). Indeed, the particular reductions in the ventricular cardiac jelly identified between 50 and 72hpf (Fig 4.15C), corresponds with the onset of trabeculation in this chamber, a process that has been linked to specific dynamics of ECM remodelling (Stankunas *et al.*, 2008; Rasouli and Stainier, 2017; del Monte-Nieto *et al.*, 2018). Notably, between these timepoints the only region of the ventricle which maintains thicker ECM is the inner curvature of this chamber (Fig 4.15C). This observation correlates effectively with the literature describing the inner curvature of the ventricle as the last ventricular region to undergo trabeculation in zebrafish heart (Rasouli and Stainier, 2017), hence confirming that the maintenance of cardiac ECM (separating the myocardium from the endocardium) is important to avoid

the early onset of trabeculation in this particular region of the ventricle (Passer *et al.*, 2016; Rasouli and Stainier, 2017; del Monte-Nieto *et al.*, 2018) and reflecting that differences in ECM organisation are required within this chamber to timely and regionally initiate trabeculation.

Quantifications of the cardiac jelly volume comprising each chamber's side (atrial/ventricular - left/right) confirms our previously published observations of an atrial-left-sided expansion of the cardiac ECM prior to looping morphogenesis (Derrick *et al.*, 2021) (see Appendix 1) and demonstrates for the first time that this expansion is maintained as the heart undergoes looping, ballooning, and early maturing (Fig 4.14I). These results are in agreement with previous studies in which the cardiac jelly of chick embryos was described as unevenly thick, displaying greater thickness in the left-right regions of the heart tube when compared to the antero-posterior regions (Männer *et al.*, 2008; Männer, Wessel and Yelbuz, 2010; Ramasubramanian *et al.*, 2013) and suggesting the asymmetry of this layer during cardiac morphogenesis may be conserved across species.

The characteristic expansion, shrinkage, and asymmetry of the cardiac ECM during early cardiac morphogenesis suggests precise spatiotemporal regulation of different ECM components that create and stabilise these asymmetries is essential for normal cardiac development. mRNA expression analysis of interstitial matrix components demonstrates dynamic spatial and temporal changes in the composition of the ECM as the heart develops, remodels, and matures. Early expression of GAG synthases, core proteins, and link proteins at disc and tube stages suggests the synthesis of heart-specific ECM may be required early in development to set up an ideal and asymmetric ECM environment that supports subsequent processes of growth during looping and ballooning morphogenesis. Furthermore, the specific expression of hyaluronidases by different tissues and within different regions of the chambers at 50hpf corroborates the cardiac ECM volume dynamics identified between 50 and 72hpf and suggests this layer undergoes regionalised HA degradation as the heart transitions to an early maturing state.

Surprisingly, none of the GAG synthases and core proteins that have previously been implicated in heart development (Mjaatvedt *et al.*, 1998; Zanin *et al.*, 1999; Patra *et al.*, 2011; Mittal *et al.*, 2013; Rambeau *et al.*, 2017) and that could be likely involved in ECM regionalisation due to their ability to sequester water within the ECM, exhibit asymmetric expression in the heart tube. Interestingly, the link proteins, *hapln1a* and *hapln1b* did exhibit asymmetric expression at this early stage, suggesting they could promote the establishment of this ECM regionalisation during early cardiac development.

7.5 NODAL SIGNALLING PROMOTES TIMELY GROWTH OF THE HEART DURING LOOPING AND BALLOONING MORPHOGENESIS

The asymmetric expression of Nodal-related genes is theorised to be the driving force of organ laterality (Levin *et al.*, 1997; Brennan, Norris and Robertson, 2002; Levin, 2005). However, in Nodal mutants, looping morphogenesis still takes place but in a randomised direction, suggesting the existence of an additional mechanism intrinsic to the organ for generating this random asymmetry (Brown and Wolpert, 1990; Noël *et al.*, 2013). While recent analysis of mouse Nodal mutants have elegantly shown the complexities in characterising heart morphogenesis and described laterality defects with 3D reconstructions and quantifications (Desgrange, Lokmer, *et al.*, 2019; Desgrange *et al.*, 2020), despite the imaging advantages offered by zebrafish, characterisation of laterality defects in zebrafish have remained relatively simplistic. Expanding on these studies, I used *morphoHeart* to characterise the dynamics of morphogenesis in zebrafish embryos with disrupted L/R patterning.

As this was the first time an in-depth 3D morphological characterisation was being performed in zebrafish *spaw*$^{-/-}$, to simplify the analysis, mutant hearts were classified according to their apparent looping directionality. Nevertheless, as mutant hearts were segmented, subtle differences in morphology were identified even in those classified with the same looping direction. Future analysis of the 3D morphometric

parameters with clustering methods (e.g. k-means, principal component analysis) could address whether zebrafish *spaw*$^{-/-}$ phenotypes represent a continuum or can be classified as distinct discrete classes -like those described in mouse Nodal mutants (Desgrange *et al.*, 2020). Implementation of this type of analysis will provide a better description of all the possible phenotypes characteristic of zebrafish embryos with disrupted L/R patterning, which combined with cardiac tissue and ECM distribution analyses will deliver revealing insights into the complex dynamics driving the morphogenesis of these mutant hearts.

Taking advantage of the enhanced morphological analysis I could attain with *morphoHeart*, *spaw* mutant hearts with different looping directions were processed at early looping, during looping and ballooning and at early maturing stages, allowing the first detailed description of the 3D morphological dynamics that characterise these hearts with altered asymmetric *spaw* expression.

Gross morphological analyses from the 3D reconstructions revealed interesting observations regarding the morphology of hearts that had undergone dextral, sinistral or no heart looping (middle/no loopers). In spite of the fact that the progression of looping morphogenesis in *spaw*$^{-/-}$ dextral loopers is in the correct anatomical direction, these hearts display abnormal morphology characterised by a loose and elongated configuration of the chambers. This result suggests that loss of L/R patterning not only has an impact upon looping directionality but also on the shaping of this organ. This dextral phenotype is corroborated with the morphology of *spaw*$^{-/-}$ sinistral loopers, which display a mirrored morphology of that of their dextral counterparts with a relaxed yet looped configuration of the chambers. In addition, 3D morphological analysis surprisingly revealed that *spaw*$^{-/-}$ middle loopers, different to how they have been described (Chen *et al.*, 1997; Grimes *et al.*, 2020), do undergo looping morphogenesis but in a dorso-ventral direction. Supporting these results and similar to mouse Nodal mutants (Desgrange *et al.*, 2020), analysis of looping morphogenesis in all *spaw* mutants regardless of their looping direction, identified looping ratio values that despite being statistically reduced when compared to that of their siblings, indicated some degree of heart looping (looping ratios >1.0, Fig 4.32).

Quantification of heart/chamber size during early heart developmental stages identified defects in chamber growth dynamics in *spaw*$^{-/-}$ hearts that span from early looping (34-36hpf) until early maturing stages (72-74hpf). Between these timepoints, both *spaw*$^{-/-}$ chambers fail to undergo the extent of expansion-compaction identified in wild-type hearts (Fig 4.1D), resulting in chambers with a significantly smaller size during looping and ballooning (48-50hpf, Fig 4.25B-B'). Interestingly, post-looping and when the hearts transition to a maturing stage (72-74hpf), similar to mouse models of laterality (Desgrange *et al.*, 2020), no defects in chamber size are identified in *spaw*$^{-/-}$ (Fig 4.25B). These chamber growth defects identified at intermediate stages (48-50hpf) suggest that *spaw*$^{-/-}$ hearts fail to undergo the same chamber- and region-specific tissue rearrangements that accompany the wild-type processes of chamber growth and compaction, possibly resulting in hearts with different tissue organisations at an early maturing stage. Further studies are required to investigate the mechanisms impacted by the loss of Nodal that produce chamber growth defects, and the possible consequences these defects might have in the continuous development of *spaw* mutant hearts. However, the analysis presented here highlights the importance of assessing morphogenesis across time to better underpin the onset and possible consequences of the dynamic defects that characterise cardiac development in hearts with disrupted L/R patterning.

Closer analysis of chamber orientation from the heart's 'ventral' and 'sagittal' face not surprisingly identified that the dynamics of the *spaw*$^{-/-}$ dorso-ventral loopers diverge from that of the *spaw*$^{-/-}$ lateralised loopers, suggesting looping direction enforces differential chamber adjustments to assist the concurrent processes of looping and ballooning morphogenesis in these hearts. One of the anatomical restrictions imposed over the dorso-ventral loopers that may hinder the rearrangement and compaction of their chambers is the connection of the atrium's IFT to the developing circulatory system, particularly the common cardinal vein, which during development is positioned over the yolk (Helker *et al.*, 2013; Eberlein *et al.*, 2021). In these mutants, the dorsal positioning of the atrium with respect to the ventricle whilst

both chambers maintain their connection to their corresponding vessels (atrium: common cardinal vein, ventricle: aortic arches) enforces an abnormal orientation (i.e. more tilted) and morphology of the dorso-ventral looped hearts within the embryo which possibly prevents the chambers from rearranging and compacting despite their loss of L/R patterning. This observation provides a possible explanation for the impaired heart packing of the *spaw* mutants, dorso-ventral loopers, suggesting that the characteristic lateralised looping of the heart constitutes an advantage in the normal process of organ packing and positioning within a restrained space in the developing embryo. Nevertheless, analysis of these parameters in *spaw*$^{-/-}$ lateralised loopers also identified a failure of the chambers to move and rearrange like wild-types into a tight side-by-side compacted shape around the AVC, suggesting a general requirement for Spaw in the tissue rearrangement processes involved in looping, ballooning and early heart maturing.

As previous studies of *spaw*$^{-/-}$ had not reported defects resulting from copy number variation, the group of sibling embryos used in the analysis of the *spaw* mutants rather than being complete wild-types, carried the *spaw* mutation in heterozygosity. Surprisingly, when the dataset of full wild-type hearts is compared to that of *spaw* heterozygous mutants, some parameters present slight variations suggesting the presence of a mild phenotype with only one copy of the wild-type gene.

7.6 ECM regionalisation and expansion in *SPAW* mutant hearts is maintained but mispositioned

Having identified the morphological defects that characterise the *spaw*$^{-/-}$ hearts, to understand if defects in L/R patterning and looping directionality result in abnormal ECM-regionalisation, a close examination of cardiac jelly distribution was carried out in *spaw* mutant hearts. Initial analysis of the cardiac jelly dynamics identified divergent progressions of cardiac ECM volume in each chamber. While the *spaw*$^{-/-}$ atria presents slower rates of ECM expansion throughout the analysed stages, the ventricular ECM undergoes constant reduction, which in the latter case results in significantly reduced ECM volumes when compared to siblings from 48-50hpf onwards. Knowing that recent studies in different animal models have described how the timing of ECM reduction in the ventricle correlates with the onset of trabeculation in this chamber (Rasouli and Stainier, 2017; del Monte-Nieto *et al.*, 2018), it is tempting to speculate that the early and accelerated reduction of ventricular cardiac jelly characteristic of *spaw*$^{-/-}$ induces a premature onset of trabeculation in this chamber. 3D analysis like the ones performed in this thesis but in *spaw* mutants at later stages of maturation (>75hpf) could easily inform if this hypothesis is correct and serve as a base to understand the functional and physiological defects that result from disrupted L/R patterning in the developing zebrafish heart.

Fascinatingly, despite the atrial cardiac jelly defects identified, analysis of ECM distribution within this chamber revealed that the ECM asymmetry recognised in developing wild-type hearts, is maintained in *spaw* mutant hearts but mispositioned (Fig 4.39-4.40). Early-looping *spaw*$^{-/-}$ heart tubes, regardless of their heart looping direction, present an atrial outer curvature ECM asymmetry which is preserved as these mutant hearts undergo looping, ballooning and early maturing (Fig 4.40). The existence of this atrial ECM asymmetry in embryos with disrupted L/R patterning suggests the identified ECM-regionalisation is independent of Nodal signalling. In addition, the recognised mispositioning of the ECM-regionalisation to the atrium's outer curvature, regardless of heart's looping direction, indicates a possible link between the axis of ECM asymmetry and the direction of looping and chamber ballooning (Fig 4.41).

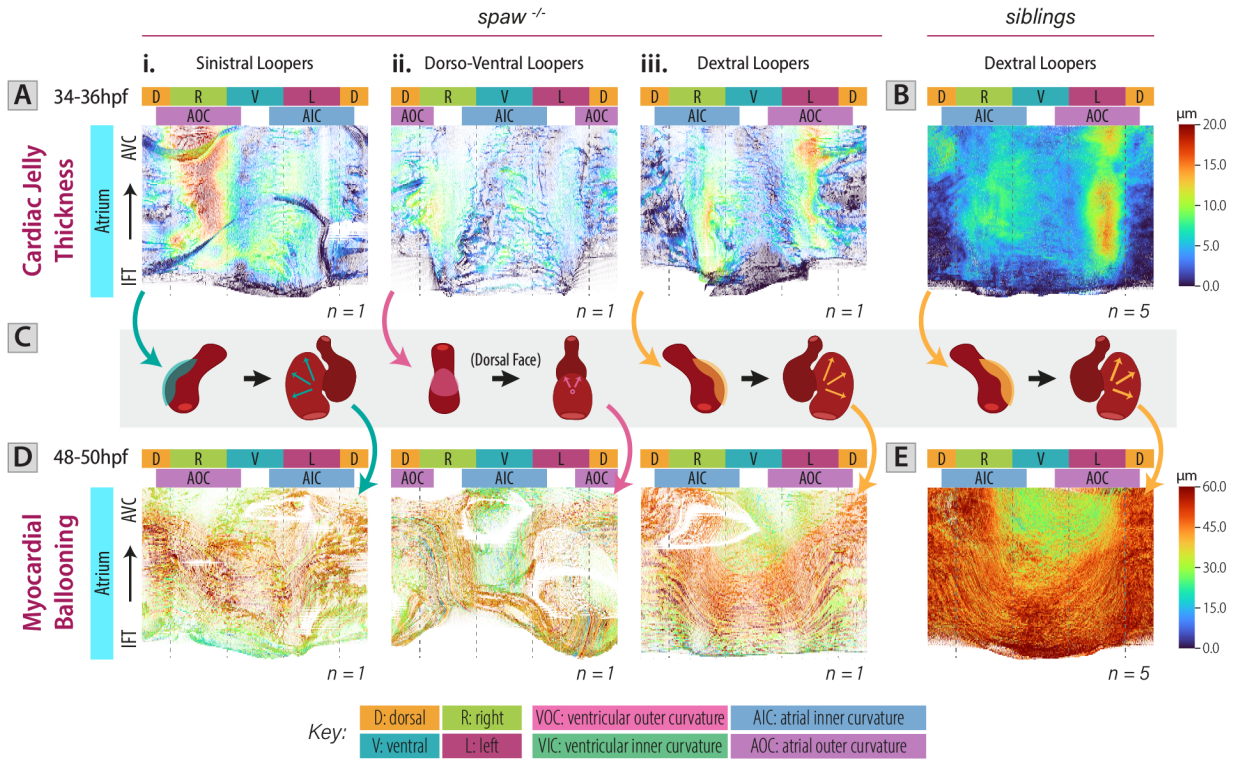

Fig 4.41. Early left-right axis of ECM regionalisation appears to be linked to the orientation of heart looping and chamber ballooning.

A-E. Cardiac jelly thickness analysis at early looping stages (34-36hpf) identified highly regionalised ECM in the atrial outer curvature, regardless of heart looping direction (A-B). This ECM-thickened region correlates at mid-looping and ballooning stages (48-50hpf) with a major extent of myocardial ballooning (D-E), suggesting that L/R patterning establishes an early atrial ECM asymmetry that intrinsically sets an axis for chamber growth and looping morphogenesis to occur (C).

These observations, combined with the multiple roles played by the ECM during embryogenesis (Feinberg and Weiss, 2009; Mittal *et al.*, 2013; Kim *et al.*, 2018; Sivakumar *et al.*, 2018; Derrick and Noël, 2021) and the distinctive cardiac ECM asymmetry identified here, raises the intriguing possibility that the regionalised differences in the cardiac jelly within the primitive heart tube (Derrick *et al.*, 2021) could be one of the intrinsic mechanisms providing directional cues and promoting asymmetric dextral looping morphogenesis. Interestingly, mRNA ISH analysis of interstitial ECM components (Fig 4.16-4.19) identified *hapln1a* and *hapln1b* as genes whose expression pattern at tube stage correlates with the expanded ECM asymmetry (Fig 4.18), suggesting them as candidate proteins for driving this regionalised cardiac jelly expansion. Consequently, to investigate the hypothesis that ECM regionalisation is linked to heart morphogenesis, in the next chapter I will first explore the role of Hapln1 proteins in the developing heart. The study of Hapln1's role, followed by the analysis of *hapln1a* and *spaw* double mutants, will provide more insights into the relationship between ECM asymmetry and intrinsic morphogenesis in the developing zebrafish heart.

Chapter 5. Hapln1a is Required to Protect the ECM Dynamics of the Early Developing Zebrafish Heart

1 INTRODUCTION

Recent studies have shown that composition and remodelling of the embryonic ECM drives organ morphogenesis in mice, chick and zebrafish, revealing that deposition, cleavage and degradation of ECM substrates not only sculpt tissue architecture but also generate bioactive ECM fragments critical to specific developmental processes (Feinberg and Weiss, 2009; Mittal *et al.*, 2013; Kim *et al.*, 2018; Sivakumar *et al.*, 2018; Derrick and Noël, 2021).

In light of the diverse roles played by the ECM during heart embryogenesis, I speculate that regionalised differences in the cardiac ECM at early stages of heart development may be important for promoting tissue intrinsic morphogenesis and consequently, precise spatiotemporal regulation of the ECM components that create and stabilise these asymmetries may be essential for normal cardiac development. mRNA *in situ* hybridisation (ISH) analysis of *hapln1a* and *hapln1b* expressions in the zebrafish heart shows they are regionally localised in a similar domain to where the expanded extracellular space on the left side of the cardiac tube was observed (Fig 4.18). Taken together, I hypothesise that regional variations in the ECM composition of the heart tube are driven by the regionalised expression of *hapln1* proteins, and that this provides varied extracellular environments that promote differential cellular behaviours essential to drive robust rightward heart looping morphogenesis.

Here, I will define the expression pattern of *hapln1a* and *hapln1b*, the two ECM component genes that appear to be asymmetrically expressed in the ECM, recapitulating the asymmetries in the cardiac ECM previously identified and described. I go on to study functionally the role of *hapln1a* using CRISPR-Cas9 mediated mutagenesis where I target the promoter of *hapln1a*, creating loss of function mutants. Detailed investigation of cardiac morphology in these mutants show that Hapln1a cross-linking protein is required to drive atrial-specific processes of chamber growth and ECM expansion-reduction dynamics in the looping and ballooning heart. Next, to identify if asymmetric *hapln1a* expression in the tube is dependent upon embryonic laterality and investigate the interactions between L/R asymmetry and regionalised ECM composition, I study cardiac morphogenesis and ECM dynamics in *spaw*$^{-/-}$, *hapln1a*$^{-/-}$ double mutants.

This work provides novel insights into role of the cardiac ECM in heart morphogenesis, specifically on how regionally expressed and deposited ECM components might drive ECM asymmetry in the heart, and the relationship of these phenomena to large scale embryo patterning.

2 *HAPLN1A* IS REGIONALLY AND TRANSIENTLY EXPRESSED IN THE HEART AND SECRETED ASYMMETRICALLY INTO THE CARDIAC JELLY

Hapln1a is part of a family of ECM link proteins that when secreted into the ECM bind hyaluronic acid and proteoglycans, forming proteoglycan aggregates (Fig 5.1A) (Spicer, Joo and Bowling, 2003; Lockhart *et al.*, 2011a). The zebrafish *hapln1a* gene is located in chromosome 5 and harbours three protein-coding transcripts (Fig 5.1B). The full-length transcript is made up of 4 exons that translate into a protein containing a pro-peptide, an immunoglobulin-like domain and two contiguous link domains (Fig 5.1B-D) (Kang *et al.*, 2008). To understand the role of *hapln1a* as a possible candidate gene driving the asymmetry in the cardiac ECM, a characterisation of its dynamics of expression and secretion was initially undertaken.

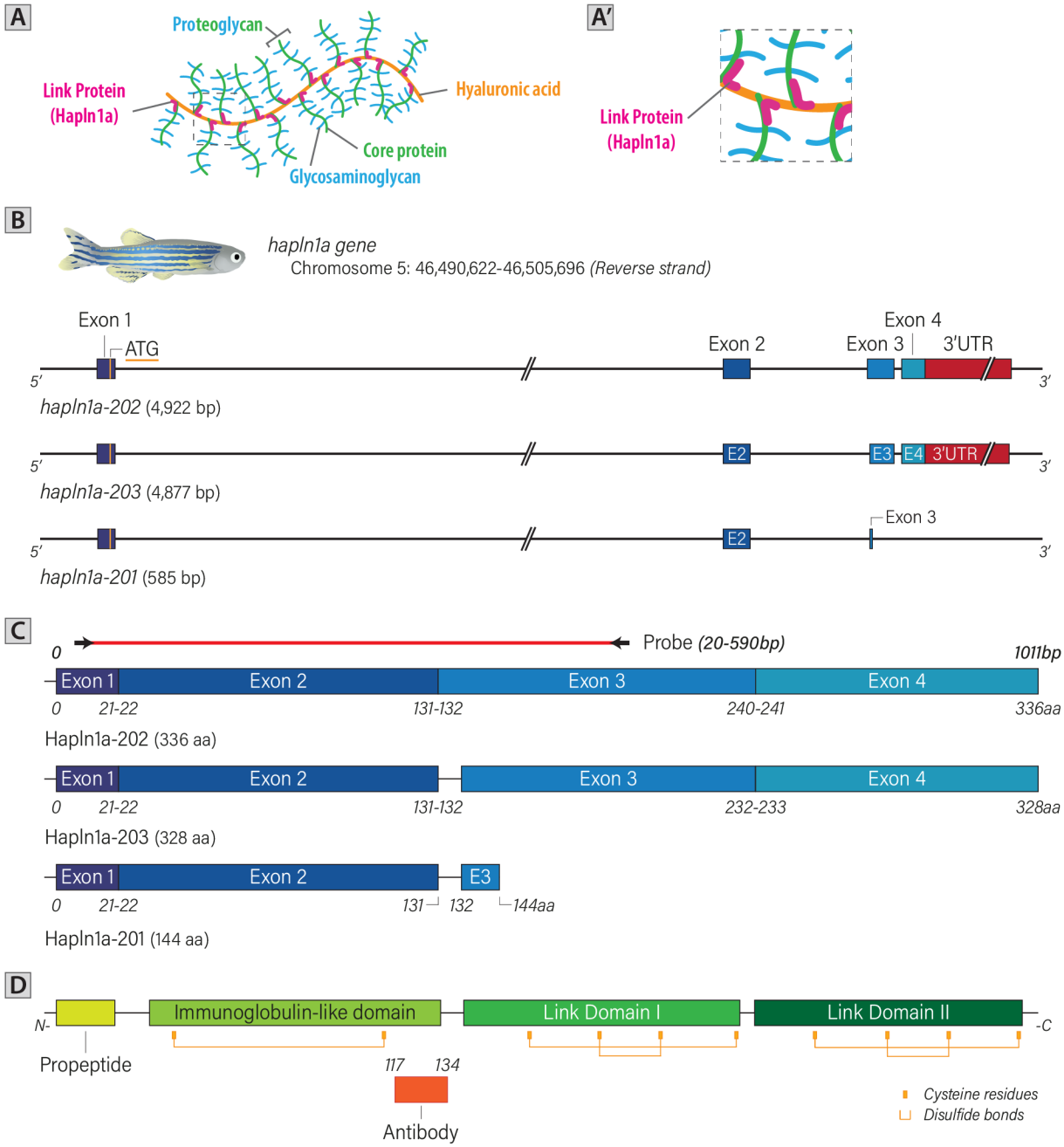

Fig 5.1. Schematic of *hapln1a* gene and Hapln1a protein organisation.
A-A'. Schematic of a proteoglycan aggregate where Hapln1a (magenta) cross-links Hyaluronic acid (orange) to proteoglycans (blue and green). **B.** *hapln1a* is in the reverse strand of zebrafish's chromosome 5. Schematic illustrating the three protein-coding transcripts of *hapln1a* genomic DNA (gDNA), ordered by base-pair (bp) length. Coding exons are shown in blue, initiating ATG in yellow and *3'UTR* in red. **C.** Schematic of the three translated coding DNA (cDNA) corresponding to the protein-coding transcripts shown in B. Coding-exons are shown in blue. *hapln1a* mRNA probe used throughout this work is illustrated in red and positioned in the region of the *hapln1a* cDNA to which it binds. **D.** Schematic showing the corresponding protein domains and features that make up the full-length Hapln1a protein (*transcript 202*). The orange region (bellow the schematic of domains and features) highlights the amino acids of the zebrafish Hapln1a protein being targeted by the Hapln1a antibody used in this study. B-D: Information based on *hapln1a* transcripts from *Danio rerio* (danRer11), GRCz11, *e!Ensembl* (Cunningham *et al.*, 2022).

2.1 *hapln1a* mRNA expression and Hapln1a Localisation Analysis

To identify the onset of regionalised expression of *hapln1a* and understand its expression dynamics more granularly during looping, ballooning and maturation stages, additional stages of zebrafish embryonic development were included in the original mRNA *in-situ* hybridisation (ISH) analysis of *hapln1a* (Fig 4.18, Fig 5.2). *hapln1a* was not observed at 6hpf indicating it is not maternally deposited during oogenesis (Fig 5.2A-B). At 18hpf, *hapln1a* expression becomes distinct in the floorplate and hypochord (corroborating a previous report from Kang *et al.* (Kang *et al.*, 2008)) and in the bilateral group of cardiac progenitor cells that will coalesce in the embryonic midline and form the heart disc or cone (Fig 5.2C-D). Interestingly, this early cardiac-specific expression is not only maintained throughout the heart disc but becomes elevated in its posterior region (Fig 5.2E). At 26hpf, *hapln1a* is present throughout the heart tube with elevated levels of expression on the left side compared to the right. Expression of *hapln1a* is maintained in the heart tube at 30hpf. However, the left-regionalisation becomes difficult to qualify as expression becomes upregulated in the embryo's head (Fig 5.2I-J). Between 18 and 30hpf, *hapln1a* continues to be detected along the midline of the embryo specifically in the hypochord and floorplate (Fig 5.2F,H,J). *hapln1a* cardiac-specific expression is transient, as overall levels of expression are reduced in the heart from 30hpf onwards, becoming restricted at 48-50hpf stage to low levels in the atrioventricular canal (Fig 5.2K-N). Between 48 and 61hpf, *hapln1a* expression is identified in the developing pectoral fins (white arrow in Fig 5.1L-R) and in the developing pharyngeal arches of the embryo (black arrows in Fig 5.2L-R). From 72 to 80hpf, whilst the pharyngeal arches expression is maintained, expression of *hapln1a* is also found in the opercles, a paired craniofacial dermal bone in the developing skull (Fig 5.2S-V).

Throughout this time-course (Fig 5.2), *hapln1a* appears to be expressed only by the myocardial tissue layer. To confirm this, fluorescent ISH analysis of *hapln1a* was undertaken in embryos at 26hpf, supporting that the cardiac tissue layer involved in the expression and secretion of Hapln1a into the ECM is the myocardium (Fig 5.2W-X) (Derrick *et al.*, 2021).

Analysis of Hapln1a protein localisation confirms the protein is secreted into the cardiac jelly asymmetrically at disc and tube stages (Fig 5.3A-H). Similar to the gene expression pattern at these stages (Fig 5.2E-H,W-X), Hapln1a is deposited by the myocardial tissue into the cardiac jelly, however due to its regionalised levels of expression this protein is strongly localised in the posterior region of the heart disc (Fig 5.3B-C) and the atrial-left side of the heart tube (Fig 5.3F,G,Hi-iii). Despite its absence of expression in the heart at 50hpf (Fig 5.2M), Hapln1a protein is still present in the ECM, particularly in the atrium and AVC (Fig 5.3J,M-O) at this stage, suggesting that the ECM environment that is established in the heart at early stages of development is maintained as the heart undergoes looping and ballooning, and its maintenance is important for promoting later processes of heart morphogenesis. As expected by the absence of cardiac-specific expression from 55hpf onwards (Fig 5.2O-V), at 72hpf, Hapln1a is no longer present in any heart-specific regions.

Fig 5.2. *hapln1a* expression is dynamic throughout zebrafish development and heart morphogenesis.
A-B. At 6hpf, *hapln1a* mRNA is not detected in the embryo. **C-D.** At 18hpf, in addition to the floorplate and hypochord, *hapln1a* expression is recognised in the bilateral group of cardiac progenitors. **E-F.** At 21hpf, *hapln1a* mRNA is identified in the posterior region of the heart disc, while it continues to be expressed in the floorplate and hypochord of the developing embryo. **G-J.** At 24hpf, cardiac-specific expression of *hapln1a* is identified asymmetrically in the heart tube (G-H). This specific-heart expression is maintained at 30hpf when it also becomes highly expressed in the embryo's head (I-J). **K-N.** At 48 and 50hpf, cardiac *hapln1a* expression is restricted to low levels in the atrioventricular canal. In addition, between these two stages, *hapln1a* mRNA

starts to be recognised in the developing pectoral fins and pharyngeal arches of the embryo. **O-V.** From 55hpf onwards, no *hapln1a* expression is detected in the developing heart. From 61 to 80hpf, whilst the pharyngeal arches expression is maintained, expression of *hapln1a* is identified in the opercles. **W.** Fluorescent ISH analysis of *hapln1a* (magenta) in *Tg(myl7:lifeActGFP)* transgenic zebrafish embryos identifies *hapln1a* is expressed by the myocardial cells at 26hpf **X.** Optical cross-section of the heart through the white dotted line in W. A-V: Heart-specific expression is indicated by arrowheads, while expression in other embryonic structures is pointed by arrows. The number of embryos matching the image shown is indicated in the bottom right of the lateral view image. Fluorescent ISH image shown in W and its corresponding cross-section X were kindly provided by Christopher Derrick. A,C,E,G,W: Dorsal views with anterior to the top. I,K,M,O,Q,S,U: Ventral views with anterior to the top. B,D,F,H,J,L,N,P,R,T,V: Lateral views with anterior to the top. X: Transverse view with dorsal to the top.

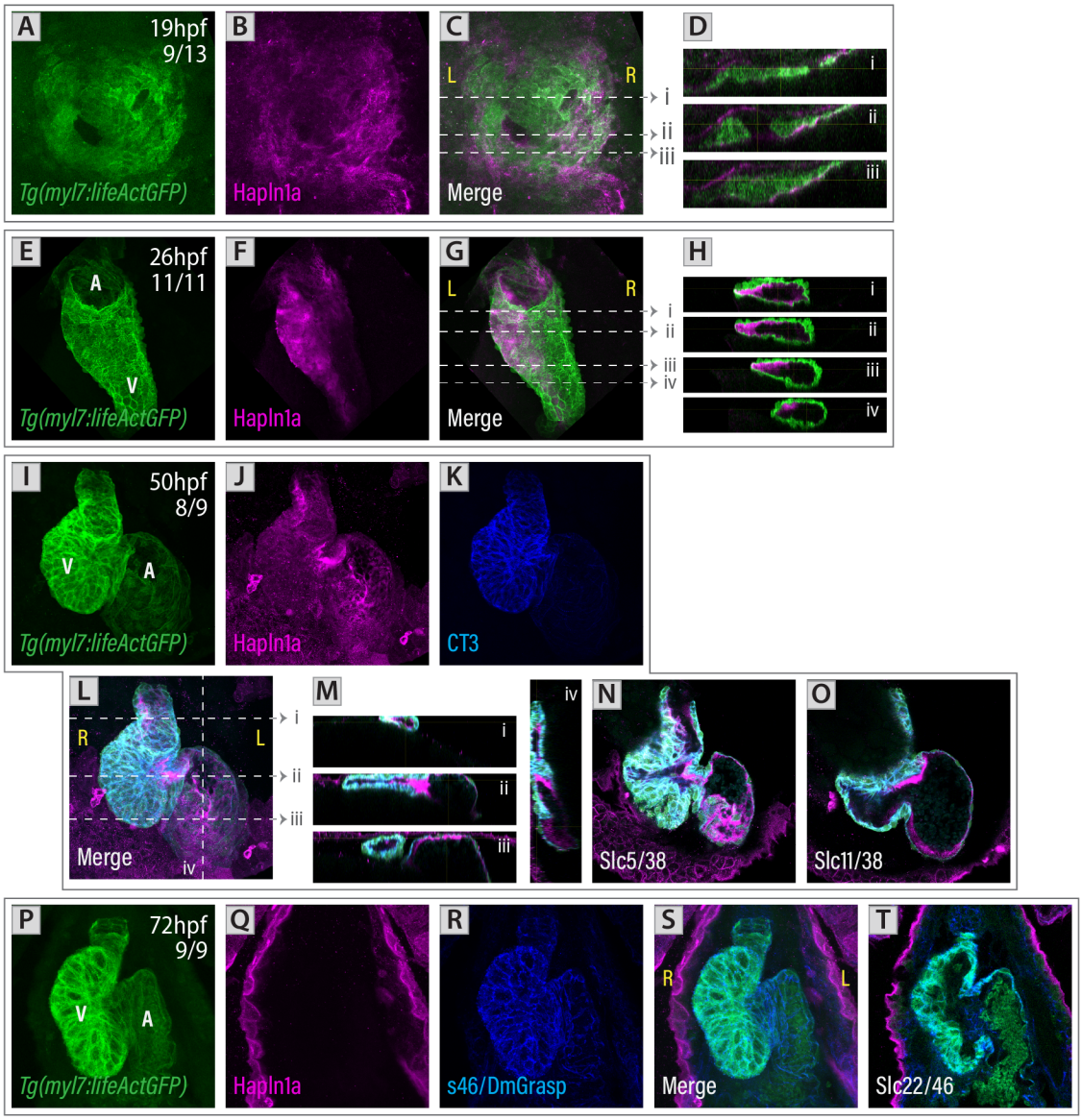

Fig 5.3. Hapln1a is dynamically deposited in the cardiac ECM throughout zebrafish heart development. Fluorescent immunostaining of Hapln1a (magenta) in *Tg(myl7:lifeActGFP)* transgenic embryos at early stages of heart development. **A-C.** Maximum-intensity projection (MIP) from two-colour fluorescent immunostaining of *Tg(myl7:lifeActGFP)* (A), and Hapln1a (B) at 19hpf. Hapln1a is secreted to the heart disc by the myocardium, and due to its asymmetric expression, this protein gets more strongly localised in the posterior region of the heart disc. **D.** Optical cross-section of the heart through the white dotted lines in C. **E-G.** MIP from two-colour fluorescent immunostaining of *Tg(myl7:lifeActGFP)* (E), and Hapln1a (F) at 26hpf. At tube stage, Hapln1a is secreted asymmetrically into the cardiac jelly on the left side of the heart tube. **H.** Optical cross-section of the heart through the white dotted lines in G. **I-L.** MIP from three-colour fluorescent immunostaining of *Tg(myl7:lifeActGFP)* (I), Hapln1a (J) and CT3 (K) at 50hpf (merge of the three channels in L). At this stage,

Hapln1a is maintained in the cardiac ECM of the developing embryo. **M-O.** Optical cross-sections of the heart through the white dotted lines in L (M) and individual slices of the heart stack (N-O) reveal that at 50hpf, Hapln1a is principally localised in the outer and inner curvature of the atrium, some regions of the ventricle, and the superior AVC cushion of the developing valve. **P-S.** MIP from three-colour fluorescent immunostaining of *Tg(myl7:lifeActGFP)* (P), Hapln1a (Q) and s46 and DmGrasp (R) at 72hpf (merge of the three channels in S). As the heart starts to mature, Hapln1a protein is no longer recognised in the developing heart. **T.** Individual slice of the heart stack reveal that at 72hpf, Hapln1a protein is no longer part of the cardiac ECM. A-T: The number of embryos matching the image shown is indicated for each timepoint in the top right of the *Tg(myl7:lifeActGFP)* channel below the stage. A-C,E-G: Dorsal views with anterior to the top. I-L,N-T: Ventral views with anterior to the top. D,H: Transverse views with dorsal to the top. Mi-iii: Transverse views with ventral to the top. Miv: Lateral view with ventral to the left. L: Left, R: Right, A: Atrium, V: Ventricle

---

2.2 *HAPLN1B* mRNA EXPRESSION ANALYSIS

As previously mentioned, zebrafish have two *hapln1* paralogs: *hapln1a* and *hapln1b.* The initial ISH screen (Fig 4.18) identified the expression profile in the heart of each paralog to be distinct during development, with *hapln1b* expressed predominantly by the endocardium. To confirm this is consistent throughout early heart development, mRNA ISH analysis of *hapln1b* was performed at similar stages as that of *hapln1a* (Fig 5.4).

Like *hapln1a*, *hapln1b* is not present at 6hpf, indicating it is not maternally deposited (Fig 5.4A-B). At 18hpf, *hapln1b* is expressed broadly in the area where the cardiac progenitor cells are located (Fig 5.4C-D), particularly where the pre-endocardial cells have been described to be migrating to form the cardiac tube (Bussmann, Bakkers and Schulte-Merker, 2007; Capon *et al.*, 2022). Additional expression of *hapln1b* can be observed in the floorplate along the trunk and in a region ventral to the tail extension. As development progresses, *hapln1b* expression becomes detectable in the eyes and downregulated throughout the rest of the embryo, while maintaining high levels of expression in the posterior cells of the developing endocardial lining of the heart cone (21hpf, Fig 5.4E-F) (Capon *et al.*, 2022). At 26hpf, *hapln1b* is present in both cardiac tissues, with stronger endocardial expression, particularly on left-side of the endocardial tube (Fig 5.4G-H). Expression of *hapln1b* is also identified at this stage in the developing eye and the cells comprising the venous pole endothelium. The weak expression in the myocardium and strong asymmetric expression of *hapln1b* within the endocardial tube and venous pole cells persists at 30hpf (Fig 5.4I-J). At 50hpf, in contrast to *hapln1a* which becomes restricted to the AVC (Fig 5.2K), *hapln1b* is strongly expressed throughout the endocardium, showing higher levels of expression in the ventricle (Fig 5.4K-L). Endocardial expression of *hapln1b* persists as the heart continues developing (56-72hpf, Fig 5.4M-P), and like *hapln1a* transiently becomes expressed in the developing pharyngeal arches (white arrows in Fig 5.4M-P). Concomitant to this expression pattern, the expression of *hapln1b* is progressively increased in what appears to be the fin bud mesenchyme, the apical ectoderm ridge and the border region of the tail, including the skin ventral to the yolk extension (50-72hpf, arrows in Fig 5.4L,N,P).

Analysis of the mRNA ISH expression time-course of both paralogs of *hapln1* (Fig 5.2, 5.4) demonstrate both genes have very distinct and complementary spatio-temporal expression patterns that suggest that they may play multiple roles in embryonic development. Remarkably, both genes are strongly and asymmetrically expressed in the heart at very early stages of development (posterior region of the myocardial disc and endocardial heart field, and left side of both myocardial and endocardial tubes), suggesting the asymmetric and tissue-specific secretion of Hapln1 into the nascent cardiac jelly might be required to establish distinct ECM environments within the early developing heart.

Together, *hapln1a* expression is 1) myocardial, just like the expression pattern of its possible interacting partners *has2* (Fig 4.16A-A') and *vcana* (Fig 4.17K-L) (Smith *et al.*, 2008), 2) dynamic (i.e. expressed and secreted at the early heart disc and tube stages, and subsequently mRNA expression is downregulated throughout the heart, while the protein remains regionally deposited in the atrial ECM), and 3) regionalised

during the very early stages of heart development. Therefore, to understand further the role of *hapln1* proteins in the zebrafish cardiac ECM and test whether its asymmetric expression/deposition is required to maintain the regionalisation of the cardiac jelly, I decided to functionally investigate the role of *hapln1a* in heart development using knockout (KO) and misexpression models of *hapln1a*.

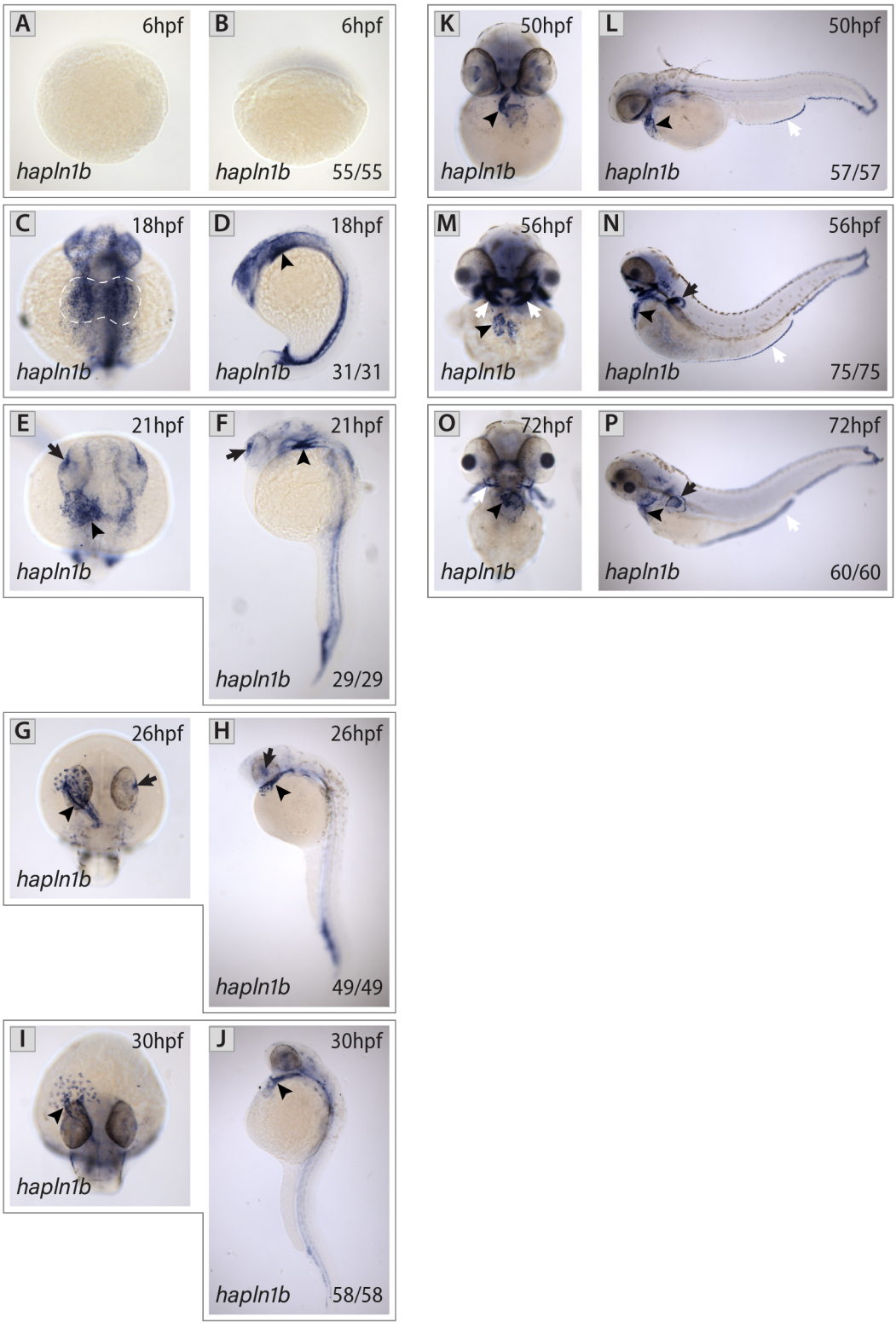

Fig 5.4. Expression dynamics of *hapln1b* mRNA throughout zebrafish development and heart morphogenesis. **A-B.** At 6hpf, *hapln1b* mRNA is not detected in the embryo. **C-D.** At 18hpf, *hapln1b* expression is recognised broadly in the area where the cardiac progenitor cells are located (white-dotted region). **E-F.** At 21hpf, *hapln1b* mRNA is identified with higher levels in the posterior cells of the developing endocardial lining of the heart cone. Additionally, *hapln1b* becomes also expressed along the trunk and in the embryo's developing eyes. **G-J.**

At 26 and 30hpf, *hapln1b* becomes clearly expressed by both cardiac tissues, with stronger endocardial expression on the left side of the heart tube. In addition to this heart tube-specific expression, *hapln1b* is also detected in cells located in inflow tract of the heart. **K-P.** Between 50 and 72hpf, cardiac *hapln1b* expression is maintained throughout the endocardial lining of the heart. In addition, between these two stages, *hapln1b* mRNA starts to be recognised in the developing pharyngeal arches and pectoral fins of the embryo. A-P: Heart-specific expression is indicated by arrowheads, while expression in other embryonic structures is pointed by arrows. The number of embryos matching the image shown is indicated in the bottom right of the lateral view image. A,C,E,G,I: Dorsal views with anterior to the top. K,M,O: Ventral views with anterior to the top. B,D,F,H,J,L,N,P: Lateral views with anterior to the top.

3 Investigating the Role of Hapln1a in Heart Morphogenesis

Two techniques were used to study of the role of *hapln1a* in heart looping morphogenesis: knockout using CRISPR-Cas9-mediated genome editing (Hwang *et al.*, 2013; Liu *et al.*, 2019) and misexpression using the *Gal4:UAS* system (Halpern *et al.*, 2008).

3.1 Generation of *hapln1a* Knockout Models using CRISPR-Cas9

While genome-editing technologies like CRISPR-Cas9 have been rapidly adopted to analyse gene function in living organisms, recent studies have identified transcriptional adaptation mechanisms, by which genes that are related to the mutated gene (i.e. exhibit sequence similarity) become upregulated upon mRNA degradation of the mutated gene, resulting in genetic compensation that can mask loss-of-function phenotypes (El-Brolosy and Stainier, 2017; El-Brolosy *et al.*, 2019). Given that alleles that fail to transcribe the mutated gene do not exhibit transcriptional adaptation (El-Brolosy *et al.*, 2019), to functionally investigate the role of *hapln1a* and avoid compensation targeted mutagenesis of the annotated promoter of *hapln1a* using CRISPR-Cas9 genome editing was undertaken.

Using the Eukaryotic Promoter Database (Dreos *et al.*, 2017), the *hapln1a* promoter was identified in the sequence upstream of the initiating ATG (see turquoise region in Fig 5.5A). To generate stable mutant lines in which transcription of *hapln1a* is prevented, two CRISPR guide RNAs (gRNAs) were designed to target the region upstream the putative promoter (*g5*) and downstream of the translation start site (ATG) (*g4*) of *hapln1a* (Fig 5.5A). Both guides were coinjected and these embryos raised to adulthood. Individuals transmitting mutations excising this region in the germline (F0) were selected and outcrossed to wildtype fish to generate F1 mutant lines. Two different mutations targeting the region of interest were recovered in the F1 generation: *hapln1a*^{promΔ187} (Fig 5.5B) and *hapln1a*^{promΔ241} (Fig 5.5C) and established as stable lines at F2.

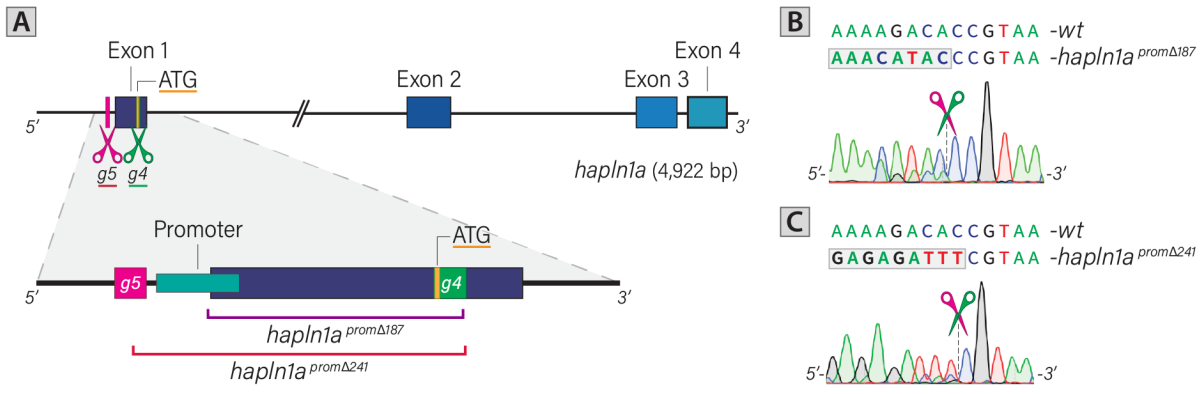

Fig 5.5. CRISPR-Cas9 mediated deletion of the *hapln1a* promoter region.
A. CRISPR-Cas9 guides (gRNA) targeting the upstream region of the putative promoter (*g5*) and the downstream region of the translation start site (ATG, *g4*) of *hapln1a* were coinjected in zebrafish embryos. Two different

germline mutations were recovered at F1: *hapln1a*^{promΔ187} and *hapln1a*^{promΔ241} and established as stable lines at F2. Box in turquoise highlights the annotated promoter of *hapln1a*, located upstream of the initiating ATG (yellow). Brackets show the region of the gDNA that was deleted in each recovered mutation. **B-C.** Sanger sequencing identified the region between the injected guides that was excised for each recovered allele. The *hapln1a*^{promΔ187} allele has a 187bp deletion, leaving a 5' region of the *hapln1a* promoter intact, yet removing the initiating ATG (B). The *hapln1a*^{promΔ241} allele has a 241bp deletion, resulting in a complete deletion of the promoter and initiating ATG (C).

3.1.1 HOMOZYGOUS *hapln1a* PROMOTER MUTANTS EXHIBIT COMPLETE LOSS OF *hapln1a* EXPRESSION

To confirm that the mutations delete the *hapln1a* promoter and prevent its transcription, whole-mount *in situ hybridisation* (ISH) analysis of *hapln1a* expression was performed in both alleles at 26hpf in F3 mutant embryos. *hapln1a* is expressed in wild-type (Fig 5.6A,A') and heterozygous siblings (Fig 5.6B,B'); however, it is absent in homozygous mutants for both alleles (Fig 5.6A'', B'') demonstrating successful deletions of the *hapln1a* promoter and validating the use of these promoter mutants as loss-of-function models. Furthermore, analysis of expression levels of *hapln1a* by ISH shows an apparent reduction in transcript levels in *hapln1a* heterozygous embryos (Fig 5.6A',B') compared to wild-type siblings (Fig 5.6A,B). Consequently, to avoid intermediate phenotypes resulting from copy number variation, the role of *hapln1a* was investigated by comparing homozygous *hapln1a* mutants with homozygous wild-type siblings.

[*Note#5.1:* To note, throughout the rest of this thesis, *hapln1a* promoter mutants carrying either of the mutations (*Δ187* or *Δ241*) in heterozygosity will be referenced as *hapln1a*^{Δ187}/+ or *hapln1a*^{Δ241}/+, while those carrying them in homozygosity will be referenced as *hapln1a*$^{Δ187/Δ187}$ (also *hapln1a*^{Δ187} mutants) or *hapln1a*$^{Δ241/Δ241}$ (also *hapln1a*^{Δ241} mutants)] .

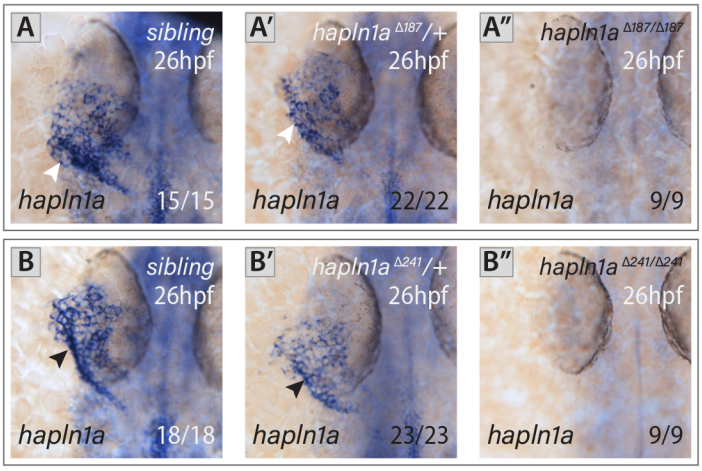

Fig 5.6. Targeted deletion of *hapln1a* promoter by CRISPR-Cas9 results in complete loss of *hapln1a* transcript. A-B''. Representative images of mRNA *in situ* hybridisation analysis of *hapln1a* at 26hpf reveals that *hapln1a* is expressed in genotyped wildtype (arrowheads in **A** and **B**) and heterozygous (arrowheads in **A'** and **B'**) embryos and absent in homozygous mutants in both of the created promoter deletion alleles (187bp: A-A'', 241bp: B-B''). A-B'': The number of embryos matching the image shown is indicated in the bottom right of each image. Dorsal views with anterior to the top.

Analysis of gross morphology revealed that homozygous *hapln1a* mutants of either allele are indistinguishable from their wild-type siblings throughout development (Fig 5.7A-D) and at juvenile stages (Fig 5.7E-H') and are viable and fertile as adults.

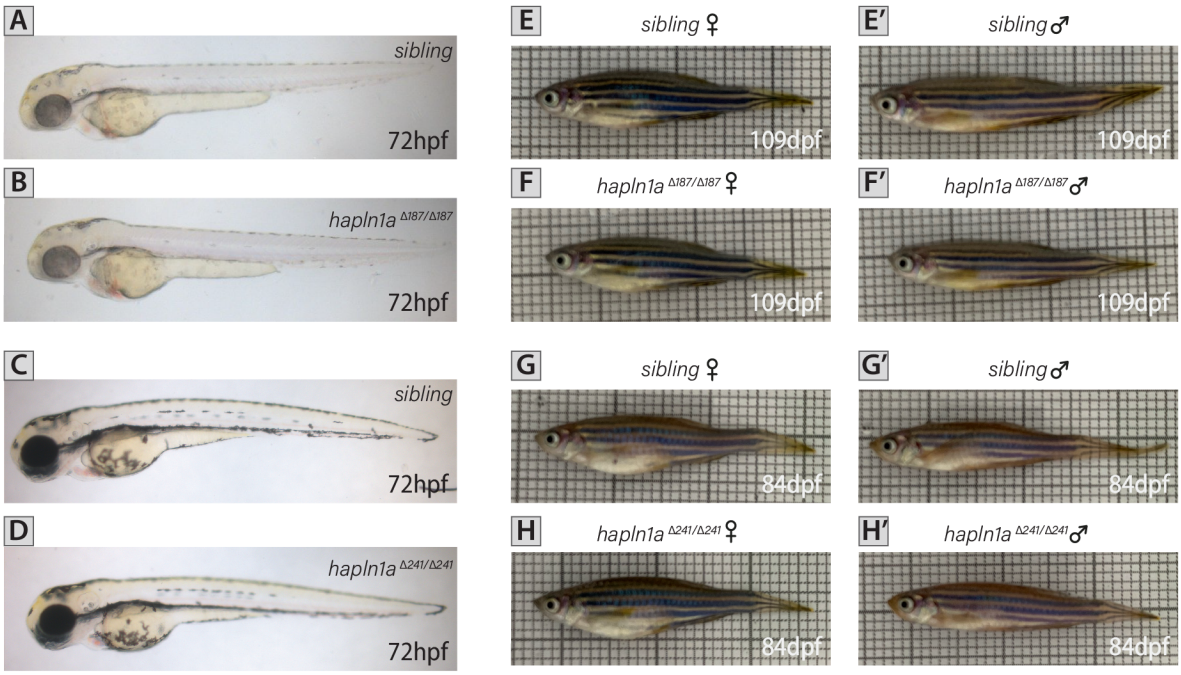

Fig 5.7. Homozygous mutants for both promoter deletion alleles do not show gross morphological defects throughout development nor at juvenile stages.
A-D. Representative brightfield images of sibling (*Δ187,* A), *hapln1a*^{Δ187} homozygous mutant (B), sibling (*Δ241,* C), and *hapln1a*^{Δ241} homozygous mutant (D) embryos at 72hpf. **E-F'.** Representative images of wild-type (E-E') and *hapln1a*^{Δ187} mutant (F-F') female (E,F) and male (E',F') juvenile fish at 109dpf. **G-H'.** Representative images of wild-type (G-G') and *hapln1a*^{Δ241} mutant (H-H') female (G,H) and male (G',H') juvenile fish at 84dpf. Homozygous mutants for both alleles do not show gross morphological defects compared to wild-type adult fish. A-H': Lateral views with anterior to the left.

3.1.2 *hapln1b* Expression is not Up-Regulated in *hapln1a* Promoter Mutants

To confirm the excision of *hapln1a* promoter is not activating genetic compensation (El-Brolosy *et al.*, 2019), mRNA ISH analysis of *hapln1b*, the most likely compensating gene, was undertaken in embryos at 26hpf obtained from in an incross of *hapln1a* heterozygous mutant F2 adults for both alleles. Expression levels of *hapln1b* are not altered by the loss of *hapln1a* (Fig 5.8A',B'), with *hapln1a* mutants showing an expression pattern similar to that in their wild-type siblings (Fig 5.8A,B). Together, this suggests that loss of *hapln1a* in the promoter homozygous mutants does not dysregulate *hapln1b* expression in the developing and that *hapln1b* is not functionally compensating for its absence.

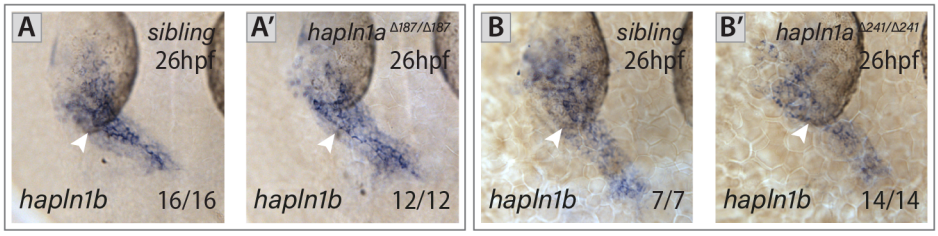

Fig 5.8. *hapln1b* expression is unaltered in *hapln1a* promoter mutants at 26hpf.
A-B'. Representative images of mRNA *in situ* hybridisation analysis if *hapln1b* expression at 26hpf in *hapln1a* promoter mutants of both alleles. *hapln1b* expression is unchanged between wild-type siblings (A,B) and *hapln1a*$^{Δ187/Δ187}$ (A') and *hapln1a*$^{Δ241/Δ241}$ (B') promoter mutants. A-B': The number of embryos matching the image shown is indicated in the bottom right of each image. Dorsal views with anterior to the top.

3.1.3 *hapln1a* PROMOTES ATRIAL GROWTH DURING CARDIAC LOOPING MORPHOGENESIS

Having recovered two promoter mutant alleles for *hapln1a*, to assess if *hapln1a* is important for heart development, mRNA ISH analysis of the pan-cardiac marker *myosin light chain 7* (*myl7*, previously *cardiac myosin light chain 2*, *cmlc2*) was performed at 26 and 50hpf for both alleles (Fig 5.9A-D') and heart morphological parameters were quantified using the methods previously described (see Chapter 2, Section 10.1). While analysis of heart morphology at both stages from the ISH images did not reveal striking abnormalities in cardiac morphogenesis, quantifications of heart area, as a proxy for heart size, displayed a significant reduction in this parameter in the *hapln1a*$^{\Delta 187}$ mutants at 26hpf compared to that of their wild-type siblings (Fig 5.9E). Heart area and looping ratio analysis at a later developmental stages (50hpf) did not show noticeable defects in the heart looping process of either *hapln1a* promoter mutant allele (Fig 5.9F,G), suggesting Hapln1a is not required for heart growth nor looping morphogenesis.

To further characterise the effect of *hapln1a* knockout, ISH expression analysis of individual chamber markers (Yelon, Horne and Stainier, 1999; Berdougo *et al.*, 2003) was carried out to analyse ventricle and atrium development (see Chapter 2, Section 10.1). Analysis of ventricular area using *myosin heavy chain 7-like* (*myh7l,* previously *vmhc*) at 50hpf (Fig 5.10A-B') did not reveal size defects in the ventricle of *hapln1a* promoter mutants (Fig 5.10E). On the contrary, analysis of atrial morphology and size using atrial *myosin heavy chain 6* (*myh6*, formerly *amhc*) at 50hpf revealed significantly smaller atria and reduced atrial outer curvature length for both alleles when compared to those of their wild-type siblings (Fig 5.10F,G). [*Note#5.2:* For a more detailed analysis of some other parameters measured from *myl7*, *myh6*, and *myh7l* ISHs in the *hapln1a* promoter mutants, see Appendix 1, FigS5J (Derrick *et al.*, 2021)].

Further analysis at 72hpf using *myl7* ISH identified that the chambers of *hapln1a* promoter mutant hearts occasionally appear mispositioned (Fig 5.11B-B', D-D') compared to their wild-type siblings (Fig 5.11A-A', C-C') rendering morphological analysis of these mutants in 2D at this stage challenging. To overcome this difficulty and be able to describe with more detail the impact that loss of Hapln1a has upon heart morphology and cardiac jelly dynamics during morphogenesis, a detailed characterisation of the *hapln1a* promoter mutants' phenotype was performed using *morphoHeart.*

[*Note#5.3:* All sample groups per genotype (*hapln1a*$^{\Delta 187/\Delta 187}$, *siblings* (*Δ187*), *hapln1a*$^{\Delta 241/\Delta 241}$ and *siblings* (*Δ241*)), were analysed for normality using Shapiro-Wilk Normality test. For each variable, if all groups were normally distributed, comparison between genotypes, per allele, were carried out using Un-paired t-test. When normal distribution could not be assumed, Mann-Whitney test was used. For all tests a statistical significance α of *0.05* was defined].

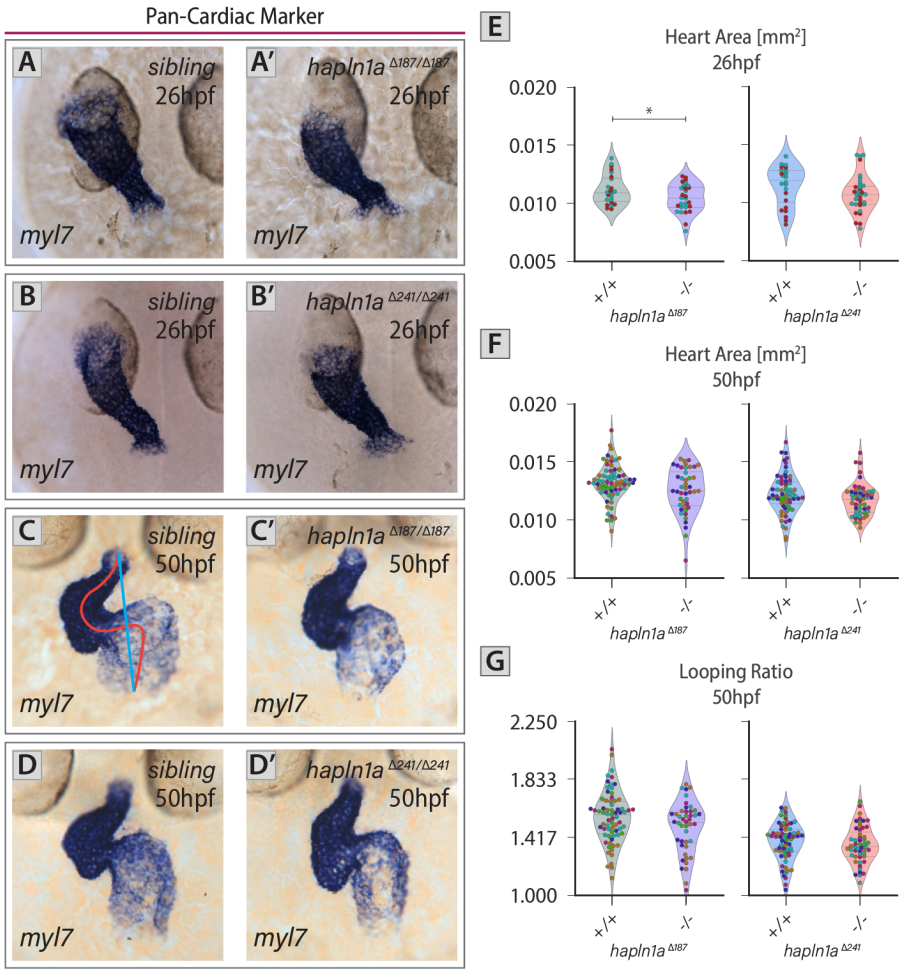

Fig 5.9. *hapln1a* promoter mutants do not exhibit heart size nor looping defects.
Quantitative analysis of heart size and looping morphology in *hapln1a* promoter mutants at 26 and 50hpf using the expression of the pan-myocardial marker *myl7* to outline the heart by mRNA *in situ* hybridisation. **A-D'** Representative images of mRNA *in situ* hybridisation analysis of *myl7* expression at 26 (A-B') and 50hpf (C-D') to examine heart morphology in sibling (*Δ187*, A,C), *hapln1a*$^{\Delta 187}$ homozygous mutant (A',C'), sibling (*Δ241*, B,D), and *hapln1a*$^{\Delta 241}$ homozygous mutant (B',D') embryos. No obvious cardiac phenotypes are apparent in *hapln1a* promoter mutants when compared to controls. **E-G.** Quantification of heart area at 26 (E) and 50hpf (F), and looping ratio at 50hpf (G) from *myl7* expression in sibling and *hapln1a* promoter mutant embryos for both alleles. The looping ratio is calculated as the quotient between the looped length or centreline of the heart (red line in C) and its linear length (blue line in C). The heart area of *hapln1a*$^{\Delta 187}$ homozygous mutants at 26hpf is significantly reduced compared to their wild-type siblings (E, *p-value=0.04053*). A-D': The number of embryos matching the image shown is indicated in the bottom right of each image. A-B': Dorsal views with anterior to the top. C-D': Ventral views with anterior to the top. E-G: Violin plots show median and quartile ranges and different colours represent different repeats. 26hpf: *siblings* (*Δ187*) *n=23*, *hapln1a*$^{\Delta 187/\Delta 187}$ *n=29*, *siblings* (*Δ241*) *n=24*, *hapln1a*$^{\Delta 241/\Delta 241}$ *n=34*; 50hpf: *siblings* (*Δ187*) *n=69*, *hapln1a*$^{\Delta 187\ /\Delta 187}$ *n=44*, *siblings* (*Δ241*) *n=65*, *hapln1a*$^{\Delta 241/\Delta 241}$ *n=51*. For details regarding the statistical analyses used to compare this set of data see *Note#5.3* (pg.177). Only significant comparisons are shown. *: *p-value*<0.05.

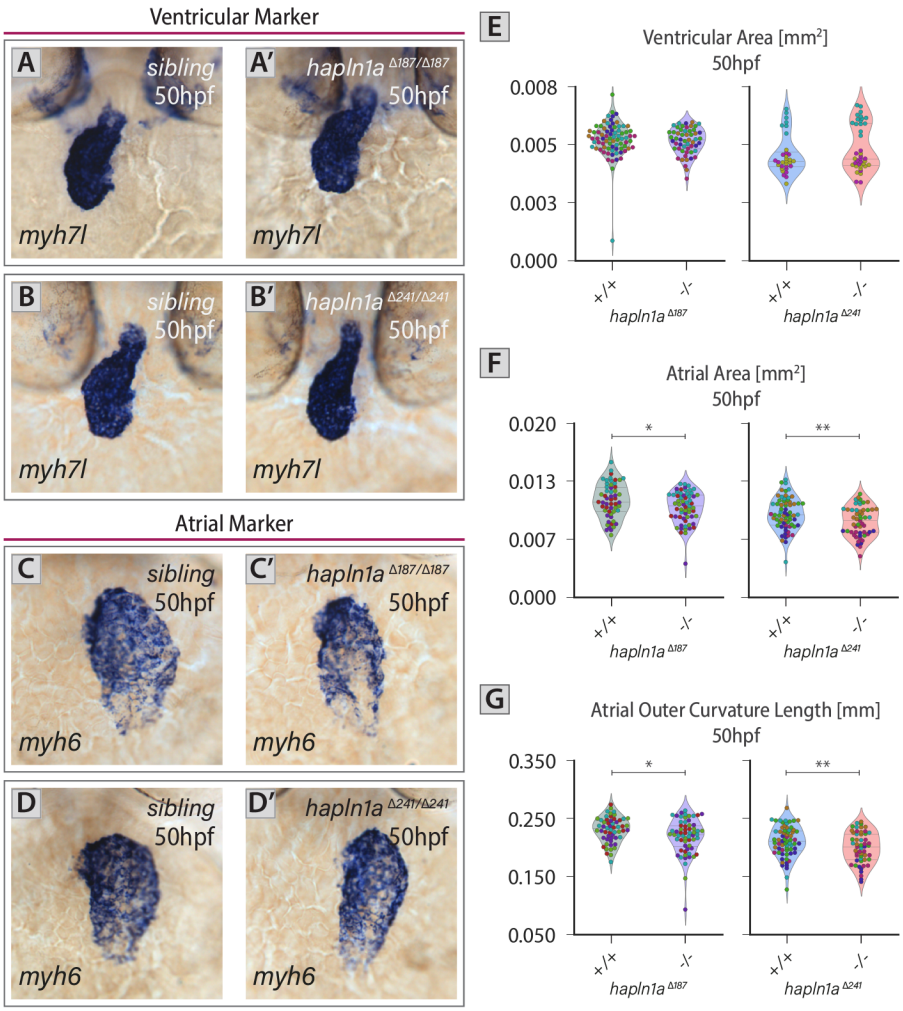

Fig 5.10. *hapln1a* promoter mutants exhibit atrial defects in size and outer curvature length. Quantitative analysis of chamber size and morphology in *hapln1a* promoter mutants at 50hpf. **A-D'.** Representative images of mRNA *in situ* hybridisation analysis of *myh6* (A-B') and *myh7l* (C-D') expression at 50hpf to examine chamber morphology in sibling (*Δ187*, A,C), *hapln1a*$^{\Delta 187}$ homozygous mutant (A',C'), sibling (*Δ241*, B,D), and *hapln1a*$^{\Delta 241}$ homozygous mutant (B',D') embryos. No obvious chamber defects are apparent in *hapln1a* promoter mutants when compared to controls. **E.** Quantification of ventricular area from *myh7l* expression in sibling and *hapln1a* promoter mutant embryos for both alleles, identified the ventricle size of *hapln1a* promoter mutants is undistinguishable from controls. **F-G.** Quantification of atrial area (F), and atrial outer curvature length (G) at 50hpf from *myh6* expression in sibling and *hapln1a* promoter mutant embryos for both alleles. *hapln1a* promoter mutants have significantly smaller atria and reduced atrial outer curvature length in both alleles (*hapln1a*$^{\Delta 187}$ vs. *siblings*: atrial area *p-value=0.04159*, atrial outer curvature length *p-value=0.03891* - *hapln1a*$^{\Delta 241}$ vs. *siblings*: atrial area *p-value=0.00746*, atrial outer curvature length *p-value=0.03540*). A-D': The number of embryos matching the image shown is indicated in the bottom right of each image. A-D': Ventral views with anterior to the top. E-G: Violin plots show median and quartile ranges and different colours represent different repeats. Ventricle area (*myh7l*): *siblings* (*Δ187*) *n=77*, *hapln1a*$^{\Delta 187/\Delta 187}$ *n=54*, *siblings* (*Δ241*) *n=32*, *hapln1a*$^{\Delta 241/\Delta 241}$ *n=39*; Atrial area and outer curvature length (*myh6*): *siblings* (*Δ187*) *n=55*, *hapln1a*$^{\Delta 187/\Delta 187}$ *n=61*, *siblings* (*Δ241*) *n=66*, *hapln1a*$^{\Delta 241/\Delta 241}$ *n=53*. For details regarding the statistical analyses used to compare this set of data see *Note#5.3* (pg.177). Only significant comparisons are shown. **: *p-value*<0.01, *: *p-value*<0.05.

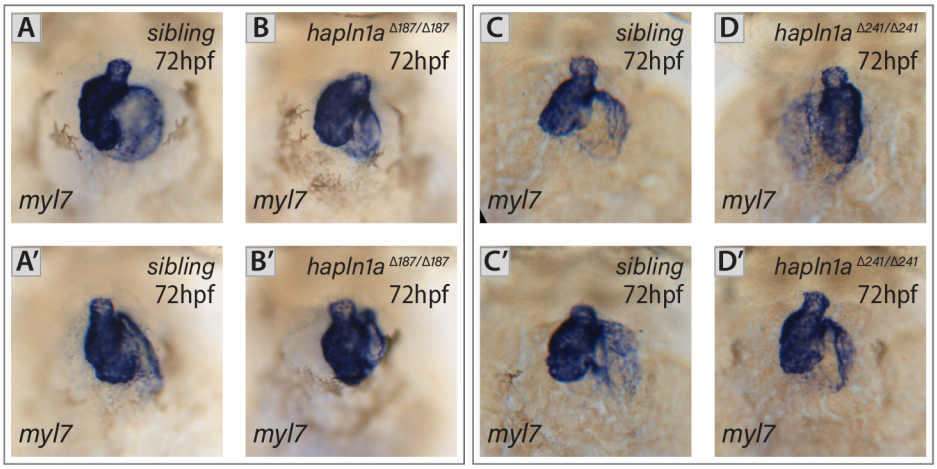

Fig 5.11. The chambers of *hapln1a* promoter mutant hearts at 72hpf rearrange differently to wild-type hearts. **A-D'** Representative images of mRNA *in situ* hybridisation analysis of the pan-cardiac marker *myl7* expression at 72hpf to examine heart morphology in sibling (*Δ187*) (A-A'), *hapln1a*$^{\Delta 187}$ homozygous mutant (B-B'), sibling (*Δ241*) (C-C'), and *hapln1a*$^{\Delta 241}$ homozygous mutant (D,D') embryos. The chambers of the heart of *hapln1a* promoter mutants are occasionally mispositioned when compared to the wild-type siblings.

Additionally, to take advantage of the time-dynamic analyses offered by *morphoHeart* and better characterise changes in heart morphology and ECM distribution in the *hapln1a* promoter mutants throughout development, the *hapln1a* promoter mutant presenting the largest deletion and most profound atrial phenotype by ISH analysis (Fig 5.10F,G) was initially analysed. Consequently, an incross of *Tg(myl7:lifeActGFP); Tg(fli1a:AC-TagRFP)* double transgenic *hapln1a*$^{\Delta 241/+}$ carriers were imaged live on the light-sheet microscope at early looping (34-36hpf), looping and ballooning (48-50hpf) and early maturing stages (72-74hpf).

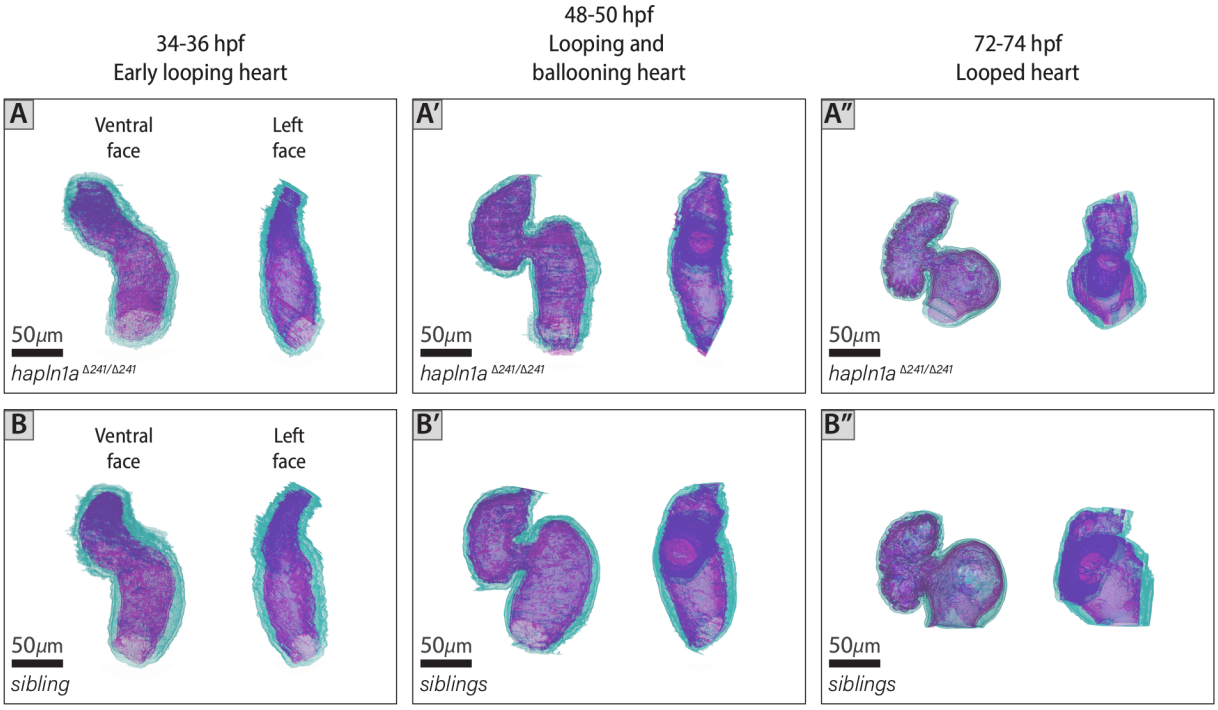

Fig 5.12. *hapln1a*$^{\Delta 241}$ promoter mutants have skinnier and 'less ballooned' atriums at 48-50hpf. **A-B''.** Representative 3D reconstructions of the myocardium (teal) and endocardium (magenta) of *hapln1a*$^{\Delta 241}$ (A-A'') and their wild-type sibling (B-B'') hearts at key developmental stages (34-36hpf: A,B; 48-50hpf: A',B'; and 72-74hpf: A'',B''). As described by the labels in Panels A and B, all panels show the ventral face(on the left) and left face (on the right) of each of the presented hearts.

Initial analysis of heart morphology from the 3D volume reconstructions of the myocardium and endocardium of *hapln1a*$^{\Delta 241}$ mutants and their siblings identified skinnier and 'less ballooned' atriums in the *hapln1a*$^{\Delta 241}$ homozygous mutants at 48-50hpf (Fig 5.12A').

Interestingly, analysis of gross heart parameters revealed differences in heart size in the *hapln1a*$^{\Delta 241}$ mutants at 34-36 and 48-50hpf (Fig 5.13A-A'), which were not captured by the ISH analysis previously described (Fig 5.9). Quantification of total heart volume at early looping stages (34-36hpf) identified that the heart tubes of *hapln1a*$^{\Delta 241}$ mutants are smaller and that this is due to reduced atrial and ventricular chamber sizes (Fig 5.13A-C). While wild-type zebrafish hearts increase in size as they transition from a linear tube to a looped organ and compact down once cardiac looping is completed, *hapln1a* mutant hearts grow slowly between 34 and 50hpf and compact slightly between 50 and 72hpf, reaching the latter stage with a similar heart size as wild-type embryos. Individual analysis of chamber volume identified that these gross size defects are driven by a failure to grow and compact of the atrium (Fig 5.13B-B'), while the size dynamics followed by the *hapln1a*$^{\Delta 241}$ mutant ventricles show no difference to that of the controls (Fig 5.13C'). These observations corroborate the results obtained for the *hapln1a*$^{\Delta 241}$ mutants when measuring the area of expression of the atrial-specific marker *myh6* as a proxy for heart size at 50hpf (Fig 5.10F), suggesting that a loss of Hapln1a has a critical effect in the atrial development process during zebrafish looping and ballooning morphogenesis.

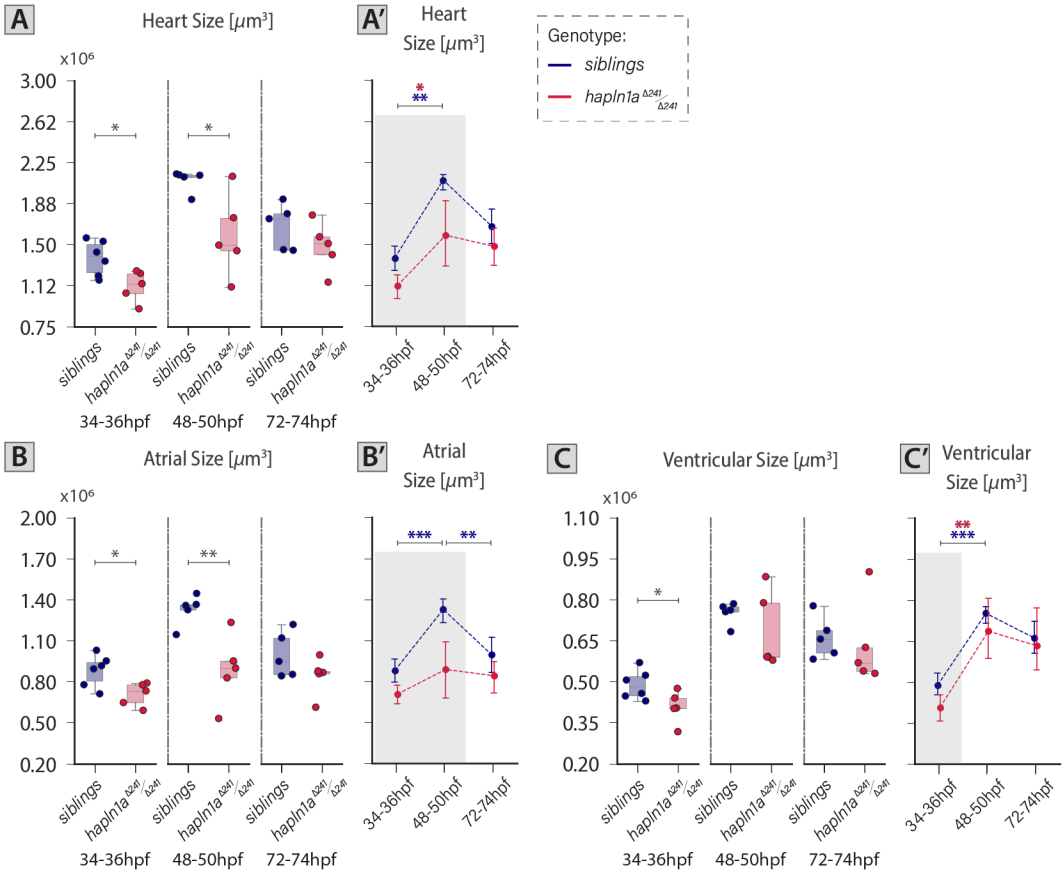

Fig 5.13. Loss of Hapln1a results in smaller heart tubes and reduced atrial size during looping and ballooning morphogenesis.

A-C'. Quantification of heart (A-A') and chambers (atrium: B-B', ventricle: C-C') size using *morphoHeart* in *hapln1a*$^{\Delta 241}$ mutants and its wild-type siblings at 34-36hpf, 48-50hpf and 72-74hpf. At early looping stages (34-36hpf), *hapln1a*$^{\Delta 241}$ mutants show a smaller heart, atrial and ventricular sizes when compared to controls (heart: *p-value=0.02198*, atrium: *p-value=0.02279*, ventricle: *p-value=0.04000*). Analysis of chamber size at 48-50hpf revealed that the heart and atrial sizes of *hapln1a*$^{\Delta 241}$ mutants remain significantly reduced when compared to its wild-type siblings, while the ventricular size shows no difference (heart: *p-value=0.03671*,

atrium: *p-value=0.00738*). A', B' and C' are point-plots of the data presented in A, B, and C, respectively. A-C': Error bars with 95% confidence interval of the mean. 34-36hpf: *siblings n=6*, *hapln1a*$^{\Delta 241/\Delta 241}$ *n=5*; 48-50hpf: *siblings n=5*, *hapln1a*$^{\Delta 241/\Delta 241}$ *n=5*; 72-74hpf: *siblings n=5*, *hapln1a*$^{\Delta 241/\Delta 241}$ *n=5*. For details regarding the statistical analyses used to compare this set of data see *Note#5.4* (pg.182). Only significant comparisons are shown. ***: *p-value*<0.001, **: *p-value*<0.01, *: *p-value*<0.05.

[*Note#5.4*: All sample groups per stage and genotype (*hapln1a*$^{\Delta 241/\Delta 241}$ and *siblings*) were analysed for normality using Shapiro-Wilk Normality test. For each variable, if all groups were normally distributed, comparison between genotypes per stage were carried out using Un-paired t-test. When normal distribution could not be assumed, Mann-Whitney test was used. For all tests a statistical significance α of *0.05* was defined].

Surprisingly, despite the heart and chamber size defects identified in the *hapln1a*$^{\Delta 241}$ mutant hearts at 34-36hpf, quantification of lumen size at this stage did not reveal differences between the mutants and the controls (Fig 5.14), suggesting instead the existence of defects in the tissue volume comprising the cardiac layers of the early looping heart. Investigation of lumen size in the heart and chambers at a later stage identified a reduced filling capacity of the *hapln1a*$^{\Delta 241/\Delta 241}$ atrium at 50hpf, which shows a gradual yet continued process of growth between 34 and 72hpf, resulting in an atrial lumen size similar to the controls at 72-74hpf (Fig 5.14B-B'). Quantifications of the ventricular lumen in *hapln1a*$^{\Delta 241}$ mutants and their wild-type siblings did not identify defects in this chamber's filling capacity nor its growth dynamics during the analysed timeframe, suggesting loss of Hapln1a mainly has an impact on atrial development.

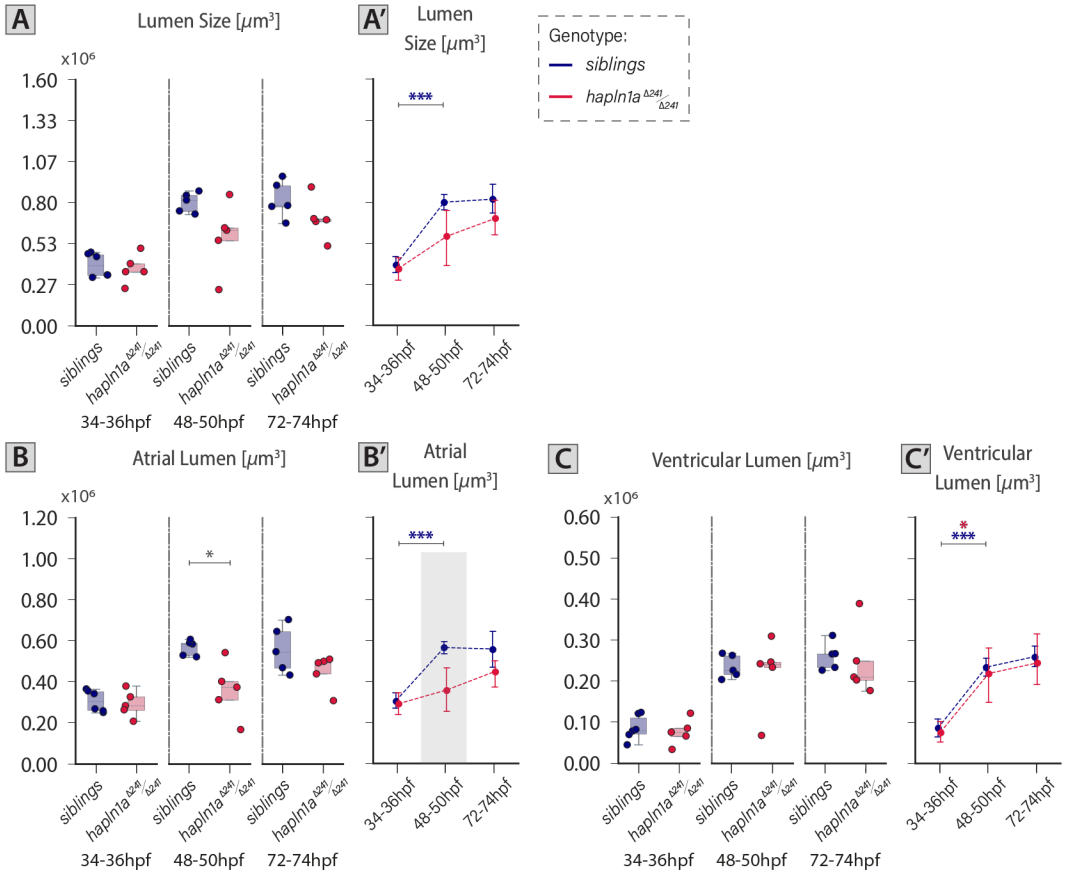

Fig 5.14. *hapln1a*$^{\Delta 241}$ mutants have reduced blood filling capacity at looping and ballooning stages.
A-C'. Lumen size (i.e. volume) quantification of the heart (A-A') and its individual chambers (atrium: B-B', ventricle: C-C') using *morphoHeart* in *hapln1a*$^{\Delta 241}$ mutants and its wild-type siblings at 34-36hpf, 48-50hpf and 72-74hpf. At 48-50hpf the atrial lumen is significantly reduced in *hapln1a*$^{\Delta 241}$ mutants compared to wild-type siblings (*p-value=0.01148*). No other lumen size defects are identified throughout the analysed stages. A', B' and C' are point-plots of the data presented in A, B, and C, respectively. A-C': Error bars with 95% confidence

interval of the mean. 34-36hpf: *siblings n=6*, *hapln1a*$^{\Delta 241/\Delta 241}$ *n=5*; 48-50hpf: *siblings n=5*, *hapln1a*$^{\Delta 241/\Delta 241}$ *n=5*; 72-74hpf: *siblings n=5*, *hapln1a*$^{\Delta 241/\Delta 241}$ *n=5*. For details regarding the statistical analyses used to compare this set of data see *Note#5.4* (pg.182). Only significant comparisons are shown. ***: *p-value*<0.001, *: *p-value*<0.05

To understand with more detail the defects in atrial morphology identified in *hapln1a*$^{\Delta 241}$ mutant hearts, chamber shape was further investigated using atrial-fitted-ellipse dimensions and myocardial ballooning heatmaps (for more details about these morphometric parameters, see Chapter 3, Fig 3.10 and Section 4.5.5 respectively). Analysis of atrial morphology using fitted ellipses identified that the small atria in the heart tube of *hapln1a*$^{\Delta 241}$ mutants are characterised by shorter and narrower dimensions (Fig 5.15B,C). Unexpectedly, at 48-50hpf, when *hapln1a*$^{\Delta 241/\Delta 241}$ display the most profound defects in atrial size (Fig 5.13B-B'), no statistical differences were found in any of the atrial morphology variables when compared *hapln1a*$^{\Delta 241}$ atria to that of controls. Closer examination of the data distribution at 48-50hpf for each variable identified an increased variance in the ellipse measurements of *hapln1a*$^{\Delta 241/\Delta 241}$ atria, particularly in the atrial depth and width (Fig 5.15A,C) driven by one heart whose measurement deviated greatly from the average. If those hearts were considered as outliers for these variables, a reduced depth and width in the atrium of *hapln1a*$^{\Delta 241}$ mutants would be the leading causes of a smaller chamber size. Interestingly, the dynamics of atrial 3D morphology in the *hapln1a*$^{\Delta 241}$ mutants appear to be only distinguishable from controls when analysing the atrial width, recognising a failure in the *hapln1a*$^{\Delta 241/\Delta 241}$ atrium to change its width throughout the analysed timeframe. These morphological defects in atrium of *hapln1a*$^{\Delta 241}$ mutants were further corroborated when comparing the atrial average 2D myocardial ballooning representations (Fig 5.16). At both stages (34-36 and 48-50hpf), *hapln1a*$^{\Delta 241}$ mutant hearts present smaller ballooning values in the 'U' shape colour pattern around the AVC region of the atrium when compared to controls (Fig 5.16A-A', B-B'), indicating that atrial failure to grow in the *hapln1a*$^{\Delta 241/\Delta 241}$ is linked to impaired chamber ballooning. No other defects are identified in looping nor ballooning of the *hapln1a*$^{\Delta 241}$ promoter mutant hearts as development progresses.

Altogether these observations suggest *hapln1a*$^{\Delta 241}$ mutants present defective atrial growth dynamics between 34 and 50hpf and suggests Hapln1a is required to promote atrial growth and ballooning in the developing heart.

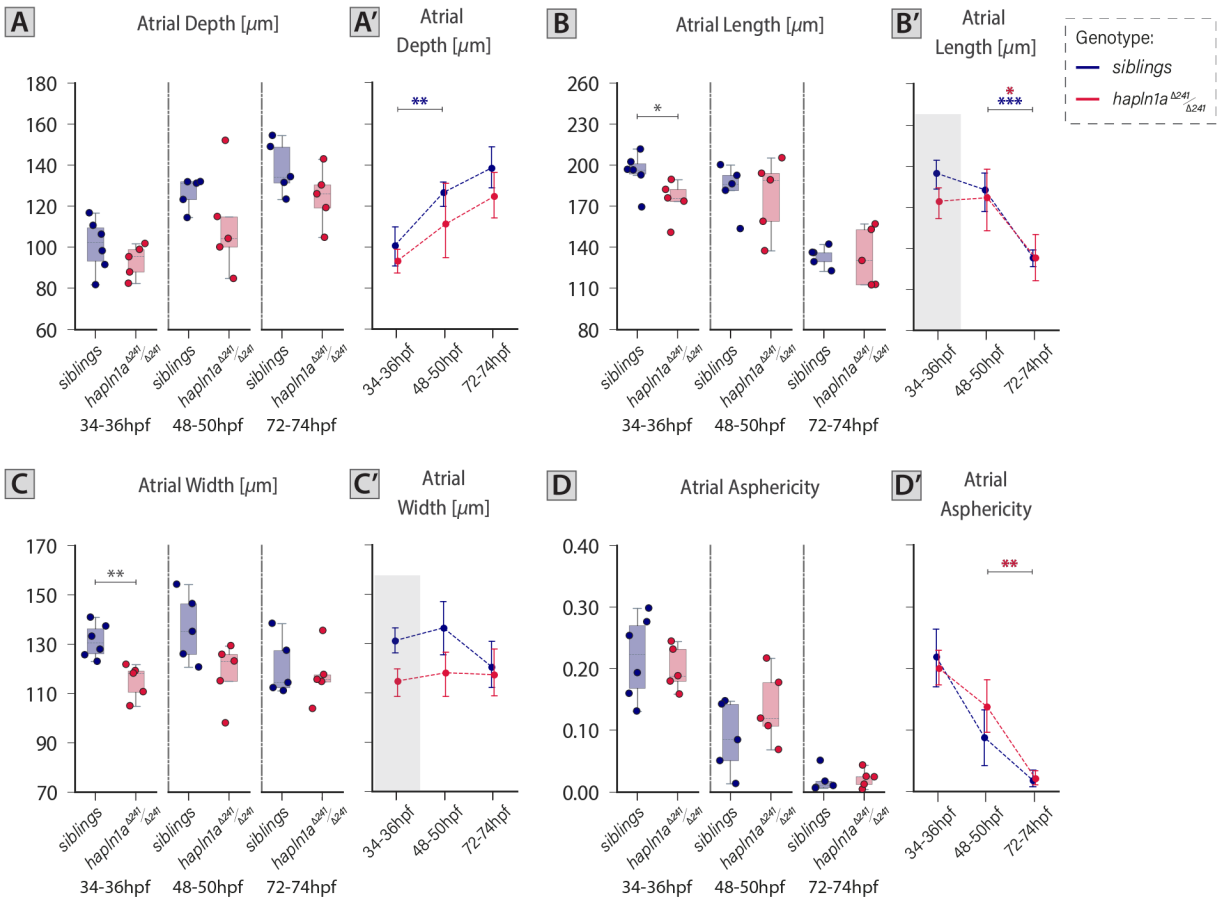

Fig 5.15. ***hapln1a$^{\Delta 241}$*** **promoter mutants present defective atrial growth dynamics during heart tube formation which remain as looping and ballooning morphogenesis progresses.**

A-D'. Quantifications of atrial depth (A-A'), length (B-B'), width (C-C'), and asphericity (D-D') using *morphoHeart* in *hapln1a$^{\Delta 241}$*mutants and wild-type siblings at 34-36hpf, 48-50hpf and 72-74hpf. At 34-36hpf the length and width of the atrium in *hapln1a$^{\Delta 241}$* mutant hearts are significantly reduced when compared to its wild-type siblings (length: *p-value=0.04231*, width: *p-value=0.00377*). As development progresses, no other defects are identified in the dimensions of *hapln1a$^{\Delta 241/\Delta 241}$* atria compared to controls. A', B' and C' are point-plots of the data presented in A, B, and C, respectively. A-D': Error bars with 95% confidence interval of the mean. 34-36hpf: *siblings n=6*, *hapln1a$^{\Delta 241/\Delta 241}$ n=5*; 48-50hpf: *siblings n=5*, *hapln1a$^{\Delta 241/\Delta 241}$ n=5*; 72-74hpf: *siblings n=5*, *hapln1a$^{\Delta 241/\Delta 241}$ n=5*. For details regarding the statistical analyses used to compare this set of data see *Note#5.4* (pg.182). Only significant comparisons are shown. ***: *p-value*<0.001, **: *p-value*<0.01, *: *p-value*<0.05.

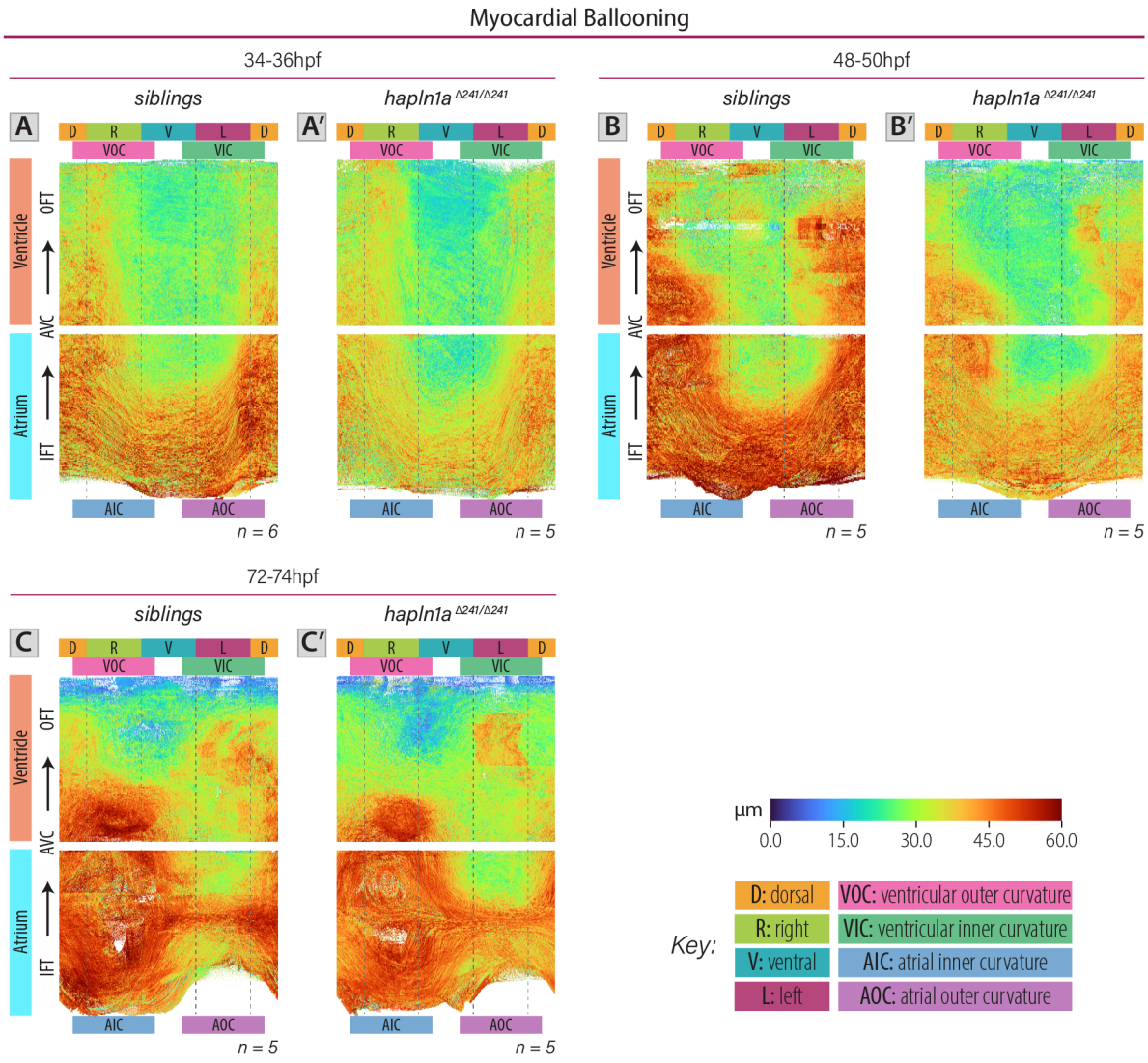

Fig 5.16. 2D myocardial ballooning heatmaps confirm atrial growth/ballooning defects in the *hapln1a*$^{\Delta 241}$ mutants at early stages of heart development.

A-C'. Average 2D myocardial ballooning heatmaps of the *hapln1a*$^{\Delta 241}$ mutants (A',B',C') and wild-type siblings (A, B, C) at 34-36hpf (A-A'), 48-50hpf (B-B') and 72-74hpf (C-C'). Myocardial ballooning heatmaps identify that *hapln1a*$^{\Delta 241}$ mutants present defective atrial ballooning dynamics between 34 and 50hpf when compared to controls. A-C' show the average planar projections of all the processed mutants and wild-type siblings at all the indicated stages. The number of heatmaps averaged per stage and genotype is indicated underneath each average heatmap. A-C' share colour-scale presented with the key below panels B-B'. D: Dorsal, R: Right, V: Ventral, L: Left, VOC: Ventricular Outer Curvature, VIC: Ventricular Inner Curvature, AOC: Atrial Outer Curvature, AIC: Atrial Inner Curvature, IFT: Inflow-tract, AVC: Atrioventricular Canal, OFT: Outflow-tract.

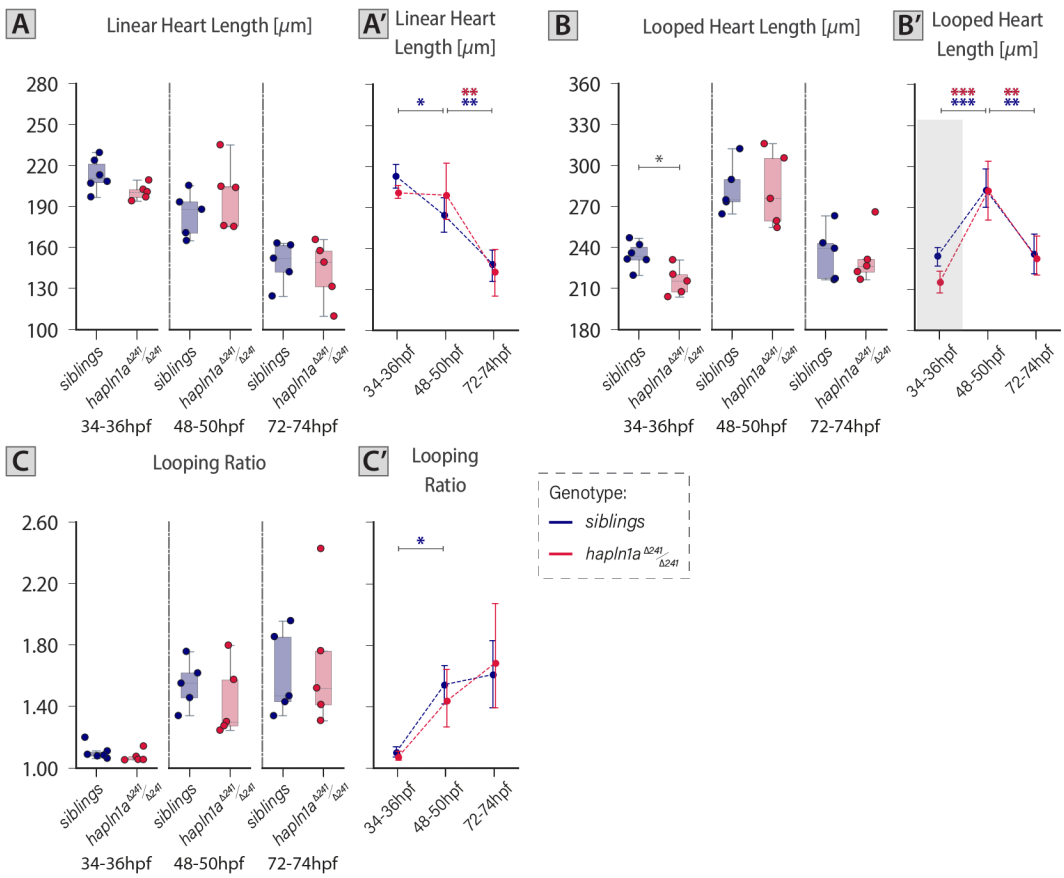

Fig 5.17. 3D looping ratio analysis confirms *hapln1a*$^{\Delta 241}$ promoter mutants do not present looping defects. **A-B.** Quantification of the linear (A) and looped (B) heart length of the heart using *morphoHeart* in *hapln1a*$^{\Delta 241}$ mutants and siblings at 34-36hpf, 48-50hpf and 72-74hpf. At 34-36hpf, the looped heart length of *hapln1a*$^{\Delta 241}$ mutants is significantly shorter when compared to the controls (*p-value=0.01295*). **C.** Quantification of looping ratio (quotient between 3D looped heart length or centreline length and 3D linear heart length) in *hapln1a*$^{\Delta 241}$ mutants and siblings at 34-36hpf, 48-50hpf and 72-74hpf. *hapln1a*$^{\Delta 241}$ mutants do not present looping defects during the analysed stages. A', B' and C' are point-plots of the data presented in A, B, and C, respectively. A-C': Error bars with 95% confidence interval of the mean. 34-36hpf: *siblings n=6*, *hapln1a*$^{\Delta 241/\Delta 241}$ *n=5*; 48-50hpf: *siblings n=5*, *hapln1a*$^{\Delta 241/\Delta 241}$ *n=5*; 72-74hpf: *siblings n=5*, *hapln1a*$^{\Delta 241/\Delta 241}$ *n=5*. For details regarding the statistical analyses used to compare this set of data see *Note#5.4* (pg.182). Only significant comparisons are shown. ***: *p-value*<0.001, **: *p-value*<0.01, *: *p-value*<0.05.

Despite the identified atrial defects during looping and ballooning and similar to the looping analysis performed using the *myl7* ISHs (Fig 5.9G), analysis of looping morphogenesis in 3D with *morphoHeart* revealed *hapln1a*$^{\Delta 241}$ promoter mutants do not present looping defects (Fig 5.17). Expectedly, because of the already identified size defect at early looping stages (Fig 5.13, 5.15B), the looped heart lengths of *hapln1a*$^{\Delta 241}$ mutants are shorter than that of the wild-type controls at 34-36hpf.

Early defects in heart tube size (Fig 5.13) yet no defects in lumen size (Fig 5.14) suggest the tissue volume of the cardiac layers comprising the primary tube might be reduced. Measurements of the myocardial and endocardial tissue volumes at early looping stages (34-36hpf) confirmed that the heart tube of *hapln1a*$^{\Delta 241}$ mutants is comprised of less cardiac tissue in the atrium when compared to their wild-type siblings (Fig 5.18A,C). This reduction in tissue volume produces an early atrial tube with a non-defective lumen (Fig 5.14B) despite this chamber's smaller size (Fig 5.13B). Regardless of these early defects, quantifications of the myocardial and endocardial tissue volume per chamber at 48-50 and 72-74hpf did not reveal differences in these variables for the *hapln1a*$^{\Delta 241}$ mutants when compared to wild-type siblings.

Interestingly, closer evaluation of the myocardial and endocardial volumes at later stages identified, similar to the analysis of atrial morphology (Fig 5.15), an increased variance in the volumetric measurements per

chamber of *hapln1a*$^{\Delta 241/\Delta 241}$ particularly at 48-50hpf. Despite this augmented variance, the tissue dynamics followed by the myocardium and endocardium in each chamber appear to be unaltered in *hapln1a*$^{\Delta 241}$ mutants between 34-36 and 48-50hpf (compare the slopes in the point-plots in Fig 5.18A',C',D'). Intriguingly, regardless of the tissue volume defects identified at early stages, the tissue volume that comprises either of the chambers in *hapln1a*$^{\Delta 241}$ mutant hearts at 72-74hpf is indistinguishable to that comprising wild-type hearts, suggesting some mechanism must be in place during development that establishes the size and tissue composition of the heart as it transitions to an early maturing stage.

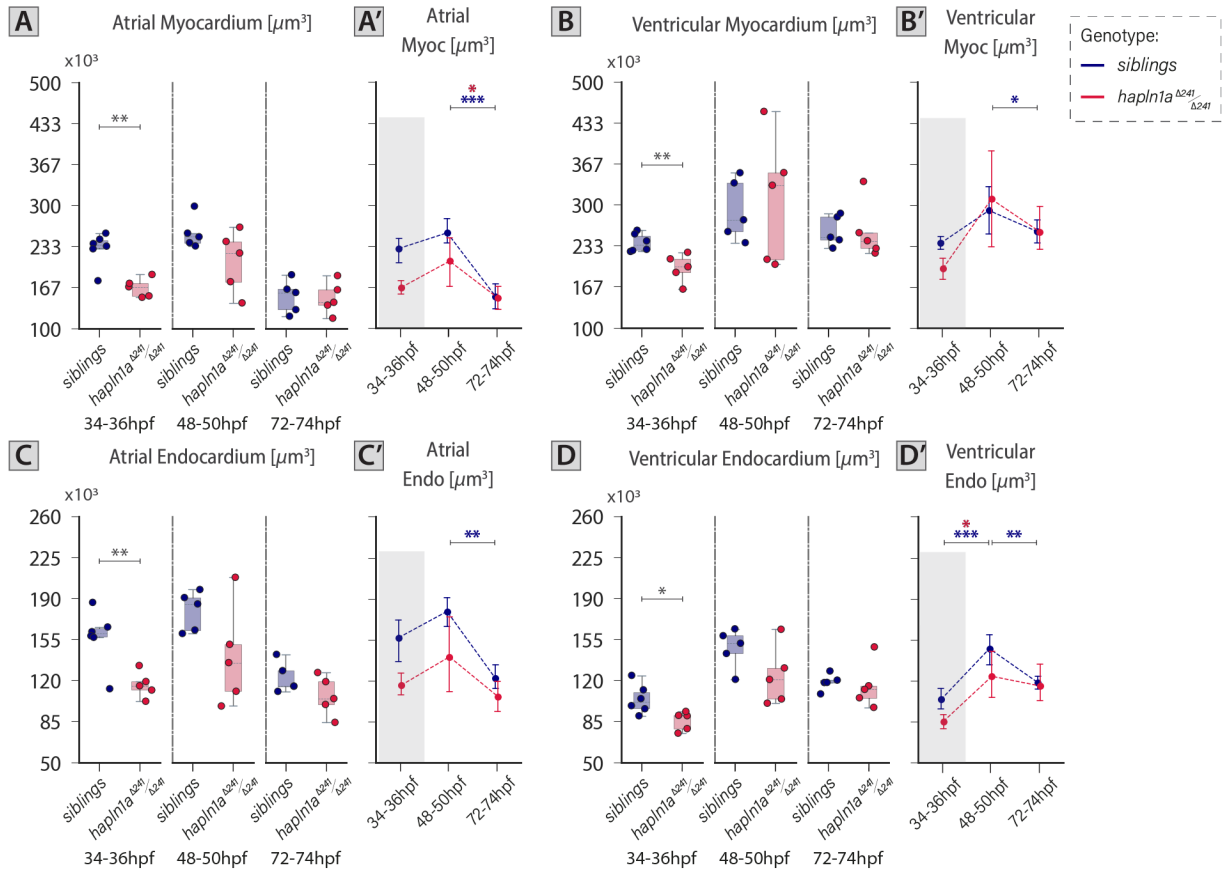

Fig 5.18. Early looping hearts of *hapln1a*$^{\Delta 241}$ mutants have reduced myocardial and endocardial tissue volume in the atrium.

A-D'. Quantification of the myocardial (A-B') and endocardial (C-D') tissue volume comprising the atrium (A-A', C-C') and ventricle (B-B', D-D') in *hapln1a*$^{\Delta 241}$ mutants and siblings at 34-36hpf, 48-50hpf and 72-74hpf. *hapln1a*$^{\Delta 241}$ mutant hearts have reduced myocardial and endocardial tissue volumes at early looping stages (34-36hpf) when compared to wild-type siblings (myocardial volume: atrium *p-value=0.00125,* ventricle *p-value=0.00589*; endocardial volume: atrium *p-value=0.00727*, ventricle *p-value=0.01843*). Non-significant differences were found when comparing the volume of the myocardium and the endocardium in both chambers at 48-50 and 72-74hpf. A', B', C' and D' are point-plots of the data presented in A, B, C, and D, respectively. A-D': Error bars with 95% confidence interval of the mean. 34-36hpf: *siblings n=6*, *hapln1a*$^{\Delta 241/\Delta 241}$ *n=5*; 48-50hpf: *siblings n=5*, *hapln1a*$^{\Delta 241/\Delta 241}$ *n=5*; 72-74hpf: *siblings n=5*, *hapln1a*$^{\Delta 241/\Delta 241}$ *n=5*. For details regarding the statistical analyses used to compare this set of data see *Note#5.4* (pg.182). Only significant comparisons are shown. ***: *p-value*<0.001, **: *p-value*<0.01, *: *p-value*<0.05.

Two mechanisms could underly the reduced atrial size phenotype in *hapln1a*$^{\Delta 241}$ mutants at 48-50hpf: reduced cell size, reduced cell number, or an additive effect of the two. To examine this further and investigate the tissue rearrangements undertaken by *hapln1a*$^{\Delta 241/\Delta 241}$ cells in an atrial chamber that has altered growth-compaction dynamics, cell counts and internuclear distance (IND) analysis were performed in a *Tg(myl7:lifeActGFP); Tg(myl7:DsRed)* double transgenic *hapln1a*$^{\Delta 241}$ heterozygous incross at 50 and 72hpf using *morphoCell* (Fig 5.19 and 5.20) (for details regarding *morphoCell* and its quantifications see

Chapter 3, Section 7.1 and Chapter 4, Fig 4.10E). Similar to the wild-type characterisation, to make sure all the DsRed positive cells were being captured, embryos were fixed at the stages of interest, immunostained to boost both fluorescent signals (i.e. GFP and DsRed) and imaged in the light-sheet microscope.

Comparative analysis of the total number of cells making the *hapln1a*$^{\Delta 241}$ mutant hearts and its individual chambers at both developmental stages did not reveal differences when compared with their wild-type siblings (Fig 5.19C,D). Just like wild-type hearts, the number of cells comprising the atrium in *hapln1a*$^{\Delta 241/\Delta 241}$ does not change between 50 and 72hpf, while it significantly increases in the ventricle (Fig 5.19D). Together, these observations validate that Hapln1a is not required to regulate cell number in either chamber within the analysed timeframe and suggest that reduced cell size might be the cause of the atrial phenotype identified during looping and ballooning.

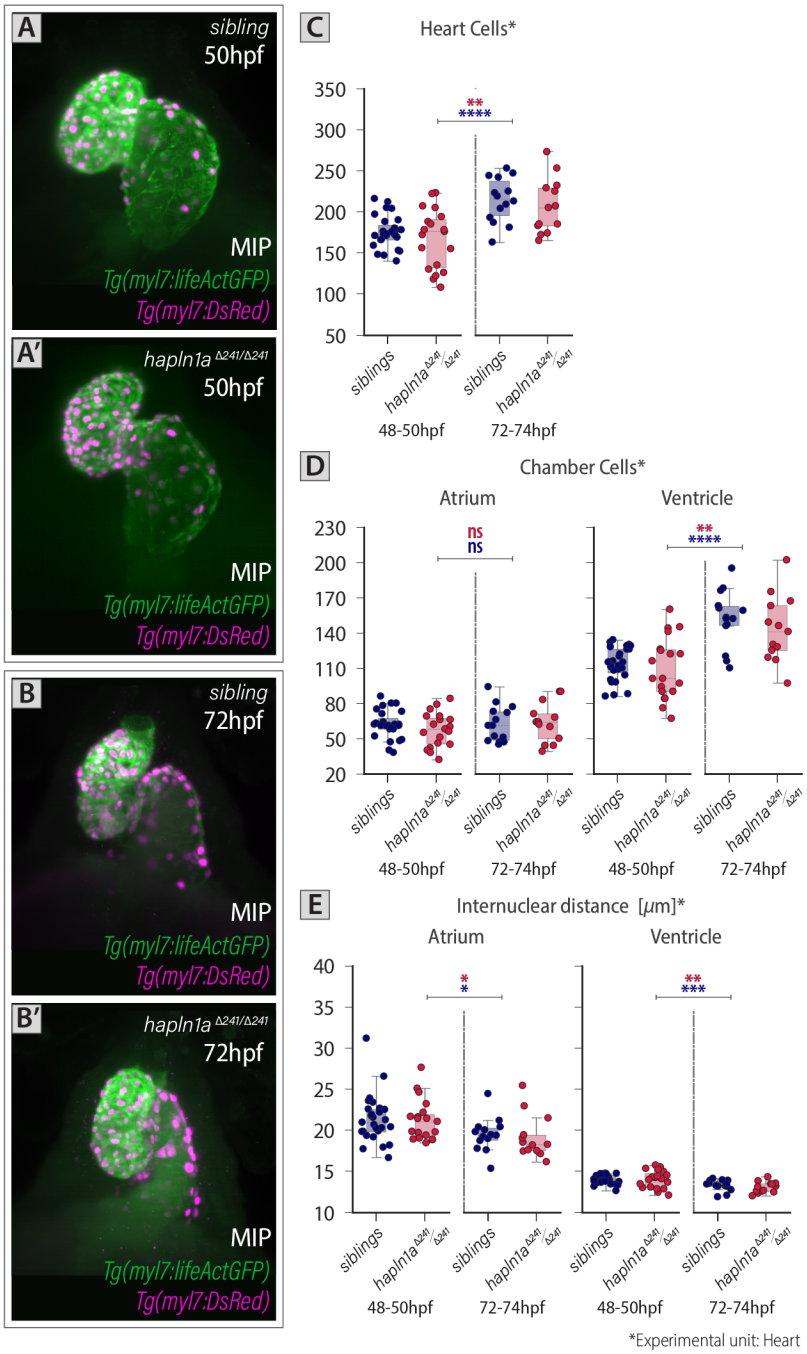

Fig 5.19. *hapln1a*$^{\Delta 241}$ promoter mutants have no defects in cell number nor cell size at 50 and 72hpf.
A-B'. Maximum intensity projections of double transgenic wild-type (A,B) and *hapln1a*$^{\Delta 241/\Delta 241}$ (A',B') zebrafish embryos with myocardial tissue and nuclear marker fixed at 50 (A-A') and 72hpf (B-B'), immunostained to boost the fluorescent signals and imaged on the light-sheet microscope. *Tg(myl7:lifeActGFP)* in green marks the

myocardium and *Tg(myl7:DsRed)* signal in magenta marks the myocardial nuclei. **C-D.** Quantification of cell number in the heart (C) and each chamber (D) using *morphoCell*. Like wild-type embryos, the number of cells making up the heart in *hapln1a*$^{\Delta 241}$ mutants increases between 50 and 72hpf, driven mainly by an increase in the number of cells making up the ventricle (heart: wild-type *p-value<0.00001*, *hapln1a*$^{\Delta 241/\Delta 241}$ *p-value=0.00385*; ventricle: wild-type *p-value<0.00001*, *hapln1a*$^{\Delta 241/\Delta 241}$ *p-value=0.00186*). **E.** Quantification of average IND identifies that the cell size per chamber in *hapln1a*$^{\Delta 241/\Delta 241}$ is unaltered when compared to controls (atrium: wild-type *p-value<0.02170*, *hapln1a*$^{\Delta 241/\Delta 241}$ *p-value=0.01133*; ventricle: wild-type *p-value<0.00089*, *hapln1a*$^{\Delta 241/\Delta 241}$ *p-value=0.00862*). A-B': Ventral views with anterior to the top. A: Atrium, V: Ventricle, IND: Internuclear-distance, MIP: Maximum intensity projection. C-E: Error bars with 95% confidence interval of the mean. 50hpf: *siblings n=27*, *hapln1a*$^{\Delta 241/\Delta 241}$ *n=19*; 72hpf: *siblings n=14, hapln1a*$^{\Delta 241/\Delta 241}$ *n=13*. For details regarding the statistical analyses used to compare this set of data see *Note#5.4* (pg.182). Only significant comparisons are shown. ****: *p-value*<0.0001, ***: *p-value*<0.001, **: *p-value*<0.01, *: *p-value*<0.05, ns: not significant.

_____

Cell size changes and rearrangements within the ventricle and its comprising regions at the analysed stages are not altered in the *hapln1a*$^{\Delta 241}$ mutants (Fig 5.19D,E and 5.20B,D), corroborating that loss of Hapln1a does not affect the morphogenesis of this chamber. Unexpectedly, analysis of IND at 50hpf in the atrium and its different chamber sections indicated that the atrial cells of *hapln1a*$^{\Delta 241}$ mutants have indistinguishable size (Fig 5.19E) and distribution (Fig 5.20A,C) as those in wild-type hearts, rejecting the hypothesis that differences in atrial cell size resulted in atrial growth defects at 48-50hpf (Fig 5.13B).

Interestingly when studying the dynamics of atrial cells' IND as the heart transitions from a looping to an early maturing state (50→72hpf), due to the fact that this chamber in *hapln1a*$^{\Delta 241}$ mutants is smaller at 50hpf, the increased cellular packing dynamics involved in the compaction of the wild-type chamber (Fig 4.11B) are not followed by the atrial cells in the *hapln1a*$^{\Delta 241}$ mutants (Fig 5.20C). However, significant reductions in cell size are still observed between these two stages in the *hapln1a*$^{\Delta 241/\Delta 241}$ atrial cells located in the ventral face and surprisingly in the outer curvature, suggesting that in spite of already exhibiting the atrial size of a wild-type heart in a maturing state, cellular rearrangements are still required within this 48-50hpf chamber of *hapln1a*$^{\Delta 241/\Delta 241}$ to support its continued development.

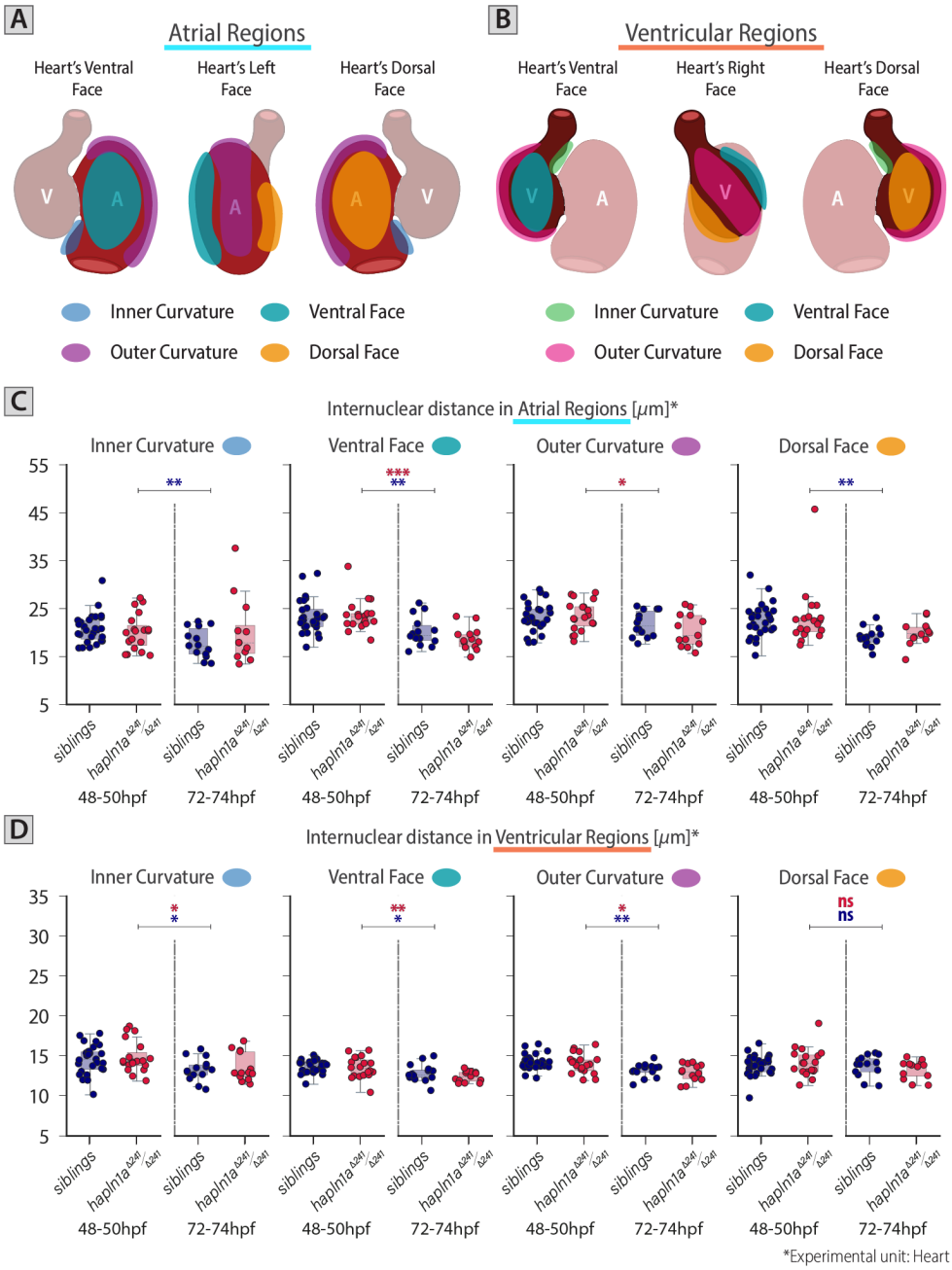

Fig 5.20. Atrial cell-shrinking dynamics are altered in *hapln1a*$^{\Delta 241}$ mutants between 50 and 72hpf.
A-B. Schematic illustrating with different colours the four different chamber regions into which atrial (A) and ventricular (B) cells can be further classified to better understand cell distribution and size in each chamber. **C.** Quantification of average internuclear distance (IND) of atrial cells positioned in the inner curvature, ventral face, outer curvature, or dorsal face of this chamber, identifies different cellular-packing events in the *hapln1a*$^{\Delta 241}$ promoter mutants when compared to that of the wild-type siblings. **D.** Quantification of average internuclear distance (IND) of ventricular cells per region, recognises that the ventricular IND and its dynamics between 50 and 72hpf are unaltered in *hapln1a*$^{\Delta 241}$ mutants. A: Atrium, V: Ventricle. C-D: Error bars with 95% confidence interval of the mean. 50hpf: *siblings n=27*, *hapln1a*$^{\Delta 241/\Delta 241}$ *n=19*; 72hpf: *siblings n=14* *hapln1a*$^{\Delta 241/\Delta 241}$ *n=13*. For details regarding the statistical analyses used to compare this set of data see *Note#5.4* (pg.182). Only significant comparisons are shown. ***: *p-value*<0.001, **: *p-value*<0.01, *: *p-value*<0.05, ns: not significant.

Altogether, analysis of chamber size and morphology, combined with quantifications of myocardial tissue volume and cell counts per chamber, suggest Hapln1a is required to promote atrial growth and ballooning during looping and ballooning morphogenesis.

3.1.4 HAPLN1A STABILISES THE CARDIAC ECM AT EARLY STAGES OF HEART DEVELOPMENT

As Hapln1a is one of the ECM components present in the early cardiac jelly as the heart tube forms and then undergoes looping (Fig 5.2E-L, 5.3A-O), is required for atrial growth and promotes ECM cross-linking (Spicer, Joo and Bowling, 2003; Lockhart *et al.*, 2011a), the next step was to determine whether the identified defects in heart size and ballooning are linked with defective cardiac jelly composition or regionalization in *hapln1a*$^{\Delta 241}$ mutants. Initial differences are easily noted in the 3D renderings of the *hapln1a*$^{\Delta 241}$ mutant cardiac jellies, especially at the early looping and ballooning stages (Fig 5.21A-B').

Initial analysis of the 3D cardiac jelly of *hapln1a*$^{\Delta 241}$ mutant embryos at 34-36 and 48-50hpf identifies that *hapln1a*$^{\Delta 241}$ mutants display a reduction in thickness and changes in the distribution of the cardiac ECM, particularly in the outer curvatures of both chambers and the ventral face of the atrium when compared to wild-type siblings (Fig 5.21A-B').

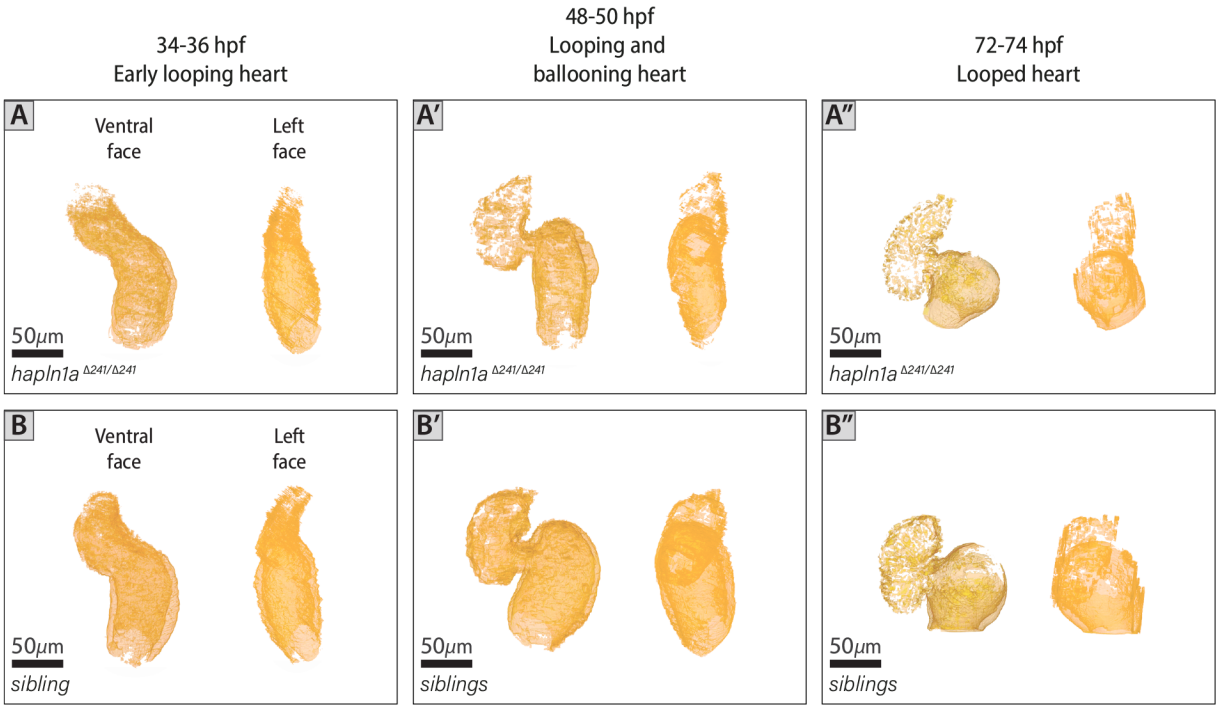

Fig 5.21. The cardiac jelly of *hapln1a*$^{\Delta 241}$ promoter mutants appear to have reduced thickness and abnormal distribution at 34-36 and 48-50hpf.
A-B''. Representative 3D reconstructions of the cardiac jelly of *hapln1a*$^{\Delta 241/\Delta 241}$ mutant (A-A'') and wild-type sibling (B-B'') hearts at key developmental stages (34-36hpf: A,B; 48-50hpf: A',B'; and 72-74hpf: A'',B''). As described by the labels in Panels A and B, all panels show the ventral face (on the left) and left face (on the right) of each of the presented hearts.

Quantification of cardiac jelly volume throughout development confirmed at 48-50hpf not only a significant reduction in the amount of cardiac jelly present in the whole heart of *hapln1a*$^{\Delta 241}$ mutants (Fig 5.22A), but also in each of its chambers (Fig 5.22B,C). Despite not being significantly different from the controls, the volume of cardiac jelly at early looping stages (34-36hpf) appears to be reduced in the atrium of the *hapln1a*$^{\Delta 241}$ mutant hearts. This result demonstrates that the early heart tube of *hapln1a*$^{\Delta 241/\Delta 241}$, in addition to being smaller in size, is comprised of less myocardial, endocardial, **and** cardiac jelly volumes and suggests Hapln1a might be required to establish an early looping heart tube with the right size and layer composition.

Starting from what appears to be a reduced volume of cardiac jelly in the early looping heart, the dynamics of expansion of the cardiac ECM in both chambers are impaired in the *hapln1a*$^{\Delta 241}$ mutants (Fig

5.22A',B',C'), evidenced by slow ECM expansion rates in the atrium and, contrary to wild-types, diminution in the ventricle. Surprisingly once the *hapln1a*$^{\Delta 241}$ mutant hearts have undergone looping and ballooning, the balance between secretion/degradation of the cardiac ECM in both chambers result in cardiac jelly volumes at early maturing stages that are undistinguishable from the controls.

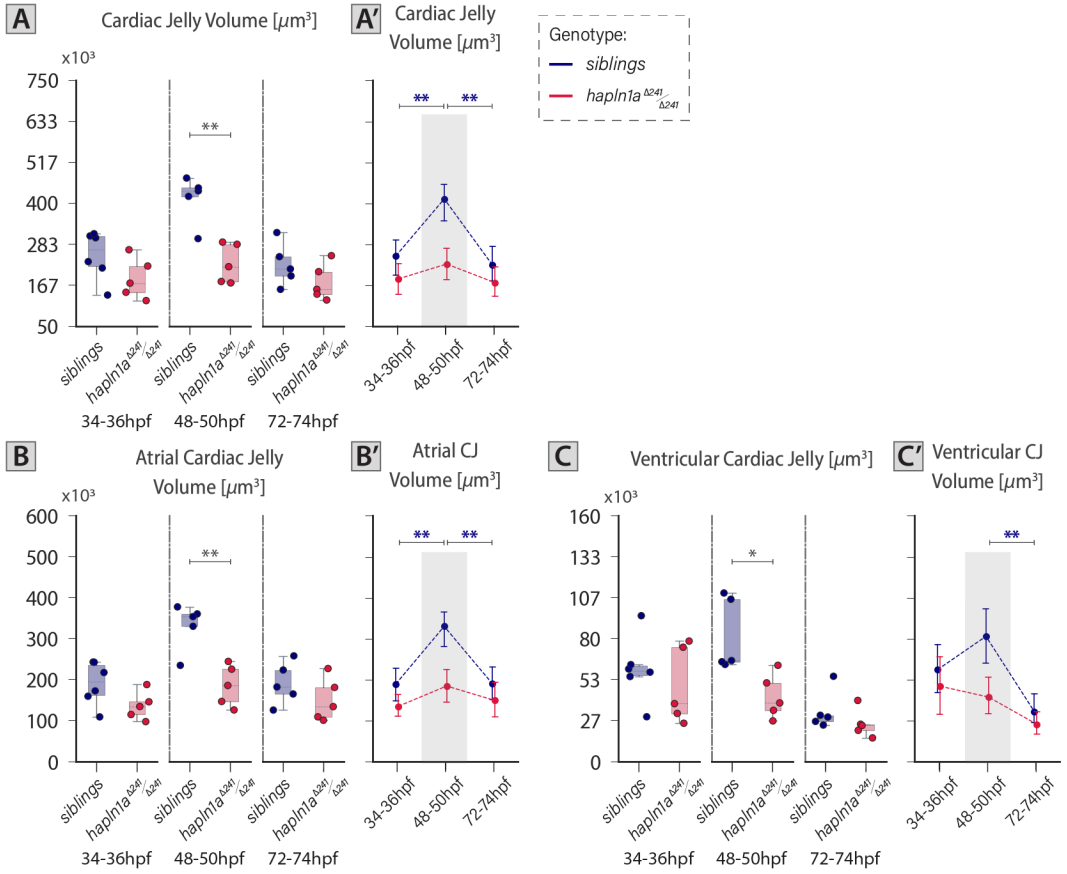

Fig 5.22. Hapln1a drives ECM expansion as the heart undergoes looping and ballooning morphogenesis.
A-C'. Quantification of cardiac jelly volume of the whole heart (A-A') and its chambers (atrium: B-B', ventricle: C-C') in *hapln1a*$^{\Delta 241}$ mutants and its wild-type siblings at 34-36hpf, 48-50hpf and 72-74hpf. At 48-50hpf, the cardiac jelly volume of *hapln1a*$^{\Delta 241}$ mutants is significantly reduced in the whole heart (A) and its individual chambers (B,C) when compared to controls (heart: *p-value=0.00142*, atrium: *p-value=0.00261*, ventricle: *p-value=0.01219*). A', B' and C' are point-plots of the data presented in A, B, and C, respectively. A-C': Error bars with 95% confidence interval of the mean. 34-36hpf: *siblings n=6*, *hapln1a*$^{\Delta 241/\Delta 241}$ *n=5*; 48-50hpf: *siblings n=5*, *hapln1a*$^{\Delta 241/\Delta 241}$ *n=5*; 72-74hpf: *siblings n=5*, *hapln1a*$^{\Delta 241/\Delta 241}$ *n=5*. For details regarding the statistical analyses used to compare this set of data see *Note#5.4* (pg.182). Only significant comparisons are shown. **: *p-value*<0.01, *: *p-value*<0.05. CJ: Cardiac Jelly.

To confirm if Hapln1a is the ECM component driving the asymmetric expansion of the cardiac ECM during early zebrafish heart development, 3D cardiac jelly meshes of *hapln1a*$^{\Delta 241}$ mutants were divided into left and right sides and volumetric measurements were acquired and quantified (Fig 5.23A-A') (for details regarding the sectioning of the cardiac jelly meshes, see Fig 4.13).

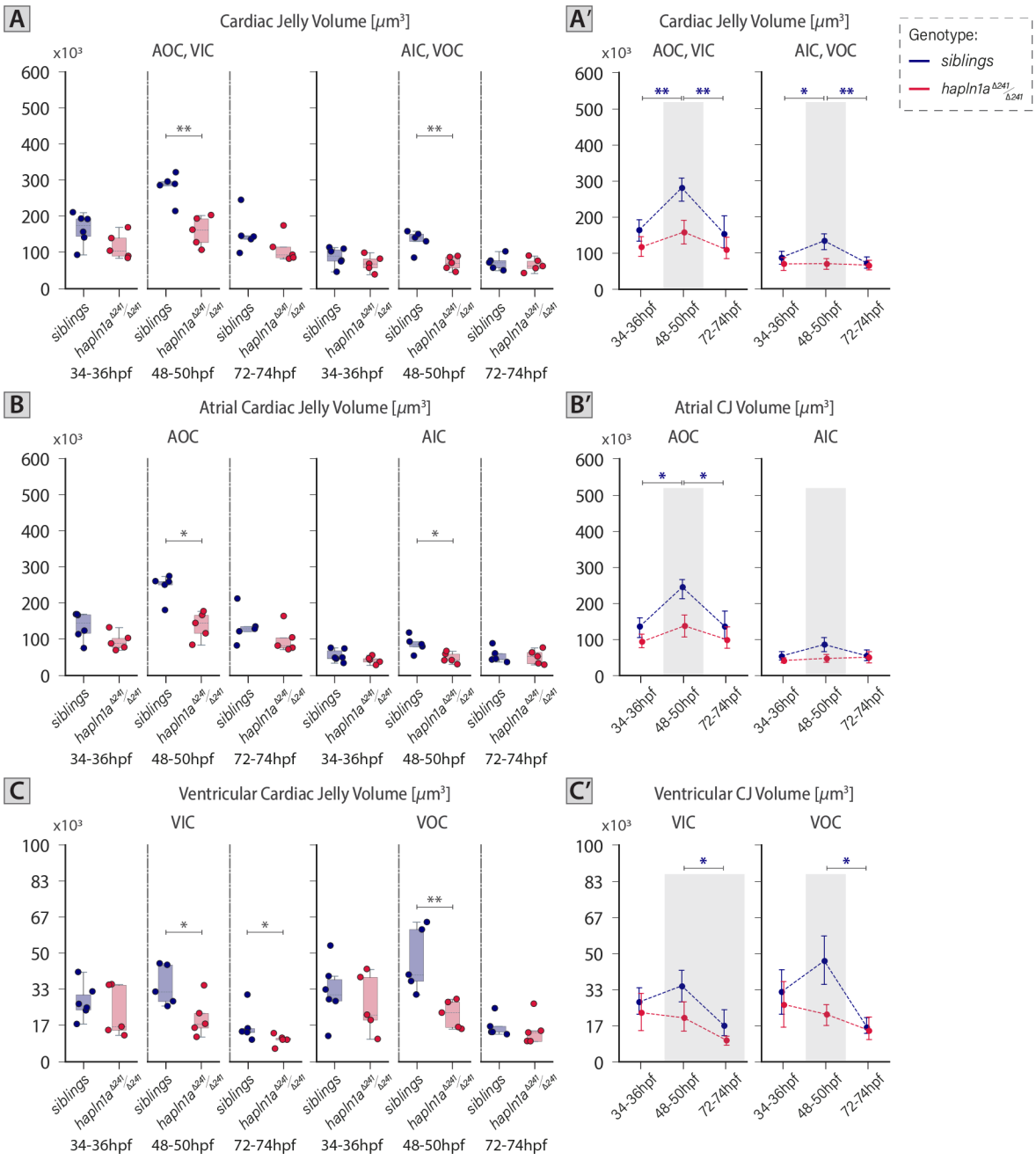

Fig 5.23. Hapln1a drives regionalised ECM expansion in the inner and outer curvatures of both heart chambers during looping and ballooning morphogenesis.

A-A'. Quantification of the volume of cardiac jelly in the AOC, VIC and AIC, VOC in *hapln1a*$^{\Delta 241}$ mutants and its wild-type siblings at 34-36hpf, 48-50hpf and 72-74hpf. At 48-50hpf the AOC, VIC and AIC, VOC cardiac jelly volumes are significantly reduced in *hapln1a*$^{\Delta 241}$ mutants when compared to its wild-type siblings (AOC, VIC: *p-value=0.00142,* AIC, VOC: *p-value=0.00342*). **B-B'.** Quantification of the volume of the atrial outer curvature (AOC) and inner curvature (AIC) in *hapln1a*$^{\Delta 241}$ mutants and its wild-type siblings at 34-36hpf, 48-50hpf and 72-74hpf. At 48-50hpf the AOC and AIC cardiac jelly volumes are significantly reduced in *hapln1a*$^{\Delta 241}$ mutants when compared to its wild-type siblings (AOC: *p-value=0.01219,* AIC: *p-value=0.01419*). **C-C'.** Quantification of the volume of the ventricular outer curvature (VOC) and inner curvature (VIC) in *hapln1a*$^{\Delta 241}$ mutants and its wild-type siblings at 34-36hpf, 48-50hpf and 72-74hpf. At 48-50hpf both the VIC and VOC cardiac jelly volumes are significantly reduced in *hapln1a*$^{\Delta 241}$ mutants when compared to its wild-type siblings (VIC: *p-value=0.03553;* VOC: *p-value=0.00947*). Later, at 72-74hpf the VIC cardiac jelly volume continues to be significantly reduced in the *hapln1a*$^{\Delta 241}$ mutants (*p-value=0.03671*). A', B' and C' are point-plots of the data presented in A, B, and C, respectively. A-C': Error bars with 95% confidence interval of the mean. 34-36hpf: *siblings n=6*, *hapln1a*$^{\Delta 241/\Delta 241}$ *n=5*; 48-50hpf: *siblings n=5*, *hapln1a*$^{\Delta 241/\Delta 241}$ *n=5*; 72-74hpf: *siblings n=5*, *hapln1a*$^{\Delta 241/\Delta 241}$ *n=5*. For details regarding the statistical analyses used to compare this set of data see *Note#5.4* (pg.182). Only significant

comparisons are shown. **: *p-value*<0.01, *: *p-value*<0.05. CJ: Cardiac jelly, AIC: Atrial Inner Curvature, AOC: Atrial Outer Curvature, VIC: Ventricular Inner Curvature, VOC: Ventricular Outer Curvature.

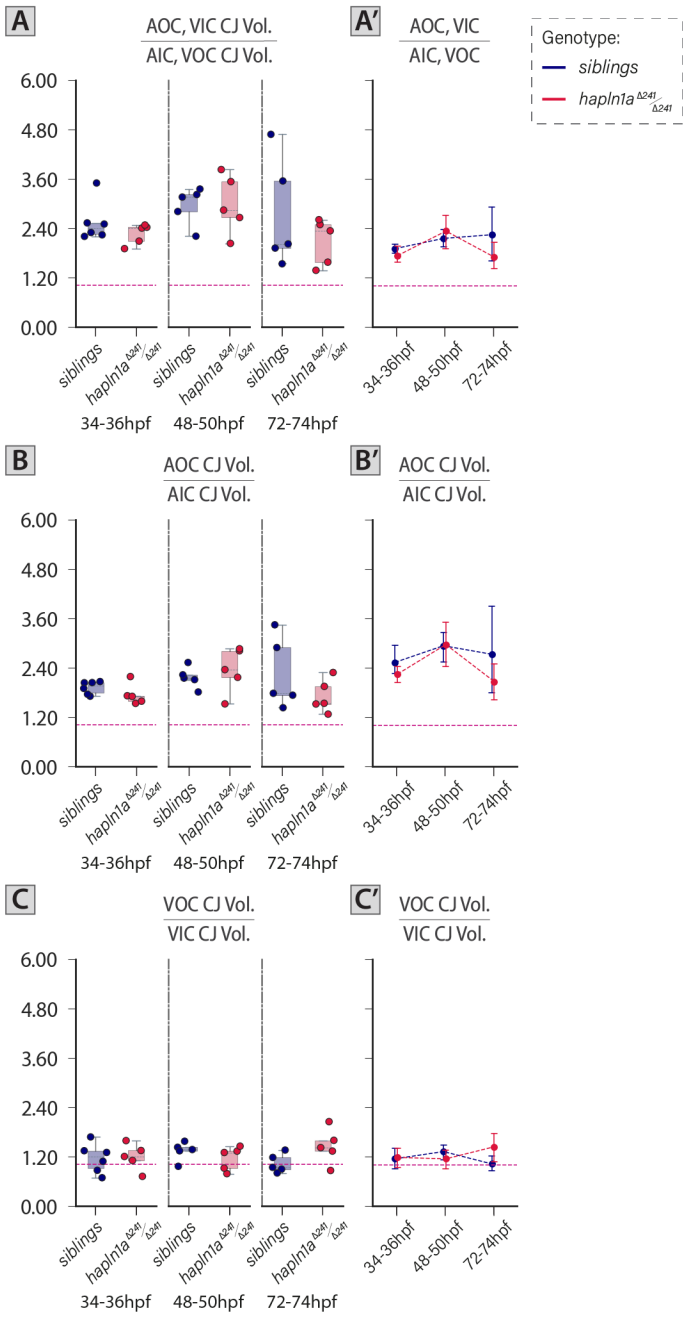

Fig 5.24. Some ECM asymmetry is retained in the atrium in the absence of Hapln1a. **A-A'.** Quantification of the quotient between AOC, VIC and AIC, VOC cardiac jelly volumes in the heart in *hapln1a*$^{\Delta 241}$ mutants and its wild-type siblings at 34-36hpf, 48-50hpf and 72-74hpf. **B-B'.** Quantification of the quotient between AOC and AIC cardiac jelly volumes in the heart in *hapln1a*$^{\Delta 241}$ mutants and its wild-type siblings at 34-36hpf, 48-50hpf and 72-74hpf. **C-C'.** Quantification of the quotient between VOC and VIC cardiac jelly volumes in the heart in *hapln1a*$^{\Delta 241}$ mutants and its wild-type siblings at 34-36hpf, 48-50hpf and 72-74hpf. A', B' and C' are point-plots of the data presented in A, B, and C, respectively. A-C': Error bars with 95% confidence interval of the mean. 34-36hpf: *siblings n=6*, *hapln1a*$^{\Delta 241/\Delta 241}$ *n=5*; 48-50hpf: *siblings n=5*, *hapln1a*$^{\Delta 241/\Delta 241}$ *n=5*; 72-74hpf: *siblings n=5*, *hapln1a*$^{\Delta 241/\Delta 241}$ *n=5*. For details regarding the statistical analyses used to compare this set of data see *Note#5.4* (pg.182). Only significant comparisons are shown. A-C'. No statistical analysis was run to compare this data. CJ: Cardiac jelly, Vol: Volume, AIC: Atrial Inner Curvature, AOC: Atrial Outer Curvature, VIC: Ventricular Inner Curvature, VOC: Ventricular Outer Curvature. Only significant comparisons are shown.

Analysis of the cardiac jelly volumes and dynamics in the left (AOC,VIC) and right (AIC,VOC) sides of the heart confirms that *hapln1a*$^{\Delta 241}$ mutant hearts fail to exhibit the normal expansion-reduction rates shown by the cardiac ECM of wild-type hearts, resulting in significantly reduced cardiac jelly volumes for both heart sides at 48-50hpf (Fig 5.23A-A'). Interestingly, while the right side of the heart (AIC,VOC) appears to maintain the cardiac ECM volume throughout the analysed timeframe, the expansion-reduction dynamics identified in the controls is observed albeit with a significantly reduced overall magnitude in the left side (AOC,VIC) of the *hapln1a*$^{\Delta 241}$ mutant hearts. Further analysis of the cardiac jelly volumes within chambers confirms this reduced expansion-reduction dynamics in the left are driven by the atrial outer curvature (AOC) (Fig 5.24B-B'), while the ventricular inner curvature (VIC, ventricular region comprising the left side

of the heart) shows a continued slow reduction of cardiac jelly volume through time (Fig 5.24C-C'). Left-to-right ratios in the whole heart and per chamber confirmed that despite the general defects in expanding the cardiac ECM, *hapln1a*$^{\Delta 241}$ mutant hearts, like wild-types, have an atrial-left-sided expansion of the cardiac ECM (ratios in Fig 5.24 B-B' for *hapln1a*$^{\Delta 241/\Delta 241}$ >1), which is established at early stages of development (earlier than 34-36hpf) and maintained as heart development of the mutant progresses.

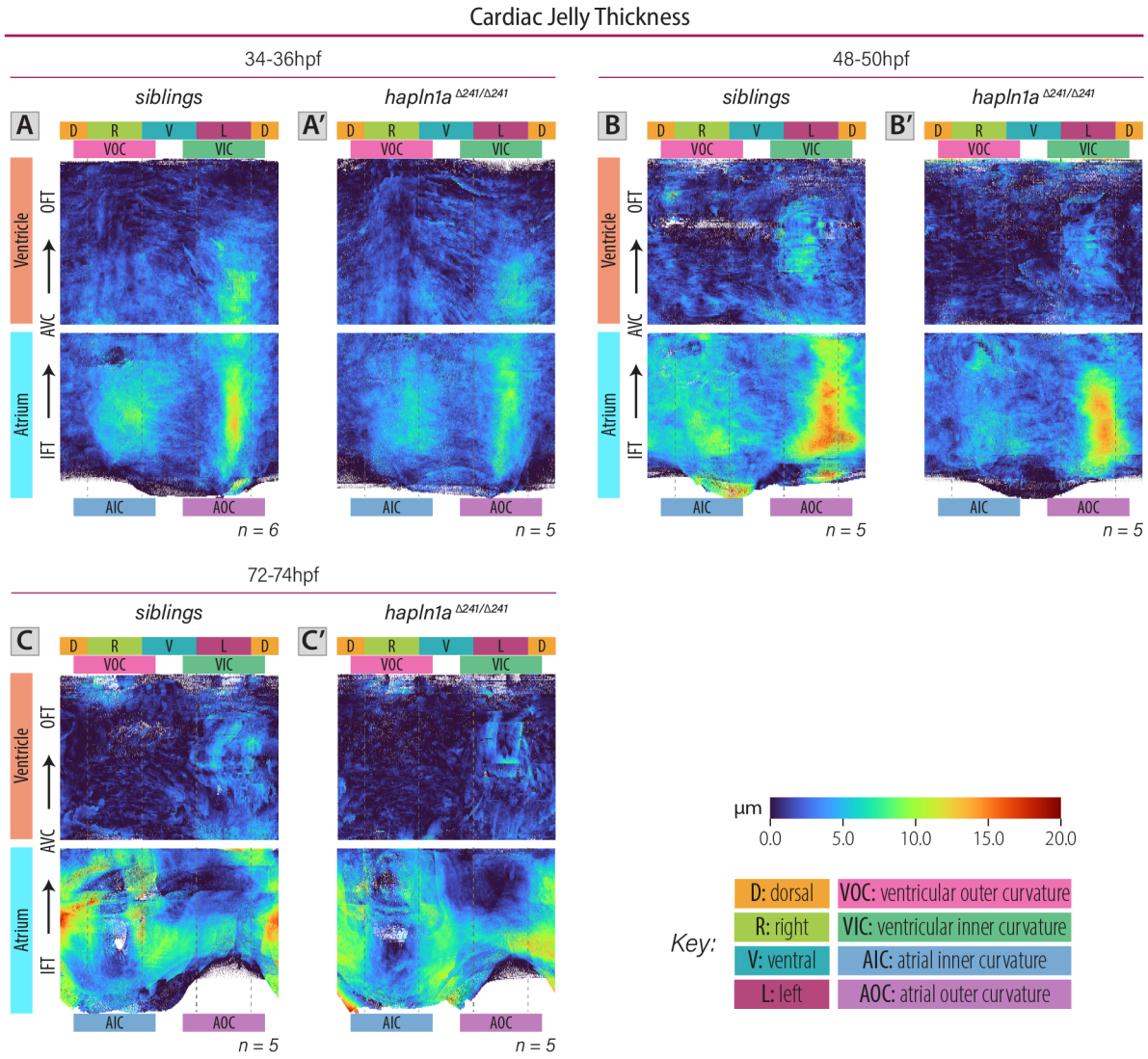

Fig 5.25. Despite residual regionalisation and asymmetry, the cardiac jelly thickness heatmap of *hapln1a*$^{\Delta 241}$ mutants identifies reduced ECM thickness values in both chambers across the analysed stages.
A-C'. Average 2D cardiac jelly thickness heatmaps of the *hapln1a*$^{\Delta 241}$ mutant (A',B',C') and wild-type siblings(A, B, C) hearts at 34-36hpf (A-A'), 48-50hpf (B-B') and 72-74hpf (C-C'). A-C' show the average planar projections of all the processed mutants and wild-type siblings at all the indicated stages. The number of heatmaps averaged per stage and genotype is indicated underneath each average heatmap. A-C' share colour-scale presented with the key below panels B-B'. D: Dorsal, R: Right, V: Ventral, L: Left, VOC: Ventricular Outer Curvature, VIC: Ventricular Inner Curvature, AOC: Atrial Outer Curvature, AIC: Atrial Inner Curvature, IFT: Inflow-tract, AVC: Atrioventricular Canal, OFT: Outflow-tract.

Characterisation of cardiac jelly distribution using average 2D heatmap plots confirmed the reduction in cardiac ECM volume of the *hapln1a*$^{\Delta 241/\Delta 241}$ atria (Fig 5.22B-B', 5.23B-B'), by exhibiting, despite residual regionalisation and asymmetry, lower ECM thickness values throughout this chamber at 34-36 and 48-50hpf (Fig 5.25A,B) when compared to wild-type (Fig 5.25A',B'). Corroborating the regional ECM volume dynamics identified in the atrium of *hapln1a*$^{\Delta 241}$ mutants (Fig 5.23B-B'), analysis of atrial cardiac jelly

thickness heatmaps reveals an increase in the thickness of this layer in the AOC between 34 and 50hpf whilst the ECM thickness in the AIC is maintained, yet somehow redistributed along the chamber's length (compare the atrial heatmaps in Fig 5.25 A' and B'). Similarly, continuous reduction of the ventricular ECM as the chamber develops is evidenced by finding progressively darker colour patterns representing thinner cardiac ECM throughout the cardiac jelly heatmaps of this chamber (compare the ventricular heatmaps in Fig 5.25 A',B' and C').

Together, analysis of cardiac jelly volume and distribution around the heart indicates that despite its regionalised expression and deposition at early stages of heart development (disc and tube, Fig 5.2E-H,W-X, Fig 5.3A-H), Hapln1a does not drive the cardiac ECM asymmetries throughout zebrafish heart development.

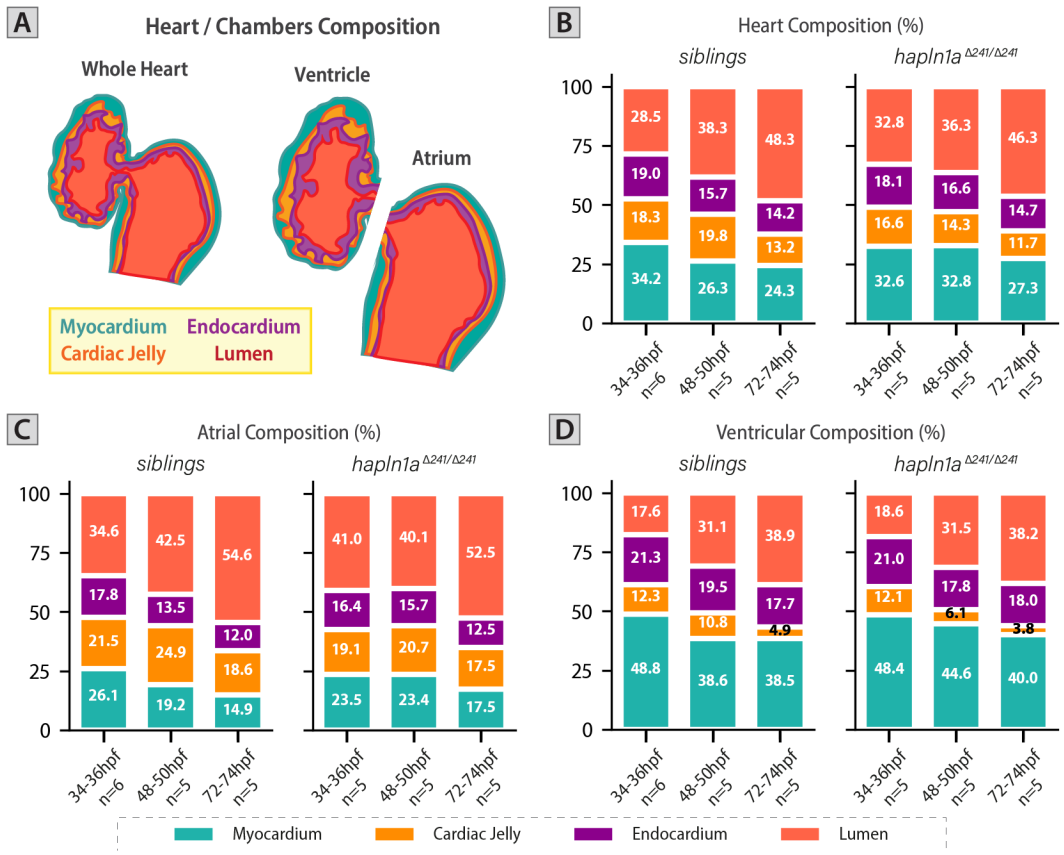

Fig 5.26. Tissue composition analysis of *hapln1a*$^{\Delta 241}$ promoter mutant confirms that loss of Hapln1a results in atria with more profound defects.

A. 2D schematic of the whole heart, atrium and ventricle illustrating the different heart layers making up the heart. **B-D.** Percentage composition of the myocardium, endocardium, cardiac jelly, and lumen, in the whole heart (B), and the individual chambers (atrium: C, ventricle: D) of *hapln1a*$^{\Delta 241}$ mutants and their wild-type siblings over the course of cardiac morphogenesis. The stacked graph bars were created using the averages of the percentage composition of each analysed heart genotype at each stage. 34-36hpf: *siblings n=6*, *hapln1a*$^{\Delta 241/\Delta 241}$ *n=5*; 48-50hpf: *siblings n=5*, *hapln1a*$^{\Delta 241/\Delta 241}$ *n=5*; 72-74hpf: *siblings n=5*, *hapln1a*$^{\Delta 241/\Delta 241}$ *n=5*.

Knowing that loss of Hapln1a results in distinct defects in chamber size, tissue and ECM volume dynamics, analysis of the percentage composition in *hapln1a*$^{\Delta 241}$ mutants was undertaken (Fig 5.26). In this type of analysis, normalising the volume of the comprising layers to the size of the heart (or chamber) allows an unbiased analysis of whether changes in heart (or chamber) size produces proportional changes in layer composition as development progresses.

Comparative chamber composition analysis at 34-36hpf between *hapln1a*$^{\Delta 241}$ mutants and wild-type siblings identifies that the composition of the atrium in the early looping hearts is altered in the mutants,

recognising reduced tissue and ECM percentages in a chamber with a proportionally bigger lumen (Fig 5.26C). Interestingly, regardless of having smaller ventricles, the ventricular percentage composition of *hapln1a*$^{\Delta 241}$ in the early looping heart tube is unaltered when compared to the controls (Fig 5.26D).

As expected, the most profound changes in percentage composition are identified in both chambers at 48-50hpf in the *hapln1a*$^{\Delta 241}$ mutants. Reduced ECM percentages in the heart at this stage result in augmented percentages in either one or both cardiac tissues comprising each chamber (atrium: myocardium and endocardium, ventricle: myocardium). Interestingly, analysis of the percentage composition of the atrium and the ventricle when the heart is transitioning to an early maturing state (72-74hpf) identifies the composition of either chamber in *hapln1a*$^{\Delta 241}$ mutants is indistinguishable from wild-type.

Altogether, morphometric analysis of the *hapln1a*$^{\Delta 241}$ mutant phenotype suggests deposition of Hapln1a is required in the nascent cardiac ECM, to promote atrial-specific morphogenetic processes during the formation of the heart tube and the establishment of a ballooned chamber morphology during looping and ballooning morphogenesis. The altered cardiac jelly dynamics in *hapln1a*$^{\Delta 241/\Delta 241}$, suggested that within this ECM, Hapln1a is indispensable for regulating chamber specific ECM deposition and degradation processes that promote and ensure the normal morphogenesis in this organ.

3.1.5 *hapln1a* $^{\Delta 187}$ AND *hapln1a* $^{\Delta 241}$ DISPLAY DIFFERENT PHENOTYPES

Having characterised the phenotype of *hapln1a*$^{\Delta 241}$ promoter mutants, the next step was to confirm if *hapln1a*$^{\Delta 187/\Delta 187}$, the other recovered *hapln1a* promoter allele (Fig 5.5), presented a similar phenotype. To simplify the analysis, knowing that *hapln1a*$^{\Delta 241}$ mutants display a more profound defective phenotype during looping and ballooning morphogenesis, *hapln1a*$^{\Delta 187}$ mutants were imaged and analysed using *morphoHeart* only at this stage (48-50hpf) (Fig 5.27).

[*Note#5.5:* To focus this section of the analysis in the comparison between the *hapln1a*$^{\Delta 187/\Delta 187}$ and the *hapln1a*$^{\Delta 241/\Delta 241}$, the wild-type siblings of both groups were combined into a single sibling group].

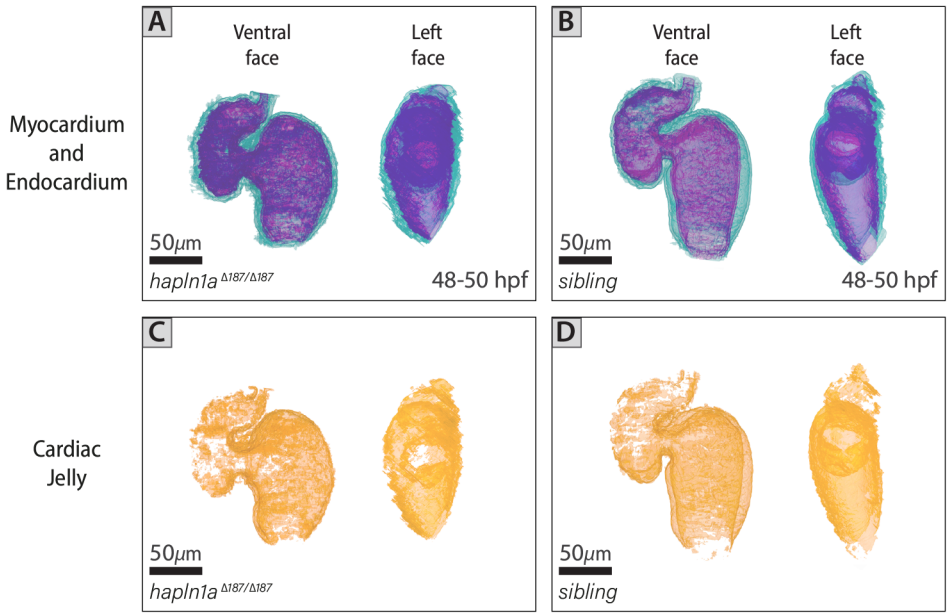

Fig 5.27. *hapln1a*$^{\Delta 187}$ mutants do not present cardiac morphology defects at 48-50hpf.
A-B. Representative 3D reconstructions of the myocardium (teal) and endocardium (magenta) of *hapln1a*$^{\Delta 187}$ (A) and wild-type sibling (B) at 48-50hpf. **C-D.** Representative 3D reconstructions of the cardiac jelly (orange) of *hapln1a*$^{\Delta 187}$ (C) and wild-type siblings (D) at 48-50hpf. As described by the labels in Panels A and B, all panels show the ventral face (on the left) and left face (on the right) of each of the presented hearts.

[*Note#5.6*: All genotype groups were analysed for normality using Shapiro-Wilk Normality test. For each analysed variable, if all groups were normally distributed, comparative statistics were carried out using ANOVA with Tukey's Multiple Comparisons as *post-hoc* test. When normal distribution could not be assumed, Kruskal-Wallis test with Dunn's Multiple Comparisons as *post-hoc* was used. For all tests a statistical significance α of *0.05* was defined].

Unexpectedly, in spite of *hapln1a* expression being lost in both alleles (Fig 5.6), the atrial growth and cardiac jelly defects identified in the *hapln1a*$^{\Delta 241}$ mutants (Fig 5.13B, Fig 5.14B, Fig 5.22B) were not observed in the *hapln1a*$^{\Delta 187}$ mutants (Fig 5.28A-D, Fig 5.29C-E). Similar to *hapln1a*$^{\Delta 241/\Delta 241}$, *hapln1a*$^{\Delta 187}$ promoter mutants do not present looping (Fig 5.28E-G), nor tissue composition (Fig 5.29A-B) defects at 48-50hpf.

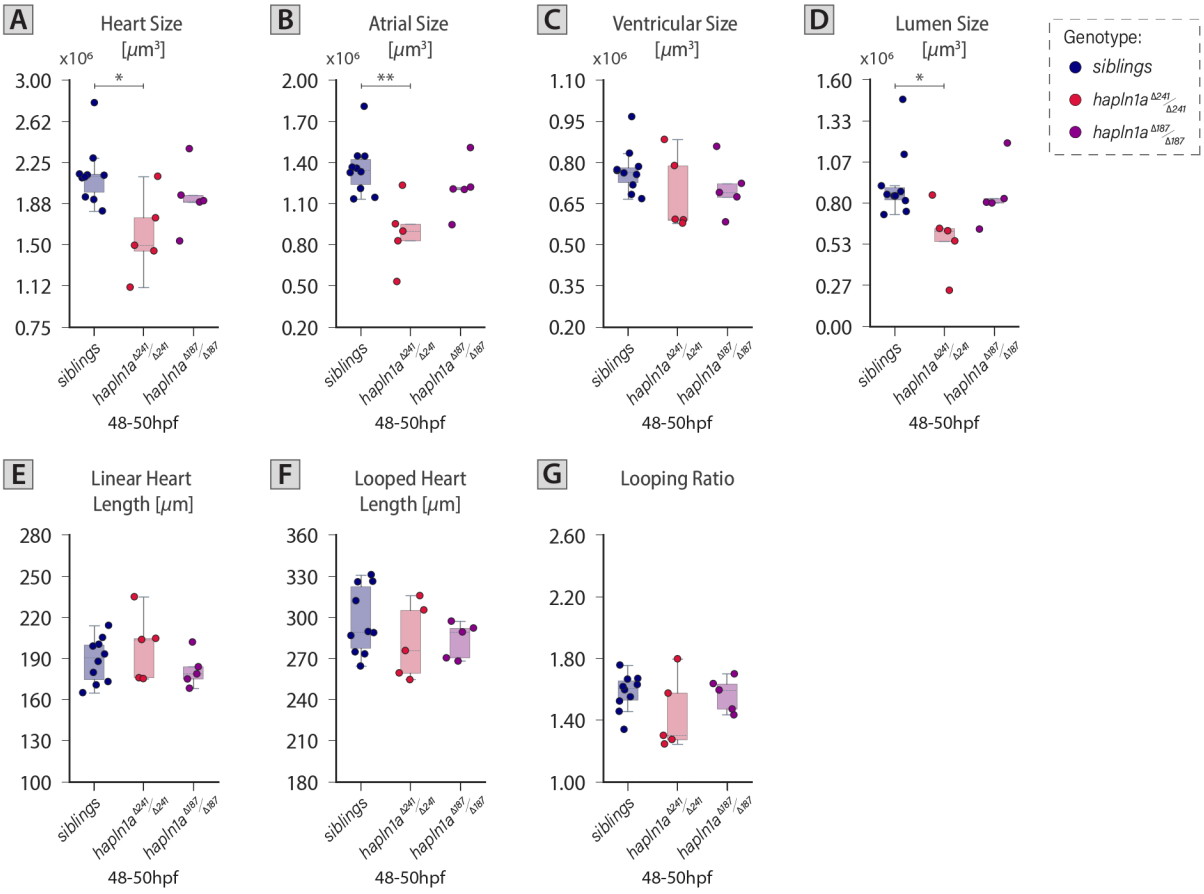

Fig 5.28. Different to *hapln1a*$^{\Delta 241}$ mutants, *hapln1a*$^{\Delta 187}$ mutants do not display heart, atrial nor lumen size defects during looping and ballooning morphogenesis.
A-G. Quantification of heart size (A), atrial size (B), ventricular size (C), total lumen size (D), linear heart length (E), looped heart length (F) and looping ratio (G) in *hapln1a*$^{\Delta 187}$ (purple), *hapln1a*$^{\Delta 241}$ (red) promoter homozygous mutants and their wild-type siblings (blue) at 48-50hpf. *hapln1a*$^{\Delta 241}$ promoter mutants show reduced heart, atria and lumen size at 48-50hpf, whilst *hapln1a*$^{\Delta 187}$ appear undistinguishable from the controls (heart size: *hapln1a*$^{\Delta 241/\Delta 241}$ vs *siblings p-value<0.02386*; atrial size: *hapln1a*$^{\Delta 241/\Delta 241}$ vs *siblings p-value<0.00219*, lumen size: *hapln1a*$^{\Delta 241/\Delta 241}$ vs *siblings p-value<0.02860*). A-G: Error bars with 95% confidence interval of the mean. 48-50hpf: *siblings n=10*, *hapln1a*$^{\Delta 241/\Delta 241}$ *n=5*, *hapln1a*$^{\Delta 187/\Delta 187}$ *n=5*. For details regarding the statistical analyses used to compare this set of data see *Note#5.6* (pg.198). Only significant comparisons are shown. **: *p-value*<0.01, *: *p-value*<0.05.

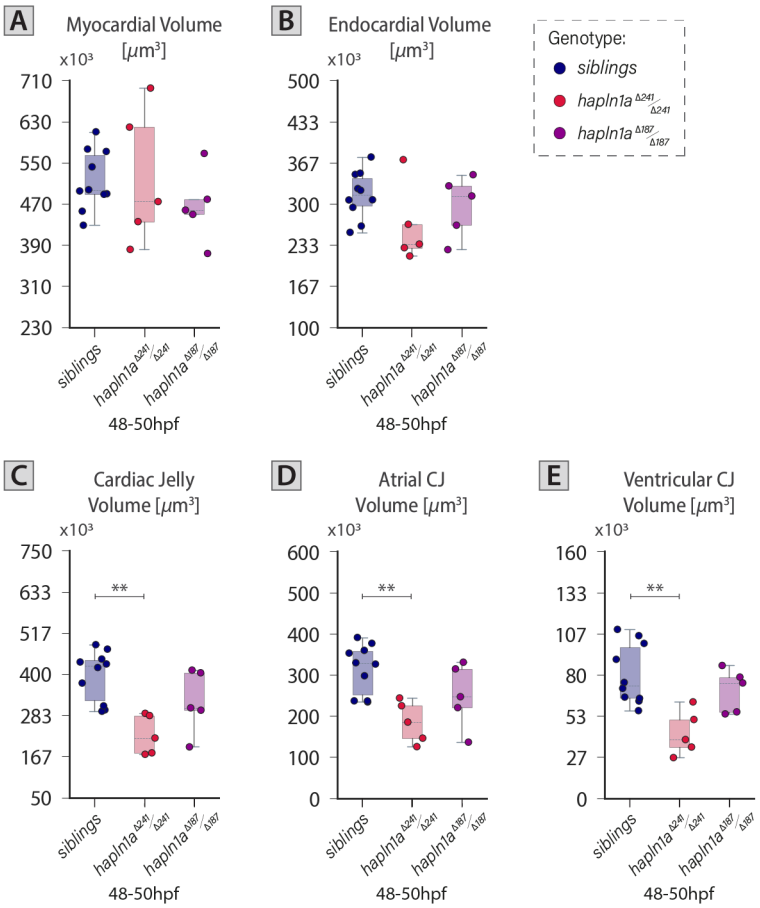

Fig 5.29. *hapln1a*$^{\Delta 187}$ mutants do not display cardiac jelly defects at looping and ballooning stages of heart development.

A-B. Quantification of myocardial (A), endocardial (B) volume in *hapln1a*$^{\Delta 187}$ (purple), *hapln1a*$^{\Delta 241}$ (red) promoter mutants and their wild-type siblings (blue) at 48-50hpf. **C-E.** Quantification of cardiac jelly volume of the whole heart (C) and its chambers (atrium: D, ventricle: E) in *hapln1a*$^{\Delta 187}$ (purple), *hapln1a*$^{\Delta 241}$ (red) promoter homozygous mutants and their wild-type siblings (blue) at 48-50hpf. Unlike *hapln1a*$^{\Delta 241}$ mutants, *hapln1a*$^{\Delta 187/\Delta 187}$ do not display defects in cardiac jelly composition at looping and ballooning stages (cardiac jelly: *hapln1a*$^{\Delta 241/\Delta 241}$ vs *siblings p-value<0.00166*; atrial cardiac jelly: *hapln1a*$^{\Delta 241/\Delta 241}$ vs *siblings p-value<0.00428*, ventricular cardiac jelly: *hapln1a*$^{\Delta 241/\Delta 241}$ vs *siblings p-value<0.00235*). A-E: Error bars with 95% confidence interval of the mean. 48-50hpf: *siblings n=10*, *hapln1a*$^{\Delta 241/\Delta 241}$ *n=5*, *hapln1a*$^{\Delta 187/\Delta 187}$ *n=5*. For details regarding the statistical analyses used to compare this set of data see *Note#5.6* (pg.198).Only significant comparisons are shown. **: *p-value*<0.01. CJ: Cardiac Jelly.

These differences in phenotype between the two promoter mutants might come from having excised a different portion of the upstream sequence of *hapln1a* in each allele, which may affect regulatory regions of other genes. A closer look at the location of the *hapln1a* gene in zebrafish genomic DNA identified that the closest protein-coding gene to *hapln1a* is *vcana* (Fig 5.30A). Mutations in *versican* in other species (i.e. mouse: (Yamamura *et al.*, 1997; Camenisch *et al.*, 2000; Hatano *et al.*, 2012; Kim *et al.*, 2018), medaka fish: (Mittal *et al.*, 2019)) result in heart defects, suggesting that disruption to this gene may contribute to a cardiac phenotype. *vcana* is located on the forward strand of chromosome 5 (opposite strand to *hapln1a*) with the 3'UTR (3' un-translated region) of each gene being separated by about 4,600bp of non-coding DNA. To examine if the expression of *vcana* was being affected differently by the excision of different upstream regions of *hapln1a*, and potentially causing differences in the phenotype between the alleles, *vcana* expression in *hapln1a* promoter mutants was analysed by ISH (Fig 5.30B-C'). No differences in the expression of *vcana* were identified between the *hapln1a* promoter mutants of either allele and their wild-

type siblings, suggesting differences in the excision length upstream of *hapln1a* is not affecting the gene expression of the closest protein-coding gene to *hapln1a*.

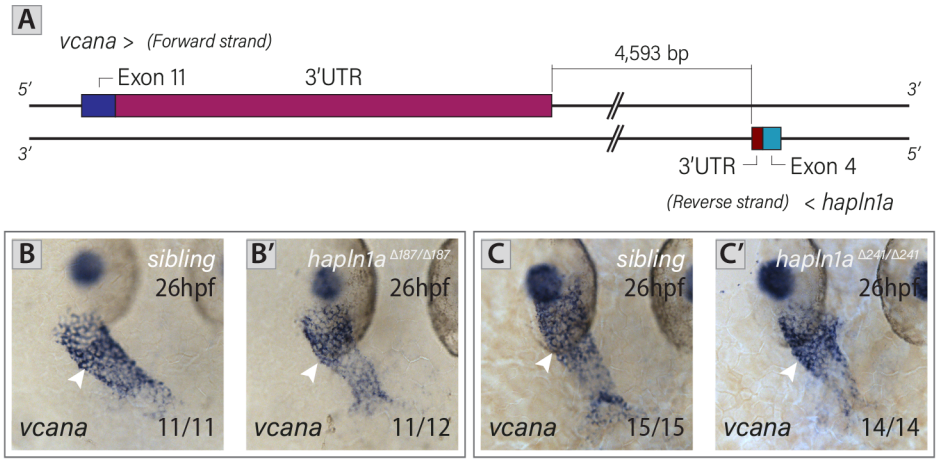

Fig 5.30. *vcana* expression is unaltered in *hapln1a* promoter mutants of either allele at 26hpf.
A. Schematic illustrating the region in between *hapln1a* and *vcana* in zebrafish's genomic DNA. Whilst *hapln1a* is in the reverse strand of zebrafish's chromosome 5, *vcana* is located on the forward strand. About 4600bp of non-coding sequence separate the annotated *3'UTRs* of both genes. Exon 11 and 3'UTR of *vcana* are shown in dark blue and purple respectively, Exon 4 and 3'UTR of *hapln1a* are illustrated in teal and dark red respectively. **B-C'.** mRNA *in situ* hybridisation of *vcana* expression at 26 hpf in *hapln1a* promoter mutants (*hapln1a*$^{\Delta 187}$: B-B', *hapln1a*$^{\Delta 241}$: C-C') reveals *vcana* expression is unaltered in the homozygous mutants of both promoter-region alleles (B', C'). B-C': The number of embryos matching the image shown is indicated in the bottom right of each image. Dorsal views with anterior to the top.

Whilst *hapln1a*$^{\Delta 241}$ and *hapln1a*$^{\Delta 187}$ mutants do not display any clear up-regulation of *hapln1b* nor an altered expression of *vcana*, this does not rule out the possibility of genetic compensation being active in either allele, potentially through the functional compensation of other link protein(s) normally expressed in the developing heart.

Previous studies using *hapln1a* morpholino (MO) had identified cardiac jelly defects in *hapln1a* morphants (Derrick *et al.*, 2021), which are in line with the results obtained for the *hapln1a*$^{\Delta 241}$ promoter mutant allele, suggesting the phenotype of the *Δ241* allele is closer to a 'real' loss-of-function phenotype in which defects are only driven by the loss of Hapln1a. Nevertheless, while expressivity of phenotype appears variable between alleles, analysis of morphological parameters from ISH images identified that both *Δ187* and *Δ241* promoter alleles exhibit significant changes in atrial morphology indicative of defective atrial growth (Fig 5.10). Consequently, it is possible that the *Δ187* allele has an intermediate phenotype between the *Δ241* and that of the wild-type siblings (as it can be seen from the parameters exhibited in Fig 5.28-5.29), which might require a higher sample size of analysed and processed embryos (*n>5*) to increase the power of the experiment and allow the identification of atrial defects in these promoter mutant hearts.

3.1.6 Heart patterning Markers are not Altered in *hapln1a* Promoter Mutants

A failure to expand the atrial chamber during looping and ballooning morphogenesis may result from improper patterning of the heart. To further characterise the effect of *hapln1a* knockout in heart patterning, ISH expression analysis of genes associated with cardiac patterning programs were evaluated in *hapln1a*$^{\Delta 241}$ homozygous mutants at 50hpf. Genes associated with the general patterning of the myocardium such as *tbx5a* (*T-box transcription factor 5a*), *tbx2b* (*T-box transcription factor 2b*), *nppa* (*natriuretic peptide a*) and *nkx2.5* (*NK homeobox 5*) were initially evaluated (Harvey, 2002; Stanley *et al.*, 2002; Bruneau, 2008; Jensen *et al.*, 2013) (for more details about these genes see Chapter 1 Section 4.1.2-

4.1.4). Patterning of the myocardium appears to be unaffected in *hapln1a*$^{\Delta 241}$ promoter mutants as *tbx5a*, *tbx2b*, *nppa* and *nkx2.5* expression appear normal (Fig 5.31A-D'). In both *hapln1a*$^{\Delta 241}$ mutants and wild-type siblings *tbx5a* and *nkx2.5* are expressed throughout the atrial and ventricular myocardium (Fig 5.31A-A' and D-D', respectively), *tbx2b* is present in the AVC myocardium (non-working myocardium), inflow tract and inner curvature of the atrium (Fig 5.31B-B'), and *nppa* expression is localised in the working myocardium in both chambers and distinctly absent in the AVC region (Fig 5.31C-C'). Additional analysis of the expression pattern of markers associated with valve development such as *notch1b* and *has2* (Bakkers *et al.*, 2004; Milan *et al.*, 2006), was performed and found to be normal in *hapln1a*$^{\Delta 241}$ mutant hearts (Fig 5.31E-F').

Together, these results suggest that the failure to grow of the *hapln1a*$^{\Delta 241/\Delta 241}$ atria is not the result of patterning defects and that *hapln1a* is not required to properly restrict the valve nor the chamber programs in the developing zebrafish heart.

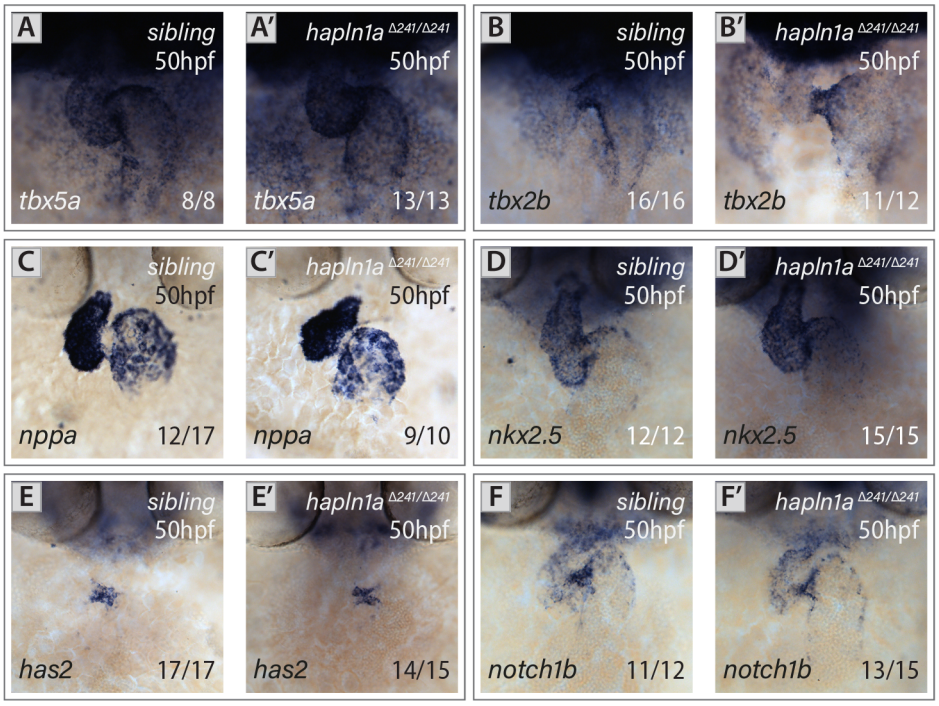

Fig 5.31. Heart patterning and valve markers are unaltered in *hapln1a*$^{\Delta 241}$ promoter mutants at 50hpf.
A-D'. mRNA ISH analysis of the cardiac patterning markers *tbx5a* (A-A'), *tbx2b* (B-B'), *nppa* (C-C') and *nkx2.5* (D-D')
in *hapln1a*$^{\Delta 241}$ promoter mutants and wild-type siblings at 50hpf, identifies the expression pattern of these genes in the homozygous mutants is unaffected. **E-F'.** mRNA ISH analysis of valve markers *has2* (E-E') and *notch1b* (F-F') at 50hpf show no detectable defects in any of these genes in the *hapln1a*$^{\Delta 241/\Delta 241}$ when compared to the expression pattern of the control embryos. A-F': The number of embryos matching the image shown is indicated in the bottom right of each image. Dorsal views with anterior to the top.

Together, knockdown of *hapln1a* results in a mild heart phenotype characterised by smaller heart tubes, atrial growth defects and altered cardiac jelly expansion/reduction dynamics (in both chambers) at looping and ballooning stages. Despite these early defects, the expression of genes involved in heart patterning during development in *hapln1a* promoter mutant hearts is comparable to controls, implying dysregulation of patterning genes is unlikely to be the basis of this phenotype, and suggesting that abnormal ECM composition, due to the loss of Hapln1a, might be the foundation of such phenotype.

3.1.7 Testing Cardiac Function in *hapln1a* Promoter Mutants

To study whether defects in cardiac jelly dynamics and reduced atrial size have an effect upon cardiac function, the heart rate of *hapln1a* promoter mutants of both alleles and their wild-type siblings were investigated using high-speed video imaging at 72hpf (Fig 5.32) (for details about methodology see Chapter 2, Section 7). Analysis of the videos showed that in both, *hapln1a* mutant embryos and their siblings, the contraction of the heart started at the inflow tract region, continuing in the atrium, and was followed by a fast contraction of the ventricle (Fig 5.32A-A'). Quantification of the heart rate identified that the embryonic *hapln1a* promoter mutant hearts of both alleles beat at a similar rate compared to controls (Fig 5.32D), suggesting loss of *hapln1a* does not have an impact in cardiac function at early stages of zebrafish development.

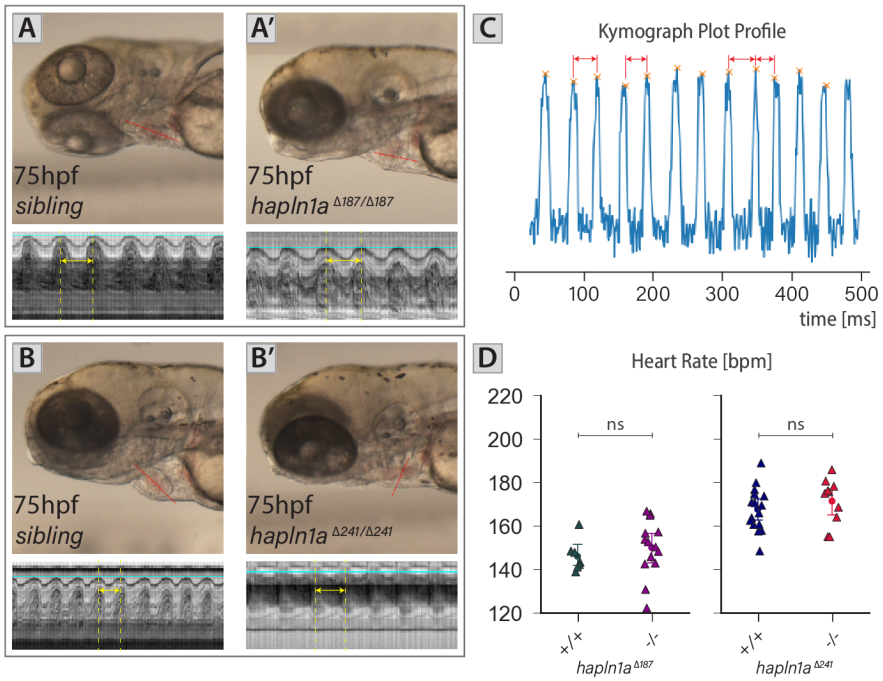

Fig 5.32. *hapln1a* promoter mutants do not display heart rate defect during early heart morphogenesis. **A-B'.** Stills of high-speed camera videos (top) and kymographs (bottom) obtained from *hapln1a* promoter mutants (*hapln1a*$^{\Delta187/\Delta187}$: A', *hapln1a*$^{\Delta241/\Delta241}$: B') and wild-type siblings (*Δ187*: A, *Δ241*: B) at 75hpf. to quantify heart rate. **C.** Profile of the kymograph presented in A' illustrating the period of the heartbeat (red double arrow and vertical lines) with which average heart rate is quantified for each embryo. **D.** Heart rate quantifications of *hapln1a* promoter mutants and wild-type siblings at 75hpf. No statistical differences are identified between in heart rate of *hapln1a* promoter mutants of either allele and their corresponding wild-type siblings. Error bars with 95% confidence interval of the mean. *siblings (Δ187) n=7, hapln1a*$^{\Delta187/\Delta187}$ *n=14, siblings* (*Δ241*) *n=16, hapln1a*$^{\Delta241/\Delta241}$ *n=10*. For details regarding the statistical analyses used to compare this set of data see *Note#5.3* (pg.177).ns: not significant. bpm: beats per minute.

Although no embryonic phenotype related to heart function was identified in *hapln1a* promoter mutants at early stages, developmental defects affecting cardiac physiology could be too subtle to be identified this early in development and yet could still become manifested later in life. To investigate whether loss of Hapln1a impacts cardiac function past embryonic stages, homozygous mutants of both alleles were grown to adulthood and their exercise tolerance, as a proxy for cardiac function, was tested using a swimming performance test (for details regarding the protocol for the test see Chapter 2, Section 9). Analysis of the test did not identify any difference in the critical swimming speed (*UCRIT*) per standard length nor standard area (proxies for fish size) (Fig 5.33C-D') of either *hapln1a* promoter mutant alleles and their wild-type siblings, suggesting loss of Hapln1a does not compromise cardiac function in the adult zebrafish heart.

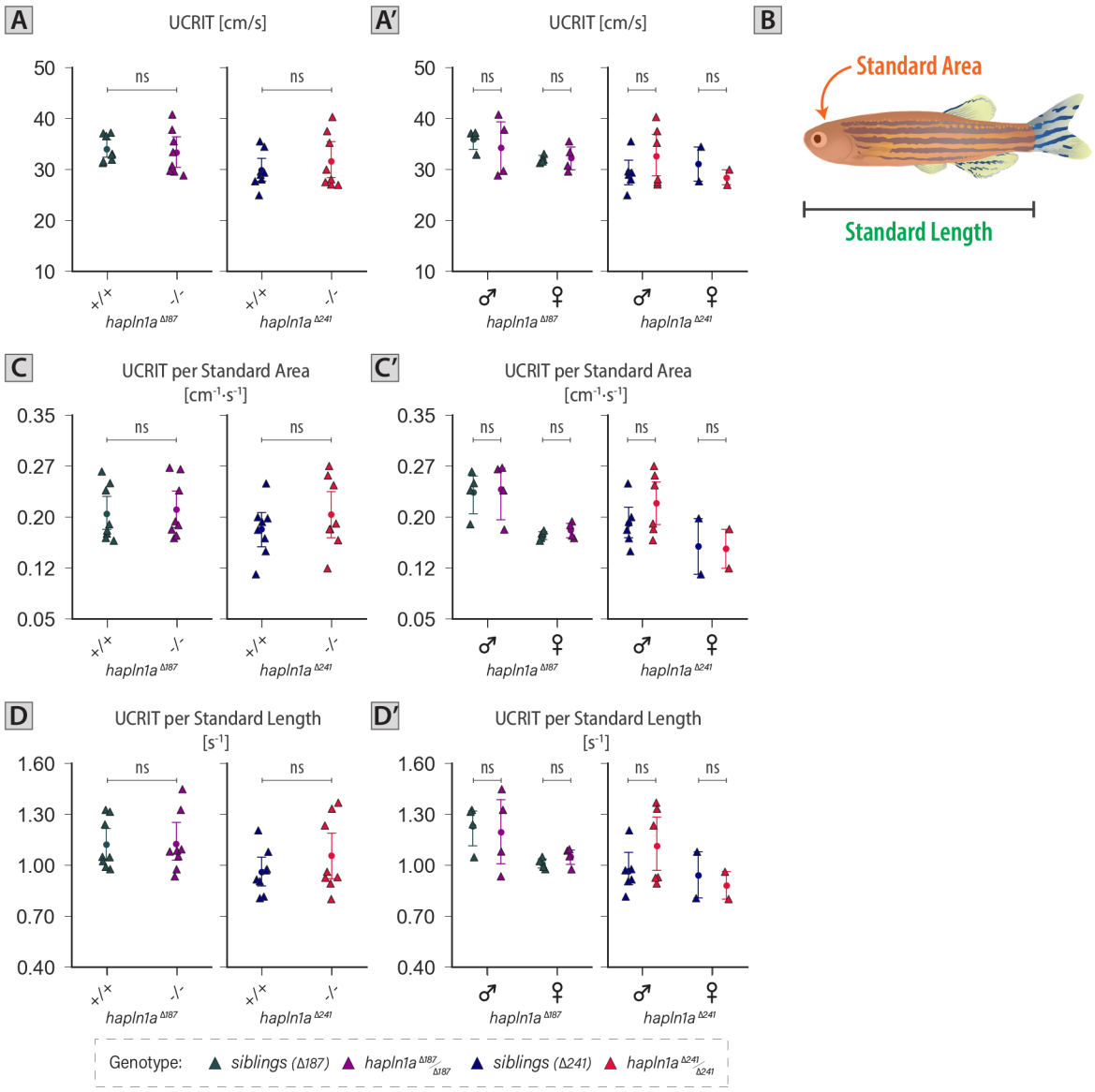

Fig 5.33. Swimming performance test suggest *hapln1a* promoter mutants do not have cardiac function defects as adults.

A-A'. Critical swimming speed (UCRIT) quantifications of all (A) or sex-segregated (A') *hapln1a* promoter mutants of either allele (-/-) and wild-type siblings (+/+).No statistical differences are identified between in UCRIT of *hapln1a* promoter mutants of either allele and their corresponding wild-type siblings. **B.** To reduce the variability of the UCRIT considering fish size, the standard length and area of the fish as a proxy for size were quantified and used to normalise the UCRIT measurements. **C-C'.** UCRIT per standard area of all (C) or sex-segregated (C) *hapln1a* promoter mutants of either allele (-/-) and wild-type siblings (+/+). **D-D'.** UCRIT per standard length of all (C) or sex-segregated (C) *hapln1a* promoter mutants of either allele (-/-) and wild-type siblings (+/+). A-A',C-D': Error bars with 95% confidence interval of the mean. *siblings (Δ187) n=8, hapln1a$^{Δ187/Δ187}$ n=8, siblings (Δ241) n=8, hapln1a$^{Δ241/Δ241}$ n=8.* For details regarding the statistical analyses used to compare this set of data see *Note#5.3* (pg.177).ns: not significant. UCRIT: Critical swimming speed.

3.2 GENERATION OF A *HAPLN1A* MISEXPRESSION MODEL

Asymmetric regionalisation of the cardiac jelly represents an intrinsic mechanism which could be driving heart looping morphogenesis. As *hapln1a* expression recapitulates the regionalisation of the cardiac ECM (Derrick *et al.*, 2021), one hypothesis is that asymmetric expression of *hapln1a* is required to promote heart morphogenesis. To understand if spatial restriction of *hapln1a* expression is important for cardiac morphogenesis, *hapln1a* misexpression was carried out by generating a transgenic line containing the full

length of *hapln1a* coding sequence under the control of *UAS* promoter (i.e. *UAS:hapln1a*) and outcrossed to a transgenic line expressing myocardial-specific *Gal4*, (i.e. *myl7:Gal4*) (Fig 5.34A-B), thus creating embryos that express *hapln1a* globally in the heart (Fig 5.34C-D). To simplify the identification of the embryos carrying the *UAS:hapln1a* construct, a *cryaa:CFP* sequence was added at the end of the *UAS:hapln1a* construct (i.e. *UAS:hapln1a, cryaa:CFP*), so that embryos could be screened by identifying the presence or absence of CFP in their eyes (Fig 5.34E-H). Additionally, to aid the comparison of heart morphology and ECM dynamics between *hapln1a* misexpression (i.e. also referred to as *hapln1a*^{ME}) and *hapln1a* knockout embryos using *morphoHeart* the *Tg(UAS:hapln1a, cryaa:CFP)* line was raised in the same transgenic background as the *hapln1a* promoter mutants (i.e. *Tg(myl7:lifeActGFP); Tg(fli1a:AC-TagRFP)*) (for details regarding the generation of the *Tg(UAS:hapln1a, cryaa:CFP)* line see Chapter 2, Section 6).

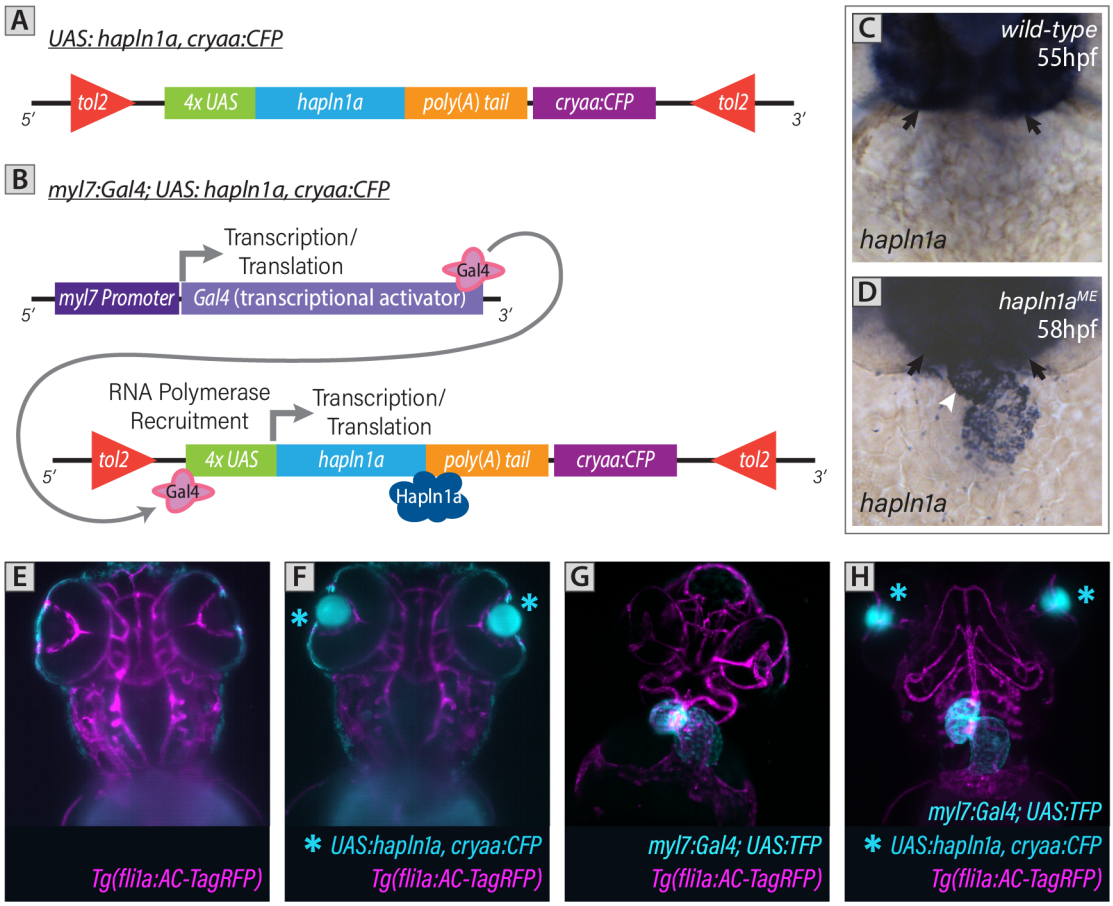

Fig 5.34. Generation of *hapln1a* misexpression tools to investigate the requirement for ECM regionalisation in cardiac morphogenesis.

A. Schematic of DNA construct which drives *hapln1a* expression under the *UAS* promoter. Embryos were injected at the 1-cell stage, and the *cryaa:CFP* construct which drives the expression of CFP in the eyes, was used to select embryos that had integrated the *UAS:hapln1a, cryaa:CFP* to raise to adulthood. **B.** Schematic representing the outcross used to identify the founder fish transmitting *UAS:hapln1a, cryaa:CFP* through the germline. Founder fish were outcrossed with the *Tg(myl7:Gal4)* transgenic fish. Embryos were grouped based on presence or absence of blue eyes and fixed. mRNA *in situ* hybridisation analysis of *hapln1a* was used to confirm overexpression of *hapln1a* in the whole heart. **C-D.** mRNA *in situ* hybridisation analysis of *hapln1a* in a wild-type embryo at 55hpf (C) and in an embryo carrying the *myl7:Gal4* and *USA:hapln1a* constructs at 58hpf (D). *hapln1a* expression is restricted to the pharyngeal region (black arrows in C and D) and to the brain at 55hpf in wild-type embryos (C), while it is highly overexpressed in the heart (white arrowhead in D) in embryos carrying both constructs. Of note, higher levels of *hapln1a* expression are shown in the brain of embryos carrying the *myl7:Gal4* and *UAS:hapln1a* construct, due to extended waiting time to allow *hapln1a* expression to become visible in embryos coming from different possible founders. **E-H.** Maximum intensity projections of light-sheet images of embryos carrying none of the constructs (E), only the *UAS:hapln1a, cryaa:CFP* construct

identified by the CFP expression in the eyes (*)- (F), only the *myl7:Gal4; UAS:TFP* construct -identified by the TFP expression in the heart- (G), and both constructs (H). C-H. Ventral views with anterior to the top.

Once the stable *Tg(UAS:hapln1a, cryaa:CFP)* line was established at F2, to confirm the misexpression of *hapln1a* in the heart throughout development an ISH of *hapln1a* expression was performed in an outcross of *Tg(UAS:hapln1a, cryaa:CFP)* and *Tg(myl7:Gal4, UAS:TFP)* fish fixed at 50, 72 and 79hpf (Fig 5.35). Whereas *hapln1a* wild-type expression between 50 and 80hpf is restricted to the pharyngeal region and the brain (Fig 5.35A,E,I), in embryos carrying both constructs (*myl7:Gal4, UAS:TFP* and *UAS:hapln1a, cryaa:CFP*) it is highly misexpressed in the whole heart at all the examined stages (Fig 5.34H, Fig 5.35D,H,L). As expected, *hapln1a* expression is not altered in embryos carrying only *UAS:hapln1a, cryaa:CFP* (Fig 5.34F, Fig 5.35B,F,J) or the *myl7:Gal4; UAS:TFP* (Fig 5.34G, Fig 5.35C,G,K) constructs. However, because in the *Tg(myl7:Gal4; UAS:TFP)* line the *myl7:Gal4* construct and *UAS:TFP* construct are not in the same cassette and thus likely not the same insertion site, some embryos screened only as *UAS:hapln1a, cryaa:CFP* carriers can also misexpress *hapln1a*, as the *myl7:Gal4* construct could have been inherited without the *UAS:TFP,* hence preventing its identification through fluorescent screening. This limitation will be considered when analysing the data obtained from these groups of experiments.

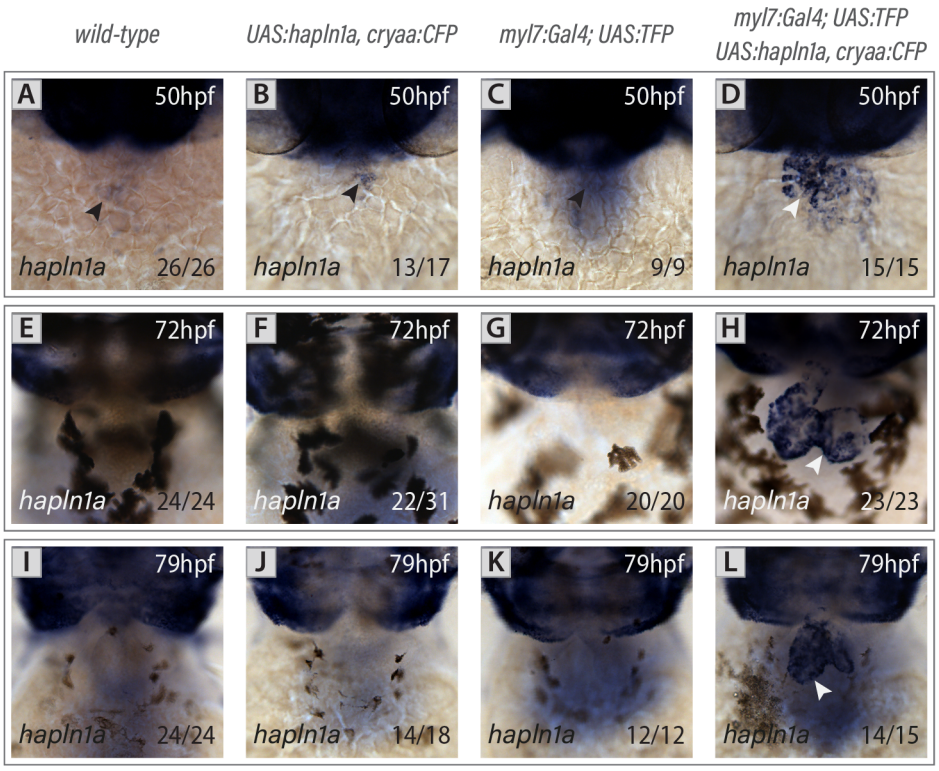

Fig 5.35. Time-course expression of *hapln1a* in *hapln1a^{ME}* model confirms *hapln1a* is misexpressed in embryos carrying the *UAS:hapln1a* and *myl7:Gal4* constructs.
A-L. mRNA *in situ* hybridisation analysis of *hapln1a* in embryos screened as non-carriers of either construct (A,E,I), carriers of the *UAS:hapln1a* only (B,F,J), carriers of the *myl7:Gal4* only (C,G,K) and carriers of both (D,H,L) at 50 (A-D), 72 (E-H) and 79hpf (I-L) to confirm *hapln1a* expression in the heart. *hapln1a* misexpression is confirmed in the whole heart (white arrowheads in D,H,L) in embryos that were screened as carriers of both *myl7:Gal4* and *USA:hapln1a* constructs. A-L. Ventral views with anterior to the top.

Knowing that *hapln1a$^{\Delta 241}$* promoter mutants display a more profound ECM defect during looping and ballooning morphogenesis, when the atrial cardiac ECM in wild-type embryos is expanded and highly regionalised, comparative analysis of morphometric parameters between *hapln1a* misexpression, *hapln1a* knockout and wild-type embryos was performed at 48-50hpf. For this *Tg(UAS:hapln1a, cryaa:CFP)* were

outcrossed to *Tg(myl7:Gal4, UAS:TFP)*, separated according to the inherited constructs (screening for blue eyes and/or teal hearts), imaged in the light-sheet microscope at 48-50hpf, and processed using *morphoHeart* (Fig 5.36).

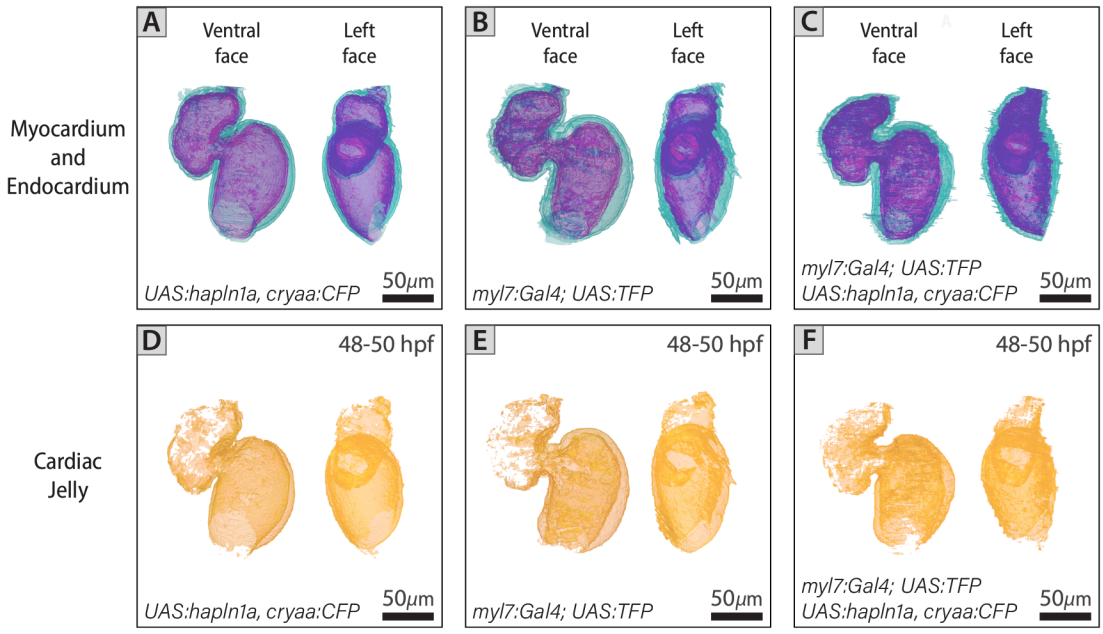

Fig 5.36. No morphological nor tissue composition defects are identified from the 3D reconstructions of the myocardium, endocardium and cardiac jelly reconstruction of *hapln1a*^{ME} embryos.
A-F. Representative 3D reconstructions of the myocardium (teal), endocardium (magenta) (A-C) and cardiac jelly (orange) (D-F) of *hapln1a*^{ME} embryos (C,F) and their controls (A-B,D-E) at 48-50hpf. As described by the labels in Panels A-C, all panels show the ventral face (on the left) and left face (on the right) of each of the presented hearts.

Initial analysis of embryos misexpressing *hapln1a* from the 3D renders of the myocardial and endocardial tissue layers (Fig 5.36) did not identify morphological defects when compared to their controls (embryos carrying either the *UAS:hapln1a, cryaa:CFP* or *myl7:Gal4, UAS:TFP* constructs).

[*Note#5.7:* To simplify the labels in the figures note that embryos screened as carriers of only the *myl7:Gal4* construct are referenced as *Gal4+,UAS-*; those screened as carrying only the *UAS:hapln1a, cryaa:CFP* are identified as *Gal4-,UAS+*; and those screened as carrying both constructs are labelled as *Gal4+,UAS+*. The first two groups (*Gal4+,UAS-* and *Gal4-,UAS+*) correspond to the control groups of the misexpression experiment here described].

Analysis of gross heart size parameters obtained from the *hapln1a*^{ME} and their controls and from the *hapln1a*$^{\Delta 241}$ promoter mutants and their controls identified an unexpected phenotype in the controls of the *hapln1a*^{ME} experiment. Comparison between the misexpression controls and the wild-type siblings (siblings of the *hapln1a*$^{\Delta 241}$ promoter mutants) identified statistical differences in ventricular size between the *Gal4-,UAS+* and the *hapln1a*$^{\Delta 241}$ siblings (Fig 5.37C), suggesting that the presence of the *UAS:hapln1a* construct results in a cardiac phenotype in these embryos. Knowing that the *Gal4-,UAS+* group might contain some embryos that misexpress *hapln1a* in the heart, the most accurate controls to which to compare the misexpression embryos (*hapln1a*^{ME}: *Gal4+,UAS+*) are the *Gal4+,UAS-*. Unexpectedly, analysis of additional morphometric parameters, such as myocardial and endocardial tissue volume (Fig 5.38), revealed statistically significant differences between both controls and the wild-type siblings from the *hapln1a*$^{\Delta 241}$ promoter mutants.

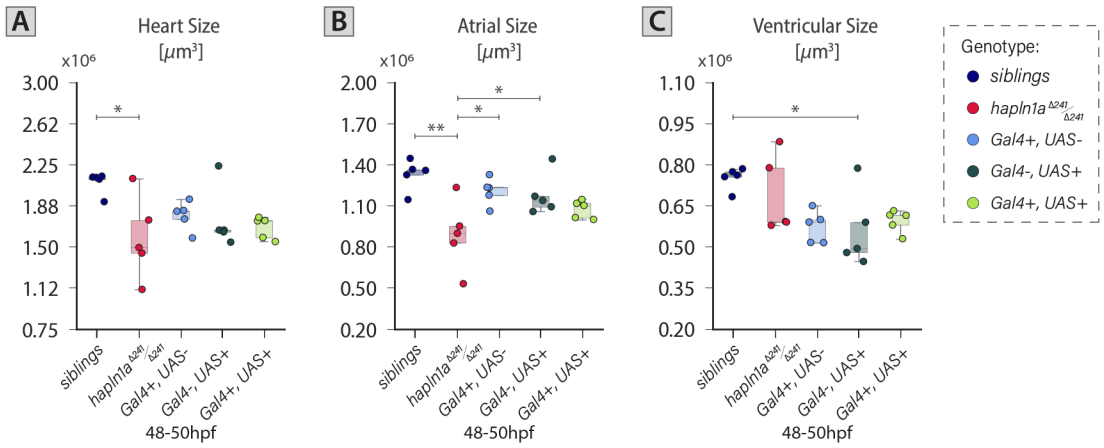

Fig 5.37. Significant differences in the ventricular size of *Gal4-,UAS+* embryos suggest control embryos of *hapln1a^{ME}* experiment have a phenotype.

A-C. Quantification of heart (A) and chambers (atrium: B, ventricle: C) size using *morphoHeart* in *Gal4+,UAS-* (light blue), *Gal4-,UAS+* (dark green), Gal4+,UAS+ (light green), *hapln1a^{Δ241}* homozygous mutants (red) and wild-type siblings (dark blue) at 50hpf. [Heart: *hapln1a^{Δ241} vs. siblings p-value=0.03992.* Atrium: *hapln1a$^{Δ241/Δ241}$ vs. siblings p-value=0.00140, hapln1a$^{Δ241/Δ241}$ vs. Gal4+,UAS- p-value=0.02414, hapln1a$^{Δ241/Δ241}$ vs. Gal4-,UAS+ p-value=0.04327.* Ventricle: *Gal4-,UAS+ vs. siblings p-value=0.03302*]. A-C: Error bars with 95% confidence interval of the mean. *siblings n=5, hapln1a$^{Δ241/Δ241}$ n=5, Gal4+,UAS- n=5, Gal4-,UAS+ n=5, Gal4+,UAS+n=5.* For details regarding the statistical analyses used to compare this set of data see *Note#5.6* (pg.198).Only significant comparisons are shown. **: *p-value*<0.01, *: *p-value*<0.05.

A possible explanation that could account for this phenotype in the *Gal4+,UAS-* controls, could be the use of different transgenic lines labelling the myocardial tissue. The myocardial channel used to segment the hearts in embryos carrying the *myl7:Gal4* construct labels the cytoplasm of the cardiomyocytes (i.e. *Tg(myl7:Gal4; UAS:TFP)*) rather than the actin contained in them (i.e. *Tg(myl7:lifeActGFP)*). Segmentation of this tissue volume using this line could hence result in differences in the quantifications of myocardial tissue volume from the segmentation process. If this was the case, myocardial tissue volumes segmented using this cytoplasmic line should result in 'higher' myocardial volumes, as the whole cell would be labelled with the fluorophore rather than only its actin. Interestingly, the tissue volumes obtained from the *Gal4+,UAS-* embryos are significantly lower than those obtained from the *hapln1a^{Δ241}* mutant controls, refuting this hypothesis. Corroborating that this justification is not accurate, analysis of the endocardium once again identifies defects in total endocardial volume between *hapln1a^{Δ241}* controls and *hapln1a^{ME}* controls. As both lines label the endocardium with the same transgene (i.e. *Tg(fli1a:AC-TagRPF)*), if none of the constructs were having an individual effect in the embryos, the endocardial tissue volume quantifications would be close to wild-type siblings for all control conditions. As this is indeed not the case (Fig 5.38D-F), this data suggests that carrying either construct (*myl7:Gal4* or *UAS:hapln1a, cryaa:CFP*) has an undesired effect in embryos' cardiac development.

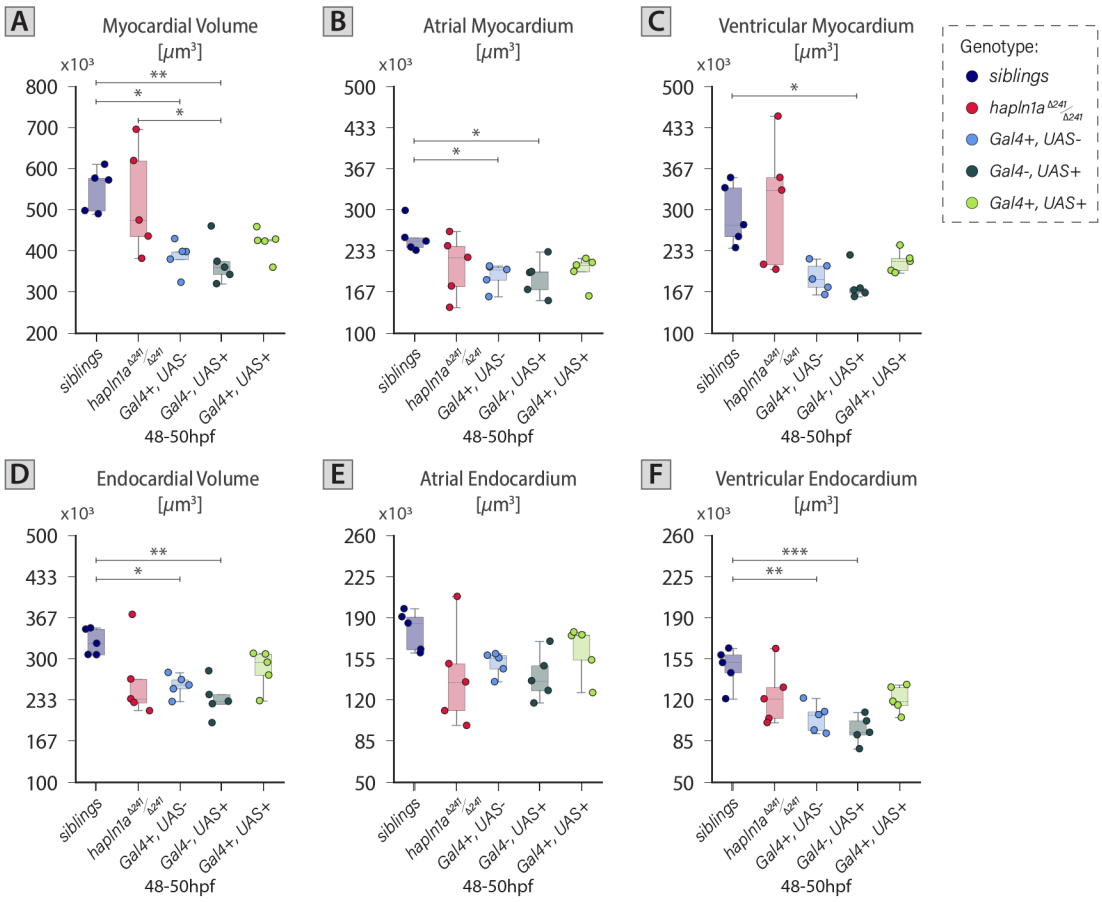

Fig 5.38. Analysis of myocardial and endocardial tissue volume in *hapln1a^{ME}* controls revealed statistically significant differences when compared to wild-type embryos.

A-F. Quantification of myocardial (A-C) and endocardial (D-F) volume of the heart (A,D) and chambers (atrium: B,E ventricle: C,F) using *morphoHeart* in *Gal4+,UAS-* (light blue), *Gal4-,UAS+* (dark green), Gal4+,UAS+ (light green), *hapln1a$^{\Delta 241}$* homozygous mutants (red) and wild-type siblings (dark blue) at 50hpf. [Myocardium: *siblings vs. Gal4+,UAS- p-value=0.01356, siblings vs. Gal4-,UAS+p-value=0.00673, hapln1a$^{\Delta 241/\Delta 241}$ vs. Gal4-,UAS+ p-value=0.02604.* Atrial myocardium: *siblings vs. Gal4+,UAS- p-value=0.04023, siblings vs. Gal4-,UAS+ p-value=0.03156.* Ventricular myocardium: *siblings vs. Gal4-,UAS+ p-value=0.01977.* Endocardium: *siblings vs. Gal4+,UAS- p-value=0.04452, siblings vs. Gal4-,UAS+ p-value=0.00608*, Ventricular endocardium: *siblings vs. Gal4+,UAS- p-value=0.00442*, *siblings vs. Gal4-,UAS+ p-value=0.00100*]. A-F: Error bars with 95% confidence interval of the mean. *siblings n=5*, *hapln1a$^{\Delta 241/\Delta 241}$ n=5*, *Gal4+,UAS- n=5*, *Gal4-,UAS+ n=5*, *Gal4+,UAS+n=5.* For details regarding the statistical analyses used to compare this set of data see *Note#5.6* (pg.198). Only significant comparisons are shown. ***: *p-value*<0.001, **: *p-value*<0.01, *: *p-value*<0.05.

Furthermore, to understand if the misexpression of *hapln1a* resulted in global deposition of Hapln1a throughout the cardiac jelly, a fluorescent immunostaining of Hapln1a was carried out in an outcross of *Tg(UAS:hapln1a, cryaa:CFP)* and *Tg(myl7:Gal4, UAS:TFP)* at 50, 72 and 80hpf (Fig 5.39). As expected at 50hpf Hapln1a is expressed in the heart of all the experimental groups (wild-type, *hapln1a^{ME}* and those containing the *UAS:hapln1a, cryaa:CFP* or the *myl7:Gal4* construct) in the atrium and AVC. Surprisingly, at this stage, despite upregulating *hapln1a* expression all around the heart (Fig 5.35D), the deposition levels of Hapln1a in the *hapln1a^{ME}* embryos appear to be indistinguishable from all controls (compare in Fig 5.35 panel D with panels A-C). This same behaviour is observed at later stages (e.g. 72 and 80hpf), where Hapln1a is not only absent in the heart in the controls (as expected, see Fig 5.3P-T), but also in the *hapln1a^{ME}* embryos.

This suggests that despite *hapln1a* being misexpressed in the heart of zebrafish embryos carrying both constructs (*UAS:hapln1a, cryaa:CFP* and *myl7:Gal4*), either the translation of Hapln1a is being prevented

or once the protein is translated other ECM components within the cardiac jelly are degrading it. Together with the previous discovery that the constructs alone appear to have an impact on heart morphology, these data invalidate the experiment and prevent further study of the *hapln1a*^{ME} phenotype.

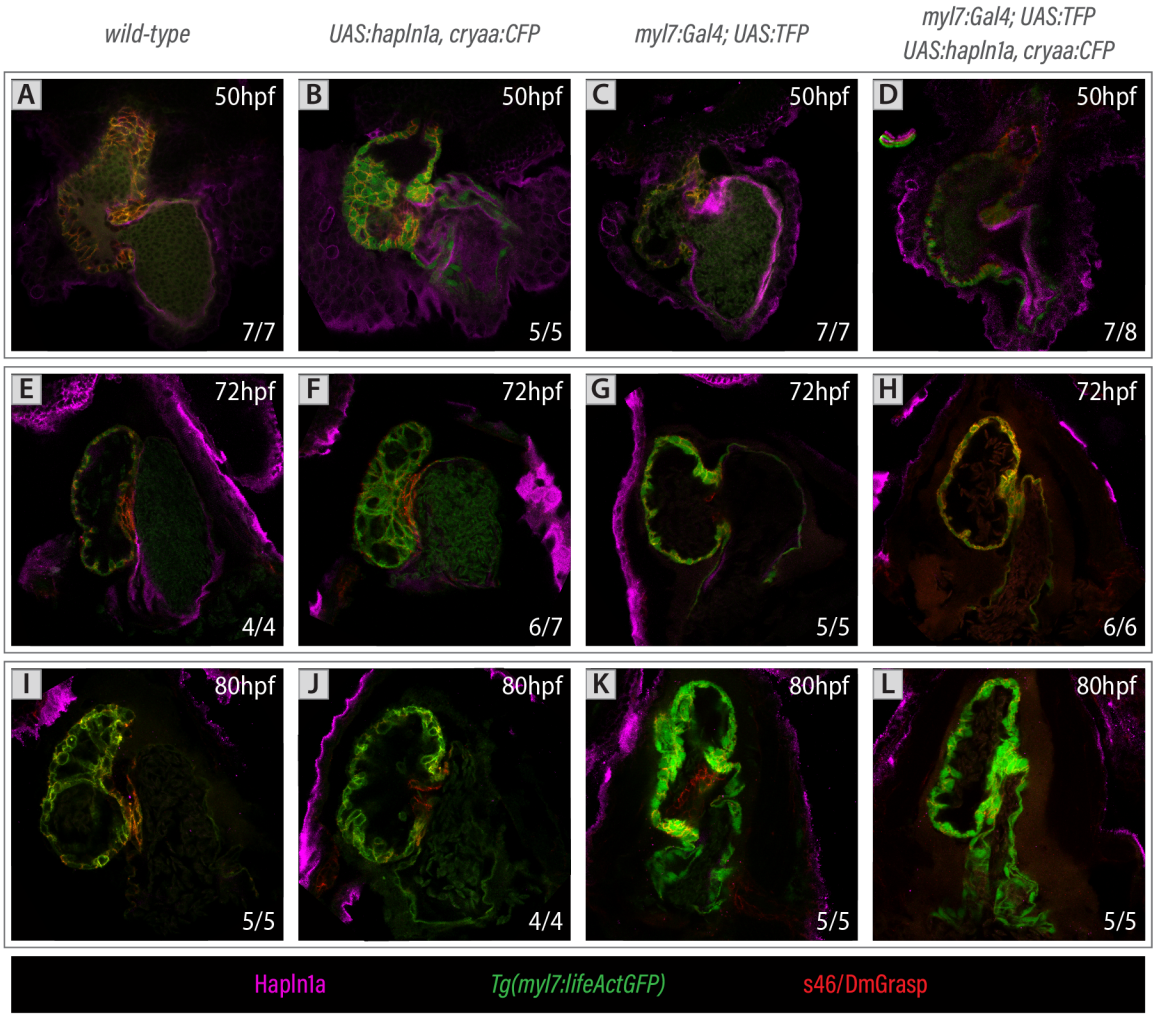

Fig 5.39. Immunohistochemistry of Hapln1a in *hapln1a*^{ME} suggests Hapln1a is not being mis-deposited despite being mis-expressed.
A-L. Fluorescent immunostaining of Hapln1a (magenta), s46/DmGrasp (red) and *Tg(myl7:lifeActGFP)* (green) in embryos screened as non-carriers of either construct (A,E,I), carriers of the *UAS:hapln1a* only (B,F,J), carriers of the *myl7:Gal4* only (C,G,K) and carriers of both (D,H,L) at 50 (A-D), 72 (E-H) and 80hpf (I-L) to confirm Hapln1a mis-deposition in the heart. A-L show individual slices of the heart stack to visualise more clearly the deposition of Hapln1a in the heart's cardiac jelly. The number of embryos matching the image shown is indicated in the bottom right of each image. A-L: Ventral views with anterior to the top.

---

4 Hapln1a and *spaw* Work both Independently and Dependently to Promote Heart Development in Zebrafish Embryos

Having confirmed that the asymmetric expression of *hapln1a* is required to promote the expansion of the cardiac ECM during looping and ballooning morphogenesis, *hapln1a* represents a candidate gene that may contribute to the previously described tissue intrinsic nature of heart looping morphogenesis (Noël *et al.*, 2013). Under this hypothesis, expression of *hapln1a* in the heart disc should be independent of external patterning processes at the embryonic scale, such as left-right laterality cues that are dictated by Nodal signalling. To confirm this model, *hapln1a* expression at 19 and 26hpf was characterised in embryos with disrupted left-right patterning (*spaw*$^{-/-}$). ISH analysis revealed that the posterior upregulation of *hapln1a*

in the heart disc was unaffected in *spaw*$^{-/-}$ hearts (Fig 5.40A-A'), yet loss of left-right patterning results in *hapln1a* being positioned in the ventral face of the heart tube at 26hpf (Fig 5.40B-B'). Together, this confirms the hypothesis that asymmetric *hapln1a* expression is independent of embryonic laterality (Fig 5.40A-A'); however, its asymmetric positioning in the tube is tightly linked to the direction in which the heart tube jogs (Fig 5.40B-B').

To examine further the interaction between intrinsic heart patterning and extrinsic left-right cues in promoting heart morphogenesis (i.e. the effect of loss of *hapln1a* in *spaw* mutant hearts), *spaw*$^{+/-}$, *hapln1a*$^{\Delta 241/+}$ adults were generated. To characterise heart morphology, double heterozygous carriers of both mutations were incrossed to obtain double homozygous mutant embryos in which live light-sheet imaging and *morphoHeart* analysis were performed.

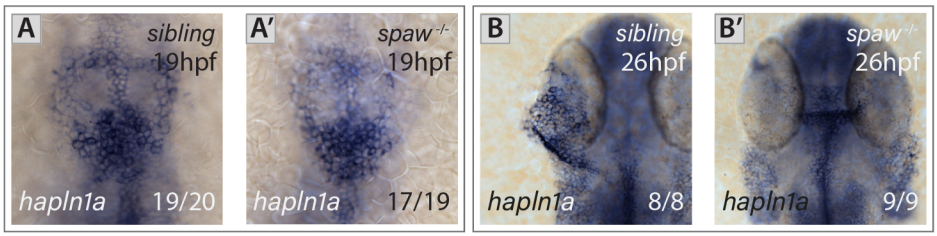

Fig 5.40. At disc stage *hapln1a* expression is independent of laterality but at tube stage it is tightly linked to the direction of heart tube position.
A-B'. mRNA *in situ* hybridisation analysis of *hapln1a* at 19 (A-A'), and 26hpf (B-B') in siblings (A,B) and *spaw*$^{-/-}$ (A',B') hearts. At disc stage, *hapln1a* expression is positioned predominantly in the posterior region of the heart disc (A), and its expression is unaffected by the loss of L/R patterning in *spaw*$^{-/-}$ hearts (A'). At tube stage, wild-type hearts express *hapln1a* throughout the heart tube with elevated levels on the left side (B). Loss of L/R patterning results in *hapln1a* being positioned in the ventral face of the heart tube in *spaw*$^{-/-}$ hearts (B'). The number of embryos matching the image shown is indicated in the bottom right of each image. A,A': Dorsal Views with anterior to the top. B,B': Ventral views with anterior to the top.

[*Note#5.8:* To note, throughout the rest of this thesis, heterozygous mutant embryos for *spaw* and *hapln1a* will be referenced as *spaw*$^{+/-}$, *hapln1a*$^{\Delta 241/+}$, while homozygous double mutants will be identified as *spaw*/*hapln1a* double mutants or *spaw*$^{-/-}$, *hapln1a*$^{\Delta 241/\Delta 241}$ doubles].

Previous analysis of individual mutants (i.e. *spaw*$^{-/-}$: Chapter 4, Section 5 and *hapln1a*$^{\Delta 241/\Delta 241}$: current chapter, Section 3.1.3) identified chamber-specific defects at particular developmental stages due to the loss of *hapln1a* or the mutation of *spaw*. Defects in chamber growth and in ECM dynamics are common to both mutants. Hence, it is possible that *spaw* and *hapln1a* may function independently to regulate chamber size and/or ECM volume, and therefore loss of both genes would result in more profound defects than those observed in the single mutants. However, if they interact together in the same pathway, these defects should be indistinguishable between either single or double mutants.

Initial inspection of myocardial and endocardial 3D reconstructions at early looping (34-36hpf), looping and ballooning (48-50hpf) and early maturing stages (72-74hpf) identify that similar to *spaw* mutants, *spaw*$^{-/-}$, *hapln1a*$^{\Delta 241/\Delta 241}$ present aberrant looping directionalities. Closer examination of the 3D reconstructions identifies besides a compaction failure, *spaw*$^{-/-}$, *hapln1a*$^{\Delta 241/\Delta 241}$ embryos have smaller and less ballooned atria at 48-50hpf (Fig 5.41).

[*Note#5.9:* In the two different 34-36hpf light-sheet imaging sessions of embryos coming from an incross of *spaw*$^{+/-}$, *hapln1a*$^{\Delta 241/+}$, none of the imaged *spaw*/*hapln1a* double embryos had a sinistral looping directionality. Consequently, in the analysis, no sinistral loopers were included within the group of *spaw*$^{-/-}$, *hapln1a*$^{\Delta 241/\Delta 241}$ at 34-36hpf].

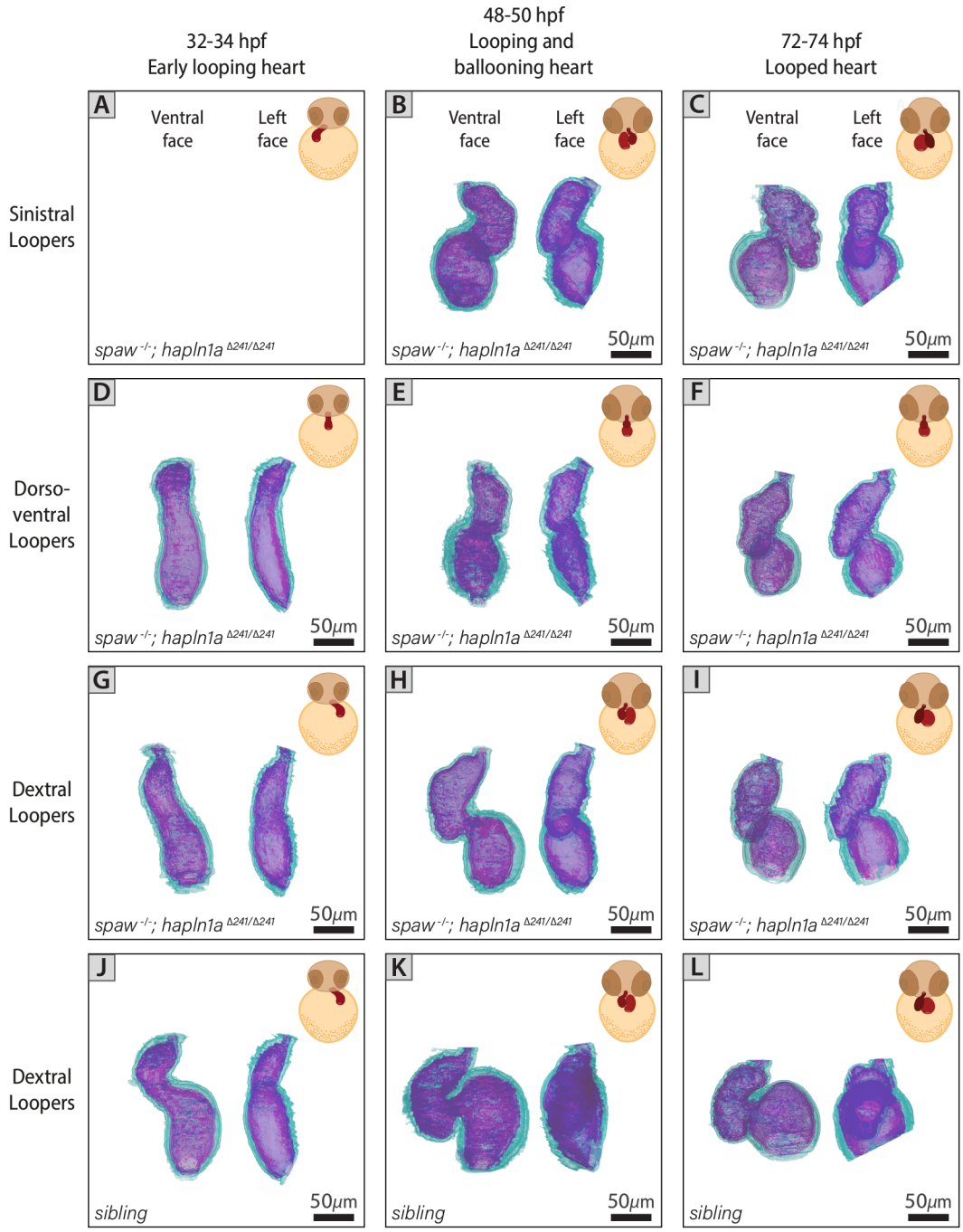

Fig 5.41. *spaw/hapln1a* double mutants hearts exhibit different directions of looping.
A-L. Representative 3D reconstructions of the myocardium (teal) and endocardium (magenta) of *spaw*$^{-/-}$, *hapln1a*$^{\Delta 241/\Delta 241}$ (A-I) and sibling (J-L) hearts at key developmental stages (34-36hpf: D,G,J; 48-50hpf: B,E,H,K; and 72-74hpf: C,F,I,L). *spaw*$^{-/-}$,*hapln1a*$^{\Delta 241/\Delta 241}$ homozygous mutants (A-I) are classified according to their direction of looping as: sinistral (B-C), middle (D-F) and dextral (G-I) loopers. A-L: As described by the labels in Panels A-C, all panels show the ventral face (on the left) and left face (on the right) of each of the presented hearts.

[*Note#5.10:* To simplify the comparisons of the *morphoHeart* parameters between the single and double mutants, wild-type siblings of the *hapln1a*$^{\Delta 241/\Delta 241}$ were combined with the siblings of *spaw*$^{-/-}$ into a single sibling group].

To investigate the interaction between *hapln1a* and *spaw*, gross heart morphometric parameters were initially quantified in the double mutants and compared to those obtained from the single mutants and

their controls (Fig 5.42). Similar to *hapln1a*$^{\Delta 241}$ promoter mutants, *spaw*$^{-/-}$,*hapln1a*$^{\Delta 241/\Delta 241}$ double mutant heart tubes have an early size defect driven by smaller atria and ventricles.

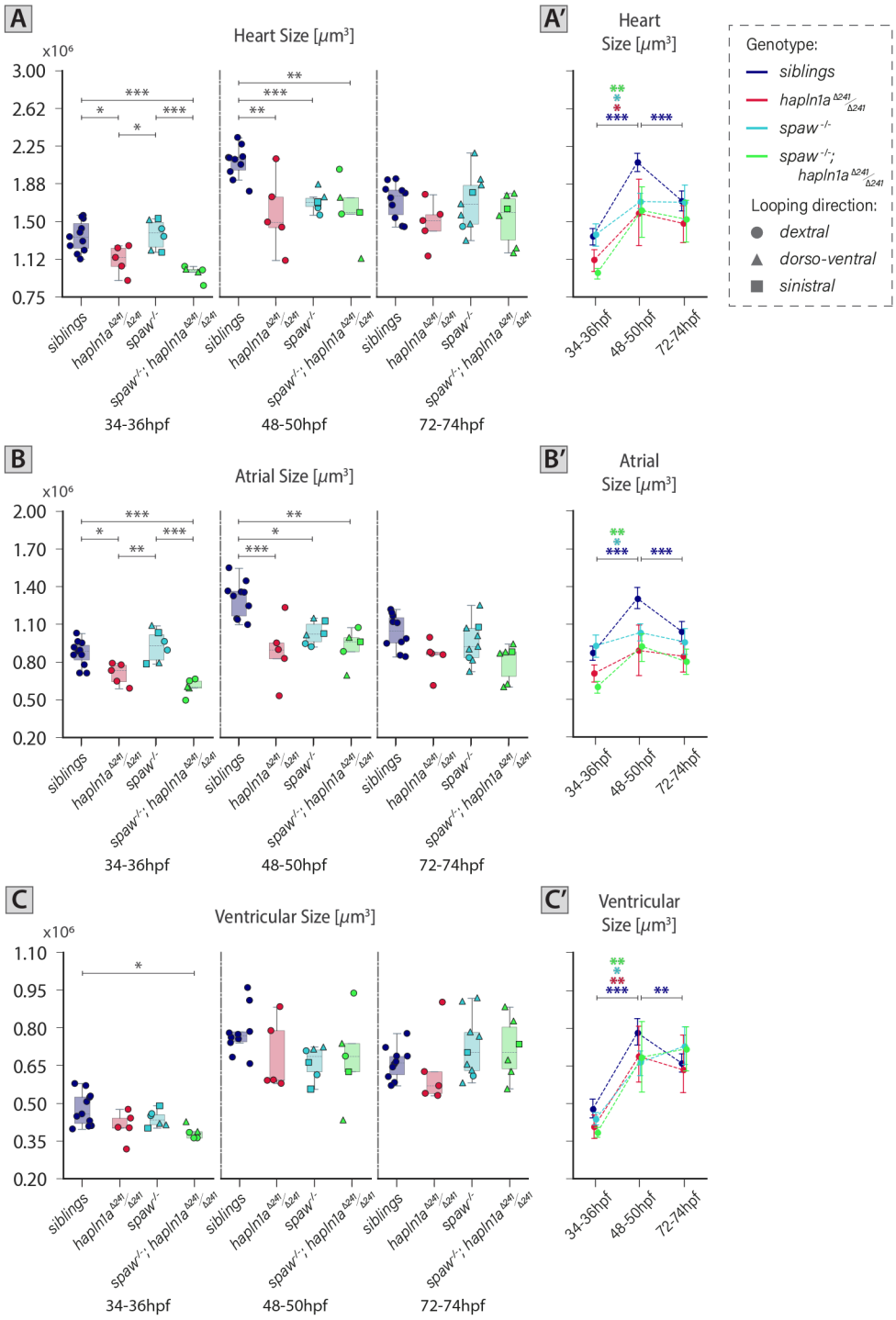

Fig 5.42. *spaw* and *hapln1a* drive independently the atrial growth dynamics of *spaw/hapln1a* double mutants during looping and ballooning morphogenesis.

A-C'. Quantification of heart (A-A') and chambers (atrium: B-B', ventricle: C-C') size using *morphoHeart* in *spaw/hapln1a* double mutants (light-green), *hapln1a*$^{\Delta 241/\Delta 241}$ (red), *spaw*$^{-/-}$ (cyan) and siblings (blue) at 34-36hpf, 48-50hpf and 72-74hpf. At early looping stages (34-36hpf), *spaw/hapln1a* double mutants, show a smaller heart driven by a smaller atrium and ventricle, when compared to controls. As the hearts undergo looping and ballooning morphogenesis (48-50hpf), both single and double mutants present a significant reduction in heart and atrial size. [Heart - 34-36hpf*: hapln1a*$^{\Delta 241/\Delta 241}$ *vs. spaw*$^{-/-}$ *p-value=0.03107, hapln1a*$^{\Delta 241/\Delta 241}$ *vs. siblings p-value=0.02433, spaw*$^{-/-}$*,hapln1a*$^{\Delta 241/\Delta 241}$ *vs. spaw*$^{-/-}$ *p-value=0.00100, spaw*$^{-/-}$*,hapln1a*$^{\Delta 241/\Delta 241}$ *vs. siblings p-value=0.00100;* 48-50hpf*: hapln1a*$^{\Delta 241/\Delta 241}$ *vs. siblings p-value=0.00424, spaw*$^{-/-}$*, spaw*$^{-/-}$*,hapln1a*$^{\Delta 241/\Delta 241}$ *vs. siblings p-value=0.00698, spaw*$^{-/-}$ *vs. siblings p-value=0.02142.* Atrium - 34-36hpf*:*

hapln1a$^{\Delta 241/\Delta 241}$ vs. spaw$^{-/-}$ p-value=0.00691, hapln1a$^{\Delta 241/\Delta 241}$ vs. siblings p-value=0.02997, spaw$^{-/-}$,hapln1a$^{\Delta 241/\Delta 241}$ vs. spaw$^{-/-}$ p-value=0.00100, spaw$^{-/-}$,hapln1a$^{\Delta 241/\Delta 241}$ vs. siblings p-value=0.00100; 48-50hpf*: hapln1a$^{\Delta 241/\Delta 241}$ vs. siblings p-value=0.00100, spaw$^{-/-}$, spaw$^{-/-}$,hapln1a$^{\Delta 241/\Delta 241}$ vs. siblings p-value=0.00148, spaw$^{-/-}$ vs. siblings p-value=0.01731.* Ventricle - 34-36hpf*: spaw$^{-/-}$,hapln1a$^{\Delta 241/\Delta 241}$ vs. siblings p-value=0.01715*]. A', B' and C' are point-plots of the data presented in A, B and C, respectively. A-C': Error bars with 95% confidence interval of the mean. 34-36hpf: *siblings n=11*, *hapln1a$^{\Delta 241/\Delta 241}$ n=5*, *spaw$^{-/-}$ n=6* (*sinistral n=2*, *dorso-ventral n=2*, *dextral n=2*), *spaw$^{-/-}$,hapln1a$^{\Delta 241/\Delta 241}$ n=5* (*dorso-ventral n=2*, *dextral n=3*)*;* 48-50hpf: *siblings n=10*, *hapln1a$^{\Delta 241/\Delta 241}$ n=5*, *spaw$^{-/-}$ n=6* (*sinistral n=2*, *dorso-ventral n=2*, *dextral n=2*), *spaw$^{-/-}$,hapln1a$^{\Delta 241/\Delta 241}$ n=5* (*sinistral n=1*, *dorso-ventral n=2*, *dextral n=2*)*;* 72-74hpf: *siblings n=10*, *hapln1a$^{\Delta 241/\Delta 241}$ n=5*, *spaw$^{-/-}$ n=9* (*sinistral n=1*, *dorso-ventral n=7*, *dextral n=1*), *spaw$^{-/-}$,hapln1a$^{\Delta 241/\Delta 241}$ n=6* (*sinistral n=1*, *dorso-ventral n=4*, *dextral n=1*). For details regarding the statistical analyses used to compare this set of data see *Note#5.11* (pg.213). Only significant comparisons are shown. ***: *p-value*<0.001, **: *p-value*<0.01, *: *p-value*<0.05.

[*Note#5.11*: All sample groups per stage and genotype (*spaw$^{-/-}$*, *hapln1a$^{\Delta 241/\Delta 241}$*, *spaw/hapln1a* double mutants and *siblings*) were analysed for normality using Shapiro-Wilk Normality test. For each variable, if all groups were normally distributed, comparison between genotypes per stage were carried out using ANOVA with Tukey's Multiple Comparisons as *post-hoc* test. When normal distribution could not be assumed, Kruskal-Wallis test with Dunn's Multiple Comparisons as *post-hoc* was used. For all tests a statistical significance α of *0.05* was defined].

As development progresses (34-36→50-72hpf), the already smaller *spaw$^{-/-}$,hapln1a$^{\Delta 241/\Delta 241}$* heart tubes fail to grow as much as the controls, resulting in hearts with significantly reduced size (Fig 5.42A). Interestingly, like *hapln1a$^{\Delta 241}$* and *spaw* single mutant embryos, defective growth of the heart during looping and ballooning is mainly driven by an atrial failure to expand (Fig 5.42B-B'), while the ventricle 'recovers' its reduced size growing, like single mutants, at a similar rate as the controls (Fig 5.42C-C'). In spite of having reduced atrial size at 34-36hpf (as a result of Hapln1a loss), the atrial size of *spaw/hapln1a* double mutants at 48-50hpf is indistinguishable from that of the *hapln1a$^{\Delta 241}$* and *spaw* single mutants, yet significantly reduced when compared to the sibling's hearts. Intriguingly, when the growth dynamics of the different mutants are analysed individually, while the atria of both single mutants grow at a reduced rate when compared to their siblings, the atrial growth of *spaw*/*hapln1a* double mutants is slightly higher than that of the single mutants (Fig 5.42B', *spaw$^{-/-}$* in cyan, *hapln1a$^{\Delta 241/\Delta 241}$* in red, *spaw$^{-/-}$, hapln1a$^{\Delta 241/\Delta 241}$* in light green). This unexpected behaviour of the double mutants suggests that Hapln1a and Spaw's L/R patterning play different and independent roles in atrial growth so that when both genes are disrupted, the interaction between the processes each gene individually regulates results in atrial expansion dynamics that resemble more closely that of the wild-type hearts. (A more in-depth explanation of the possible hypothesis that explains this peculiar, yet recurrent behaviour will be presented later in the discussion of this chapter).

At 72-74hpf, no defects in size are identified in the whole heart nor in its individual chambers in *spaw$^{-/-}$, hapln1a$^{\Delta 241/\Delta 241}$* double mutants. Similar to *hapln1a$^{\Delta 241}$* and *spaw* single mutants, the atrial chamber size of double mutant hearts shows a slight trend towards compaction between 50 and 72hpf (Fig 5.42B'), however, their final size at 72-74hpf is not significantly different to the size these hearts had already acquired by 48-50hpf. Surprisingly, the abnormal continued ventricular growth pattern previously identified in *spaw$^{-/-}$* mutant hearts is replicated in the *spaw$^{-/-}$, hapln1a$^{\Delta 241/\Delta 241}$* double mutants (Fig 5.42C'), suggesting an ongoing requirement for Spaw's L/R patterning to regulate ventricular heart size at post-looping stages.

Total lumen size throughout the examined stages did not show defects in the double mutants when compared to controls (Fig 5.43A-A'). Interestingly, analysis of the lumen size per chamber identified a reduced atrial capacity at 34-36hpf in the *spaw$^{-/-}$, hapln1a$^{\Delta 241/\Delta 241}$* double mutants when compared to controls and to *spaw* single mutants (Fig 5.43B-B'), reinforcing the previous finding of an early requirement of Hapln1a to regulate heart tube size. At 48-50hpf, like both *spaw* and *hapln1a* single mutants, defective

atrial growth results in reduced atrial blood filling capacity in the double mutants (Fig 5.43B-B'), whilst the ventricular lumen expands just like the controls (Fig 5.43C-C'). These results build on the hypothesis that during looping and ballooning, the combined effect of the mechanisms driven independently by Hapln1a and Spaw control atrial growth, including its lumen size.

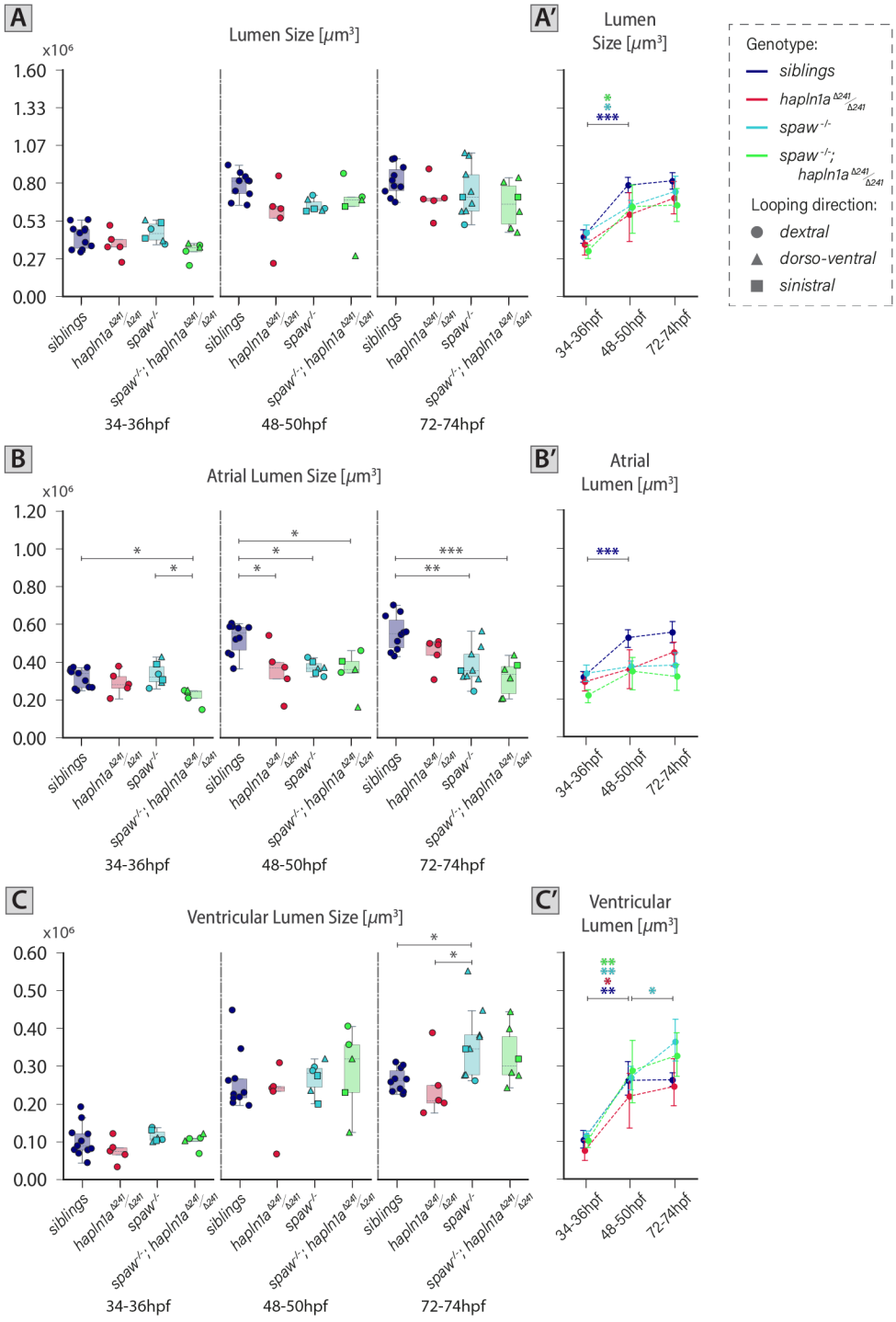

Fig 5.43. *spaw*$^{-/-}$, *hapln1a*$^{\Delta241/\Delta241}$ exhibit defects in atrial and ventricular lumen size, resulting from altered dynamics in chamber growth.

A-C'. Quantification of the lumen size of the heart (A-A') and its chambers (atrium: B-B', ventricle: C-C') using *morphoHeart* in *spaw/hapln1a* double mutants (light-green), *hapln1a*$^{\Delta241/\Delta241}$ (red), *spaw*$^{-/-}$ (cyan) and siblings (blue) at 34-36hpf, 48-50hpf and 72-74hpf. At early looping stages (34-36hpf), *spaw/hapln1a* double mutants, show a smaller atrial lumen, when compared to controls and *spaw*$^{-/-}$. As the hearts undergo looping and ballooning morphogenesis (48-50hpf), both single and double mutants present a significant reduction in atrial lumen size, which is preserved in *spaw/hapln1a* doubles and *spaw*$^{-/-}$ as the hearts transition to an early maturing stage. At 72-74hpf, the ventricles of *spaw*$^{-/-}$ are significantly larger than controls. [Atrium - 34-36hpf: *spaw*$^{-/-}$

,hapln1a$^{\Delta241/\Delta241}$ vs. spaw$^{-/-}$ p-value=0.01965, spaw$^{-/-}$,hapln1a$^{\Delta241/\Delta241}$ vs. siblings p-value=0.02696; 48-50hpf*: hapln1a$^{\Delta241/\Delta241}$ vs. siblings p-value=0.01793, spaw$^{-/-}$, spaw$^{-/-}$,hapln1a$^{\Delta241/\Delta241}$ vs. siblings p-value=0.01065, spaw$^{-/-}$ vs. siblings p-value=0.02121;* 72-74hpf*: spaw$^{-/-}$,hapln1a$^{\Delta241/\Delta241}$ vs. siblings p-value=0.00100, spaw$^{-/-}$ vs. siblings p-value=0.00220.* Ventricle - 72-74hpf*: hapln1a$^{\Delta241/\Delta241}$ vs. spaw$^{-/-}$ p-value=0.03374, spaw$^{-/-}$ vs. siblings p-value=0.02770*]. A', B' and C' are point-plots of the data presented in A, B and C, respectively. A-C': Error bars with 95% confidence interval of the mean. 34-36hpf: *siblings n=11*, *hapln1a$^{\Delta241/\Delta241}$ n=5*, *spaw$^{-/-}$ n=6* (*sinistral n=2*, *dorso-ventral n=2*, *dextral n=2*), *spaw$^{-/-}$,hapln1a$^{\Delta241/\Delta241}$ n=5* (*dorso-ventral n=2*, *dextral n=3*); 48-50hpf: *siblings n=10*, *hapln1a$^{\Delta241/\Delta241}$ n=5*, *spaw$^{-/-}$ n=6* (*sinistral n=2*, *dorso-ventral n=2*, *dextral n=2*), *spaw$^{-/-}$,hapln1a$^{\Delta241/\Delta241}$ n=5* (*sinistral n=1*, *dorso-ventral n=2*, *dextral n=2*); 72-74hpf: *siblings n=10*, *hapln1a$^{\Delta241/\Delta241}$ n=5*, *spaw$^{-/-}$ n=9* (*sinistral n=1*, *dorso-ventral n=7*, *dextral n=1*), *spaw$^{-/-}$,hapln1a$^{\Delta241/\Delta241}$ n=6* (*sinistral n=1*, *dorso-ventral n=4*, *dextral n=1*). For details regarding the statistical analyses used to compare this set of data see *Note#5.11* (pg.213). Only significant comparisons are shown. ***: *p-value*<0.001, **: *p-value*<0.01, *: *p-value*<0.05.

As looping and ballooning terminate and the heart transitions to an early maturing stage (48-50→72-74hpf) the atrial lumen of *spaw$^{-/-}$, hapln1a$^{\Delta241/\Delta241}$*, like that of *spaw$^{-/-}$* and siblings, is maintained constant, sustaining a significantly reduced atrial capacity when compared to controls (Fig 5.43B-B'). This preserved behaviour between the wild-types and double mutants to maintain the acquired atrial lumen size between 50 and 72hpf suggests loss of Spaw or Hapln1a does not influence the atrial lumen dynamics of *spaw$^{-/-}$*, *hapln1a$^{\Delta241/\Delta241}$* doubles during maturing stages.

Interestingly, between 50 and 72hpf, the ventricular lumen of *spaw$^{-/-}$, hapln1a$^{\Delta241/\Delta241}$* doubles continue growing at an increased rate like the *spaw* mutants resulting in ventricular capacities that appear to be larger than controls yet not significantly different (Fig 5.43C'). This result reiterates the possible role of Spaw's L/R patterning in regulating ventricular growth (chamber and lumen size) dynamics during maturing stages.

Together, analysis of the heart/chambers size and blood filling capacity in the single and double *spaw*/*hapln1a* suggests an early requirement for Hapln1a to regulate heart tube size at early looping stages (34-36hpf), an intermediate requirement for Spaw's L/R patterning and Hapln1a during looping and ballooning to drive independently atrial chamber and lumen growth, and a late requirement for Spaw to control ventricular chamber dynamics as the heart transitions to a maturing stage.

To further characterise heart morphogenesis and specifically heart looping in the *spaw$^{-/-}$, hapln1a$^{\Delta241/\Delta241}$* double mutants, the 3D linear and looped heart lengths were measured, and the looping ratio was quantified across the four genotypes. Analysis of these parameters revealed that disrupted L/R patterning due to loss of *spaw* is the main factor responsible for the looping defects identified in the double mutants.

Analysis of these parameters initially identifies that *spaw$^{-/-}$*, *hapln1a$^{\Delta241/\Delta241}$* doubles, similar to *spaw$^{-/-}$* hearts have significantly longer linear heart lengths when compared to their siblings at early maturing stages (72-74hpf, Fig 5.44A-A'). Examination of the looped heart length identifies only an early significant reduction in this variable in the *hapln1a$^{\Delta241/\Delta241}$* mutants, which appear to be also impacting the *spaw*/*hapln1a* doubles yet not in a significant way (Fig 5.44B-B'). Interestingly, the fact that no other defects are identified in this parameter confirms that despite the loss of Hapln1a or Spaw, the centrelines of these hearts are lengthening between looping and ballooning and then shortening due to the remodelling processes occurring in the heart when it transitions to a maturing stage. Consequently, the looping ratio defects identified in the *spaw$^{-/-}$* (at 48-50hpf) and *spaw/hapln1a* doubles (at 72-74hpf) when compared to their siblings are the result of a failure to rearrange the chambers around the AVC and bring the IFT and OFT closer, which in turn result in significantly longer linear heart lengths in these mutant hearts (Fig 5.41B,E,H, Fig 5.44A-A').

Together, this suggests that loss of Spaw does not result in the absence of heart looping (in single and double mutants), but instead that Spaw's L/R patterning is required to support the compaction and rearrangement process of the chambers during looping and ballooning morphogenesis.

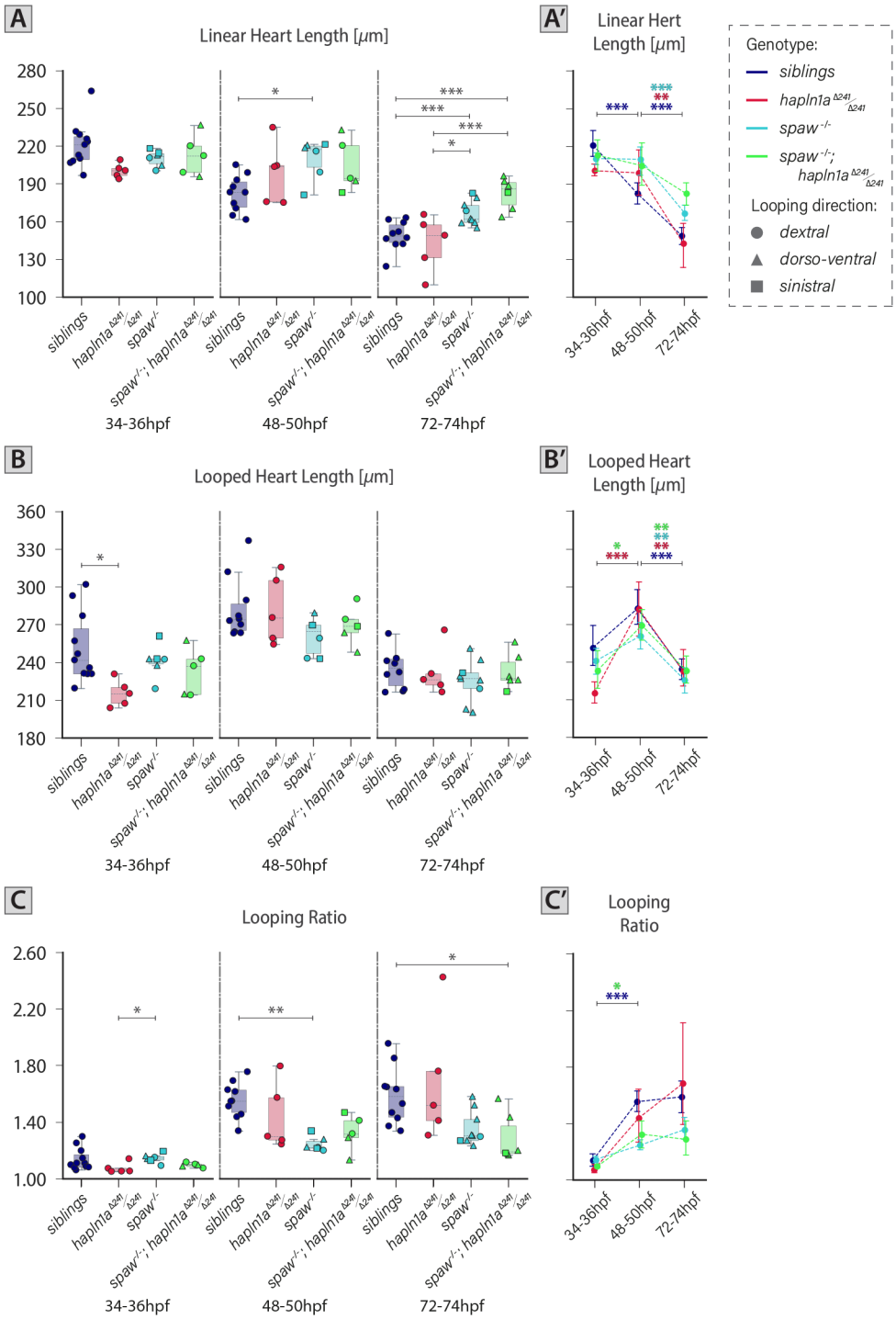

Fig 5.44. L/R patterning is required to support chamber compaction and rearrangement during looping and ballooning morphogenesis.

A-B'. Quantification of the linear (A-A') and looped (B-B') heart length of the heart using *morphoHeart* in *spaw/hapln1a* double mutants (light-green), *hapln1a*$^{\Delta241/\Delta241}$ (red), *spaw*$^{-/-}$ (cyan) and siblings (blue) at 34-36hpf, 48-50hpf and 72-74hpf. At 48-50hpf, *spaw*$^{-/-}$ have significantly larger linear heart lengths when compared to controls. At 72-74hpf, driven by the loss of *spaw*, the linear heart length of *spaw*$^{-/-}$ and *spaw*$^{-/-}$, *hapln1a*$^{\Delta241/\Delta241}$ is significantly larger than that of *hapln1a*$^{\Delta241/\Delta241}$ and the controls. *hapln1a*$^{\Delta241}$ promoter homozygous mutants exhibit a significantly shorter looped heart length at 34-36hpf when compared to controls. **C-C'.** Quantification of looping ratio (quotient between looped heart length and linear heart length) across the four phenotypes described in A-B' at 34-36hpf, 48-50hpf and 72-74hpf. Failure in heart compaction,

results in significantly reduced looping ratios in the *hapln1a*$^{\Delta 241}$ mutant at 34-36hpf (when compared to *spaw* mutants), in the *spaw*$^{-/-}$ at 48-50hpf (when compared to siblings) and in *spaw*/*hapln1a* double mutants at 72-74hpf (when compared to siblings). [Linear length - 48-50hpf*: spaw*$^{-/-}$ *vs. siblings p-value=0.03952;* 72-74hpf*: hapln1a*$^{\Delta 241/\Delta 241}$ *vs. spaw*$^{-/-}$*,hapln1a*$^{\Delta 241/\Delta 241}$ *p-value=0.00100, hapln1a*$^{\Delta 241/\Delta 241}$ *vs. spaw*$^{-/-}$ *p-value=0.01822, spaw*$^{-/-}$*,hapln1a*$^{\Delta 241/\Delta 241}$ *vs. siblings p-value=0.00100, spaw*$^{-/-}$ *vs. siblings p-value=0.03805.* Looped heart length - 34-36hpf*: hapln1a*$^{\Delta 241/\Delta 241}$ *vs. siblings p-value=0.02209.* Looping ratio - 34-36hpf*: hapln1a*$^{\Delta 241/\Delta 241}$ *vs. spaw*$^{-/-}$ *p-value=0.03392;* 48-50hpf*: spaw*$^{-/-}$ *vs. siblings p-value=0.00356;* 72-74hpf*: spaw*$^{-/-}$*,hapln1a*$^{\Delta 241/\Delta 241}$ *vs. siblings p-value=0.02487*]. A', B' and C' are point-plots of the data presented in A, B and C, respectively. A-C': Error bars with 95% confidence interval of the mean. 34-36hpf: *siblings n=11*, *hapln1a*$^{\Delta 241/\Delta 241}$ *n=5*, *spaw*$^{-/-}$ *n=6* (*sinistral n=2*, *dorso-ventral n=2*, *dextral n=2*), *spaw*$^{-/-}$*,hapln1a*$^{\Delta 241/\Delta 241}$ *n=5* (*dorso-ventral n=2*, *dextral n=3*); 48-50hpf: *siblings n=10*, *hapln1a*$^{\Delta 241/\Delta 241}$ *n=5*, *spaw*$^{-/-}$ *n=6* (*sinistral n=2*, *dorso-ventral n=2*, *dextral n=2*), *spaw*$^{-/-}$*,hapln1a*$^{\Delta 241/\Delta 241}$ *n=5* (*sinistral n=1*, *dorso-ventral n=2*, *dextral n=2*); 72-74hpf: *siblings n=10*, *hapln1a*$^{\Delta 241/\Delta 241}$ *n=5*, *spaw*$^{-/-}$ *n=9* (*sinistral n=1*, *dorso-ventral n=7*, *dextral n=1*), *spaw*$^{-/-}$*,hapln1a*$^{\Delta 241/\Delta 241}$ *n=6* (*sinistral n=1*, *dorso-ventral n=4*, *dextral n=1*). For details regarding the statistical analyses used to compare this set of data see *Note#5.11* (pg.213). Only significant comparisons are shown. ***: *p-value*<0.001, **: *p-value*<0.01, *: *p-value*<0.05.

Analysis of chamber size and looping morphogenesis parameters identified that Hapln1a and Spaw appear to regulate separately heart growth and morphogenesis in *spaw*$^{-/-}$, *hapln1a*$^{\Delta 241/\Delta 241}$ double mutants. To characterise chamber growth and identify whether the loss of *hapln1a* affects chamber morphology differently in hearts with different looping directions, the ballooning heatmaps of dextral, dorso-ventral and sinistral *spaw*$^{-/-}$, *hapln1a*$^{\Delta 241/\Delta 241}$ hearts were obtained and analysed (Fig 5.45A-B: 34-36hpf, C-D: 48-50hpf, and E-F: 72-74hpf). [*Note#5.12:* Like with *spaw*$^{-/-}$ hearts, to assist the 2D heatmap analysis of *spaw/hapln1a* double mutant hearts with different looping directions refer to Fig 4.33].

Analysis of chamber ballooning in *spaw*$^{-/-}$, *hapln1a*$^{\Delta 241/\Delta 241}$ hearts identifies that regardless of looping direction, double mutant heart tubes are thinner (reduced ballooning values identified by green-yellow colours in both chambers' heatmaps) at 34-36hpf when compared to controls (Fig 5.45A,B). Despite this reduction in the heart tube dimensions, the myocardial ballooning heatmaps of the double mutants display the characteristic 'U' shape around the AVC region of the atrium, while the ventricle remains tubular, suggesting these hearts, just like wild types, have already started to undergo ballooning morphogenesis in the atrium. The already identified defect in atrial growth at 48-50hpf (Fig 5.42B-B') is clearly visible in the reduced ballooning values present in the heatmaps of *spaw*$^{-/-}$, *hapln1a*$^{\Delta 241/\Delta 241}$ atria at this stage (Fig 5.45Ci-iii). Similar to *spaw*$^{-/-}$ hearts, according to the direction of looping, different specific ballooning patterns characterising the chamber's outer curvatures and apexes are readily recognised. At 72-74hpf, just like the single *hapln1a*$^{\Delta 241}$ and *spaw* mutants, no morphological defects are identified in the chambers of *spaw*$^{-/-}$, *hapln1a*$^{\Delta 241/\Delta 241}$ double mutants, confirming these hearts, irrespective of their looping direction at this stage attain a comparable size and shape to that of the control siblings.

To identify if loss of *hapln1a* combined with loss L/R patterning result in hearts with abnormal cardiac tissue dynamics, the myocardial and endocardial tissue volumes per chamber were quantified (myocardium: Fig 5.46, endocardium: Fig 5.47). Interestingly, *spaw*$^{-/-}$, *hapln1a*$^{\Delta 241/\Delta 241}$ hearts present an early defect in the myocardial and endocardial tissue volume comprising both chambers in the early looping heart, which can be directly linked to the loss of *hapln1a* (Fig 5.18A,B), supporting the early requirement of Hapln1a in the establishment of the cardiac tissues comprising the early looping heart tube.

Interestingly, aside from the early volumetric defects, analysis of the transition dynamics of each tissue layer volume comprising each heart chamber between timepoints allows to pinpoint altered expansion/reduction dynamics and link them to defects resulting from the loss of either or both genes.

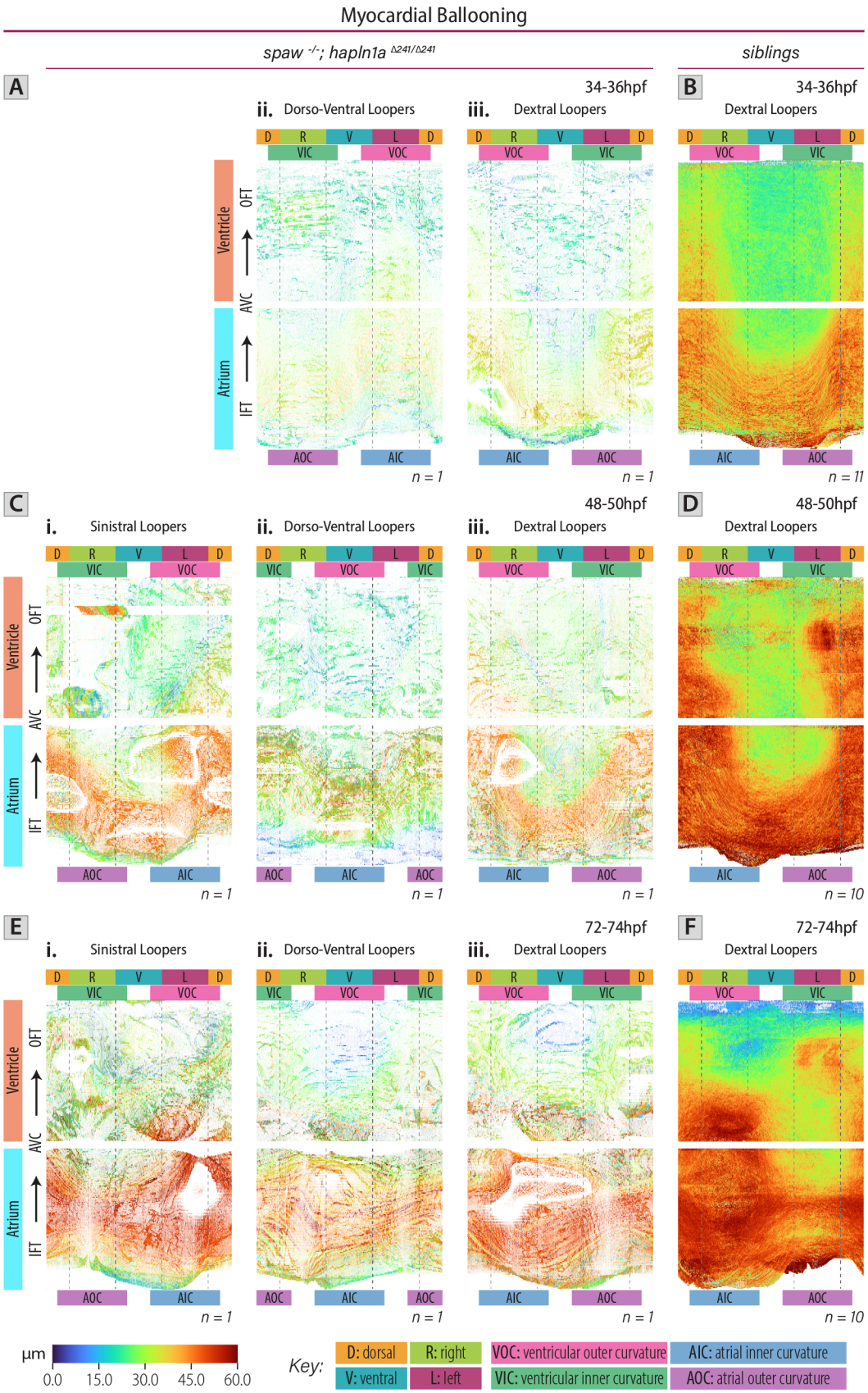

Fig 5.45. Myocardial ballooning heatmaps corroborate defective atrial growth in *spaw/hapln1a* double mutants during looping and ballooning morphogenesis

A-F. 2D representations of the myocardial ballooning of *spaw*$^{-/-}$, *hapln1a*$^{\Delta 241/\Delta 241}$ (A,C,E) and sibling (B, D, F) hearts at 34-36hpf (A-B), 48-50hpf (C-D) and 72-74hpf (E-F). *spaw/hapln1a* homozygous mutants are classified according to their direction of looping as: sinistral (i), dorso-ventral (ii) and dextral (iii) loopers. While A, C and E show examples of planar projection plots of individual embryos, B, D and F show the average planar

projections of all the processed siblings at all the indicated stages. A-F share colour-scale presented with the key at the bottom-left of the figure. D: Dorsal, R: Right, V: Ventral, L: Left, VOC: Ventricular Outer Curvature, VIC: Ventricular Inner Curvature, AOC: Atrial Outer Curvature, AIC: Atrial Inner Curvature, IFT: Inflow-tract, AVC: Atrioventricular Canal, OFT: Outflow-tract.

While the ventricular myocardium dynamics during looping and ballooning in the *spaw*$^{-/-}$, *hapln1a*$^{\Delta241/\Delta241}$ follow that of the *spaw*$^{-/-}$ (characterised by a slow tissue expansion, Fig 5.46B'), the atrial myocardium dynamics appear to follow the growth rate of sibling hearts, suggesting that despite the loss of Hapln1a and Spaw the dynamics of myocardial growth in the atrium of double mutant hearts is not affected (36→48hpf , Fig 5.46A'). As development progresses and the heart starts to mature, like the individual mutants, no defects are identified in the atrial myocardium of double mutant hearts. Interestingly, within this timeframe (50→72hpf), while the ventricular myocardium dynamics of the siblings (and *hapln1a*$^{\Delta241/\Delta241}$) show a compaction process in this tissue layer, the double mutants (following the ventricular myocardium dynamics of the *spaw*$^{-/-}$), show a continued expansion of this tissue volume, resulting in a final tissue volume indistinguishable from that of sibling hearts.

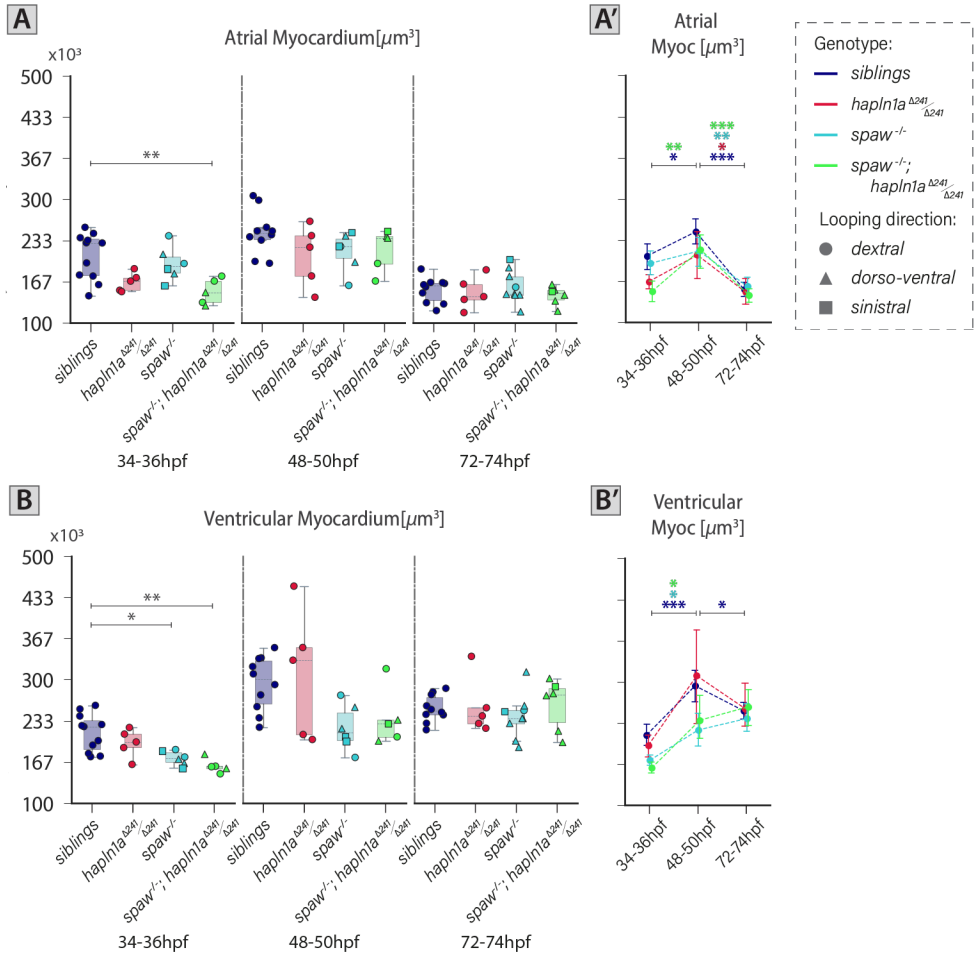

Fig 5.46. Regulation of the myocardial volume dynamics by *hapln1a* and *spaw* during looping and ballooning are chamber-specific.

A-B'. Quantification of the atrial (A-A') and ventricular (B-B') myocardium of *spaw/hapln1a* double mutants (light-green), *hapln1a*$^{\Delta241/\Delta241}$ (red), *spaw*$^{-/-}$ (cyan) and siblings (blue) at 34-36hpf, 48-50hpf and 72-74hpf. At 34-36hpf, *spaw/hapln1a* double mutants have a significantly reduced myocardial volume in the atrium and ventricle when compared to controls. [Atrial myocardium - 34-36hpf*: spaw*$^{-/-}$*,hapln1a*$^{\Delta241/\Delta241}$ *vs. siblings p-value=0.00934.* Ventricular myocardium - 34-36hpf*: spaw*$^{-/-}$*,hapln1a*$^{\Delta241/\Delta241}$ *vs. siblings p-value=0.00150, spaw*$^{-/-}$ *vs. siblings p-value=0.01033*]. A' and B' are point-plots of the data presented in A, and B, respectively. A-B': Error bars with 95% confidence interval of the mean. 34-36hpf: *siblings n=11*, *hapln1a*$^{\Delta241/\Delta241}$ *n=5*, *spaw*$^{-/-}$ *n=6* (*sinistral n=2*, *dorso-ventral n=2*, *dextral n=2*), *spaw*$^{-/-}$*,hapln1a*$^{\Delta241/\Delta241}$ *n=5* (*dorso-ventral n=2*, *dextral n=3*); 48-

50hpf: *siblings n=10*, *hapln1a$^{\Delta241/\Delta241}$ n=5*, *spaw$^{-/-}$ n=6* (*sinistral n=2*, *dorso-ventral n=2*, *dextral n=2*), *spaw$^{-/-}$;hapln1a$^{\Delta241/\Delta241}$ n=5* (*sinistral n=1*, *dorso-ventral n=2*, *dextral n=2*); 72-74hpf: *siblings n=10*, *hapln1a$^{\Delta241/\Delta241}$ n=5*, *spaw$^{-/-}$ n=9* (*sinistral n=1*, *dorso-ventral n=7*, *dextral n=1*), *spaw$^{-/-}$;hapln1a$^{\Delta241/\Delta241}$ n=6* (*sinistral n=1*, *dorso-ventral n=4*, *dextral n=1*). For details regarding the statistical analyses used to compare this set of data see *Note#5.11* (pg.213). Only significant comparisons are shown. ***: *p-value*<0.001, **: *p-value*<0.01, *: *p-value*<0.05.

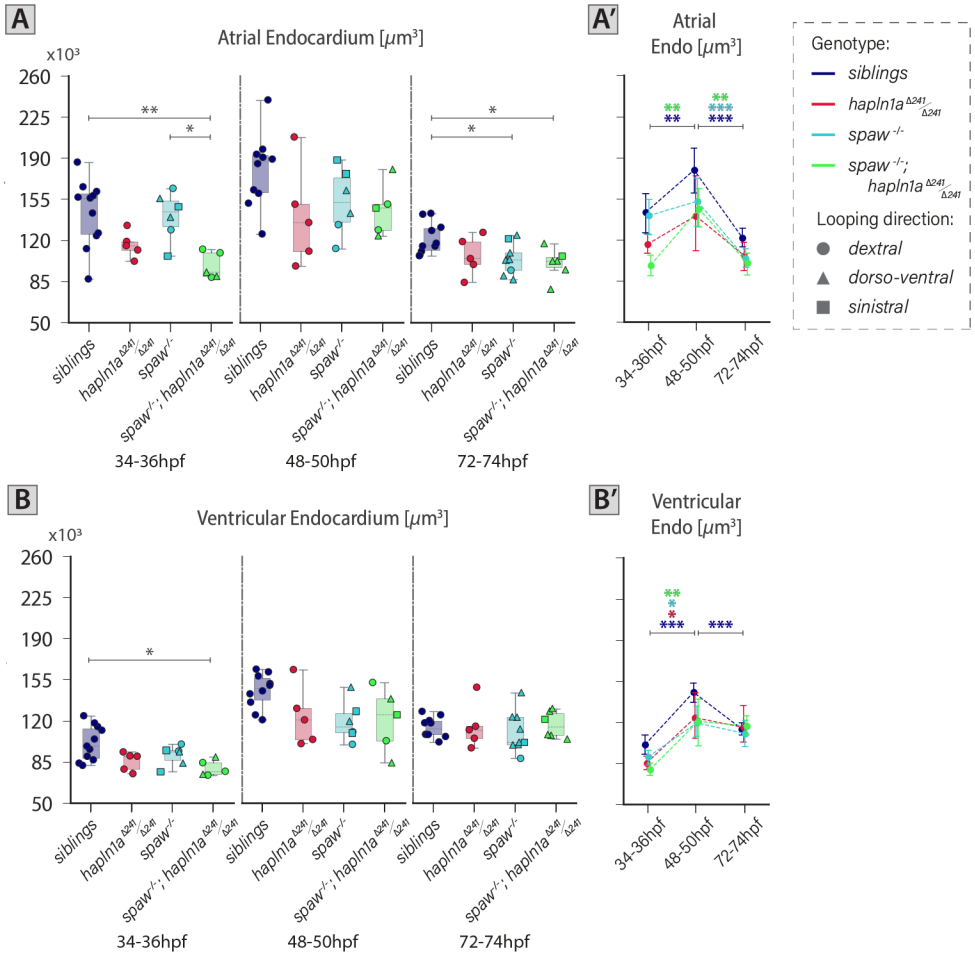

Fig 5.47. *hapln1a* and *spaw* are required during early heart development to regulate the atrial endocardial tissue volume of the developing zebrafish hearts.
A-B'. Quantification of the atrial (A-A') and ventricular (B-B') endocardium of *spaw/hapln1a* double mutants (light-green), *hapln1a$^{\Delta241/\Delta241}$* (red), *spaw$^{-/-}$* (cyan) and siblings (blue) at 34-36hpf, 48-50hpf and 72-74hpf. At 34-36hpf, [Atrial endocardium - 34-36hpf: *spaw$^{-/-}$;hapln1a$^{\Delta241/\Delta241}$ vs. spaw$^{-/-}$ p-value=0.02125*, *spaw$^{-/-}$;hapln1a$^{\Delta241/\Delta241}$ vs. siblings p-value=0.00501*; 72-74hpf: *spaw$^{-/-}$;hapln1a$^{\Delta241/\Delta241}$ vs. siblings p-value=0.02866*, *spaw$^{-/-}$ vs. siblings p-value=0.04597*. Ventricular endocardium - 34-36hpf: *spaw$^{-/-}$;hapln1a$^{\Delta241/\Delta241}$ vs. siblings p-value=0.01082*]. A' and B' are point-plots of the data presented in A, and B, respectively. A-B': Error bars with 95% confidence interval of the mean. 34-36hpf: *siblings n=11*, *hapln1a$^{\Delta241/\Delta241}$ n=5*, *spaw$^{-/-}$ n=6* (*sinistral n=2*, *dorso-ventral n=2*, *dextral n=2*), *spaw$^{-/-}$;hapln1a$^{\Delta241/\Delta241}$ n=5* (*dorso-ventral n=2*, *dextral n=3*); 48-50hpf: *siblings n=10*, *hapln1a$^{\Delta241/\Delta241}$ n=5*, *spaw$^{-/-}$ n=6* (*sinistral n=2*, *dorso-ventral n=2*, *dextral n=2*), *spaw$^{-/-}$;hapln1a$^{\Delta241/\Delta241}$ n=5* (*sinistral n=1*, *dorso-ventral n=2*, *dextral n=2*); 72-74hpf: *siblings n=10*, *hapln1a$^{\Delta241/\Delta241}$ n=5*, *spaw$^{-/-}$ n=9* (*sinistral n=1*, *dorso-ventral n=7*, *dextral n=1*), *spaw$^{-/-}$;hapln1a$^{\Delta241/\Delta241}$ n=6* (*sinistral n=1*, *dorso-ventral n=4*, *dextral n=1*). For details regarding the statistical analyses used to compare this set of data see *Note#5.11* (pg.213). Only significant comparisons are shown. ***: *p-value*<0.001, **: *p-value*<0.01, *: *p-value*<0.05.

Analysis of the endocardial volume dynamics as the heart undergoes looping and ballooning identifies that despite the reduced endocardial growth identified in the single mutants (Fig 5.47A'), no defects in tissue expansion are identified in either of the doubles' chambers when compared to controls. Interestingly, as

the heart transition to a maturing stage (50→72hpf), although the atrial endocardial reduction dynamics appear to be unaffected in the double mutants, as the atrial endocardial volume at 48-50hpf in the doubles appeared to be smaller than that of the siblings (yet not significant), the unaffected reduction dynamics between 50 and 72hpf result in *spaw/hapln1a* double mutants with a significantly reduced atrial endocardium. The ventricular endocardial dynamics are unaltered as the heart transitions to an early maturing stage, resulting in double mutant ventricles with endocardial volumes comparable to the siblings (Fig 5.47B-B').

Altogether, analysis of heart/chamber size and cardiac tissue volumes in the *spaw*$^{-/-}$, *hapln1a*$^{\Delta 241/\Delta 24}$ suggests different critical windows for Hapln1a and Spaw activities to regulate chamber and tissue dynamics during early zebrafish heart development. While an early requirement for Hapln1a during heart tube assembly is necessary to establish correct heart tube tissue composition and size, a later requirement for Spaw's L/R patterning is essential in regulating ventricular chamber size (and lumen), and chamber rearrangement as the heart undergoes looping, ballooning and early maturing.

Next, to examine the interaction between *hapln1a* asymmetric expression and laterality, the cardiac ECM of embryos with disrupted L/R patterning and loss of Hapln1a were reconstructed and morphologically characterised using *morphoHeart* (Fig 5.48). Examination of the 3D volumes identifies time- and chamber-specific abnormal cardiac ECM dynamics in the double mutants compared to controls, characterised by reduced atrial (Fig 5.48B,E,H) and ventricular (Fig 5.48B,C,F,I) cardiac ECM at 48-50 and 72-74hpf, respectively.

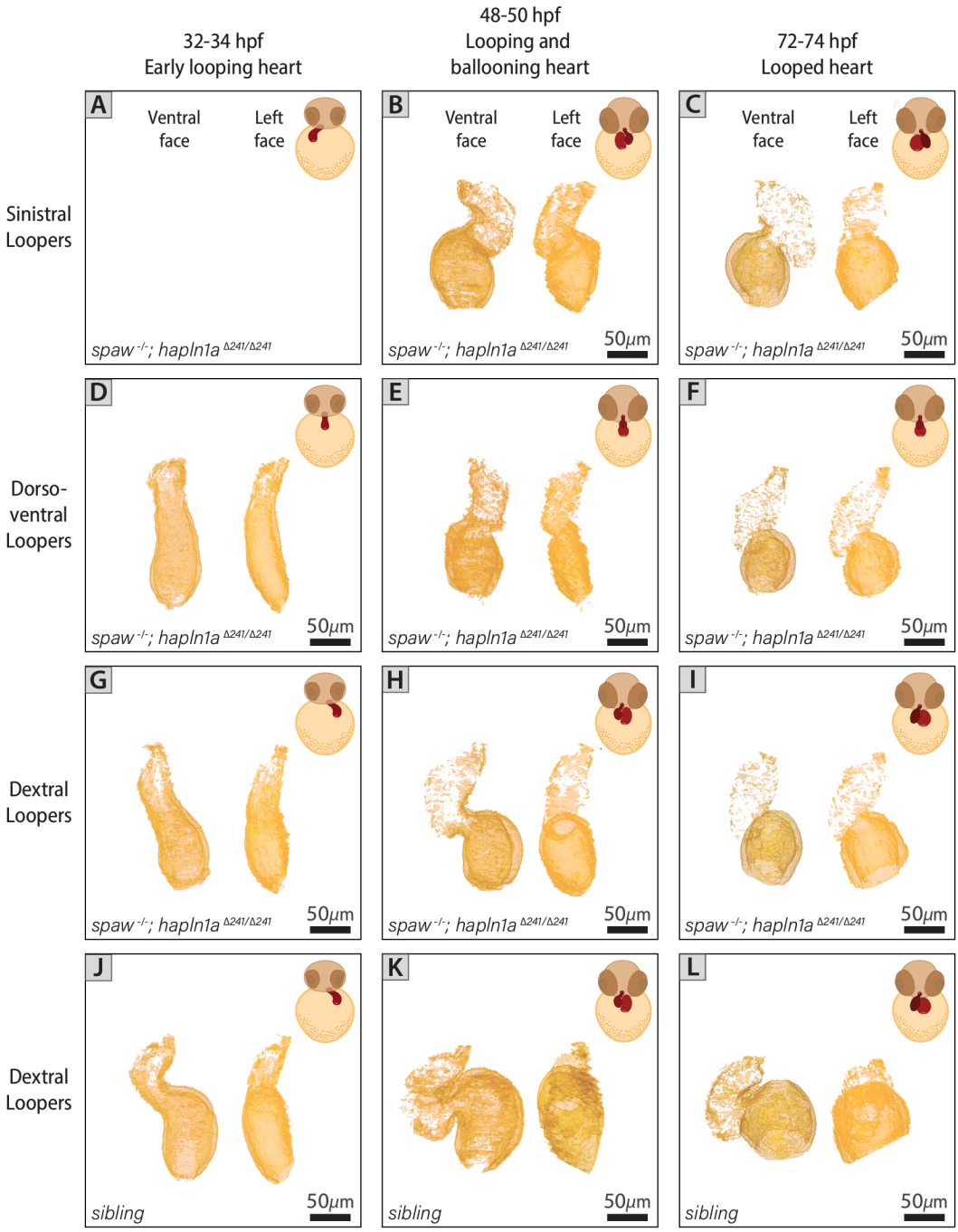

Fig 5.48. 3D cardiac jelly volume reconstructions of *spaw*$^{-/-}$, *hapln1a*$^{\Delta 241/\Delta 241}$ hearts exhibit time- and chamber-specific defects in the cardiac ECM volume present in these hearts.

A-L. Representative 3D reconstructions of the cardiac jelly (orange) of *spaw*$^{-/-}$, *hapln1a*$^{\Delta 241/\Delta 241}$ (A-I) and sibling (J-L) hearts at key developmental stages (34-36hpf: D,G,J; 48-50hpf: B,E,H,K; and 72-74hpf: C,F,I,L). *spaw/hapln1a* double homozygous mutants (A-I) are classified according to their direction of looping as: sinistral (B-C), middle (D-F) and dextral (G-I) loopers. A-L: As described by the labels in Panels A-C, all panels show the ventral face(on the left) and left face (on the right) of each of the presented hearts.

Further quantifications of the cardiac ECM volume identified early defects in the total cardiac ECM of *spaw*$^{-/-}$, *hapln1a*$^{\Delta 241/\Delta 241}$ mutant hearts when compared to the *spaw*$^{-/-}$ and siblings (34-36hpf, Fig 5.49A). Like *hapln1a*$^{\Delta 241/\Delta 241}$, this early defect (34-36hpf) in the cardiac ECM of *spaw*$^{-/-}$;*hapln1a*$^{\Delta 241/\Delta 241}$ double mutants is mainly driven by a reduced amount of atrial ECM (Fig 5.49B), while the ECM volume in the ventricle is unaffected (Fig 5.49C).

Interestingly, the chamber-specific ECM dynamics of the *spaw*/*hapln1a* double mutants between 34 and 72hpf appear to be distinctly regulated at different timeframes, showing in some instances individual yet in others shared roles for Hapln1a and Spaw in the regulation of cardiac jelly volume at early stages of heart development.

In the atrium, as expected from the phenotypes in the individual *hapln1a*$^{\Delta 241}$ and *spaw* mutants, as the heart undergoes looping and ballooning (34-36→48-50hpf), the expansion rate of the cardiac jelly in the *spaw*$^{-/-}$, *hapln1a*$^{\Delta 241/\Delta 241}$ is reduced compared to the controls (Fig 5.49B') resulting in significantly reduced atrial cardiac ECM volume in the double mutant hearts (Fig 5.49B). Interestingly, the fact that the atrial ECM volume dynamics between 34 and 50hpf in the double mutants are slightly higher than that of the single mutants suggests once again that Hapln1a and Spaw regulate separately the atrial cardiac jelly specific-expansion between 34 and 50hpf. As development progresses in this chamber (48-50→72-74hpf), the atrial cardiac jelly dynamics of the *spaw*/*hapln1a* double mutants, different to the siblings in which the ECM is reduced, continue expanding but at a slower rate than that between 34 and 50hpf (Fig 5.49B'). Because the atrial cardiac ECM volume in the double mutants' atria at 48-50hpf was already significantly smaller than the cardiac jelly in the siblings, this slow ECM production between 50 and 72hpf results in a *spaw*$^{-/-}$, *hapln1a*$^{\Delta 241/\Delta 241}$ chamber with a cardiac ECM volume comparable to controls. This result suggests that during this timeframe, Spaw's L/R patterning is the factor required to regulate atrial ECM reduction as the heart transitions to a maturing stage (50→72hpf).

In the ventricle, on the contrary, during looping and ballooning, the ventricular cardiac ECM dynamics of the double mutants fail to follow the expansion of the controls, resulting in a chamber with a significantly reduced ECM at 48-50hpf (Fig 5.49C). Not surprisingly, this ventricular defect in ECM expansion was recognised in the analysis of the single mutants (*spaw*$^{-/-}$ and *hapln1a*$^{\Delta 241/\Delta 241}$) (Fig 4.36C, 5.22C). Additionally, the fact that the extent of the defect observed in the double mutants is similar to that observed in the singles (Fig 5.49C) corroborates the hypothesis that Hapln1a and Spaw interact in the same pathway to regulate the cardiac jelly expansion of the **ventricle** as the heart undergoes looping and ballooning morphogenesis.

As the ventricle transitions to a maturing stage (48-50→72-74hpf), the ECM reduction dynamics identified in the siblings are also recognised in the *spaw*/*hapln1a* double mutants (Fig 5.49C'). Even though the ECM reduction rate in the double mutants is slower than that of the siblings, the observation that the ECM volume present in the *spaw*$^{-/-}$, *hapln1a*$^{\Delta 241/\Delta 241}$ ventricle at 48-50hpf is already smaller than the controls (Fig 5.49C), explains why the cardiac jelly volume at 72-74hpf in the ventricle of the double mutant embryos remains significantly reduced. As the ventricular ECM dynamics for all the sibling and mutant groups between 50 and 72hpf point towards reduction, it makes it difficult to identify if the described dynamics of the double mutants are the result of the loss of Hapln1a and/or Spaw or simply the normal activation of the ECM degradation processes within this chamber.

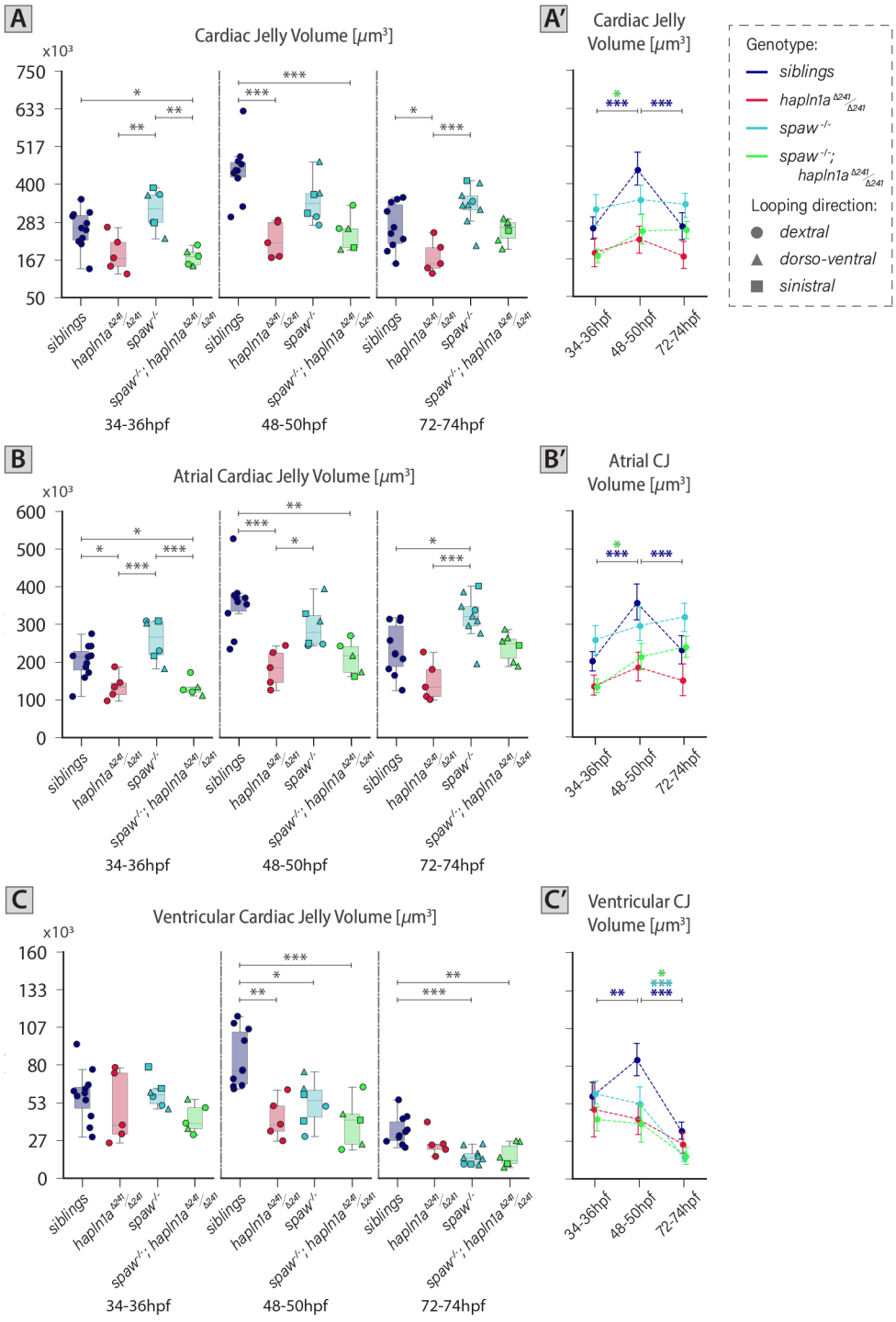

Fig 5.49. Throughout development Hapln1a and Spaw regulate the cardiac jelly volume dynamics in the developing heart.

A-C'. Quantification of the total cardiac jelly comprising the heart (A-A') and the chambers (atrium: B-B', ventricle: C-C') of *spaw/hapln1a* double mutants (light-green), *hapln1a*$^{\Delta241/\Delta241}$ (red), *spaw*$^{-/-}$ (cyan) and siblings (blue) at 34-36hpf, 48-50hpf and 72-74hpf. At 34-36hpf, *spaw/hapln1a* double mutants, similar to *hapln1a*$^{\Delta241/\Delta241}$ have a significantly reduced cardiac jelly volume in the heart and atrium when compared to controls and *spaw*$^{-/-}$. As the heart undergoes looping and ballooning, the ECM volume comprising the total heart and both chambers in the *spaw/hapln1a* double mutants is significantly reduced when compared to siblings. At 72-74hpf as the hearts transition to a maturing state, like *spaw* mutants, *spaw*$^{-/-}$, *hapln1a*$^{\Delta241/\Delta241}$ exhibit only significantly reduced cardiac ECM in the ventricle. [Cardiac jelly - 34-36hpf: *hapln1a*$^{\Delta241/\Delta241}$ *vs. spaw*$^{-/-}$ *p-value=0.00300, spaw*$^{-/-}$*,hapln1a*$^{\Delta241/\Delta241}$ *vs. spaw*$^{-/-}$ *p-value=0.00148, spaw*$^{-/-}$*,hapln1a*$^{\Delta241/\Delta241}$ *vs. siblings p-value=0.03909;* 48-50hpf*: hapln1a*$^{\Delta241/\Delta241}$ *vs. siblings p-value=0.00100, spaw*$^{-/-}$*,hapln1a*$^{\Delta241/\Delta241}$ *vs. siblings p-value=0.00100;* 72-74hpf*: hapln1a*$^{\Delta241/\Delta241}$ *vs. spaw*$^{-/-}$ *p-value=0.00100, hapln1a*$^{\Delta241/\Delta241}$ *vs. siblings p-value=0.04340.* Atrial CJ - 34-36hpf*: hapln1a*$^{\Delta241/\Delta241}$ *vs. spaw*$^{-/-}$ *p-value=0.00100, hapln1a*$^{\Delta241/\Delta241}$ *vs. siblings p-*

value=0.04084, spaw$^{-/-}$,hapln1a$^{\Delta241/\Delta241}$ vs. spaw$^{-/-}$ p-value=0.00100, spaw$^{-/-}$,hapln1a$^{\Delta241/\Delta241}$ vs. siblings p-value=0.03147; 48-50hpf*: hapln1a$^{\Delta241/\Delta241}$ vs. spaw$^{-/-}$ p-value=0.04747, hapln1a$^{\Delta241/\Delta241}$ vs. siblings p-value=0.00100, spaw$^{-/-}$,hapln1a$^{\Delta241/\Delta241}$ vs. siblings p-value=0.00314;* 72-74hpf*: hapln1a$^{\Delta241/\Delta241}$ vs. spaw$^{-/-}$ p-value=0.00100, spaw$^{-/-}$ vs. siblings p-value=0.01605.* Ventricular CJ - 48-50hpf*: hapln1a$^{\Delta241/\Delta241}$ vs. siblings p-value=0.00167, spaw$^{-/-}$,hapln1a$^{\Delta241/\Delta241}$ vs. siblings p-value=0.00100, spaw$^{-/-}$ vs. siblings p-value=0.01404;* 72-74hpf*: spaw$^{-/-}$,hapln1a$^{\Delta241/\Delta241}$ vs. siblings p-value=0.00220, spaw$^{-/-}$ vs. siblings p-value=0.00100*]. A' and B' are point-plots of the data presented in A, and B, respectively. A-B': Error bars with 95% confidence interval of the mean. 34-36hpf: *siblings n=11*, *hapln1a$^{\Delta241/\Delta241}$ n=5*, *spaw$^{-/-}$ n=6* (*sinistral n=2*, *dorso-ventral n=2*, *dextral n=2*), *spaw$^{-/-}$,hapln1a$^{\Delta241/\Delta241}$ n=5* (*dorso-ventral n=2*, *dextral n=3*); 48-50hpf: *siblings n=10*, *hapln1a$^{\Delta241/\Delta241}$ n=5*, *spaw$^{-/-}$ n=6* (*sinistral n=2*, *dorso-ventral n=2*, *dextral n=2*), *spaw$^{-/-}$,hapln1a$^{\Delta241/\Delta241}$ n=5* (*sinistral n=1*, *dorso-ventral n=2*, *dextral n=2*); 72-74hpf: *siblings n=10*, *hapln1a$^{\Delta241/\Delta241}$ n=5*, *spaw$^{-/-}$ n=9* (*sinistral n=1*, *dorso-ventral n=7*, *dextral n=1*), *spaw$^{-/-}$,hapln1a$^{\Delta241/\Delta241}$ n=6* (*sinistral n=1*, *dorso-ventral n=4*, *dextral n=1*). For details regarding the statistical analyses used to compare this set of data see *Note#5.11* (pg.213). Only significant comparisons are shown. ***: *p-value*<0.001, **: *p-value*<0.01, *: *p-value*<0.05.

To identify if the whole-chamber ECM dynamics just described characterise the different curvature regions comprising either heart chamber, the atrial and ventricular cardiac jelly meshes of *spaw/hapln1a* double mutant hearts were divided into inner and outer curvature meshes (Fig 4.37A''-C'') and their volumes quantified.

Analysis of the cardiac jelly volume in the atrium curvature regions at 34-36hpf confirms that the reduced ECM volume of *spaw*/*hapln1a* double in the AOC region is driven by the loss of Hapln1a, while the cardiac ECM volume in the AIC is comparable to controls. This result corroborates the requirement for Hapln1a in the early developing heart to establish a heart tube with the correct layer composition (Fig 5.50A-A'').

As the atrium undergoes looping and ballooning, while the ECM dynamics described for the atrium of *spaw*/*hapln1a* double mutants are recapitulated in the ECM dynamics of the AOC (i.e. slow expansion of the cardiac ECM yet slightly faster than that of *hapln1a$^{\Delta241}$* or *spaw* single mutants, Fig 5.50A''), the cardiac jelly of the AIC mimics the behaviour of this same ECM region the sibling's hearts. Subsequently, as the atrium transitions to a maturing stage, rather than reducing the cardiac jelly volume in both atrial curvature regions (i.e. siblings' behaviour), the AOC and AIC cardiac ECM of double mutants follow the slow ECM expansion dynamics of *spaw* single mutants, resulting in comparable and significantly larger cardiac jelly volumes, respectively, and suggesting dysregulation of these dynamics due to loss of L/R patterning in the double mutant hearts.

Analysis of the ventricular curvature-specific cardiac jelly volumes in the *spaw$^{-/-}$*, *hapln1a$^{\Delta241/\Delta241}$* doubles at early stages of development (34-36hpf), similar to the total ventricular ECM volume (Fig 5.49C), shows no defects in the VIC or VOC cardiac ECM volume (Fig 5.50B-B'). As development progresses and the heart undergoes looping, ballooning and early maturing, the cardiac jelly dynamics specific to both curvatures of the ventricle (Fig 5.50B'') follow similar dynamics to those identified in the total ventricular cardiac jelly (i.e. slow reduction of cardiac ECM between 34 and 72hpf, similar to *hapln1a$^{\Delta241}$* and *spaw* single mutants, Fig 5.49C'). As this continued and slow reduction in cardiac jelly volume within this timeframe is opposite to the expansion-reduction dynamics of the cardiac ECM in the ventricular curvatures in sibling's hearts (Fig 5.50B''), *spaw$^{-/-}$*, *hapln1a$^{\Delta241/\Delta241}$* doubles (like *spaw$^{-/-}$*) have a significantly smaller volume of cardiac ECM in both the IC and OC of this chamber.

Together, analysis of the chamber- and region-specific cardiac jelly volumes and dynamics suggests: 1) an early requirement of Hapln1a to establish a heart tube with the correct atrial cardiac jelly composition, 2) as the heart undergoes looping and ballooning (34→ 50hpf), both Hapln1a and Spaw play a crucial role in regulating the ECM expansion in both chambers (and chamber-regions), and 3) as the heart transitions to an early maturing stage, Spaw becomes the predominant gene involved in promoting the reduction of the cardiac ECM in both atrial and ventricular curvature regions.

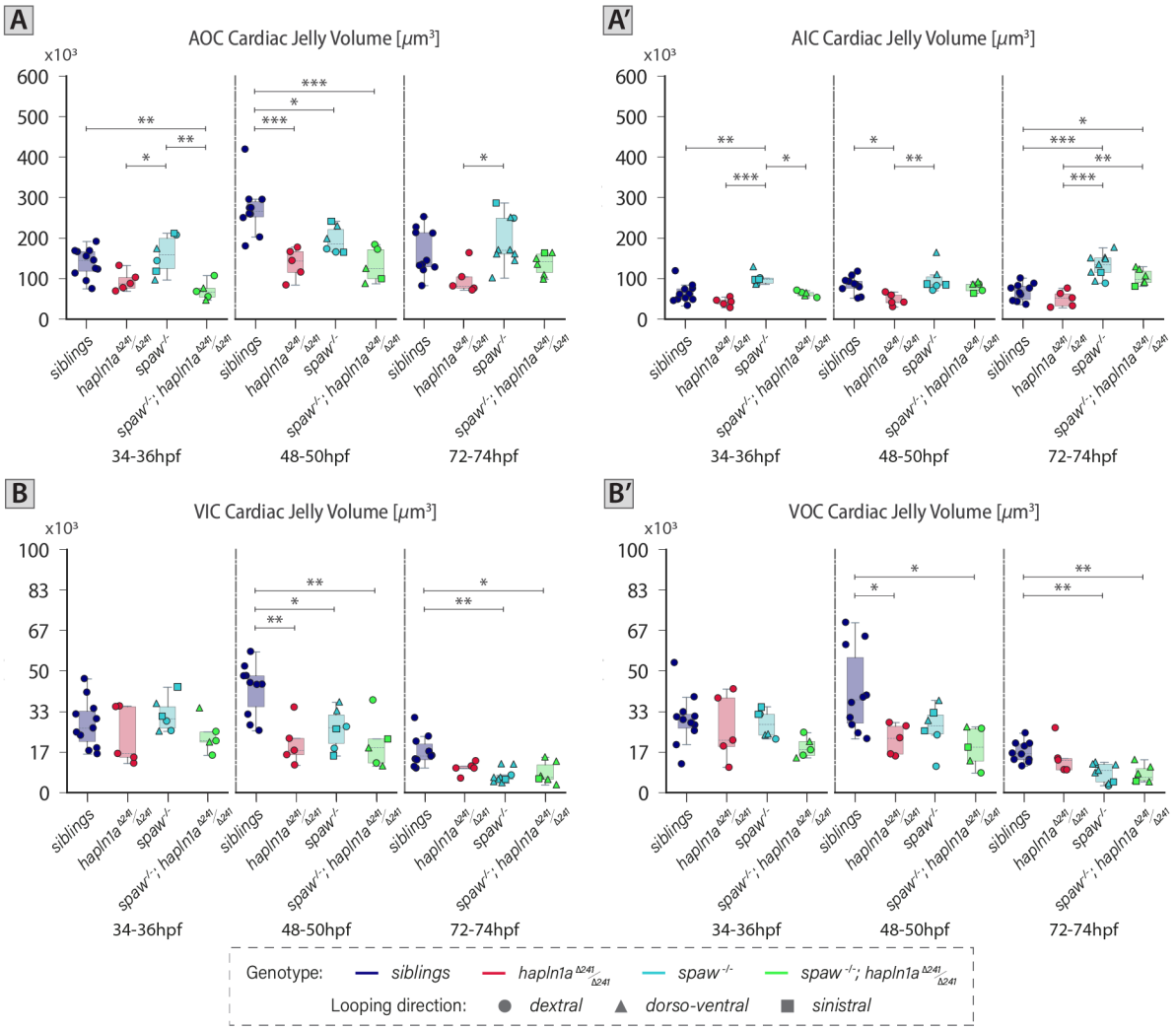

Fig 5.50. Hapln1a and L/R patterning are required to regulate the ECM dynamics in chamber curvature-specific regions throughout heart development. *(Figure continues in the next page)*

A-B''. Quantification of the cardiac jelly comprising the atrium outer curvature (AOC, A), atrium inner curvature (AIC, A'), ventricle inner curvature (VIC, B), ventricle outer curvature (VOC, B') of *spaw/hapln1a* double mutants (light-green), *hapln1a*$^{\Delta241/\Delta241}$ (red), *spaw*$^{-/-}$ (cyan) and siblings (blue) at 34-36hpf, 48-50hpf and 72-74hpf. At 34-36hpf, *spaw/hapln1a* double mutants, similar to *hapln1a*$^{\Delta241/\Delta241}$, have a significantly reduced cardiac jelly volume in both of its atrial curvature regions. As the hearts undergo looping and ballooning, double mutants, similar to single mutants, exhibit reductions in cardiac jelly volumes in the AOC, VIC and VOC when compared to controls. At 72-74hpf, defects in cardiac jelly are identified in the AIC, VIC, and VOC of the *spaw*$^{-/-}$ and *spaw/hapln1a* double mutants. [AOC - 34-36hpf: *hapln1a*$^{\Delta241/\Delta241}$ *vs. spaw*$^{-/-}$ *p-value=0.02766, spaw*$^{-/-}$*,hapln1a*$^{\Delta241/\Delta241}$ *vs. spaw*$^{-/-}$ *p-value=0.00214, spaw*$^{-/-}$*,hapln1a*$^{\Delta241/\Delta241}$ *vs. siblings p-value=0.00784;* 48-50hpf*: hapln1a*$^{\Delta241/\Delta241}$ *vs. siblings p-value=0.00100, spaw*$^{-/-}$*,hapln1a*$^{\Delta241/\Delta241}$ *vs. siblings p-value=0.00100, spaw*$^{-/-}$ *vs. siblings p-value=0.03833;* 72-74hpf*: hapln1a*$^{\Delta241/\Delta241}$ *vs. spaw*$^{-/-}$ *p-value=0.02040.* AIC - 34-36hpf*: hapln1a*$^{\Delta241/\Delta241}$ *vs. spaw*$^{-/-}$ *p-value=0.00100, spaw*$^{-/-}$*,hapln1a*$^{\Delta241/\Delta241}$ *vs. spaw*$^{-/-}$ *p-value=0.01119, spaw*$^{-/-}$ *vs. siblings p-value=0.00344;* 48-50hpf*: hapln1a*$^{\Delta241/\Delta241}$ *vs. spaw*$^{-/-}$ *p-value=0.00486, hapln1a*$^{\Delta241/\Delta241}$ *vs. siblings p-value=0.03247;* 72-74hpf*: hapln1a*$^{\Delta241/\Delta241}$ *vs. spaw*$^{-/-}$*,hapln1a*$^{\Delta241/\Delta241}$ *p-value=0.00507, hapln1a*$^{\Delta241/\Delta241}$ *vs. spaw*$^{-/-}$ *p-value=0.00100, spaw*$^{-/-}$*,hapln1a*$^{\Delta241/\Delta241}$ *vs. siblings p-value=0.03033, spaw*$^{-/-}$ *vs. siblings p-value=0.00100.* VIC - 48-50hpf*: hapln1a*$^{\Delta241/\Delta241}$ *vs. siblings p-value=0.00267, spaw*$^{-/-}$*,hapln1a*$^{\Delta241/\Delta241}$ *vs. siblings p-value=0.00270, spaw*$^{-/-}$ *vs. siblings p-value=0.02183;* 72-74hpf*: spaw*$^{-/-}$*,hapln1a*$^{\Delta241/\Delta241}$ *vs. siblings p-value=0.02665, spaw*$^{-/-}$ *vs. siblings p-value=0.00157.* VOC - 48-50hpf*: hapln1a*$^{\Delta241/\Delta241}$ *vs. siblings p-value=0.04414, spaw*$^{-/-}$*,hapln1a*$^{\Delta241/\Delta241}$ *vs. siblings p-value=0.01584;* 72-74hpf*: spaw*$^{-/-}$*,hapln1a*$^{\Delta241/\Delta241}$ *vs. siblings p-value=0.00418, spaw*$^{-/-}$ *vs. siblings p-value=0.00301*]. A'' and B'' are point-plots of the data presented in A-A', and B-B', respectively. A-B'': Error bars with 95% confidence interval of the mean. 34-36hpf: *siblings n=11, hapln1a*$^{\Delta241/\Delta241}$ *n=5, spaw*$^{-/-}$ *n=6* (*sinistral n=2, dorso-ventral n=2, dextral n=2*), *spaw*$^{-/-}$*,hapln1a*$^{\Delta241/\Delta241}$ *n=5* (*dorso-ventral n=2, dextral n=3*); 48-50hpf: *siblings n=10, hapln1a*$^{\Delta241/\Delta241}$ *n=5, spaw*$^{-/-}$ *n=6* (*sinistral n=2, dorso-ventral n=2, dextral n=2*), *spaw*$^{-/-}$*,hapln1a*$^{\Delta241/\Delta241}$ *n=5* (*sinistral n=1, dorso-ventral n=2, dextral n=2*); 72-

74hpf: *siblings n=10*, *hapln1a*$^{\Delta 241/\Delta 241}$ *n=5*, *spaw*$^{-/-}$ *n=9* (*sinistral n=1*, *dorso-ventral n=7*, *dextral n=1*), *spaw*$^{-/-}$ *,hapln1a*$^{\Delta 241/\Delta 241}$ *n=6* (*sinistral n=1*, *dorso-ventral n=4*, *dextral n=1*). For details regarding the statistical analyses used to compare this set of data see *Note#5.11* (pg.213). Only significant comparisons are shown. ***: *p-value*<0.001, **: *p-value*<0.01, *: *p-value*<0.05.

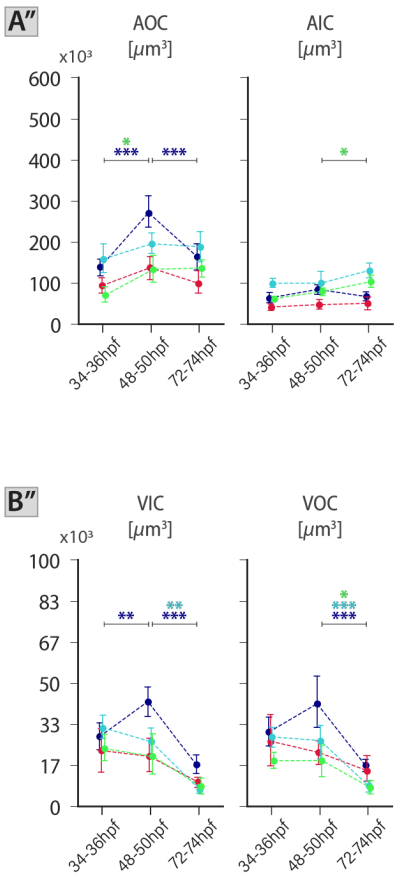

Having quantified the cardiac jelly volume in each of the chamber's curvature regions and its dynamics throughout early heart development, to deepen our understanding about the extent of the asymmetries within individual chambers the ratio between the cardiac jelly volume comprising the outer and inner curvatures (OC-to-IC) was calculated (Fig 5.51A-B').

OC-to-IC ratios per chamber confirm that despite the loss of Hapln1a and the L/R patterning defect, *spaw*$^{-/-}$, *hapln1a*$^{\Delta 241/\Delta 241}$ doubles, like siblings, throughout the analysed stages have an atrial ECM-asymmetry and ventricular ECM-symmetry, (Fig 5.51 atrium: A-A', AOC-to-AIC >1.0, ventricle: B-B', VOC-to-VIC ≈1.0)

Despite this preserved atrial ECM asymmetry, an initial comparison of the atrial OC-to-IC ratio between the siblings and the single mutants (Fig 5.51B-B') identifies that throughout the analysed stages, the atrial ECM asymmetry of the *spaw*$^{-/-}$ is more impaired (i.e. asymmetry more reduced) than that of the *hapln1a*$^{\Delta 241/\Delta 241}$ when compared to controls. This enhanced reduction of ECM asymmetry in the *spaw*$^{-/-}$ (yet maintaining a ratio > 1.0), combined with the reduced ECM asymmetry of the *hapln1a*$^{\Delta 241}$ mutants, generates double mutants in which disruption of both genes results in an ECM-asymmetry with even lower OC-to-IC values. Together, these data suggest that both Hapln1a and Spaw, are required during early heart development to create and sustain the atrial-OC ECM-asymmetry characteristic of the wild-type developing heart.

To complement this ECM volume analysis and visualise the remaining asymmetries in the cardiac jelly of *spaw*/*hapln1a* double mutant hearts, 2D tissue thickness heatmaps of the cardiac ECM of the double mutants were acquired and analysed at the same stages of development (Fig 5.51A-B: 34-36hpf, C-D: 48-50hpf, and E-F: 72-74hpf). Closer analysis of the 2D cardiac jelly thickness heatmaps identifies that similar to *spaw*$^{-/-}$ hearts, **regardless of the direction of looping, *spaw*/*hapln1a* double mutants have thicker ECM regions in the OC of the atrium** (i.e. AOC). The significantly reduced ECM volume characteristic of the double mutants at early stages of development driven by the loss of Hapln1a (Fig 5.49A, 5.50A) can be identified by the reduced ECM thickness values present in the cardiac jelly thickness heatmaps of these hearts (Fig 5.52Aii-iii) when compared to siblings. Likewise, the heightened expansion of the atrial ECM (Fig 5.50A) and reduction of the ventricular ECM (Fig 5.50B) that characterise the double and *spaw* single mutants, can be readily recognised in the *spaw*/*hapln1a* double mutant heatmaps at 72-74hpf, with increased red-orange areas in the atrium and darker blue colours in the ventricle, further supporting the hypothesis that Spaw's L/R patterning is required in the maturing heart to support tightly controlled ECM reduction in both chambers.

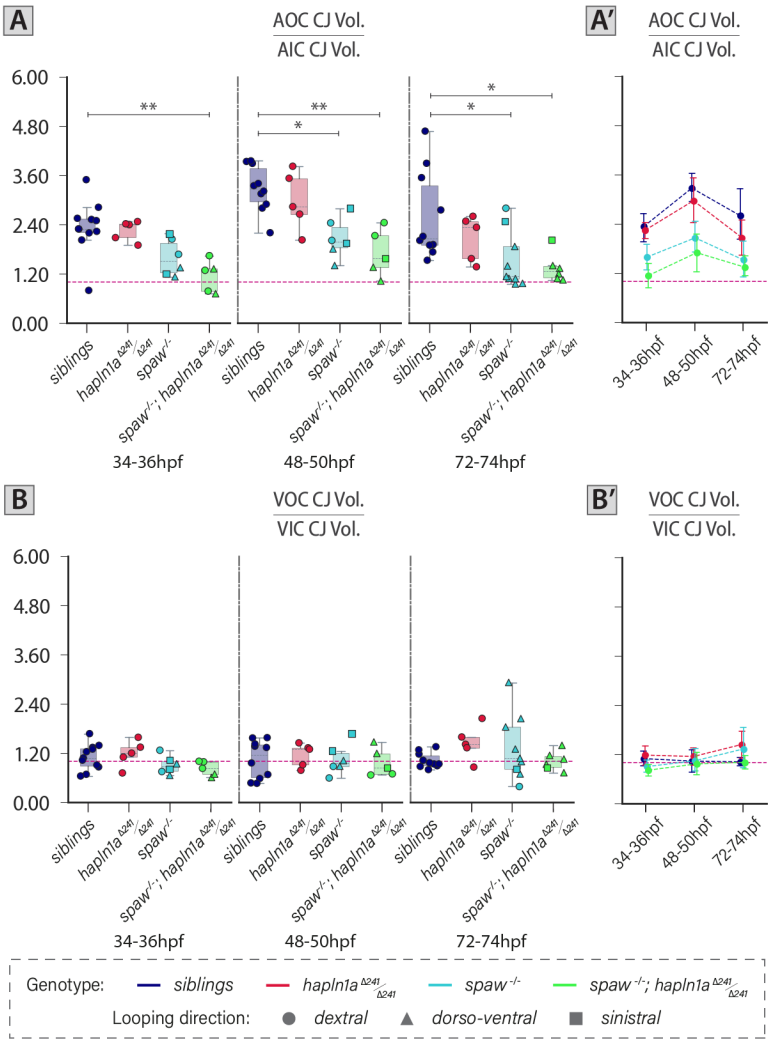

Fig 5.51. Disruption of *hapln1a* and *spaw* significantly affects atrial ECM-asymmetry of zebrafish developing hearts.

A-B'. Quantification of the cardiac jelly AOC-to-AIC (A-A') and VOC-to-VIC (B-B') volumes ratio in the heart of *spaw/hapln1a* double mutants (light-green), *hapln1a*$^{\Delta 241/\Delta 241}$ (red), *spaw*$^{-/-}$ (cyan) and siblings (blue) at 34-36hpf, 48-50hpf and 72-74hpf. [AOC/AIC - 34-36hpf: *spaw*$^{-/-}$,*hapln1a*$^{\Delta 241/\Delta 241}$ *vs. siblings p-value=0.00598;* 48-50hpf: *spaw*$^{-/-}$ *vs. siblings p-value=0.01641, spaw*$^{-/-}$,*hapln1a*$^{\Delta 241/\Delta 241}$ *vs. siblings p-value=0.00544;* 72-74hpf: *spaw*$^{-/-}$ *vs. siblings p-value=0.04857, spaw*$^{-/-}$,*hapln1a*$^{\Delta 241/\Delta 241}$ *vs. siblings p-value=0.04666*]. A' and B' are point-plots of the data presented in A, and B, respectively. A-B': Error bars with 95% confidence interval of the mean. 34-36hpf: *siblings n=11, hapln1a*$^{\Delta 241/\Delta 241}$ *n=5, spaw*$^{-/-}$ *n=6* (*sinistral n=2, dorso-ventral n=2, dextral n=2*), *spaw*$^{-/-}$,*hapln1a*$^{\Delta 241/\Delta 241}$ *n=5* (*dorso-ventral n=2, dextral n=3*); 48-50hpf: *siblings n=10, hapln1a*$^{\Delta 241/\Delta 241}$ *n=5, spaw*$^{-/-}$ *n=6* (*sinistral n=2, dorso-ventral n=2, dextral n=2*), *spaw*$^{-/-}$,*hapln1a*$^{\Delta 241/\Delta 241}$ *n=5* (*sinistral n=1, dorso-ventral n=2, dextral n=2*); 72-74hpf: *siblings n=10, hapln1a*$^{\Delta 241/\Delta 241}$ *n=5, spaw*$^{-/-}$ *n=9* (*sinistral n=1, dorso-ventral n=7, dextral n=1*), *spaw*$^{-/-}$,*hapln1a*$^{\Delta 241/\Delta 241}$ *n=6* (*sinistral n=1, dorso-ventral n=4, dextral n=1*). For details regarding the statistical analyses used to compare this set of data see *Note#5.11* (pg.213). Only significant comparisons are shown. **: *p-value*<0.01, *: *p-value*<0.05.

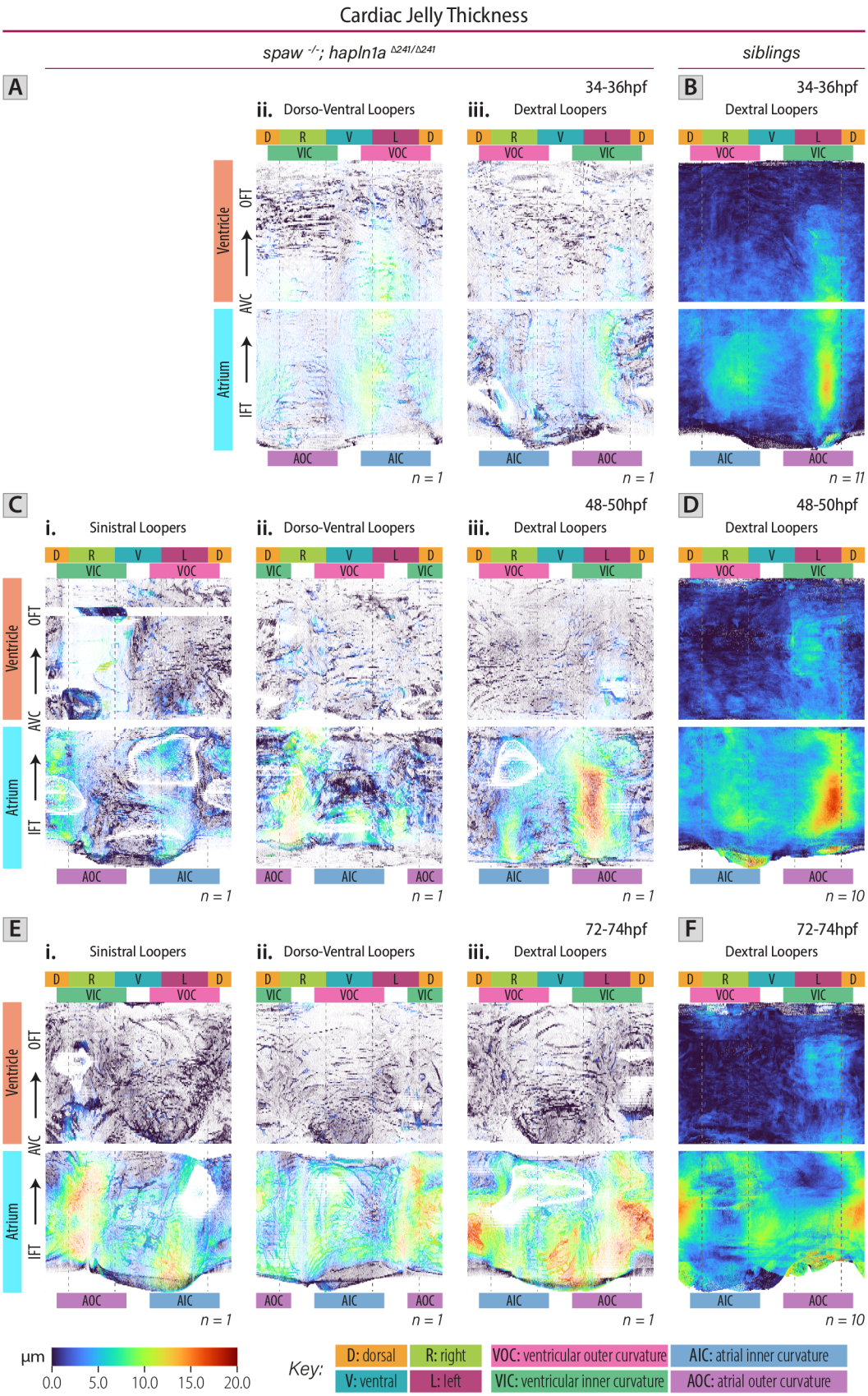

Fig 5.52. Despite the reduced ECM-asymmetry, ECM regionalisation in the early *spaw/hapln1a* double mutant hearts is maintained and, similar to *spaw*$^{-/-}$, mispositioned.

A-F. 2D representations of the cardiac jelly thickness heatmap of *spaw*$^{-/-}$, *hapln1a*$^{\Delta 241/\Delta 241}$ (A,C,E) and sibling (B, D, F) hearts at 34-36hpf (A-B), 48-50hpf (C-D) and 72-74hpf (E-F). *spaw/hapln1a* homozygous mutants are classified according to their direction of looping as: sinistral (i), dorso-ventral (ii) and dextral (iii) loopers. While A, C and E show examples of planar projection plots of individual embryos, B, D and F show the average planar

projections of all the processed siblings at all the indicated stages. A-F share colour-scale presented with the key at the bottom-left of the figure. D: Dorsal, R: Right, V: Ventral, L: Left, VOC: Ventricular Outer Curvature, VIC: Ventricular Inner Curvature, AOC: Atrial Outer Curvature, AIC: Atrial Inner Curvature, IFT: Inflow-tract, AVC: Atrioventricular Canal, OFT: Outflow-tract.

_____

5 Chapter Conclusions

- The ECM cross-linking protein Hapln1a is secreted asymmetrically into the cardiac jelly of the developing zebrafish heart at disc and tube stages.
- Hapln1a prevents cardiac jelly degradation during cardiac looping and ballooning, promoting regionalised atrial ECM expansion and growth.
- The regionalised deposition of Hapln1a in the heart aids the maintenance of the ECM asymmetry in wild-type hearts; however, it is not the only component involved in its establishment.
- Hapln1a has a 'limited lifespan' effect based on the stages in which the protein is present within the cardiac ECM.
- L/R-patterning events driven by *spaw* have a longer-lasting role in ensuring that early heart patterning perdures during the early stages of cardiac morphogenesis.

6 Chapter Discussion

6.1 Hapln1a is required for atrial growth during zebrafish looping morphogenesis

hapln1a encodes an extracellular protein that mediates the interaction between hyaluronic acid and other proteoglycans in the ECM (Fig 5.1A). mRNA ISH analysis revealed that *hapln1a is* regionally expressed through the early stages of heart development, mainly when the heart disc transitions into a tube. At these stages, *hapln1a* expression is preferentially localised in the posterior region of the heart disc (Fig 5.2E) and is maintained as the heart undergoes tube formation, repositioning its expression primarily to the atrial-left side of the tube (Fig 5.2G) and notably in a similar domain to where the expanded ECM was observed (Derrick *et al.*, 2021) (Fig 4.14F, 4.15A''). Analysis of Hapln1a localisation confirms the protein is secreted asymmetrically at disc and tube stages (Fig 5.3A-H). Despite the absence of *hapln1a* mRNA expression in the heart chambers at 50hpf (Fig 5.2M), Hapln1a protein is still present in the chamber ECM, particularly in the atrium (Fig 5.3I-O), suggesting that the ECM environment that is established at early stages of heart development is maintained as the heart undergoes looping, and its maintenance is important for promoting later processes of heart morphogenesis.

Despite its significance in stabilising the ECM, the role of Hapln1a in specific developmental processes has not been explored. Hapln1 (previously known as Cartilage Link Protein 1, Crtl1) has been recognised for its role in cartilage formation in pigs and zebrafish, where it links aggregates of aggrecan and hyaluronan, providing the cartilage with strength and elasticity (Hardingham, 1979; Kang *et al.*, 2008). Additionally, a recently published study in human foetal neocortex tissue culture identified that HAPLN1 combined with lumican and collagen I, upregulate the expression, deposition and cross-linking of HA establishing a permissive stiffer environment that induces the formation of the cortical folds in the developing brain (Long *et al.*, 2018). Other studies demonstrated an upregulation of *hapln1a* during zebrafish fin regeneration suggesting an important role for this protein during skeletal growth and patterning (Govindan and Iovine, 2015). Furthermore, *Hapln1* expression in the developing mouse heart was described by Wirrig *et al.* (2007) at early stages of cardiac development, where it was identified to be co-expressed with HA and Versican in the endothelial lining of the heart, in addition to regions of the

atrioventricular junction and the outflow tract. At later stages, this co-expression becomes restricted to small populations of mesenchymal cells derived from the endocardium (Wirrig *et al.*, 2007). Importantly, the same study showed that knockdown of this gene in mice resulted in a broad spectrum of cardiac malformations, including atrioventricular septal and myocardial defects (Wirrig *et al.*, 2007), pointing to an important role for Hapln1 in heart development.

To investigate the role of *hapln1a* in zebrafish heart morphogenesis and ECM modulation, I generated *hapln1a* promoter mutants by removing the sequence upstream of the gene containing the promoter and translation-initiating ATG using CRISPR-Cas9 genome editing (Fig 5.5) and recovered two promoter alleles that lack *hapln1a* transcript (Fig 5.6), validating the use of the promoter mutant as a loss of function model (Derrick *et al.*, 2021).

Having established stable promoter mutant lines at F2, to assess if *hapln1a* is required for heart development, analysis of heart morphology of *hapln1a* mutants and wild-type siblings at early-, during- and post-looping stages was performed. Quantification of total heart size revealed a failure of *hapln1a*$^{\Delta 241}$ promoter mutant hearts to exhibit the growth-compaction dynamics shown by wild-type hearts (Fig 5.13A-A'). Further analysis of chamber-specific size and myocardial ballooning heatmaps recognised that these defects were mainly driven by an atrial growth defect during looping and ballooning morphogenesis (34→50hpf, Fig 5.13B, 5.16B-B'), confirming the defects recognised by the ISH analysis (Fig 5.10C-D',F,G) and suggesting a specific role for Hapln1a in atrial expansion and chamber ballooning in the developing heart. Unfortunately, as the interest of the study describing Hapln1-deficient mice was to gain insights regarding the role of Hapln1 in the formation of the atrioventricular junction, the cardiac phenotype of Hapln1-deficient mice was studied only at post-looping stages (E≥13.0) (Wirrig *et al.*, 2007), thus making it impossible to confirm if atrial growth defects during looping morphogenesis are also characteristic of other Hapln1(a) mutants.

Reduced atrial size in *hapln1a*$^{\Delta 241}$ mutants at 48-50hpf, could be explained by two mechanisms: reduced cell size, reduced cell number, or an additive effect of the two. To investigate this further and characterise the rearrangement dynamics of *hapln1a*$^{\Delta 241}$ mutant hearts, cell counts and IND analysis were performed in the homozygous mutants and their wild-type siblings at 50 and 72hpf. Resulting quantifications identified no defects in the cell number comprising either of mutant chambers nor in their IND per region (Fig 5.19-20) at any of the two analysed stages, suggesting Hapln1a loss does not affect cell ingression to the developing heart nor cell rearrangement within its myocardium, yet failing to provide support to any of the proposed underlying mechanisms resulting in a small atrial size at 48-50hpf.

Interestingly, individual analysis of the IND dynamics within the different chamber regions between timepoints for both genotype groups acknowledged differences in atrial cellular rearrangements between the *hapln1a*$^{\Delta 241}$ mutants and the controls as they transition to an early maturing stage. While wild-type atrial cardiomyocytes shrink in size across the dorso-ventral axis and inner-curvature of the chamber, atrial cardiomyocytes in *hapln1a*$^{\Delta 241}$ promoter mutants become smaller in the ventral face and unexpectedly in the outer-curvature face of this chamber. This altered atrial-cell dynamics suggest that even though the atrial size of the mutants does not change between 50 and 72hpf (Fig 5.13B-B'), different cellular rearrangements are still required within the *hapln1a*$^{\Delta 241}$ promoter mutant chamber to support its maturing and continued development (Fig 5.20C).

The cardiac jelly is a hydrated structure in which multiple components interact in a network, and their structure can therefore be greatly affected by the environment and conditions in which it is being studied. Following this line of thought, a plausible explanation as to why the methodology used in this experiment might not have been suitable to identify the mechanism behind atrial growth failure could be associated with the differences in cardiac jelly compositions between the *hapln1a*$^{\Delta 241}$ mutants and the wild-type siblings combined to the fixation and processing required for the immunohistochemistry. As mentioned, Hapln1a is a cross-linking protein that mediates the interaction between HA and proteoglycans in the ECM

(Spicer, Joo and Bowling, 2003; Kang *et al.*, 2008; Attili and Richter, 2013), which in turn provides structure to the tissues (Barry, 1948; Nakamura and Manasek, 1978, 1981; Camenisch *et al.*, 2000). Less ECM volume and less cross-linking in the atrial cardiac ECM of *hapln1a*$^{\Delta 241}$ mutants could signify that the turgor pressure and tissue stabilisation abilities of the cardiac jelly are not as high as in the wild-type hearts. Hence any fixation and processing induce even more morphological variations in the atrial morphology of the mutants, which result in quantifications of these parameters that are not reflective of the real live tissue organisation.

To address this question and remove the possible side-effects sample processing may have upon chamber morphology and tissue organisation, analysis of ***live*** images from *hapln1a*$^{\Delta 241}$ homozygous mutant and wild-type embryos with arrested hearts is proposed. Suitable transgenes to label the cell membranes or nuclei of all cardiomyocytes should be carefully considered so that all cells can be counted, their size quantified, and distribution within the tissue characterised.

Cross-linking proteins, like Hapln1a, are known to stabilise the bond between PG and HA in the ECM (Kohda *et al.*, 1996; Lockhart *et al.*, 2011a; Attili and Richter, 2013). Although PG and HA proteins can interact and form complexes in the absence of link proteins, *in vitro* studies have shown that addition of cross-linking proteins to matrices containing PG and HA, increases its stability and density, allowing it to sustain more load (i.e. increased compressible resistance) whilst maintaining an elastic structure (Matsumoto *et al.*, 2003; Attili and Richter, 2013). In addition, a stable matrix advocates the possibility of forming a more elaborate network of multiple HA-PG complexes into which GAG chains can sequester water, forming a hydrated and expanded cardiac jelly that facilitates cellular proliferation, motility and signal transduction (Nakamura and Manasek, 1978; Toole, 1990, 2001).

6.2 Regionalised deposition of Hapln1a at disc and tube stages stabilises the cardiac ECM preventing the premature degradation of its components

In addition to the atrial growth defects, analysis of cardiac jelly volume in the *hapln1a*$^{\Delta 241}$ mutants through time identified altered ECM-expansion dynamics during looping and ballooning morphogenesis, which resulted not only in a significantly reduced cardiac ECM volume present in the whole heart of *hapln1a*$^{\Delta 241/\Delta 241}$ at 48-50hpf (Fig 5.22A) but also in each of its chambers (Fig 5.22B-C). This failure to increase the cardiac jelly volume agrees with the ECM modification abilities of cross-linking proteins previously described, suggesting Hapln1a cross-linking is required to stabilise the expanding cardiac ECM as the heart undergoes looping and ballooning morphogenesis.

Moreover, despite the transient mRNA expression of *hapln1a* (Fig 5.2), Hapln1a protein is preserved in the cardiac jelly in regions where the ECM is expanded (i.e. AOC) and at stages where the expression of regionalised hyaluronidases is upregulated (50hpf, Fig 4.19). These results demonstrate that Hapln1a's role in stabilising the ECM is still required by this stage and might be important to prevent HA modifications or degradation in precise regions of the heart, supporting ECM asymmetry and ongoing cardiac development. Building upon this protective role, studies in Hapln1 mutant mice identified reduced levels of Versican at E13.0 (Wirrig *et al.*, 2007), while analysis of *hapln1a* KOs in adult zebrafish reveals the presence of less HA in the regenerative cardiac muscle (Sun *et al.*, 2022), together suggesting that Hapln1(a) cross-linking stabilises the ECM and promotes its expansion by protecting HA and the proteoglycan aggregate components from degradation. To further confirm this protective and stabilising role for HA and other PG, the organisation of the ECM within the atrial cardiac jelly of *hapln1a*$^{\Delta 241}$ mutants could be assessed by scanning electron microscopy (SEM) (Fransen and Lemanski, 1991). In addition, quantification of fluorescent intensity and formation of aggregates in confocal microscopy images using fluorescent dyes (Toole, Yu and Underhill, 2001) (or antibodies) to label HA and/or the PGs of interest could provide insights about differences in ECM organisation and composition in the presence/absence of Hapln1a.

mRNA *in situ* hybridisation analysis of interstitial ECM components identified that aside from *hapln1a*, *has2*, *chsy1*, *hapln1b*, *vcana* and *hyal2a* are proteins that are likely involved in cardiac ECM volume regulation as the heart undergoes early morphogenesis (Fig 4.16-19). Interestingly, the fact that the expression pattern of all of these components is transient and, in some cases, regionalised (i.e. *has2*-Fig 4.16, *hapln1a*-Fig 5.2E-H, *hapln1b*-Fig 5.4E-J) during early heart development, suggests it is at very early stages (disc and tube stage) where the precise asymmetric ECM environment is established to support continued morphogenesis of this organ.

Supporting this hypothesis, similar to the transient expression of *hapln1a*, *has2* left-sided expression is identified in the early heart disc (Fig 4.16A) (Chen *et al.*, 1997; Smith *et al.*, 2008; Lenhart *et al.*, 2013; Veerkamp *et al.*, 2013) and the endothelial lining of the heart tube (Fig 4.16B) before its expression becomes restricted to the developing AVC. Despite this transient expression, the HA that is deposited in the nascent cardiac ECM is maintained in the cardiac jelly of zebrafish embryos at 72 and 120hpf (Grassini *et al.*, 2018; Gunawan *et al.*, 2020), thus confirming that the cardiac ECM that accompanies the early processes of cardiac morphogenesis is set up very early on, and its composition and organisation is unique to assist in the asymmetric process of heart development.

Supporting an early requirement for Hapln1a, analysis of multiple morphometric parameters in *spaw*/*hapln1a* double mutants, recognised that most of the identified early looping defects (i.e. 34-36hpf) and looping and ballooning morphogenesis dynamics are driven by the loss of Hapln1a rather than by the disruption of L/R patterning. Further analysis of the double mutants identified that none of the defective dynamics nor parameters identified between 50 and 72hpf and at 72-74hpf (not even those related to the cardiac jelly), were linked to the *hapln1a* mutation. These results are in line with the current hypothesis, proposing not only an early role for Hapln1a in heart development, but a role for Hapln1a during the time window in which the protein is present in the heart (i.e. from disc stage ~ 19-21hpf until after 50hpf).

Although mRNA expression analysis of PGs throughout early stages of development suggests multiple roles for these ECM components in heart development, so far, the only PG identified as a possible interacting partner of Hapln1a, due to its comparable expression dynamics in conjunction with *has2*, is *versicana* (see expression dynamics between disc and tube stages of *vcana*, *has2*, and *hapln1a* in Figs 4.17K-L, 4.16A-B and 5.2E-H, respectively). Similar to zebrafish, in mouse embryos, *Has2* and *Versican* are expressed in comparable domains at E9.5 (Camenisch *et al.*, 2000). Furthermore, targeted deletion of hyaluronan synthase 2 in mice resulted in cardiac defects closely resembling those of the *hdf* mouse mutant, in which Versican expression is disrupted by a transgene insertion (Yamamura *et al.*, 1997; Mjaatvedt *et al.*, 1998). Moreover, in addition to medaka mutants with a recessive point mutation in the versican 3'UTR, *Versican* and *Has2* mutant mice exhibit multiple heart defects along with an absent or uniformly thin cardiac jelly (Yamamura *et al.*, 1997; Mjaatvedt *et al.*, 1998; Mittal *et al.*, 2019). These results, combined with the reduction in Versican protein identified in Hapln1 mice mutants (Wirrig *et al.*, 2007), and the HA-reduction recognised in *hapln1a* zebrafish mutants (Sun *et al.*, 2022), suggest a conserved functional role of these three ECM binding partners in heart development in mice, medaka and zebrafish, and imply that *vcana* is the main PG interacting with Hapln1a in the zebrafish heart. Nevertheless, as the expression patterns of all known proteoglycans have not been analysed (e.g. Neurocan, Perlecan and Agrin), the presence of other PG in the developing zebrafish heart and hence other possible interacting partners of Hapln1a cannot be discarded.

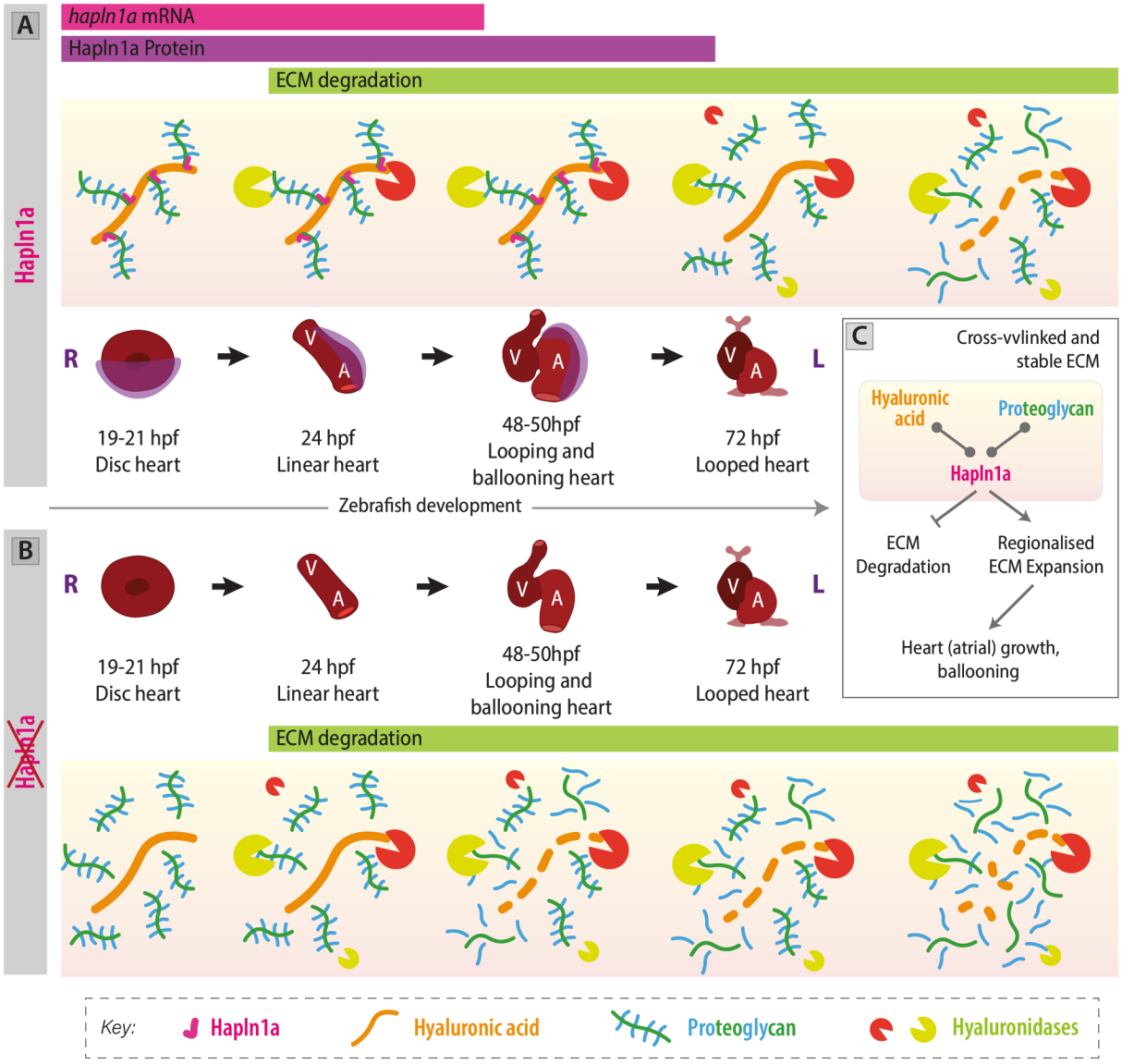

Fig 5.53. Hapln1a cross-linking prevents early ECM degradation promoting atrial growth and ballooning during heart morphogenesis.
A-B. Schematics depicting Hapln1a's role in stabilising the cardiac ECM at early stages of heart development in a wild-type (A) and a *hapln1a* mutant scenario (B) (see text for details). Hapln1a protein localisation is highlighted in the wild-type hearts in purple. **C.** Summary diagram illustrating the mechanism proposed. L: Left, R: Right, A: Atrium, V: Ventricle.

Taking together all that has been discussed, I propose that regionalised deposition of Hapln1a during early stages of heart development, prior to tube morphogenesis (i.e. 19-21hpf), stabilises the cardiac ECM as the heart develops, preventing the premature degradation of its components (i.e. HA and PGs). This permits regionalised ECM expansion to occur at the regions where Hapln1a is positioned: initially in the atrial left-side of the heart tube and subsequently in the outer- and inner-curvature of the atrium, driving atrial growth and chamber ballooning while ensuring robust cardiac morphogenesis (Fig 5.53). This proposed model supports a role for Hapln1a cross-linking protein in regionally regulating cardiac ECM size to promote normal cardiac morphogenesis.

In addition to highlighting the importance of Hapln1a in early heart morphogenesis, analysis of the *spaw/hapln1a* double mutants identified a requirement for Spaw's L/R patterning in regulating processes such as ventricular size maintenance (Fig 5.42C-C', 5.43C-C'), and cardiac jelly degradation dynamics in

both chambers and curvature regions (Fig 5.49B-C, 5.50) as the heart transitions to a maturing state (50→72hpf).

Captivatingly, between 34 and 50hpf, examination of different **atrial** parameters identified that the dynamics of the *spaw*/*hapln1a* double mutants resembled more the dynamics of the controls (siblings) than that of any of the single mutants (see the atrial dynamics for myocardium, endocardium and cardiac jelly in Fig 5.46A', 5.47A', 5.49B', 5.50A-A'). For instance, the expansion exhibited by the atrium of the double mutants during looping and ballooning morphogenesis (34→50hpf, Fig 5.42B') followed the dynamics of growth identified in the group of siblings, while individually, *hapln1a*$^{\Delta 241}$ and *spaw* single mutants displayed reduced growth. As disruption of both genes results in altered (i.e. reduced) dynamics of growth, the 'recovery' identified in the doubles is curious and suggests some interaction might be happening downstream of the regulatory processes that *spaw* and *hapln1a* individually regulate, setting up a novel and uncharacterised scenario that 'recovers' the defect, permitting atrial expansion. If Hapln1a's role is to stabilise the ECM and avoid its early degradation, and *spaw* is involved, for instance, in regulating the regionalised deposition of ECM proteolytic components (e.g. hyaluronidases) one could speculate that once the heart has undergone looping and ballooning (50hpf), in a scenario where both genes are lost, dysregulation of the regionalised expression of the proteolytic components in regions of the heart where normally Hapln1a would be positioned to protect the ECM means the heart no longer requires Hapln1a's protective role, resulting in a permissive environment for chamber growth. This hypothetical scenario proposes Nodal signalling is involved in regulating the expression of different ECM components of the cardiac ECM during heart development, which is corroborated by studies in Nodal-deficient mice downregulate genes encoding the deposition of ECM components, receptors and modifiers (Desgrange *et al.*, 2020).

Contrary to what I had hypothesised and despite the defects in ECM expansion, the left-sided atrial ECM asymmetry characteristic of wild-type hearts is preserved in *hapln1a*$^{\Delta 241}$ promoter mutants, however, with a reduced magnitude (Fig 5.24, 5.25). The reduction yet maintenance of the atrial ECM asymmetry suggests Hapln1a facilitates the strengthening of this asymmetry in wild-type hearts, but it is not the only component involved in its establishment. In line with this, the other possible component whose expression pattern is regionalised, recapitulating the ECM expansion, and that could be involved in stabilising the ECM-asymmetry when Hapln1a is lost, is Hapln1b. Characterisation of cardiac jelly distribution in *hapln1a*$^{\Delta 241}$ mutants using average 2D heatmap plots confirmed that despite residual regionalisation, the cardiac ECM of *hapln1a* mutants is particularly reduced in the inner and outer curvatures of the atrium.

Hapln1a and Hapln1b are comprised of the same functional domains (Sun *et al.*, 2022), yet time-course expression analysis suggests each paralog is expressed by a different cardiac tissue (myocardium: *hapln1a*, endocardium: *hapln1b*), and their expression patterns are complementary (Fig 5.2 and 5.4). Interestingly, different to *hapln1a,* cardiac-specific expression of *hapln1b* is not transient, starting from the early heart cone and maintained until after 72hpf, suggesting both paralogs have differential *in vivo* roles and interacting partners. Double KO of *hapln1a* and *hapln1b* would be invaluable to confirm if *hapln1b* is indeed the ECM component that in conjunction with *hapln1a*, stabilises the cardiac jelly and promotes the ECM asymmetries throughout zebrafish development.

Nevertheless, establishing an ECM environment that is complex at early stages of development, and together with the additional asymmetries identified in *hapln1b* and hyaluronidase expression this still supports the hypothesis that regionalised ECM asymmetry could still be the driving factor for tissue intrinsic looping morphogenesis. Analysis of this hypothesis will be discussed in the next chapter with more detail.

6.3 Additional remarks

6.3.1 Loss-of-Function Model

As mentioned, recent studies have found that upregulation of mutant gene-related compensatory genes is a transcriptional adaptation strategy triggered when high levels of mutant mRNA decay is detected within the cell (El-Brolosy *et al.*, 2019), and this compensation can complicate the analysis of specific gene function. Therefore, the strategy I used to generate *hapln1a* loss-of-function model was to remove the promoter region of *hapln1a* thus preventing its transcription and avoiding mutants with an absence of phenotype caused by genetic compensation. Surprisingly, despite the fact that in both *hapln1a* mutant alleles the annotated promoter was excised and *hapln1a* expression throughout the embryo was lost at 26hpf, analysis of their morphometric parameters at 48-50hpf show different phenotypes, with the phenotype of the *hapln1a*$^{\Delta 241}$ being more profound than that of the *hapln1a*$^{\Delta 187}$.

Different hypotheses could explain these phenotype differences. 1) Excision of different portions of *hapln1a* gene could be disrupting the regulatory regions of other genes in the embryo, which, if involved in heart development, could produce dissimilar heart phenotypes in each allele. 2) Differences in excision regions of the promoter could be dysregulating the expression of *hapln1b* in a different way in either allele. Although *hapln1b* expression was evaluated in both alleles at 26hpf, considering that *hapln1a* expression starts very early in heart development (Fig 5.2C-D), analysis of *hapln1b* expression at earlier stages (e.g. disc stage) could have identified if there was an upregulation of *hapln1b* as a consequence of *hapln1a* loss. If this was the case, defects in the mutants could have recovered by 26hpf, accounting for the variations in phenotype between the promoter mutants. 3) Although both promoter alleles were recovered from the same batch of injected embryos (F0 generation), the outcrosses performed to generate the stable generations (F1 and F2) could have introduced different genetic backgrounds into each of the lines, which could be producing different phenotypes (El-Brolosy and Stainier, 2017).

To test any of these hypotheses, transcriptomic analysis of both alleles at the first stage in which *hapln1a* is highly expressed (e.g. 21hpf) could be carried out looking for differential up/down regulation of gene expression, which could account for the variation in phenotype between the *hapln1a* alleles.

6.3.2 Mis-Expression Model

Whilst I generated a novel transgenic line to stably misexpress *hapln1a* in zebrafish and investigate the role of regional-specific expression of this gene and deposition of its corresponding protein, I was unable to perform this analysis. However, the development of this tool has the potential to study the regionalised expression of this gene and how its misexpression might affect cardiac morphogenesis. Development of region-specific Gal4 lines in conjunction with the *UAS:hapln1a* would provide a powerful method to investigate the role of regionalised ECM expansion in a spatially-controlled manner.

Further work will need to be performed to try and understand the cause of the phenotype identified in the embryos carrying either the *UAS:hapln1a, cryaa:CFP* or *myl7:Gal4* constructs.

Finally, to confirm that *hapln1a* expression needs to be regionalised in the atrium to promote looping and ballooning morphogenesis, other regional specific drivers could be used in conjunction with a verified version of the *UAS:hapln1a, cryaa:CFP* line, to stably misexpress *hapln1a* in different domains of the chamber and examine the effect of altering the axis of regionalisation of the ECM within the chamber.

Chapter 6. General Discussion

1 MAJOR CONTRIBUTIONS OF THIS THESIS TO THE FIELD

Despite the rapid technological development of tools used acquire high-resolution 3D datasets from live embryos, methods for visualising and objectively quantifying these datasets have fallen behind and remain limited. Consequently, I developed *morphoHeart*, an open-access quantitative image analysis tool that allows the segmentation of the cardiac layers -including the extracellular matrix- and quantification of tissue organisation and morphology throughout zebrafish heart development. *morphoHeart* is an exciting alternative to free and commercially available software, offering a comprehensive pipeline that provides semi-automated segmentation capabilities and improves the suite of tools and quantifications available in the biological field to characterise organ morphology and tissue distribution. While *morphoHeart* was initially developed for the study of zebrafish heart development, its modular nature for 3D segmentation and morphometric analysis gives this tool an application plasticity that the broader community can use to study a wide range of morphogenetic processes in other organs and organisms, contributing to the understanding of the tissue-organisation mechanisms underpinning them.

The ECM is a highly dynamic structure, and its continuous deposition, modification and degradation allow the regional generation of specialised extracellular environments important in mediating chemical and biomechanical signalling at cellular and tissue levels (Lu *et al.*, 2011; Humphrey, Dufresne and Schwartz, 2014). In spite of its described importance in driving the embryonic morphogenesis of organs in different animal models (Feinberg and Weiss, 2009; Mittal *et al.*, 2013; Kim *et al.*, 2018; Sivakumar *et al.*, 2018; Derrick and Noël, 2021) and the early traditional studies suggesting a requirement of this cardiac layer in cardiac development (Davis, 1924; Barry, 1948; Nakamura and Manasek, 1978, 1981) the role of the cardiac jelly has been under-investigated. To fill this gap and understand in more detail how the ECM helps sculpt the heart during cardiac morphogenesis, I used *morphoHeart* to acquire, for **the first time,** 3D reconstructions of the cardiac jelly at different zebrafish developmental stages. Quantitative analysis of the cardiac ECM through time allowed me to describe **comprehensively and in 3D** cardiac morphology and ECM-positioning and use such information to link morphology and ECM dynamics to heart development. Combined with candidate-driven functional models, these analyses facilitated the recognition of biologically relevant relationships between cardiac ECM regionalisation, embryo's L/R patterning and early heart morphogenesis.

Some of the main biological findings described in this thesis are summarised below:

- During early heart morphogenesis the ECM undergoes a dynamic expansion and subsequent degradation that correlates with specific cardiac development and maturation phases: while ECM expansion is associated with initial growth of the heart during looping and ballooning morphogenesis, the later ECM degradation is linked to regionalised tissue shrinkage accompanying chamber morphogenesis.
- Detailed analysis of ECM distribution in wild-type embryos confirmed that the atrial-specific left-sided ECM expansion we had previously described at tube stage (26hpf) (Derrick et al., 2021) is maintained as the heart undergoes looping and ballooning morphogenesis.
- The ECM is regionalised in the atrium, and the axis of regionalisation appears to be linked to the direction of atrial ballooning.
- Contrary to the established paradigm, 'middle' or 'non-looping' hearts undergo looping morphogenesis in the dorso-ventral axis, positioning the ventricle ventral to the atrium.
- Asymmetric Nodal signalling in zebrafish regulates chamber growth and regionalised ECM expansion as the heart undergoes looping morphogenesis.
- In spite of the disruption of L/R patterning, Nodal mutants exhibit atrial ECM asymmetry suggesting ECM-regionalisation is independent of Nodal signalling.

- The ECM cross-linking protein Hapln1a prevents cardiac jelly degradation during cardiac looping and ballooning, promoting atrial growth.
- The regionalised presence of Hapln1a in the heart throughout development facilitates the strengthening of the ECM asymmetry in wild-type hearts; however, it is not the only component involved in its establishment.
- While Hapln1a has a 'limited lifespan' effect based on the stages in which the protein is present in the cardiac ECM, L/R-patterning events driven by *spaw* have a longer lasting role in ensuring that early patterning of the heart has a lasting effect on morphogenesis.

In line with all these findings and with the working hypothesis that intrinsic information within the tissues of the developing heart must promote heart tube morphogenesis and provide directional cues (Brown and Wolpert, 1990; Noël *et al.*, 2013) it is tempting to speculate a model whereby regionalised differences in the cardiac jelly of the early heart tube are the driving factor for tissue intrinsic looping morphogenesis providing the cues that promote asymmetric dextral looping morphogenesis.

Next, I will discuss my work in the wide context of developmental biology, further describing how my data support this general hypothesis. I will propose new studies/experiments to investigate further the link between ECM and tissue morphogenesis in the development of the heart. Finally, I will describe limitations and further directions of the present study.

2 3D Quantification of Heart Development

To describe complex and dynamic processes such as heart development, advances in high-resolution microscopy now provide the possibility to image 3D organs in live organisms over time. In line with these advances, characterisation of cardiac morphology and remodelling during organogenesis has started to evolve from a simple description of cardiac looping direction in 2D, to volumetric and 3D directional and orientational descriptions, supporting not only a more detailed characterisation of morphogenesis in wild-type and defective scenarios but also the creation of higher resolution predictive models that provide novel insights into the mechanisms underpinning development (Le Garrec *et al.*, 2017; Desgrange, Lokmer, *et al.*, 2019; Desgrange *et al.*, 2020).

While great effort has been invested in developing tools for visualising 3D objects from grey-scale images (Semple, Peakall and Tatarnic, 2019; Rasse, Hollandi and Horvath, 2020), segmentation and analysis approaches in 3D are computationally demanding, and objective quantification of such datasets remains limited. In this study, I present *morphoHeart*, a quantitative image analysis tool that allows the segmentation of the heart layers -including the cardiac jelly- and quantification of heart morphology throughout development. As images obtained from ***live*** embryos are the tool's primary input, *morphoHeart* offers a standardised framework to characterise ongoing heart morphogenesis, capturing spatiotemporal changes in heart morphology and cardiac layer volume and distribution throughout development and avoiding alterations in tissue/chamber morphology due to fixation, processing and mounting.

morphoHeart facilitates multiparametric morphometric analysis of the chambers and their comprising cardiac layers. When all these metrics are analysed in wild-type hearts at different developmental stages, a thorough analysis of the evolution of each morphological parameter can be performed, gaining further insights into the processes supporting the morphogenesis of this organ (Chapter 4). Likewise, if similar analyses are performed in mutant hearts at different stages, deeper characterisations of heart malformations and the emergence of phenotypes can be attained enhancing the understanding of the impact of such mutations in heart development (see Chapter 4 and 5).

To demonstrate the scientific utility of *morphoHeart*, I processed datasets from 5 different experiments and extracted all the readouts included in *morphoHeart*'s 3D morphometric analysis library. The use of this tool in the analysis of zebrafish embryos with different mutations throughout this thesis demonstrated *morphoHeart*'s ability to:

- extract novel, high-resolution 3D morphometric data from zebrafish hearts at different developmental stages;
- identify and quantify morphological changes undergone by the chambers (i.e. size, orientation/rotation) and the tissue layers (i.e. volume, 3D distribution) as the heart undergoes morphogenesis;
- detect statistically significant differences with relatively small group sizes (when compared for example to heart morphology analysis using ISH images) in embryos with relatively mild morphological defects;
- recognise biologically relevant relationships between variables, allowing a deeper understanding of the interactions between processes that co-occur within an organ as it develops.

Organogenesis of the heart in zebrafish spans from late segmentation (~10hpf) (Keegan, Meyer and Yelon, 2004) until about ~5-14dpf when specific structures characteristic to each chamber continue to develop (Hu *et al.*, 2000; Foglia *et al.*, 2016). Although critical morphogenetic processes occur prior to the earliest stage analysed here (i.e. 34hpf), the positioning and movement of the cardiac progenitors that form the heart disc/cone and the subsequent tissue involution and jogging movements that constitute the formation and positioning of the heart tube pose imaging and segmentation challenges to analyse these very early stages of heart morphogenesis in 3D. Continuous improvements of mounting techniques within the systems, combined with algorithms to correct changes in focus and frame reference as development progresses, will enable a high-resolution 3D understanding of the morphogenetic processes involved in shaping the nascent heart, thus allowing a more detailed and comprehensive study of embryonic cardiac development.

Moreover, to correlate the morphology of the heart at multiple stages, understand how chamber and tissue dynamics evolve, and pinpoint the onset of key biological processes, imaging with the same embryo is required. However, as the heart is a beating organ and its beating is required for normal morphogenesis (Sehnert *et al.*, 2002; Hoog *et al.*, 2018; Sidhwani and Yelon, 2019; Foo *et al.*, 2021), to reduce the possible side effects of long-term imaging, yet acquire high-resolution datasets that image the genuine developmental process, the use of computational strategies that control the acquisition or aid the post-processing of 3D images of beating hearts would be strongly recommended.

The use of *morphoHeart* in the analysis of wild-type heart morphogenesis allowed me to describe comprehensively **in 3D** and **throughout development** *cardiac morphology* and *ECM-positioning* and use such information to link morphology and ECM dynamics to heart development. Furthermore, the use of *morphoHeart* combined with candidate-driven functional analysis, allowed me to better comprehend the tight relationship between ECM asymmetry, embryonic laterality, and heart morphogenesis, supporting the novelty and importance of the biological insights obtained when using *morphoHeart.* The further use of *morphoHeart* within the field will hopefully enhance the description of mutant heart phenotypes and understanding of the synergies underpinning heart organogenesis.

3 THE EARLY SET-UP OF AN ASYMMETRIC ECM

The ECM is a complex and dynamic array of highly cross-linked macromolecules that provides structural support and generates specialised extracellular environments important in mediating signalling at cellular and tissue levels (Byron, Humphries and Humphries, 2013; Mouw, Ou and Weaver, 2014; Keeley *et al.*, 2020). I have hypothesised that the ECM regionalisation is the tissue-intrinsic process, that, together with

Nodal signalling, promotes asymmetric heart morphogenesis, but questions remain around how this early asymmetric ECM is set up in the heart.

I have shown that concomitant to early cardiac developmental processes such as the formation of the heart disc from the bilateral group of heart progenitors, and the foundation of the heart tube from the involution of the heart disc, the expression and possible deposition of multiple ECM components is activated within the heart cells. Interestingly, while the expression pattern of most of these ECM components is homogeneous throughout the heart disc or tube, others have distinct regionalised expression patterns, like that of *hapln1a*, *hapln1b* (Chapter 4) or *has2* (Smith *et al.*, 2008).

Moreover, I have presented that the regionalised expression pattern of *hapln1a* on the posterior region of the heart disc (19-21hpf) and left side of the heart tube (24-26hpf) translates into a regionalised deposition of the protein at both stages. Interestingly, these early dynamics of expression of *hapln1a* and *hapln1b*/secretion of Hapln1a are in line with studies that characterise the formation of the heart tube from the heart disc, in which, as a consequence of the rotation and involution events, the cardiomyocytes that originated in the posterior compartment of the cardiac disc, get repositioned to the left side of the heart tube (Rohr, Otten and Abdelilah-Seyfried, 2008; Smith *et al.*, 2008; Guerra *et al.*, 2018). The fact that Hapln1a early deposition in the heart disc is maintained as the heart undergoes these complex morphogenetic events, suggests that the nascent ECM in the heart disc not only sets a permissive environment in the embryo for these set of rotation and folding events to occur, but also sets-up up the composition and mechanical properties of the nascent ECM that is going to transform into the asymmetric cardiac jelly of the primitive heart tube.

I have identified that the nascent cardiac jelly is composed at 19-21hpf of homogeneous myocardial deposition of Versicana (from *vcana* expression), left side deposition of HA (from *has2* expression) (Smith *et al.*, 2008), and posterior deposition of Hapln1a. Endocardially expressed *hapln1b* (and possibly deposited Hapln1b) is also present at this stage in the heart field, and so far is the only contributing ECM component forming the nascent cardiac ECM originating from this cardiac tissue layer. This particular composition containing Hyaluronic Acid, Versicana (as the PG) and two cross-linking proteins (Hapln1a and Hapln1b), suggests the requirement and interaction of these ECM components to generate **a stable and asymmetrically expanded** nascent cardiac jelly (see Chapter 5, Discussion). In addition, these genes' individual patterning and expression create a nascent ECM with four quadrants of regionally distinct environments within a small and simple disc (Fig 6.1A-A'').

During heart tube formation, rotation of the heart disc and folding of the epithelium repositions not only the cardiomyocytes expressing ECM components but also the already deposited ECM (Fig 6.1A''). These movements result in theory in a heart tube with elevated levels of HA in the ventral face, homogeneous presence of Versicana throughout the tube and elevated levels of Hapln1a on the left side (Fig 6.1B-B''). Indeed, analysis of Hapln1a deposition at 26hpf (Chapter 5) supports the repositioning of the four quadrants of regionally distinct environments in the disc to longitudinal sections in the heart tube: the originally posterior Hapln1a-rich ECM is repositioned to form the left side of the cardiac jelly in the heart tube (Fig 6.1B''). Consequently, this set of movements is required to establish the previously described left-sided expansion of the cardiac jelly (Derrick *et al.*, 2021) (Appendix 1).

Once the heart tube is formed with a regionally diverse ECM, the already asymmetric ECM goes through a process of regionalised expansion as the heart undergoes looping and ballooning morphogenesis. During this expansion, concomitantly to Hapln1a protein maintenance in the left side of the atrium and supporting its role in protecting the ECM from early degradation, the cardiac ECM maintains the left-sided asymmetry, which as the chamber loops and balloons transforms into an outer-curvature asymmetry. Interestingly, during this timeframe (>30hpf) the expression of *hapln1a*, *vcana* and *has2* are downregulated throughout the heart. The transient expression of these genes, combined with the unique ECM environments set up

in the heart disc and subsequently in the tube, suggests that the ECM environment established at early stages of heart development is the ECM that drives continued morphogenesis of the heart.

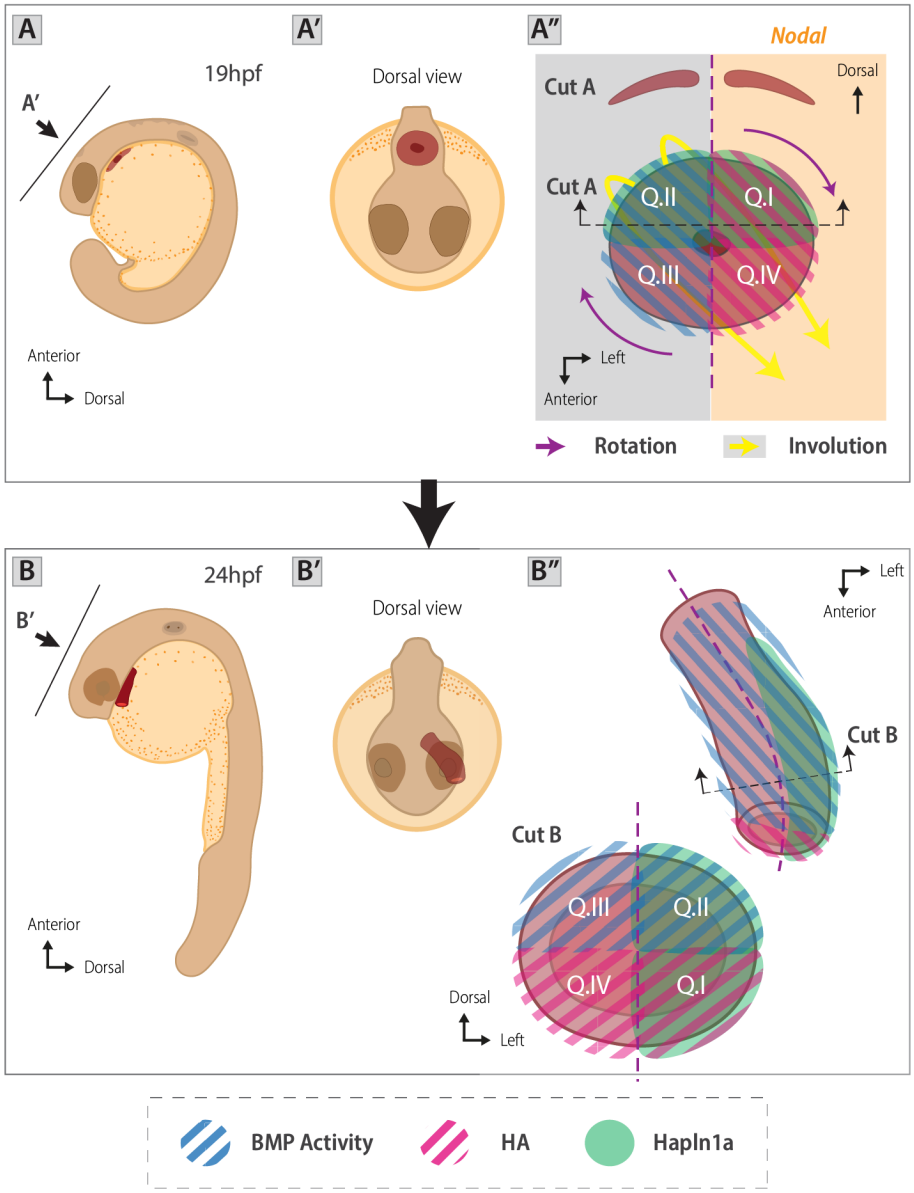

Fig 6.1. Regionalised gene expression of ECM components in the early heart disc establishes four distinct ECM environments required to create the asymmetric expansion of the cardiac jelly during zebrafish heart morphogenesis.

Current model of heart jogging and establishment of the nascent cardiac jelly at disc (A-A'') and tube (B-B'') stages. **A-B''.** The heart disc and nascent cardiac ECM displays A/P asymmetry due to the regionalised expression and deposition of Hapln1a in the posterior compartment of the disc. Alongside, L/R asymmetry dependant on the expression of *Nodal* (orange) signalling pathway (*spaw* in zebrafish) is established in the heart disc. This initial Nodal-*dependent* patterning restricts the expression of *has2* (and deposition of HA, pink stripes) to the left side of the disc, downregulating BMP activity (blue stripes) and consequently promoting cell motility. These asymmetries result in a heart disc with a nascent cardiac jelly comprised of four quadrants with regionally distinct ECM environments (Q.I: Versican, Hapln1a and HA, Q.II: Versican, Hapln1a and BMP activity, Q.III: Versican and BMP activity, Q.IV: Versican, and HA). Faster migration speeds of the cells located on the posterior-left compartment of the disc promotes the extension and formation of the heart tube towards the anterior-left side of the embryo. The combination of rotation and involution events position the Hapln1-rich ECM environment to the left side of the heart tube (Q.I and Q.II), where the continued expression of *hapln1a*, *hapln1b*, *versicana* and *has2* and deposition of the proteins they encode, drives the expansion of the ECM with a characteristic atrial-specific left-sided asymmetry. A,B: Left view of the embryo illustrating the position of the

heart disc at 19 (A) and 24hpf (B). A''',B''': Schematic of the embryo and heart viewed from the position of the arrows depicted in A and B, respectively (dorsal view of the heart).

_____

Furthermore, simultaneous analysis of 2D myocardial ballooning and cardiac jelly thickness heatmaps between 34-36hpf and 48-50hpf (Chapter 4, Fig 4.41) proposes a link between the ECM asymmetries present in the early heart tube and the final direction of chamber ballooning as the heart undergoes morphogenesis.

Together, I propose the following model: In the presence of asymmetric Nodal signalling, *has2* expression is restricted to the left compartment of the heart disc where it downregulates *bmp4* expression establishing different migration velocities within the cardiomyocytes forming the heart disc. Within this disc Hapln1a, independent of Nodal is deposited in the posterior compartment while Versicana is expressed and deposited homogeneously throughout, creating four distinct quadrants (or regions) within the heart disc with differences in ECM composition, mechanical properties and patterning markers (Fig 6.1A-A''). During tube formation, due to differences in cell migration speed, the heart disc undergoes a clockwise rotation (from a dorsal view) and a simultaneous asymmetric folding of the disc epithelium towards the anterior-left side of the embryo (Fig 6.1B-B''). These rotation and folding events position the Hapln1-rich ECM environment to the left side of the heart tube, where the continued expression of *hapln1a*, *hapln1b*, *versicana* and *has2* and deposition of the proteins they encode, drives the expansion of the ECM with a characteristic atrial-specific left-sided asymmetry. The establishment of this asymmetry within the heart tube, provides tissue-intrinsic directional cues to the heart tube, setting up the left-right axis as the orientation in which chamber growth and looping morphogenesis will occur.

4 The Role of Left-Right Patterning

Disruption of Nodal patterning in zebrafish (i.e. *spaw*$^{-/-}$) results in homogeneous expression of *has2* throughout the heart disc (Smith *et al.*, 2008). This in turn produces uniform inhibition of *bmp4* activity which fails to create asymmetric migration directionality of the cardiomyocytes in the posterior region of the heart disc. As a result, heart discs fail to rotate and rather than folding and extending asymmetrically to the anterior-left, fold and extend the disc down the midline of the embryo creating hearts which lack directionality in cardiac jogging (i.e. 'no jogged hearts') (Baker, Holtzman and Burdine, 2008; Lenhart *et al.*, 2013; Veerkamp *et al.*, 2013). In this scenario, despite the loss of L/R patterning, as *hapln1a* expression is independent of laterality cues (Chapter 5) (Derrick *et al.*, 2021), deposition of Hapln1a and that of Versicana is maintained intact in the heart disc (i.e. *hapln1a*/Hapln1a: posterior and *vcana*/Versicana*:* uniform) producing a cardiac jelly in the disc with only two distinct ECM compositions rather than four (Fig 6.2A-A'').

In line with the current model (Fig 6.1A-C), this altered composition of the nascent ECM in the *spaw*$^{-/-}$ heart, combined with the absence of rotations in the heart disc as the heart tube forms (Fig 6.2A''), predicts the Hapln1a-rich ECM will end up forming the ventral face of the heart tube (Fig 6.2B-B''). These mispositioned ECM asymmetries could provide tissue-intrinsic directional cues to the *spaw*$^{-/-}$ heart, setting a D/V axis for chamber growth and looping morphogenesis to occur. Therefore, the set of events just described would result in *spaw*$^{-/-}$ hearts that display dorso-ventral looping directionality.

Interestingly, although *spaw*$^{-/-}$ dorso-ventral loopers do undergo looping morphogenesis and present an AOC-asymmetric ECM expansion, the reduced AOC/AIC ratio values when compared to lateralised *spaw*$^{-/-}$ suggests a more profound dysregulation of the ECM dynamics in the atrium of these mutant hearts (i.e. dorso-ventral loopers). These observations, strengthens the proposed relationship between the axis of ECM asymmetry and directionality of looping morphogenesis (Fig 6.2A), and suggests that absence of

rotations and asymmetric expression of ECM components in the cardiac ECM of the heart disc creates an unfavourable ECM environment for chamber growth and rearrangement.

Furthermore, to describe with more detail the features that characterise the different looping directionalities in *spaw*$^{-/-}$, the sample size for each looping direction should be increased, allowing a more direct comparison of the morphometric parameters within groups.

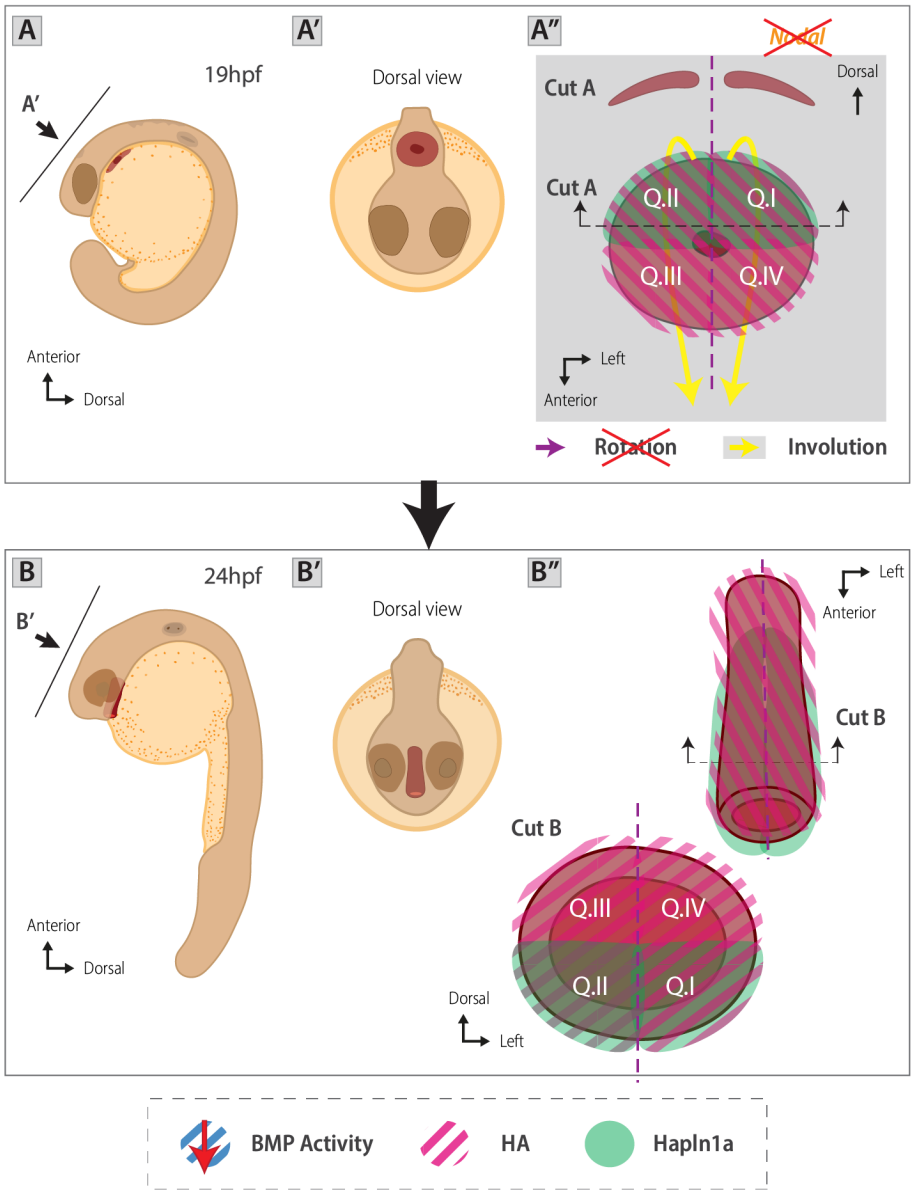

Fig 6.2. Disrupted L/R patterning fail to create the four distinct ECM environments required to generate the left-sided asymmetric expansion of the cardiac jelly during zebrafish heart morphogenesis.
Current model of heart jogging and establishment of the nascent cardiac jelly at disc (A-A'') and tube (B-B'') stages in a *spaw* mutant scenario. **A-B''.** The heart disc and nascent cardiac ECM displays A/P asymmetry due to the regionalised expression and deposition of Hapln1a in the posterior compartment of the disc. Alongside, disruption of L/R patterning fails to restrict the expression of *has2* (and deposition of HA, pink stripes) to the left side of the disc resulting in a homogeneous deposition of HA and downregulation of BMP activity (blue stripes) throughout the heart disc. The asymmetries established by Hapln1a deposition, result in a heart disc with a nascent cardiac jelly comprised of two halves with regionally distinct ECM environments (Q.I-Q.II (posterior compartment): Versican, Hapln1a and HA, Q.III-Q.IV (anterior compartment): Versican and HA). Similar migration speeds of the cells located on the posterior compartment of the disc promotes the extension and formation of the heart tube towards the anterior of the embryo, resulting in midline jogged hearts. These events position the Hapln1-rich ECM environment to the ventral side of the heart tube (Q.I and Q.II). A,B: Left view of the embryo illustrating the position of the heart disc of a *spaw*$^{-/-}$ at 19 (A) and 24hpf (B). A''',B''':

Schematic of the embryo and heart viewed from the position of the arrows depicted in A and B, respectively (dorsal view of the heart).

_____

The fact that a greater proportion of *spaw*$^{-/-}$ midline joggers loop dextrally (Noël *et al.*, 2013; Grimes *et al.*, 2020), indicates that either an additional intrinsic mechanism (other than the asymmetric ECM) is active in the developing heart providing the required directional cues to establish robust dextral looping, or that despite the midline jogging, stochastic deposition of ECM components could set a slightly biased D/V axis setting in motion a directionality in these hearts.

In line with the first hypothesis, a previous study identified that drug-treatment of explanted heart tubes with pharmacological compounds such as myosin II- or actin polymerisation-inhibitors abrogated looping morphogenesis, suggesting that cytoskeletal remodelling at cellular-scale level may regulate tissue-intrinsic cardiac morphogenesis required to promote dextral looping (Noël *et al.*, 2013). Yet, further studies will need to be performed to understand the role played by cellular cytoskeleton remodelling as a possible tissue-intrinsic mechanism driving heart looping directionality. Importantly, in this same study, it was shown that although most *spaw*$^{-/-}$ exhibit 'no jogged' heart tubes, during heart tube formation, they display a minor rotation of the disc, which was correlated to their final looping direction (Noël *et al.*, 2013). Using this information to build on the second hypothesis and the presented model, the slight rotation of the heart disc, added to a spontaneous/stochastic non-homogeneous expression of *has2* in the disc, could create regionalised inhibition of *bmp4* and in turn small differences in cardiomyocyte migration velocities within the cone. These set of conditions, could result in a *spaw* mutant heart tube that despite exhibiting no jogging direction, has a tissue-intrinsic axis set for chamber growth that is not precisely D/V, resulting in *spaw*$^{-/-}$ hearts with lateralised loops.

Reconstruction and quantification of the cardiac jelly from time-lapse imaging of *spaw* mutants starting from the moment the heart tube is formed (~24hpf) until early looping stages (~32-34hpf) could test whether a 'mild' L/R asymmetry (i.e. predominantly D/V asymmetry, but with a slight L/R skew) in the cardiac jelly of the 'just formed' heart tube could predict the final direction of looping, hence supporting the presented model. Furthermore, in these experiments, the use of additional cell markers with multiple colours (Staudt *et al.*, 2014; Foglia *et al.*, 2016; Lombardo *et al.*, 2019) could be used to follow the position of the cells as the heart tube descends ventrally over the embryo's yolk while undergoing looping and ballooning morphogenesis, aiding the investigation of tissue rotations, cellular-rearrangements and -size changes (if any) involved in the development of Nodal mutant hearts with different directionalities (Lombardo *et al.*, 2019; Tessadori *et al.*, 2021). Additional experiments in *pkd2* (polycystic kidney disease 2) mutants in which heart laterality is randomised (Schottenfeld, Sullivan-Brown and Burdine, 2007; Bataille *et al.*, 2011), could also provide novel insights regarding the link between looping directionality, left-right patterning and ECM regionalisation.

In addition to these experiments in which Nodal signalling as the extrinsic cue driving heart looping directionality is disrupted, complementary experiments modifying the composition and regionalisation of the cardiac jelly could deliver further understandings of the features that characterise this asymmetric ECM and its role in driving robust dextral looping morphogenesis. Here I described the phenotype of Hapln1a loss-of-function mutants (Chapter 5) and identified the early requirement for this cross-linking protein to expand and stabilise the nascent cardiac ECM and promote atrial growth. Despite the defects in ECM expansion, the atrial L/R ECM-asymmetries in *hapln1a*$^{\Delta 241}$ mutants were reduced, suggesting Hapln1a is not the only ECM component driving the asymmetries in the cardiac jelly. *hapln1b*, the paralog gene of *hapln1a*, also displays an asymmetric expression at early stages of heart development. Thus, double knockout of both *hapln1* genes would confirm if both link proteins are required to establish asymmetries in the cardiac ECM and, if so, corroborate if the complete absence of ECM asymmetry as a tissue-intrinsic mechanism result in hearts with abrogated looping morphogenesis.

spaw is expressed in a posterior-to-anterior pattern on the zebrafish left LPM from 10 through to 22 somites (14-20hpf) (Ahmad, Long and Rebagliati, 2004). Interestingly, most of the defects identified in *spaw*$^{-/-}$ mutant hearts initiate in a timeframe where active *spaw* expression is no longer present in the embryo (Chapter 4 and 5), suggesting the existence of a long-lasting mechanism whereby *spaw* ensures that the early patterning has a lasting effect on morphogenesis. Two different mechanisms could explain this phenomenon.

1) During the stages in which the heart is a disc and *spaw* is still expressed, Spaw restricts or induces regional expression (and possibly deposition) of ECM components or remodelling enzymes. During heart formation, these ECM factors get positioned in a region within the heart tube where they are maintained. At later stages, additional ECM components are deposited which may act as interacting partners or modifiers of the established regionalised ECM, and so the presence of these later-expressed ECM components plays an active role in modifying the early patterned ECM. When Nodal signalling is disrupted, loss of regional expression of these genes would either create an early ECM in which these factors are either not produced or are homogeneously deposited (like the previously described expression of *has2* in *spaw*$^{-/-}$). In both scenarios, the later deposition of ECM interacting partners or modifiers, in conjunction with the abnormal early ECM environment, result in a 'retarded' amplification of these early defects. This mechanism could be tested by mRNA ISH of different possible ECM components or remodelling enzymes that are expressed at disc stage and whose expression could be induced or restricted by the expression of *spaw* in the left LPM. Performing the ISH analysis of these components in wild-type and *spaw*$^{-/-}$ would identify if their expression is Nodal-dependent, and if so, further studies investigating the role of these factors, their possible interacting partners and its link to long-lasting L/R patterning would be required.

2) Recent studies have shown that signalling pathways, such as Nodal, can orchestrate transcriptional responses during development via epigenetic changes (Dahle, Kumar and Kuehn, 2010; Brown *et al.*, 2011; Bertero *et al.*, 2015). In line with these studies, L/R patterning of the heart by *spaw* could change the epigenetic landscape of the cardiomyocytes comprising the left compartment of the heart disc which in turn could alter the transcription of ECM genes required later during ongoing morphogenesis. Disruption of L/R patterning, could result in no differential epigenetic landscapes between both sides of the heart disc, resulting in the later amplification of these early 'patterning defects' when differential expression of the target ECM-related genes is required. Although this hypothesis could represent a straightforward explanation to the long-lasting impact of patterning defects in *spaw*$^{-/-}$, understanding how exactly could the ECM be epigenetically regulated during heart development is a poorly studied research area (Song and Zhang, 2020).

5 THE TIGHTLY CONTROLLED COMPOSITION OF THE CARDIAC ECM

The characteristic expansion, shrinkage, and asymmetry of the cardiac ECM during early cardiac morphogenesis suggests precise spatiotemporal regulation of production, modification and turnover of its different components to create and stabilise the asymmetries hypothesised to be essential for normal cardiac development (Fig 6.1A-B''). Indeed, multiple studies investigating the role of different ECM components in development have highlighted the importance of a fine balance and spatially controlled levels necessary for the progression of normal development.

For instance, when regulating the levels of HA during heart development, mutations in *cemip2* (*cell migration inducing hyaluronidase 2*, formerly *tmem2*) results in zebrafish with angiogenesis defects, abnormal heart looping and increased deposition of HA around the major vessels and the cardiac jelly (De Angelis *et al.*, 2017). As *cemip2* is required to degrade HA, disruption of *cemip2* activity fails to control the elevated deposition of HA, which in turn results in defects confining the AVC markers such as *has2* and Wnt, required for normal AVC development (De Angelis *et al.*, 2017; Hernandez *et al.*, 2019). Other studies

have also described the importance of spatially restricting the expression of *has2* in the development of the AVC, and have shown that failure to restrict its expression results in cardiac jelly expansion and looping defects (Lagendijk *et al.*, 2011; Patra *et al.*, 2011; Grassini *et al.*, 2018)

Moreover, multiple studies have confirmed the early requirement of Versican and HA in heart morphogenesis. Mittal *et al.*, for instance described the importance of *versican* expression in medaka heart morphogenesis. Medaka embryos lacking Versican exhibited arrest of cardiac development at the linear heart tube stage, with an absence of cardiac looping, and no cardiac jelly or cardiac valves (Mittal et al., 2019). Interestingly, these phenotypic characteristics are similar to those found in the hearts of the *Hyaluronan synthase-2* (*has2*)-deficient and *Versican*-deficient mouse embryos (Yamamura *et al.*, 1997; Camenisch *et al.*, 2000; Hatano *et al.*, 2012), confirming the importance of these two ECM components in the modulation of continued heart morphogenesis. Moreover, drug treatments using a HA-synthase from the onset of myocardial expression of *has2* until looping stages (18→48hpf) resulted in failure of the heart to form, while inhibition only between disc and cone stage (18→22hpf) resulted in the formation of a tube whose subsequent morphogenetic processes were disrupted (Derrick *et al.*, 2021). These results support the hypothesis that HA synthesis is required prior to the formation of the tube to support ongoing heart morphogenesis.

Interestingly, three out of the four ECM components comprising the ECM at disc stage (i.e. HA, Versican, Hapln1a and Hapln1b) have an asymmetric mRNA expression. As described, previous studies have identified *has2* as a downstream target of Nodal signalling, elevating or restricting its expression to the left side of the disc (Chen *et al.*, 1997; Smith *et al.*, 2008; Lenhart *et al.*, 2013). As for *hapln1a*, the only other gene that has been so far identified to be specifically expressed in the posterior compartment of the zebrafish heart disc and left side of the heart tube is the transcription factor *meis2b* (Guerra *et al.*, 2018). To confirm *hapln1a* expression is indeed downstream of *meis2b*, mRNA ISH analysis of *hapln1a* in *meis2b* mutants could be performed uncovering the interactions between them and establishing the first link of the transcriptional network that regulates the antero-posterior regionalisation of genes in the developing myocardium. Until now, no genes have been identified to drive the antero-posterior patterning of the endocardial cells, making it difficult to identify the gene(s) driving the upregulated posterior expression of *hapln1b* in the heart field.

Aside from *hapln1a*, *hapln1b* and *has2*, asymmetric deposition of other ECM components in this nascent ECM cannot be ruled out. As mentioned in the previous chapter, the full composition of the zebrafish cardiac ECM at the different stages of development investigated here is still unknown. In addition, although the mRNA expression pattern of some of the analysed ECM-related genes seem symmetrical, the actual deposition of some of these ECM components into the cardiac ECM requires the presence of other components inside the cell either to aid its synthesis (e.g. Has2 for HA (Weigel and DeAngelis, 2007)) or to create the final assembly that is then deposited into the cardiac jelly (e.g. laminin subunits that form the laminin trimer (Hamill *et al.*, 2009)). Hence, it could be the asymmetric expression of these other components that could generate an asymmetric deposition of the ECM component of interest. Moreover, all components once deposited into the ECM can experience degradation by specific proteolytic enzymes. If these proteolytic enzymes are instead the ones asymmetrically deposited, then the regionalised degradation of components could indeed create an asymmetric deposition of a particular ECM component without its synthesis needing to be regionalised. Together this highlights the complexity of the ECM and exposes the myriad ways in which the identified asymmetric expansion could be established and maintained throughout development.

HA, one of the most common ECM components, is involved in the modulation of numerous cellular processes during development. The multiple functions attributed to HA are thought to result from the large structural variability of the macromolecule in terms of size, conformation, and interactions with different binding proteins, that trigger different biological effects (Cowman and Matsuoka, 2005; Cyphert,

Trempus and Garantziotis, 2015). Illustrating the complexities in understanding the ECM and its multiple roles, a recent study performed in chick and mice described an asymmetric ECM expansion of the right side of the gut's dorsal mesentery (a mesodermal structure that suspends the gut), necessary for driving midgut rotation during gut development (Sivakumar *et al.*, 2018). This ECM expansion is the result of the accumulation of an enzymatically modified HA on the right side of the dorsal mesentery, which created dissimilar cellular environments on both sides of the midgut. Analysis of HA synthesis indicate that despite bilateral HA synthesis, it is the degradation of HA on the left and accumulation of a modified HA on the right, which drives regionally distinct downstream HA signalling mechanisms, triggering distinct cellular behaviours on either side of the midgut necessary for driving directional gut rotation during the looping morphogenesis of this organ (Sivakumar *et al.*, 2018).

Despite the complexity of the ECM and the multiple ways in which its components could be involved in heart development, one way in which a clearer picture of the composition of the zebrafish ECM could be attained is by performing proteomic analysis of individual hearts, and if possible, of individual chambers at different stages of development. The results from these experiments could provide a much richer appreciation of all the different ECM components comprising the cardiac jelly of the zebrafish developing heart, allowing a more straightforward characterisation of the interactions within these components and its dynamics as development progresses. These type of analyses, combined with transcriptomics datasets (Junker *et al.*, 2014; Burkhard and Bakkers, 2018) at the same developmental stages could serve as a basis for the definition of future investigations in which the role of new ECM components and its possible interacting partners could be investigated.

Although there is still much that is not known, the ECM components investigated here had been previously described in multiple studies to be required in heart development. Additionally, their conserved functional role as binding partners in the cardiac jelly in mice, medaka and zebrafish (Chapter 5, Discussion), suggest that the asymmetric ECM environment established in the nascent cardiac jelly of the heart disc and tube establishes an ECM environment that provides the tissue-intrinsic directional cues to the heart tube, setting a L/R axis for chamber growth and looping morphogenesis to occur.

6 THE ECM ROLES IN HEART DEVELOPMENT

Having stated the hypothesis that regionalised differences in the cardiac jelly of the early heart tube are the tissue-intrinsic factors that provide directional cues and promote asymmetric dextral looping morphogenesis, I will finally speculate the possible mechanisms by which this could be happening.

Interestingly, this is not the first study in which asymmetries of the cardiac jelly during early stages of heart development are identified. In the early 1900, traditional studies described the cardiac jelly in chick embryos as a gelatinous sheath surrounding the epithelium with distinctly thinner ECM at the primary ventral and dorsal midlines (Patten, 1922; Davis, 1924). Although differences in the L/R axis are not reported, the conserved asymmetric deposition of the cardiac ECM within animal models hints an early requirement for an asymmetric ECM in the primitive heart tube, implying an important role in its existence.

These difference in ECM distribution between sides of the heart tube driven by dissimilar ECM compositions could play a number of roles in early heart development.

As mentioned, during embryonic development, the heart is the first organ to function, even before it has acquired its mature structure. The fact that blood flow is established already at these early stages, particularly in zebrafish and chick embryos where diffusion is a sufficient means of oxygen, nutrient and metabolic waste transport up until about 7dpf and HH20, respectively (Pelster and Bagatto, 2010; Lindsey, Butcher and Yalcin, 2014), suggests a critical role for blood flow in the patterning, development and maturation of the early endothelial and cardiac muscle cells comprising the primitive heart. In fact, recent

studies in the field of cardiac tissue engineering have highlighted the importance of precise mechanical and electrical stimuli to direct *in vitro* the differentiation of stem cells into mature cardiomyocytes (Stoppel, Kaplan and Black, 2016). In addition, other studies have identified the importance of wall shear stresses in the maturation of endothelial cells (Roux *et al.*, 2020).

Following the assembly of the heart tube and the onset of blood flow, endothelial cells within the heart tube start to be exposed to hemodynamic forces in the form of laminar or turbulent shear stresses. In addition to this boundary forces, contractility of the heart tube combined with blood being sucked-in and pumped-out through its lumen, create variations in the hydrostatic pressure which stretches the endothelial cells as a result of radial wall pressure. This set of biophysical forces (i.e. wall shear stress combined with cyclical stretching-contracting) experienced by the endothelial cells make the endocardium the flow-sensitive tissue and its transduction of signals to the myocardium has been shown to facilitate morphogenetic adaptations of the developing heart in response to changing hemodynamic conditions (Auman *et al.*, 2007; Yalcin *et al.*, 2011; Dietrich *et al.*, 2014).

With this in mind and considering that the ECM asymmetries identified in the early heart tube creates a lumen that is not symmetrical, one could hypothesise that the morphological changes induced by these asymmetries, creates particular mechanical environments within the heart tube, that in the absence of an asymmetric ECM would not exists (Fig 6.3A). Consistent with this hypothesis, a computational fluid dynamic (CFD) model of the OFT in chick embryos in which realistic 3D curvatures were investigated, identified differential shear stresses in the OFT lumen which correlated to the tissue morphology being studied (Liu *et al.*, 2011). Higher wall shear stresses were identified in the narrower lumen regions and in the inner curvature of the OFT, while lower shear stresses were recognised in the outer curvature of this structure. In fact, this particular difference in shear stresses between inner and outer curvatures was described by Hierck *et al.* in 2007 where shear stress distribution was investigated in developing chich hearts at HH17 (Hierck *et al.*, 2007). This heterogeneous distribution of wall shear stress due to tissue morphology, supports the hypothesis that asymmetric tissue morphologies create distinct biomechanical environments within the lumen of a structure which in turn may modulate differential cellular responses required for directional growth.

In order to maintain structural integrity and functionality, cells are able to sense forces from the ECM and neighbouring cells by means of receptors and cell adhesions (Hay, 1991; Bachir *et al.*, 2017). This mechanosensing mechanism allow cells to adapt to differential forces exerted by their environment and translate them into intracellular signalling. Indeed, studies investigating the influence of ECM mechanical properties in developing and remodelling tissues have shown that the structure and elasticity of the ECM provides an outline for tissues to either bend, twist or break-off to form complex morphologies (Gjorevski and Nelson, 2010; Walker, Mojares and del Río Hernández, 2018). As the biomechanical properties of the ECM are tightly controlled by its specific composition (Cox and Erler, 2011; Attili and Richter, 2013), it is possible that differences in link-protein deposition (like the case of the early heart tube) creates environment with different stiffness or elasticities inducing different cellular behaviours (Rodriguez and Roughley, 2006; Jeon *et al.*, 2007). Hence, early ECM asymmetries in heart tube combined with these observations suggest a role for the ECM in creating via tight deposition of ECM components specific mechanical microenvironments within the tissue for cells to sense and respond. Supporting this hypothesis, recent studies in the field of regeneration have highlighted the importance of precise mechanical ECM environments to control tissue regenerative potential in myocardial muscle regeneration (Notari *et al.*, 2018). On the other hand, and relating these observations to hemodynamics, studies investigating the impact of vessel wall stiffness on blood flow dynamics identified that stiffer aortas resulted in variations in velocity patterns, increased peak velocities and higher systolic pressures when compared to compliant aortas (Zimmermann *et al.*, 2021).

Incorporating the ideas described so far, the biophysical forces induced by blood flow to the endothelial cells, the multiple mechanical environments that can be created via differences in ECM composition, and the ECM asymmetries identified in the heart tube, result in a setup of very distinctive mechanical microenvironments within the heart. This set of conditions could indeed provide regionalised tissue-intrinsic directional cues to the heart tube and induce patterning events that support directional growth and continued morphogenesis.

Moreover, as the heart undergoes ballooning, crosstalk between the two cardiac tissue layers has been shown to be important in regulating chamber growth. Different studies have shown how this crosstalk is bidirectional, as both tissues secrete different biochemical signalling molecules to communicate with the other, inducing changes in cellular morphology, proliferation and differentiation (Staudt and Stainier, 2012; Haack and Abdelilah-Seyfried, 2016). For these signals to be transmitted appropriately between the cardiac tissue, they must traverse the cardiac ECM. In this process, depending on the composition of the ECM, some signals might get sequestered, preventing its free diffusion, while others might require additional post-translational modifications in the matrix prior to be delivered to the other tissue (Stankunas *et al.*, 2008; Bonnans, Chou and Werb, 2014). These phenomena suggest that the establishment of the correct cardiac jelly composition within both tissue layers is critical in ensuring appropriate reception of signals and highlight an additional mechanism by which signalling across ECMs with different compositions can result in regionalised responses (Bonnans, Chou and Werb, 2014; Walker, Mojares and del Río Hernández, 2018). In this way, by providing permissive (or non-permissive) environments for diffusion or posttranslational modifications of signalling molecules (e.g. Notch, Neuregulin, VEGF), the ECM serves as a 'signalling barrier', that assists and regulates the crosstalk between tissues, hence impacting tissue morphogenesis.

Taken together I propose the following model. Following the assembly of the heart tube, asymmetries in the cardiac ECM generate a tube with an asymmetric lumen and four different ECM environments. The onset of blood flow, combined with these different environments, creates distinct hemodynamic patterns as the blood flows through the heart. Specific hemodynamic patterns sensed for instance by the cells comprising the left side of the tube in which a thicker cardiac ECM is comprised between the cardiac tissues, sets an atrial outer curvature fate to these cells activating the genetic and morphogenetic changes required within them to direct tissue growth and directional looping morphogenesis. In this way, early asymmetric ECM combined with the mechanical forces induced by blood flow to the heart, conduce regionalised and specific myocardial-endocardial patterning necessary to attune changes in cellular sizes and shapes driving the onset of ballooning and dextral looping morphogenesis. As development progresses, the complex communication between all the entities (endocardium as the flow sensitive tissue, cardiac jelly and myocardium) makes this process a closed loop in which changes in cell shapes and size drive changes in chamber morphology. These morphological changes accompanied by ECM expansion (driven by both cardiac tissues), results in changes in blood hemodynamics that are sensed by the endocardium and feedback back to the whole system, altogether driving asymmetric cardiac morphogenesis.

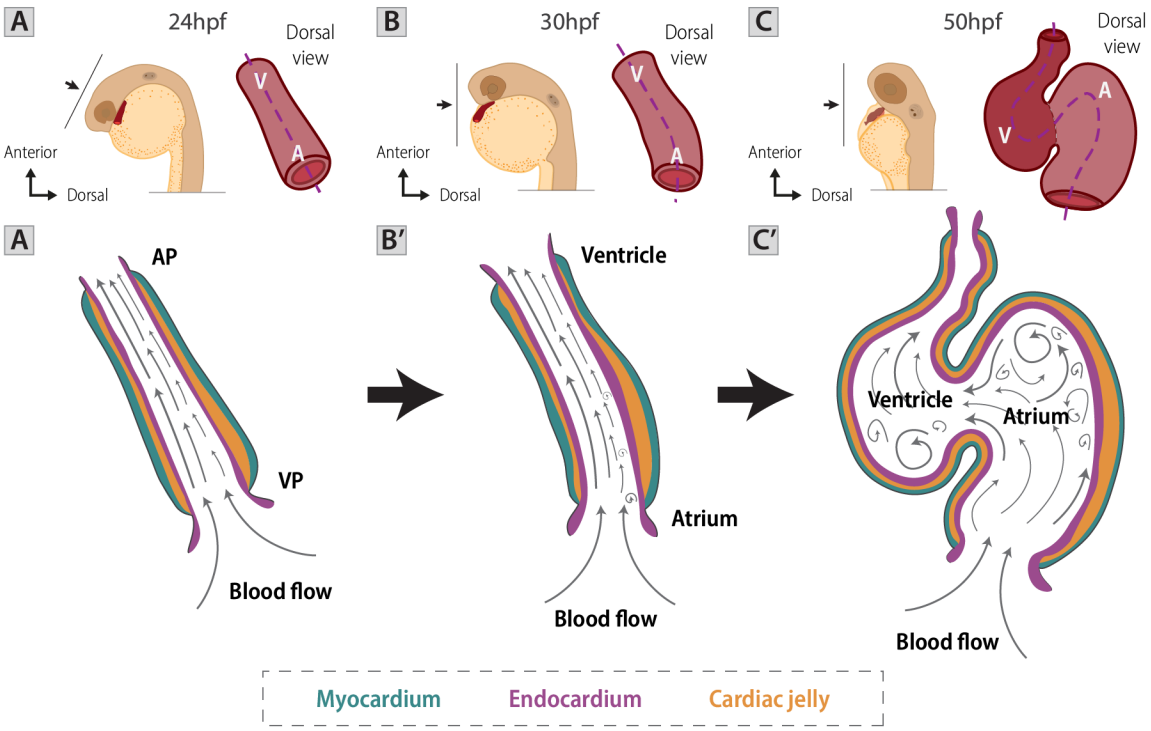

Fig 6.3. Regionalised differences in the cardiac jelly of the early heart tube are the tissue-intrinsic factors that provide directional cues and promote asymmetric dextral looping morphogenesis
A-C'. Biomechanical asymmetries setup by the ECM during the formation of the heart tube combined with the mechanical forces induced by blood flow in the heart (specifically, the differential shear stresses imparted on the endothelial wall), induce the myocardial and endocardial changes necessary to drive looping and ballooning morphogenesis of the heart, resulting in robust dextral looping directionality (see text for details). A'-C': Laminar flows which result in higher shear stresses are depicted by thicker and longer arrows. Turbulent flows with lower shear stresses are depicted by thinner and curly arrows.

Being such a complex process different experiments could be proposed to test individually the requirements for an asymmetric ECM and blood flow during this process. If KO of both *hapln1* paralogs indeed results in loss of ECM asymmetries in the heart, characterisation of cardiac morphology in these mutants could help elucidate whether symmetric hemodynamics in the tube correlate with an absence of looping. Additionally, CFD models using the 3D reconstruction of mutant and wild-type heart tube could help investigate the differences in wall shear stress experienced by a symmetric and an asymmetric tube and how they relate to the progression of looping morphogenesis. Additional insights regarding the composition of the cardiac ECM at early stages of development (i.e. proteomics and transcriptomics experiments previously proposed) could further help set up a real 3D model of the cardiac jelly, in which the mechanical properties of this ECM and their influence in tissue contraction could be explored.

Moreover, to further investigate the importance of blood flow and contractility the cardiac morphology of hearts with reduced blood shear stress (i.e. by injecting *gata1/gata2* MO (Lin, Swinburne and Yelon, 2012)) or with disrupted contractility (e.g. *tnnt2a* mutants (Sehnert *et al.*, 2002)), could provide interesting insights into the mechanisms by which the mechanical stimuli induced by blood flow regulates continued morphogenesis.

7 Limitations and Future Perspectives

One of the main limitations in the scope of this thesis stems from the fact that no other analysis approaches have been published quantifying the zebrafish cardiac layers (including the cardiac jelly) or chambers with

the resolution and detail provided by *morphoHeart*. Although the absence of such analysis with which to compare *morphoHeart* in the field dismisses the possibility of validating its results, the morphometric characterisation of wild-type embryos delivered by this study can become the benchmark against which future studies can compare their results.

As it was demonstrated throughout this study *morphoHeart* offers a novel suite of morphometric parameters for performing detailed quantifications and characterisations of heart morphogenesis in zebrafish embryos. The open-source nature of *morphoHeart* will allow future studies to enhance the analysis capabilities of the tool, implementing new quantifications or descriptors that support the description of this complex morphogenetic processes in model organisms other than zebrafish.

The processing and filtering steps of *morphoHeart* was mainly optimized for the myocardial and endothelial markers in the *Tg(myl7:lifeActGFP); Tg(fli1a:AC-TagRFP)* double transgenic line. Hence, applying the suggested processing and filtering to other transgenic lines, will likely require optimization to allow accurate contour demarcation and tissue layer segmentation in the following processing steps.

Due to the approach used to obtain undisturbed 3D image datasets of the whole heart (i.e. high-dose of anaesthetic and low temperature), all hearts were analysed with both chambers in a 'relaxed' state which is not representative of any cardiac stage during the zebrafish heartbeat. Despite this limitation, as the same approach was used for all the analysed embryos in this thesis, the morphometric parameters obtained at the multiple developmental stages and with the different genotypes were comparable and facilitated a more in-depth characterisation of cardiac tissue dynamics and chamber morphology throughout development in wild-type and mutant scenarios. The use of adaptive prospective optical gating (Taylor *et al.*, 2019) or macroscopic-phase stamping (Trivedi *et al.*, 2020) imaging techniques in future studies will allow the acquisition of datasets at specific or throughout the whole cardiac cycle, which, combined with *morphoHeart*'s segmentation and morphometric analysis capabilities, will enhance the investigation of not only the dynamics between developmental stages but also within every heartbeat.

As mentioned, the use of *ssNcan-GFP* as an HA sensor (De Angelis *et al.*, 2017) has allowed multiple groups to follow the deposition of this ECM component *live* (De Angelis *et al.*, 2017; Grassini *et al.*, 2018; Gunawan *et al.*, 2020; Derrick *et al.*, 2021). Since HA is one of the major components of the cardiac ECM, to validate the cardiac jelly segmentation approach used by *morphoHeart* (i.e. from negative space), segmentation of the cardiac ECM from *Tg(ubi:ssNcan-EGFP)* transgenic embryos (Grassini *et al.*, 2018) at the same developmental stages as those analysed in this study could be carried out. Additionally, to further understand the contribution of the myocardium and endocardium in the deposition of HA in the cardiac ECM, tissue-specific transgenic lines driving the expression of this HA sensor under the promoter of the pan-myocardial marker *myl7* or the endothelial markers *fli1a* or *kdrl*, respectively would serve useful. The quantification of the cardiac jelly volume contributed by each cellular tissue layer in these transgenic lines will also provide information regarding the tissue involved in establishing the ECM asymmetries identified in the early-developing zebrafish heart.

Analysis of the *spaw*/*hapln1a* double mutants exposed that most defects identified at early looping stages (i.e. 34-36hpf) are driven by the loss of Hapln1a link protein. As Hapln1a is expressed and deposited at disc stage, the altered composition of the nascent cardiac ECM in embryos with the *hapln1a* mutation could affect the morphogenetic events involved in the formation and jogging of the heart tube (i.e. disc rotation and involution). As this is the first study in which the cardiac jelly is investigated at heart disc stage, it is still unknown whether this early deposited ECM is used by the cardiomyocytes and endocardial cells as a substrate to migrate and form the tube or if it remains attached to the cellular layers whilst the rotation and involution events take place. An interesting way in which this could be investigated could be by creating a transgenic zebrafish line with a photoconvertible fluorophore (e.g. kaede fluorescent protein (Hatta, Tsujii and Omura, 2006)) fused to the HA sensor *ssNcan* (De Angelis *et al.*, 2017) and driven under myocardial and endocardial promoters (e.g. *Tg(myl7:ssNcan-kaede)*; *Tg(kdrl:ssNcan-kaede)*). Irreversible

photoconversion of this fluorescent protein from green to red in the heart disc before the onset of jogging will label the early deposited cardiac ECM. Imaging of the photoconverted embryos at stages post-tube formation (e.g. 28hpf) will aid the localisation of the photoconverted ECM confirming either of the described hypotheses.

Finally, to investigate if the regionalised ECM asymmetry is a driving factor for tissue intrinsic looping morphogenesis, experiments in which localised manipulations of the cardiac ECM components involved in its volumetric expansion or proteolytic degradation could be performed. For instance, taking advantage of the ECM protective properties of the Hapln1 proteins, a transgenic line driving the mis-expression (and deposition) of *hapln1a* or *hapln1b* at the anterior portion of the heart disc, the right side of the heart tube, or the inner curvature of the atrium using the *Gal4:UAS* system, could create symmetric cardiac jelly environments on either side of the heart, aiding the investigation the role of ECM asymmetries during heart looping. Inactivation of the endogenous transcription of proteolytic proteins (e.g. *cemip2*, *hyal2a*, *hyal2b*) could be attained using gene-specific caged morpholinos (cMO) in which the 3'-amine and 5'-carboxylic acid ends of the linear oligonucleotide is circularised using a photocleavable linker (Yamazoe *et al.*, 2012; Feng *et al.*, 2022). Activation of cMO knockdown activity of such hyaluronidases by targeted illumination of specific heart regions (e.g. right side of the heart tube) would avoid its endogenous expression and restrict its capability in maintaining ECM asymmetries. A similar experiment in which specific hyaluronidase activity can be regionally constrained could be achieved by using the Cre-*loxP* system with a fish line reporter in which the Cre DNA recombination is optically controlled (Brown and Deiters, 2019). For this experiment, for instance, a *myl7:Cre* line could be outcrossed to a line containing a '*lox-STOP-lox*' cassette placed upstream of the hyaluronidase of interest. In the resulting embryos, while the stop-cassette would prevent the translational expression of the selected hyaluronidase in myocardial cells without Cre recombination, photoactivation of the Cre would excise the stop-cassette allowing the endogenous expression of the gene. Both techniques (cMO and optically controlled Cre-*loxP* system) offer high spatial and temporal resolution, aiding the ability to manipulate regionally (i.e. in targeted regions of the heart) the expression and deposition of proteolytic components into the ECM, potentially informing its temporal requirement for ECM asymmetry maintenance, further testing the role of ECM regionalisation in directing looping morphogenesis.

Thesis References

1 References

Ahmad, N., Long, S. and Rebagliati, M. (2004) 'A Southpaw Joins the Roster: The Role of the Zebrafish nodal-related Gene Southpaw in Cardiac LR Asymmetry', *Trends in Cardiovascular Medicine*, 14(2), pp. 43–49. Available at: https://doi.org/10.1016/j.tcm.2003.11.001.

Akerberg, A.A. *et al.* (2019) 'Deep learning enables automated volumetric assessments of cardiac function in zebrafish', *Disease Models & Mechanisms*, 12(10), p. dmm040188. Available at: https://doi.org/10.1242/dmm.040188.

Alazmani, A. *et al.* (2016) 'Quantitative assessment of colorectal morphology: Implications for robotic colonoscopy', *Medical Engineering & Physics*, 38(2), pp. 148–154. Available at: https://doi.org/10.1016/j.medengphy.2015.11.018.

Andrey, P. and Boudier, T. (2006) 'Adaptive active contours (snakes) for the segmentation of complex structures in biological images'. Centre de Recherche Public Henri Tudor.

Antiga, L. *et al.* (2008) 'An image-based modeling framework for patient-specific computational hemodynamics', *Medical & Biological Engineering & Computing*, 46(11), pp. 1097–1112. Available at: https://doi.org/10.1007/s11517-008-0420-1.

Arrenberg, A.B. *et al.* (2010) 'Optogenetic Control of Cardiac Function', *Science*, 330(6006), pp. 971–974. Available at: https://doi.org/10.1126/science.1195929.

Aspberg, A. (2012) 'The Different Roles of Aggrecan Interaction Domains', *Journal of Histochemistry & Cytochemistry*, 60(12), pp. 987–996. Available at: https://doi.org/10.1369/0022155412464376.

Attili, S. and Richter, R.P. (2013) 'Self-assembly and elasticity of hierarchical proteoglycan–hyaluronan brushes', *Soft Matter*, 9(44), p. 10473. Available at: https://doi.org/10.1039/c3sm51213d.

Auman, H.J. *et al.* (2007) 'Functional Modulation of Cardiac Form through Regionally Confined Cell Shape Changes', *PLoS Biology*. Edited by B.L.M. Hogan, 5(3), pp. e53–e53. Available at: https://doi.org/10.1371/journal.pbio.0050053.

Bachir, A.I. *et al.* (2017) 'Actin-Based Adhesion Modules Mediate Cell Interactions with the Extracellular Matrix and Neighboring Cells', *Cold Spring Harbor Perspectives in Biology*, 9(7), pp. a023234–a023234. Available at: https://doi.org/10.1101/cshperspect.a023234.

Bajolle, F. *et al.* (2006) 'Rotation of the Myocardial Wall of the Outflow Tract Is Implicated in the Normal Positioning of the Great Arteries', *Circulation Research*, 98(3), pp. 421–428. Available at: https://doi.org/10.1161/01.RES.0000202800.85341.6e.

Baker, K., Holtzman, N.G. and Burdine, R.D. (2008) 'Direct and indirect roles for Nodal signaling in two axis conversions during asymmetric morphogenesis of the zebrafish heart', *Proceedings of the National Academy of Sciences*, 105(37), pp. 13924–13929. Available at: https://doi.org/10.1073/pnas.0802159105.

Bakkers, J. *et al.* (2004) 'Has2 is required upstream of Rac1 to govern dorsal migration of lateral cells during zebrafish gastrulation', *Development (Cambridge, England)*, 131(3), pp. 525–537. Available at: https://doi.org/10.1242/dev.00954.

Bakkers, J. (2011) 'Zebrafish as a model to study cardiac development and human cardiac disease.', *Cardiovascular research*, 91(2), pp. 279–88. Available at: https://doi.org/10.1093/cvr/cvr098.

Bakkers, J., Verhoeven, M.C. and Abdelilah-Seyfried, S. (2009) 'Shaping the zebrafish heart: From left-right axis specification to epithelial tissue morphogenesis', *Developmental Biology*, 330(2), pp. 213–220. Available at: https://doi.org/10.1016/j.ydbio.2009.04.011.

Baldwin, H.S. and Dees, E. (2012) 'Chapter 50 - Embryology and Physiology of the Cardiovascular System', in Gleason Christine A. and S.U. Devaskar (eds) *Avery's Diseases of the Newborn (Ninth Edition)*. Philadelpia: W.B. Saunders, pp. 699–713. Available at: https://doi.org/10.1016/B978-1-4377-0134-0.10050-2.

Barry, A. (1948) 'The functional significance of the cardiac jelly in the tubular heart of the chick embryo', *The Anatomical Record*, 102(3), pp. 289–298. Available at: https://doi.org/10.1002/ar.1091020304.

Bataille, S. *et al.* (2011) 'Association of PKD2 (Polycystin 2) Mutations With Left-Right Laterality Defects', *American Journal of Kidney Diseases*, 58(3), pp. 456–460. Available at: https://doi.org/10.1053/j.ajkd.2011.05.015.

Bayer, S. *et al.* (2019) 'Registration of vascular structures using a hybrid mixture model', *International Journal of Computer Assisted Radiology and Surgery*, 14(9), pp. 1507–1516. Available at: https://doi.org/10.1007/s11548-019-02007-y.

Becker, J.R. *et al.* (2012) 'In vivo natriuretic peptide reporter assay identifies chemical modifiers of hypertrophic cardiomyopathy signalling', *Cardiovascular Research*, 93(3), pp. 463–470. Available at: https://doi.org/10.1093/cvr/cvr350.

Beis, D. *et al.* (2005) 'Genetic and cellular analyses of zebrafish atrioventricular cushion and valve development', *Development (Cambridge, England)*, 132(18), pp. 4193–4204. Available at: https://doi.org/10.1242/dev.01970.

Berdougo, E. *et al.* (2003) 'Mutation of weak atrium/atrial myosin heavy chain disrupts atrial function and influences ventricular morphogenesis in zebrafish', *Development (Cambridge, England)*, 130(24), pp. 6121–6129. Available at: https://doi.org/10.1242/dev.00838.

Bertero, A. *et al.* (2015) 'Activin/Nodal signaling and NANOG orchestrate human embryonic stem cell fate decisions by controlling the H3K4me3 chromatin mark', *Genes & Development*, 29(7), pp. 702–717. Available at: https://doi.org/10.1101/gad.255984.114.

Bode-Lesniewska, B. *et al.* (1996) 'Distribution of the large aggregating proteoglycan versican in adult human tissues.', *Journal of Histochemistry & Cytochemistry*, 44(4), pp. 303–312. Available at: https://doi.org/10.1177/44.4.8601689.

de Boer, B.A. *et al.* (2012) 'Growth of the developing mouse heart: An interactive qualitative and quantitative 3D atlas', *Developmental Biology*, 368(2), pp. 203–213. Available at: https://doi.org/10.1016/j.ydbio.2012.05.001.

Boland, E., Quondamatteo, F. and Van Agtmael, T. (2021) 'The role of basement membranes in cardiac biology and disease', *Bioscience Reports*, 41(8), p. BSR20204185. Available at: https://doi.org/10.1042/BSR20204185.

Bonnans, C., Chou, J. and Werb, Z. (2014) 'Remodelling the extracellular matrix in development and disease', *Nature reviews. Molecular cell biology*, 15(12), pp. 786–801. Available at: https://doi.org/10.1038/nrm3904.

Bornhorst, D. *et al.* (2019) 'Biomechanical signaling within the developing zebrafish heart attunes endocardial growth to myocardial chamber dimensions', *Nature Communications*, 10(1), p. 4113. Available at: https://doi.org/10.1038/s41467-019-12068-x.

Bowley, G. *et al.* (2022) 'Zebrafish as a tractable model of human cardiovascular disease', *British Journal of*

Pharmacology, 179(5), pp. 900–917. Available at: https://doi.org/10.1111/bph.15473.

Bradski, G. (2000) 'The OpenCV Library', *Dr. Dobb's Journal of Software Tools* [Preprint].

Brennan, J., Norris, D.P. and Robertson, E.J. (2002) 'Nodal activity in the node governs left-right asymmetry.', *Genes & development*, 16(18), pp. 2339–44. Available at: https://doi.org/10.1101/gad.1016202.

Brett, J.R. (1964) 'The Respiratory Metabolism and Swimming Performance of Young Sockeye Salmon', *Journal of the Fisheries Research Board of Canada*, 21(5), pp. 1183–1226. Available at: https://doi.org/10.1139/f64-103.

Brown, D.R. *et al.* (2016) 'Advances in the Study of Heart Development and Disease Using Zebrafish.', *Journal of cardiovascular development and disease*, 3(2). Available at: https://doi.org/10.3390/jcdd3020013.

Brown, N.A. and Wolpert, L. (1990) 'The development of handedness in left/right asymmetry', *Development*, 109(1), pp. 1–9. Available at: https://doi.org/10.1242/dev.109.1.1.

Brown, S. *et al.* (2011) 'Activin/Nodal signaling controls divergent transcriptional networks in human embryonic stem cells and in endoderm progenitors', *Stem Cells (Dayton, Ohio)*, 29(8), pp. 1176–1185. Available at: https://doi.org/10.1002/stem.666.

Brown, W. and Deiters, A. (2019) 'Light-Activation of Cre Recombinase in Zebrafish Embryos through Genetic Code Expansion', *Methods in enzymology*, 624, pp. 265–281. Available at: https://doi.org/10.1016/bs.mie.2019.04.004.

Bruneau, B.G. (2008) 'The developmental genetics of congenital heart disease', *Nature*, 451(7181), pp. 943–948. Available at: https://doi.org/10.1038/nature06801.

Buckingham, M., Meilhac, S. and Zaffran, S. (2005) 'Building the mammalian heart from two sources of myocardial cells', *Nature Reviews Genetics*, 6(11), pp. 826–835. Available at: https://doi.org/10.1038/nrg1710.

Buijtendijk, M.F.J., Barnett, P. and van den Hoff, M.J.B. (2020) 'Development of the human heart', *American Journal of Medical Genetics. Part C, Seminars in Medical Genetics*, 184(1), pp. 7–22. Available at: https://doi.org/10.1002/ajmg.c.31778.

Burkhard, S.B. and Bakkers, J. (2018) 'Spatially resolved RNA-sequencing of the embryonic heart identifies a role for Wnt/β-catenin signaling in autonomic control of heart rate', *eLife*, 7, p. e31515. Available at: https://doi.org/10.7554/eLife.31515.

Bussmann, J., Bakkers, J. and Schulte-Merker, S. (2007) 'Early Endocardial Morphogenesis Requires Scl/Tal1', *PLOS Genetics*, 3(8), p. e140. Available at: https://doi.org/10.1371/journal.pgen.0030140.

Byron, A., Humphries, J.D. and Humphries, M.J. (2013) 'Defining the extracellular matrix using proteomics', *International Journal of Experimental Pathology*, 94(2), pp. 75–92. Available at: https://doi.org/10.1111/iep.12011.

Cai, C.-L. *et al.* (2003) 'Isl1 Identifies a Cardiac Progenitor Population that Proliferates Prior to Differentiation and Contributes a Majority of Cells to the Heart', *Developmental Cell*, 5(6), pp. 877–889. Available at: https://doi.org/10.1016/S1534-5807(03)00363-0.

Camenisch, T.D. *et al.* (2000) 'Disruption of hyaluronan synthase-2 abrogates normal cardiac morphogenesis and hyaluronan-mediated transformation of epithelium to mesenchyme', *The Journal of Clinical Investigation*, 106(3), pp. 349–360. Available at: https://doi.org/10.1172/JCI10272.

Campione, M. and Franco, D. (2016) 'Current Perspectives in Cardiac Laterality', *Journal of Cardiovascular*

Development and Disease, 3(4), p. 34. Available at: https://doi.org/10.3390/jcdd3040034.

Capon, S.J. *et al.* (2022) 'Endocardial identity is established during early somitogenesis by Bmp signalling acting upstream of *npas4l* and *etv2*', *Development*, 149(9), p. dev190421. Available at: https://doi.org/10.1242/dev.190421.

Captur, G. *et al.* (2016) 'Morphogenesis of myocardial trabeculae in the mouse embryo', *Journal of Anatomy*, 229(2), pp. 314–325. Available at: https://doi.org/10.1111/joa.12465.

Chang, H. *et al.* (2000) 'Smad5 is essential for left-right asymmetry in mice', *Developmental Biology*, 219(1), pp. 71–78. Available at: https://doi.org/10.1006/dbio.1999.9594.

Chen, J.N. *et al.* (1997) 'Left-right pattern of cardiac BMP4 may drive asymmetry of the heart in zebrafish', *Development (Cambridge, England)*, 124(21), pp. 4373–4382. Available at: https://doi.org/10.1242/dev.124.21.4373.

Chen, W.C.W. *et al.* (2016) 'Decellularized zebrafish cardiac extracellular matrix induces mammalian heart regeneration', *Science Advances*, 2(11), p. e1600844. Available at: https://doi.org/10.1126/sciadv.1600844.

Chi, Neil C. *et al.* (2008) 'Foxn4 directly regulates tbx2b expression and atrioventricular canal formation', *Genes & Development*, 22(6), pp. 734–739. Available at: https://doi.org/10.1101/gad.1629408.

Chi, Neil C *et al.* (2008) 'Genetic and Physiologic Dissection of the Vertebrate Cardiac Conduction System', *PLoS Biology*. Edited by B.L.M. Hogan, 6(5), p. e109. Available at: https://doi.org/10.1371/journal.pbio.0060109.

Chow, R.W.-Y. *et al.* (2018) 'Following Endocardial Tissue Movements via Cell Photoconversion in the Zebrafish Embryo', *Journal of Visualized Experiments: JoVE* [Preprint], (132). Available at: https://doi.org/10.3791/57290.

Chow, R.W.-Y. and Vermot, J. (2017) 'The rise of photoresponsive protein technologies applications in vivo: a spotlight on zebrafish developmental and cell biology', *F1000Research*, 6, p. 459. Available at: https://doi.org/10.12688/f1000research.10617.1.

Chowdhury, B. *et al.* (2017) 'Hyaluronidase 2 Deficiency Causes Increased Mesenchymal Cells, Congenital Heart Defects, and Heart Failure', *Circulation: Cardiovascular Genetics*, 10(1), p. e001598. Available at: https://doi.org/10.1161/CIRCGENETICS.116.001598.

Christoffels, V.M. *et al.* (2000) 'Chamber formation and morphogenesis in the developing mammalian heart', *Developmental Biology*, 223(2), pp. 266–278. Available at: https://doi.org/10.1006/dbio.2000.9753.

Christoffels, V.M., Burch, J.B.E. and Moorman, A.F.M. (2004) 'Architectural Plan for the Heart: Early Patterning and Delineation of the Chambers and the Nodes', *Trends in Cardiovascular Medicine*, 14(8), pp. 301–307. Available at: https://doi.org/10.1016/j.tcm.2004.09.002.

Colombo, S. *et al.* (2017) '*nkx* genes establish SHF cardiomyocyte progenitors at the arterial pole and pattern the venous pole through Isl1 repression', *Development*, p. dev.161497. Available at: https://doi.org/10.1242/dev.161497.

Cowman, M.K. and Matsuoka, S. (2005) 'Experimental approaches to hyaluronan structure', *Carbohydrate Research*, 340(5), pp. 791–809. Available at: https://doi.org/10.1016/j.carres.2005.01.022.

Cox, T.R. and Erler, J.T. (2011) 'Remodeling and homeostasis of the extracellular matrix: implications for fibrotic diseases and cancer', *Disease Models & Mechanisms*, 4(2), pp. 165–178. Available at: https://doi.org/10.1242/dmm.004077.

Crucean, A. *et al.* (2017) 'Re-evaluation of hypoplastic left heart syndrome from a developmental and morphological perspective', *Orphanet Journal of Rare Diseases*, 12(1), p. 138. Available at: https://doi.org/10.1186/s13023-017-0683-4.

de la Cruz, M.V. *et al.* (1977) 'Experimental study of the development of the truncus and the conus in the chick embryo.', *Journal of Anatomy*, 123(Pt 3), pp. 661–686.

Cui, Y. *et al.* (2019) 'Single-Cell Transcriptome Analysis Maps the Developmental Track of the Human Heart', *Cell Reports*, 26(7), pp. 1934-1950.e5. Available at: https://doi.org/10.1016/j.celrep.2019.01.079.

Cunningham, F. *et al.* (2022) 'Ensembl 2022', *Nucleic Acids Research*, 50(D1), pp. D988–D995. Available at: https://doi.org/10.1093/nar/gkab1049.

Cyphert, J.M., Trempus, C.S. and Garantziotis, S. (2015) 'Size Matters: Molecular Weight Specificity of Hyaluronan Effects in Cell Biology', *International Journal of Cell Biology*, 2015, pp. 1–8. Available at: https://doi.org/10.1155/2015/563818.

Dahle, Ø., Kumar, A. and Kuehn, M.R. (2010) 'Nodal Signaling Recruits the Histone Demethylase Jmjd3 to Counteract Polycomb-Mediated Repression at Target Genes', *Science signaling*, 3(127), p. ra48. Available at: https://doi.org/10.1126/scisignal.2000841.

Davis, C.L. (1924) 'The cardiac jelly of the chick embryo', *The Anatomical Record*, 27(4), pp. 201–202.

Davis, N.M. *et al.* (2008) 'The Chirality of Gut Rotation Derives from Left-Right Asymmetric Changes in the Architecture of the Dorsal Mesentery', *Developmental Cell*, 15(1), pp. 134–145. Available at: https://doi.org/10.1016/j.devcel.2008.05.001.

De Angelis, J.E. *et al.* (2017) 'Tmem2 Regulates Embryonic Vegf Signaling by Controlling Hyaluronic Acid Turnover', *Developmental Cell*, 40(2), pp. 123–136. Available at: https://doi.org/10.1016/j.devcel.2016.12.017.

De La Cruz, M.V., Sánchez-Gómez, C. and Palomino, M.A. (1989) 'The primitive cardiac regions in the straight tube heart (Stage 9-) and their anatomical expression in the mature heart', *Journal of Anatomy*, 165, pp. 121–131.

DeLaughter, D.M. *et al.* (2016) 'Single-Cell Resolution of Temporal Gene Expression during Heart Development', *Developmental Cell*, 39(4), pp. 480–490. Available at: https://doi.org/10.1016/j.devcel.2016.10.001.

Derrick, C.J. *et al.* (2021) 'Asymmetric Hapln1a drives regionalised cardiac ECM expansion and promotes heart morphogenesis in zebrafish development', *Cardiovascular Research* [Preprint]. Available at: https://doi.org/10.1093/cvr/cvab004.

Derrick, C.J. and Noël, E.S. (2021) 'The ECM as a driver of heart development and repair', *Development*, 148(dev191320). Available at: https://doi.org/10.1242/dev.191320.

Desgrange, A., Lokmer, J., *et al.* (2019) 'Standardised imaging pipeline for phenotyping mouse laterality defects and associated heart malformations, at multiple scales and multiple stages', *Disease Models & Mechanisms*, 12(7), p. dmm038356. Available at: https://doi.org/10.1242/dmm.038356.

Desgrange, A., Garrec, J.-F.L., *et al.* (2019) 'Transient Nodal signalling in left precursors coordinates opposed asymmetries shaping the heart loop', *bioRxiv*, p. 854463. Available at: https://doi.org/10.1101/854463.

Desgrange, A. *et al.* (2020) 'Transient Nodal Signaling in Left Precursors Coordinates Opposed Asymmetries Shaping the Heart Loop', *Developmental Cell*, 55(4), pp. 413-431.e6. Available at: https://doi.org/10.1016/j.devcel.2020.10.008.

Desgrange, A., Le Garrec, J.-F. and Meilhac, S.M. (2018) 'Left-right asymmetry in heart development and disease: forming the right loop', *Development*, 145(22), pp. dev162776–dev162776. Available at: https://doi.org/10.1242/DEV.162776.

Dewan, S. *et al.* (2017) 'Model of Human Fetal Growth in Hypoplastic Left Heart Syndrome: Reduced Ventricular Growth Due to Decreased Ventricular Filling and Altered Shape', *Frontiers in Pediatrics*, 5. Available at: https://doi.org/10.3389/fped.2017.00025.

Dietrich, A.-C. *et al.* (2014) 'Blood Flow and Bmp Signaling Control Endocardial Chamber Morphogenesis', *Developmental Cell*, 30(4), pp. 367–377. Available at: https://doi.org/10.1016/j.devcel.2014.06.020.

Domínguez, J.N. *et al.* (2012) 'Asymmetric Fate of the Posterior Part of the Second Heart Field Results in Unexpected Left/Right Contributions to Both Poles of the Heart', *Circulation Research*, 111(10), pp. 1323–1335. Available at: https://doi.org/10.1161/CIRCRESAHA.112.271247.

Dreos, R. *et al.* (2017) 'The eukaryotic promoter database in its 30th year: focus on non-vertebrate organisms', *Nucleic Acids Research*, 45(D1), pp. D51–D55. Available at: https://doi.org/10.1093/nar/gkw1069.

Eberlein, J. *et al.* (2021) 'Molecular and Cellular Mechanisms of Vascular Development in Zebrafish', *Life*, 11(10), p. 1088. Available at: https://doi.org/10.3390/life11101088.

El-Brolosy, M.A. *et al.* (2019) 'Genetic compensation triggered by mutant mRNA degradation', *Nature*, 568(7751), pp. 193–197. Available at: https://doi.org/10.1038/s41586-019-1064-z.

El-Brolosy, M.A. and Stainier, D.Y.R. (2017) 'Genetic compensation: A phenomenon in search of mechanisms', *PLOS Genetics*. Edited by C. Moens, 13(7), pp. e1006780–e1006780. Available at: https://doi.org/10.1371/journal.pgen.1006780.

Epstein, J.A., Aghajanian, H. and Singh, M.K. (2015) 'Semaphorin Signaling in Cardiovascular Development', *Cell Metabolism*, 21(2), pp. 163–173. Available at: https://doi.org/10.1016/j.cmet.2014.12.015.

Faltz, L.L. *et al.* (1979) 'Structure of the complex between hyaluronic acid, the hyaluronic acid-binding region, and the link protein of proteoglycan aggregates from the swarm rat chondrosarcoma.', *Journal of Biological Chemistry*, 254(4), pp. 1381–1387. Available at: https://doi.org/10.1016/S0021-9258(17)34213-8.

Fedorov, A. *et al.* (2012) '3D Slicer as an image computing platform for the Quantitative Imaging Network', *Magnetic Resonance Imaging*, 30(9), pp. 1323–1341. Available at: https://doi.org/10.1016/j.mri.2012.05.001.

Fei, P. *et al.* (2016) 'Cardiac Light-Sheet Fluorescent Microscopy for Multi-Scale and Rapid Imaging of Architecture and Function', *Scientific Reports*, 6(1), p. 22489. Available at: https://doi.org/10.1038/srep22489.

Feinberg, T. and Weiss, S.J. (2009) 'Developmental ECM Sculpting: Laying It Down and Cutting It Up', *Developmental Cell*, 17(5), pp. 584–586. Available at: https://doi.org/10.1016/j.devcel.2009.10.020.

Feng, Z. *et al.* (2022) 'The Development and Application of Opto-Chemical Tools in the Zebrafish', *Molecules*, 27(19), p. 6231. Available at: https://doi.org/10.3390/molecules27196231.

Foglia, M.J. *et al.* (2016) 'Multicolor mapping of the cardiomyocyte proliferation dynamics that construct the atrium', p. 9.

Foo, Y.Y. *et al.* (2021) 'Effects of extended pharmacological disruption of zebrafish embryonic heart biomechanical environment on cardiac function, morphology, and gene expression', *Developmental Dynamics*, 250(12), pp. 1759–1777. Available at: https://doi.org/10.1002/dvdy.378.

Fouquet, B. *et al.* (1997) 'Vessel Patterning in the Embryo of the Zebrafish: Guidance by Notochord', *Developmental Biology*, 183(1), pp. 37–48. Available at: https://doi.org/10.1006/dbio.1996.8495.

Fransen, M.E. and Lemanski, L.F. (1991) 'Extracellular matrix of the developing heart in normal and cardiac lethal mutant axolotls, Ambystoma mexicanum', *The Anatomical Record*, 230(3), pp. 387–405. Available at: https://doi.org/10.1002/ar.1092300312.

Frantz, C., Stewart, K.M. and Weaver, V.M. (2010) 'The extracellular matrix at a glance', *Journal of Cell Science*, 123(24), pp. 4195–4200. Available at: https://doi.org/10.1242/jcs.023820.

Frazier, D.T. and Narahashi, T. (1975) 'Tricaine (MS-222): effects on ionic conductances of squid axon membranes', *European Journal of Pharmacology*, 33(2), pp. 313–317. Available at: https://doi.org/10.1016/0014-2999(75)90175-2.

Fujiwara, T. *et al.* (2002) 'Distinct requirements for extra-embryonic and embryonic bone morphogenetic protein 4 in the formation of the node and primitive streak and coordination of left-right asymmetry in the mouse.', *Development*, 129(20), pp. 4685–4696.

Furtado, M.B. *et al.* (2008) 'BMP/SMAD1 signaling sets a threshold for the left/right pathway in lateral plate mesoderm and limits availability of SMAD4.', *Genes & development*, 22(21), pp. 3037–49. Available at: https://doi.org/10.1101/gad.1682108.

Geng, F.-S. *et al.* (2013) 'Semicircular canal morphogenesis in the zebrafish inner ear requires the function of *gpr126* (*lauscher*), an adhesion class G protein-coupled receptor gene', *Development*, 140(21), pp. 4362–4374. Available at: https://doi.org/10.1242/dev.098061.

Gittenberger-de Groot, A.C. *et al.* (2013) 'Embryology of the heart and its impact on understanding fetal and neonatal heart disease', *Seminars in Fetal and Neonatal Medicine*, 18(5), pp. 237–244. Available at: https://doi.org/10.1016/j.siny.2013.04.008.

Gjorevski, N. and Nelson, C.M. (2010) 'Endogenous patterns of mechanical stress are required for branching morphogenesis', *Integrative Biology*, 2(9), pp. 424–434. Available at: https://doi.org/10.1039/c0ib00040j.

Glickman, N.S. and Yelon, D. (2002) 'Cardiac development in zebrafish: coordination of form and function', *Seminars in Cell & Developmental Biology*, 13(6), pp. 507–513. Available at: https://doi.org/10.1016/S1084952102001040.

Gluck, J.M. *et al.* (2017) 'Biochemical and biomechanical properties of the pacemaking sinoatrial node extracellular matrix are distinct from contractile left ventricular matrix.', *PloS one*, 12(9), p. e0185125. Available at: https://doi.org/10.1371/journal.pone.0185125.

Goenezen, S., Rennie, M.Y. and Rugonyi, S. (2012) 'Biomechanics of early cardiac development', *Biomechanics and Modeling in Mechanobiology*, 11(8), pp. 1187–204. Available at: https://doi.org/10.1007/s10237-012-0414-7.

Govindan, J. and Iovine, M.K. (2015) 'Dynamic remodeling of the extra cellular matrix during zebrafish fin regeneration', *Gene Expression Patterns*, 19(1–2), pp. 21–29. Available at: https://doi.org/10.1016/j.gep.2015.06.001.

Grant, M.G. *et al.* (2017) 'Modeling Syndromic Congenital Heart Defects in Zebrafish', in *Current Topics in Developmental Biology*. Elsevier, pp. 1–40. Available at: https://doi.org/10.1016/bs.ctdb.2016.11.010.

Grassini, D.R. *et al.* (2018) 'Nppa and Nppb act redundantly during zebrafish cardiac development to confine AVC marker expression and reduce cardiac jelly volume.', *Development (Cambridge, England)*, 145(12), pp. dev160739–dev160739. Available at: https://doi.org/10.1242/dev.160739.

Grimes, D.T. *et al.* (2020) 'Left-right asymmetric heart jogging increases the robustness of dextral heart

looping in zebrafish', *Developmental Biology*, 459(2), pp. 79–86. Available at: https://doi.org/10.1016/j.ydbio.2019.11.012.

Grimes, D.T. and Burdine, R.D. (2017) 'Left–Right Patterning: Breaking Symmetry to Asymmetric Morphogenesis', *Trends in Genetics*, 33(9), pp. 616–628. Available at: https://doi.org/10.1016/j.tig.2017.06.004.

Gros, J. *et al.* (2009) 'Cell Movements at Hensen's Node Establish Left/Right Asymmetric Gene Expression in the Chick', *Science*, 324(5929), pp. 941–944. Available at: https://doi.org/10.1126/science.1172478.

Guerra, A. *et al.* (2018) 'Distinct myocardial lineages break atrial symmetry during cardiogenesis in zebrafish', *eLife*, 7, p. e32833. Available at: https://doi.org/10.7554/eLife.32833.

Gunawan, F. *et al.* (2019) 'Focal adhesions are essential to drive zebrafish heart valve morphogenesis', *Journal of Cell Biology*, 218(3), pp. 1039–1054. Available at: https://doi.org/10.1083/jcb.201807175.

Gunawan, F. *et al.* (2020) 'Nfatc1 Promotes Interstitial Cell Formation During Cardiac Valve Development in Zebrafish', *Circulation Research*, 126(8), pp. 968–984. Available at: https://doi.org/10.1161/CIRCRESAHA.119.315992.

Haack, T. and Abdelilah-Seyfried, S. (2016) 'The force within: endocardial development, mechanotransduction and signalling during cardiac morphogenesis', *Development*, 143(3), pp. 373–386. Available at: https://doi.org/10.1242/dev.131425.

Halpern, M.E. *et al.* (2008) 'Gal4/UAS Transgenic Tools and Their Application to Zebrafish', *Zebrafish*, 5(2), pp. 97–110. Available at: https://doi.org/10.1089/zeb.2008.0530.

Hami, D. *et al.* (2011) 'Zebrafish cardiac development requires a conserved secondary heart field', *Development*, 138(11), pp. 2389–2398. Available at: https://doi.org/10.1242/dev.061473.

Hamill, K.J. *et al.* (2009) 'Laminin deposition in the extracellular matrix: a complex picture emerges', *Journal of Cell Science*, 122(24), pp. 4409–4417. Available at: https://doi.org/10.1242/jcs.041095.

Handorf, A.M. *et al.* (2015) 'Tissue stiffness dictates development, homeostasis, and disease progression', *Organogenesis*, 11(1), pp. 1–15. Available at: https://doi.org/10.1080/15476278.2015.1019687.

Hardingham, T.E. (1979) 'The role of link-protein in the structure of cartilage proteoglycan aggregates.', *The Biochemical journal*, 177(1), pp. 237–47.

Harris, C.R. *et al.* (2020) 'Array programming with NumPy', *Nature*, 585(7825), pp. 357–362. Available at: https://doi.org/10.1038/s41586-020-2649-2.

Harvey, R.P. (2002) 'Patterning the vertebrate heart.', *Nature reviews. Genetics*, 3(7), pp. 544–556. Available at: http://dx.doi.org/10.1038/nrg843.

Hatano, S. *et al.* (2012) 'Versican/PG-M is essential for ventricular septal formation subsequent to cardiac atrioventricular cushion development', *Glycobiology*, 22(9), pp. 1268–1277. Available at: https://doi.org/10.1093/glycob/cws095.

Hatta, K., Tsujii, H. and Omura, T. (2006) 'Cell tracking using a photoconvertible fluorescent protein', *Nature Protocols*, 1(2), pp. 960–967. Available at: https://doi.org/10.1038/nprot.2006.96.

Hay, E.D. (ed.) (1991) *Cell Biology of Extracellular Matrix*. 2nd Ed. Boston, MA: Springer US. Available at: https://doi.org/10.1007/978-1-4615-3770-0.

Heckel, E. *et al.* (2015) 'Oscillatory Flow Modulates Mechanosensitive klf2a Expression through trpv4 and trpp2 during Heart Valve Development', *Current biology: CB*, 25(10), pp. 1354–1361. Available at: https://doi.org/10.1016/j.cub.2015.03.038.

Helker, C.S.M. *et al.* (2013) 'The zebrafish common cardinal veins develop by a novel mechanism: lumen

ensheathment', *Development*, 140(13), pp. 2776–2786. Available at: https://doi.org/10.1242/dev.091876.

Hernandez, L. *et al.* (2019) 'Tmem2 restricts atrioventricular canal differentiation by regulating degradation of hyaluronic acid', *Developmental Dynamics*, 248(12), pp. 1195–1210. Available at: https://doi.org/10.1002/dvdy.106.

Hierck, B.P. *et al.* (2007) 'Fluid shear stress controls cardiovascular development. A functionomic approach', *Wiener Klinische Wochenschrift*, 119(11-12 Suppl 1), pp. 10–13.

Hoebe, R.A. *et al.* (2007) 'Controlled light-exposure microscopy reduces photobleaching and phototoxicity in fluorescence live-cell imaging', *Nature Biotechnology*, 25(2), pp. 249–53. Available at: https://doi.org/10.1038/nbt1278.

Hoffman, J.I.E. (2013) 'The global burden of congenital heart disease : review article', *Cardiovascular Journal Of Africa*, 24(4), pp. 141–145. Available at: https://doi.org/10.5830/CVJA-2013-028.

Holtzman, N.G. *et al.* (2007) 'Endocardium is necessary for cardiomyocyte movement during heart tube assembly', *Development*, 134(12), pp. 2379–2386. Available at: https://doi.org/10.1242/dev.02857.

Holtzman, N.G. *et al.* (2016) 'Learning to fish with genetics: A primer on the vertebrate model Danio rerio', *Genetics*, 203(3), pp. 1069–1089. Available at: https://doi.org/10.1534/genetics.116.190843.

Honda, H. (2021) 'Left-handed cardiac looping by cell chirality is mediated by position-specific convergent extensions', *Biophysical Journal*, 120(23), pp. 5371–5383. Available at: https://doi.org/10.1016/j.bpj.2021.10.025.

Honda, H., Abe, T. and Fujimori, T. (2020) 'The Chiral Looping of the Embryonic Heart Is Formed by the Combination of Three Axial Asymmetries', *Biophysical Journal*, 118(3), pp. 742–752. Available at: https://doi.org/10.1016/j.bpj.2019.11.3397.

Hoog, T.G. *et al.* (2018) 'The effects of reduced hemodynamic loading on morphogenesis of the mouse embryonic heart', *Developmental Biology*, 442(1), pp. 127–137. Available at: https://doi.org/10.1016/j.ydbio.2018.07.007.

Howe, K. *et al.* (2013) 'The zebrafish reference genome sequence and its relationship to the human genome.', *Nature*, 496(7446), pp. 498–503. Available at: https://doi.org/10.1038/nature12111.

Hu, N. *et al.* (2000) 'Structure and function of the developing zebrafish heart', *The Anatomical Record*, 260(2), pp. 148–157. Available at: https://doi.org/10.1002/1097-0185(20001001)260:2<148::AID-AR50>3.0.CO;2-X.

Huisken, J. *et al.* (2004) 'Optical Sectioning Deep inside Live Embryos by Selective Plane Illumination Microscopy', *Science*, 305(5686), pp. 1007–1009. Available at: http://www.jstor.org/stable/3837569 (Accessed: 25 April 2022).

Humphrey, J.D., Dufresne, E.R. and Schwartz, M.A. (2014) 'Mechanotransduction and extracellular matrix homeostasis', *Nature Reviews Molecular Cell Biology*, 15(12), pp. 802–812. Available at: https://doi.org/10.1038/nrm3896.

Hunter, J.D. (2007) 'Matplotlib: A 2D Graphics Environment', *Computing in Science Engineering*, 9(3), pp. 90–95. Available at: https://doi.org/10.1109/MCSE.2007.55.

Hwang, W.Y. *et al.* (2013) 'Efficient genome editing in zebrafish using a CRISPR-Cas system', *Nature Biotechnology*, 31(3), pp. 227–229. Available at: https://doi.org/10.1038/nbt.2501.

Icardo, J.M. and Fernandez-Terán, A. (1987) 'Morphologic study of ventricular trabeculation in the embryonic chick heart', *Acta Anatomica*, 130(3), pp. 264–274. Available at:

https://doi.org/10.1159/000146455.

Itano, N. *et al.* (1999) 'Three isoforms of mammalian hyaluronan synthases have distinct enzymatic properties', *The Journal of Biological Chemistry*, 274(35), pp. 25085–25092. Available at: https://doi.org/10.1074/jbc.274.35.25085.

Ivanovitch, K., Temiño, S. and Torres, M. (2017) 'Live imaging of heart tube development in mouse reveals alternating phases of cardiac differentiation and morphogenesis', *eLife*. Edited by R.P. Harvey, 6, p. e30668. Available at: https://doi.org/10.7554/eLife.30668.

Jam, F.A. *et al.* (2018) 'Identification of juvenility-associated genes in the mouse hepatocytes and cardiomyocytes', *Scientific Reports*, 8(1), p. 3132. Available at: https://doi.org/10.1038/s41598-018-21445-3.

Jensen, B. *et al.* (2013) 'Evolution and development of the building plan of the vertebrate heart', *Biochimica et Biophysica Acta (BBA) - Molecular Cell Research*, 1833(4), pp. 783–794. Available at: https://doi.org/10.1016/j.bbamcr.2012.10.004.

Jeon, O. *et al.* (2007) 'Mechanical properties and degradation behaviors of hyaluronic acid hydrogels cross-linked at various cross-linking densities', *Carbohydrate Polymers*, 70(3), pp. 251–257. Available at: https://doi.org/10.1016/j.carbpol.2007.04.002.

Jonkman, J. *et al.* (2020) 'Tutorial: guidance for quantitative confocal microscopy', *Nature Protocols*, 15(5), pp. 1585–1611. Available at: https://doi.org/10.1038/s41596-020-0313-9.

Jou, C.J., Spitzer, K.W. and Tristani-Firouzi, M. (2010) 'Blebbistatin Effectively Uncouples the Excitation-Contraction Process in Zebrafish Embryonic Heart', *Cellular Physiology and Biochemistry*, 25(4–5), pp. 419–424.

Junker, J.P. *et al.* (2014) 'Genome-wide RNA Tomography in the Zebrafish Embryo', *Cell*, 159(3), pp. 662–675. Available at: https://doi.org/10.1016/j.cell.2014.09.038.

Kang, J.S. *et al.* (2004) 'Characterization of dermacan, a novel zebrafish lectican gene, expressed in dermal bones', *Mechanisms of Development*, 121(3), pp. 301–312. Available at: https://doi.org/10.1016/j.mod.2004.01.007.

Kang, J.S. *et al.* (2008) 'Molecular Cloning and Developmental Expression of a Hyaluronan and Proteoglycan Link Protein Gene, crtl1/hapln1 , in Zebrafish', *Zoological Science*, 25(9), pp. 912–918. Available at: https://doi.org/10.2108/zsj.25.912.

Karlsson, J., von Hofsten, J. and Olsson, P.-E. (2001) 'Generating Transparent Zebrafish: A Refined Method to Improve Detection of Gene Expression During Embryonic Development', *Marine Biotechnology*, 3(6), pp. 0522–0527. Available at: https://doi.org/10.1007/s1012601-0053-4.

Kaufmann, A. *et al.* (2012) 'Multilayer mounting enables long-term imaging of zebrafish development in a light sheet microscope', *Development*, 139(17), pp. 3242–3247. Available at: https://doi.org/10.1242/dev.082586.

Keegan, B.R., Meyer, D. and Yelon, D. (2004) 'Organization of cardiac chamber progenitors in the zebrafish blastula', 131(13), p. 11.

Keeley, D.P. *et al.* (2020) 'Comprehensive Endogenous Tagging of Basement Membrane Components Reveals Dynamic Movement within the Matrix Scaffolding', *Developmental Cell*, 54(1), pp. 60-74.e7. Available at: https://doi.org/10.1016/j.devcel.2020.05.022.

Kelly, R.G., Buckingham, M.E. and Moorman, A.F. (2014) 'Heart Fields and Cardiac Morphogenesis', *Cold Spring Harbor Perspectives in Medicine*, 4(10), pp. a015750–a015750. Available at: https://doi.org/10.1101/cshperspect.a015750.

Kiani, C. *et al.* (2002) 'Structure and function of aggrecan', *Cell Research*, 12(1), pp. 19–32. Available at: https://doi.org/10.1038/sj.cr.7290106.

Kidokoro, H. *et al.* (2018) 'The heart tube forms and elongates through dynamic cell rearrangement coordinated with foregut extension', *Development*, p. dev.152488. Available at: https://doi.org/10.1242/dev.152488.

Kim, K.H. *et al.* (2018) 'Myocardial Angiopoietin-1 Controls Atrial Chamber Morphogenesis by Spatiotemporal Degradation of Cardiac Jelly', *Cell Reports*, 23(8), pp. 2455–2466. Available at: https://doi.org/10.1016/j.celrep.2018.04.080.

Kimmel, C.B. *et al.* (1995) 'Stages of embryonic development of the zebrafish', *Developmental Dynamics*, 203(3), pp. 253–310. Available at: https://doi.org/10.1002/aja.1002030302.

Kiruthika, M. *et al.* (2019) 'Artery and Vein classification for hypertensive retinopathy', in *2019 3rd International Conference on Trends in Electronics and Informatics (ICOEI). 2019 3rd International Conference on Trends in Electronics and Informatics (ICOEI)*, pp. 244–248. Available at: https://doi.org/10.1109/ICOEI.2019.8862719.

Knudson, C.B. and Knudson, W. (1993) 'Hyaluronan-binding proteins in development, tissue homeostasis, and disease', *The FASEB Journal*, 7(13), pp. 1233–1241. Available at: https://doi.org/10.1096/fasebj.7.13.7691670.

Koefoed, K. *et al.* (2014) 'Cilia and coordination of signaling networks during heart development', *Organogenesis*, 10(1), pp. 108–125. Available at: https://doi.org/10.4161/org.27483.

Kohda, D. *et al.* (1996) 'Solution Structure of the Link Module: A Hyaluronan-Binding Domain Involved in Extracellular Matrix Stability and Cell Migration', *Cell*, 86(5), pp. 767–775. Available at: https://doi.org/10.1016/S0092-8674(00)80151-8.

Kugler, E.C. *et al.* (2022) 'Zebrafish vascular quantification: a tool for quantification of three-dimensional zebrafish cerebrovascular architecture by automated image analysis', *Development*, 149(3), p. dev199720. Available at: https://doi.org/10.1242/dev.199720.

Kula-Alwar, D. *et al.* (2021) 'Mef2c factors are required for early but not late addition of cardiomyocytes to the ventricle', *Developmental Biology*, 470, pp. 95–107. Available at: https://doi.org/10.1016/j.ydbio.2020.11.008.

Kwan, K.M. *et al.* (2007) 'The Tol2kit: A multisite gateway-based construction kit forTol2 transposon transgenesis constructs', *Developmental Dynamics*, 236(11), pp. 3088–3099. Available at: https://doi.org/10.1002/dvdy.21343.

Labun, K. *et al.* (2019) 'CHOPCHOP v3: expanding the CRISPR web toolbox beyond genome editing', *Nucleic Acids Research*, 47(W1), pp. W171–W174. Available at: https://doi.org/10.1093/nar/gkz365.

Lagendijk, A.K. *et al.* (2011) 'MicroRNA-23 restricts cardiac valve formation by inhibiting has2 and extracellular hyaluronic acid production', *Circulation Research*, 109(6), pp. 649–657. Available at: https://doi.org/10.1161/CIRCRESAHA.111.247635.

Lagendijk, A.K. *et al.* (2013) 'Hyaluronan: A critical regulator of endothelial-to-mesenchymal transition during cardiac valve formation', *Trends in Cardiovascular Medicine*, 23(5), pp. 135–142. Available at: https://doi.org/10.1016/j.tcm.2012.10.002.

Lagendijk, A.K. *et al.* (2017) 'Live imaging molecular changes in junctional tension upon VE-cadherin in zebrafish', *Nature Communications*, 8(1), p. 1402. Available at: https://doi.org/10.1038/s41467-017-01325-6.

Lazic, S. and Scott, I.C. (2011) 'Mef2cb regulates late myocardial cell addition from a second heart field-

like population of progenitors in zebrafish', *Developmental Biology*, 354(1), pp. 123–133. Available at: https://doi.org/10.1016/j.ydbio.2011.03.028.

Le Garrec, J.-F. *et al.* (2017) 'A predictive model of asymmetric morphogenesis from 3D reconstructions of mouse heart looping dynamics', *eLife*, 6. Available at: https://doi.org/10.7554/eLife.28951.

Lee, J. *et al.* (2013) 'Moving Domain Computational Fluid Dynamics to Interface with an Embryonic Model of Cardiac Morphogenesis', *PLOS ONE*, 8(8), p. e72924. Available at: https://doi.org/10.1371/journal.pone.0072924.

Lee, S. *et al.* (2012) 'Real-time in vivo imaging of the beating mouse heart at microscopic resolution', *Nature Communications*, 3(1), p. 1054. Available at: https://doi.org/10.1038/ncomms2060.

Legland, D., Arganda-Carreras, I. and Andrey, P. (2016) 'MorphoLibJ: integrated library and plugins for mathematical morphology with ImageJ', *Bioinformatics*, 32(22), pp. 3532–3534. Available at: https://doi.org/10.1093/bioinformatics/btw413.

Lenhart, K.F. *et al.* (2013) 'Integration of Nodal and BMP Signals in the Heart Requires FoxH1 to Create Left-Right Differences in Cell Migration Rates That Direct Cardiac Asymmetry', *PLoS Genetics*, 9(1). Available at: https://doi.org/10.1371/journal.pgen.1003109.

Levin, M. *et al.* (1997) 'Left/Right Patterning Signals and the Independent Regulation of Different Aspects ofSitusin the Chick Embryo', *Developmental Biology*, 189(1), pp. 57–67. Available at: https://doi.org/10.1006/dbio.1997.8662.

Levin, M. (2005) 'Left–right asymmetry in embryonic development: a comprehensive review', *Mechanisms of Development*, 122(1), pp. 3–25. Available at: https://doi.org/10.1016/j.mod.2004.08.006.

Lin, Y.-F., Swinburne, I. and Yelon, D. (2012) 'Multiple influences of blood flow on cardiomyocyte hypertrophy in the embryonic zebrafish heart', *Developmental Biology*, 362(2), pp. 242–253. Available at: https://doi.org/10.1016/j.ydbio.2011.12.005.

van der Linde, D. *et al.* (2011) 'Birth Prevalence of Congenital Heart Disease Worldwide: A Systematic Review and Meta-Analysis', *Journal of the American College of Cardiology*, 58(21), pp. 2241–2247. Available at: https://doi.org/10.1016/J.JACC.2011.08.025.

Lindsey, S.E., Butcher, J.T. and Yalcin, H.C. (2014) 'Mechanical regulation of cardiac development.', *Frontiers in physiology*, 5, pp. 318–318. Available at: https://doi.org/10.3389/fphys.2014.00318.

Lischik, C.Q., Adelmann, L. and Wittbrodt, J. (2019) 'Enhanced in vivo-imaging in medaka by optimized anaesthesia, fluorescent protein selection and removal of pigmentation', *PLOS ONE*, 14(3), p. e0212956. Available at: https://doi.org/10.1371/journal.pone.0212956.

Liu, A. *et al.* (2011) 'Quantifying blood flow and wall shear stresses in the outflow tract of chick embryonic hearts', *Computers & Structures*, 89(11), pp. 855–867. Available at: https://doi.org/10.1016/j.compstruc.2011.03.003.

Liu, J. *et al.* (2010) 'A dual role for ErbB2 signaling in cardiac trabeculation', *Development (Cambridge, England)*, 137(22), pp. 3867–3875. Available at: https://doi.org/10.1242/dev.053736.

Liu, J. *et al.* (2017) 'CRISPR/Cas9 in zebrafish: an efficient combination for human genetic diseases modeling', *Human Genetics*, 136(1), pp. 1–12. Available at: https://doi.org/10.1007/s00439-016-1739-6.

Liu, K. *et al.* (2019) 'Expanding the CRISPR Toolbox in Zebrafish for Studying Development and Disease', *Frontiers in Cell and Developmental Biology*, 7. Available at: https://www.frontiersin.org/articles/10.3389/fcell.2019.00013 (Accessed: 15 August 2022).

Lockhart, M. *et al.* (2011a) 'Extracellular matrix and heart development', *Birth Defects Research Part A: Clinical and Molecular Teratology*, 91(6), pp. 535–550. Available at: https://doi.org/10.1002/bdra.20810.

Lockhart, M. *et al.* (2011b) 'Extracellular matrix and heart development', *Birth Defects Research Part A: Clinical and Molecular Teratology*, 91(6), pp. 535–550. Available at: https://doi.org/10.1002/bdra.20810.

Lombardo, V.A. *et al.* (2019) 'Morphogenetic control of zebrafish cardiac looping by Bmp signaling', *Development*, p. dev.180091. Available at: https://doi.org/10.1242/dev.180091.

Long, K.R. *et al.* (2018) 'Extracellular Matrix Components HAPLN1, Lumican, and Collagen I Cause Hyaluronic Acid-Dependent Folding of the Developing Human Neocortex', *Neuron*, 99(4), pp. 702-719.e6. Available at: https://doi.org/10.1016/j.neuron.2018.07.013.

Long, S., Ahmad, N. and Rebagliati, M. (2003) 'The zebrafish nodal-related gene southpaw is required for visceral and diencephalic left-right asymmetry', *Development*, 130(11), pp. 2303–2316. Available at: https://doi.org/10.1242/dev.00436.

Lu, P. *et al.* (2011) 'Extracellular matrix degradation and remodeling in development and disease.', *Cold Spring Harbor perspectives in biology*, 3(12), pp. a005058–a005058. Available at: https://doi.org/10.1101/cshperspect.a005058.

Manasek, F.J., Burnside, M.B. and Waterman, R.E. (1972) 'Myocardial cell shape change as a mechanism of embryonic heart looping', *Developmental Biology*, 29(4), pp. 349–371. Available at: https://doi.org/10.1016/0012-1606(72)90077-2.

Männer, J. (2000) 'Cardiac looping in the chick embryo: a morphological review with special reference to terminological and biomechanical aspects of the looping process', *The Anatomical Record*, 259(3), pp. 248–262. Available at: https://doi.org/10.1002/1097-0185(20000701)259:3<248::AID-AR30>3.0.CO;2-K.

Männer, J. (2004) 'On rotation, torsion, lateralization, and handedness of the embryonic heart loop: New insights from a simulation model for the heart loop of chick embryos: Cardiac Looping', *The Anatomical Record Part A: Discoveries in Molecular, Cellular, and Evolutionary Biology*, 278A(1), pp. 481–492. Available at: https://doi.org/10.1002/ar.a.20036.

Männer, J. *et al.* (2008) 'High-resolution in vivo imaging of the cross-sectional deformations of contracting embryonic heart loops using optical coherence tomography', *Developmental Dynamics*, 237(4), pp. 953–961. Available at: https://doi.org/10.1002/dvdy.21483.

Männer, J. (2009) 'The anatomy of cardiac looping: A step towards the understanding of the morphogenesis of several forms of congenital cardiac malformations', *Clinical Anatomy*, 22(1), pp. 21–35. Available at: https://doi.org/10.1002/ca.20652.

Männer, J., Wessel, A. and Yelbuz, T.M. (2010) 'How does the tubular embryonic heart work? Looking for the physical mechanism generating unidirectional blood flow in the valveless embryonic heart tube', *Developmental Dynamics*, 239(4), pp. 1035–1046. Available at: https://doi.org/10.1002/dvdy.22265.

Marks, T.S. (2022) 'playsound'. Available at: https://github.com/TaylorSMarks/playsound (Accessed: 6 September 2022).

Matsumoto, K. *et al.* (2003) 'Distinct Interaction of Versican/PG-M with Hyaluronan and Link Protein*', *Journal of Biological Chemistry*, 278(42), pp. 41205–41212. Available at: https://doi.org/10.1074/jbc.M305060200.

Meilhac, S.M. *et al.* (2004) 'Oriented clonal cell growth in the developing mouse myocardium underlies

cardiac morphogenesis', *Journal of Cell Biology*, 164(1), pp. 97–109. Available at: https://doi.org/10.1083/jcb.200309160.

Meilhac, S.M. and Buckingham, M.E. (2018) 'The deployment of cell lineages that form the mammalian heart', *Nature Reviews Cardiology*, 15(11), pp. 705–724. Available at: https://doi.org/10.1038/s41569-018-0086-9.

Melching, L.I. and Roughley, P.J. (1990) 'Studies on the interaction of newly secreted proteoglycan subunits with hyaluronate in human articular cartilage', *Biochimica et Biophysica Acta (BBA) - General Subjects*, 1035(1), pp. 20–28. Available at: https://doi.org/10.1016/0304-4165(90)90168-V.

Merry, C.L.R. *et al.* (2022) 'Proteoglycans and Sulfated Glycosaminoglycans', in A. Varki et al. (eds) *Essentials of Glycobiology*. 4th edn. Cold Spring Harbor (NY): Cold Spring Harbor Laboratory Press. Available at: http://www.ncbi.nlm.nih.gov/books/NBK579925/ (Accessed: 26 September 2022).

Miao, Y. *et al.* (2020) 'Intrinsic Endocardial Defects Contribute to Hypoplastic Left Heart Syndrome', *Cell Stem Cell*, 27(4), pp. 574-589.e8. Available at: https://doi.org/10.1016/j.stem.2020.07.015.

Mickoleit, M. *et al.* (2014) 'High-resolution reconstruction of the beating zebrafish heart', *Nature Methods*, 11(9), pp. 919–922. Available at: https://doi.org/10.1038/nmeth.3037.

Mikhailov, A. (2019) 'Turbo, An Improved Rainbow Colormap for Visualization', *Google AI Blog*, 20 August. Available at: http://ai.googleblog.com/2019/08/turbo-improved-rainbow-colormap-for.html (Accessed: 2 June 2022).

Milan, D.J. *et al.* (2006) 'Notch1b and neuregulin are required for specification of central cardiac conduction tissue', *Development (Cambridge, England)*, 133(6), pp. 1125–1132. Available at: https://doi.org/10.1242/dev.02279.

Mine, N., Anderson, R.M. and Klingensmith, J. (2008) 'BMP antagonism is required in both the node and lateral plate mesoderm for mammalian left-right axis establishment', *Development*, 135(14), pp. 2425–2434. Available at: https://doi.org/10.1242/dev.018986.

Mittal, A. *et al.* (2013) 'Fibronectin and integrin alpha 5 play requisite roles in cardiac morphogenesis', *Developmental Biology*, 381(1), pp. 73–82. Available at: https://doi.org/10.1016/J.YDBIO.2013.06.010.

Mittal, N. *et al.* (2019) 'Versican is crucial for the initiation of cardiovascular lumen development in medaka (Oryzias latipes)', *Scientific Reports*, 9(1), p. 9475. Available at: https://doi.org/10.1038/s41598-019-45851-3.

Mjaatvedt, C.H. *et al.* (1998) 'The Cspg2 Gene, Disrupted in the hdf Mutant, Is Required for Right Cardiac Chamber and Endocardial Cushion Formation', *Developmental Biology*, 202(1), pp. 56–66. Available at: https://doi.org/10.1006/dbio.1998.9001.

Mjaatvedt, C.H. *et al.* (2001) 'The Outflow Tract of the Heart Is Recruited from a Novel Heart-Forming Field', *Developmental Biology*, 238(1), pp. 97–109. Available at: https://doi.org/10.1006/dbio.2001.0409.

del Monte-Nieto, G. *et al.* (2018) 'Control of cardiac jelly dynamics by NOTCH1 and NRG1 defines the building plan for trabeculation', *Nature*, 557(7705), pp. 439–445. Available at: https://doi.org/10.1038/s41586-018-0110-6.

Moorman, A.F.M., Brown, N. and Anderson, R.H. (2010) 'Chapter 3 - Embryology of the Heart', in *Paediatric Cardiology*. Elsevier, pp. 37–55. Available at: https://doi.org/10.1016/B978-0-7020-3064-2.00003-5.

Moorman et al. (2003) 'Development of the heart (1): formation of the cardiac chambers and arterial trunks', *Heart*, 89(1), pp. 806–14. Available at: https://doi.org/10.1136/heart.89.7.806.

Mouw, J.K., Ou, G. and Weaver, V.M. (2014) 'Extracellular matrix assembly: a multiscale deconstruction', *Nature Reviews Molecular Cell Biology*, 15(12), pp. 771–785. Available at: https://doi.org/10.1038/nrm3902.

Musy, M. *et al.* (2022) 'vedo: A python module for scientific analysis and visualization of 3D objects and point clouds based on VTK.' Zenodo. Available at: https://doi.org/10.5281/zenodo.6416103.

Nakamura, A. and Manasek, F.J. (1978) 'Experimental studies of the shape and structure of isolated cardiac jelly', *Development*, 43(1), pp. 167–183. Available at: https://doi.org/10.1242/dev.43.1.167.

Nakamura, A. and Manasek, F.J. (1981) 'An experimental study of the relation of cardiac jelly to the shape of the early chick embryonic heart', *Development*, 65(1), pp. 235–256. Available at: https://doi.org/10.1242/dev.65.1.235.

Nakanishi, T. *et al.* (eds) (2016) *Etiology and Morphogenesis of Congenital Heart Disease: From Gene Function and Cellular Interaction to Morphology*. Tokyo: Springer Japan. Available at: https://doi.org/10.1007/978-4-431-54628-3.

Necas, J. *et al.* (2008) 'Hyaluronic acid (hyaluronan): a review', *Veterinární Medicína*, 53(No. 8), pp. 397–411. Available at: https://doi.org/10.17221/1930-VETMED.

Noël, E.S. *et al.* (2013) 'A Nodal-independent and tissue-intrinsic mechanism controls heart-looping chirality', *Nature Communications*, 4. Available at: https://doi.org/10.1038/ncomms3754.

Notari, M. *et al.* (2018) 'The local microenvironment limits the regenerative potential of the mouse neonatal heart', *Science Advances*, 4(5), p. eaao5553. Available at: https://doi.org/10.1126/sciadv.aao5553.

Osher, S. and Fedkiw, R. (2003) 'Signed Distance Functions', in S. Osher and R. Fedkiw (eds) *Level Set Methods and Dynamic Implicit Surfaces*. New York, NY: Springer (Applied Mathematical Sciences), pp. 17–22. Available at: https://doi.org/10.1007/0-387-22746-6_2.

Passer, D. *et al.* (2016) 'Atypical Protein Kinase C-Dependent Polarized Cell Division Is Required for Myocardial Trabeculation', *Cell Reports*, 14(7), pp. 1662–1672. Available at: https://doi.org/10.1016/j.celrep.2016.01.030.

de Pater, E. *et al.* (2009) 'Distinct phases of cardiomyocyte differentiation regulate growth of the zebrafish heart', *Development*, 136(10), pp. 1633–1641. Available at: https://doi.org/10.1242/dev.030924.

Patra, C. *et al.* (2011) 'Nephronectin regulates atrioventricular canal differentiation via Bmp4-Has2 signaling in zebrafish', *Development*, 138(20), pp. 4499–4509. Available at: https://doi.org/10.1242/dev.067454.

Patten, B.M. (1922) 'The formation of the cardiac loop in the chick', 30(3), pp. 373–397. Available at: https://doi.org/10.1002/aja.1000300304.

Peal, D.S. *et al.* (2009) 'Chondroitin sulfate expression is required for cardiac atrioventricular canal formation', *Developmental Dynamics*, 238(12), pp. 3103–3110. Available at: https://doi.org/10.1002/dvdy.22154.

Pelster, B. and Bagatto, B. (2010) '7 - Respiration', in S.F. Perry et al. (eds) *Fish Physiology*. Academic Press (Zebrafish), pp. 289–309. Available at: https://doi.org/10.1016/S1546-5098(10)02907-9.

Peshkovsky, C., Totong, R. and Yelon, D. (2011) 'Dependence of cardiac trabeculation on neuregulin signaling and blood flow in zebrafish', *Developmental Dynamics: An Official Publication of the American Association of Anatomists*, 240(2), pp. 446–456. Available at: https://doi.org/10.1002/dvdy.22526.

Piccinelli, M. *et al.* (2009) 'A Framework for Geometric Analysis of Vascular Structures: Application to

Cerebral Aneurysms', *IEEE Transactions on Medical Imaging*, 28(8), pp. 1141–1155. Available at: https://doi.org/10.1109/TMI.2009.2021652.

Power, R.M. and Huisken, J. (2017) 'A guide to light-sheet fluorescence microscopy for multiscale imaging', *Nature Methods*, 14(4), pp. 360–373. Available at: https://doi.org/10.1038/nmeth.4224.

Priya, R. *et al.* (2020) 'Tension heterogeneity directs form and fate to pattern the myocardial wall', *Nature*, 588(7836), pp. 130–134. Available at: https://doi.org/10.1038/s41586-020-2946-9.

Quammen, C., Weigle, C. and Taylor II, R.M. (2011) 'Boolean Operations on Surfaces in VTK Without External Libraries', *The VTK Journal* [Preprint]. Available at: https://doi.org/10.54294/216g01.

Rahman, A. *et al.* (2021) 'A mouse model of hypoplastic left heart syndrome demonstrating left heart hypoplasia and retrograde aortic arch flow', *Disease Models & Mechanisms*, 14(11), p. dmm049077. Available at: https://doi.org/10.1242/dmm.049077.

Ramasubramanian, A. *et al.* (2013) 'On the role of intrinsic and extrinsic forces in early cardiac S-looping', *Developmental Dynamics*, 242(7), pp. 801–816. Available at: https://doi.org/10.1002/dvdy.23968.

Rambeau, P. *et al.* (2017) 'Reduced aggrecan expression affects cardiac outflow tract development in zebrafish and is associated with bicuspid aortic valve disease in humans', *International Journal of Cardiology*, 249, pp. 340–343. Available at: https://doi.org/10.1016/j.ijcard.2017.09.174.

Ramsdell, A.F. (2005) 'Left–right asymmetry and congenital cardiac defects: Getting to the heart of the matter in vertebrate left–right axis determination', *Developmental Biology*, 288(1), pp. 1–20. Available at: https://doi.org/10.1016/J.YDBIO.2005.07.038.

Rasouli, S.J. and Stainier, D.Y.R. (2017) 'Regulation of cardiomyocyte behavior in zebrafish trabeculation by Neuregulin 2a signaling', *Nature Communications*, 8(1), p. 15281. Available at: https://doi.org/10.1038/ncomms15281.

Rasse, T.M., Hollandi, R. and Horvath, P. (2020) 'OpSeF: Open Source Python Framework for Collaborative Instance Segmentation of Bioimages', *Frontiers in Bioengineering and Biotechnology*, 8. Available at: https://www.frontiersin.org/article/10.3389/fbioe.2020.558880 (Accessed: 25 April 2022).

Ray, P. *et al.* (2018) 'Intrinsic cellular chirality regulates left–right symmetry breaking during cardiac looping', *Proceedings of the National Academy of Sciences*, 115(50), pp. E11568–E11577. Available at: https://doi.org/10.1073/pnas.1808052115.

Reischauer, S. *et al.* (2014) 'Actin Binding GFP Allows 4D In Vivo Imaging of Myofilament Dynamics in the Zebrafish Heart and the Identification of Erbb2 Signaling as a Remodeling Factor of Myofibril Architecture', *Circulation Research*, 115(10), pp. 845–856. Available at: https://doi.org/10.1161/CIRCRESAHA.115.304356.

Reynaud, E.G. *et al.* (2008) 'Light sheet-based fluorescence microscopy: more dimensions, more photons, and less photodamage', *HFSP Journal*, 2(5), pp. 266–275. Available at: https://doi.org/10.2976/1.2974980.

Rodriguez, E. and Roughley, P. (2006) 'Link protein can retard the degradation of hyaluronan in proteoglycan aggregates', *Osteoarthritis and Cartilage*, 14(8), pp. 823–829. Available at: https://doi.org/10.1016/j.joca.2006.02.008.

Rohr, S., Otten, C. and Abdelilah-Seyfried, S. (2008) 'Asymmetric Involution of the Myocardial Field Drives Heart Tube Formation in Zebrafish', *Circulation Research*, 102(2), pp. e12–e19. Available at: https://doi.org/10.1161/CIRCRESAHA.107.165241.

Rottbauer, W. *et al.* (2002) 'Reptin and Pontin Antagonistically Regulate Heart Growth in Zebrafish Embryos', *Cell*, 111(5), pp. 661–672. Available at: https://doi.org/10.1016/S0092-8674(02)01112-1.

Roughley, P.J. and Mort, J.S. (2014) 'The role of aggrecan in normal and osteoarthritic cartilage', *Journal of Experimental Orthopaedics*, 1(1), p. 8. Available at: https://doi.org/10.1186/s40634-014-0008-7.

Roux, E. *et al.* (2020) 'Fluid Shear Stress Sensing by the Endothelial Layer', *Frontiers in Physiology*, 11. Available at: https://www.frontiersin.org/articles/10.3389/fphys.2020.00861 (Accessed: 30 September 2022).

Rozario, T. and DeSimone, D.W. (2010) 'The extracellular matrix in development and morphogenesis: A dynamic view', *Developmental Biology*, 341(1), pp. 126–140. Available at: https://doi.org/10.1016/j.ydbio.2009.10.026.

Samsa, L.A., Yang, B. and Liu, J. (2013) 'Embryonic cardiac chamber maturation: Trabeculation, conduction, and cardiomyocyte proliferation', *American Journal of Medical Genetics Part C: Seminars in Medical Genetics*, 163(3), pp. 157–168. Available at: https://doi.org/10.1002/ajmg.c.31366.

Savage, A.M. *et al.* (2019) 'tmem33 is essential for VEGF-mediated endothelial calcium oscillations and angiogenesis', *Nature Communications*, 10(1), p. 732. Available at: https://doi.org/10.1038/s41467-019-08590-7.

Schindelin, J. *et al.* (2012) 'Fiji: an open-source platform for biological-image analysis', *Nature Methods*, 9(7), pp. 676–682. Available at: https://doi.org/10.1038/nmeth.2019.

Schlaeppi, A. *et al.* (2021) 'Light Sheet Microscopy of Fast Cardiac Dynamics in Zebrafish Embryos', *JoVE (Journal of Visualized Experiments)*, (174), p. e62741. Available at: https://doi.org/10.3791/62741.

Schleich, J.-M. *et al.* (2013) 'An overview of cardiac morphogenesis', *Archives of Cardiovascular Diseases*, 106(11), pp. 612–623. Available at: https://doi.org/10.1016/J.ACVD.2013.07.001.

Schmid, B. *et al.* (2010) 'A high-level 3D visualization API for Java and ImageJ', *BMC Bioinformatics*, 11(1), p. 274. Available at: https://doi.org/10.1186/1471-2105-11-274.

Schottenfeld, J., Sullivan-Brown, J. and Burdine, R.D. (2007) 'Zebrafish curly up encodes a Pkd2 ortholog that restricts left-side-specific expression of southpaw', *Development*, 134(8), pp. 1605–1615. Available at: https://doi.org/10.1242/dev.02827.

Scuderi, G.J. and Butcher, J. (2017) 'Naturally Engineered Maturation of Cardiomyocytes', *Frontiers in Cell and Developmental Biology*, 5. Available at: https://www.frontiersin.org/article/10.3389/fcell.2017.00050 (Accessed: 9 June 2022).

Sehnert, A.J. *et al.* (2002) 'Cardiac troponin T is essential in sarcomere assembly and cardiac contractility', *Nature Genetics*, 31(1), pp. 106–110. Available at: https://doi.org/10.1038/ng875.

Sekiguchi, R. and Yamada, K.M. (2018) 'Basement membranes in development and disease', *Current topics in developmental biology*, 130, pp. 143–191. Available at: https://doi.org/10.1016/bs.ctdb.2018.02.005.

Semple, T.L., Peakall, R. and Tatarnic, N.J. (2019) 'A comprehensive and user-friendly framework for 3D-data visualisation in invertebrates and other organisms', *Journal of Morphology*, 280(2), pp. 223–231. Available at: https://doi.org/10.1002/jmor.20938.

Shewale, B. and Dubois, N. (2021) 'Of form and function: Early cardiac morphogenesis across classical and emerging model systems', *Seminars in Cell & Developmental Biology*, 118, pp. 107–118. Available at: https://doi.org/10.1016/j.semcdb.2021.04.025.

Shi, Y. *et al.* (2014) 'Bending and twisting the embryonic heart: a computational model for c-looping based on realistic geometry', *Frontiers in Physiology*, 5. Available at: https://www.frontiersin.org/articles/10.3389/fphys.2014.00297 (Accessed: 11 September 2022).

Shiratori, H. and Hamada, H. (2014) 'TGFβ signaling in establishing left–right asymmetry', *Seminars in Cell & Developmental Biology*, 32, pp. 80–84. Available at: https://doi.org/10.1016/j.semcdb.2014.03.029.

Sidhwani, P. and Yelon, D. (2019) 'Chapter Eleven - Fluid forces shape the embryonic heart: Insights from zebrafish', in D.M. Wellik (ed.) *Current Topics in Developmental Biology*. Academic Press (Organ Development), pp. 395–416. Available at: https://doi.org/10.1016/bs.ctdb.2018.12.009.

Simpson, M. *et al.* (2022) 'Hyaluronan', in A. Varki et al. (eds) *Essentials of Glycobiology*. 4th edn. Cold Spring Harbor (NY): Cold Spring Harbor Laboratory Press. Available at: http://www.ncbi.nlm.nih.gov/books/NBK579913/ (Accessed: 26 September 2022).

Sivakumar, A. *et al.* (2018) 'Midgut Laterality Is Driven by Hyaluronan on the Right', *Developmental Cell*, 46(5), pp. 533-551.e5. Available at: https://doi.org/10.1016/j.devcel.2018.08.002.

Smistad, E., Elster, A.C. and Lindseth, F. (2014) 'GPU accelerated segmentation and centerline extraction of tubular structures from medical images', *International Journal of Computer Assisted Radiology and Surgery*, 9(4), pp. 561–575. Available at: https://doi.org/10.1007/s11548-013-0956-x.

Smith, K.A. *et al.* (2008) 'Rotation and Asymmetric Development of the Zebrafish Heart Requires Directed Migration of Cardiac Progenitor Cells', *Developmental Cell*, 14(2), pp. 287–297. Available at: https://doi.org/10.1016/j.devcel.2007.11.015.

Song, R. and Zhang, L. (2020) 'Cardiac ECM: Its Epigenetic Regulation and Role in Heart Development and Repair', *International Journal of Molecular Sciences*, 21(22), p. 8610. Available at: https://doi.org/10.3390/ijms21228610.

Spicer, A.P., Joo, A. and Bowling, R.A. (2003) 'A Hyaluronan Binding Link Protein Gene Family Whose Members Are Physically Linked Adjacent to Chrondroitin Sulfate Proteoglycan Core Protein Genes', *Journal of Biological Chemistry*, 278(23), pp. 21083–21091. Available at: https://doi.org/10.1074/jbc.M213100200.

Srivastava, D. (2006) 'Making or Breaking the Heart: From Lineage Determination to Morphogenesis', *Cell*, 126(6), pp. 1037–1048. Available at: https://doi.org/10.1016/j.cell.2006.09.003.

Srivastava, D. and Olson, E.N. (2000) 'A genetic blueprint for cardiac development', *Nature*, 407(6801), pp. 221–226. Available at: https://doi.org/10.1038/35025190.

Stainier, D.Y. *et al.* (1996) 'Mutations affecting the formation and function of the cardiovascular system in the zebrafish embryo', *Development*, 123(1), pp. 285–292. Available at: https://doi.org/10.1242/dev.123.1.285.

Stainier, D.Y., Lee, R.K. and Fishman, M.C. (1993) 'Cardiovascular development in the zebrafish. I. Myocardial fate map and heart tube formation', *Development*, 119(1), pp. 31–40. Available at: https://doi.org/10.1242/dev.119.1.31.

Stainier, D.Y.R. and Fishman, M.C. (1992) 'Patterning the zebrafish heart tube: Acquisition of anteroposterior polarity', *Developmental Biology*, 153(1), pp. 91–101. Available at: https://doi.org/10.1016/0012-1606(92)90094-W.

Stankunas, K. *et al.* (2008) 'Endocardial Brg1 Represses ADAMTS1 to Maintain the Microenvironment for Myocardial Morphogenesis', *Developmental Cell*, 14(2), pp. 298–311. Available at: https://doi.org/10.1016/j.devcel.2007.11.018.

Stanley, E.G. *et al.* (2002) 'Efficient Cre-mediated deletion in cardiac progenitor cells conferred by a 3'UTR-ires-Cre allele of the homeobox gene Nkx2-5', *The International Journal of Developmental Biology*, 46(4), pp. 431–439.

Staudt, D. and Stainier, D. (2012) 'Uncovering the Molecular and Cellular Mechanisms of Heart

Development Using the Zebrafish', *Annual Review of Genetics*, 46(1), pp. 397–418. Available at: https://doi.org/10.1146/annurev-genet-110711-155646.

Staudt, D.W. *et al.* (2014) 'High-resolution imaging of cardiomyocyte behavior reveals two distinct steps in ventricular trabeculation', *Development*, 141(3), pp. 585–593. Available at: https://doi.org/10.1242/dev.098632.

Steed, E., Boselli, F. and Vermot, J. (2016) 'Hemodynamics driven cardiac valve morphogenesis', *Biochimica et Biophysica Acta (BBA) - Molecular Cell Research*, 1863(7), pp. 1760–1766. Available at: https://doi.org/10.1016/j.bbamcr.2015.11.014.

Stidham, R.W. *et al.* (2020) 'Assessing Small Bowel Stricturing and Morphology in Crohn's Disease Using Semi-automated Image Analysis', *Inflammatory Bowel Diseases*, 26(5), pp. 734–742. Available at: https://doi.org/10.1093/ibd/izz196.

Stoppel, W.L., Kaplan, D.L. and Black, L.D. (2016) 'Electrical and mechanical stimulation of cardiac cells and tissue constructs', *Advanced drug delivery reviews*, 96, pp. 135–155. Available at: https://doi.org/10.1016/j.addr.2015.07.009.

Strate, I., Tessadori, F. and Bakkers, J. (2015) 'Glypican4 promotes cardiac specification and differentiation by attenuating canonical Wnt and Bmp signaling', *Development*, 142(10), pp. 1767–1776. Available at: https://doi.org/10.1242/dev.113894.

Sun, J. *et al.* (2022) 'hapln1 Defines an Epicardial Cell Subpopulation Required for Cardiomyocyte Expansion During Heart Morphogenesis and Regeneration', *Circulation*, 146(1), pp. 48–63. Available at: https://doi.org/10.1161/CIRCULATIONAHA.121.055468.

Swinburne, I.A. *et al.* (2015) 'Improved Long-Term Imaging of Embryos with Genetically Encoded α-Bungarotoxin', *PLOS ONE*, 10(8), p. e0134005. Available at: https://doi.org/10.1371/journal.pone.0134005.

Sylva, M., Van den Hoff, M.J.B. and Moorman, A.F.M. (2014) 'Development of the human heart', *American Journal of Medical Genetics, Part A*, 164(6), pp. 1347–1371. Available at: https://doi.org/10.1002/ajmg.a.35896.

Taber, L.A. (2006) 'Biophysical mechanisms of cardiac looping', *International Journal of Developmental Biology*, 50(2–3), pp. 323–332. Available at: https://doi.org/10.1387/ijdb.052045lt.

Taber, L.A. and Perucchio, R. (2000) 'Modeling Heart Development', *Journal of elasticity and the physical science of solids*, 61(1), pp. 165–197. Available at: https://doi.org/10.1023/A:1011082712497.

Taylor, J.M. *et al.* (2011) 'Real-time optical gating for three-dimensional beating heart imaging', *Journal of Biomedical Optics*, 16(11), p. 116021. Available at: https://doi.org/10.1117/1.3652892.

Taylor, J.M. *et al.* (2019) 'Adaptive prospective optical gating enables day-long 3D time-lapse imaging of the beating embryonic zebrafish heart', *Nature Communications*, 10(1), p. 5173. Available at: https://doi.org/10.1038/s41467-019-13112-6.

Terpilowski, M.A. (2019) 'scikit-posthocs: Pairwise multiple comparison tests in Python', *Journal of Open Source Software*, 4(36), p. 1169. Available at: https://doi.org/10.21105/joss.01169.

Tessadori, F. *et al.* (2021) 'Twisting of the zebrafish heart tube during cardiac looping is a tbx5-dependent and tissue-intrinsic process', *eLife*. Edited by D.Y. Stainier, S.M. Meilhac, and M. Furthauer, 10, p. e61733. Available at: https://doi.org/10.7554/eLife.61733.

The pandas development team *et al.* (2022) 'pandas-dev/pandas: Pandas 1.4.2'. Zenodo. Available at: https://doi.org/10.5281/zenodo.6408044.

Thisse, C. and Thisse, B. (2008) 'High-resolution in situ hybridization to whole-mount zebrafish embryos', *Nature Protocols*, 3(1), pp. 59–69. Available at: https://doi.org/10.1038/nprot.2007.514.

Thompson, M.A. *et al.* (1998) 'The cloche and spadetail genes differentially affect hematopoiesis and vasculogenesis', *Developmental Biology*, 197(2), pp. 248–269. Available at: https://doi.org/10.1006/dbio.1998.8887.

Thompson, R.P., Abercrombie, V. and Wong, M. (1987) 'Morphogenesis of the truncus arteriosus of the chick embryo heart: Movements of autoradiographic tattoos during septation', *The Anatomical Record*, 218(4), pp. 434–440. Available at: https://doi.org/10.1002/ar.1092180411.

Tien, J.Y.L. and Spicer, A.P. (2005) 'Three vertebrate hyaluronan synthases are expressed during mouse development in distinct spatial and temporal patterns', *Developmental Dynamics: An Official Publication of the American Association of Anatomists*, 233(1), pp. 130–141. Available at: https://doi.org/10.1002/dvdy.20328.

Toole, B.P. (1990) 'Hyaluronan and its binding proteins, the hyaladherins', *Current Opinion in Cell Biology*, 2(5), pp. 839–844. Available at: https://doi.org/10.1016/0955-0674(90)90081-o.

Toole, B.P. (2001) 'Hyaluronan in morphogenesis', *Seminars in Cell & Developmental Biology*, 12(2), pp. 79–87. Available at: https://doi.org/10.1006/scdb.2000.0244.

Toole, B.P., Yu, Q. and Underhill, C.B. (2001) 'Hyaluronan and hyaluronan-binding proteins. Probes for specific detection', *Methods in Molecular Biology (Clifton, N.J.)*, 171, pp. 479–485. Available at: https://doi.org/10.1385/1-59259-209-0:479.

Trivedi, V. *et al.* (2020) 'Imaging the Beating Heart with Macroscopic Phase Stamping', *arXiv:2011.01688 [q-bio]* [Preprint]. Available at: http://arxiv.org/abs/2011.01688 (Accessed: 25 April 2022).

Truong, T.V. *et al.* (2020) 'High-contrast, synchronous volumetric imaging with selective volume illumination microscopy', *Communications Biology*, 3(1), pp. 1–8. Available at: https://doi.org/10.1038/s42003-020-0787-6.

Tu, S. and Chi, N.C. (2012) 'Zebrafish models in cardiac development and congenital heart birth defects', *Differentiation*, 84(1), pp. 4–16. Available at: https://doi.org/10.1016/j.diff.2012.05.005.

Uribe, V. *et al.* (2018) 'In vivo analysis of cardiomyocyte proliferation during trabeculation', *Development*, 145(14). Available at: https://doi.org/10.1242/dev.164194.

Üveges, Á. *et al.* (2019) 'Three-dimensional evaluation of the spatial morphology of stented coronary artery segments in relation to restenosis', *The International Journal of Cardiovascular Imaging*, 35(10), pp. 1755–1763. Available at: https://doi.org/10.1007/s10554-019-01628-3.

Vedula, V. *et al.* (2017) 'A method to quantify mechanobiologic forces during zebrafish cardiac development using 4-D light sheet imaging and computational modeling', *PLOS Computational Biology*. Edited by S.L. Diamond, 13(10), p. e1005828. Available at: https://doi.org/10.1371/journal.pcbi.1005828.

Veerkamp, J. *et al.* (2013) 'Unilateral Dampening of Bmp Activity by Nodal Generates Cardiac Left-Right Asymmetry', *Developmental Cell*, 24(6), pp. 660–667. Available at: https://doi.org/10.1016/j.devcel.2013.01.026.

Verigakis, G. (2022) 'verigak/progress'. Available at: https://github.com/verigak/progress (Accessed: 6 September 2022).

Vermot, J. *et al.* (2009) 'Reversing Blood Flows Act through klf2a to Ensure Normal Valvulogenesis in the Developing Heart', *PLoS Biology*. Edited by H. Hamada, 7(11), p. e1000246. Available at: https://doi.org/10.1371/journal.pbio.1000246.

Virtanen, P. *et al.* (2020) 'SciPy 1.0: fundamental algorithms for scientific computing in Python', *Nature Methods*, 17(3), pp. 261–272. Available at: https://doi.org/10.1038/s41592-019-0686-2.

Waldo, K.L. *et al.* (2001) 'Conotruncal myocardium arises from a secondary heart field', *Development (Cambridge, England)*, 128(16), pp. 3179–3188. Available at: https://doi.org/10.1242/dev.128.16.3179.

Walker, C., Mojares, E. and del Río Hernández, A. (2018) 'Role of Extracellular Matrix in Development and Cancer Progression', *International Journal of Molecular Sciences*, 19(10), p. 3028. Available at: https://doi.org/10.3390/ijms19103028.

Walma, D.A.C. and Yamada, K.M. (2020) 'The extracellular matrix in development', *Development*, 147(10). Available at: https://doi.org/10.1242/dev.175596.

Walsh, E.C. and Stainier, D.Y. (2001) 'UDP-glucose dehydrogenase required for cardiac valve formation in zebrafish', *Science (New York, N.Y.)*, 293(5535), pp. 1670–1673. Available at: https://doi.org/10.1126/science.293.5535.1670.

Walt, S. van der *et al.* (2014) 'scikit-image: image processing in Python', *PeerJ*, 2, p. e453. Available at: https://doi.org/10.7717/peerj.453.

Warren, K.S. and Fishman, M.C. (1998) '"Physiological genomics": mutant screens in zebrafish', *American Journal of Physiology-Heart and Circulatory Physiology*, 275(1), pp. H1–H7. Available at: https://doi.org/10.1152/ajpheart.1998.275.1.H1.

Weber, M. *et al.* (2017) 'Cell-accurate optical mapping across the entire developing heart', *eLife*, 6, p. e28307. Available at: https://doi.org/10.7554/eLife.28307.

Weigel, P.H. and DeAngelis, P.L. (2007) 'Hyaluronan Synthases: A Decade-plus of Novel Glycosyltransferases*', *Journal of Biological Chemistry*, 282(51), pp. 36777–36781. Available at: https://doi.org/10.1074/jbc.R700036200.

Westin, J. and Lardelli, M. (1997) 'Three novel Notch genes in zebrafish: implications for vertebrate Notch gene evolution and function', *Development Genes and Evolution*, 207(1), pp. 51–63. Available at: https://doi.org/10.1007/s004270050091.

Wirrig, E.E. *et al.* (2007) 'Cartilage link protein 1 (Crtl1), an extracellular matrix component playing an important role in heart development', *Developmental Biology*, 310(2), pp. 291–303. Available at: https://doi.org/10.1016/J.YDBIO.2007.07.041.

Wittig, J.G. and Münsterberg, A. (2016) 'The Early Stages of Heart Development: Insights from Chicken Embryos', *Journal of Cardiovascular Development and Disease*, 3(2), p. 12. Available at: https://doi.org/10.3390/jcdd3020012.

Wittig, J.G. and Münsterberg, A. (2020) 'The Chicken as a Model Organism to Study Heart Development', *Cold Spring Harbor Perspectives in Biology*, 12(8), p. a037218. Available at: https://doi.org/10.1101/cshperspect.a037218.

Wu, Y.J. *et al.* (2005) 'The interaction of versican with its binding partners', *Cell Research*, 15(7), pp. 483–494. Available at: https://doi.org/10.1038/sj.cr.7290318.

Yalcin, H.C. *et al.* (2011) 'Hemodynamic patterning of the avian atrioventricular valve', *Developmental Dynamics: An Official Publication of the American Association of Anatomists*, 240(1), pp. 23–35. Available at: https://doi.org/10.1002/dvdy.22512.

Yamaguchi, Y. (2000) 'Lecticans: organizers of the brain extracellular matrix', *Cellular and Molecular Life Sciences CMLS*, 57(2), pp. 276–289. Available at: https://doi.org/10.1007/PL00000690.

Yamamura, H. *et al.* (1997) 'A heart segmental defect in the anterior-posterior axis of a transgenic mutant mouse', *Developmental Biology*, 186(1), pp. 58–72. Available at: https://doi.org/10.1006/DBIO.1997.8559.

Yamazoe, S. *et al.* (2012) 'Cyclic Caged Morpholinos: Conformationally Gated Probes of Embryonic Gene Function', *Angewandte Chemie International Edition*, 51(28), pp. 6908–6911. Available at: https://doi.org/10.1002/anie.201201690.

Yelon, D., Horne, S.A. and Stainier, D.Y.R. (1999) 'Restricted Expression of Cardiac Myosin Genes Reveals Regulated Aspects of Heart Tube Assembly in Zebrafish', *Developmental Biology*, 214(1), pp. 23–37. Available at: https://doi.org/10.1006/dbio.1999.9406.

Zanin, M.K.B. *et al.* (1999) 'Distinct spatial and temporal distributions of aggrecan and versican in the embryonic chick heart', *The Anatomical Record*, 256(4), pp. 366–380. Available at: https://doi.org/10.1002/(SICI)1097-0185(19991201)256:4<366::AID-AR4>3.0.CO;2-#.

Zhou, Y. *et al.* (2011) 'Latent TGF-β binding protein 3 identifies a second heart field in zebrafish', *Nature*, 474(7353), pp. 645–648. Available at: https://doi.org/10.1038/nature10094.

Zimmermann, J. *et al.* (2021) 'On the impact of vessel wall stiffness on quantitative flow dynamics in a synthetic model of the thoracic aorta', *Scientific Reports*, 11(1), p. 6703. Available at: https://doi.org/10.1038/s41598-021-86174-6.

APPENDIX 1

ESC European Society of Cardiology

Cardiovascular Research
doi:10.1093/cvr/cvab004

Asymmetric Hapln1a drives regionalized cardiac ECM expansion and promotes heart morphogenesis in zebrafish development

Christopher J. Derrick [1,‡], Juliana Sánchez-Posada [1,‡], Farah Hussein [1], Federico Tessadori [2], Eric J.G. Pollitt [1], Aaron M. Savage [3], Robert N. Wilkinson [3†], Timothy J. Chico[3], Fredericus J. van Eeden[1], Jeroen Bakkers [2], and Emily S. Noël [1*]

[1]Department of Biomedical Science, University of Sheffield, Western Bank, Sheffield, S10 2TN, UK[2]Hubrecht Institute for Developmental and Stem Cell Biology, Uppsalalaan 8, 3584 CT, Utrecht, Netherlands[3]Department of Infection, Immunity and Cardiovascular Disease, University of Sheffield, Medical School, Beech Hill Road, Sheffield, S10 2RX, UK

Received 26 November 2019; editorial decision 30 December 2020; accepted 8 January 2021

Aims Vertebrate heart development requires the complex morphogenesis of a linear tube to form the mature organ, a process essential for correct cardiac form and function, requiring coordination of embryonic laterality, cardiac growth, and regionalized cellular changes. While previous studies have demonstrated broad requirements for extracellular matrix (ECM) components in cardiac morphogenesis, we hypothesized that ECM regionalization may fine tune cardiac shape during heart development.

Methods and results Using live *in vivo* light sheet imaging of zebrafish embryos, we describe a left-sided expansion of the ECM between the myocardium and endocardium prior to the onset of heart looping and chamber ballooning. Analysis using an ECM sensor revealed the cardiac ECM is further regionalized along the atrioventricular axis. Spatial transcriptomic analysis of gene expression in the heart tube identified candidate genes that may drive ECM expansion. This approach identified regionalized expression of *hapln1a,* encoding an ECM cross-linking protein. Validation of transcriptomic data by *in situ* hybridization confirmed regionalized *hapln1a* expression in the heart, with highest levels of expression in the future atrium and on the left side of the tube, overlapping with the observed ECM expansion. Analysis of CRISPR-Cas9-generated *hapln1a* mutants revealed a reduction in atrial size and reduced chamber ballooning. Loss-of-function analysis demonstrated that ECM expansion is dependent upon Hapln1a, together supporting a role for Hapln1a in regionalized ECM modulation and cardiac morphogenesis. Analysis of *hapln1a* expression in zebrafish mutants with randomized or absent embryonic left–right asymmetry revealed that laterality cues position *hapln1a*-expressing cells asymmetrically in the left side of the heart tube.

Conclusion We identify a regionalized ECM expansion in the heart tube which promotes correct heart development, and propose a novel model whereby embryonic laterality cues orient the axis of ECM asymmetry in the heart, suggesting these two pathways interact to promote robust cardiac morphogenesis.

* Corresponding author. Tel: +44 1142 222311; fax: +44 1142 222787, E-mail: e.s.noel@sheffield.ac.uk
† Present address. School of Life Sciences, University of Nottingham, Queen's Medical Centre, Nottingham, NG7 2UH, UK.
‡ The first two authors contributed equally to the study.

Graphical Abstract

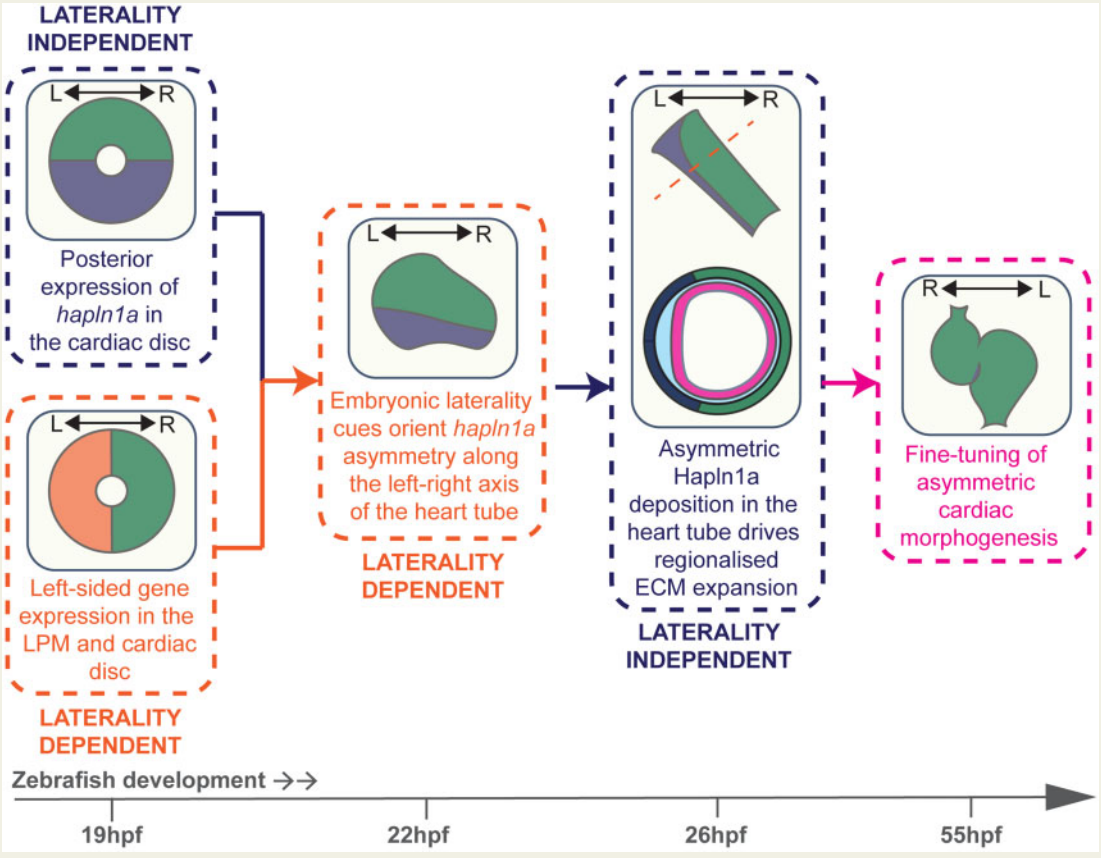

Keywords Heart morphogenesis • Extracellular matrix • Laterality • Zebrafish • Heart development

1. Introduction

Congenital heart defects are the most common human birth abnormality, with an incidence of approximately 1% of live births.[1] These structural malformations arise due to abnormal morphogenesis and maturation of the heart during embryonic development. A key stage in cardiac development occurs when the heart transitions from a linear tube to an asymmetric organ, a process including initial looping morphogenesis of the tube and subsequent ballooning of the cardiac chambers. Correct cardiac morphogenesis is vital for ensuring normal blood flow through the heart, proper chamber and vessel alignment, valve formation and septation, and is therefore a tightly controlled process requiring intricate coordination of heart-extrinsic signalling cues, cardiac growth, and tissue-intrinsic changes in cell shape.[2]

The requirement for embryonic left–right signalling pathways in promoting directionality of heart morphogenesis is well established, with asymmetric Nodal signalling playing a key role in driving rightward looping of the linear heart tube in multiple organisms.[3–6] However, while embryos with defective asymmetric Nodal signalling display disrupted directionality of heart looping, the heart still undergoes looping morphogenesis.[5–7] This indicates that while extrinsic asymmetric cues provide directional information to the heart, regionalized intrinsic signals may help to promote morphogenesis. How the interplay of both extrinsic and intrinsic regionalized signalling and cell behaviours ensures the coordination of directionality and morphogenesis required to orient and shape the heart remains unknown.

The developing heart tube is composed of two tissue layers: an outer tube of myocardium surrounding an inner layer of specialized endothelial cells (endocardium). These two layers are separated by an extracellular matrix (ECM), termed the cardiac jelly. The ECM consists of collagens, glycosaminoglycans, and glycoproteins and plays a pivotal role in providing mechanical cues and modulating extracellular signalling in the heart during cardiac development.[8] Classic embryological experiments demonstrated that the cardiac jelly is important for heart morphogenesis[9] while more recent studies have begun to identify specific ECM constituents with distinct roles in heart development.[10–16] Hyaluronic acid (HA) is a glycosaminoglycan with conserved roles in heart tube formation, cardiac morphogenesis and atrioventricular valve development,[10,17,18] suggesting multiple requirements for HA at various stages during cardiac development. While broad disruption of the cardiac ECM has profound effects on heart morphology,[17,19] it is likely that the ECM plays distinct functions in regulating regionalized morphogenesis of the heart tube.

In this study, we demonstrate that the cardiac ECM of the zebrafish heart tube exhibits regionalized expansion prior to onset of heart tube morphogenesis, with a thicker ECM in both the left side and future atrium of the heart tube. Loss-of-function analyses demonstrate that this

ECM expansion is dependent upon the ECM cross-linking protein Hyaluronan and Proteoglycan Link Protein 1a (Hapln1a), and that Hapln1a promotes heart morphogenesis. Finally, we show that while asymmetric *hapln1a* expression is independent of laterality cues, the axis of *hapln1a* asymmetry in the heart is dictated by embryonic laterality, supporting a new model where embryonic left–right asymmetry tightly defines the orientation of ECM asymmetry in the heart tube, and together these pathways fine tune asymmetric cardiac morphogenesis.

2. Methods

2.1 Zebrafish maintenance

Adult zebrafish were maintained according to standard laboratory conditions. The following lines were used: AB, *Tg(myl7:eGFP)*,[20] *Tg(myl7:lifeActGFP)*,[21] *Tg(fli1a:AC-TagRFP)*,[22] *spaw*^{t30973} [7], *Tg(lft2BAC:Gal4FF); Tg(UAS;RFP)*, *pkd2*^{hu2173}, *hapln1a*$^{\Delta187}$ (allele designation *hapln1a*^{sh611}), *hapln1a*$^{\Delta241}$ (allele designation *hapln1a*^{sh580}). Embryos older than 24hpf were treated with 0.2 mM 1-phenyl-2-thiourea (PTU) in E3 medium to inhibit melanin production. All animals were euthanized by immersion in overdose of Tricaine methanesulfonate (1.33 g/L). Animal work was approved by the local Animal Welfare and Ethical Review Body (AWERB) at the University of Sheffield, conducted in accordance with UK Home Office Regulations under PPLs 70/8588 and PA1C7120E, and in line with the guidelines from Directive 2010/63/EU of the European Parliament on the protection of animals used for scientific purposes.

2.2 Generation of *hapln1a* mutants

CRISPR guide RNAs (gRNAs) were designed to target the putative promoter region of *hapln1a* (GRCz11: ENSDART00000122966.4, g1: 5′-TCGTCTCTCTCTAAGGGGAGGGG-3′) and downstream of the translation start site (g2: 5′-GATGATTGCTCTGTTTTCTGTGG-3′). Sequence-specific CRISPR RNAs (crRNA, Merck) were resuspended in MilliQ water to 21.4 µM, and injected with equimolar tracrRNA (Merck) together with Cas9 protein (NEB M0386T) into 1-cell stage embryos in a volume of 1nl. CRISPR-Cas9-injected embryos were raised to adulthood and individuals transmitting germline promoter deletions were identified by PCR using the following primers: forward 5′-ACATTTTGCATGCCCTCGAA-3′; reverse 5′-TGCATCCTGGACCTTCATTCA-3′. Promoter deletions were identified by Sanger sequencing. F0 founders transmitting a desirable mutation were established as stable lines at F2. Two *hapln1a* promoter deletion alleles were recovered: *hapln1a*$^{\Delta187}$ and *hapln1a*$^{\Delta241}$.

2.3 mRNA *in situ* hybridization

Embryos were fixed overnight in 4% PFA, and mRNA *in situ* hybridizations carried out as previously described.[7] Fluorescent *in situ* hybridizations were performed using the TSA kit (Perkin-Elmer).[23] Primers used to generate new mRNA *in situ* probe constructs and information on published probes are detailed in Supplementary material online, *Methods*. Riboprobes were transcribed from linearized template in the presence of DIG-11-UTP or Fluorescein-11-UTP (Roche).

2.4 Immunohistochemistry

Embryos were fixed overnight in 4% PFA with 4% sucrose at 4°C. For Hapln1a immunostaining samples were stored overnight in MeOH at -20°C. After rehydration if applicable, embryos were blocked for 1 h at room temperature in 0.2% PBS-Triton-X (PBS-Tx) with 10% goat serum. Embryos were incubated overnight at 4°C with primary and secondary antibodies diluted in PBS-Tx/10% goat serum with 1% DMSO. The following commercially available primary antibodies were used: αGFP (1:1000 Aves lab), αCT3 (1:100, Developmental Studies Hybridoma Bank), αCdh5[24] (1:100). A rabbit polyclonal antibody targeting amino acids 117–134 (DGMNDMTLEVDLEVQGKD) of zebrafish Hapln1a was designed and produced by Proteintech. Test bleeds were used to determine cross-reactivity with Hapln1a by comparing protein localization at 26hpf with mRNA *in situ* hybridization. Subsequently, affinity-purified Hapln1a antibody was used at 1:100. Fluorophore-conjugated secondary antibodies (Jackson labs) were used at 1:200.

2.5 Tomo-seq

Hearts were dissected from *Tg(myl7: eGFP)* zebrafish embryos at 26hpf and placed into OCT cryofreezing medium (Sakura Finetek). Blue Affygel beads (BioRad) were placed at each end of the heart tube to aid visualization during sectioning, and the hearts were rapidly frozen and stored at -80°C. Hearts were sectioned using a cryostat at 9 nm resolution. RNA extraction, aRNA synthesis, library preparation, sequencing, and data analysis were performed as previously described.[25,26]

2.6 Morpholino-mediated knockdown and *hapln1a* overexpression construct generation and analysis

A morpholino was designed to target the translational start site of *hapln1a* (5′-AGAGCAAT[CAT]CTTCACGTTTGTTA-3′, brackets denote *hapln1a* ATG reverse complement). Morpholinos blocking *tp53*,[27] (Zfin *tp53* MO-4) and *has2*[28] (Zfin *has2* MO-1) are previously described. All morpholinos were supplied by GeneTools and diluted to a 1 mM stock. Working concentrations were as follows: *hapln1a* 500 nM or 250 nM, *has2* 250 nM, combinatorial *has2/hapln1a* 250 nM each, *tp53* 250 nM. *has2* and *hapln1a* morpholinos were co-injected together with *tp53* morpholino. Embryos were injected with 1 nL of morpholino solution.

The *hapln1a* coding sequence was amplified using the following primers containing AttB sequences for Gateway cloning and a Kozak sequence (underlined): forward: 5′ggggacaagtttgtacaaaaaagcaggctTCGCCGCCACCATGATTGCTCTGTTTTCTGT 3′; reverse: 5′GGGGACCACTTTGTACAAGAAAGCTGGGTTTTACTGCTGGGCTTTGTAGCAATA-3′. The resulting PCR product was ligated into the pDONR221 middle entry Gateway vector, generating a pME*hapln1a*CDS vector. Full-length *hapln1a* was subsequently recombined with a p5E *myl7* promoter sequence,[29] and a p3E polyA sequence into the pDestTol2pA3 destination vector[30] to generate the pDest*myl7*: *hapln1a* construct. Gateway cloning was performed using the Tol2kit via standard protocols.[30] 60 pg of pDest*myl7: hapln1a* was co-injected with 25 pg of *tol2* mRNA into the cell of 1-cell stage embryos. Analysis of *hapln1a* overexpression and cardiac morphogenesis was performed using double *in situ* hybridization to assess *hapln1a* and *myl7* expression.

2.7 RNA injections

ssNcan-GFP mRNA was synthesized from the *ssNcan-GFP* plasmid as previously described.[31] Embryos were injected with 100 pg of mRNA in 1 nL volume at the 1-cell stage and screened for GFP at 24hpf.

2.8 Imaging and image quantification

Live zebrafish embryos were imaged on a ZEISS Lightsheet Z.1 microscope. To assess cardiac morphology at 50hpf and 72hpf embryos were

anesthetized by immersion in 8.4% Tricaine (Merck 10521) before mounting in 1% low melting point agarose in E3 with 8.4% Tricaine. To stop the heart the imaging chamber was filled with E3 with 8.4% Tricaine and the temperature maintained at 10°C. All samples were imaged using a 20× lens and 1.0 zoom at 0.47–0.65 µm z-step size, with sufficient z slices to capture the entire heart. Dual side lasers with dual side fusion and pivot scan were used for sample illumination.

Embryos injected with *ssNcan-GFP* mRNA were fixed overnight in 4% PFA with 4% sucrose, and the GFP signal amplified by immunohistochemistry. Dissected embryos were imaged using a Zeiss Airyscan microscope, z stacks were obtained with a step size of 1 µm.

Detailed image quantification methodology is included in Supplementary material online.

3. Results

3.1 The cardiac ECM is asymmetrically expanded at early stages of heart looping morphogenesis

During cardiac development the myocardial and endocardial layers of the heart are separated by the cardiac ECM. We hypothesized there may be regional differences in the ECM of the zebrafish heart tube which could promote local changes in tissue shape to drive cardiac morphogenesis. To examine regional ECM thickness in the heart tube, we used live *in vivo* light-sheet microscopy to image quadruple transgenic zebrafish embryos at 26 h post-fertilization (hpf).

Tg(myl7:lifeActGFP); Tg(fli1a:AC-TagRFP); Tg(lft2BAC:Gal4FF); Tg(UAS:RFP) zebrafish express actin-tagged GFP in the myocardium[21] and actin-localized RFP in the endothelium including the endocardium,[22] allowing visualization of the two tissue layers in the heart tube. The *Tg(lft2BAC:Gal4FF); Tg(UAS:RFP)* double transgenic drives RFP in *lefty2*-expressing cells, comprising the dorsal myocardium of the heart tube at 26hpf (*Figure 1A* and Supplementary material online, *Figure S1*).[18,32] This combination of transgenes allowed imaging of optical cross-sections through the heart tube at 26hpf, just before the onset of looping morphogenesis, and enabled dorsal–ventral axis orientation of the heart tube (*Figure 1A–G* and Supplementary material online, *Movie S1*). We consistently observed an asymmetry in the extracellular space between the myocardial and endocardial layers of the heart in the future atrium, with an apparent thickening of the ECM on the left side of the tube which is maintained throughout the cardiac cycle (*Figure 1D and G*). We quantified the extracellular space between the two tissue layers and calculated the ECM left: right ratio (left ECM thickness divided by right ECM thickness, where >1 indicates a left sided expansion). Using this method, we detected a reproducible expansion of the ECM in the left side of the heart tube (*Figure 1H*) which is maintained in the atrium at 50hpf (Supplementary material online, *Figure S2*).

Due to technical limitations in imaging deeper cardiac tissue with sufficient resolution at 26hpf, we could only image the superficially located venous pole/atrium of the heart tube in live embryos. Therefore, to determine whether ECM left–right asymmetry is restricted to the venous pole or is maintained along the atrioventricular axis of the heart, we performed fixed tissue imaging. Previous studies have demonstrated that hyaluronic acid (HA) is present in the cardiac jelly during vertebrate heart development.[17,33,34] To visualize the HA-rich ECM, wild-type embryos were injected with the HA sensor *ssNcan-GFP*[31] at the 1-cell stage, fixed at 26hpf, and the GFP signal detected by immunohistochemistry before imaging the entire heart tube as a z-stack using confocal microscopy (*Figure 1I–K*). Optical reslicing of z-stacks generated cross-sections of the heart tube from the venous pole to the arterial pole, allowing us to quantify the width of the *ssNcan-GFP*-positive ECM on left and right sides of the tube along the entire pole-to-pole length of the heart (*Figure 1L–N*). We confirmed that the ECM is thicker on the left side of the heart tube compared to the right, however this asymmetry is more profound at the venous pole/future atrium than at the arterial pole/future ventricle (*Figure 1N and O*). Furthermore, the cardiac ECM is thicker in the future atrium when compared to the ventricle (*Figure 1L–N*). Together these data demonstrate that the heart tube exhibits a regionally expanded ECM prior to onset of looping morphogenesis.

3.2 *hapln1a* exhibits regionalized cardiac expression prior to heart tube formation and looping morphogenesis

The asymmetric expansion of the cardiac ECM could be due to regionalized synthesis of ECM components. However, we did not observe any clear asymmetry in levels of HA deposition in the cardiac ECM in either live embryos injected with the *ssNcan-GFP* sensor (Supplementary material online, *Figure S3*) or in fixed hearts (*Figure 1I–K*). We also did not find left–right asymmetry in the heart tube in the expression of *hyaluronan synthase 2 (has2*, the major HA producing enzyme), *chondroitin sulfate synthase 1* (*chsy1*), or the ECM proteoglycans *versican* (*vcana/b), aggrecan (acana/b*), all of which have previously been implicated in heart development[11,17–19,35,36] (Supplementary material online, *Figure S3*), suggesting that regionalized synthesis of these proteins is not responsible for ECM asymmetry. We therefore hypothesized that a protein required for HA modification or cross-linking may be regionally expressed in the heart tube.

To identify candidate genes which modulate cardiac ECM expansion, we took a genome-wide unbiased approach to identify genes expressed in the heart tube at 26hpf, prior to the onset of looping morphogenesis. Since we observed the strongest left-sided ECM expansion in the putative atrium, as well as a generally more expanded ECM at the venous pole of the heart compared to the arterial pole, we used the previously described Tomo-seq technique to generate a regionalized map of gene expression from pole-to-pole in the heart tube[25,26] (*Figure 2A*). We sectioned two individual hearts along the atrioventricular axis, identifying 6787 and 8916 expressed genes (Supplementary material online, *Tables S2–S5*), of which approximately half were expressed in more than one section. By identifying which sections express the atrial marker *myh6* (*myosin, heavy chain 6, cardiac muscle, alpha*), we defined a subset of sections with atrial identity. We subsequently filtered genes that were up-regulated in atrial sections compared to ventricular sections in both hearts and examined this list for genes implicated in ECM modification.

Using this approach, we identified *hyaluronan and proteoglycan link protein 1a (hapln1a*, formerly *crtl1)* as a candidate to drive regionalized ECM expansion (*Figure 2B*). The Hapln family of proteins are secreted into the ECM where they cross-link HA to proteoglycans,[37] suggesting Hapln1a may modify the cardiac ECM environment. mRNA *in situ* hybridization analysis revealed that *hapln1a* is expressed in the posterior of the heart disc and cardiac cone prior to formation of the linear heart tube (*Figure 2C and D*). At 26hpf, *hapln1a* expression is up-regulated on the left side of the heart tube with elevated levels of expression in the future atrium compared to the future ventricle, recapitulating the regionalized ECM expansion in the heart (compare *Figures 2E and 1K*). This dynamic *hapln1a* expression is in line with recent studies demonstrating that the

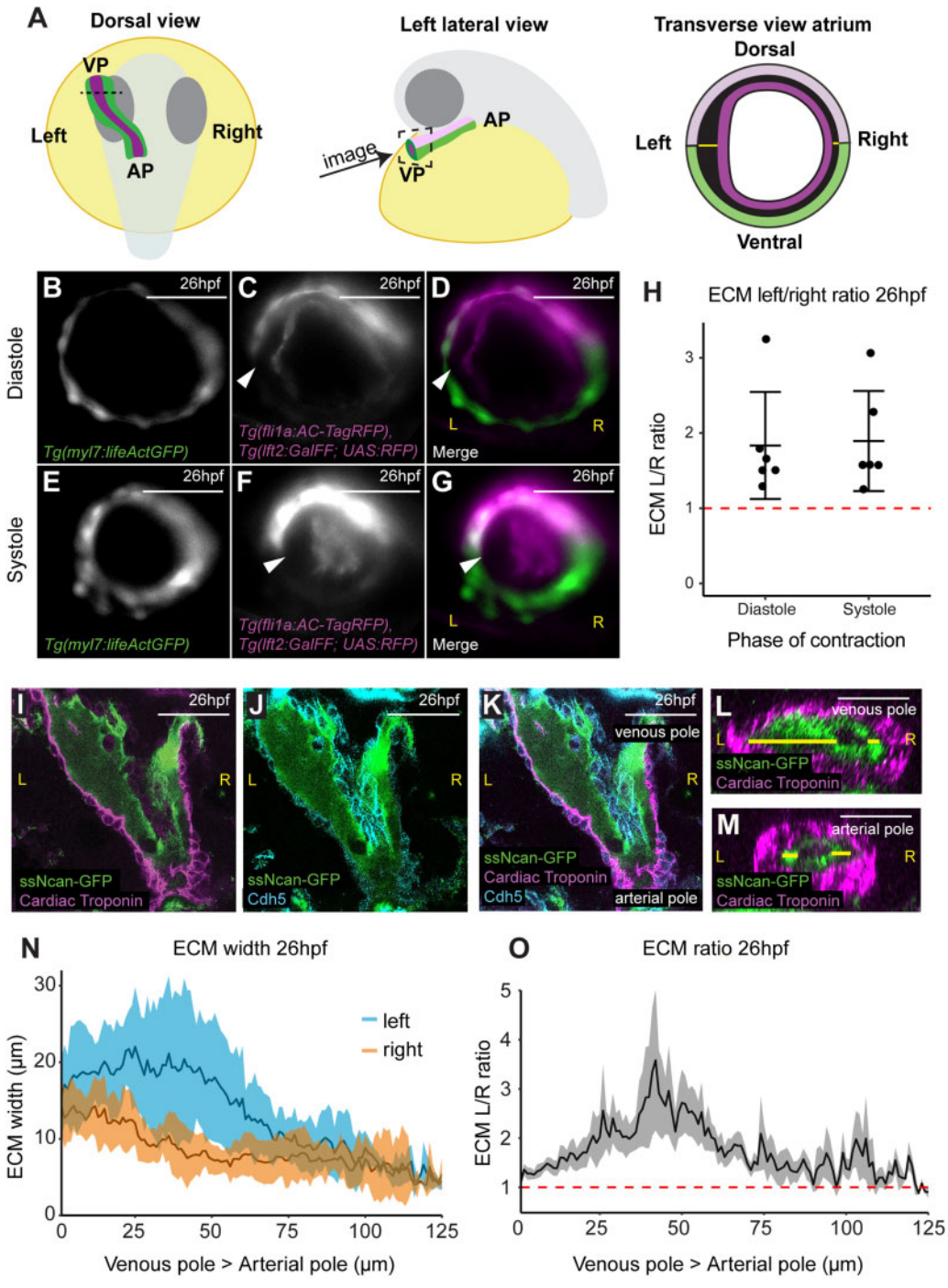

Figure 1 The hyaluronan-rich ECM is asymmetric during early zebrafish heart development. (*A*) Schematic depicting the developmental stage and orientation of zebrafish embryos used in live imaging experiments. Optical transverse sections of the heart tube are imaged at the position of the dotted line/dotted square. Green, myocardium; magenta, endocardium; light pink, dorsal myocardium. (*B–G*) Light-sheet optical cross-sections through the heart tube of a 26hpf *Tg(myl7:lifeActGFP); Tg(fli1a:AC-TagRFP); Tg(lft2BAC:Gal4FF); Tg(UAS:RFP)* transgenic embryo during diastole (*B–D*) and systole (*E–G*) at the level of the dotted line in (*A*). The myocardium is marked in green (*B, D, E*, and *G*), and the dorsal myocardium and endocardium are marked in magenta (*C, D, F*, and *G*). The extracellular space between myocardium and endocardium is expanded on the left side of the heart tube (white arrowhead). Scale bar = 50 μm. (*H*) Quantification of left–right ECM ratio in heart tubes, >1 (red dotted line) denotes left-sided expansion. Mean ± SD are plotted, $n = 6$. (*I–K*) Single confocal *z*-planes longitudinally through the heart at 26hpf of embryos injected with *ssNcan-GFP* (green), counterstained with cardiac troponin (magenta, *I, K*) and VE-Cadherin (cyan *J, K*). (*L* and *M*) Transverse optical reslice through the heart tube the venous pole (*L*) or arterial pole (*M*). ECM width is measured using the ssNcan-GFP signal (yellow line) on left and right sides of the tube. (*N*) Quantification of ECM width on the left (blue) and right (orange) sides of the heart tube from venous pole to arterial pole at 26hpf. Mean ± SD are plotted, $n = 7$. (*O*) Left–right ECM ratio in the heart tube from venous pole to arterial pole, where >1 (red dotted line) indicates a left-sided expansion. Mean ± SEM are plotted, $n = 7$. The mean L/R ratio across the heart is 1.667, and analysis using a one-sample *t*-test shows this significantly differs from 1, $P < 0.0001$ L, left; R, right; VP, venous pole; AP, arterial pole. Scale bar = 50μm.

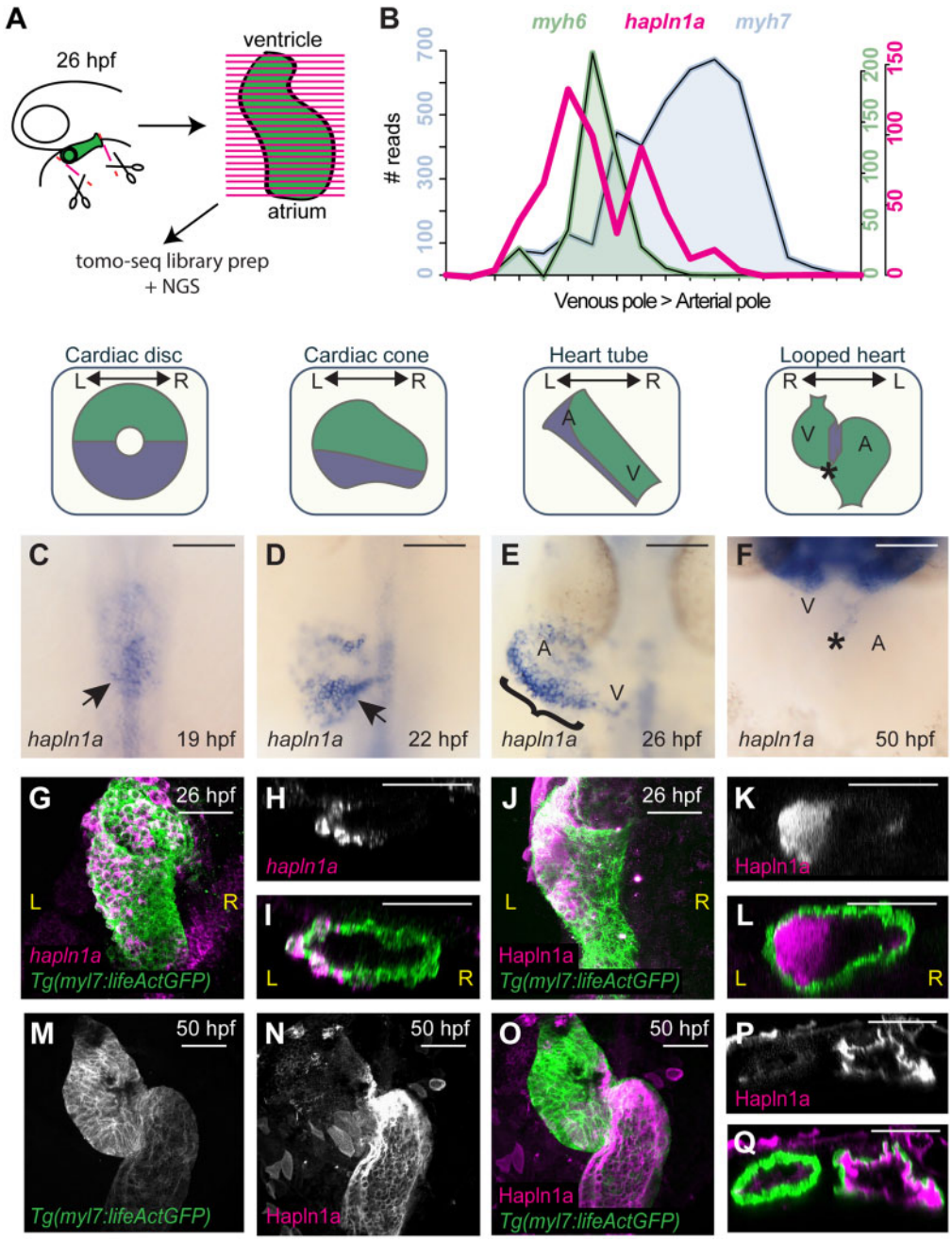

Figure 2 *hapln1a* is regionally expressed in the heart tube and secreted asymmetrically into the cardiac jelly. (*A*) Schematic representation of Tomo-seq pipeline. GFP-expressing hearts are manually excised from embryos at 26hpf, and frozen in tissue freezing medium. Heart tubes are sectioned along the atrioventricular axis. RNA extracted from individual slices is labelled with a slice-specific molecular barcode during reverse transcription before generating sequencing libraries. (*B*) Example Tomo-seq traces from a single 26hpf heart tube, with individual slices from venous pole to arterial pole along the *x*-axis and normalized read number along the *y*-axis. Read numbers for atrial marker *myh6* (green) and ventricular marker *myh7* (blue) allows identification of chamber position within the dataset. *hapln1a* expression (magenta) is up-regulated in atrial sections. (*C–F*) mRNA *in situ* hybridization analysis of *hapln1a* expression in the heart between 19hpf and 50hpf. At cardiac disc stage, *hapln1a* is up-regulated in the posterior (arrow *C*), which is maintained as the heart forms the cardiac cone prior to tube formation (arrow *D*), with lower expression in the anterior cone. Once the heart cone has extended to form the tube, the previously posterior *hapln1a* expression is positioned on the left side of the tube (bracket, *E*), and expressed at higher levels in the atrium (A) than the ventricle (V). By 50hpf *hapln1a* expression in the heart is restricted to low levels in the atrioventricular canal (AVC, asterisk, *F*). Schematics above *in situ* panels indicate heart morphology at each stage, and *hapln1a* expression domain within the heart (blue) V, Ventricle; A, Atrium. Scale bar = 100 μm. (*G–I*) Fluorescent *in situ* hybridization analysis of *hapln1a* (magenta) in *Tg(myl7:lifeActGFP)* transgenic embryos shows *hapln1a* is expressed in myocardial cells at 26hpf. (*J–L*) Fluorescent immunostaining of Hapln1a (magenta) in *Tg(myl7:lifeActGFP)* transgenic embryos demonstrating the protein is secreted into the extracellular space predominantly on the left side of the heart tube (magenta) at 26hpf. (*G* and *J*) Dorsal views. (*H* and *I*, *K* and *L*) Transverse views. (*M–Q*) Fluorescent immunostaining of Hapln1a (magenta) in *Tg(myl7:lifeActGFP)* transgenic embryos at 50hpf revealing Hapln1a is maintained in the cardiac ECM as looping progresses. (*M–O*) Ventral views. (*P* and *Q*) Transverse views. L, left; R, right, scale bar = 50 μm

posterior compartment of the cardiac disc is re-positioned to the left side of the heart tube.[38] By 50hpf *hapln1a* expression is restricted to low levels in the atrioventricular canal (*Figure 2F*). Fluorescent *in situ* hybridization demonstrates *hapln1a* is expressed in the myocardium (*Figure 2G–I*), while analysis of Hapln1a protein localization confirms it is deposited in the ECM (*Figure 2J–L*). Despite the absence of *hapln1a* expression in the heart at 50hpf (*Figure 2F*), Hapln1a protein is maintained in the ECM at 50hpf (*Figure 2M–Q*), suggesting that the ECM environment established during early stages prior to heart tube formation is maintained during heart development and may be important for subsequent cardiac morphogenesis.

3.3 Hapln1a is required for heart morphogenesis and promotes ECM expansion

To determine whether Hapln1a is required for cardiac morphogenesis, we used CRISPR-Cas9-mediated genome editing to generate *hapln1a* mutants by deleting the putative *hapln1a* promoter therefore abolishing *hapln1a* expression (Supplementary material online, *Figure S4*). We recovered two alleles; a 187-bp deletion (*hapln1a*$^{\Delta 187}$) and a 241-bp deletion (*hapln1a*$^{\Delta 241}$) and established both as stable lines at F2. Both alleles remove the initiating ATG and upstream sequence. To confirm both deletions removed the *hapln1a* promoter and abrogated transcription, *hapln1a* expression was analyzed at 26hpf in F3 mutant embryos. Homozygous *hapln1a* promoter mutants of either allele exhibit a complete loss of *hapln1a* expression at 26hpf compared to wild-type embryos (*Figure 3A–C* and Supplementary material online, *Figure S4*), demonstrating successful deletion of the *hapln1a* promoter. While analysis of heart development in *hapln1a* $^{\Delta 241}$ mutants at 50hpf by *in situ* hybridization of the pan-cardiac marker *myl7 (myosin light chain 7)* did not reveal striking abnormalities in cardiac morphogenesis (*Figure 3D–F*), we did observe mild heart malformations and an apparent reduction in atrial size. To investigate this further, we quantified heart size and chamber morphology at 50hpf by *in situ* hybridization analysis of *myl7*, the atrial marker *myh6* and the ventricular marker *myh7l* (*myosin heavy chain 7-like*)[39] (*Figure 3* and Supplementary material online, *Figures S4* and *S5*). We observed a reduction in atrial size in *hapln1a*$^{\Delta 241}$ mutants and a reduction in the length of the outer curvature of the atrium in both *hapln1a*$^{\Delta 241}$ and *hapln1a*$^{\Delta 187}$ mutants, suggesting a defect in atrial growth (*Figure 3J and K*). We performed similar analyses by generating z-projections of live light-sheet images of *Tg(myl7:lifeActGFP); Tg(fli1a:AC-TagRFP)* transgenic wild-type sibling and *hapln1a* mutant hearts at 50hpf and 72hpf, allowing us to assess ongoing heart morphogenesis without chamber morphology being altered during fixation and processing (*Figure 3L–O* and Supplementary material online, *Figure S6*). We confirmed a reduction in atrial size and ballooning of the atrial outer curvature in live *hapln1a*$^{\Delta 241}$ mutants at 50hpf (*Figure 3P and Q*), as well as reductions in atrial perimeter and elongation at 72hpf in *hapln1a*$^{\Delta 187}$ mutants (Supplementary material online, *Figure S6*), with similar trends in reduction in all atrial parameters across alleles. At 72hpf *hapln1a* mutants also display abnormally positioned atria compared to wild-type siblings, with reduced compaction of the heart, and mispositioning of the atrium and ventricle relative to each other (Supplementary material online, *Figure S6*). While expressivity of phenotype appears variable between alleles, both exhibit significant changes in morphological parameters indicative of defective atrial growth. Supporting a requirement in atrial growth specifically after heart tube formation, we did not observe significant defects in heart size or tube position at 26hpf, or in looping morphology, or ventricular growth at 50hpf in *hapln1a* mutants (Supplementary material online, *Figure S5*). Both *hapln1a* mutant alleles are adult viable and we did not observe more profound defects in maternal-zygotic *hapln1a* mutants (data not shown). Together this demonstrates that similar to mouse,[15] *hapln1a* is required for atrial morphogenesis in zebrafish.

Hapln1 functions as an ECM binding protein and its localization recapitulates the regionalized ECM expansion in the heart tube, therefore, we hypothesized that Hapln1a promotes cardiac morphogenesis by driving regionalized ECM expansion in the heart. Since both *hapln1a* promoter deletion alleles carry the *Tg(myl7:lifeActGFP)* transgene, this prevented analysis of ECM width throughout the heart tube of *hapln1a* mutants using the *ssNcan-GFP* HA sensor. We instead injected a morpholino (MO) against *hapln1a* into zebrafish embryos at the 1-cell stage together with a *tp53* MO control and the *ssNcan-GFP* HA sensor and assessed ECM expansion in the heart tube at 26hpf. Analysis of Hapln1a protein levels in *hapln1a* morphants confirms successful blocking of Hapln1a translation in the morphants (Supplementary material online, *Figure S7*). Control embryos injected with *tp53* MO demonstrate the regionalized ECM expansion previously observed, with a left-sided expansion of the ECM (*Figure 4A and B*), and a higher level of ECM expansion in the atrium vs. the ventricle (*Figure 4C*), although overall ECM width was slightly reduced compared to uninjected embryos (compare *Figures 4C and 1N*). Embryos injected with *hapln1a* MO + *tp53* MO did not exhibit either atrial or left-sided ECM expansion (*Figure 4A, B, and D*), suggesting that Hapln1a drives regionalized ECM expansion in the heart tube. To confirm a role for Hapln1a in ECM regionalization, we analyzed ECM size in a series of optical cross-sections from live light-sheet images of wild-type and *hapln1a* mutant *Tg(myl7:lifeActGFP); Tg(fli1a:AC-TagRFP)* transgenic embryos, taking sections from the atrioventricular canal through the atrium towards the venous pole at 50hpf and 72hpf (*Figure 4E–H* and Supplementary material online, *Figure S8*). Analysis of radial ECM width in the atrium of *hapln1a* mutants revealed a reduction in ECM specifically in the outer curvature of the atrium proximal to the AVC (*Figure 4H* and Supplementary material online, *Figure S8*, cross-sections 2–4), where ECM expansion is most profound in wild-type hearts and defects in atrial morphology occur in *hapln1a* mutants (*Figure 3K and Q*). Together this supports a role for Hapln1a in regionally regulating cardiac ECM size to promote normal cardiac morphogenesis.

3.4 Hapln1a and HA interact to drive heart morphogenesis

Hapln1a is a member of a family of ECM binding proteins which cross-link HA with proteoglycans.[37] Since *hapln1a* is transiently expressed during early heart development at cardiac disc and early tube stage (*Figure 2*), this suggests that the cardiac ECM driving continued morphogenesis of the heart is established at early stages of heart development and requires the interaction of Hapln1a with HA. To interrogate the temporal requirements for HA in heart looping, we applied the HA synthesis inhibitor 4-methylumbelliferone (4-MU[40,41]) to embryos prior to the onset of heart tube formation at 18hpf, and either washed the drug off at 22hpf, or left the embryos to develop to 48hpf, when we assessed heart morphology. Inhibiting HA synthesis from cardiac disc stage (18hpf) until 48hpf often arrested heart development mid-way during tube formation (Supplementary material online, *Figure S9*), a more profound phenotype than that observed in *has2* zebrafish morphants or *Has2* mouse mutants.[17,18] However, inhibition of HA synthesis during the short time window between cardiac disc (18hpf) and cardiac cone (22hpf) stage, prior to tube formation, resulted in normal tube formation

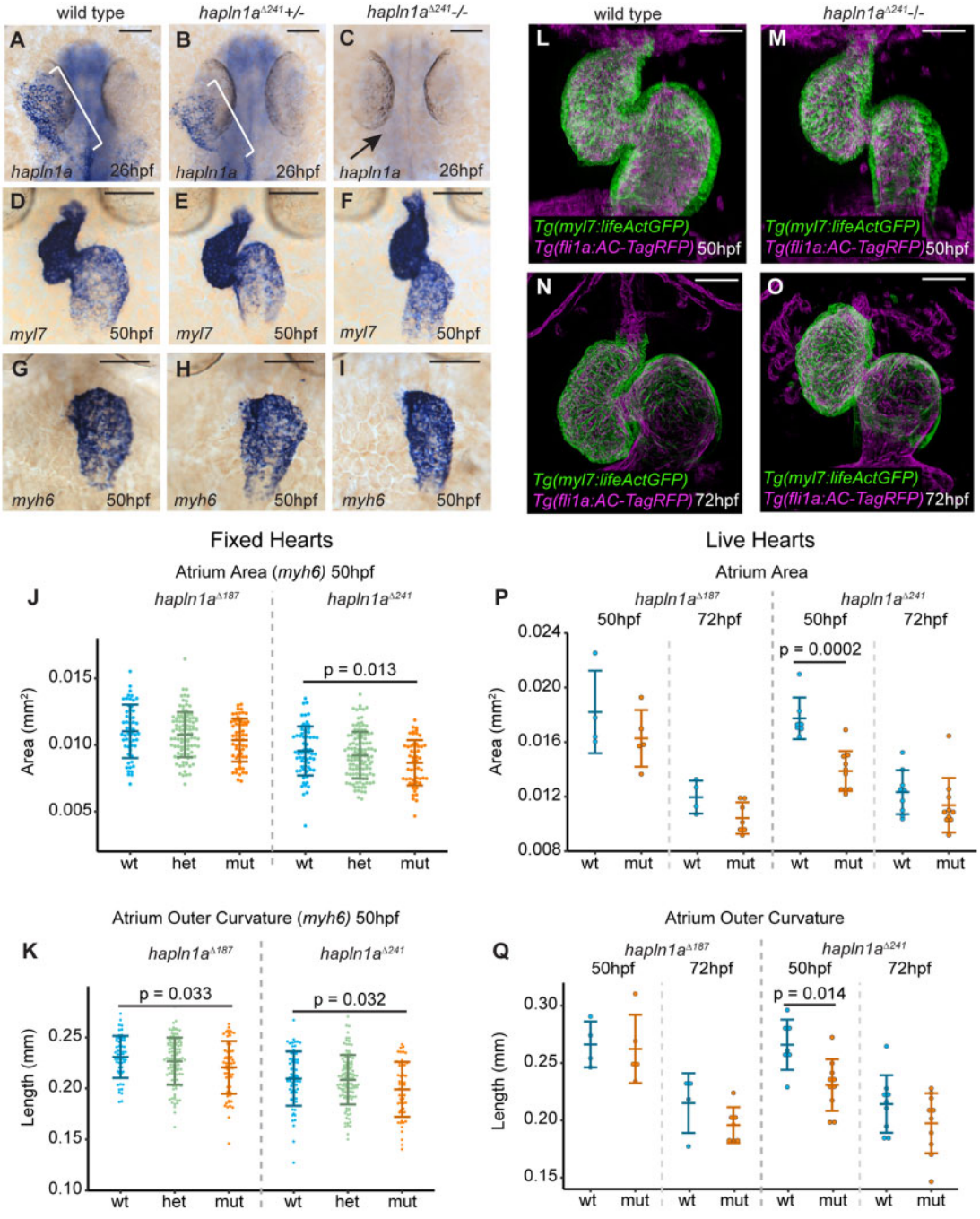

Figure 3 Hapln1a promotes atrial growth. (*A–C*) mRNA *in situ* hybridization analysis of *hapln1a* expression at 26hpf in embryos from an incross of *hapln1a*$^{\Delta 241}$ heterozygous carriers. Wild-type and heterozygous siblings express *hapln1a* in the heart (bracket *A*, *B*, respectively), whereas *hapln1a* is absent in homozygous mutants (arrow *C*). (*D–I*) mRNA *in situ* hybridization expression analysis at 50hpf of *myl7* (*D–F*) and *myh6* (*G–I*) in wild-type siblings (*D* and *G*), *hapln1a*$^{\Delta 241}$ heterozygous siblings (*E* and *H*) or *hapln1a*$^{\Delta 241}$ homozygous mutant embryos (*F* and *I*). Scale bar = 50 µm. (*J* and *K*) Quantification of atrial area (*J*), and atrial outer curvature (*K*) in ISH-processed sibling embryos (wt/het) and *hapln1a*$^{\Delta 241}$ or *hapln1a*$^{\Delta 187}$ mutants (mut) at 50hpf. Atrial area is significantly reduced in *hapln1a*$^{\Delta 241}$ mutants compared to wild-type siblings ($P = 0.013$), and atrial outer curvature is significantly reduced in both *hapln1a*$^{\Delta 187}$ and *hapln1a*$^{\Delta 241}$ mutants ($P = 0.033$ and $P = 0.032$). In both *J* and *K*, $n = 54$ *hapln1a*$^{\Delta 187}$ wt; 104 *hapln1a*$^{\Delta 187}$ het; 60 *hapln1a*$^{\Delta 187}$ mut, 66 *hapln1a*$^{\Delta 241}$ wt; 116 *hapln1a*$^{\Delta 241}$ het; 53 *hapln1a*$^{\Delta 241}$ mut. (*L–O*) Maximum intensity projections of light-sheet z-stacks of live 50hpf (*L* and *M*) and 72hpf (*N* and *O*) *Tg(myl7:lifeActGFP); Tg(fli1a:AC-TagRFP)* transgenic wild-type (*L* and *N*), and *hapln1a*$^{\Delta 241}$ mutant embryos (*M* and *O*). Scale bar = 50µm. (*P* and *Q*) Quantification of atrial area (*P*), and atrial outer curvature (*Q*) in live light-sheet z-projections from wild-type sibling embryos and *hapln1a*$^{\Delta 241}$ or *hapln1a*$^{\Delta 187}$ mutants at 50hpf and 72hpf. Atrial area and atrial outer curvature are significantly reduced in *hapln1a*$^{\Delta 241}$ mutants (mut) compared to wild-type siblings (wt/het) at 50hpf ($P = 0.0002$, and $P = 0.014$). In both (*P*) and (*Q*), $n = 4$ *hapln1a*$^{\Delta 187}$ 50hpf wt; 5 *hapln1a*$^{\Delta 187}$ 50hpf mut, 7 *hapln1a*$^{\Delta 241}$ 50hpf wt; 10 *hapln1a*$^{\Delta 241}$ 50hpf mut; 4 *hapln1a*$^{\Delta 187}$ 72hpf wt; 7 *hapln1a*$^{\Delta 187}$ 72hpf mut, 9 *hapln1a*$^{\Delta 241}$ 72hpf wt; 10 *hapln1a*$^{\Delta 241}$ 72hpf mut. Comparative statistics carried out using a Kruskal–Wallis test with multiple comparisons.

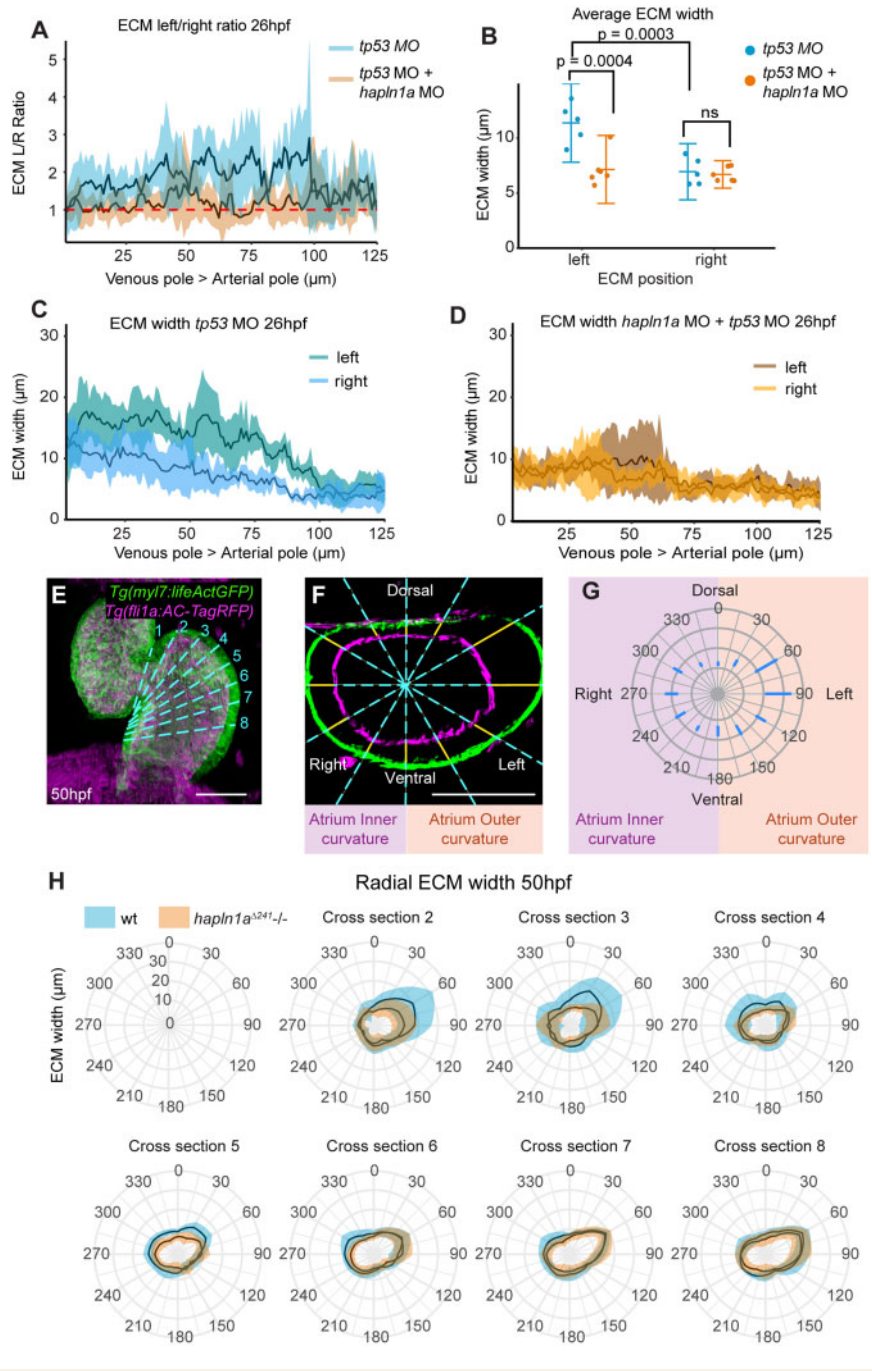

Figure 4 Hapln1a drives regionalized ECM expansion. (*A*) Quantification of ECM left/right width along the longitudinal axis of the heart at 26hpf in embryos injected with either *tp53* MO (blue, $n = 5$) or *hapln1a* MO + *tp53* MO (orange, $n = 6$). Mean ± SD are plotted. (*B*) Average ECM width on the left or right side of the heart tube in embryos injected with *tp53* MO (blue, $n = 5$) or *hapln1a* MO + *tp53* MO (orange, $n = 6$). *tp53*-injected controls display an expanded ECM on the left side of the heart tube compared to the right, ($P = 0.0003$, 2-way ANOVA) whereas embryos injected with *hapln1a* MO + *tp53* MO have a reduced left ECM size when compared to *tp53* MO injected ($P = 0.0004$), resulting in loss of left-sided ECM expansion. Mean ± SD are plotted. (*C* and *D*) Quantification of ECM width on the left and right sides of the heart tube from venous pole to arterial pole at 26hpf in embryos injected with *tp53* MO (*C*, $n = 5$) or *hapln1a* MO + *tp53* MO (*D*, $n = 6$). Mean ± SD are plotted. The cardiac ECM in *tp53* morphants exhibits atrial and left side expansion, whereas the ECM in *hapln1a* morphants is more uniform in width from atrium to ventricle and is not expanded on the left side. Mean ± SD are plotted. (*E*) Maximum intensity projection of light-sheet z-stacks of 50hpf *Tg(myl7:lifeActGFP); Tg(fli1a:AC-TagRFP)* transgenic embryo. Dashed cyan line indicates position of optical cross-sections. (*F*) Example orthogonal view through the atrium of wild-type embryo in (*E*). Blue dashed lines indicate radial positions for measuring ECM thickness (yellow lines). Scale bar = 50μm. (*G*) Schematic of radial plot corresponding to radial ECM positions in (*F*). (*H*) Quantification of ECM width in atrial cross-sections at defined angular positions along the longitudinal axis of the atrium from AVC (cross-section 2) towards the venous pole (cross-section 8) at 50hpf in wild-type (blue) or *hapln1a*$^{\Delta 241}$ mutants (orange). Asymmetric ECM width is reduced in the outer curvature close to the AVC (cross-sections 2–4) in *hapln1a*$^{\Delta 241}$ mutants compared to wild-type siblings. Mean ± SD are plotted, radial-axis is consistent between plots, $n \geq 4$ at each location.

but a specific disruption to subsequent cardiac looping morphogenesis (Supplementary material online, *Figure S9*). This supports the hypothesis that HA synthesized prior to formation of the heart tube is required for ongoing morphogenesis of the heart.

Having demonstrated a requirement for HA synthesis in heart morphogenesis during early cardiac development when *hapln1a* expression is initiated, we wanted to confirm the interaction of *hapln1a* and HA in heart looping morphogenesis. Injection of sub-phenotypic doses of morpholinos targeting either *has2* or *hapln1a* did not result in significant defects in cardiac morphology at 48hpf (Supplementary material online, *Figure S9*). However, co-injection of both *has2* and *hapln1a* morpholinos results in profound defects in heart development at 48hpf (Supplementary material online, *Figure S9*), including a reduction in heart looping ratio, and abnormal atrial morphology. This is a more severe phenotype than that observed by either injection of *hapln1a* MO + *tp53* MO, *has2* MO + *tp53* MO, 4MU treatment or deletion of the *hapln1a* promoter, suggesting that while timely HA synthesis drives heart morphogenesis subsequent to tube formation, *hapln1a* is an important regional modulator of this process.

3.5 Hapln1a misexpression results in abnormal heart morphogenesis

While analysis of *hapln1a* mutants demonstrates a requirement for Hapln1a in heart development (*Figure 3* and Supplementary material online, *Figure S6*), we wished to investigate whether the regionalization of *hapln1a* expression is important for cardiac morphogenesis. We generated a DNA construct in which the full-length *hapln1a* coding sequence is driven by the pan-myocardial *myl7* promoter, flanked by Tol2 transposon sites to allow integration into the genome (*Figure 5A*). We co-injected *myl7*: *hapln1a* DNA with *tol2* transposase mRNA at the 1-cell stage and analyzed both *myl7* and *hapln1a* expression at 55hpf, allowing us to visualize heart morphology alongside assessing the extent of *hapln1a* misexpression (*Figure 5B–G*). We analyzed heart morphology by quantifying looping ratio and assessed this as a function of percentage coverage of *hapln1a* expression in the whole heart (*Figure 5H*). Increasing the domain of *hapln1a* expression in the heart results in a reduction in looping morphogenesis (*Figure 5H*), suggesting that regionalized expression of *hapln1a* in the heart is important for cardiac morphogenesis. Since *hapln1a* expression and ECM asymmetry is greater in the atrium than the ventricle, we hypothesized that *hapln1a* misexpression in each chamber may impact differently on heart morphogenesis. We quantified *hapln1a* misexpression in each chamber by calculating the percentage of the chamber which expresses *hapln1a* (*Figure 5I–M*), and found that while misexpression of *hapln1a* in the ventricle did not impact upon heart morphogenesis, misexpression of *hapln1a* in the atrium decreased looping ratio (*Figure 5N*). Conversely, we did not find significant changes in chamber area upon *hapln1a* overexpression (*Figure 5O*). Together with our observations of abnormal heart morphology in *hapln1a* mutants this suggests that spatially restricted *hapln1a* expression in the atrium drives cardiac morphogenesis.

3.6 Embryonic left–right asymmetry orients the axis of ECM asymmetry in the heart tube

Finally, since *hapln1a* is asymmetrically expressed on the left side of the heart tube, and is required for heart morphogenesis, we hypothesized that it may contribute to a previously-described tissue-intrinsic mechanism of heart looping morphogenesis[7] and thus is expressed independent of embryonic left–right asymmetry cues. Embryos with mutations in *pkd2 (polycystic kidney disease 2)*, which is required for Kupffer's Vesicle function,[42] exhibit defects in left–right asymmetry including a disruption to normal leftward displacement of the heart tube,[42] while *spaw* mutants lack asymmetric Nodal expression prior to asymmetric organ morphogenesis resulting in midline positioning of the heart tube.[7] We hypothesized that induction of *hapln1a* expression occurs independent of embryonic laterality cues, but that asymmetric positioning of *hapln1a*-expressing cells in the heart tube may be tightly linked to the direction of heart tube position, and therefore dictated by embryonic left–right asymmetry. We analyzed *hapln1a* expression in an incross of *pkd2*^{hu2173} and *spaw* heterozygotes and found that consistent with our hypothesis *hapln1a* is always expressed in the posterior of the heart disc in both *pkd2*^{hu2173} mutants and *spaw* mutants at 19hpf (*Figure 6A–D*). Importantly, at 26hpf, we observed that positioning of *hapln1a*-expressing cells is dependent upon cardiac position—in *pkd2*^{hu2173} mutants where the heart is positioned to the right, *hapln1a* is up-regulated on the right side of the tube, whereas if the heart remains midline, *hapln1a* does not exhibit a clear left–right asymmetry in up-regulation (*Figure 6E–H*). Similarly, analysis of Hapln1a deposition in *spaw* mutants at 26hpf reveals Hapln1a is no longer positioned on the left side of the heart tube, but instead is secreted into the cardiac ECM on the ventral face of the heart (*Figure 6I–P*). These data support a model where laterality cues do not initiate *hapln1a* expression but are required for its subsequent position in the heart tube.

Together, this supports a model where initiation of *hapln1a* expression in the posterior cardiac disc is independent of laterality cues, but the subsequent cell movements which occur during heart tube formation reposition this population of cells to the left side of the heart, dictating the axis of ECM asymmetry in the heart tube.

4. Discussion

The process of forming the complex heart from a simple linear tube requires careful coordination of spatially restricted extrinsic signals and highly regionalized changes in cell shape and tissue growth to ensure correct shaping of the developing tissue. Our data show that the zebrafish heart tube exhibits regionalized ECM expansion that is dependent upon localized expression of the ECM binding protein *hapln1a* and this promotes cardiac morphogenesis. Our finding that while the onset of *hapln1a* in the posterior cardiac disc is independent of embryonic left–right asymmetry, laterality cues are required to orient asymmetric Hapln1a deposition along the left–right axis of the heart tube, allows us to propose a new model in which heart-extrinsic embryonic asymmetry orients tissue-intrinsic cardiac ECM asymmetry, ensuring that directionality and growth of the heart are tightly coordinated to fine tune cardiac morphogenesis (*Figure 7*).

Interestingly, the only other gene thus far identified specifically in the posterior cardiac disc/left heart tube in zebrafish is *meis2b*.[38] *meis2b* mutants exhibit defects in atrial morphology at juvenile and adult stages, supporting our conclusion that early anterior–posterior asymmetry in the heart disc/left–right asymmetry in the heart tube are important for continual cardiac morphogenesis. However, contrary to our study which reveals a reduced atrial size in *hapln1a* mutants, *meis2b* mutant adult zebrafish exhibit an enlarged atrium,[38] suggesting these two genes play opposing roles in atrial morphogenesis. Investigating *hapln1a* expression in *meis2b* mutants may uncover any interactions between these two genes in heart development. Similarly, *hapln1a* mutants are adult viable,

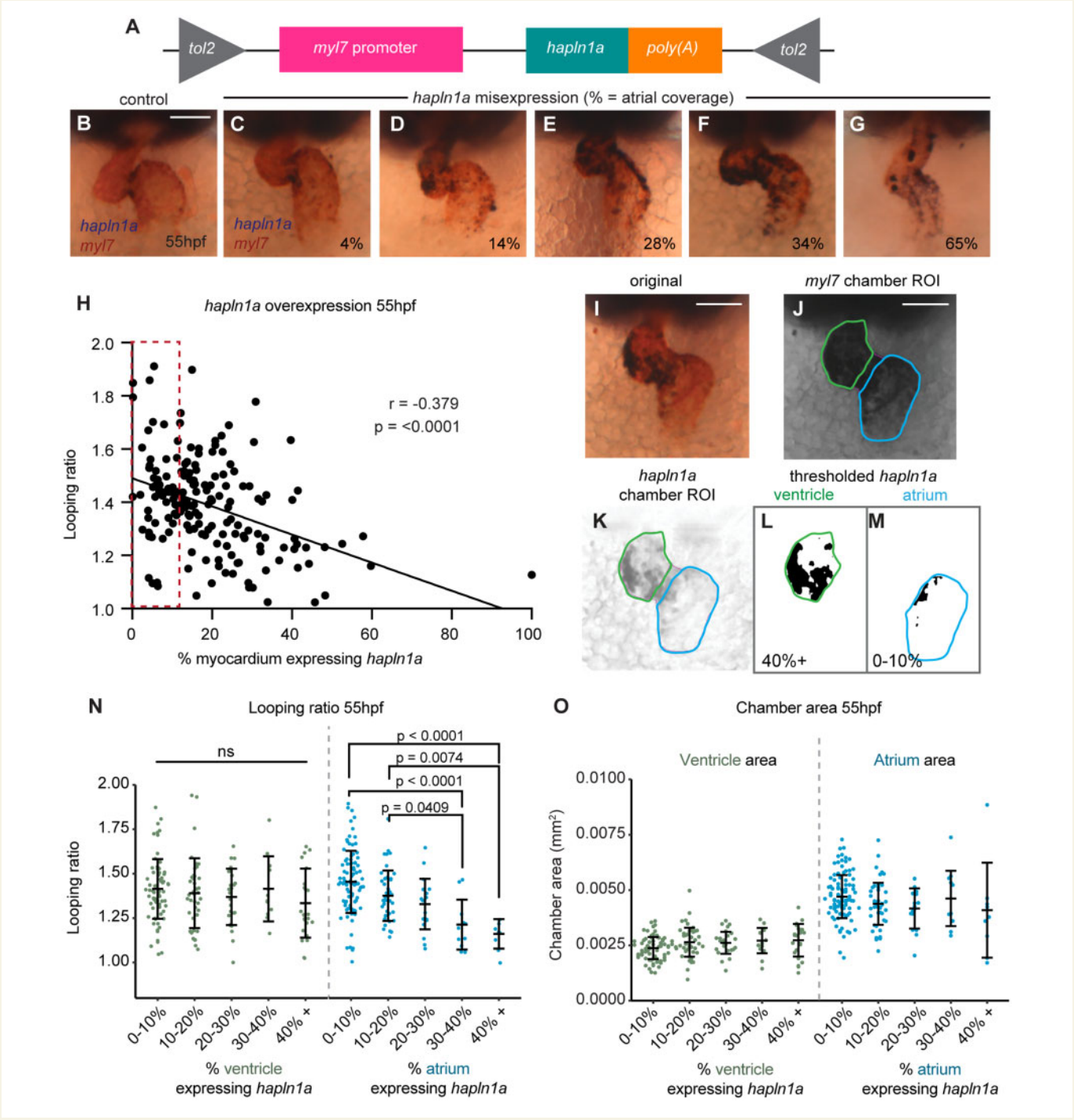

Figure 5 Regionalized *hapln1a* expression in the atrium promotes heart morphogenesis. (*A*) Schematic of DNA construct used to misexpress *hapln1a* specifically in cardiomyocytes. (*B–G*) Example images of heart morphology (*myl7*, red) upon different levels of *hapln1a* misexpression (blue) at 55hpf, related to the quantification method depicted in (*I–M*). Percentage indicates *hapln1a* coverage of the atrium. (*H*) Scatter plot depicting looping ratio as a function of percentage of the heart covered by *hapln1a* expression together with linear regression of the data ($n = 174$). Spearman's correlation coefficient (r) deviates significantly from zero ($P < 0.0001$) demonstrating that increased coverage of *hapln1a* in the myocardium results in reduced heart looping morphogenesis. Red dashed box indicates embryos with wild-type levels of *hapln1a* expression. (*I–M*) Quantification approach to analyze pan-cardiac or chamber-specific *hapln1a* misexpression at 55hpf. The number of *hapln1a*-positive pixels within each chamber is measured alongside the total chamber area, quantifying the percentage of the chamber expressing *hapln1a*. (*N–O*) Analysis of looping ratio (*N*) and chamber area (*O*) as a function of the level of *hapln1a* expression in each chamber of the heart. Embryos are categorized depending on the percentage of the chamber expressing *hapln1a*. Misexpression of *hapln1a* in the ventricle does not affect looping ratio, whereas misexpression of *hapln1a* in the atrium significantly reduces looping ratio at ≥30% coverage (*N*). *hapln1a* misexpression in either chamber does not appear to alter overall heart size (*O*). ns = not significant. In both (*N*) and (*O*), atrium misexpression categories: $n = 92$ (0–10%); 43 (10–20%); 17 (20–30%); 12 (30–40%); 9 (40+%); ventricle misexpression categories: $n = 73$ (0–10%); 41 (10–20%); 25 (20–30%); 12 (30–40%); 23 (40+%). Comparative statistics carried out using a Kruskal–Wallis test with multiple comparisons.

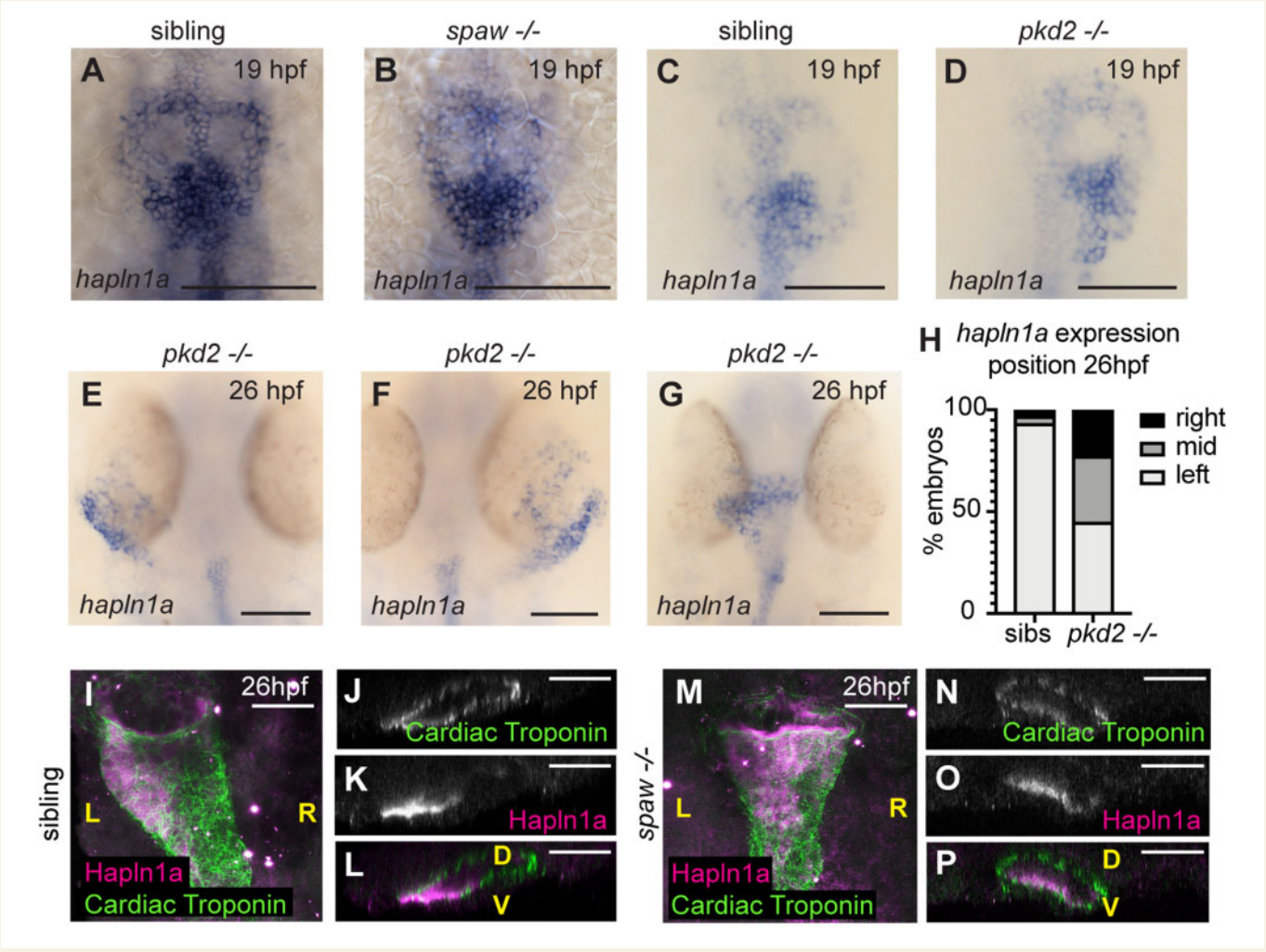

Figure 6 Posterior up-regulation of *hapln1a* in the cardiac disc is independent of left–right asymmetry. (*A–G*) mRNA *in situ* hybridization analysis of *hapln1a* expression in an incross of *spaw* (*A* and *B*) or *pkd2*^{hu2173} (*C–G*) heterozygous carriers. At 19hpf *hapln1a* is expressed in the posterior cardiac disc of both *spaw* mutant embryos (*B*, $n = 17/19$), and *pkd2* mutant embryos (*D*, $n = 13/13$), similar to sibling embryos. At 26hpf *pkd2* mutant hearts that have jogged to the left exhibit left side up-regulation of *hapln1a* (*E*, $n = 18$), *pkd2* mutant hearts on the right have right side up-regulation of *hapln1a* (*F*, $n = 9$), and *pkd2* mutant hearts that remain at the midline have no clear left–right asymmetry in expression (*G*, $n = 13$). (*H*) Quantification of position of *hapln1a* expression in sibling and *pkd2*^{hu2173} mutant embryos at 26hpf, $n = 138$ *pkd2*^{hu2173} siblings, 40 *pkd2*^{hu2173} mutants. (*I–P*) Fluorescent immunostaining of Hapln1a (magenta) and cardiac troponin (green) at 26hpf in wild-type siblings (*I–L*) or *spaw* mutant embryos (*M–P*). Wild-type siblings exhibit left-sided deposition of Hapln1a in the heart tube (*I–L*, $n = 6$), whereas *spaw* mutant embryos exhibit ventral localization of Hapln1a (*M–P*, $n = 6$). (*I* and *M*) Dorsal views. (*J–L* and *N–P*) Optical transverse sections. Scale bar = 50μm. L, left; R, right; D, dorsal; V, ventral.

and comparing atrial phenotypes in juveniles and adults will better define the phenotypic relationship between these two genes, as well as the impact of abnormal embryonic morphology on adult heart form and function. Furthermore, recent studies have shown that cross-talk between the myocardium and endocardium modulates atrial growth,[43] and our study suggests that differential ECM composition and/or degradation may help regionally fine tune this process to dictate chamber morphology.

The mechanism by which regionalized ECM composition modulates cardiac morphogenesis remains unclear. A major role of the ECM in tissue morphogenesis is to provide structural or biomechanical cues to neighbouring tissues. Alternatively, Hapln1a-mediated cross-linking may modulate regional stiffness of the cardiac ECM, and differential matrix stiffness has been shown to regulate cardiomyocyte form and function.[44–47] Importantly, we do not see defects in heart rate in *hapln1a* mutants (Supplementary material online, *Figure S5*), suggesting this regionalized ECM is not regulating cardiac function. In addition to provision of mechanical cues to the surrounding cells, the ECM also modulates diffusion and availability of extracellular signalling molecules.[48] It is therefore tempting to speculate that the specific ECM environment allows precise regionalized cellular responses to pan-cardiac or chamber specific signalling pathways.

Hapln proteins cross-link HA to proteoglycans. HA and Versican have previously been implicated in heart development, however global loss of these genes throughout the heart result in profound morphological defects.[17,19] We suggest that regionalized modification of the ECM by Hapln1a allows the developing heart to generate different regional responses to globally deposited ECM components, resulting in spatial

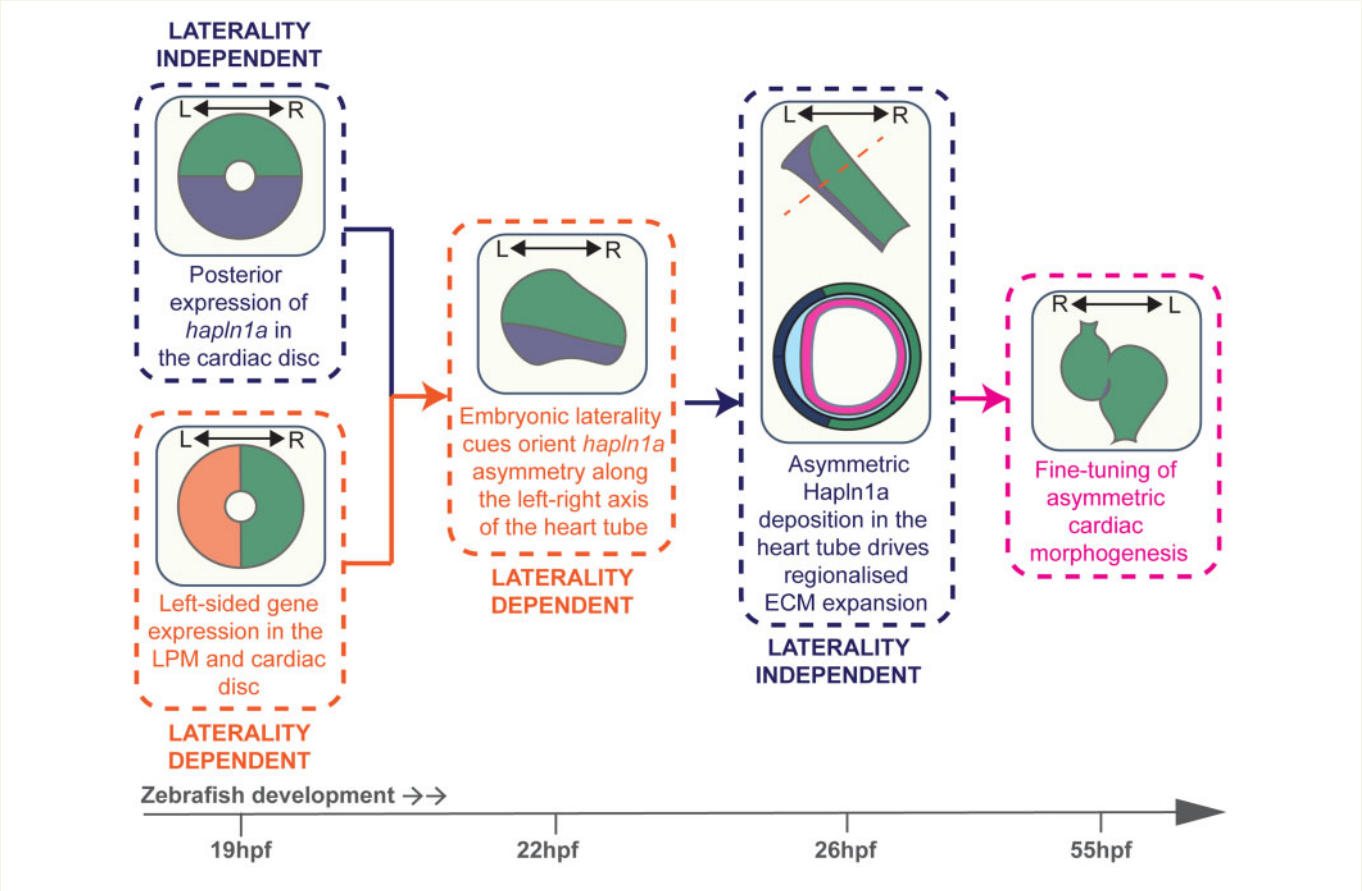

Figure 7 Left–right asymmetry orients ECM asymmetry in the heart tube to fine tune cardiac morphogenesis. Model depicting the interaction between embryonic laterality and ECM regionalization in cardiac morphogenesis. LPM, lateral plate mesoderm; L, left; R, right.

fine-tuning of the specific morphological rearrangements required for complex tissue shaping. While regional ECM cross-linking may change the biomechanical properties of the ECM by stabilizing these components in specific regions of the heart tube, HA and proteoglycan cleavage products can also act as signalling molecules.[49] Our finding that *hapln1a* and *has2* work synergistically to promote heart morphogenesis suggests that Hapln1a could promote regional atrial growth by regulating HA signalling in the heart.

Importantly, while our data show that ECM regionalization appears to be the result of asymmetric *hapln1a* expression and deposition, other factors may support and maintain ECM regionalization during development. Although we do not observe asymmetric *has2* expression, we cannot rule out asymmetries in deposition which current analytical methods are not sensitive enough to detect. Similarly, we cannot discard the possibility that asymmetric activity of additional ECM modifiers or hyaluronidases enhance ECM regionalization through localized degradation, and there is some evidence that hyaluronidases themselves are regionally localized in the heart tube.[50] This suggests multiple regulatory mechanisms may interact to regionalize HA/ECM activity in the developing heart. Comparative quantitative analysis of cardiac morphology in single and combinatorial knockout models will help define how ECM components and modifiers interact to contribute to heart morphogenesis. Our relatively simplistic analysis of 3D chamber morphology suggests that 2D analyses do not capture all aspects of cardiac morphology during development, and thus defining the links between spatiotemporal ECM dynamics and cardiac morphology requires better definition of changes in ECM composition and morphological cardiac parameters in 3D.

Additionally, *Hapln1* mouse mutants exhibit decreased protein levels of the proteoglycan Versican,[15] suggesting that Hapln1-mediated HA-Versican cross-linking prevents degradation of one or both of these components. Further supporting an interaction between Hapln1a, Versican, and HA in heart morphogenesis, both mice and medaka lacking Versican exhibit severe cardiac malformations.[19,36] Versican proteins can be subject to cleavage by ADAMTS proteases,[51] depending on isoform and domain structure, and reduction in ADAMTS protease activity results in reduced Versican cleavage and cardiac abnormalities.[52,53] We have shown that of the two zebrafish versican paralogs, only *vcana* expression overlaps the *hapln1a* expression domain (Supplementary material online, *Figure S3*). Zebrafish Vcana appears to be a small V3 or V4-like isoform which is not predicted to undergo cleavage (Uniprot ID A0A2R8Q3K1). This suggests that in zebrafish Hapln1a may not stabilize Versican in the ECM, and alternatively Hapln1a cross-linking may promote regional degradation of HA in the heart tube.

Hapln1 mutant mouse embryos also exhibit relatively mild structural cardiac malformations consistent with abnormal early cardiac morphogenesis.[15] However, while that study describes *Hapln1* expression in the

valve leaflets it does not address a potentially conserved role for transiently asymmetric *Hapln1* expression during earlier heart development. Zebrafish have two *hapln1* paralogs, each with a distinct expression profile in the heart during development, with *hapln1b* expressed primarily in the endocardium (data not shown). Thus, zebrafish provide an opportunity to define tissue-specific requirements for Hapln1 function in either the myocardium or endocardium during cardiac morphogenesis.

Together this study identifies a novel functional role for ECM regionalization in the developing heart, mediated by the HA cross-linking protein Hapln1a, and provides a new model in which ECM regionalization acts together with embryonic laterality cues to drive cardiac morphogenesis.

Supplementary material

Supplementary material is available at *Cardiovascular Research* online.

Authors' contributions

C.J.D. and E.S.N. conceived the study and designed the experiments. C.J.D., J.S.-P., F.H., E.J.G.P., and E.S.N. carried out experimental work. A.M.S., R.N.W., and T.J.C. shared the *Tg(fli1a: AcTagRFP)* transgenic line prior to publication. F.T. and J.B. generated the *Tg(lft2BAC: Gal4FF)* transgenic line, and F.J.v.E. characterized the *pkdhu2173* allele. J.B. provided financial support for the Tomo-seq experiments. E.S.N. wrote the manuscript with input from C.J.D., J.S.-P., E.J.G.P., F.T., and T.J.C.

Acknowledgements

Additional imaging work was performed at the Wolfson Light Microscopy Facility, using Airyscan and Nikon A1 microscopes. We thank Kelly Smith for the *ssNcan-GFP* construct, Markus Affolter for the VE-Cadherin antibody, and Aylin Metzner for help characterizing the *pkd2*^{hu2173} allele. We also thank Tanya Whitfield, David Strutt, and Simon Johnston for helpful comments on the manuscript.

Conflict of interest: none declared.

Funding

This work was supported by the British Heart Foundation (FS/16/37/32347 to E.S.N.; IG/15/1/31328) and the Academy of Medical Sciences (Springboard Award to E.S.N.). J.B. and F.T. acknowledge support from the Netherlands Cardiovascular Research Initiative: An initiative with support of the Dutch Heart foundation, CVON2014-18 CONCOR-GENES.

Data availability

The data underlying this article will be shared on reasonable request to the corresponding author.

References

1. Linde D V D, Konings EEM, Slager MA, Witsenburg M, Helbing WA, Takkenberg JJM, Roos-Hesselink JW. Birth prevalence of congenital heart disease worldwide: a systematic review and meta-analysis. *J Am Coll Cardiol* 2011;**58**:2241–2247.
2. Desgrange A, Garrec J-FL, Meilhac SM. Left-right asymmetry in heart development and disease: forming the right loop. *Development* 2018;**145**:dev162776.
3. Levin M, Johnson RL, Sterna CD, Kuehn M, Tabin C. A molecular pathway determining left-right asymmetry in chick embryogenesis. *Cell* 1995;**82**:803–814.
4. Long S, Ahmad N, Rebagliati M. The zebrafish nodal-related gene southpaw is required for visceral and diencephalic left-right asymmetry. *Development* 2003;**130**:2303–2316.
5. Brennan J, Norris DP, Robertson EJ. Nodal activity in the node governs left-right asymmetry. *Genes Dev* 2002;**16**:2339–2344.
6. Toyoizumi R, Ogasawara T, Takeuchi S, Mogi K. Xenopus nodal related-1 is indispensable only for left-right axis determination. *Int J Dev Biol* 2005;**49**:923–938.
7. Noël ES, Verhoeven M, Lagendijk AK, Tessadori F, Smith K, Choorapoikayil S, Hertog J D, Bakkers J. A Nodal-independent and tissue-intrinsic mechanism controls heart-looping chirality. *Nat Commun* 2013;**4**:2754.
8. Rozario T, DeSimone DW. The extracellular matrix in development and morphogenesis: a dynamic view. *Dev Biol* 2010;**341**:126–140.
9. Barry A. The functional significance of the cardiac jelly in the tubular heart of the chick embryo. *Anat Rec* 1948;**102**:289–298.
10. Chowdhury B, Xiang B, Liu M, Hemming R, Dolinsky VW, Triggs-Raine B. Hyaluronidase 2 deficiency causes increased mesenchymal cells, congenital heart defects, and heart failure. *Circ Cardiovasc Genet* 2017;**10**:e001598.
11. Rambeau P, Faure E, Théron A, Avierinos J-F, Jopling C, Zaffran S, Faucherre A. Reduced aggrecan expression affects cardiac outflow tract development in zebrafish and is associated with bicuspid aortic valve disease in humans. *Int J Cardiol* 2017;**249**:340–343.
12. Strate I, Tessadori F, Bakkers J. Glypican4 promotes cardiac specification and differentiation by attenuating canonical Wnt and Bmp signaling. *Development* 2015;**142**:1767–1776.
13. Mittal A, Pulina M, Hou S-Y, Astrof S. Fibronectin and integrin alpha 5 play essential roles in the development of the cardiac neural crest. *Mech Dev* 2010;**127**:472–484.
14. Tao G, Levay AK, Peacock JD, Huk DJ, Both SN, Purcell NH, Pinto JR, Galantowicz ML, Koch M, Lucchesi PA, Birk DE, Lincoln J. Collagen XIV is important for growth and structural integrity of the myocardium. *J Mol Cell Cardiol* 2012;**53**:626–638.
15. Wirrig EE, Snarr BS, Chintalapudi MR, O'Neal JL, Phelps AL, Barth JL, Fresco VM, Kern CB, Mjaatvedt CH, Toole BP, Hoffman S, Trusk TC, Argraves WS, Wessels A. Cartilage link protein 1 (Crtl1), an extracellular matrix component playing an important role in heart development. *Dev Biol* 2007;**310**:291–303.
16. Trinh LA, Stainier DYR. Fibronectin regulates epithelial organization during myocardial migration in zebrafish. *Dev Cell* 2004;**6**:371–382.
17. Camenisch TD, Spicer AP, Brehm-Gibson T, Biesterfeldt J, Augustine ML, Calabro A, Kubalak S, Klewer SE, McDonald JA. Disruption of hyaluronan synthase-2 abrogates normal cardiac morphogenesis and hyaluronan-mediated transformation of epithelium to mesenchyme. *J Clin Invest* 2000;**106**:349–360.
18. Smith KA, Chocron S, S von der H, E de P, Soufan A, Bussmann J, Schulte-Merker S, Hammerschmidt M, Bakkers J. Rotation and asymmetric development of the zebrafish heart requires directed migration of cardiac progenitor cells. *Dev Cell* 2008;**14**:287–297.
19. Mjaatvedt CH, Yamamura H, Capehart AA, Turner D, Markwald RR. TheCspg2Gene, disrupted in the hdf mutant, is required for right cardiac chamber and endocardial cushion formation. *Dev Biol* 1998;**202**:56–66.
20. Huang C, Tu C, Hsiao C, Hsieh F, Tsai H. Germ-line transmission of a myocardium-specific GFP transgene reveals critical regulatory elements in the cardiac myosin light chain 2 promoter of zebrafish. *Dev Dyn* 2003;**228**:30–40.
21. Reischauer S, Arnaout R, Ramadass R, Stainier DYR. Actin binding GFP allows 4D in vivo imaging of myofilament dynamics in the zebrafish heart and the identification of Erbb2 signaling as a remodeling factor of myofibril architecture. *Circ Res* 2014;**115**:845–856.
22. Savage AM, Kurusamy S, Chen Y, Jiang Z, Chhabria K, MacDonald RB, Kim HR, Wilson HL, van Eeden FJM, Armesilla AL, Chico TJA, Wilkinson RN. tmem33 is essential for VEGF-mediated endothelial calcium oscillations and angiogenesis. *Nat Commun* 2019;**10**:732.
23. Welten MCM, Haan S. D, Boogert N, van den Noordermeer JN, Lamers GEM, Spaink HP, Meijer AH, Verbeek FJ. ZebraFISH: fluorescent in situ hybridization protocol and three-dimensional imaging of gene expression patterns. *Zebrafish* 2006;**3**:465–476.
24. Blum Y, Belting H-G, Ellertsdottir E, Herwig L, Lüders F, Affolter M. Complex cell rearrangements during intersegmental vessel sprouting and vessel fusion in the zebrafish embryo. *Dev Biol* 2008;**316**:312–322.
25. Burkhard SB, Bakkers J. Spatially resolved RNA-sequencing of the embryonic heart identifies a role for Wnt/β-catenin signaling in autonomic control of heart rate. *Elife* 2018;**7**:e31515.
26. Junker JP, Noël ES, Guryev V, Peterson KA, Shah G, Huisken J, McMahon AP, Berezikov E, Bakkers J, Oudenaarden A. V. Genome-wide RNA tomography in the zebrafish embryo. *Cell* 2014;**159**:662–675.
27. Robu ME, Larson JD, Nasevicius A, Beiraghi S, Brenner C, Farber SA, Ekker SC. p53 activation by knockdown technologies. *PLoS Genet* 2007;**3**:e78.
28. Bakkers J, Kramer C, Pothof J, Quaedvlieg NEM, Spaink HP, Hammerschmidt M. Has2 is required upstream of Rac1 to govern dorsal migration of lateral cells during zebrafish gastrulation. *Development* 2004;**131**:525–537.
29. Veerkamp J, Rudolph F, Cseresnyes Z, Priller F, Otten C, Renz M, Schaefer L, Abdelilah-Seyfried S. Unilateral dampening of Bmp activity by nodal generates cardiac left-right asymmetry. *Dev Cell* 2013;**24**:660–667.
30. Kwan KM, Fujimoto E, Grabher C, Mangum BD, Hardy ME, Campbell DS, Parant JM, Yost HJ, Kanki JP, Chien C. The Tol2kit: a multisite gateway-based construction kit for Tol2 transposon transgenesis constructs. *Dev Dyn* 2007;**236**:3088–3099.

31. Angelis JED, Lagendijk AK, Chen H, Tromp A, Bower NI, Tunny KA, Brooks AJ, Bakkers J, Francois M, Yap AS, Simons C, Wicking C, Hogan BM, Smith KA. Tmem2 regulates embryonic vegf signaling by controlling hyaluronic acid turnover. *Dev Cell* 2017;**40**:123–136.
32. Baker K, Holtzman NG, Burdine RD. Direct and indirect roles for Nodal signaling in two axis conversions during asymmetric morphogenesis of the zebrafish heart. *Proc Natl Acad Sci U S A* 2008;**105**:13924–13929.
33. Grassini DR, Lagendijk AK, Angelis JED, Silva JD, Jeanes A, Zettler N, Bower NI, Hogan BM, Smith KA. Nppa and Nppb act redundantly during zebrafish cardiac development to confine AVC marker expression and reduce cardiac jelly volume. *Development* 2018;**145**:dev.160739.
34. Lagendijk AK, Goumans MJ, Burkhard SB, Bakkers J. MicroRNA-23 restricts cardiac valve formation by inhibiting Has2 and extracellular hyaluronic acid production. *Circ Res* 2011;**109**:649–657.
35. Peal DS, Burns CG, Macrae CA, Milan D. Chondroitin sulfate expression is required for cardiac atrioventricular canal formation. *Dev Dyn* 2009;**238**: 3103–3110.
36. Mittal N, Yoon SH, Enomoto H, Hiroshi M, Shimizu A, Kawakami A, Fujita M, Watanabe H, Fukuda K, Makino S. Versican is crucial for the initiation of cardiovascular lumen development in medaka. *Sci Rep* 2019;**9**:9475.
37. Spicer AP, Joo A, Bowling RA. A hyaluronan binding link protein gene family whose members are physically linked adjacent to chrondroitin sulfate proteoglycan core protein genes The Missing Links. *J Biol Chem* 2003;**278**:21083–21091.
38. Guerra A, Germano RFV, Stone O, Arnaout R, Guenther S, Ahuja S, Uribe V, Vanhollebeke B, Stainier DYR, Reischauer S. Distinct myocardial lineages break atrial symmetry during cardiogenesis in zebrafish. *Elife* 2018;**7**:e32833.
39. Yelon D, Horne SA, Stainier DYR. Restricted expression of cardiac myosin genes reveals regulated aspects of heart tube assembly in zebrafish. *Dev Biol* 1999;**214**: 23–37.
40. Nakamura T, Funahashi M, Takagaki K, Munakata H, Tanaka K, Saito Y, Endo M. Effect of 4-methylumbelliferone on cell-free synthesis of hyaluronic acid. *Biochem Mol Biol Int* 1997;**43**:263–268.
41. Ouyang X, Panetta NJ, Talbott MD, Payumo AY, Halluin C, Longaker MT, Chen JK. Hyaluronic acid synthesis is required for zebrafish tail fin regeneration. *PLoS One* 2017;**12**:e0171898.
42. Schottenfeld J, Sullivan-Brown J, Burdine RD. Zebrafish curly up encodes a Pkd2 ortholog that restricts left-side-specific expression of southpaw. *Development* 2007; **134**:1605–1615.
43. Bornhorst D, Xia P, Nakajima H, Dingare C, Herzog W, Lecaudey V, Mochizuki N, Heisenberg C-P, Yelon D, Abdelilah-Seyfried S. Biomechanical signaling within the developing zebrafish heart attunes endocardial growth to myocardial chamber dimensions. *Nat Commun* 2019;**10**:4113.
44. Wan W, Bjorkman KK, Choi ES, Panepento AL, Anseth KS, Leinwand LA. Cardiac myocytes respond differentially and synergistically to matrix stiffness and topography. *bioRxiv* 2019;682930.
45. Bhana B, Iyer RK, Chen WLK, Zhao R, Sider KL, Likhitpanichkul M, Simmons CA, Radisic M. Influence of substrate stiffness on the phenotype of heart cells. *Biotechnol Bioeng* 2010;**105**:1148–1160.
46. Ingber DE. Mechanical signaling and the cellular response to extracellular matrix in angiogenesis and cardiovascular physiology. *Circ Res* 2002;**91**:877–887.
47. Majkut S, Idema T, Swift J, Krieger C, Liu A, Discher DE. Heart-specific stiffening in early embryos parallels matrix and myosin expression to optimize beating. *Curr Biol* 2013;**23**:2434–2439.
48. Müller P, Schier AF. Extracellular movement of signaling molecules. *Dev Cell* 2011;**21**: 145–158.
49. Iozzo RV, Schaefer L. Proteoglycan form and function: a comprehensive nomenclature of proteoglycans. *Matrix Biol* 2015;**42**:11–55.
50. Smith KA, Lagendijk AK, Courtney AD, Chen H, Paterson S, Hogan BM, Wicking C, Bakkers J. Transmembrane protein 2 (Tmem2) is required to regionally restrict atrioventricular canal boundary and endocardial cushion development. *Development* 2011; **138**:4193–4198.
51. Nandadasa S, Foulcer S, Apte SS. The multiple, complex roles of versican and its proteolytic turnover by ADAMTS proteases during embryogenesis. *Matrix Biol* 2014;**35**:34–41.
52. Kern CB, Wessels A, McGarity J, Dixon LJ, Alston E, Argraves WS, Geeting D, Nelson CM, Menick DR, Apte SS. Reduced versican cleavage due to Adamts9 haploinsufficiency is associated with cardiac and aortic anomalies. *Matrix Biol* 2010;**29**: 304–316.
53. Kim KH, Nakaoka Y, Augustin HG, Koh GY. Myocardial angiopoietin-1 controls atrial chamber morphogenesis by spatiotemporal degradation of cardiac jelly. *Cell Rep* 2018;**23**:2455–2466.

Translational Perspective

This study reveals that the cardiac ECM exhibits regional specialization required for heart morphogenesis, and sheds light on how embryonic left–right asymmetry acts in concert with ECM regionalization to fine tune heart shape. This work can help us understand the origins of congenital heart defects, and in particular the nature of morphological heart abnormalities in patients with heterotaxia-associated heart malformations. Furthermore, recent studies suggest the ECM is a key regulator of regenerative potential in the heart, thus defining how distinct ECM composition impacts upon heart form and function has implications for developing regenerative therapies in the future.

CVR-2019-1247R1

Supplementary Material

Asymmetric Hapln1a drives regionalised cardiac ECM expansion and promotes heart morphogenesis in zebrafish development

Christopher J Derrick[*], Juliana Sánchez-Posada[*], Farah Hussein, Federico Tessadori, Eric JG Pollitt, Aaron M Savage, Robert N Wilkinson, Timothy J Chico, Fredericus J van Eeden, Jeroen Bakkers, Emily S Noël[+].

[*] These authors contributed equally to this work

[+] Corresponding author: Email: e.s.noel@sheffield.ac.uk

Supplementary Figures

Figure S1: **Generation of the *Tg(lft2BAC:Gal4FF)* transgenic zebrafish**

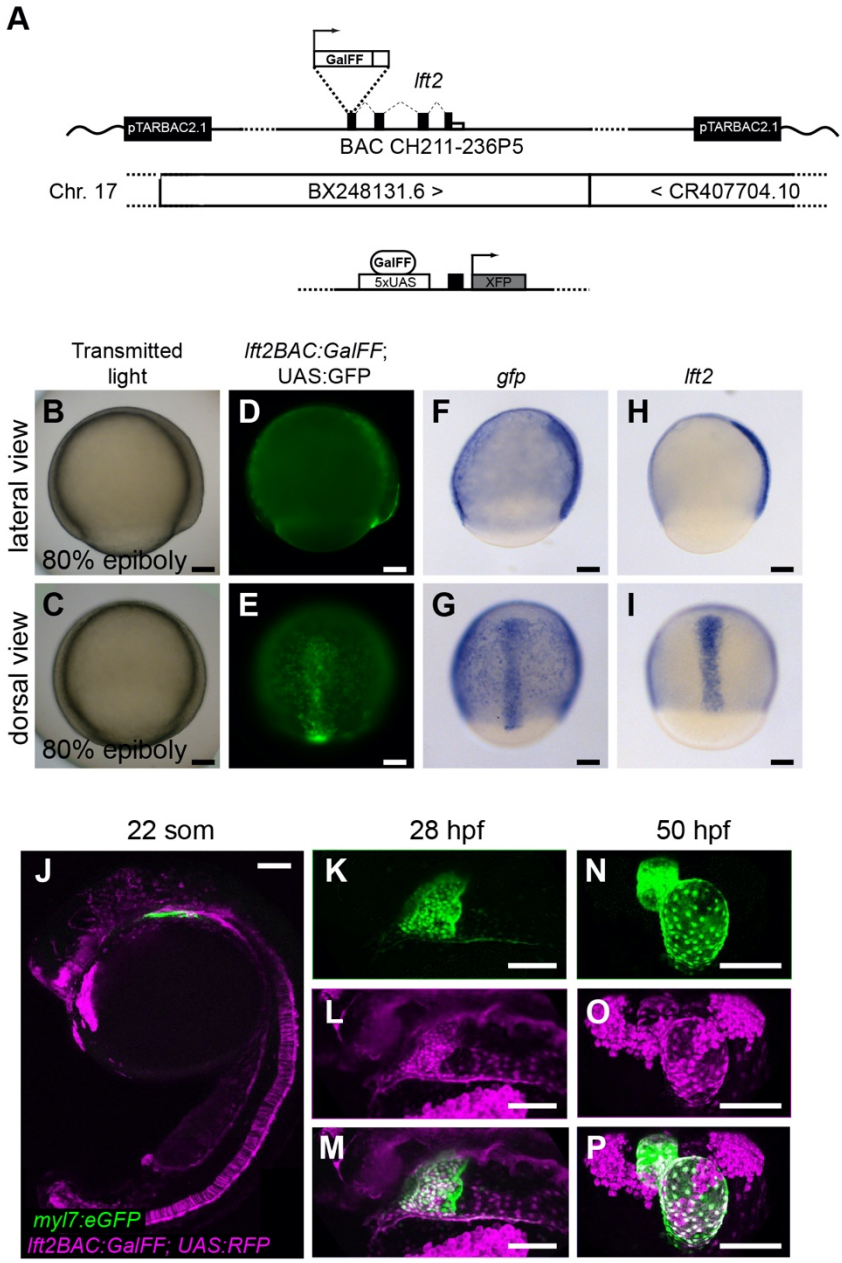

Characterisation of the *Tg(lft2BAC:Gal4FF)* reporter line. (A) An expression cassette containing Gal4FF was recombined into BAC CH211-236P5 at the ATG site of the 1st exon of the *lft2* gene. B-E: Brightfield images (B, C) and corresponding GFP expression domain (D, E) of the *Tg(lft2BAC:Gal4FF)*; *Tg(UAS:GFP)* double transgenic embryos at 80% epiboly. F-G: mRNA *in situ* hybridisation analysis of *gfp* mRNA (F,G). (H-I) mRNA *in situ* hybridisation analysis of *lft2* expression at 80% epiboly. Note the overlap of expression at the forming

midline (compare E, G, I). (J-P) Reporter expression (RFP) in *Tg(lft2BAC:Gal4FF); Tg(UAS:RFP*); *Tg(myl7:eGFP)* triple transgenic embryos at 22 somites (lateral view, J) and in the cardiac region at 28 hpf (lateral view, K-M) and at 50 hpf (frontal view, N-P). Scale bars = 100μm

Figure S2: Cardiac jelly in the atrium is asymmetrically expanded at 50hpf

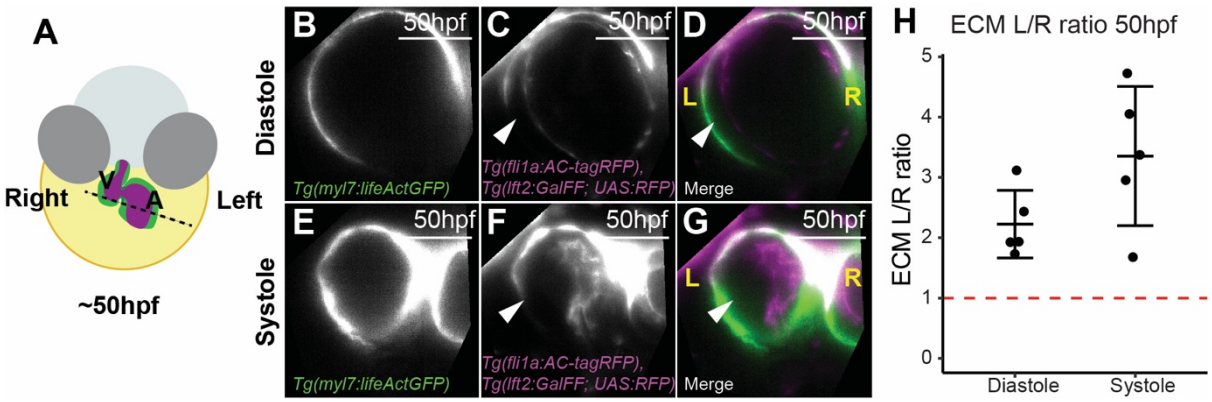

A: Schematic representing the positioning of the heart in a zebrafish embryo at 50hpf (ventral view). Dotted line demarcates the optical transverse sections imaged in panels B-G. B-G: Light-sheet optical cross-sections through the atrium of a 50hpf *Tg(myl7:lifeActGFP); Tg(fli1a:AC-TagRFP); Tg(lft2BAC:Gal4FF); Tg(UAS:RFP*) transgenic embryo during diastole (B-D) and systole (E-G). The myocardium is highlighted in green (B, D, E, G), and the dorsal myocardium and endocardium are highlighted in magenta (C, D, F, G). The extracellular space between the myocardium and endocardium is expanded on the left side of the atrium (white arrowhead). Scale bar = 50µm. H: Quantification of left-right ECM ratio in the atrium at 50hpf, where a value greater than 1 (red dotted line) denotes a left-sided expansion (n=6).

Figure S3: The ECM constituents HA, *versican* and *aggrecan,* and the ECM synthases *has2* and *chsy1* are not asymmetrically expressed in the heart tube

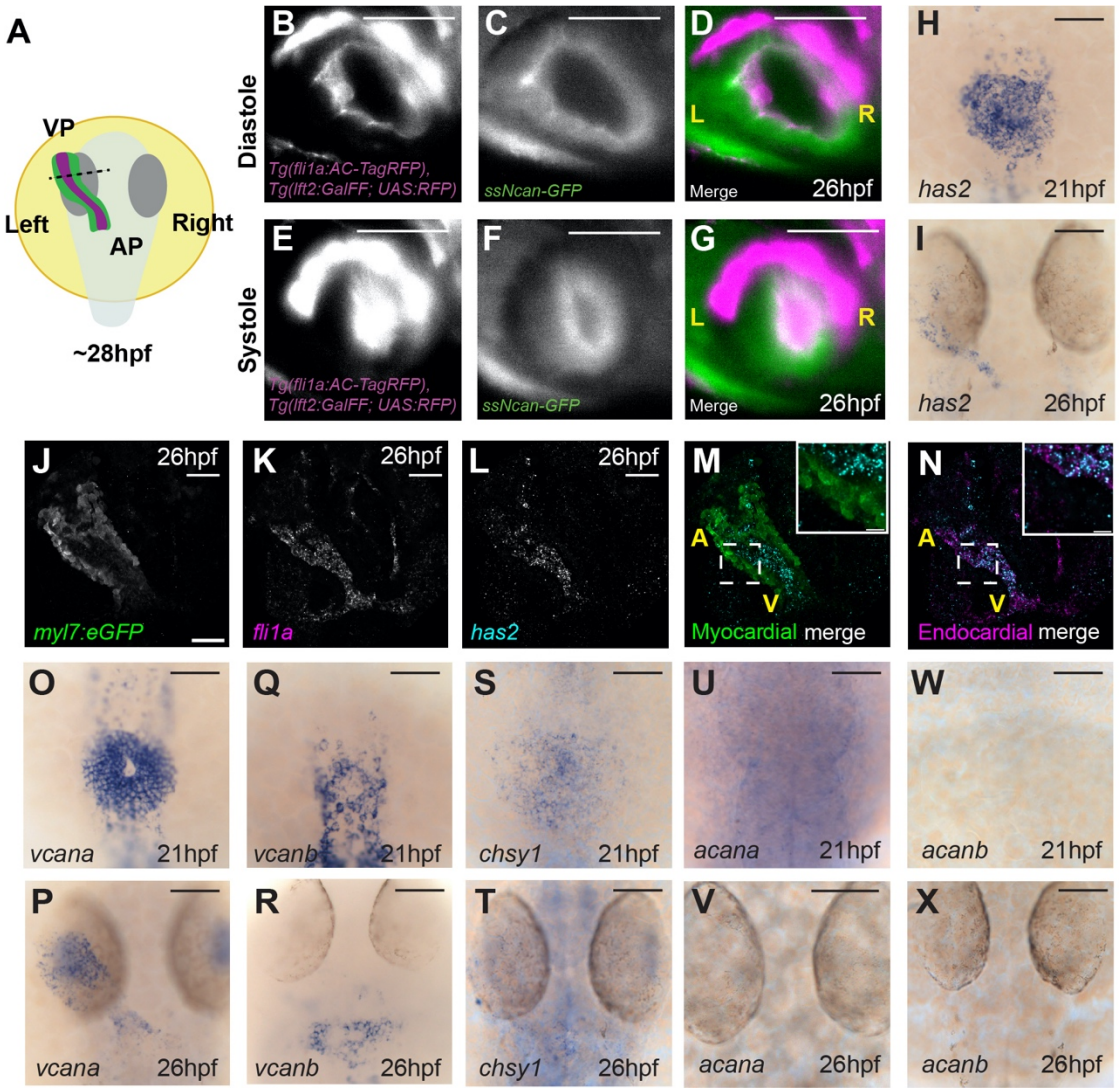

A: Schematic representing the positioning of the heart in a zebrafish embryos at 28hpf (dorsal view), with the dotted line representing the optical transverse sections imaged in panels B-G. B-G: Light-sheet optical cross-sections through the heart tube of a 28hpf *Tg(fli1a:AC-TagRFP); Tg(lft2BAC:Gal4FF); Tg(UAS:RFP)* transgenic embryo injected with *ssNcan-GFP* RNA, imaged during diastole (B-D) and systole (E-G). The *ssNcan-GFP* sensor is highlighted in green (C, D, F, G), and the dorsal myocardium and endocardium are highlighted in magenta (B, D, E, G). The *ssNcan-GFP* binds to HA and is found in the extracellular space between the myocardium and endocardium and does not appear to display asymmetric distribution. L – left,

R – right. Scale bar = 50μm H-I: mRNA *in situ* hybridisation analysis of *has2* reveals it does not display anterior-posterior asymmetry in the heart disc at 21hpf (H) or left-right asymmetry in the tube at 26hpf (I). J-N: Single slice images from two-colour fluorescent mRNA in situ hybridisation analysis of *has2* (L) and *fli1a* (K) expression in *Tg(myl7:GFP)* transgenic embryos (J) at 26hpf confirms that *has2* colocalises with *fli1a* in the endocardium (N). O-X: mRNA *in situ* hybridisation analysis of *vcana* (O, P), *vcanb* (Q, R), *chsy1* (S, T), *acana* (U, V), and *acanb* (W, X) at 21hpf and 26hpf respectively. *vcana* is broadly expressed in the cardiomyocytes of the heart disc at 21hpf, (O) and in the heart tube at 26hpf. (P) Conversely at 21hpf *vcanb* is expressed only in a small ring of cells at the centre of the heart disc (Q), which at 26hpf constitute the outflow tract of the heart tube (R). *chsy1* is expressed at low levels in the heart disc at 21hpf (S), but appears to be absent in the heart tube at 26hpf (T). Neither *aggrecan* paralogs are detected in the heart at these stages (U-X). None of the genes analysed display anterior-posterior asymmetry in the heart disc or left-right asymmetry in the heart tube. H-X: Dorsal views, anterior to top. Scale bar = 50μm

Figure S4: Generation of *hapln1a* mutants and quantification of heart morphology

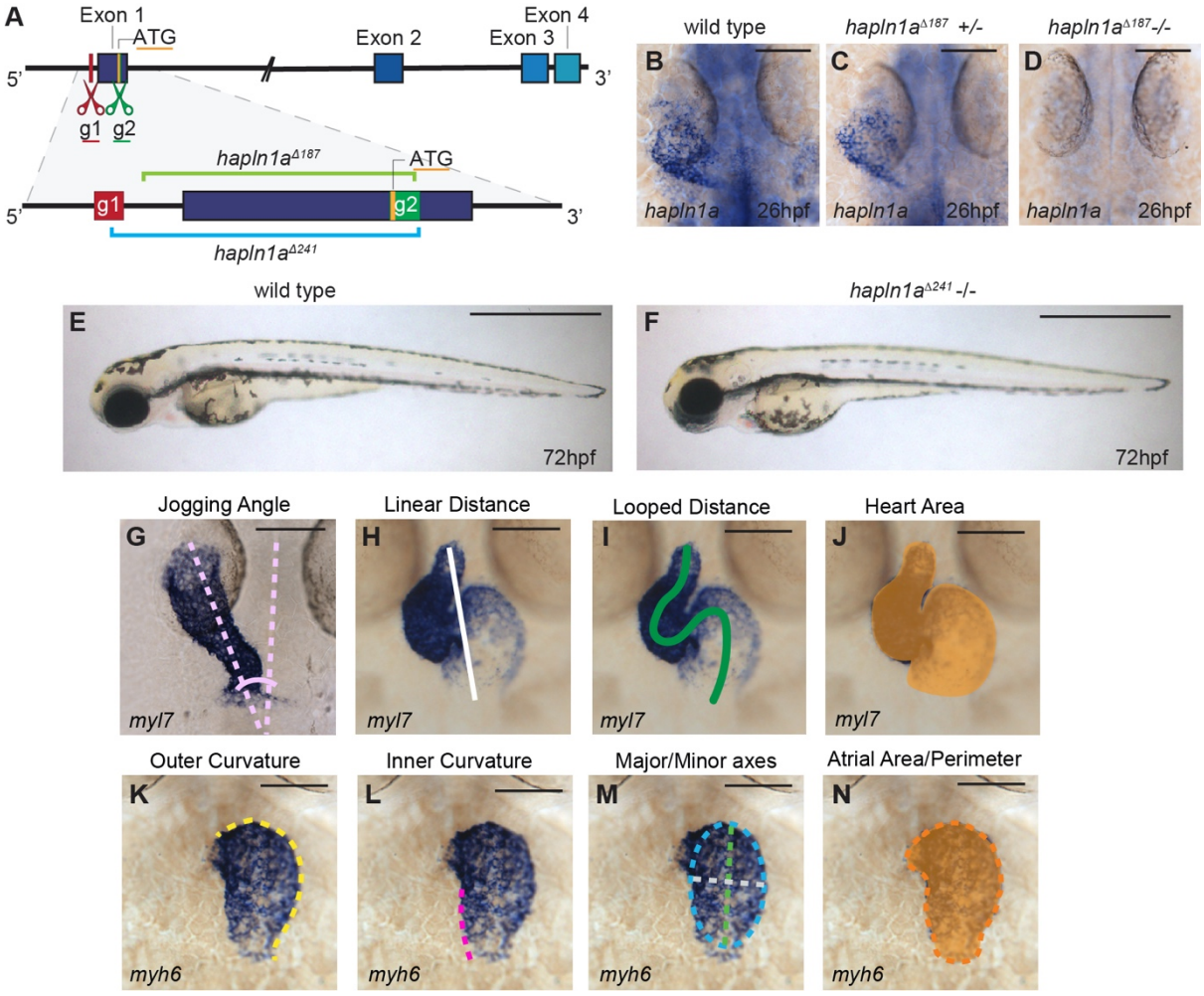

A: Schematic of deletion of putative promoter in *hapln1a* mutants by CRISPR-Cas9 mediated genome editing, based on Ensembl GRCz11 *hapln1a* transcript ID ENSDART00000122966.4. B-D: mRNA *in situ* hybridisation analysis of *hapln1a* expression at 26hpf in embryos from an incross of *hapln1a*$^{\Delta 187}$ heterozygous carriers. Wild type and heterozygous siblings express *hapln1a,* whereas *hapln1a* is absent in homozygous mutants (D). Scale bar = 50µm. E-F: Brightfield images of wild type siblings (E) and *hapln1a*$^{\Delta 241}$ mutants (F) at 72hpf. *hapln1a*$^{\Delta 241}$ mutants do not exhibit any gross morphological defects. Scale bar = 500µm. G-J: Illustration of methods to quantify jogging angle (G, pink angle), linear heart distance (H, length of white line), looped heart distance (I, length of green line) and heart area (J, orange shaded area) from *myl7* mRNA *in situ* hybridisation expression analysis at 26hpf (G) and 50hpf (H-I). Looping

ratio is the quotient of the looped and linear distances. K-N: Illustration of method to quantify atrial outer curvature (K, length of yellow dashed line), atrial inner curvature (L, length of magenta dashed line), atrial major and minor axes (M, fitted elipse - blue dashed line, major axis - length of green dashed line, minor axis - length of white dashed line) and atrial area and perimeter (N, orange shaded area and length of orange dashed line, respectively) from *myh6* mRNA *in situ* hybridisation expression analysis at 50hpf. Scale bar = 50μm.

Figure S5 - *hapln1a* is dispensable for heart jogging, ventricle size and heart function.

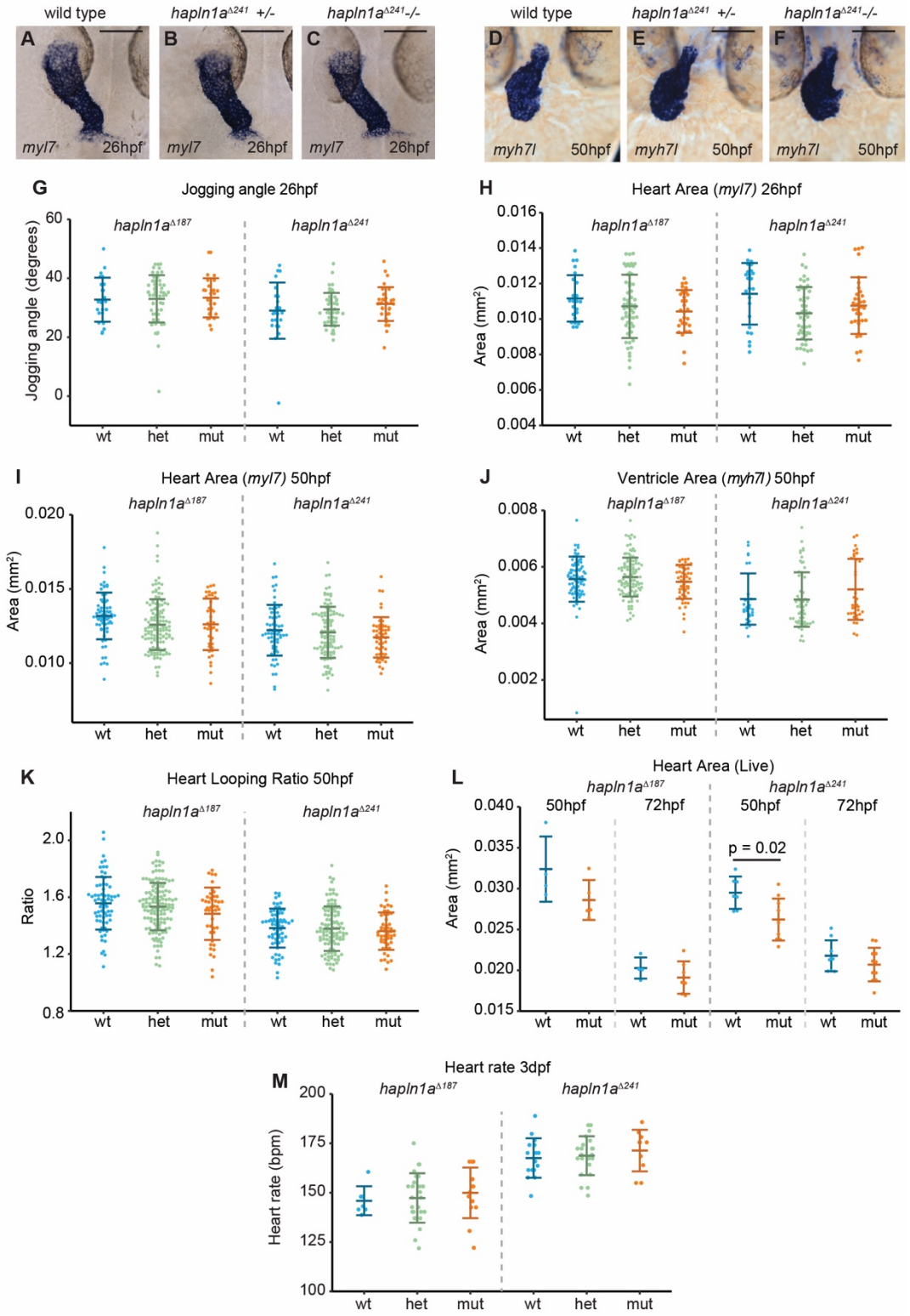

A-C: mRNA *in situ* hybridisation expression analysis at 26hpf of *myl7* in wild-type siblings (A), *hapln1a*$^{\Delta 241}$ heterozygous siblings (B) or *hapln1a*$^{\Delta 241}$ homozygous mutant embryos (C). D-F: mRNA *in situ* hybridisation expression analysis at 50hpf of *myh7l* in wild-type siblings

(D), *hapln1a*$^{\Delta 241}$ heterozygous siblings (E) or *hapln1a*$^{\Delta 241}$ homozygous mutant embryos (F). Scale bar = 50μm. G-H: Quantification of heart jogging angle (J) and heart size (K) from *myl7* expression at 26hpf in sibling and *hapln1a* mutant embryos. n = 23 *hapln1a*$^{\Delta 187}$ wt; 56 *hapln1a*$^{\Delta 187}$ het; 29 *hapln1a*$^{\Delta 187}$ mut, 24 *hapln1a*$^{\Delta 241}$ wt; 50 *hapln1a*$^{\Delta 241}$ het; 34 *hapln1a*$^{\Delta 241}$ mut. I: Quantification of heart size from *myl7* expression at 50hpf in sibling (wt/het) and *hapln1a* mutant embryos (mut). n = 69 *hapln1a*$^{\Delta 187}$ wt; 133 *hapln1a*$^{\Delta 187}$ het; 43 *hapln1a*$^{\Delta 187}$ mut, 65 *hapln1a*$^{\Delta 241}$ wt; 104 *hapln1a*$^{\Delta 241}$ het; 51 *hapln1a*$^{\Delta 241}$ mut. J: Quantification of ventricle size from *myh7l* expression at 50hpf in sibling (wt/het) and *hapln1a* mutant embryos (mut). n = 77 *hapln1a*$^{\Delta 187}$ wt; 113 *hapln1a*$^{\Delta 187}$ het; 43 *hapln1a*$^{\Delta 187}$ mut, 32 *hapln1a*$^{\Delta 241}$ wt; 60 *hapln1a*$^{\Delta 241}$ het; 39 *hapln1a*$^{\Delta 241}$ mut. K: Quantification of looping ratio from *myl7* expression at 50hpf in sibling (wt/het) and *hapln1a* mutant embryos (mut), number of embryos same as in (K). L: Quantification of heart size from live light-sheet images of sibling (wt) and *hapln1a* mutant embryos (mut) at 50hpf and 72hpf. n = 4 *hapln1a*$^{\Delta 187}$ wt; 5 *hapln1a*$^{\Delta 187}$ mut, 7 *hapln1a*$^{\Delta 241}$ wt; 10 *hapln1a*$^{\Delta 241}$ mut. Heart area is significantly reduced in *hapln1a*$^{\Delta 241}$ mutants at 50hpf. M: Quantification of heart rate at 3dpf in sibling (wt/het) and *hapln1a* mutant embryos (mut). n = 7 *hapln1a*$^{\Delta 187}$ wt; 26 *hapln1a*$^{\Delta 187}$ het; 14 *hapln1a*$^{\Delta 187}$ mut, 16 *hapln1a*$^{\Delta 241}$ wt; 22 *hapln1a*$^{\Delta 241}$ het; 10 *hapln1a*$^{\Delta 241}$ mut. Mean ± SD is plotted. Comparative statistics carried out using a Kruskal-Wallis test with multiple comparisons.

Figure S6: *hapln1a* mutants have defects in atrial growth and morphology.

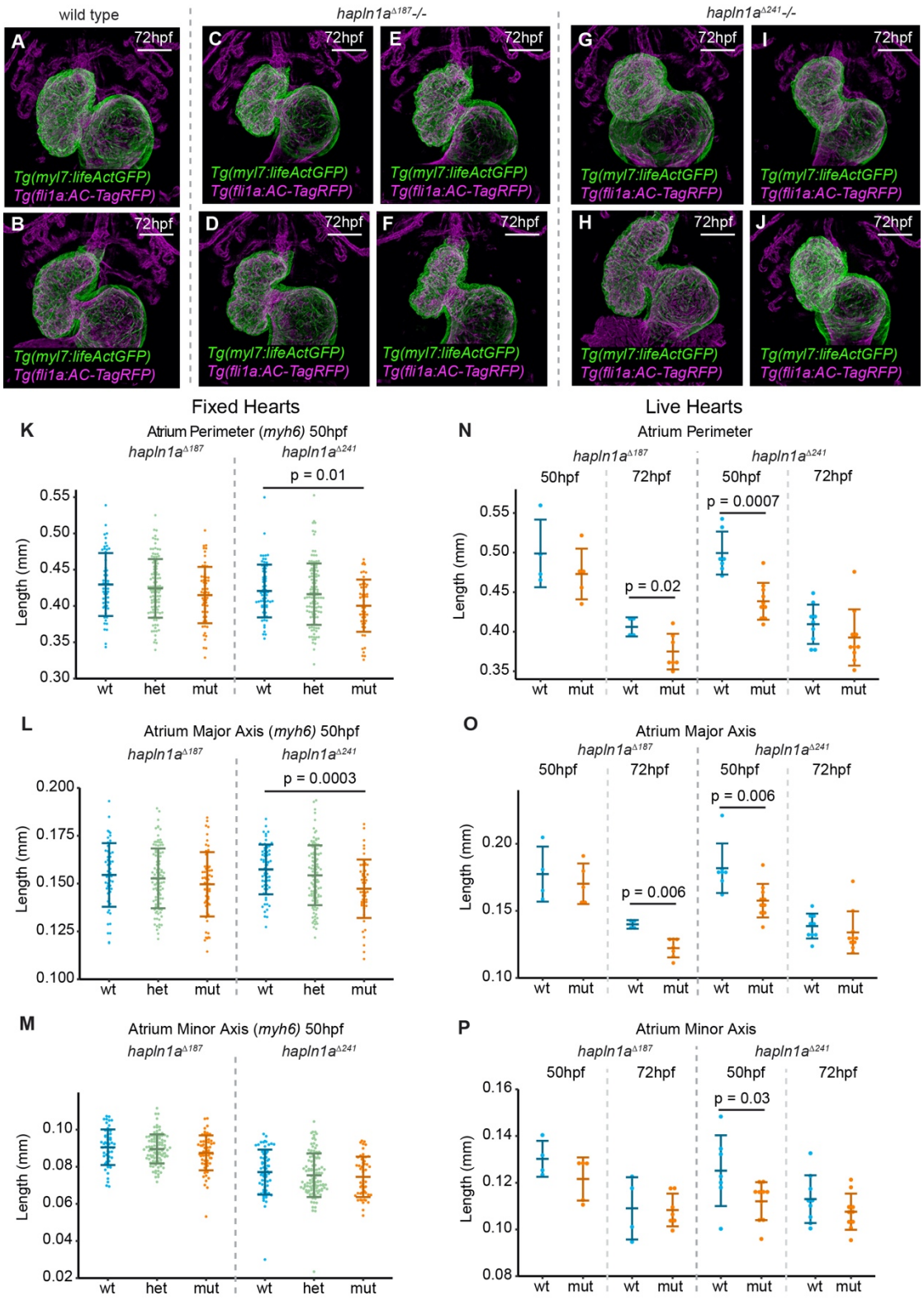

A-J: Maximum intensity projections of light-sheet z-stacks of live 72hpf *Tg(myl7:lifeActGFP); Tg(fli1a:AC-TagRFP)* transgenic wild-type (A, B), *hapln1a*$^{\Delta 187}$ mutant embryos (C-F) and

hapln1a$^{\Delta 241}$ mutant embryos (G-J). Scale bar = 50μm. K-M: Quantification of atrial perimeter (K) atrial major axis (L) and atrial minor axis (M) in *myh6*-stained ISH-processed sibling embryos (wt/het) and *hapln1a*$^{\Delta 187}$ or *hapln1a*$^{\Delta 241}$ mutants (mut) at 50hpf. Atrial perimeter and major axis is significantly reduced in *hapln1a*$^{\Delta 241}$ mutants compared to wild type siblings. In K-M n = 54 *hapln1a*$^{\Delta 187}$ wt; 104 *hapln1a*$^{\Delta 187}$ het; 60 *hapln1a*$^{\Delta 187}$ mut, 66 *hapln1a*$^{\Delta 241}$ wt; 116 *hapln1a*$^{\Delta 241}$ het; 53 *hapln1a*$^{\Delta 241}$ mut. N-P: Quantification of atrial perimeter (N) atrial major axis (O), and atrial minor axis (P) in live light-sheet z-projections from sibling embryos (wt/het) and *hapln1a*$^{\Delta 187}$ or *hapln1a*$^{\Delta 241}$ mutants (mut) at 50hpf and 72hpf. Atrial perimeter, major axis and minor axis are significantly reduced in *hapln1a*$^{\Delta 241}$ mutants compared to wild type siblings at 50hpf, and atrial perimeter and major axis are significantly reduced in *hapln1a*$^{\Delta 187}$ mutants at 72hpf. In N-P n = 4 *hapln1a*$^{\Delta 187}$ 50hpf wt; 5 *hapln1a*$^{\Delta 187}$ 50hpf mut, 7 *hapln1a*$^{\Delta 241}$ 50hpf wt; 10 *hapln1a*$^{\Delta 241}$ 50hpf mut; 4 *hapln1a*$^{\Delta 187}$ 72hpf wt; 7 *hapln1a*$^{\Delta 187}$ 72hpf mut, 9 *hapln1a*$^{\Delta 241}$ 72hpf wt; 10 *hapln1a*$^{\Delta 241}$ 72hpf mut. Comparative statistics carried out using a Kruskal-Wallis test with multiple comparisons.

Figure S7: *hapln1a* morpholino is a loss-of-function model.

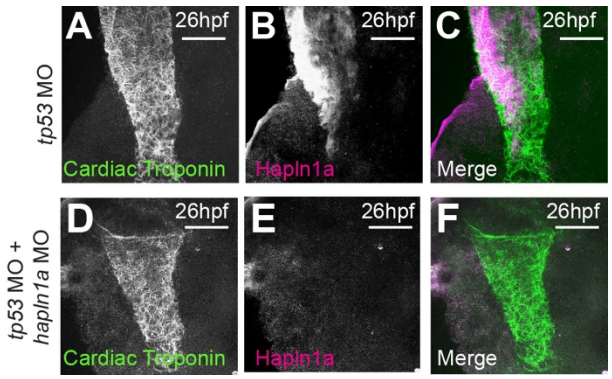

A-F: Immunohistochemistry analysis of Hapln1a (magenta) in embryos injected with either *tp53* MO (A-C) or *hapln1a* MO + *tp53* MO (D-F). Cardiac Troponin (green) outlines the heart. Hapln1a is present in *tp53* MO-injected embryos (n=5) but is absent in embryos injected with *hapln1a* MO + *tp53* MO (n=6). Scale bar = 50μm.

Figure S8: Regionalised ECM thickness is disrupted in *hapln1a* mutants

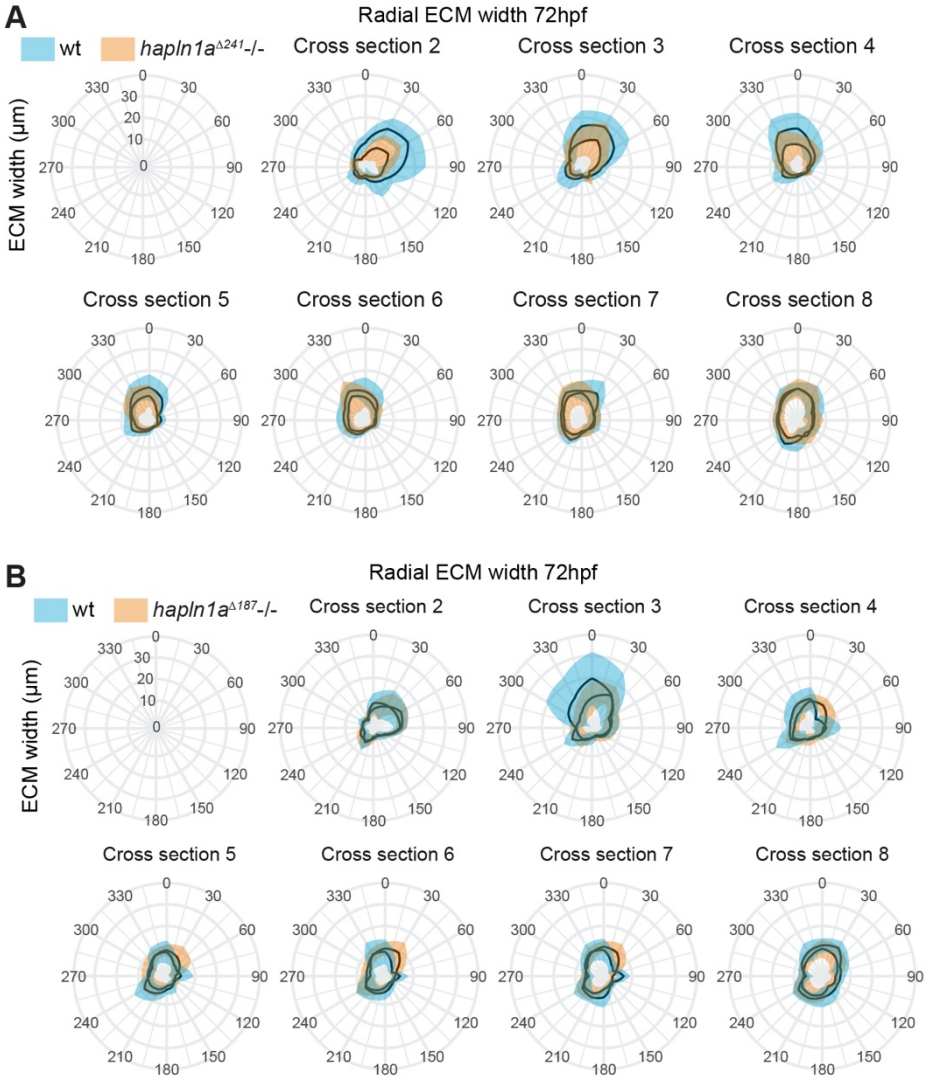

A-B: Quantification of ECM width of atrial cross sections at defined positions along the longitudinal axis of the atrium from AVC (cross-section 2) towards venous pole (cross-section 8) at 72hpf in *hapln1a*$^{\Delta 241}$ mutants (A) or *hapln1a*$^{\Delta 187}$ mutants (B). Wild type - blue, *hapln1a* mutant - orange. Mean ± SD are plotted. n ≥ 4 at each location.

Figure S9: HA is required at early stages of heart development for cardiac morphogenesis and interacts with Hapln1a

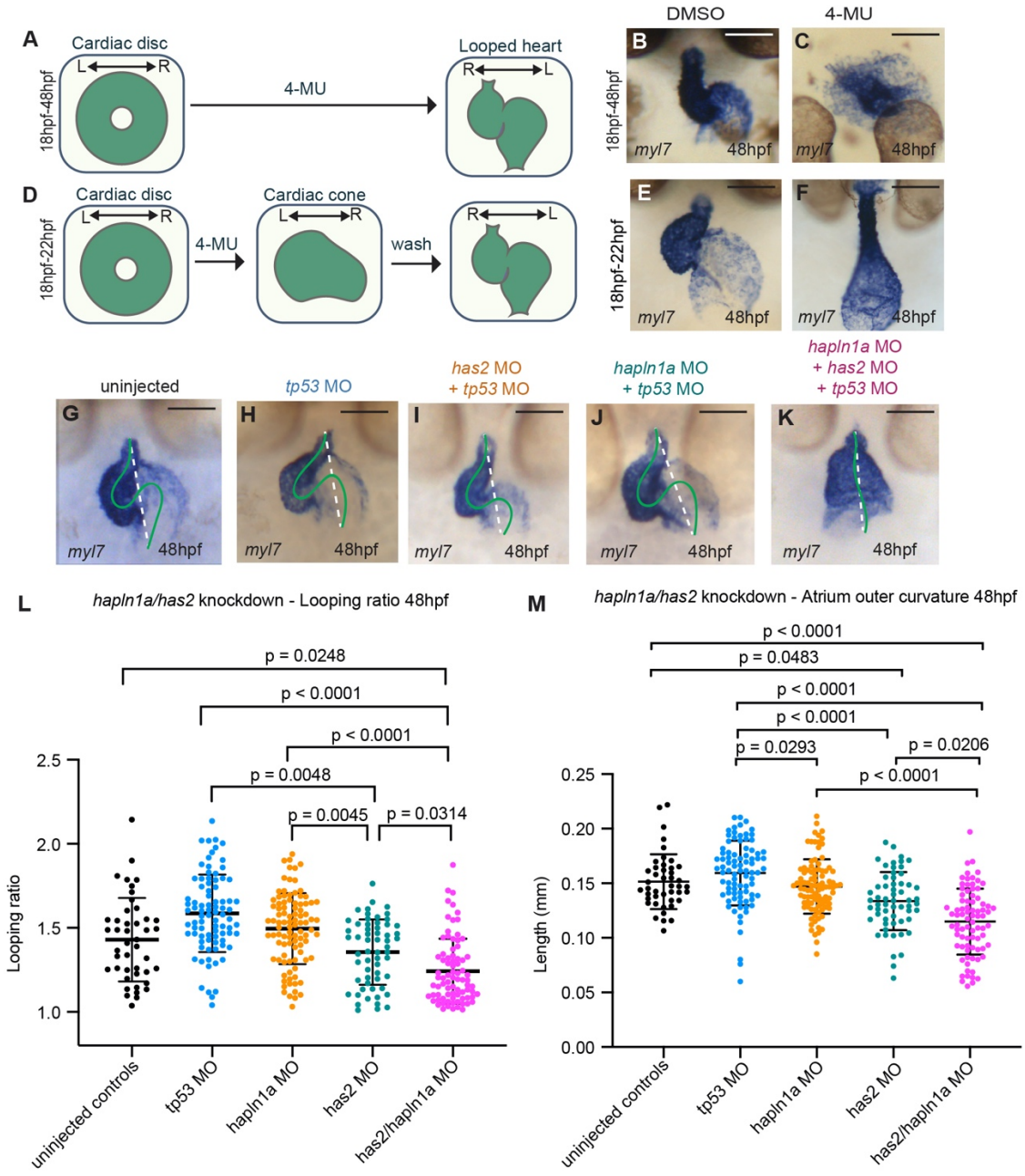

A, D: Schematic depicting timing of 4-MU treatments. B-C, E-F: *in situ* hybridisation analysis of *myl7* expression at 48hpf in embryos treated either with DMSO (B, E) or 4-MU (C, F). Embryos treated with 4-MU from 18hpf to 48hpf exhibit severe defects in heart development, characterised by a failure to correctly form the heart tube (C). In comparison, embryos treated with 4-MU in a shorter time window from 18hpf to 22hpf exhibit milder defects in heart

morphogenesis, characterised by a specific failure in heart looping morphogenesis (F). G-K: mRNA *in situ* hybridisation analysis at 48hpf of *myl7* expression in embryos injected with *tp53* MO (H), sub-phenotypic doses of either *has2* MO + *tp53* MO (I) or *hapln1a* MO + *tp53* MO (J), or a co-injection of sub-phenotypic doses of both *has2* and *hapln1a* MOs together with *tp53* MO (K). Embryos injected with sub-phenotypic doses of either *has2* MO + *tp53* MO or *hapln1a* MO + *tp53* MO do not exhibit heart defects, whereas embryos co-injected with both morpholinos together with *tp53* MO display unlooped hearts with dilated atria (K). Scale bar = 100μm. White dashed line = linear heart length, green line = looped heart length. L-M: Quantification of heart looping ratio (L) and atrial outer curvature (M) at 48hpf in embryos injected with *tp53* MO, sub-phenotypic doses of single *has2* or *hapln1a* MO, or co-injection of *has2* and *hapln1a* MOs. Embryos co-injected with *has2* and *hapln1a* MOs exhibit significantly reduced heart looping and atrial ballooning compared with single injected or uninjected controls. In L and M n = 44 uninjected controls; 85 *tp53* MO; 59 *tp53* + *hapln1a* MO; 95 *tp53* + *has2* MO; 81 *tp53* + *hapln1a* + *has2* MO. Median ± interquartile range are plotted, comparative statistics performed using Kruskal Wallis with multiple comparisons.

Movie S1: The cardiac ECM is asymmetric in the zebrafish heart tube

Live light-sheet optical cross-sections through the beating heart tube of a 26hpf *Tg(myl7:lifeActGFP); Tg(fli1a:AC-TagRFP); Tg(lft2BAC:Gal4FF); Tg(UAS:RFP)* at the level of the future atrium. The myocardium is marked in green and the dorsal myocardium and endocardium are marked in magenta. Movie speed is not in real-time.

Table S1: Number of embryos analysed for *hapln1a* morphant, *hapln1a* mutant and *pkd2* mutant experiments

Genotype	Stage/gene	Wild type	Heterozygous	Homozygous mutants
hapln1a$^{\Delta 187}$ mutants	26hpf/*myl7*	23	56	29
	50hpf/*myl7*	69	133	43
	50hpf/*myh7l*	77	113	54
	50hpf/*myh6*	54	104	60
	50hpf live	4	-	5
	72hpf live	4	-	7
hapln1a$^{\Delta 241}$ mutants	26hpf/*myl7*	24	50	34
	50hpf/*myl7*	65	104	51
	50hpf/*myh7l*	32	60	39
	50hpf/*myh6*	66	116	53
	50hpf live	7	-	10
	72hpf live	9	-	10
pkd2^{hu2173} mutants	19hpf/*hapln1a*		72	13
	26hpf/*hapln1a*		138	40
spaw mutants	19hpf/*hapln1a*		69	19

Experiment	Stage/ gene	Uninj.	*tp53* MO	*tp53* MO + *hapln1a* MO	*tp53* MO + *has2* MO	*tp53* MO + *hapln1a MO* +*has2* MO
hapln1a/	50hpf/	44	85	59	95	81

has2 MO	*myl7*				
Experiment	Stage/ gene	DMSO 18hpf – 48hpf	4MU 18hpf – 48hpf	DMSO 18hpf – 22hpf	4MU 18hpf – 22hpf
HA inhibition	48hpf/ *myl7*	38	36	36	44

Table S2: Raw Tomo-seq transcriptional analysis of Heart #1 at 26hpf

Heart 1 sectioned from venous pole to arterial pole, table includes Ensembl gene identifiers, raw read numbers per section, and ERCC spike in read numbers

Table S3: Spike-in normalised transcriptional analysis of Heart #1 at 26hpf

Heart 1 sectioned from venous pole to arterial pole, read numbers per section normalised to spike-in RNA, and including gene names.

Table S4: Raw Tomo-seq transcriptional analysis of Heart #2 at 26hpf

Heart 1 sectioned from arterial pole to venous pole, table includes Ensembl gene identifiers, raw read numbers per section, and ERCC spike in read numbers

Table S5: Spike-in normalised transcriptional analysis of Heart #2 at 26hpf

Heart 2 sectioned from venous pole to arterial pole, read numbers per section normalised to spike-in RNA, and including gene names.

Supplementary Methods

Generation of the Tg(lft2BAC:Gal4FF) transgenic line

The *Tg(lft2BAC:Gal4FF)* line was generated by recombineering of bacterial artificial chromosome (BAC) CH211-236P5 as previously described[1,2]. A Gal4FF_kan cassette was inserted at the ATG start codon of the first exon of the *lft2* gene. Amplification from a pCS2+Gal4FF_kanR plasmid was achieved with primers :

F_LFT2_GAL4FF

5'-

cctcagagcttcagtcagtcattcattctttcactggcatcgttagatcaACCATGAAGCTACTGTCTTCTATCGAAC-3'

R_LFT2_NEO

5'-

tgtgtgagtgagatcgctgtggtcaaaatgaacagctggatgaacagagcTCAGAAGAACTCGTCAAGAAGGCG-3'

Sequences homologous to the genomic locus in lower case. Recombineering was essentially carried out following the manufacturer's protocol (Red/ET recombination; Gene Bridges GmbH). BAC DNA isolation was carried out using a Midiprep kit (Life Technologies BV). BAC DNA was injected at a concentration of 300 ng/µl in the presence of 0.75U PI-SceI meganuclease (New England Biolabs) in 1-cell stage *Tg(UAS:GFP)* or *Tg(UAS:RFP)* embryos (both UAS lines[3]). At 1dpf, healthy embryos displaying robust *lft2*-specific fluorescence were selected and grown to adulthood. Founder fish (F0) were identified by outcrossing and the progeny (F1) was grown to establish the transgenic line.

Generation of *pkd2*^{hu2173} allele

The *pkd2*^{hu2173} allele was generated using ENU mutagenesis and consists of an A->T transversion at base position 1327 which results in a premature stop codon at amino acid 302 of 904. The truncation occurs in the first extracellular loop, before the channel pore, and is

predicted to be a null. The *pkd2*^{hu273} allele can be identified by PCR amplification with the following primers: forward primer 5'- GATTTATTGCTCTGTTTGTTTGTAAGGA-3' and reverse primer 5' -GAAGTCCAAGAACACCGCTC-3', followed by XmnI restriction of the PCR product. The primers contain a mismatch which together with the *pkd2*^{hu2173} mutation introduces an XmnI recognition site into the mutant strand.

in situ hybridisation mRNA probes

The following primers were used to amplify a region of the CDS from the gene of interest:

Gene	Forward Primer	Reverse Primer	Size (bp)
hapln1a	5' – TGGCATTGATGGTGTTTGCA - 3'	5' – ACAGTTCCGTCACTAAGCCA - 3'	860
has2	5' – GTTCACGCAGACCTCATCAC – 3'	5' – CATCCAATACCTCACGCTGC – 3'	1050
acana	5'- CGGATCAAGTGGAGTCTGGT -3'	5'- GAAGGGAGGACGTGGGAAAT -3'	1067
acanb	5'- ATCAAGACAGCACCCTCAGT -3'	5'- TTTCTGGAAATGGCGTGGTC -3'	1035
chsy1	5'- CACCATTCAGCTCCATCGTG-3'	5'- TCGGCTTTGGGGTACTTCAT-3'	801

All probe sequences were ligated into the PCR2-TOPO vector (Invitrogen). *myl7*, *fli1a*, *vcana* and *vcanb* mRNA probes have been previously described[4–6].

Pharmacological treatments

To block HA synthesis, 4-Methylumbelliferone (4-MU, Sigma-Aldrich) was dissolved in DMSO to a stock concentration of 100mM, and subsequently diluted to a working concentration of 1mM in E3 medium. Embryos were dechorionated and incubated in 4-MU or an equal concentration of DMSO (1%). For timed treatments, at the end of the treatment window embryos were washed 3 x 5 mins in E3 to remove the 4MU, before being placed in fresh E3 until fixation.

Heart rate analysis

Embryos were transferred individually from a 28.5°C incubator and positioned laterally on an agarose mold (2% agarose in E3 medium) for imaging. Once the heart was in focus under the stereoscope (using 5x magnification), image sequences of 5000ms in duration were acquired at 120 frames per second, using a High Speed Camera (Chameleon3 USB3, FLIR Integrated Imaging Solutions Inc) together with SpinView software (Spinnaker v. 2.0.0.147). Image sequences were imported to Fiji[7] and heart rate obtained through a custom-written macro incorporating the MultiKymograph plugin to obtain a time-space plot that captured the motion of the heart, and Plot Profile plugin to measure the time between heart beats. Individual points plotted in graphs show average heart rate for each embryo over the 5000ms imaging window.

Image quantification

Light-sheet images of heart morphology: Image stacks were initially processed using Vision4D (Arivis AG, Germany) and Fiji. Processing steps included noise removal, background correction, and subsequent application of individual morphological filters to each channel to sharpen the edges of the myocardial and endocardial tissue layers. Maximum intensity z-projections of the composite channels were used to visualise cardiac morphology.

Analysis of ECM width in *ssNcan-GFP* mRNA injected embryos: Images were acquired on an Airyscan microscope with a z-resolution of 1µm step size. Images were Airyscan processed using Zen Black software (Zeiss), and the resulting image stacks were optically resliced using Fiji. ECM width was manually measured in Fiji. ECM measurements were aligned between samples at the venous pole of the heart for plotting.

Analysis of radial ECM width in live embryos: Maximum intensity projections of 50hpf and 72hpf light-sheet images of live *Tg(myl7:lifeActGFP); Tg(fli1a:AC-TagRFP)* transgenic hearts were used to draw the outer and inner curvatures of the atrium. Using a custom-written ImageJ

macro these two splines were then divided into segments of equal length by 12 equidistant points. Corresponding points from each of the two curvature splines were subsequently connected to define the cross-section positions starting from the AVC towards the venous pole (Figure 4E). Cross-section slices at the inflow tract and atrioventricular canal where the atrial signal is not complete were removed from the analysis. All cross sections were blinded, and a radial grid with 30° gridlines placed on each image, manually centred at the middle of the chamber lumen, where 0° represents the dorsal face and 180° the ventral face of the heart. The width of the ECM was manually measured at each position on the radial grid where both myocardial and endocardial layers were visible. Where myocardium and endocardium were touching, ECM width was set to 1px (0.2μm). To visualise radial ECM spread, the average ECM width and deviation at each radial position was calculated for each slice.

Looping morphology: Looping ratio was calculated from images of *myl7* expression detected by ISH. All samples from one experimental set were blinded using the ImageJ Blind_Analysis plugin (https://github.com/quantixed/imagej-macros/blob/master/Blind_Analysis.ijm). The linear distance from arterial to venous poles of the heart was measured as a straight-line distance, and looped distance was drawn from the same positions at each pole through the centre of each chamber, down the centreline of the looped heart. Looping ratio was determined by dividing looped distance by the linear distance. Statistical testing of average looping ratio between experimental conditions was carried out using Kruskal-Wallis with Dunn's multiple comparisons.

Heart jogging: The angle of heart jogging was calculated from images of *myl7* expression detected by ISH. A line was drawn down the midline of the embryo, and a second line drawn through the midline of the heart tube, using the centre of the inflow and outflow tracts to standardise line positioning. The angle of intersection between these two lines defines heart jogging angle.

Heart and chamber parameters: whole-heart, ventricle or atrium parameters at 26hpf and 50hpf were quantified from *in situ* hybridisations by manually drawing round either *myl7*, *myh7l* or *myh6* staining area in Fiji. Heart and atrial parameters in live embryos at 50hpf and 72hpf were quantified from maximum intensity projections of z-stacks obtained on the light-sheet by manually drawing round the heart or atrium using the *Tg(myl7:lifeActGFP)* channel. Atrial curvatures were quantified by manually drawing along the atrium from the AVC to the inflow tract of the heart. Atrial major and minor axes quantifications were derived from an ellipse fit to the outline of the atrium. In embryos where heart looping morphology is profoundly affected, the atrioventricular boundary is defined using a combination of mild changes in tissue morphology (from concave to convex indicating transition from an area of tissue restriction (canal) to expansion (chamber)) together with intensity of *myl7 in situ* hybridisation staining, which is more intense in ventricular tissue when compared to atrial tissue.

Statistical testing of heart or chamber parameters between genotypes was carried out using Kruskal-Wallis with Dunn's multiple comparisons.

For examples of the quantifications of cardiac and chamber parameters described above, please refer to Figure S4.

hapln1a overexpression: Quantification of *hapln1a* overexpression was performed by imaging overexpression embryos where *myl7* expression was detected using INT/BCIP and *hapln1a* expression detected using NBT/BCIP. All embryos were imaged using the same microscope settings, and individual images combined into a composite of all experiments. Using the composite, channels were split in Fiji, resulting in the blue and green channels carrying the *myl7* stain, and the red channel carrying the *hapln1a* stain. Background was subtracted in the red channel. The *myl7* staining was used to calculate looping ratio for each heart. In addition, each *myl7* signal was used to manually trace the whole heart, atrium, AVC and ventricle for each heart, which was saved as a region of interest (ROI) and the area of each chamber was

measured in pixels. Next, the *hapln1a* image was thresholded to generate a binary image. The whole-heart, or chamber-specific ROI was applied to the thresholded *hapln1a* channel, and the number of positive pixels in each ROI recorded. Number of positive pixels as a percentage (%) of the total number of pixels comprising the heart or the specific chamber was calculated and plotted against looping ratio for each heart. Spearmann's correlation coefficient (r) was calculated in GraphPad Prism, with 95% confidence intervals.

Data was visualised using the ggplot2 package in R, or using GraphPad Prism.

References

1. Bussmann J, Schulte-Merker S. Rapid BAC selection for tol2-mediated transgenesis in zebrafish. *Development* 2011;**138**:4327–4332.

2. Tessadori F, Weerd JH van, Burkhard SB, Verkerk AO, Pater E de, Boukens BJ, Vink A, Christoffels VM, Bakkers J. Identification and Functional Characterization of Cardiac Pacemaker Cells in Zebrafish. *PLoS One* 2012;**7**:e47644.

3. Asakawa K, Kawakami K. Targeted gene expression by the Gal4-UAS system in zebrafish. *Dev Growth Differ* 2008;**50**:391–399.

4. Yelon D, Horne SA, Stainier DYR. Restricted Expression of Cardiac Myosin Genes Reveals Regulated Aspects of Heart Tube Assembly in Zebrafish. *Dev Biol* 1999;**214**:23–37.

5. Kang JS, Oohashi T, Kawakami Y, Bekku Y, Belmonte JCI, Ninomiya Y. Characterization of dermacan, a novel zebrafish lectican gene, expressed in dermal bones. *Mech Dev* 2004;**121**:301–312.

6. Brown LA, Rodaway AR, Schilling TF, Jowett T, Ingham PW, Patient RK, Sharrocks AD. Insights into early vasculogenesis revealed by expression of the ETS-domain transcription factor Fli-1 in wild-type and mutant zebrafish embryos. *Mech Dev* 2000;**90**:237–252.

7. Schindelin J, Arganda-Carreras I, Frise E, Kaynig V, Longair M, Pietzsch T, Preibisch S, Rueden C, Saalfeld S, Schmid B, Tinevez J-Y, White DJ, Hartenstein V, Eliceiri K, Tomancak P, Cardona A. Fiji: an open-source platform for biological-image analysis. *Nat Methods* 2012;**9**:676–682.